STRATEGIC CONSTRUCTION OF DIVERSE METAL ORGANIC COORDINATION NETWORKS AND THEIR APPLICATIONS IN GUEST ENCAPSULATION, ION EXCHANGE, CATALYSIS AND SENSING

Sandeep Kumar

A thesis submitted for the partial fulfillment of

the degree of Doctor of Philosophy

Department of Chemical Sciences

Indian Institute of Science Education and Research Mohali

Knowledge city, Sector 81, SAS Nagar, Manauli PO, Mohali 140306, Punjab, India.

October 2018

Dedicated
To My Family (specially Parents)
and Friends

Declaration

The work presented in this thesis has been carried out by me under the guidance of Prof. Sanjay K. Mandal at the Indian Institute of Science Education and Research Mohali. This work has not been submitted in part or in full for a degree, a diploma, or a fellowship to any other university or institute. Whenever contributions of others are involved, every effort is made to indicate this clearly, with due acknowledgment of collaborative research and discussions. This thesis is a bona fide record of original work done by me and all sources listed within have been detailed in the bibliography.

Sandeep Kumar

In my capacity as the supervisor of the candidate's thesis work, I certify that the above statements by the candidate are true to the best of my knowledge.

Prof. Sanjay K. Mandal

Acknowledgments

It is my pleasure to express my sincere appreciation to each and every one, who have contributed in their own way for the completion of this fruitful and unforgettable journey.

First and foremost, I would like to express my deepest appreciation to Professor Sanjay K. Mandal, my supervisor, for his excellent guidance, incredible support and valuable suggestions to carry out this research work. I will always be thankful for his wisdom, knowledge, and deep concern. I owe special honor to him for introducing me to many fascinating interdisciplinary projects. His critical and logical thinking, never say impossible attitude and disciplined behavior has helped me in growing as a better person both professionally and personally. The joy and enthusiasm he has for his research was a source of constant motivation for me, even during the tough times during this work.

I wish to express my gratitude to the members of my doctoral committee, Dr. Ramesh Ramachandran and Dr. K. R. Shmasunder for their valuable suggestions.

I gratefully acknowledge Dr. Sadhika Khullar (for building the initial base of research for me). With her, I started my research work and learned how to do systematic work, analyze data, handling of instruments and so many things. I would like to acknowledge Dr. Navnita Kumar (for valuable discussion) for her understanding and encouragement which has helped me a lot. I am also thankful to all my lab members Biswajit Laha (for teaching some instruments and CHN analysis), Vijay Gupta, Datta Markad, Gouri Chakraborty, Prasenjit Das, Shradha Gandhi, Smriti Thakur, Alisha Gogia and Sheeba Khan for creating a fun-filled and affectionate environment in the lab which made research so much enjoyable.

I would never forget the beautiful moments shared with the project students: Gaurav Verma, Karan, Nitish, Sandhya, and Manpreet and summer students (Sujeeth, Priyakshi, Kaushik, Gaurav, Neeraj, Sunny Das, Shibna, Justin, Jigyasa, Shubashini, Annapurna, Shelly, Razia, Jagdeep, Monika, Zinnia).

I would like to thank my all my best friends Dr. Vinod Khatri, Dr. Naveen Malik, Dr. Kuldeep Jaishwal, Sunil Chahal, Dr. Ramarao Parela, Dr. Nayyer, Dr. Manjeet Saini, Pankaj Bhatiya, Dr. Badri Parsad, Deepak, Ravinder, Sonu, Bhagat, Narender, Neeraj Rana and Mayank, who were with me in my good and bad times. Along with these, I would like to thank all my batch mates (Dr. Monika, Biswajit Laha, Abhijeet, Hema, Dr. Kanupriya, Dr. Dibyendu, Dr. Ginny) for their help in initial times. I would like to especially thank Vijay Gupta, Datta Markad, Sheeba Khan and Alisha Gogia for sharing all good and bad times with me during this journey.

Without the help and support of my family members maybe I could not achieve this. Thus, I would like to heartily acknowledge especially my parents, brothers (Naveen, Pardeep, and Sunder) and sisters (Manju, Meena, Usha, and Jyoti). I would like to acknowledge my loveable wife (Sonia) for her patience, support, and unconditional love and to build my confidence to do this work. I would like to acknowledge Sh. Suresh Kashyap (mosa), Munesh, Sultan, Dinesh, Yashpal, Sonu and Rishi for their support. I would also like to acknowledge my relatives who helped me directly or indirectly. I would like to acknowledge my hostel friends Yuvraj, Sajal, Vishal, PBD, Harsit Jain, Yash Rana, Ankit yadav and Ivan for creating funny environment in hostel.

I would like to take this opportunity to thank all my teachers who have influenced my life in some way or the other.

I am indebted to MHRD, India, for providing me with a fellowship and IISER Mohali for the state-of-art infrastructure for my research.

I also wish to thank Mr. Bahadur, Mr. Mangat, Mr. Satinder, Mr. Prahlad, and Mr. Ganesh, lab assistants of chemistry teaching lab for their help.

Last but not the least, I thank the Almighty for giving me the courage and dedication to accomplish this journey.

List of Figures

Chapter I (Introduction)

Chapter III (Results and Discussion)

List of Schemes

Chapter III (Results and Discussion)

List of Tables

Chapter III (Results and discussion)

Appendix

Acronyms and Abbreviations

adc	acetylene dicarboxylate
H_2fumarate	Fumaric acid
H_2succinate	Succinic acid
H_2adc	acetylene dicarboxylic acid
4,4′-bipy	4,4′-bipyridine
H_3BTC	1,3,5-benzene tricarboxylic acid
6-Mebpta	2-methyl-N-((6-methylpyridin-2-yl)methyl)-N-(pyridin-2-ylmethyl)propan-2-amine
6-Mebpea	N-((6-methylpyridin-2-yl)methyl)-N-(pyridin-2-ylmethyl)ethanamine
6,6-Me_2bpta	2-methyl-N,N-bis((6-methylpyridin-2-yl)methyl)propan-2-amine
2,2-terpyBA	4'-(4-(prop-2-yn-1-yloxy)phenyl)-2,2':6',2"-terpyridine
4,4-terpyBA	4'-(4-(prop-2-yn-1-yloxy)phenyl)-4,2':6',4"-terpyridine
H_2bpaipa	5-(bis(pyridin-2-ylmethyl)amino)isophthalic
2,4-H_2bpaipa	5-((pyridin-2-ylmethyl)(pyridin-3-ylmethyl)amino)isophthalic
H_3pbaipa	5-((4-carboxybenzyl)(pyridin-2-ylmethyl)amino)isophthalic acid
H_4daib	5,5'-((1,3-phenylenebis(methylene))bis(azanediyl))diisophthalic
H_4bdaib	5,5'-((1,3-phenylenebis(methylene))bis(azanediyl))diisophthalic acid
B.p.	Boiling point
M.p.	melting point
CP	Coordination Polymer
DMF	N,N'-dimethylformamide
DMSO	dimethylsulfoxide
MOF	Metal Organic Frameworks
MOCN	Metal Organic Coordination Networks
1D	one dimensional
2D	two dimensional
3D	three dimensional
HT	hydrothermal
RT	room temperature
SC	Single Crystal
SCNs	Supramolecular Coordination Networks
FTIR	Fourier Transform Infrared
UV-Vis	Ultraviolet-Visible
FESEM	Field emission scanning electron microscopy
TEM	Transmission electron microscopy
EDX	Electron dispersion X-ray spectroscopy
TGA	Thermogravimetric analysis
NMR	Nuclear magnetic resonance
PXRD	Powder X-ray diffractometry
SCXRD	Single crystal X-ray diffractometry

Contents

Abstract

Based on the rapid growth in industrialization for human needs and comfort, one of the major programs in recent times is focused on multidisciplinary research efforts to deal with energy and environment issues. Chemistry plays a critical role in how our societies will contend with broader global effects related to such issues. For this reason, different kinds of new multifunctional materials are designed and evaluated for their possible applications in various related topics with special attention to cost and efficiency. In the past two decades, there is a giant leap in the sphere of strategic design of diverse functional materials namely supramolecular coordination assemblies, coordination polymers (CPs) and metal organic frameworks (MOFs), which are collectively termed as Metal Organic Coordination Networks (MOCNs), for various applications such as carbon capture, gas storage/separation, catalysis, sensing, water purification, drug delivery, guest encapsulation, magnetism, etc. The construction of such functional materials via coordination-driven self-assembly of metal ions/clusters and multitopic organic linkers depends on coordination bonds and supramolecular interactions, such as hydrogen bonds, π–π and/or C-H···O interactions, etc. Through judicious choice of the components in making such coordination architectures, it is possible to generate materials with tunable structures varying dimensionality and topology and targeted physicochemical properties and functionality.

This thesis work focused on the strategic designs to obtain a variety of MOCNs under ambient, hydro- or solvothermal conditions in good to high yields via self-assembly of both two-component (metal ions and custom-designed mixed pyridyl-carboxylate linkers) and three-component (metal ions, neutral ancillary ligands, and carboxylate linkers) systems. These have been extensively characterized by various analytical techniques including elemental analysis, FT-IR, Raman and UV-Vis spectroscopy, TGA, single crystal and powder X-ray diffraction, and ESI-MS analysis. Their applications in four different areas, namely (i) guest encapsulation (water clusters including rare cyclic dimers and cyclic pentamers, and common organic solvents in supramolecular coordination assemblies), (ii) ion exchange (waste water purification and separation of dyes by anionic MOFs), (iii) catalysis (cascade N-alkylation reaction and the Knoevenagel condensation reaction by Pd NPs@MOFs) and (iv) sensing (ketones, amines and nitroaromatic compounds by luminescent MOFs), have been explored to contribute tremendously to the targeted efforts sought in the multidisciplinary approach mentioned above. There are four chapters in this thesis.

CHAPTER I

Introduction

During the past few decades, the design and synthesis of metal organic coordination networks (MOCNs) by using various ligands and linkers has attracted considerable attention owing to their potential application in catalysis,[1–4] separation,[5,6] sensor,[7–9] gas storage,[10–12] luminescent materials,[9,13–16] ion exchange,[17,18,19] magnetism,[20,21] wastewater purification,[22] etc. MOCNs can form 1D, 2D and 3D coordination networks through coordinate bond and/or various weak interactions like hydrogen bonding, π–π stacking of aromatic moieties, C-H···O interactions etc.[23] Furthermore, an association of 1D or 2D networks results in the formation of 3D supramolecular networks through non-covalent interactions.[24,25] Thus, the major force to form building blocks of MOCNs is the coordination between the metal and the ligand. For the formation of this type of bond, the HSAB (hard and soft acids and bases) principle plays a very important role for the different pre-defined coordination networks.[26] According to this theory, a soft acid prefers to accommodate a soft base, while a hard acid prefers to accommodate a hard base.[26] In MOCNs, metal ions act as acids while ligands with donor atoms act as bases. The components of MOCNs (Figure 1.1) are: a metal ion or metal clusters, ancillary ligand, organic linker, counter ions and guest molecules (usually solvent molecules used in the synthesis).[27] With a variation of these constituents, diverse materials differing in the structure as well as properties can be created. Thus, the solvent (like water), the molar ratio of reactants, pH and temperature of the reaction, and counter ions (if present for charge balance) direct the formation of the final architectures of these networks.[25] MOCNs synthesized using these components can be classified into three different categories. These can be discrete coordination complexes,[28,29] which can form a supramolecular assembly of different dimensions based on supramolecular interactions, the presence of lattice solvent molecules playing an important role.[30] Another class of MOCNs is the coordination polymers having 1D structures.[31] These can have a linear chain, a zig-zag polymeric chain, or a ladder-shaped architecture.[32,33] The most important class of MOCNs is 2D or 3D porous coordination polymers, known as Metal Organic Frameworks (MOFs).[34–38] These porous networks with tunable structures have been found to be very useful in various applications mentioned in Figure 1.1.[39,40] For the synthesis of these MOCNs, various

methods are reported in the literature, like one pot self-assembly under ambient conditions, hydro-/solvothermal, sonochemical, electrochemical and microwave.[27] However, the method under ambient conditions and the hydro-/solvothermal method are used frequently. However, the hydro-/solvothermal method is challenging due to the formation of different products from the same components at high temperature and autogenous pressure. However, products formed by hydro-/solvothermal method show very high thermal stability. In the present work, we have used both ambient as well as hydro-/solvothermal protocols for the synthesis of various MOCNs with high purity and good yields. These MOCNs have been used for various applications, such as guest encapsulation, ion exchange, catalysis, and sensing, which are discussed further.

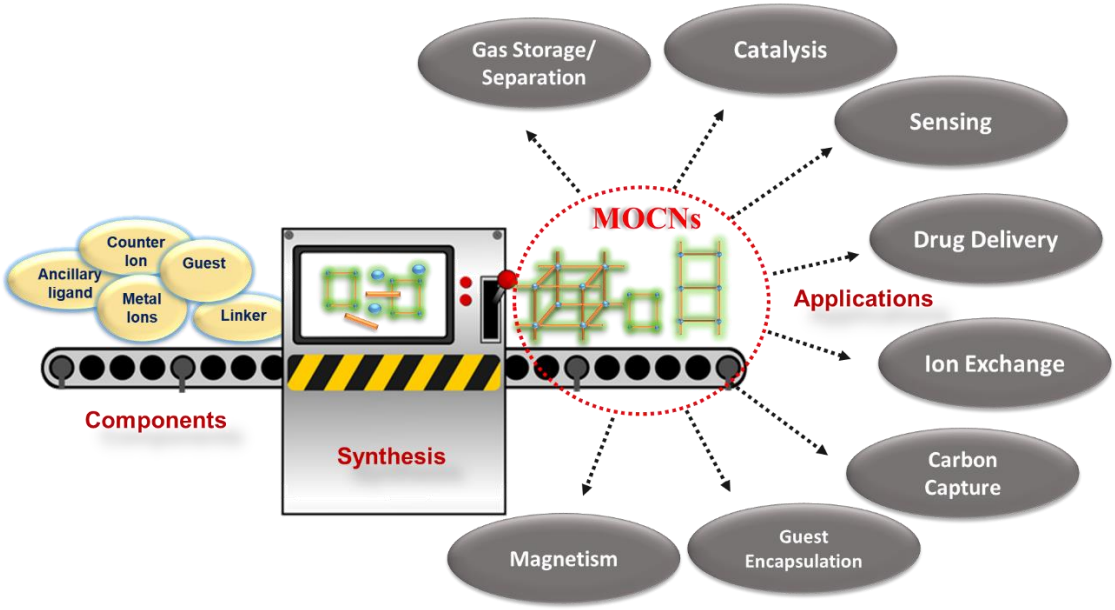

Figure 1.1. Schematic representation showing the components, synthesis, and applications of MOCNs.

Guest Encapsulation

Guest encapsulation is one of the very important applications for porous materials. These materials can be utilized for the encapsulation of different types of guest molecules inside the pores.[41] These can be small molecules like organic solvents, explosives, biological molecules, water, ions, drugs, pesticides, fungicides, dyes, etc., in all three different states.[42,43] Using the guest encapsulation capability of a material, some important applications, such as purification of water,[44] drying of the organic solvents, drug delivery,[45] and removal of harmful substances[46,47] from a mixture, have been demonstrated.[48,49] There are many methods reported in the literature for the encapsulation of guest molecules in the coordination networks. Three common protocols are: (1) in-situ encapsulation of guest

molecules, (2) encapsulation of solvents in the network which has real porosity, and (3) replacing the guest, which is already present, by another guest (Figure 1.2). Guest encapsulation is strongly dependent on the size of guest molecules, interaction of guest with framework, and pore sizes.[50,51] At the time of synthesis, some solvent molecules like water are usually entrapped within the framework, which is known as in-situ encapsulation.[52,53] These encapsulated solvent molecules help in the formation of diverse supramolecular assemblies, and arrange in clusters of different shapes and sizes; this is further discussed below. In the second method, the framework that does not have any guest can absorb guests upon exposure. For the the third method, solvents in the framework are first removed by pretreating it at a certain temperature followed by sorption of other solvent molecules. Solvent sorption isotherms give the amount of guest solvent loading. The encapsulation of guest molecules is a very challenging task because of the low stability of the networks under the applied conditions of pretreatment. These may fall apart during activation.[54]

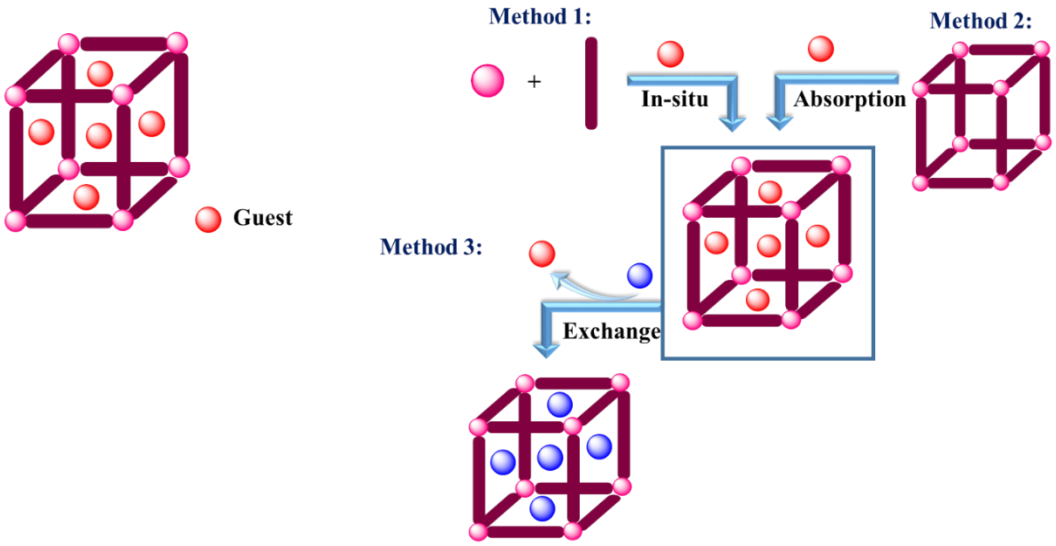

Figure 1.2. Schematic representation of strategies for the encapsulation of guests in MOCNs.

Thus, the stability of these MOCNs is very important for this type of solvent encapsulation. Several analytical techniques like elemental analysis, TGA, FTIR, PXRD, and SCXRD can be used to follow this at the molecular level. In case of gas adsorption studies, the pretreatment of coordination polymers at a certain temperature is done but sometimes the results obtained are less than expected. In these type of cases, it becomes important to understand the observed data at the molecular level due to the treatment. One of the ways, which is not an easy task,[55–58] is through single-crystal-to-single-crystal (SC-SC) transformation.[59] Although many literature reports are there for post-synthetic modification

like ion exchange, ligand exchange and desolvation/resolvation via SC-SC transformation,[60,61] it is difficult because the mother crystal may not sustain the applied conditions or may crack or decompose. Sometimes ions can also be trapped with the solvent molecules in the supramolecular assembly. These ionic guests can be exchanged by another ion, which results in a tremendous change in the supramolecular assembly as well as in the formation of a water cluster.[62] This exchange of ionic guest can also be followed by single-crystal-to-single-crystal (SC-SC) transformation.[63]

Encapsulation of water cluster is a very important subclass of guest encapsulation.[64-66] The identification, characterization, and classification of various water assemblies in different crystalline materials have recently become a popular research field, namely towards understanding the properties of bulk water in its liquid and solid phases as well as interpretation of water–water interaction in various environments including inorganic materials, supramolecular systems, and biomolecules. Water clusters play an important role in the stabilization of supramolecular systems both in solution as well as in the solid state.[67–69] There is clearly a need for better understanding of how such water aggregations are influenced by the overall structure. Due to this aggregation, different types of water cluster are formed, which can be linear (n = 2-20), cyclic (n = 2-8) and cages (n > 20).[70–72] In some cases, theoretical calculations provide their existence; however, still a lot more experimental evidence is required to ascertain the predictions. Thus, we have explored the encapsulated water molecules for better understanding of the existence of rare water clusters in the solid state. Also, diversification in the water clusters can be explored by SC-SC transformation.

For our interests to explore and identify the factors governing the formation of supramolecular assemblies vs. discrete polygons such as squares and rectangles, and their further association through supramolecular interactions, a systematic study has been carried out using multidentate polypyridyl ancillary ligands and multitopic carboxylate linkers with Ni(II) as the metal center.[73–75] There are several factors which decide the formation of water clusters, such as, ligands and metal center as well as the reaction conditions and the presence of different ions. In this regard, carboxylate ions can merely function as charge balancing groups in the coordination networks rather than playing a role in providing structural diversity to the overall architecture, such as the formation of bridges, helical structures, higher dimensional networks, etc.[76] Anions in coordinated or uncoordinated forms (hydrogen bonded with solvent molecules) or both, support the aggregation of water

clusters and are helpful in the construction of supramolecular architectures (mentioned above). It is evident that the free anion can be exchanged with other anions under favorable conditions, causing a change in the arrangement of water clusters and supramolecular architectures as well. Although various methods are reported in the literature, we like to follow the SC-SC transformation as well as wet methods (liquid-liquid and solid-liquid post-synthetic exchange) for the anion exchange.[77,78]

Ion Exchange

Both cations and anions function for balancing the charge in coordination networks. While most of the ionic networks are cationic in nature requiring an anion for overall neutrality, there are examples where a cation resulting from the protonation followed by degradation of a solvent is used in the synthesis, stabilizes an anionic architecture. Such anionic architectures with channels containing exchangeable cations are very important for their applications in separation/absorption of dyes from a mixture. This type of research is the basis for purification of water.

Separation of Dyes. Dyes are the compounds used in the coloring of clothes and textiles.[79,80] These can be natural or synthetic. Nowadays, the production of synthetic dyes is increasing, due to their high demands in textile and other industries. Although their use is increasing day by day but the disposal of dyes waste in water makes a bad impact on the environment. Furthermore, the wastewater containing dyes is very harmful to human health and aquatic life.

The removal of dyes from wastewater is a challenging issue in environmental engineering. Different dyes have different pysico-chemical properties. Both cationic and anionic dyes are extensively used. Some of the dyes are carcinogenic.[81,82] However, the carcinogenicity of many dyes is due to their cleaved product such as benzidine, p-phenylenediamine, and other amine-containing aromatic compounds. These components, particularly benzidine, induce tumor in the human body. Moreover, these components are responsible for allergies, which affect the nervous system of humans. Some of the dyes are used in food, which can also cause allergy in the body. There are many techniques used for the purification of wastewater that comes out of the industries. Among the techniques employed, adsorption technology is generally considered highly efficient. Various clays and zeolites have been extensively used for this purpose.[83–88] With an increase in the number of MOFs reported in the literature, their use for dye separation and adsorption has been sought. A cationic

framework can selectively take the anionic dyes inside the MOFs and leave behind the cationic dyes in a mixture. Similarly, an anionic framework operates in a reverse way.

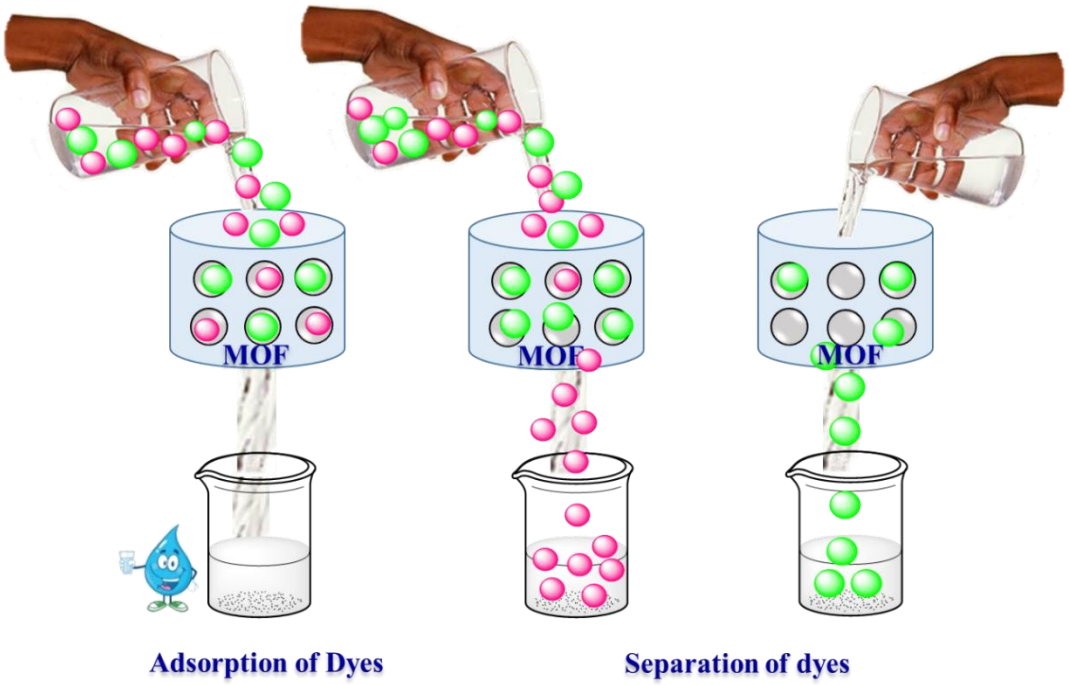

Figure 1.3. Schematic representation showing adsorption and separation of dyes from wastewater by MOF.

Thus, we can easily separate the cationic or anionic dyes from the mixture of dyes as shown in Figure 1.3. An important factor is a compatibility between the size of pores and the size of the dyes. This type of adsorption is based on the size selectivity.[87,89,90] In this work, we have been able to make few anionic MOFs and used them for showcasing the separation of dyes from a mixture.

Catalysis

In the last two decades, the use of MOFs as heterogeneous catalysts has greatly increased for the consideration of a new green protocol that presents an eco-friendly alternative in catalysis. In particular, heterogeneous catalysis by MOFs in various organic transformation reactions has emerged as an attractive field with advantages over homogeneous ones (such as easy separation from products and recyclability).[91–93] There are many approaches for the introduction of catalytically active sites into the framework via functionalized linkers and coordinatively unsaturated or modified metal nodes as well as using the external surface of MOF as a support for metal nanoparticles (Figure 1.4). Due to various scopes available for tuning their structures through modification in organic linkers, MOFs provides diversity in these catalytic sites.[94] The Lewis acidic and/or basic sites in the frameworks interact with

different substrates molecules.[95–99] Therefore, catalysis depends on the type of metal and/or linker used in the framework. For such diversity, many organic transformations that require catalysts are possible with MOFs.[100–102]

However, it is a very challenging task to synthesize new catalysts with the above-mentioned requirements. Furthermore, both stability (chemical and thermal) and recyclability of the catalyst are very important for sustainable chemistry.[103–105] In the literature, catalysts for various C-C bond forming reactions and one pot N-alkylation reaction are reported but the demand for good catalysts, which give excellent conversion and efficiency, for such reactions is huge.

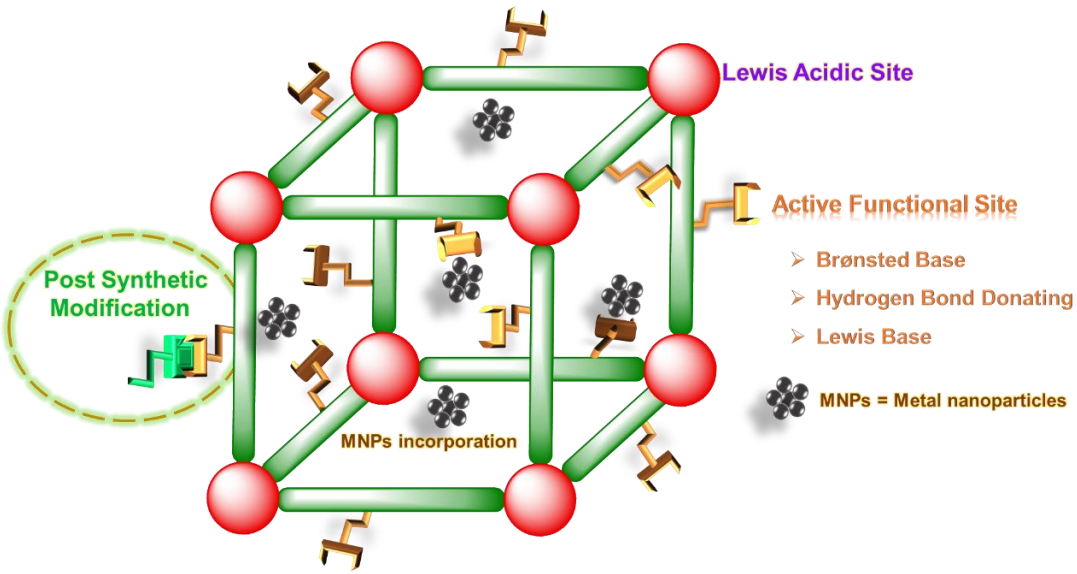

Figure 1.4. Schematic representation of various interaction sites in MOFs for catalysis.

The formation of nanoparticles like Ag, Pd or Pt inside the porous metal organic framework with functionality, such as free acetylene moiety, is a good and effective path to synthesize a NPs@MOF catalyst. These catalysts exploit the crystalline structure and uniform pore size of the MOF to direct the access of reacants to the encapsulated catalytic nanoparticles. Due to the implementation of nanoparticles, these MOFs become dual functional catalysts.[41,106,107]

Sensing

With an increase in industrialization and globalization, there has been a vast change in the atmosphere resulting in environmental pollution and health issues. Another important reason is the increase in antisocial activities all over the world, for which it is essential to develop such sensors for detecting the explosives and other harmful chemicals with fast response time to reduce the damage risk. Thus, several sensors have been developed such

as discrete molecules, polymeric architectures like MOFs, supramolecular complexes and metal nanoparticles for detecting hazardous entities like explosives, toxic gases, neutral molecules, solvent molecules, temperature, pH, acids/bases, vapors, anions, cations, fungicides, fumigants, biological entities like cells, virus, antibodies, and pesticides, etc.[9,13–16,108,109,110–113]

Sensing by these materials is strongly dependent on the molecular recognition and self-assembly of these chemical structures by various supramolecular interactions, which create changes in the properties.[114,115] These changes can be observed by using different techniques, and after analyzing the data, we can understand the mechanism of action for, and efficiency of, a sensor. From ancient times, different methods have been used for sensing of a wide variety of materials.[116–118] Till now, various sophisticated instruments have been used for sensing, such as electrochemistry, mass spectrometry, surface enhanced Raman spectroscopy and fluorescence spectroscopy. Among these, the fluorescence technique is mostly preferred for fast response time, low cost, and reliable detection. From past few decades, many luminescent MOFs have come into picture, which are potential candidates for the detection of various analytes with very high efficiency as well as excellent detection limits (see Figure 1.5).[15,119,120] The importance of these materials has extensively increased because of their exceptional structural tunability as well as morphological properties. A luminescent MOF can interact with different analytes due to the presence of different interaction sites which results in the change in the fluorescence properties.[121] Mostly, d^{10} metal centers (Zn(II) and Cd(II)) based MOFs in combination with fluorescent-tagged organic systems are utilized for fluorescence-based sensing.[114,115] There are four ways by which a change in the fluorescence can be observed. First is the turn-on fluorescence in which enhancement in the fluorescence intensity (hyperchromic shift) occurs while second is the turn-off fluorescence in which a decrease in the fluorescence intensity (hypochromic shift) takes place (see Figure 1.6). Other two are related to a change in λ_{max}: shift to a higher wavelength which is red-shift (bathochromic shift) and the change towards lower wavelength or blue shift (hypsochromic shift). All these changes in the fluorescence are due to the different interactions of the analyte with the framework by which a change in the electron and energy transfers takes place.[112,122–124] Sensing of the small molecules like solvents is one of the essential assignments to accomplish. A luminescent MOF can behave differently in different solvents like DMF, H_2O, methanol, ethanol, toluene, DMSO, acetonitrile, etc.[16,125–128] The enhancement or

quenching in the emission intensity strongly depends on the interaction of these solvent molecules with the framework. One of the important solvent molecules to detect is acetone. Acetone can interact with the metal center or the ligand part to reduce the electron transfer from metal to ligand or ligand to metal that can result in the change in the fluorescence intensity.[126] Most of the literature reports are based on the fluorescent tagged MOFs or lanthanide-based luminescent MOFs.[121,129–135] On the other hand, very few reports on sensing of acetone are reported. Interestingly, Zn(II) based MOFs for sensing of small molecules and ketones are very less.[136]

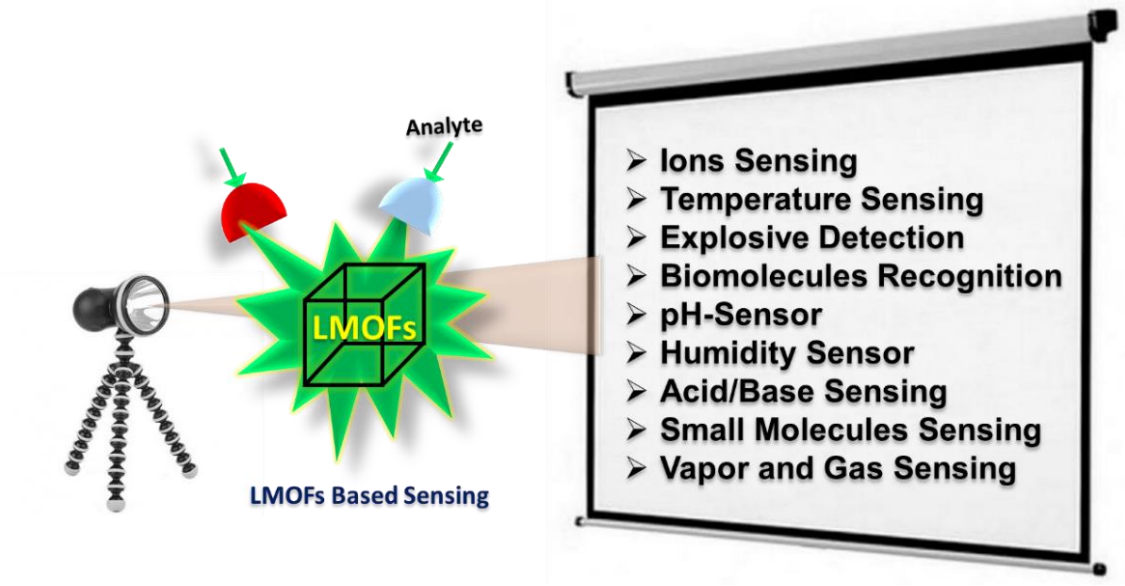

Figure 1.5. Schematic representation of sensing application for different analytes by luminescent MOFs.

To explore this further, sensing of ketones is yet another significant task. Some of the ketones like cyclohexanone are used for the crystallization of the RDX which is an explosive material used in terrorist activities. It was the second most used explosive in World War II. Therefore, it is worthwhile to sense this type of material concerning national and international security. In this regard, sensing of cyclohexanone among other ketones is the alternative approach towards indirect detection of RDX. On the other hand, detection of other explosives mainly nitro-compounds, like TNT and TNP, is also very important to control environmental pollution as well as for homeland security and safety. Selective sensing of TNT and TNP among other nitro-compounds is one of the challenging but achievable tasks.[13,137]

Furthermore, it is a very challenging task to detect the compounds in the vapor state with similar vapor pressure. In this context, vapors of aliphatic and aromatic amines are very harmful to human health, which cause various infections in the respiratory tract.[138,139] For

example, exposure to high concentration of aniline can lead to the formation of methemoglobin, resulting in a decrease in the oxygen-carrying capacity of the blood. Its carcinogenic nature is responsible for causing severe damage to the human body. Although various methods of sensing of these vapors are reported,[139] the strategic design of metal-organic coordination networks by utilizing different metal centers and functionality can allow to achieve this with better efficiency. This type of sensing can be carried out in the solid state where turn-on or turn-off behavior is observed (Figure 1.6).[140–143]

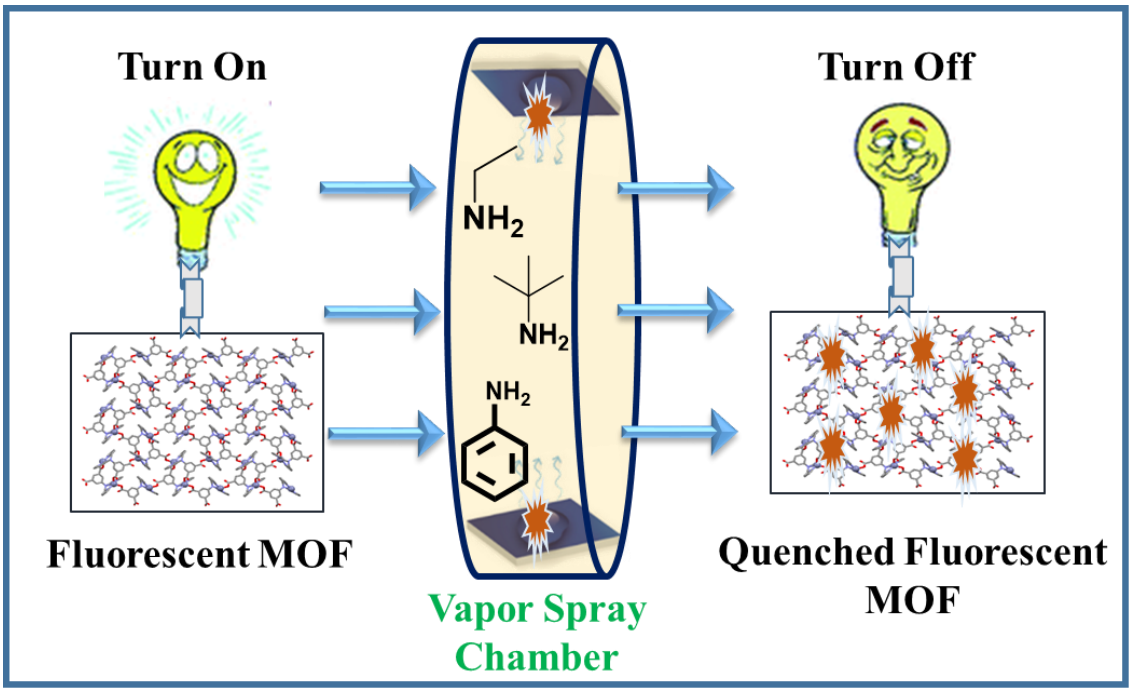

Figure 1.6. Schematic representation showing vapor sensing of aliphatic and aromatic amines by luminescent MOFs.

Scope and Significance of Present work

In order to make new MOCNs, the most important theme is the design of multitopic ligands with a consideration of coordination chemistry of various metal ions. In the literature, a majority of MOCNs are made through the exploitation of existing or new polycarboxylates in a combination of various metal centers under hydro-/solvothermal conditions.

Thus, the two-component systems with mostly carboxylates have been exhausted. On the other hand, mostly bifunctional neutral N-donor ligands have been used in combination of carboxylates in the three-component systems. However, very little is exploited where the ligands are mixed anionic-neutral organic species. In this work, four different types of new ligands have been synthesized in good yield and high purity (Figure 1.7).

(a) Pyridyl-based ligands

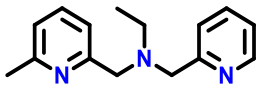

N-((6-methylpyridin-2-yl)methyl)
-*N*-(pyridin-2-ylmethyl)ethanamine
(6-Mebpea)

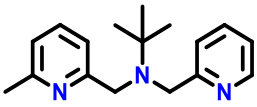

2-methyl-*N*-((6-methylpyridin-2-yl)
methyl)-*N*-(pyridin-2-ylmethyl)propan-2-amine
(6-Mebpta)

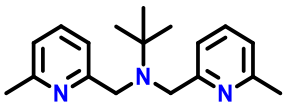

2-methyl-*N*,*N*-bis((6-methylpyridin-2-yl)
methyl)propan-2-amine
(6,6'-Me$_2$bpta)

(b) Functionalised pyridyl-based ligands

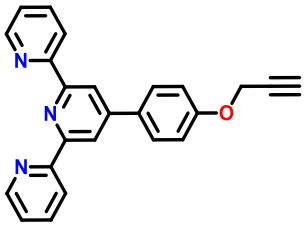

4'-(4-(prop-2-yn-1-yloxy)phenyl)-2,2':6,4'-(4-(prop-
2-yn-1-yloxy)phenyl)-2,2':6',2''-terpyridine
(2,2'-terpyBA)

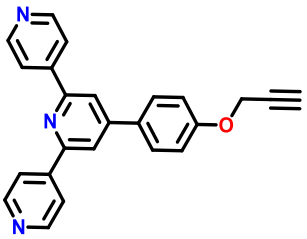

4'-(4-(prop-2-yn-1-yloxy)phenyl)-4,2':6',4''-terpyridine
(4,4'-terpyBA)

(c) Mixed pyridyl-carboxylate ligands

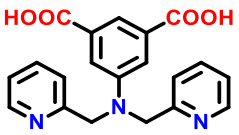

5-(bis(pyridin-2-ylmethyl)
amino)isophthalic acid
(2,2'-H$_2$bpaipa)

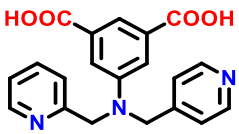

5-((pyridin-2-ylmethyl)(pyridin-4-
ylmethyl)amino)isophthalic acid
(2,4-H$_2$bpaipa)

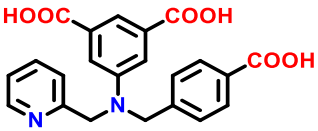

5-((4-carboxybenzyl)(pyridin-2-
ylmethyl)amino)isophthalic acid
(H$_3$pbaipa)

(d) Functionalized tetracarboxylate ligands

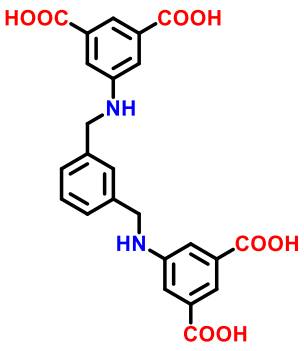

5,5'-((1,3-phenylenebis(methylene))
bis(azanediyl))diisophthalic acid
(H$_2$diab)

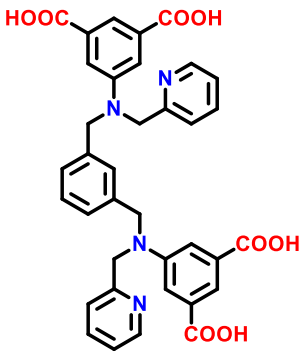

5,5'-((1,3-phenylenebis(methylene))
bis((pyridin-2-ylmethyl)azanediyl))diisophthalic acid
(H$_2$bdiab)

Figure 1.7. Organic ligands prepared for this study.

The first type is the pyridyl-based tridentate ancillary ligands. The second category of ligands is pyridyl-based ligands having additional functionality which can be used for various applications; these ligands can act as an ancillary ligand and also behave like a linker when the position of donor atoms is changed. The third category includes the mixed pyridyl-carboxylate ligands. The strategy behind the synthesis of the mixed ligands is to combine both ancillary ligand and carboxylate linker together to generate highly porous networks. The fourth category includes functionalized tetracarboxylates based ligands with a xylyl spacer: one with noncoordinating secondary amine groups and the second is a mixed pyridyl-carboxylate. Wherever required, for the three-component systems various dicarboxylates, functionalized dicarboxylates, tricarboxylates and pyridyl linkers (shown in Figure 1.8) are used.

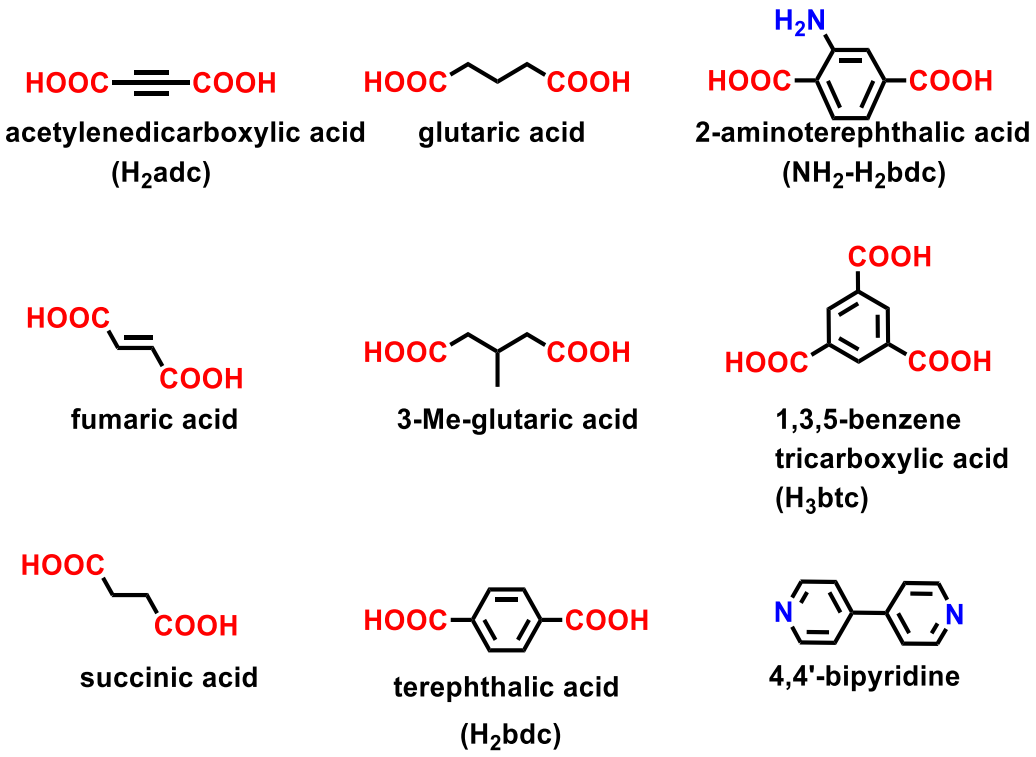

Figure 1.8. Organic linkers used in this study.

Thus, the scope for this work was defined by the ligand systems described above. In making over seventy six MOCNs, two different strategies as shown in Figure 1.9 are explored. The three- component strategy consists of two different subsections categorized based on tridentate and functionalized tridentate ligands with dicarboxylates and tricarboxylates as linkers. For the two-component strategy, either mixed ligands or tetracarboxylates are the

second component. With these vast number of MOCNs, their applications in four different important areas (mentioned above) make this work significant.

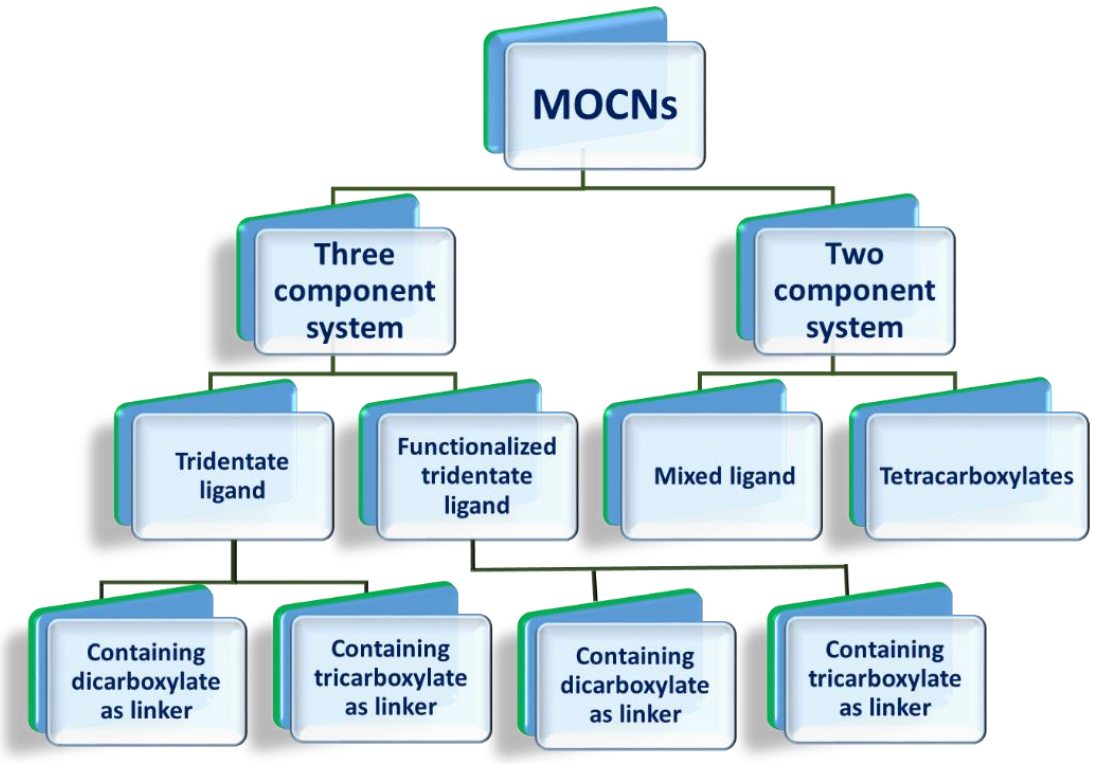

Figure 1.9. Flow diagram of the present research.

CHAPTER II

Experimental Section

2.1 Materials and Methods

All chemicals and solvents used for synthesis were obtained from commercial sources and were used as received, without further purification. All reactions were carried out under aerobic conditions. All the ligands were synthesized either by reported procedure or by modifying the reported procedures in the literature.

2.2 Physical Measurements

^{1}H NMR spectra of the synthesized ligands were obtained in deuterated solvents at 25 °C on a Bruker ARX-400 spectrometer; chemical shifts are reported relative to the residual solvent signals. Each sample was prepared by taking 5-10 mg of the compound in approx. 0.5 mL of the deuterated solvent. Each data obtained was analyzed and plotted using either TOPSPIN software by Bruker or Spinworks.

Melting points (M.pt.) were measured on a Büchi Melting and Boiling Point Apparatus. All melting points have been measured in open melting point capillaries.

FTIR spectra were measured in the range of 4000-400 cm^{-1} on a Perkin-Elmer Spectrum I spectrometer with samples prepared as KBr pellets.

Raman spectra were recorded on a Renishaw InVia Raman microscope equipped with a 785 nm high-power near-infrared laser working at 300 mW power and a Renishaw CCD detector. Analysis of the Raman spectra was performed in reflection mode on powder samples placed on the sample stage and aligned in optical path by using a camera, with 0.1-0.5% laser power and by using 50X optics in the range of 400-2000 cm^{-1}.

Elemental analysis (C, H, N) was carried out using either a Leco-USA Tru Spec CHNS micro version 2.7x analyzer at IISER Mohali or Mettler CHNS analyzer at NIPER Mohali.

Thermogravimetric analysis was carried out from 25 to 500 °C (at a heating rate of 10 °C/min) under dinitrogen atmosphere on a Shimadzu DTG-60. The sample to be analyzed was weighed using an analytical balance, put in a pan and weighed again using the microbalance of the instrument to avoid any discrepancy. The data obtained were analyzed using TA 60 software.

UV-Vis spectra of the compounds in different solvents were recorded in an Agilent Technologies Cary60 UV-Vis spectrophotometer using a cuvette of path length 10 mm. Solid state reflectance of solid samples was recorded in Cary5000 UV-Vis spectrophotometer using KBr medium.

Fluorescence emission spectra were obtained using a Horiba Jobin Yvon Fluorimeter 3 instrument with a cuvette of 10 mm path length. To obtain the spectrum, a slurry of the compound was prepared in a suitable solvent by stirring for 15 minutes.

Powder X-ray data were recorded on a Rigaku Ultima IV diffractometer equipped with a 3 kW sealed tube Cu Kα X-ray radiation (generator power settings: 40 kV and 40 mA) and a DTex Ultra detector using parallel beam geometry (2.5° primary and secondary solar slits, 0.5° divergence slit with 10 mm height limit slit). Each sample grounded into a fine powder using a mortar and a pestle was placed on a glass sample holder that was placed on the sample rotation stage (120 rpm) attachment. The data were collected over an angle range 5° to 50° with a scanning speed of 1° per minute with 0.02° step with XRF reduction for the metals.

Hot stage microscopy experiments were performed on a ZEISS Discovery V12 microscope using a LIKAM hot stage controlled by the Linksys32 software. The growth of the crystals was observed by taking an image after one second for 45 minutes at room temperature.

Single crystal X-ray analysis were performed by initial crystal evaluation, and data collection were performed on a Kappa APEX II diffractometer equipped with a CCD detector (with the crystal-to-detector distance fixed at 60 mm) and sealed-tube monochromated Mo Kα radiation using the program APEX2.[144] By using the program SAINT[144] for the integration of the data, reflection profiles were fitted, and values of F^2 and $\sigma(F^2)$ for each reflection were obtained. In some cases, a lot of efforts were invested to recollect data sets with new crystals a few times, but no better data sets that are used here could be obtained. Data were also corrected for Lorentz and polarization effects. The subroutine XPREP[144] was used for the processing of data that included determination of space group, application of an absorption correction (SADABS),[144] merging of data, and generation of files necessary for solution and refinement. Using Olex2,[145] the structure was solved with the ShelXT[146] structure solution program using Intrinsic Phasing and refined with the ShelXL[147] refinement package using least squares minimization. The space group was chosen based on systematic absences and confirmed by the successful refinement of

the structure. Positions of most of the non-hydrogen atoms were obtained from a direct methods solution. Several full-matrix least-squares/difference Fourier cycles were performed, locating the remainder of the non-hydrogen atoms. Some cases the solvents molecules are highly disordered. Therefore, the Olex2[145] masking program were used to remove those peaks. In order to obtain reasonable thermal parameters compared to other atoms, the lowest residual factors and optimum goodness of fit with the convergence of refinement, occupancy factors of some of the atoms were adjusted accordingly. The occupancy factors of some of the atoms were adjusted to obtain favorable thermal parameters. All non-hydrogen atoms for all structures were refined with anisotropic displacement parameters except where mentioned. Crystallographic parameters and basic information pertaining to data collection and structure refinement for all compounds are summarized in the appendix. All figures were drawn using, and MERCURY V 3.10.2[148] and hydrogen bonding parameters were generated using PLATON.[149,150]

Solvent adsorption measurements were recorded for pressure in the range 0–1.2 bar by the volumetric method using a BELSORP instrument. Each solid sample was transferred to pre-weighed analysis tubes, which were capped with transeals and evacuated by heating at a temperature between 110-150 °C (based on thermal profile obtained from TGA) under dynamic vacuum until an outgassing rate of less than 2 mTorr min^{-1} (0.27 Pa min^{-1}) was achieved (ca. 12-24 hrs). The evacuated analysis tubes containing the degassed sample was then carefully transferred to an electronic balance and weighed again to determine the mass of the sample. The tube was then placed back on the analysis port of the gas adsorption instrument. The outgassing rate was again confirmed to be less than 2 mTorr min^{-1} (0.27 Pa min^{-1}). For all isotherms, warm and cold free-space (dead volume) correction measurements were performed using ultra-high-purity He gas (UHP grade 5.0, 99.999% purity). The change of the pressure was monitored, and the degree of adsorption was determined by the decrease in pressure at the equilibrium state via computer controlled automatic operations that are set up at the start of each measurement. Oil-free vacuum pumps and oil-free pressure regulators were used for all measurements to prevent contamination of the samples during the evacuation process or of the feed gases during the isotherm measurements.

2.3 Synthesis of Ligands

N-((6-methylpyridin-2-yl)methyl)-N-(pyridin-2-ylmethyl)ethanamine (6-Mebpea).

Step 1, N-((6-methylpyridin-2-yl)methyl)ethanamine). To a methanolic solution of 6-methyl-2-pyridinecarboxaldehyde (242 mg, 2 mmol) in a 25 mL RBF, ethylamine solution (90 mg, 2 mmol in water) was added followed by stirring for 12 h at room temperature. An excess of sodium borohydride (1.5 equivalents) was added slowly to the above stirred mixture at 0-4 °C and further stirred for another 12 h. The resulting reduced Schiff base was extracted using chloroform followed by drying over anhydrous sodium sulfate. The solvent was evaporated to dryness using reduced pressure affording a yellow oily substance. Yield: 210 mg (70%). ^{1}H NMR ($CDCl_3$): δ 7.46 (t, 1H), 7.05 (d, 1H), 6.96 (d, 1H), 3.80 (s, 2H), 2.66 (m, 2H), 2.47 (s, 3H), 1.11 (t, 3H).

In *Step 2*, 2-picolylchloride hydrochloride (143 mg, 0.87 mmol) was added to the aqueous solution of the reduced Schiff base (171 mg, 0.87 mmol) obtained in *Step-1*. Furthermore, sodium hydroxide solution (80 mg, 2 mmol in 2 mL water) was added to the above mixture dropwise and stirred for another 24 h. The product was extracted with chloroform followed by drying the organic layer over anhydrous sodium sulfate. The solvent was evaporated to dryness under reduced pressure affording a light yellow semi-solid product. Yield: 244 mg (88%). ^{1}H NMR ($CDCl_3$): δ 8.48 (d, 1H), 7.44 (m, 2H), 7.40 (d, 1H), 7.34 (m, 2H), 7.01 (d, 1H), 3.95 (s, 4H), 2.72 (m, 2H) 2.45 (s, 3H), 1.18 (t, 9H). HRMS (ESI-TOF): *m/z* calcd for $[(6\text{-Mebpea})H]^+$, 242.1613; found, 242.1607.

2-methyl-N-((6-methylpyridin-2-yl)methyl)-N-(pyridin-2-ylmethyl)propan-2-amine (6-Mebpta). *Step 1*, 2-methyl-N-((6-methylpyridin-2-yl)methyl)propan-2-amine. To a methanolic solution of 6-methyl-2-pyridinecarboxaldehyde (242 mg, 2 mmol), tertiary butyl amine (146 mg, 2 mmol) was added and stirred for 12 h at room temperature. An excess of sodium borohydride (1.5 equivalent) was added slowly to the above reaction mixture at 0-4 °C and stirred for another 12 h. The resulting reduced Schiff base was isolated from the reaction mixture by extracting with chloroform followed by drying with anhydrous sodium sulfate. The solvent was evaporated to dryness using reduced pressure affording a yellow oily substance. Yield: 155 mg (60%). ^{1}H NMR ($CDCl_3$): δ 7.49 (t, 1H), 7.12 (d, 1H), 6.99 (d, 1H), 3.83 (s, 2H), 2.52 (s, 3H), 1.18 (s, 9H).

Step 2, To an aqueous solution of the reduced Schiff base (150 mg, 0.84 mmol) obtained in *step 1*, picolylchloride hydrochloride (138 mg, 0.84 mmol) was added. A sodium hydroxide solution (80 mg, 2 mmol in 2 mL water) was added dropwise to the above reaction mixture

and stirred for another 24 h. The product was extracted with chloroform followed by drying the organic layer over anhydrous sodium sulfate. The solvent was evaporated to dryness using reduced pressure affording a light yellow semi-solid. Yield: 178 mg (79%). ^{1}H NMR ($CDCl_3$): δ 8.48 (d, 1H), 7.44 (d, 2H), 7.40 (d, 1H), 7.34 (d, 1H), 7.01 (t, 1H), 6.80 (d, J = 7.6 Hz, 1H), 3.95 (s, 4H), 2.45 (s, 3H), 1.18 (s, 9H). HRMS (ESI-TOF): *m/z* calcd for [(6-Mebpta)H]$^+$, 270.1926; found, 270.1913.

2-methyl-N,N-bis((6-methylpyridin-2-yl)methyl)propan-2-amine (6,6′-Me$_2$bpta). To a stirred mixture of 6-methylpyridine-2-carboxyaldehyde (605 mg, 5 mmol) in 8 mL of dry dichloroethane, tertiary butyl amine (146 mg, 2 mmol) was added and stirred for another 3 h under inert conditions at room temperature. To the above stirred reaction mixture, sodium triacetoxy borohydride (1.2 g, 6 mmol) was added very carefully at 0-4 °C in an inert atmosphere followed by the addition of 5 mL DCE and was stirred for another 24 h. A saturated solution of sodium bicarbonate (19 mL) was added to make it slightly alkaline. The product was extracted with chloroform, dried over anhydrous sodium sulfate to remove the moisture, the solvent was evaporated to dryness under reduced pressure affording a yellow liquid substance which was further recrystallized using ethyl acetate and hexane mixture affording white crystals. Yield: 435 mg (62%). ^{1}H NMR ($CDCl_3$): δ 7.45 (t, 2H), 7.41 (d, 2H), 6.89 (d, 2H), 3.94 (s, 4H), 2.46 (s, 6H), 1.16 (s, 9H). HRMS (ESI-TOF): *m/z* calcd for [(6-Mebpta)H]$^+$, 284.2082; found, 284.2079.

4'-(4-(prop-2-yn-1-yloxy)phenyl)-4,2':6',4''-terpyridine (4,4-terpyBA). This ligand was achieved in two steps as follows. *Step 1*, 4-(prop-2-yn-1-yloxy)benzaldehyde). In a 25 mL round bottom flask, p-hydroxy benzaldehyde (122 mg, 1 mmol) was dissolved in 5 mL DMF followed by addition of K_2CO_3 (3 eq.). To the above stirred mixture, propargyl bromide solution (178 mg, 1.5 mmol) was added under inert conditions. This reaction mixture was then refluxed for 5 h during which its color changed from colorless to light yellow and then finally dark brown. Furthermore, the reaction mixture was poured into ice-cold water resulting in the formation of a yellow precipitate immediately. Upon filtering through a G4-crucible, the precipitate was washed with water and dried using a vacuum aspirator. Yield: 144 mg (90%). ^{1}H NMR ($CDCl_3$): δ 9.93 (s, 1H), 7.90 (s, 2H), 7.11 (s, 2H), 4.81 (d, 2H), 2.60 (s, 1H).

In *Step 2*, product formed in the *Step 1*, 4-(prop-2-yn-1-yloxy)benzaldehyde (160 mg, 1 mmol) was added in 8 mL ethanolic solution of 2-acetyl pyridine (242 mg, 2 mmol). Upon addition of potassium hydroxide (112 mg, 2 mmol), a clear solution was formed which was

stirred for 10 minutes. Furthermore, an aqueous NH_3 solution (15 mL) was added dropwise using a dropping funnel with constant stirring over 30 minutes. After 15 minutes, white precipitate started to appear. The reaction mixture was stirred overnight, a white precipitate was filtered, washed with water and dried in air. Yield: 300 mg (82%). Melting point: 118 ^oC. ^1H NMR ($CDCl_3$): δ 8.81 (d, 4H), 8.09 (d, 2H), 8.02 (d, 4H), 7.75 (d, 2H), 7.19 (d, 2H), 4.82 (s, 2H), 2.62 (s, 1H). HRMS (ESI-TOF): *m/z* calcd for $[(4,4\text{-terpyBA})H]^+$, 364.1405; found, 364.1408.

4'-(4-(prop-2-yn-1-yloxy)phenyl)-2,2':6',2''-terpyridine (2,2-terpyBA). In a 20 mL RB, 4-(prop-2-yn-1-yloxy)benzaldehyde (160 mg, 1 mmol) was added to an ethanolic solution of 2-acetylenepyridine (242 mg, 2 mmol) with constant stirring at room temperature. Upon addition of potassium hydroxide (112 mg, 2 mmol), a clear solution was formed which was stirred for 10 minutes. Furthermore, an aqueous NH_3 solution (20 mL) was added dropwise using a drooping funnel with constant stirring over 30 minutes. After 15 minutes, greenish white precipitate started appearing and the reaction mixture was stirred overnight. The green color precipitate was filtered, washed with water and dried in air. The precipitate was then dissolved in $CHCl_3$ and passed through a silica-column to obtain the pure product. A pale-yellow solution eluted out from the column was then evaporated under reduced pressure to dryness. A pale-yellow solid product was obtained. Yield: 285 mg (78%). Melting point: 175-178 ^oC. ^1H NMR ($CDCl_3$): δ 8.76 (d, 2H), 8.72 (t, 2H), 7.95 (d, 2H), 7.93 (d, 2H), 7.40 (d, 2H), 7.13 (d, 2H), 4.80 (s, 2H), 2.59 (s, 1H). HRMS (ESI-TOF): *m/z* calcd for $[(2,2\text{-terpyBA})H]^+$, 364.1405; found, 364.1421.

5-(bis(pyridin-2-ylmethyl)amino)isophthalic acid (H_2-bpaipa). In *step 1*, 5-(bis(pyridin-2-ylmethyl)amino)isophthalic acid was prepared with some modifications in the reported procedure. In a 50 mL RBF, 10 mL methanolic solution of 5-aminoisophthalic acid (1.81 g, 10 mmol) was taken, to which trimethylamine (2 mL) was added and stirred for 15 min. Subsequently, 2-pyridinecarboxaldehyde (0.98 mL, 10 mmol) was added and stirred for 8 h. An excess of sodium borohydride (2 eq.) was added slowly to the above solution at 0 °C and stirred for another 10 h. Upon evaporation of most of the solvent under reduced pressure, the resulting slurry was poured into 20 mL of ice-cold water followed by addition of few drops of acetic acid to make the pH 5–6. A yellow-white precipitate was isolated after evaporation of the solvent. Its melting point and ^1H NMR data were matched with the literature values, confirming its identity and purity. This was used in the next step without any purification. Yield: 1.35 g (52%).

In *step 2*, to an aqueous solution (8 mL) of the reduced Schiff base obtained in the first step (0.5 g, 2 mmol), picolyl chloride hydrochloride (0.32 g, 2 mmol) was added and the mixture was stirred for 5 min. After adding sodium hydroxide solution (0.16 g in 1 mL of water) dropwise over a period of 20 min, the mixture was stirred for 24 h at room temperature. The aqueous reaction mixture was washed 3–4 times with chloroform followed by the addition of 1 mL of dil. HCl. A yellow solid was obtained. Further work-up to remove NaCl using dry MeOH provided the desired product. Yield: 583 mg (85%).^{1}H NMR (D_2O): δ 8.33 (d, 2H), 7.65 (d, 2H), 7.48 (s, 1H), 7.21 (d, 2H), 7.19 (d, 2H), 4.76 (s, 4H). HRMS (ESI-TOF): *m/z* calcd for [(2,2-H_2bpaipa)H]$^{+}$, 364.1252; found, 364.1284.

5-((pyridin-2-ylmethyl)(pyridin-3-ylmethyl)amino)isophthalic acid (2,4-H_2bpaipa). It was synthesized by following the same procedure as above, except that 4-pyridine carboxyaldehyde was used instead of 2-pyridine carboxaldehyde. *Step 1* (5-((4-carboxybenzyl)amino)isophthalic acid), To a stirred solution of 5-aminoisophthalic acid (724 mg, 4 mmol) dissolved in 6 mL MeOH placed in a 25 mL RBF, triethylamine (2 mL) was added, followed by the addition of 4-pyridine carboxaldehyde (428 mg, 4 mmol). The resulting reaction mixture was then allowed to stir for 5 h at room temperature. The mixture was cooled by placing the RBF in an ice bath. To the yellow reaction mixture, $NaBH_4$ (303 mg, 8 mmol) was added slowly and stirred for 12 h to yield a light yellow solution. Methanol was evaporated under reduced pressure and the product was poured into ice cold water. After the addition of a few drops of acetic acid, a white solid was formed. The solid was filtered and washed with water several times followed by drying in air. Yield: 707 mg (65%). Its melting point and ^{1}H NMR data were matched with the literature values, confirming its identity and purity. This was used in the next step without any purification.
In *Step 2,* ((4-carboxybenzyl)amino)isophthalic acid (544 mg, 2 mmol) was added in 5 mL water followed by addition of 4-picolyl chloride solution (328 mg, 2 mmol in 1 mL water). After this, sodium hydroxide solution (120 mg, 3 mmol in 2 mL water) was added dropwise upon which the reaction mixture turns from light yellow to dark red. The reaction mixture was allowed to stir for 24 h at room temperature. The aqueous reaction mixture was washed 3–4 times with chloroform followed by the addition of 1 mL of dil. HCl. A yellow solid was formed after some time which was collected by filtration through filter paper. Yield: 443 mg (60%). Melting point: 300 ^{o}C. ^{1}H NMR (D_2O): δ 8.54 (m, 3H), 7.90 (m, 1H), 7.74 (m, 3H), 7.32 (m, 4H), 4.90 (s, 2 H), 4.82 (s, 2 H). HRMS (ESI-TOF): *m/z* calcd for [(2,4-H_2bpaipa)H]$^{+}$, 364.1253; found, 364.1267.

5-((4-carboxybenzyl)(pyridin-2-ylmethyl)amino)isophthalic acid (H_3pbaipa). *Step 1,* To a stirred solution of 5-aminoisophthalic acid (181 mg, 1 mmol) in 6 mL MeOH placed in a 25 mL RBF, triethylamine (1 mL) was added followed by the addition of 4-formyl benzoic acid (150 mg, 1 mmol). The reaction mixture was then allowed to stir for 6 h at room temperature. The reaction mixture was cooled to 0-4 °C by placing the RBF in an ice bath. To this stirred cooled yellow reaction mixture, excess $NaBH_4$ (2 eq.) was added slowly and then stirred further for another 12 h. After some time, the color of the reaction mixture faints from the original. The solvent was evaporated under reduced pressure and the resulting slurry was poured into ice cold water. After the addition of a few drops of acetic acid, a white precipitate started to appear. This was filtered and washed with water 5-6 times followed by drying in air. Yield: 160 mg (51%). Melting point: 300 ^oC. ^1H NMR (D_2O): δ 7.55 (s, 2H), 7.39 (s, 1H), 7.18 (d, 2H), 7.09 (d, 2H), 4.13 (s, 2 H).

Step 2, In a 10 mL RBF, the product formed from the first step ((4-carboxybenzyl)amino)isophthalic acid (100 mg, 0.32 mmol) was mixed in 6 mL water. A solution of 2-picolyl chloride (53 mg, 0.32 mmol) dissolved in 1 mL water was added to this stirred solution. After that, a solution of sodium hydroxide (51 mg, 1.2 mmol in 2 mL water) was added dropwise to the above stirred reaction mixture. The color of the compound changed to dark red from light yellow. It was allowed to stir for another 24 h. It was the poured into ice cold water followed by an addition of 1 mL dilute HCl solution dropwise. After some time, white precipitate started to appear. The solid was filtered, washed with water and dried in air. Yield: 85 mg (60%). Melting point: 292-296 ^oC. ^1H NMR (D_2O): δ 8.51 (d, 2H), 8.07 (d, 2H), 7.96 (s, 1H), 7.82 (s, 2H), 7.52 (d, 2H), 7.41 (m, 4H), 4.95 (s, 4H). HRMS (ESI-TOF): *m/z* calcd for $[(H_3pbaipa)H]^+$, 407.1198; found, 407.1219.

5,5'-((1,3-phenylenebis(methylene))bis(azanediyl))diisophthalic acid (H_4daib). In a 25 mL RBF, 5-aminoisopthalic acid (362 g, 2 mmol) was added to a 10 mL methanol followed by addition of isophthaldehyde (134 mg, 1 mmol). To this stirred reaction mixture, triethylamine (2 mL) was added and stirred for 5 h at room temperature. Furthermore, this reaction mixture was cooled to 0-4 °C using an ice bath and excess of $NaBH_4$ was added slowly. The reaction mixture was stirred for 4 h at 4 °C and again 10 h at room temperature. The solvent was evaporated under reduced pressure and the resulting slurry was poured into 15 mL ice cold water followed by addition of few drop of hydrochloride solution to get the pH 3-4. At this pH, white precipitate was formed which was filtered, washed several times with water and dried in air. Yield: 705 mg (76%). Melting Point: 321 °C. ^1H NMR

(D_2O): δ 7.48 (s, 2H), 7.27 (s, 1H), 7.15-7.19 (m, 7H), 4.18 (s, 4 H). HRMS (ESI-TOF): *m/z* calcd for $[(H_4pbaipa)Na]^+$, ; 488.1151, found; 488.1100

5,5'-((1,3-phenylenebis(methylene))bis(azanediyl))diisophthalic acid (H_4bdaib). To an aqueous solution of the H_4daib (232 mg, 0.5 mmol), 2-picolylchloride hydrochloride salt (164 mg, 1 mmol) was added. A sodium hydroxide solution (160 mg, 2 mmol in 5 mL water) was added to the above stirred reaction mixture dropwise and was stirred for another 24 h. The resulting slurry was poured into ice cold water followed by addition of a few drop of dil. HCl to get the pH 3-4. The white precipitate thus obtained was filtered and washed 4-5 times with water followed by drying in air. Yield: 200 mg, melting point: 218 °C. ^{1}H NMR (D_2O): δ 8.53 (d, 2H), 7.70 (m, 4H), 7.40 (m, 4H), 7.26-7.184 (m, 8H).81 (s, 4H), 4.74 (s, 4H). HRMS (ESI-TOF): *m/z* calcd for $[(H_4pbaipa)Na]^+$, 669.1961; found, 669.1917.

2.4 Synthesis of Compounds

$[Ni_2(adc)_2(6\text{-mebpta})_2]\cdot 2H_2O$ (1) To a stirred solution of $Ni_2(OAc)_2\cdot 4H_2O$ (49.6 mg, 0.2 mmol) and 6-Mebpta (53.8 mg, 0.2 mmol) in 4 mL methanol, acetylene dicarboxylic acid (22.8 mg, 0.2 mmol) was added. The reaction mixture was stirred for another 4 h at room temperature. The resulting slurry was evaporated to dryness and treated with 4 mL of an acetonitrile-toluene mixture (50:50 v/v) to get rid-off the acetic acid by-product affording a green solid. Yield: 65 mg (72%). Single crystals were obtained by slow evaporation of its aqueous solution. Anal. Calcd for $C_{42}H_{54}N_6O_{12}Ni_2$ (MW 952.29) (4 H_2O): C, 52.97; H, 5.72; N, 8.82. Found: C, 52.88; H, 5.35; N, 7.95. It should be noted that the formula used for the calculation of CHN analysis was with four water molecules although other characterizations including X-ray crystallography indicated that it has two water molecules. Selected FTIR peaks (KBr, cm^{-1}): 3408 (br), 1624 (m), 1607 (s), 1596 (s), 1552 (m), 1401 (m), 1377 (s), 1352 (s), 1195 (m), 792 (m), 779 (m), 772 (m), 690 (m). Selected Raman peaks (cm^{-1}): 2203, 1575, 1399, 1027, 772.

$[Ni_2(fumarate)(6\text{-}Mebpta)_2(H_2O)_2](fumarate)\cdot 9H_2O$ (2⊃fumarate) To a stirred solution of $Ni(OAc)_2\cdot 4H_2O$ (49.6 mg, 0.2 mmol) and 6-Mebpta (53.8 mg, 0.2 mmol) in 4 mL methanol, fumaric acid (23.2 mg, 0.2 mmol) was added. The reaction mixture was stirred for 4 h at room temperature. The resulting slurry was evaporated to dryness under reduced pressure, treated with acetonitrile-toluene mixture (50:50 v/v) to get rid-off of the acetic acid affording a green solid. Yield: 75 mg (69%). Single crystals were obtained by slow evaporation of its solution of water and acetonitrile. Anal. Calcd for $C_{42}H_{62}N_6O_{14}Ni_2$ (MW

992.36) ($6H_2O$): C, 50.83; H, 6.30; N, 8.47. Found: C, 50.36; H, 5.91; N, 8.40. Selected FTIR peaks (KBr, cm^{-1}): 3403 (br), 3274 (br), 2971 (m), 1704 (w), 1605 (s), 1581 (s), 1561 (s), 1403 (m), 1385 (s), 1262 (m), 1126 (m), 1023 (m), 978 (m), 803 (m), 776 (m), 680 (m). Selected Raman peaks (cm^{-1}): 1665, 1607, 1577, 1272, 1024, 772.

$[Ni_2(succinate)(6\text{-}Mebpta)_2(H_2O)_2](Hsuccinate)_2{\cdot}4H_2O$ (3⊃Hsuccinate) To a stirred solution of $Ni(OAc)_2{\cdot}4H_2O$ (49.6 mg, 0.2 mmol) and 6-Mebpta (53.8 mg, 0.2 mmol) in 4 mL methanol, succinic acid (23.6 mg, 0.2 mmol) was added. The reaction mixture was stirred for 4 h at room temperature. The resulting slurry was evaporated to dryness under reduced pressure, treated with acetonitrile-toluene mixture (50:50 v/v) to get rid-off of the acetic acid affording a green solid. Yield: 65 mg (67%). Single crystals were obtained by slow evaporation of its solution of water and acetonitrile. Anal. Calcd for $C_{42}H_{68}N_6O_{16}Ni_2$ (MW 1078.33): C, 51.23; H, 6.36; N, 7.79. Found: C, 48.40; H, 6.39; N, 7.64. Selected FTIR peaks (KBr, cm^{-1}): 3411 (br), 3221 (br), 2984 (m), 1718 (w), 1653 (m), 1608 (s), 1570 (m), 1542 (m), 1434 (m), 1404 (s), 1190 (m), 778 (m), 684 (m). Selected Raman peaks (cm^{-1}): 1577, 1449, 1272, 1024, 833.

$[Ni_2(glutarate)(6\text{-}Mebpta)_2(H_2O)_2](ClO_4){\cdot}H_2O$ (4) To a stirred solution of $Ni(OAc)_2{\cdot}4H_2O$ (25 mg, 0.1 mmol) and 6-Mebpta (27 mg, 0.1 mmol) in 4 mL methanol, glutaric acid (13.2 mg, 0.1 mmol) was added. The reaction mixture was stirred for 4 h at room temperature. The resulting slurry was evaporated to dryness under reduced pressure, treated with acetonitrile-toluene mixture (50:50 v/v) to get rid-off of the acetic acid affording a green sticky substances. This sticky substance was again dissolved in water and sodium perchlorate (0.05 mmol) was added to it, after evaporation of the solvent green color solid compound was formed. Yield: 29 mg (60%). Anal. Calcd for $C_{39}H_{58}N_6O_{11}ClNi_2$ (MW 939.75): C, 49.84; H, 6.22; N, 8.94. Found: C, 49.98; H, 7.01; N, 9.03. Selected FTIR peaks (KBr, cm^{-1}): 3460 (br), 1607 (m), 1546 (s), 1466 (s), 1438 (s), 1181 (m), 757 (m), 623 (m).

$[Ni_2(Me\text{-}glutarate)(6\text{-}Mebpta)_2(H_2O)_2](ClO_4){\cdot}3H_2O$ (5) To a stirred solution of $Ni(OAc)_2{\cdot}4H_2O$ (25 mg, 0.1 mmol) and 6-Mebpta (27 mg, 0.1 mmol) in 4 mL methanol, 3-methylglutaric acid (14.6 mg, 0.1 mmol) was added. The reaction mixture was stirred for 4 h at room temperature. The resulting slurry was evaporated to dryness under reduced pressure, treated with acetonitrile-toluene mixture (50:50 v/v) to get rid-off of the acetic acid affording a green color sticky substances, which was dissolved in water and sodium perchlorate (0.05 mmol) was added to it, and after evaporation of the solvent green color solid compound was formed. Yield: 39 mg (78%). Anal. Calcd for $C_{40}H_{64}N_6O_{13}ClNi_2$ (MW

989.80): C, 48.54; H, 6.52; N, 8.49. Found: C, 47.99; H, 6.85; N, 8.01. Selected FTIR peaks (KBr, cm^{-1}): 3468 (br), 1607 (m), 1579 (s), 1551 (s), 1462 (s), 1438 (m), 1084 (s), 763 (m), 625 (m).

{[Zn_2(adc)$_2$(6-mebpta)$_2$]·2H_2O}$_n$ (6) To the stirred solution of $Zn(OAc)_2{\cdot}2H_2O$ (22 mg, 0.1 mmol) and 6-Mebpta (27 mg, 0.1 mmol) in 4 mL methanol, acetylene dicarboxylic acid (12 mg, 0.1 mmol) was added. The reaction mixture was stirred for another 4-5 h at room temperature. The resulting precipitate was filtered through filter paper, washed with methanol and dried in air affording a yellow solid. Yield: 37 mg (79%). Anal. Calcd for $C_{42}H_{50}N_6O_{10}Zn_2$ (MW 929.64): C, 54.26; H, 5.42; N, 9.04. Found: C, 54.10; H, 4.87; N, 8.29. Selected FTIR peaks (KBr, cm^{-1}): 3445 (br), 1628 (s), 1614 (s), 1327 (s), 1018 (m), 758 (m), 676 (m).

{[Cd_2(adc)$_2$(6-mebpta)$_2$]·4H_2O}$_n$ (7) To the stirred solution of $Cd(OAc)_2{\cdot}2H_2O$ (26 mg, 0.1 mmol) and 6-Mebpta (27 mg, 0.1 mmol) in 4 mL methanol, acetylene dicarboxylic acid (22.8 mg, 0.2 mmol) was added. The reaction mixture was stirred for another 4-5 h at room temperature. The resulting precipitate was filtered through filter paper, washed with methanol and dried in air affording a yellow solid. Yield: 45 mg (83%). Anal. Calcd for $C_{42}H_{54}N_6O_{12}Cd_2$ (MW 1059.73): C, 47.60; H, 5.14; N, 7.93. Found: C, 48.20; H, 5.97; N, 8.10. Selected FTIR peaks (KBr, cm^{-1}): 3424 (b), 1605 (s), 1452 (w), 1346 (s), 772 (m), 685 (m).

{[Zn_2(bdc)$_2$(6-mebpta)$_2$]·2H_2O}$_n$ (8) To the stirred solution of $Zn(OAc)_2{\cdot}2H_2O$ (22 mg, 0.1 mmol) and 6-Mebpta (27 mg, 0.1 mmol) in 4 mL methanol, 1,4-benzene dicarboxylic acid (16.6 mg, 0.1 mmol) was added. The reaction mixture was stirred for another 2 h at room temperature till all the components get dissolved in solution. After this, white precipitate started appearing so, it was stirred further for 6 h at room temperature. The resulting precipitate was filtered through a filter paper, washed with methanol and acetonitrile toluene mixture (1:1) and dried in air affording a white solid. Yield: 45 mg (86%). Anal. Calcd for $C_{50}H_{58}N_6O_{10}Zn_2$ (MW 1033.78): C, 58.09; H, 5.65; N, 8.13. Found: C, 58.95; H, 6.10; N, 8.83. Selected FTIR peaks (KBr, cm^{-1}): 3440 (br), 1608 (s), 1367 (s), 1027 (m), 822 (w), 781 (m), 753 (m).

{[Cd_2(bdc)$_2$(6-mebpta)$_2$]·3H_2O}$_n$ (9) To the stirred solution of $Cd(OAc)_2{\cdot}2H_2O$ (26 mg, 0.1 mmol) and 6-Mebpta (27 mg, 0.1 mmol) in 4 mL methanol, 1,4-benzene dicarboxylic acid (16.6 mg, 0.1 mmol) was added. The reaction mixture was stirred for another 2 h at room temperature till all the components get dissolved in solution. After this, yellow precipitate started appearing so, it was stirred further for 6 h at room temperature. The

resulting precipitate was filtered through filter paper, washed with methanol and acetonitrile toluene mixture (1:1) followed by drying in air affording a yellow--white solid. Yield: 30 mg (52%). Anal. Calcd for $C_{50}H_{60}N_6O_{11}Cd_2$ (MW 1145.86): C, 52.41; H, 5.28; N, 7.33. Found: C, 53.35; H, 5.01; N, 7.98. Selected FTIR peaks (KBr, cm^{-1}): 3422 (br), 1603 (w), 1571 (s), 1385 (s), 1016 (w), 835 (m), 753 (m).

$\{[Cu_2(bdc)_2(6\text{-mebpta})_2]\cdot 4H_2O\}_n$ (10) To the stirred solution of $Cu(OAc)_2\cdot H_2O$ (20 mg, 0.1 mmol) and 6-Mebpta (27 mg, 0.1 mmol) in 4 mL methanol, 1,4-benzene dicarboxylic acid (16.6 mg, 0.1 mmol) was added. The reaction mixture was stirred for another 2 h at room temperature till all the components get dissolved in solution. After this, blue green precipitate started appearing so, it was stirred further for 6 h at room temperature. The resulting precipitate was filtered through filter paper, washed with methanol and acetonitrile toluene mixture (1:1) and dried in air affording a blue green solid. Yield: 33 mg (62%). Anal. Calcd for $C_{50}H_{62}N_6O_{12}Cu_2$ (MW 1066.15): C, 56.33; H, 5.86; N, 7.88. Found: C, 55.01; H, 6.11; N, 7.82. Selected FTIR peaks (KBr, cm^{-1}): 3422 (br), 1686 (m), 1607 (s), 1589 (s), 1391 (s), 1355 (s), 1290 (m), 1016 (w), 749 (s).

$\{[Mn_2(bdc)_2(6\text{-mebpta})_2]\cdot 5H_2O\}_n$ (11) To the stirred solution of $Mn(OAc)_2\cdot 4H_2O$ (25 mg, 0.1 mmol) and 6-Mebpta (27 mg, 0.1 mmol) in 4 mL methanol, 1,4-benzene dicarboxylic acid (16.6 mg, 0.1 mmol) was added. The reaction mixture was stirred for another 2 h at room temperature till all the components get dissolved in solution. After this, white precipitate started appearing so, it was stirred further for 6 h at room temperature. The resulting precipitate was filtered through filter paper, washed with methanol and acetonitrile toluene mixture (1:1) and dried in air affording a white solid. Yield: 37 mg (68%). Anal. Calcd for $C_{50}H_{64}N_6O_{13}Mn_2$ (MW 1066.95): C, 56.29; H, 6.05; N, 7.88. Found: C, 55.72; H, 7.10; N, 7.10. Selected FTIR peaks (KBr, cm^{-1}): 3404 (br), 1577 (s), 1392 (s), 1017 (w), 750 (m), 522 (m).

$\{[Co_2(bdc)_2(6\text{-mebpta})_2]\}_n$ (12) To the stirred solution of $Co(OAc)_2\cdot 4H_2O$ (25 mg, 0.1 mmol) and 6-Mebpta (27 mg, 0.1 mmol) in 4 mL methanol, 1,4-benzene dicarboxylic acid (16.6 mg, 0.1 mmol) was added. The reaction mixture was stirred for another 2 h at room temperature till all the components get dissolved in solution. After this, dark pink precipitate started appearing so, it was stirred further for 6 h at room temperature. The resulting precipitate was filtered through filter paper, washed with methanol and of acetonitrile toluene mixture (1:1) and dried in air affording a dark pink solid. Yield: 41 mg (82%). Anal. Calcd for $C_{50}H_{54}N_6O_8Co_2$ (MW 984.86): C, 58.82; H, 5.73; N, 8.23. Found:

C, 59.10; H, 5.99; N, 7.97. Selected FTIR peaks (KBr, cm^{-1}): 3422 (br), 1571 (s), 1385 (m), 1356 (s), 1018 (m), 820 (m), 750 (m), 516 (w).

{[Ni_2(adc)$_2$(6-mebpea)$_2$]·7H_2O}$_n$ (13) To a mixture of $Ni(OAc)_2{\cdot}4H_2O$ (49 mg, 0.2 mmol) and 6-Mebpea (49 mg, 0.2 mmol) in 4 mL methanol, acetylene dicarboxylic acid (22 mg, 0.2 mmol) was added. The reaction mixture was stirred for another 4 h at room temperature. The resulting slurry was evaporated to dryness using reduced pressure, treated with 4 mL of an acetonitrile-toluene mixture (50:50 v/v) to get rid-off the acetic acid by-product affording a green solid. Yield: 70 mg (74%). Anal. Calcd for $C_{38}H_{52}N_6O_{15}Ni_2$ (MW 950.23): C, 48.03; H, 5.52; N, 8.84. Found: C, 49.01; H, 5.95; N, 8.54. Selected FTIR peaks (KBr, cm^{-1}): 3382 (br), 1590 (s), 1355 (s), 774 (m), 685 (m).

{[Ni_2(fumarate)$_2$(6-mebpea)$_2$]·2H_2O·3MeOH}$_n$ (14) To a mixture of $Ni(OAc)_2{\cdot}4H_2O$ (49 mg, 0.2 mmol) and 6-Mebpea (49 mg, 0.2 mmol) in 4 mL methanol, fumaric acid (22 mg, 0.2 mmol) was added. The reaction mixture was stirred for another 4 h at room temperature. The resulting slurry was evaporated to dryness using reduced pressure, treated with 4 mL of an acetonitrile-toluene mixture (50:50 v/v) to get rid-off the acetic acid by-product affording a green solid. Yield: 40 mg (41%). Anal. Calcd for $C_{41}H_{58}N_6O_{13}Ni_2$ (MW 960.31): C, 51.28; H, 5.91; N, 8.75. Found: C, 50.34; H, 6.97; N, 8.90. Selected FTIR peaks (KBr, cm^{-1}): 3392 (br), 1559 (s), 1393 (s), 1213 (w), 980 (w), 802 (m), 689 (m).

{[Zn_2(adc)$_2$(6-mebpea)$_2$]·9H_2O}$_n$ (15) To a mixture of $Zn(OAc)_2{\cdot}2H_2O$ (44 mg, 0.2 mmol) and 6-Mebpea (49 mg, 0.2 mmol) in 4 mL methanol, acetylene dicarboxylic acid (22 mg, 0.2 mmol) was added. The reaction mixture was stirred for another 4 h at room temperature. The resulting slurry was evaporated to dryness using reduced pressure, treated with 4 mL of an acetonitrile-toluene mixture (50:50 v/v) to get rid-off the acetic acid by-product affording a yellow solid. Yield: 58 mg (58%). Anal. Calcd for $C_{38}H_{56}N_6O_{17}Zn_2$ (MW 999.64): C, 45.66; H, 5365; N, 8.41. Found: C, 44.96; H, 6.25; N, 8.97. Selected FTIR peaks (KBr, cm^{-1}): 3377 (br), 1636 (s), 1602 (s), 1379 (s), 1327 (s), 1171 (w), 1018 (w), 768 (m), 686 (m).

{[Cd_2(adc)$_2$(6-mebpea)$_2$]·8H_2O}$_n$ (16) To a mixture of $Cd(OAc)_2{\cdot}2H_2O$ (53 mg, 0.2 mmol) and 6-Mebpea (49 mg, 0.2 mmol) in 4 mL methanol, acetylene dicarboxylic acid (22 mg, 0.2 mmol) was added. The reaction mixture was stirred for another 4 h at room temperature. The resulting slurry was evaporated to dryness using reduced pressure, treated with 4 mL of an acetonitrile-toluene mixture (50:50 v/v) to get rid-off the acetic acid by-product affording a yellow solid. Yield: 70 mg (65%). Anal. Calcd for $C_{38}H_{56}N_6O_{17}Cd_2$ (MW 1093.70): C, 41.73; H, 5.16; N, 7.68. Found: C, 42.32; H, 4.83; N, 7.67. Selected FTIR

peaks (KBr, cm^{-1}): 3415 (br), 1619 (s), 1351 (s), 1328 (s), 1169 (w), 990 (w), 779 (m), 673 (m).

[Ni(adc)(6,6′-Me$_2$bpta)(H$_2$O)]·H$_2$O (17) To a solution of Ni(OAc)$_2$·4H$_2$O (24 mg, 0.1 mmol) and 6,6′-Me$_2$bpta (28 mg, 0.1 mmol) in 4 mL methanol, acetylene dicarboxylic acid (11 mg, 0.1 mmol) was added. The reaction mixture was stirred for 4 h at room temperature. The resulting slurry was evaporated to dryness under reduced pressure, treated with acetonitrile-toluene mixture (50:50 v/v) to get rid-off of the acetic acid affording a green solid. Yield: 30 mg (66%). Single crystals were obtained by slow evaporation of its water-acetonitrile aqueous solution. Anal. Calcd for $C_{22}H_{29}N_3O_6Ni$ (MW 490.17): C, 52,91; H, 5.96; N, 8.57. Found: C, 52.70; H, 5.79; N, 8.41. CHN calculation is with 1.5 water molecules. Selected FTIR peaks (KBr, cm^{-1}): 3435 (br), 3221 (br), 1704 (m), 1607 (s), 1590 (s), 1407 (m), 1340 (s), 1226 (m), 1192 (m), 1022 (m), 789 (m), 690 (m). Selected Raman peaks (cm^{-1}): 2233, 1401, 1003, 775.

[Ni$_2$(fumarate)$_2$(6,6′-Me$_2$bpta)$_2$]·5H$_2$O (18) To a solution of Ni(OAc)$_2$·4H$_2$O (24 mg, 0.1 mmol) and 6,6′-Me$_2$bpta (28 mg, 0.1 mmol) in 4 mL methanol, fumaric acid (11 mg, 0.1 mmol) was added. The reaction mixture was stirred for 4 h at room temperature. The resulting slurry was evaporated to dryness under reduced pressure, treated with acetonitrile-toluene mixture (50:50 v/v) to get rid-off of the acetic acid affording a green solid. Yield: 40 mg (83%). Anal. Calcd for $C_{44}H_{64}N_6O_{13}Ni_2$ (MW 1002.39): C, 52,72; H, 6.44; N, 8.38. Found: C, 52.04; H, 5.76; N, 7.52. Selected FTIR peaks (KBr, cm^{-1}): 3411 (br), 1607 (m), 1579 (s), 1466 (w), 1372 (s), 1227 (w), 1188 (w), 982 (w), 784 (m), 679 (m). Selected Raman peaks (cm^{-1}): 1652, 1580, 1400, 1014, 776

[Ni$_2$(succinate)$_2$(6,6′-Me$_2$bpta)$_2$]·6H$_2$O (19) To a solution of Ni(OAc)$_2$·4H$_2$O (24 mg, 0.1 mmol) and 6,6′-Me$_2$bpta (28 mg, 0.1 mmol) in 4 mL methanol, succinic acid (11 mg, 0.1 mmol) was added. The reaction mixture was stirred for 4 h at room temperature. The resulting slurry was evaporated to dryness under reduced pressure, treated with acetonitrile-toluene mixture (50:50 v/v) to get rid-off of the acetic acid affording a green solid. Yield: 31 mg (63%). Anal. Calcd for $C_{44}H_{70}N_6O_{14}Ni_2$ (MW 1024.44): C, 51,59; H, 6.88; N, 8.20. Found: C, 51.17; H, 6.10; N, 7.70. Selected FTIR peaks (KBr, cm^{-1}): 3400 (br), 1606 (s), 1566 (s), 1466 (m), 1436 (m), 1407 (s), 1219 (w), 1193 (w), 1010 (w), 786 (m), 665 (m), 657 (m). Selected Raman peaks (cm^{-1}): 1605, 1580, 1278, 1014, 767.

[Mn$_2$(adc)$_2$(6,6′-Me$_2$bpta)$_2$]·2H$_2$O (20) To a solution of Mn(OAc)$_2$·4H$_2$O (24 mg, 0.1 mmol) and 6,6′-Me$_2$bpta (28 mg, 0.1 mmol) in 4 mL methanol, acetylene dicarboxylic acid (11 mg, 0.1 mmol) was added. The reaction mixture was stirred for 4 h at room temperature.

The resulting slurry was evaporated to dryness under reduced pressure, treated with acetonitrile-toluene mixture (50:50 v/v) to get rid-off of the acetic acid affording a light yellow solid. Yield: 29 mg (63%). Anal. Calcd for $C_{44}H_{54}N_6O_{10}Mn_2$ (MW 936.80): C, 56.41; H, 5.81; N, 8.97. Found: C, 56.20; H, 6.10; N, 8.31. Selected FTIR peaks (KBr, cm^{-1}): 3454 (br), 1583 (s), 1463 (s), 1361 (s), 774 (m), 693 (m).

[Mn_2(fumarate)$_2$(6,6′-Me_2bpta)$_2$]·H_2O (21) To a solution of $Mn(OAc)_2{\cdot}4H_2O$ (24 mg, 0.1 mmol) and 6,6′-Me_2bpta (28 mg, 0.1 mmol) in 4 mL methanol, fumaric acid (11 mg, 0.1 mmol) was added. The reaction mixture was stirred for 4 h at room temperature. The resulting slurry was evaporated to dryness under reduced pressure, treated with acetonitrile-toluene mixture (50:50 v/v) to get rid-off of the acetic acid affording a light yellow solid. Yield: 31 mg (68%). Anal. Calcd for $C_{44}H_{56}N_6O_9Mn_2$ (MW 922.82): C, 57.27; H, 6.12; N, 9.11. Found: C, 56.92; H, 6.35; N, 8.97. Selected FTIR peaks (KBr, cm^{-1}): 3417 (br), 1565 (s), 1398 (s), 1218 (m), 836 (m), 663 (m).

{[Zn_2(adc)$_2$(6,6′-Me_2bpta)$_2$]}$_n$ (22) To a solution of $Zn(OAc)_2{\cdot}2H_2O$ (21 mg, 0.1 mmol) and 6,6′-Me_2bpta (28 mg, 0.1 mmol) in 4 mL methanol, acetylene dicarboxylic acid (11 mg, 0.1 mmol) was added. The reaction mixture was stirred for 4 h at room temperature. The resulting white precipitate were filtered through filter paper and washed with acetonitrile-toluene mixture (50:50 v/v) to get rid-off of the acetic acid. Yield: 33 mg (75%). Anal. Calcd for $C_{44}H_{50}N_6O_8Zn_2$ (MW 921.66) (2 H_2O): C, 57.34; H, 5.47; N, 9.12. Found: C, 56.10; H, 6.21; N, 8.89. Selected FTIR peaks (KBr, cm^{-1}): 3417 (br), 1642 (s), 1614 (s), 1467 (m), 1332 (s), 1093 (m), 779 (m), 674 (m).

{[Cd_2(adc)$_2$(6,6′-Me_2bpta)$_2$]·2H_2O}$_n$ (23) To a solution of $Cd(OAc)_2{\cdot}2H_2O$ (26 mg, 0.1 mmol) and 6,6′-Me_2bpta (28 mg, 0.1 mmol) in 4 mL methanol, acetylene dicarboxylic acid (11 mg, 0.1 mmol) was added. The reaction mixture was stirred for 4 h at room temperature. The resulting yellow- white precipitate were filtered through filter paper and washed with acetonitrile-toluene mixture (50:50 v/v) to get rid-off of the acetic acid. Yield: 37 mg (73%). Anal. Calcd for $C_{44}H_{54}N_6O_{10}Cd_2$ (MW 1051.75): C, 50.25; H, 5.18; N, 7.99. Found: C, 51.01; H, 5.89; N, 8.92. Selected FTIR peaks (KBr, cm^{-1}): 3417 (br), 1618 (s), 1604 (s), 1585 (s), 1464 (m), 1327 (s), 1089 (m), 837 (m), 777 (m), 688 (m).

{[Cd_2(Hbtc)$_2$(6-mebpea)$_2$]}$_n$ (24) A mixture of $Cd(OAc)_2{\cdot}2H_2O$ (26.6 mg, 0.1 mmol), 6-mebpea (24 mg, 0.1 mmol), H_3btc (14 mg, 0.066 mmol) in 0.5 mL distilled H_2O and 0.5 mL MeOH was sealed in a 10 mL Teflon-lined stainless steel container and heated at 120 °C for 3 days. The mixture was cooled to room temperature at a rate of 5 °C/h, colorless block crystals of compound were obtained with mother liquor. The solution with crystals

was evaporated to dryness and then treated with 2 mL of an acetonitrile-toluene mixture (50:50 v/v) to get rid-off the acetic acid by-product affording an off yellow solid. Yield: 37 mg (67%). Anal. Calcd for $C_{48}H_{46}N_6O_{12}Cd_2$ (MW 1123.73): Calc. C, 51.30; H, 4.12; N, 7.47. Found: C, 49.20; H, 4.19; N, 7.45. Selected FTIR peaks (KBr, cm^{-1}): 3406 (Br), 3101 (m), 2968 (m), 2938 (m), 1683 (m), 1613 (s), 1575 (s), 1567 (s), 1557 (s), 1440 (m), 1368 (m), 1170 (m), 1099 (w), 1015 (w), 785 (w), 758 (w), 730 (w), 675 (m), 521 (m).

$\{[Cd_2(H_2btc)(btc)(6\text{-mebpta})_2]\}_n$ (25) A mixture of $Cd(OAc)_2{\cdot}2H_2O$ (26.6 mg, 0.1 mmol), 6-mebpta (27 mg, 0.1 mmol), H_3btc (14 mg, 0.066 mmol) in 0.5 mL distilled H_2O and 0.5 mL MeOH was sealed in a 10 mL Teflon-lined stainless steel container and heated at 120 °C for 3 days. After the mixture cooled to room temperature at a rate of 5 °C/h, colorless block crystals were obtained. The resulting slurry was evaporated to dryness and then treated with 2 mL of an acetonitrile-toluene mixture (50:50 v/v) to get rid-off the acetic acid by-product affording a yellow solid. Yield: 42 mg (73%). Anal. Calcd for $C_{52}H_{54}N_6O_{12}Cd_2$ (MW 1179.84): Calc. C, 52.94; H, 4.61; N, 7.12. Found: C, 50.96; H, 4.46; N, 6.60. Selected FTIR peaks (KBr, cm^{-1}): 3315 (Br), 2913 (m), 2542 (m), 1682 (s), 1610 (s), 1570 (m), 1401 (s), 1399 (m), 1367 (m), 1281 (m), 1247 (m), 1199 (m), 1111 (w), 744 (w), 690 (m), 525, (m) 420 (w).

$\{[Zn_2(bdc)_2(2,2\text{-terpyBA})_2]{\cdot}3DMF{\cdot}2H_2O\}_n$ (26) To the stirred solution of 2,2-terpyBA (36 mg, 0.1 mmol) and H_2bdc (16 mg, 0.1 mmol) in 2 mL DMF, $Zn(OAc)_2{\cdot}2H_2O$ (22 mg, 0.1 mmol) was added which results in a greenish color suspension. Upon addition of 1:1 water /EtOH solution (2 mL) to this a clear solution was obtained. Yellow precipitate started appearing after 15 min. Further this, the reaction mixture was stirred for another 5 h. The resulting yellow- precipitate was filtered through a filter paper and washed with DMF and EtOH, dried in air and weighed. Yield: 43 mg (60%). Anal. Calc. for $C_{73}H_{67}N_9O_{15}Zn_2$ (MW 1441.12): Calc. C, 60.84; H, 4.69; N, 8.75. Found: C, 60.02; H, 5.01; N, 7.32. Selected FTIR peaks (KBr, cm^{-1}): 3430 (br), 2114 (for acetylene C-H), 1664 (m, for DMF), 1599 (s), 1521 (w), 1475 (m) 1356 (s), 1230 (m), 1191 (m), 1016 (m), 833 (w), 792 (m), 748 (m), 659 (w), 515 (w).

$\{[Cd_2(bdc)_2(2,2\text{-terpyBA})_2]{\cdot}2DMF{\cdot}5H_2O\}_n$ (27) To the stirred solution of 2,2-terpyBA (36 mg, 0.1 mmol) and H_2bdc (16 mg, 0.1 mmol) in 4 mL mixture of DMF, H_2O and EtOH (1:1:1), $Cd(OAc)_2{\cdot}2H_2O$ (26 mg, 0.1 mmol) was added. Yellow precipitate started appearing after 15 min. Further this, the reaction mixture was stirred for another 5 h. The resulting yellow- precipitate were filtered through a filter paper and washed with DMF and EtOH, dried in air and weighed. Yield: 40 mg (54%). Anal. Calc. for $C_{70}H_{68}N_8O_{18}Cd_2$ (MW

1534.15): Calc. C, 55.45; H, 4.39; N, 7.39. Found: C, 55.58; H, 3.74; N, 6.55. Selected FTIR peaks (KBr, cm^{-1}): 3426 (br), 2114 (for acetylene C-H), 1663 (m, for DMF), 1598 (s), 1571 (s), 1519 (m) 1476 (w) 1432 (m), 1378 (s), 1231 (m) 1189 (m), 1014 (m), 838 (m), 790 (m), 746 (m), 659 (w), 518 (m).

{[Cu_2(bdc)$_2$(2,2-terpyBA)$_2$]·DMF·3H_2O}$_n$ (28) To the stirred solution of 2,2-terpyBA (72.8 mg, 0.2 mmol) and 1,4-H_2bdc (16 mg, 0.1 mmol) in 4 mL mixture of DMF, H_2O and EtOH (1:1:1), $Cu(OAc)_2 \cdot H_2O$ (40 mg, 0.2 mmol) was added and the reaction mixture was stirred for 5 h at room temperature. After stirring for 5 h, reaction mixture turned green with appearance of green precipitate. Resulting green precipitate were filtered through filter paper and washed with DMF and EtOH, dried in air and weighed. Yield: 89 mg (68%). Anal. Calc. for $C_{67}H_{55}N_7O_{14}Cu_2$ (MW 1309.28): Calc. C, 61.46; H, 4.23; N, 7.49. Found: C, 60.32; H, 5.01; N, 7.01. Selected FTIR peaks (KBr, cm^{-1}): 3435 (br), 2117 (for acetylene C-H), 1660 (s, for DMF), 1599 (s), 1366 (s), 1242 (s), 1191(m), 794 (m), 751 (s).

{[Mn_2(bdc)$_2$(2,2-terpyBA)$_2$]·4H_2O}$_n$ (29) To the stirred solution of 2,2-terpyBA (36 mg, 0.1 mmol) and 1,4-H_2bdc (16 mg, 0.1 mmol) in 4 mL mixture of DMF, H_2O and EtOH (1:1:1), $Mn(OAc)_2 \cdot 4H_2O$ (25 mg, 0.1 mmol) was added. After stirring for 5 h, yellow precipitate started appearing which were filtered through filter paper and washed with DMF and EtOH, dried in air and weighed. Yield: 51 mg (80%). Anal. Calc. for $C_{64}H_{50}N_6O_{14}Mn_2$ (MW 1236.98): Calc. C, 62.14; H, 4.07; N, 6.79. Found: C, 61.95; H, 4.78; N, 7.12. Selected FTIR peaks (KBr, cm^{-1}): 3450 (Br), 2123 (for acetylene C-H), 1600 (s), 1560 (s), 1474 (w), 1384 (s), 1231 (w) 1189 (w), 1015 (m), 792 (m), 751 (m), 517 (w).

{[Co_2(bdc)$_2$(2,2-terpyBA)$_2$]·DMF·H_2O}$_n$ (30) To the stirred solution of 2,2-terpyBA (36 mg, 0.1 mmol) and 1,4-H_2bdc (16 mg, 0.1 mmol) in 4 mL mixture of DMF, H_2O and EtOH (1:1:1), $Co(OAc)_2 \cdot 4H_2O$ (25 mg, 0.1 mmol) was added. A pink precipitate started appearing after 15 min. Furthermore, the reaction mixture was stirred for another 5 h at room temperature. The resulting pink precipitate were filtered through a filter paper and washed with DMF and EtOH, dried in air and weighed. Yield: 39 mg (62%). Anal. Calc. for $C_{67}H_{51}N_7O_{12}Co_2$ (MW 1264.02): Calc. C, 63.66; H, 4.07; N, 7.76. Found: C, 60.25; H, 3.99; N, 7.85. Selected FTIR peaks (KBr, cm^{-1}): 3366 (br), 2114 (for acetylene C-H), 1653 (m, for DMF), 1600 (s), 1575 (s), 1521 (m), 1474 (w) 1434 (w) 1381 (s), 1230 (m) 1190 (w), 1016 (m), 832 (m), 792 (m), 753 (m), 659 (w), 518 (w).

{[Zn_2(NH_2bdc)$_2$(2,2-terpyBA)$_2$]·DMF·2H_2O}$_n$ (31) To the stirred solution of 2,2-terpyBA (36 mg, 0.1 mmol) and NH_2bdc (18 mg, 0.1 mmol) in 4 mL mixture of DMF, H_2O and EtOH (1:1:1), $Zn(OAc)_2 \cdot 2H_2O$ (22 mg, 0.1 mmol) was added. A yellow-white precipitate

started appearing after 15 min. Furthermore, the reaction mixture was stirred for another 5 h. The resulting yellow- precipitate were filtered through a filter paper and washed with DMF and EtOH, dried in air and weighed. Yield: 44 mg (66%). Anal. Calc. for $C_{67}H_{55}N_9O_{13}Zn_2$ (MW 1324.96): Calc. C, 60.73; H, 4.18; N, 9.51. Found: C, 59.41; H, 4.95; N, 9.86. Selected FTIR peaks (KBr, cm^{-1}): 3431, 3336 (-NH_2), 2118 (for acetylene C-H), 1664 (s, for DMF), 1576 (s), 1600 (s), 1519 (m) 1476 (m) 1434 (m), 1362 (s), 1253 (m) 1188 (m), 1016 (m), 833 (m), 793 (m), 773 (m), 659 (w).

{[$Cd_2(NH_2bdc)_2(2,2\text{-}terpyBA)_2$]·DMF·$3H_2O$}$_n$ (32) To the stirred solution of 2,2-terpyBA (36 mg, 0.1 mmol) and NH_2bdc (18 mg, 0.1 mmol) in 4 mL mixture of DMF, H_2O and EtOH (1:1:1), $Cd(OAc)_2{\cdot}2H_2O$ (26 mg, 0.1 mmol) was added. Yellow- white precipitate starts appearing after 15 min. Furthermore, the reaction mixture was stirred for another 5 h. The resulting yellow- precipitate were filtered through a filter paper and washed with DMF and EtOH, dried in air and weighed. Yield: 52 mg (74%). Anal. Calc. for $C_{67}H_{57}N_9O_{14}Cd_2$ (MW 1437.04): Calc. C, 56.00; H, 4.00; N, 8.17. Found: C, 55.12; H, 4.52; N, 9.45. Selected FTIR peaks (KBr, cm^{-1}): 3426, 3314 (-NH_2), 2123 (for acetylene C-H), 1666 (s, for DMF), 1599 (s), 1550 (s), 1519 (m) 1477 (w) 1430 (m), 1372 (s), 1230 (m) 1189 (m), 1014 (m), 843 (m), 791 (m), 773 (m), 659 (w).

{[$Cu_2(NH_2bdc)_2(2,2\text{-}terpyBA)_2$]·DMF·$H_2O$}$_n$ (33) To the stirred solution of 2,2-terpyBA (72.8 mg, 0.2 mmol) and NH_2bdc (36 mg, 0.1 mmol) in 4 mL mixture of DMF, H_2O and EtOH (1:1:1), $Cu(OAc)_2{\cdot}H_2O$ (40 mg, 0.2 mmol) was added. After stirring for 5 h reaction mixture turned green with appearance of green precipitate. Resulting green precipitate were filtered through filter paper and washed with DMF and EtOH, dried in air and weighed. Yield: 75 mg (58%). Anal. Calc. for $C_{67}H_{53}N_9O_{12}Cu_2$ (MW 1303.28) Calc. C, 61.75; H, 4.10; N, 9.67. Found: C, 59.78; H, 4.64; N, 9.79. Selected FTIR peaks (KBr, cm^{-1}): 3420 (br), 2118 (for acetylene C-H), 1659 (s, for DMF), 1598 (s), 1571 (s), 1522 (m) 1435 (w) 1360 (s), 1255 (m), 1237 (m), 1192 (m), 1022 (m), 833 (m), 792 (m), 622 (w).

Crystals of this compound were grown by the layering method using a premixed stock solution of 2,2-terpyBA and $Cu(OAc)_2$ in 5 mL of DMF named as solution A and NH_2-bdc in 5 mL of EtOH and water (2:1 named as solution B) were prepared and stirred for 30 min. Then 1 mL of premixed solution B was slowly and carefully layered over 1 mL of solution A using 1 mL of 1:1 (v/v) buffer solution of H_2O and EtOH. The light green rectangular crystals were obtained after 10 days.

{[$Mn_2(NH_2bdc)_2(2,2\text{-}terpyBA)_2$]·DMF·$H_2O$}$_n$ (34) To the stirred solution of 2,2-terpyBA (72.8 mg, 0.2 mmol) and NH_2bdc (36 mg, 0.2 mmol) in 4 mL mixture of DMF, H_2O and

EtOH (1:1:1), $Mn(OAc)_2 \cdot 4H_2O$ (50 mg, 0.2 mmol) was added. After stirring for 5 h, yellow precipitate started appearing, which were filtered through filter paper and washed with DMF and EtOH, dried in air and weighed. Yield: 76 mg (58%). Anal. Calc. for $C_{67}H_{53}N_9O_{12}Mn_2$ (MW 1286.06): Calc. C, 62.57; H, 4.15; N, 9.80. Found: C, 60.62; H, 4.84; N, 9.78. Selected FTIR peaks (KBr, cm^{-1}): 3424 (br), 3323 (m, for NH_2), 2121 (w, for acetylene C-H), 1668 (s, for DMF), 1600 (s), 1573 (s), 1555 (m) 1519 (w) 1478 (m), 1433 (s), 1406 (m), 1374 (s), 1254 (m), 1191 (m), 1016 (m), 842 (m), 794 (m), 775 (m), 660 (w).

Crystals of this compound were grown by the layering method using a premixed stock solution of 2,2-terpyBA and $Mn(OAc)_2$ in 5 mL of DMF named as solution A and NH_2-bdc in 5 mL of EtOH and water (2:1 named as solution B) were prepared and stirred for 30 min. Then 1 mL of premixed solution B was slowly and carefully layered over 1 mL of solution A using 1 mL of 1:1 (v/v) buffer solution of H_2O and EtOH. The light green rectangular crystals of $\{[Cu(NH_2\text{-bdc})(2,2\text{-terpyBA})]\cdot DMF\cdot H_2O\}_n$ were obtained after 10 days. Scale up of this compound was done at room temperature stirring for 5 h.

$\{[Ni_2(NH_2bdc)_2(2,2\text{-terpyBA})_2]\cdot 2DMF\cdot 4H_2O\}_n$ (35) To the stirred solution of 2,2-terpyBA (36 mg, 0.1 mmol) and NH_2bdc (18 mg, 0.1 mmol) in 4 mL mixture of DMF, H_2O and EtOH (1:1:1), $Ni(OAc)_2 \cdot 4H_2O$ (24 mg, 0.1 mmol) was added. A green precipitate started appearing after 15 min. Furthermore, the reaction mixture was stirred for another 5 h. The resulting greenish precipitate was filtered through a filter paper, washed with DMF and EtOH, dried in air and weighed. Yield: 50 mg (74%). Anal. Calc. for $C_{70}H_{64}N_{10}O_{15}Ni_2$ (MW 1402.70): Calc. C, 59.94; H, 4.60; N, 9.99. Found: C, 59.93; H, 4.28; N, 8.23. Selected FTIR peaks (KBr, cm^{-1}): 3428, 3347 (-NH_2), 2127 (for acetylene C-H), 1661 (m, for DMF), 1603 (s), 1572 (s), 1474 (w) 1420 (m) 1379 (s), 1237 (m) 1188 (w), 1018 (w), 854 (m), 793 (m), 775 (m), 659 (w).

$\{[Co_2(NH_2bdc)_2(2,2\text{-terpyBA})_2]\cdot 2DMF\cdot H_2O\}_n$ (36) To the stirred solution of 2,2-terpyBA (36 mg, 0.1 mmol) and NH_2bdc (18 mg, 0.1 mmol) in 4 mL mixture of DMF, H_2O and EtOH (1:1:1), $Co(OAc)_2 \cdot 4H_2O$ (25 mg, 0.1 mmol) was added. A pink precipitate started appearing after 15 min, the reaction mixture was stirred for another 5 h. The resulting pink precipitate was filtered through a filter paper, washed with DMF and EtOH, dried in air and weighed. Yield: 35 mg (52%). Anal. Calc. for $C_{70}H_{60}N_{10}O_{13}Co_2$ (MW 1367.15): Calc. C, 61.50; H, 4.42; N, 10.25. Found: C, 60.25; H, 3.99; N, 9.85. Selected FTIR peaks (KBr, cm^{-1}): 3473, 3339 (-NH_2), 2117 (for acetylene C-H), 1617 (m, for DMF), 1563 (s), 1498 (w) 1420 (s) 1381 (s), 1307 (w) 1165 (w), 1035 (m), 848 (m), 773 (m), 578 (w), 543 (w).

{[Zn_2(bdc)$_2$(4,4-terpyBA)$_2$]·DMF·H_2O}$_n$ (37) To the stirred solution of 4,4-terpyBA (72.8 mg, 0.2 mmol) and 1,4-H_2bdc (33 mg, 0.2 mmol) in 4 mL mixture of DMF:H_2O:EtOH (1:1:1), $Zn(OAc)_2 \cdot 2H_2O$ (42 mg, 0.2 mmol) was added. After stirring for 15 min, a white precipitate started appearing which was stirred for another 5 h and filtered through a filter paper, washed with DMF and MeOH, dried in air and weighed. Yield: 96 mg (80%). Anal. Calc. for $C_{67}H_{59}N_7O_{16}Zn_2$ (MW 1348.98) (DMF·$5H_2O$): Calc. C, 59.65; H, 4.41; N, 7.27. Found: C, 58.57; H, 3.92; N, 6.24. Selected FTIR peaks (KBr, cm^{-1}): 3419 (br), 2114 (for acetylene C-H), 1661 (s, for DMF), 1616 (s), 1599 (s), 1505 (s), 1386 (s), 1227 (m), 1185 (w), 1018 (m), 828 (m), 752 (m), 651 (m).

{[Cd(bdc)(4,4-terpyBA)]·DMF·$5H_2O$}$_n$ (38) To the stirred solution of 4,4-terpyBA (72.8 mg, 0.2 mmol) and 1,4-H_2bdc (33 mg, 0.2 mmol) in 4 mL mixture of DMF:H_2O:EtOH (1:1:1), $Cd(OAc)_2 \cdot 2H_2O$ (53 mg, 0.2 mmol) was added. After stirring for 15 min, a white precipitate started appearing which was stirred for another 5 h and filtered through a filter paper, washed with DMF and MeOH, dried in air and weighed. Yield: 100 mg (70%). Anal. Calc. for $C_{67}H_{59}N_7O_{16}Zn_2$ (MW 1443.04): Calc. C, 55.77; H, 4.12; N, 6.79. Found: C, 57.01; H, 4.10; N, 6.75. Selected FTIR peaks (KBr, cm^{-1}): 3435 (br), 2116 (for acetylene C-H), 1664 (s, for DMF), 1614 (s), 1598 (s), 1559 (s), 1410 (s), 1363 (s), 1220 (m), 1183 (w), 1027 (m), 832 (m), 729 (m), 651 (m).

{[Cu_2(bdc)$_2$(4,4-terpyBA)$_2$]·DMF·$4H_2O$}$_n$ (39) To the stirred solution of 4,4-terpyBA (72.8 mg, 0.2 mmol) and 1,4-H_2bdc (33 mg, 0.2 mmol) in 4 mL mixture of DMF:H_2O:EtOH (1:1:1), $Cu(OAc)_2 \cdot H_2O$ (40 mg, 0.2 mmol) was added. After stirring for 15 min, a white precipitate started appearing. Further it was stirred for another 5 h, the precipitate obtained was filtered through filter paper and washed with DMF and MeOH, dried in air and weighed. Yield: 107 mg (81%). Anal. Calc. for $C_{67}H_{57}N_7O_{15}Cu_2$ (MW 1327.29): Calc. C, 60.63; H, 4.33; N, 7.39. Found: C, 58.06; H, 4.39; N, 7.11. Selected FTIR peaks (KBr, cm^{-1}): 3419 (br), 2114 (for acetylene C-H), 1664 (s, for DMF), 1616 (s), 1599 (s), 1395 (s), 1361 (s), 1225 (m), 1182 (w), 1018 (m), 830 (m), 753 (m), 654 (m).

{[Ni(bdc)(4,4-terpyBA)$_2$(H_2O)$_2$]·CH_3CH_2OH·H_2O}$_n$ (40) To the stirred solution of 4,4-terpyBA (72 mg, 0.2 mmol) and 1,4-H_2bdc (16 mg, 0.1 mmol) in 4 mL mixture of DMF, H_2O and EtOH (1:1:1), $Ni(OAc)_2 \cdot 4H_2O$ (24 mg, 0.1 mmol) was added. After stirring for 15 min, a green precipitate started appearing. Further it was stirred for another 5 h, the precipitate obtained was filtered through filter paper and washed with DMF and MeOH, dried in air and weighed. Yield: 28 mg (86%). Anal. Calc. for $C_{58}H_{46}N_6O_8Ni$ (MW 1013.71): Calc. C, 68.72; H, 4.57; N, 8.27. Found: C, 68.68; H, 5.98; N, 9.95. Selected

FTIR peaks (KBr, cm^{-1}): 3409 (br), 2114 (for acetylene C-H), 1664 (s, for DMF), 1600 (s), 1559 (s), 1515 (s), 1435 (w), 1382 (s), 1226 (m), 1183 (m), 1017 (m), 827 (m), 753 (m), 663 (m), 527 (w).

{[Co(bdc)(4,4-terpyBA)$_2$(H$_2$O)$_2$]·DMF·H$_2$O}$_n$ (41) To the stirred solution of 4,4-terpyBA (72 mg, 0.2 mmol) and 1,4-H$_2$bdc (16 mg, 0.1 mmol) in 4 mL mixture of DMF:H$_2$O:EtOH (1:1:1), Co(OAc)$_2$·4H$_2$O (25 mg, 0.1 mmol) was added. After stirring for 15 min, a pink precipitate started appearing. Further it was stirred for another 5 h, the precipitate obtained was filtered through filter paper and washed with DMF and MeOH, dried in air and weighed. Yield: 60 mg (53%). Anal. Calc. for $C_{62}H_{56}N_8O_{10}Co$ (MW 1132.08)(2 DMF and 2 H_2O): Calc. C, 65.78; H, 4.99; N, 9.90. Found: C, 67.01; H, 4.40; N, 8.82. Selected FTIR peaks (KBr, cm^{-1}): 3409 (br), 2114 (for acetylene C-H), 1664 (s, for DMF), 1599 (s), 1559 (s), 1515 (s), 1435 (w), 1375 (s), 1226 (m), 1183 (m), 1017 (m), 827 (m), 753 (m), 663 (m), 527 (w).

{[Zn$_2$(NH$_2$bdc)$_2$(4,4-terpyBA)$_2$]·DMF·2H$_2$O}$_n$ (42) To the stirred solution of 4,4-terpyBA (72.8 mg, 0.2 mmol) and NH$_2$bdc (33 mg, 0.2 mmol) in 4 mL mixture of DMF:H$_2$O:EtOH (1:1:1), Zn(OAc)$_2$·2H$_2$O (44 mg, 0.2 mmol) was added. After stirring for 15 min, a white precipitate started appearing. Further it was stirred for another 5 h, the precipitate obtained was filtered through filter paper and washed with DMF and MeOH, dried in air and weighed. Yield: 86 mg (65%). Anal. Calc. for $C_{67}H_{55}N_9O_{13}Zn_2$ (MW 1324.96): Calc. C, 60.73; H, 4.18; N, 9.51. Found: C, 59.88; H, 4.26; N, 9.09. Selected FTIR peaks (KBr, cm^{-1}): 3434 (br), 2118 (for acetylene C-H), 1662 (s, for DMF), 1597 (s), 1574 (s), 1515 (s), 1436 (m), 1367 (m), 1256 (s), 1227 (m), 1027 (s), 827 (m), 772 (m), 651 (m).

{[Cd$_2$(NH$_2$bdc)$_2$(4,4-terpyBA)$_2$]·2DMF·3H$_2$O}$_n$ (43) To the stirred solution of 4,4-terpyBA (72.8 mg, 0.2 mmol) and NH$_2$bdc (33 mg, 0.2 mmol) in 4 mL mixture of DMF:H$_2$O:EtOH (1:1:1), Cd(OAc)$_2$·2H$_2$O (53 mg, 0.2 mmol) was added. After stirring for 15 min, a yellow precipitate started appearing. Further it was stirred for another 5 h, the precipitate obtained was filtered through filter paper and washed with DMF and MeOH, dried in air and weighed. Yield: 120 mg (80%). Anal. Calc. for $C_{70}H_{64}N_{10}O_{15}Cd_2$ (MW 1510.37): Calc. C, 55.67; H, 4.27; N, 9.28. Found: C, 55.61; H, 5.92; N, 9.20. Selected FTIR peaks (KBr, cm^{-1}): 3414 (br), 2118 (for acetylene C-H), 1699 (s, for DMF), 1598 (s), 1412 (s), 1378 (s), 756 (m), 698 (m).

{[Cu$_2$(NH$_2$bdc)$_2$(4,4-terpyBA)$_2$]·2DMF·3H$_2$O}$_n$ (44) To the stirred solution of 4,4-terpyBA (72.8 mg, 0.2 mmol) and NH$_2$bdc (33 mg, 0.2 mmol) in 4 mL mixture of DMF:H$_2$O:EtOH (1:1:1), Cu(OAc)$_2$·H$_2$O (40 mg, 0.2 mmol) was added. After stirring for

15 min, a green precipitate started appearing. Further it was stirred for another 5 h, the precipitate obtained was filtered through filter paper and washed with DMF and MeOH, dried in air and weighed. Yield: 105 mg (80%). Anal. Calc. for $C_{67}H_{55}N_6O_{13}Cu_2$ (MW 1321.29): Calc. C, 60.90; H, 4.20; N, 9.54. Found: C, 58.95; H, 4.50; N, 9.87. Selected FTIR peaks (KBr, cm^{-1}): 3441 (br), 3336 (m, for NH_2), 2114 (for acetylene C-H), 1664 (s, for DMF), 1600 (s), 1574 (s), 1515 (s), 1434 (m), 1384 (m), 1256 (s), 1227 (m), 1028 (s), 829 (m), 772 (m), 654 (m).

{[Ni(NH_2bdc)(4,4-terpyBA)]·DMF·$4H_2O$}$_n$ (45) To the stirred solution of 4,4-terpyBA (72.8 mg, 0.2 mmol) and NH_2bdc (33 mg, 0.2 mmol) in 4 mL mixture of DMF:H_2O:EtOH (1:1:1), Ni(OAc)$_2$·$4H_2O$ (49 mg, 0.2 mmol) was added. After stirring for 15 min, a green precipitate started appearing. Further it was stirred for another 5 h, the precipitate obtained was filtered through filter paper and washed with DMF and MeOH, dried in air and weighed. Yield: 118 mg (88%). Anal. Calc. for $C_{67}H_{59}N_9O_{15}Ni_2$ (MW 1347.62): Calc. C, 59.71; H, 4.41; N, 8.71. Found: C, 61.62; H, 4.00; N, 7.99. Selected FTIR peaks (KBr, cm^{-1}): 3432 (br), 3347 (m, for NH_2), 2114 (for acetylene C-H), 1662 (s, for DMF), 1600 (s), 1544 (s), 1515 (s), 1421 (m), 1375 (s), 1228 (m), 1182 (m), 1026 (m), 829 (m), 773 (m), 639 (m).

{[Co(NH_2bdc)(4,4-terpyBA)]·DMF·$5H_2O$}$_n$ (46) To the stirred solution of 4,4-terpyBA (72.8 mg, 0.2 mmol) and NH_2bdc (33 mg, 0.2 mmol) in 4 mL mixture of DMF:H_2O:EtOH (1:1:1), Co(OAc)$_2$·$4H_2O$ (50 mg, 0.2 mmol) was added. After stirring for 15 min, a pink precipitate started appearing. Further it was stirred for another 5 h, the precipitate obtained was filtered through filter paper and washed with DMF and MeOH, dried in air and weighed. Yield: 89 mg (65%). Anal. Calc. for $C_{67}H_{61}N_9O_{16}Co_2$ (MW 1365.91): Calc. C, 58.91; H, 4.50; N, 9.23. Found: C, 59.16; H, 4.68; N, 9.86. Selected FTIR peaks (KBr, cm^{-1}): 3424 (br), 3347 (m-NH_2), 2123 (for acetylene C-H), 1663 (s, for DMF), 1598 (s), 1568 (s), 1515 (s), 1419 (s), 1367 (s), 1256 (s), 1228 (m), 1020 (s), 826 (m), 772 (m), 647 (m).

{[Zn_3(btc)$_2$(2,2-terpyBA)$_3$]·DMF·$2H_2O$}$_n$ (47) To the stirred solution of 2,2-terpyBA (36 mg, 0.1 mmol) and H_3btc (14 mg, 0.06 mmol) in 4 mL mixture of DMF, EtOH and water (1:1:1), Zn(OAc)$_2$·$2H_2O$ (22 mg, 0.1 mmol) was added. After stirring for 15 min, a yellow precipitate started appearing. Further it was stirred for another 5 h, the precipitate obtained was filtered through a filter paper and washed with DMF and EtOH, dried in air and weighed. Yield: 50 mg (83%). Anal. Calc. for $C_{93}H_{68}N_{10}O_{18}Zn_3$ (MW 1809.73): Calc. C, 61.72; H, 3.79; N, 7.74. Found: C, 59.91; H, 3.61; N, 7.75. Selected FTIR peaks (KBr, cm^{-1}

^{1}): 3410 (br), 2118 (for acetylene C-H), 1618 (s), 1575 (m), 1436 (m) 1362 (s), 1231 (m), 1017 (m), 832 (w), 766 (m), 728 (w).

{[Cd_3(btc)$_2$(2,2-terpyBA)$_3$]·3H_2O}$_n$ (48) To the stirred solution of 2,2-terpyBA (36 mg, 0.1 mmol) and H_3btc (14 mg, 0.06 mmol) in 4 mL mixture of DMF, EtOH and water (1:1:1), $Cd(OAc)_2 \cdot 2H_2O$ (26 mg, 0.1 mmol) was added. After stirring for 15 min, a yellow precipitate started appearing. Further it was stirred for another 5 h, the precipitate obtained was filtered through a filter paper and washed with DMF and EtOH, dried in air and weighed. Yield: 61.76 mg (69%). Anal. Calc. for $C_{90}H_{63}N_9O_{18}Cd_3$ (MW 1895.74): Calc. C, 57.02; H, 3.35; N, 6.65. Found: C, 58.15; H, 4.01; N, 7.00. Selected FTIR peaks (KBr, cm^{-1}): 3401 (br), 2114 (for acetylene C-H), 1610 (s), 1549 (w), 1437 (m) 1369 (s), 1232 (m), 1190 (m), 1015 (m), 832 (w), 791 (m), 729 (w).

{[Cu_3(btc)$_2$(2,2-terpyBA)$_3$]·2DMF·2H_2O}$_n$ (49) To the stirred solution of 2,2-terpyBA (36 mg, 0.1 mmol) and H_3btc (14 mg, 0.06 mmol) in 4 mL mixture of DMF, EtOH and water (1:1:1), $Cu(OAc)_2 \cdot H_2O$ (20 mg, 0.1 mmol) was added. After stirring for 15 min, blue precipitate started appearing. Further it was stirred for another 5 h, the precipitate obtained was filtered through a filter paper and washed with DMF and EtOH, dried in air and weighed. Yield: 39 mg (62%). Anal. Calc. for $C_{96}H_{75}N_{11}O_{19}Cu_3$ (MW 1877.32): Calc. C, 61.42; H, 4.03; N, 8.21. Found: C, 61.32; H, 5.24; N, 8.37. Selected FTIR peaks (KBr, cm^{-1}): 3420 (br), 2114 (for acetylene C-H), 1659 (DMF), 1602 (s), 1544 (m), 1435 (m) 1361 (s), 1230 (m), 1190 (m), 1015 (m), 829 (w), 792 (m), 729 (w).

[Co(2,2-terpyBA)$_2$](Hbtc)·H_2O (50) To the stirred solution of 2,2-terpyBA (145 mg, 0.4 mmol) and H_3btc (42 mg, 0.2 mmol) in 4 mL mixture of DMF, EtOH and water (1:1:1), $Co(OAc)_2 \cdot 4H_2O$ (50 mg, 0.2 mmol) was added. After stirring for 15 min, pink precipitate started appearing. Further it was stirred for another 5 h, the precipitate obtained was filtered through a filter paper and washed with DMF and EtOH, dried in air and weighed. Yield: 121 mg (60%). Anal. Calc. for $C_{57}H_{40}N_6O_9Co_2$ (MW 1011.89): Calc. C, 66.47; H, 4.11; N, 8.16. Found: C, 65.82; H, 3.76; N, 9.82. Selected FTIR peaks (KBr, cm^{-1}): 3407 (br), 2109 (for acetylene C-H), 1660 (m), 1625 (s), 1577 (m), 1438 (m) 1371 (s), 1232 (m), 1191 (m), 1015 (m), 831 (w), 792 (m), 766 (m), 711 (w).

{[Zn_2(Hbtc)$_2$(4,4-terpyBA)$_2$]}$_n$ (51) To the stirred solution of 4,4-terpyBA (36 mg, 0.1 mmol) and H_3btc (21 mg, 0.1 mmol) in 4 mL mixture of DMF, EtOH and water (1:1:1), $Zn(OAc)_2 \cdot 2H_2O$ (22 mg, 0.1 mmol) was added. After stirring for 15 min, white precipitate started appearing. Further it was stirred for another 5 h, the precipitate obtained was filtered through a filter paper and washed with DMF and EtOH, dried in air and weighed. Yield:

52 mg (81%). Anal. Calc. for $C_{66}H_{42}N_6O_{14}Zn_2$ (MW 1273.83): Calc. C, 62.23; H, 3.32; N, 6.60. Found: C, 61.25; H, 3.98; N, 7.30. Selected FTIR peaks (KBr, cm^{-1}): 3431 (br), 2112 (for acetylene C-H), 1702 (free carboxylate), 1627 (s), 1578 (m), 1438 (m) 1369 (s), 1257 (m), 1184 (m), 1027 (m), 833 (w), 759 (m), 734 (m), 652 (w).

{[Cd_2(OAc)(btc)(4,4-terpyBA)$_2$(H_2O)]·DMF·H_2O}$_n$ (52) To the stirred solution of 2,2-terpyBA (36 mg, 0.1 mmol) and H_3btc (21 mg, 0.1 mmol) in 4 mL mixed solution of DMF, EtOH and water (1:1:1), $Cd(OAc)_2·2H_2O$ (26 mg, 0.1 mmol) was added. After stirring for 15 min, yellow precipitate started appearing. Further it was stirred for anothe ther 5 h, the precipitate obtained was filtered through a filter paper and washed with DMF and EtOH, dried in air and weighed. Yield: 55 mg (83%). Anal. Calc. for $C_{62}H_{53}N_7O_{14}Cd_2$ (MW 1344.94): Calc. C, 55.37; H, 3.97; N, 7.29. Found: C, 54.93; H, 4.22; N, 7.99. Selected FTIR peaks (KBr, cm^{-1}): 3424 (br), 3234 (br), 2114 (for acetylene C-H), 1669 (DMF), 1609 (s), 1561 (m), 1434 (m) 1366 (s), 1229 (m), 1185 (m), 1020 (m), 826 (w), 765 (m), 729 (m), 646 (w).

{[Cu_3(btc)$_2$(4,4-terpyBA)$_3$]}$_n$ (53) To the stirred solution of 2,2-terpyBA (36 mg, 0.1 mmol) and H_3btc (14 mg, 0.06 mmol) in 4 mL mixture of DMF, EtOH and water (1:1:1), $Cu(OAc)_2·H_2O$ (20 mg, 0.1 mmol) was added. After stirring for 15 min, blue green precipitate started appearing. Further it was stirred for another 5 h, the precipitate obtained was filtered through a filter paper and washed with DMF and EtOH, dried in air and weighed. Yield: 30 mg (53%). Anal. Calcd for $C_{90}H_{57}N_9O_{15}Cu_3$ (MW 1695.10): Calc. C, 63.77; H, 3.39; N, 7.44. Found: C, 64.25; H, 4.78; N, 6.35. Selected FTIR peaks (KBr, cm^{-1}): 3422 (br), 3283 (br), 2114 (for acetylene C-H), 1664 (DMF), 1616 (s), 1516 (m), 1436 (m) 1363 (s), 1226 (m), 1186 (m), 1028 (m), 828 (w), 766 (m), 727 (m), 654 (w).

{[Mn_3(btc)$_2$(4,4-terpyBA)$_3$]·2H_2O}$_n$ (54) To the stirred solution of 2,2-terpyBA (36 mg, 0.1 mmol) and H_3btc (14 mg, 0.06 mmol) in 4 mL mixture of DMF, EtOH and water (1:1:1), $Mn(OAc)_2·4H_2O$ (25 mg, 0.1 mmol) was added. After stirring for 15 min, a yellow precipitate started appearing. Further it was stirred for another 5 h, the precipitate obtained was filtered through a filter paper and washed with DMF and EtOH, dried in air and weighed. Yield: 40 mg (68%). Anal. Calcd for $C_{90}H_{61}N_9O_{17}Mn_3$ (MW 1705.13): Calc. C, 63.39; H, 3.61; N, 7.39. Found: C, 62.95; H, 3.45; N, 7.98. Selected FTIR peaks (KBr, cm^{-1}): 3400 (br), 2113 (for acetylene C-H), 1649 (DMF), 1628 (s), 1614 (s), 1574 (s), 1435 (s) 1374 (s), 1252 (m), 1105 (m), 1060 (w), 769 (m), 727 (m), 709 (w), 674 (w).

{[Co_3(btc)$_2$(4,4-terpyBA)$_3$]·2H_2O}$_n$ (55) To the stirred solution of 2,2-terpyBA (36 mg, 0.1 mmol) and H_3btc (14 mg, 0.06 mmol) in 4 mL mixture of DMF, EtOH and water (1:1:1),

$Co(OAc)_2 \cdot 4H_2O$ (25 mg, 0.1 mmol) was added. After stirring for 15 min, a pink precipitate started appearing. Further it was stirred for another 5 h, the precipitate obtained was filtered through a filter paper and washed withe th DMF and EtOH, dried in air and weighed. Yield: 38 mg (66%). Anal. Calcd for $C_{90}H_{61}N_9O_{17}Co_3$ (MW 1717.29): Calc. C, 62.95; H, 3.58; N, 7.34. Found: C, 63.75; H, 4.92; N, 7.36. Selected FTIR peaks (KBr, cm^{-1}): 3400 (br), 2114 (for acetylene C-H), 1654 (DMF), 1610 (s), 1560 (m), 1432 (m) 1372 (s), 1227 (m), 1184 (w), 1020 (w), 828 (m), 768 (m), 718 (m).

$\{[Zn(bpaipa)]\cdot DMF\cdot 2H_2O\}_n$ (56) A mixture of $Zn(OAc)_2 \cdot 2H_2O$ (22 mg, 0.1 mmol), and bpaipa (36.3 mg, 0.1 mmol) in DMF–H_2O (1 mL:1 mL) was heated in a 5 mL capacity Teflon lined stainless-steel reactor at 120 °C for 48 h and then cooled to room temperature in 24 h. Colorless block-shaped crystals were collected via filtration and washed with a 1:1 mixture of acetonitrile and toluene to remove the acetic acid by-product followed by dried in air. Yield: 38 mg (71%) Anal. Calcd for $C_{20}H_{17}N_3O_5Zn$ (MW 444.75): C, 54.01; H, 3.85; N, 9.45. Found: C, 53.85; H, 3.80; N, 9.15. Selected FTIR peaks (KBr, cm^{-1}): 3344 (br), 1662 (m), 1633 (s), 1607 (s), 1567 (s), 1443 (s), 1345 (s), 1297 (m), 783 (m), 725 (m).

$\{[Zn(bpaipa)]\cdot 6H_2O\}_n$ (57) A mixture of $Zn(OAc)_2 \cdot 2H_2O$ (22 mg, 0.1 mmol), and bpaipa (36.3 mg, 0.1 mmol) in MeOH (4 mL) was stirred at room temperature for 5 h, resulted in the formatthe ion of pale yellow color solid. It was filtered through filter paper and washed with toluene and acetonitrile mixture (1:1) and air dried. Yield, 42 mg (79%). Anal. Calcd for $C_{20}H_{31}N_3O_{12}Zn$ (MW 570.85)(8 H_2O): C, 42.08; H, 5.47; N, 7.36. Found: C, 42.3; H, 4.00; N, 7.30. Selected FTIR peaks (KBr, cm^{-1}): 3429 (br), 1608 (m), 1577 (s), 1442 (s), 1398 (s), 1025 (m), 782 (m).

$\{[Cd(bpaipa)]\cdot DMF\cdot 2H_2O\}_n$ (58) A mixture of $Cd(OAc)_2 \cdot 2H_2O$ (26 mg, 0.1 mmol), and bpaipa (36.3 mg, 0.1 mmol) in DMF:H_2O (1:1) was heated in a 5 mL capacity Teflon lined stainless-steel reactor at 120 °C for 48 h and then cooled to room temperature in 24 h. Colorless block-shaped crystals were collected via filtration and washed with a 1:1 mixture of acetonitrile and toluene to remove the acetic acid by-product followed by air drying. Yield, 33 mg (53%). Anal. Calcd for $C_{23}H_{32}O_{10}N_4Cd$ (MW 636.93) (DMF and 5 H_2O):, C, 47.37; H, 5.06; N, 8.80. Found: C, 46.5; H, 5.92; N, 8.6. Selected FTIR peaks (KBr, cm^{-1}): 3434 (br), 1662 (m), 1604 (m), 1560 (s), 1498 (s), 1439 (s), 1386 (s), 1055 (m), 858 (s), 789 (m).

$\{[Cd(bpaipa)]\cdot 4H_2O\}_n$ (59) A mixture of $Cd(OAc)_2 \cdot 2H_2O$ (26 mg, 0.1 mmol), and bpaipa (36.3 mg, 0.1 mmol) in MeOH (4 mL) was stirred at room temperature for 5 h which result in the formation of pale yellow colour solid. It was filtered through filter paper and washed

with toluene and acetonitrile mixture (1:1) to remove the acetic acid by-product followed by air drying. Yield: 47 mg (88%). Anal. Calcd for $C_{20}H_{23}N_3O_8Cd$ (MW 545.82): C, 44.01; H, 4.25; N, 7.70. Found: C, 44.3; H, 3.30; N, 7.00. Selected FTIR peaks (KBr, cm^{-1}): 3445 (s, br), 1708 (m), 1604 (s), 1548 (s), 1442 (s), 1376 (s), 1132 (s), 767 (m).

{[Zn(2,4-bpaipa)]·CH_3OH·$2H_2O$}$_n$ (60) A mixture of $Zn(OAc)_2·2H_2O$ (22 mg, 0.1 mmol), and 2,4-H_2bpaipa (36.3 mg, 0.1 mmol) in 4 mL methanol was stirred in a 10 mL round bottom flask at room temperature for 5 h. A white precipitate was formed which was separated from the mixture by filtration and the solid was washed with a 1:1 mixture of acetonitrile and toluene to remove the acetic acid by-product followed by air drying. Yield: 43 mg (83%). Anal. Calc. for $C_{22}H_{25}N_3O_7Zn$ (MW 508.82): C, 51.93; H, 4.95; N, 8.26. Found: C, 50.02; H, 3.87; N, 9.35. Selected FTIR peaks (KBr, cm^{-1}): 3439 (br) 3236 (br), 1629 (s), 1577 (s), 1430 (s), 1366 (s), 778 (m).

{[Cd(2,4-bpaipa)]·$3H_2O$}$_n$ (61) A mixture of $Cd(OAc)_2·2H_2O$ (26 mg, 0.1 mmol), and 2,4-H_2bpaipa (36.3 mg, 0.1 mmol) in 4 mL methanol was stirred in a 10 mL round bottom flask at room temperature for 5 h. A yellow precipitate was formed which were separated from the mixture by filtration, washed with a 1:1 mixture of acetonitrile and toluene to remove the acetic acid by-product followed by air drying. Yield: 39 mg (75%). Anal. Calc. for $C_{20}H_{21}N_3O_7Cd$ (MW 527.80): C, 45.51; H, 4.01; N, 7.96. Found: C, 45.45; H, 3.92; N, 8.53. Selected FTIR peaks (KBr, cm^{-1}): 3439 (br), 1615 (m), 1555 (s), 1424 (s), 1378 (m), 781 (m).

{[Ni(2,4-bpaipa)]·H_2O}$_n$ (62) A mixture of $Ni(OAc)_2·4H_2O$ (22 mg, 0.1 mmol), and bpaipa (36.3 mg, 0.1 mmol) in DMF/H_2O (1:1) was stirred in a 5 mL round bottom flask at room temperature for 5 h. Green precipitate was formed, collected via filtration, washed with a 1:1 mixture of acetonitrile and toluene to remove the acetic acid by-product followed by air drying. Yield: 32 mg (76%). Anal. Calc. for $C_{20}H_{15}N_3O_4Ni$ (MW 420.04): C, 57.19; H, 3.50; N, 10.00. Found: C, 58.35; H, 3.50; N, 11.17. Selected FTIR peaks (KBr, cm^{-1}): 3442 (br), 1617 (s), 1633(s), 1545 (s), 1567(s), 1414 (m), 1370 (s), 1041 (s), 776 (m), 698 (m), 533 (w).

{[Co(2,4-bpaipa)]}$_n$ (63) A mixture of $Co(OAc)_2·4H_2O$ (20 mg, 0.1 mmol), and 2,4-H_2bpaipa (36.3 mg, 0.1 mmol) in 4 mL methanol was stirred in a 10 mL round bottom flask at room temperature for 5 h. A pink precipitate was formed, which were separated from the mixture by filtration, washed with 1:1 mixture of acetonitrile and toluene to remove the acetic acid by-product followed by air drying. Yield: 30 mg (71%). Anal. Calc. for $C_{20}H_{15}N_3O_4Co$ (MW 420.28): C, 57.16; H, 3.60; N, 10.00. Found: C, 56.32; H, 3.05;

N, 9.72. Selected FTIR peaks (KBr, cm^{-1}): 3439 (br) 3236 (br), 1621 (s), 1569 (s), 1414 (s), 1367 (s), 778 (m).

{[$(CH_3)_2NH_2$][Zn(bpaipa)]·$4H_2O$}$_n$ (64) A mixture of $Zn(OAc)_2·2H_2O$ (44 mg, 0.1 mmol), and H_3pbaipa (72 mg, 0.1 mmol) in DMF/H_2O (1:1) was heated in a 5 mL capacity Teflon lined stainless-steel reactor at 120 °C for 48 h and then cooled to room temperature in 24 h. Colorless block-shaped crystals were collected via filtration and washed with a 1:1 mixture of acetonitrile and toluene to remove the acetic acid by-product followed by drying in air. Yield: 77 mg (65%). Anal. Calc. for $C_{24}H_{31}N_3O_{10}Zn$ (MW 586.89): C, 49.12; H, 5.32; N, 7.16. Found: C, 50.73; H, 5.95; N, 7.10. Selected FTIR peaks (KBr, cm^{-1}): 3342 (br), 1686 (m), 1598 (s), 1425 (s), 1300 (s), 1096 (s), 945 (w), 753 (m), 630 (m).

[Cd_3(bpaipa)$_2$]·$4H_2O$}$_n$ (65) A mixture of $Cd(OAc)_2·2H_2O$ (26 mg, 0.1 mmol), and H_3pbaipa (24.3 mg, 0.06 mmol) in DMF/H_2O (1:1) was heated in a 5 mL capacity Teflon lined stainless-steel reactor at 120 °C for 48 h and then cooled to room temperature in 24 h. Colorless block-shaped crystals were collected via filtration and washed with a 1:1 mixture of acetonitrile and toluene to remove the acetic acid by-product followed by drying in air. Yield: 27 mg (69%). Anal. Calcd for $C_{44}H_{38}O_{16}N_4Cd_3$ (MW 1216.02): C, 43.32; H, 3.15; N, 4.61. Found: C, 43.32; H, 4.95; N, 4.72. Selected FTIR peaks (KBr, cm^{-1}): 3404 (br), 1600 (m), 1594 (m), 1542 (s), 1385 (s), 772 (m).

{[$(CH_3)_2NH_2$][Cu(bpaipa)]·H_2O}$_n$ (66) A mixture of $Cu(OAc)_2·H_2O$ (20 mg, 0.1 mmol), and H_3pbaipa (36.3 mg, 0.1 mmol) in MeOH (4 mL) was stirred at room temperature for 5 h which result in the formation of pale yellow color solid. It was filtered through filter paper, washed with toluene and acetonitrile mixture (1:1) and air dried. Yield: 42 mg (79%). Anal. Calcd for $C_{24}H_{25}N_3O_7Cu$ (MW 531.01): C, 54.28; H, 4.75; N, 7.91. Found: C, 53.19; H, 4.70; N, 7.65. Selected FTIR peaks (KBr, cm^{-1}): 3414 (br), 1699 (m), 1570 (s), 1386 (s), 1261 (s), 767 (m), 671 (m).

{[$(CH_3)_2NH_2$][Co(bpaipa)]·$5H_2O$}$_n$ (67) A mixture of $Co(OAc)_2·4H_2O$ (25 mg, 0.1 mmol), and H_3pbaipa (36.3 mg, 0.1 mmol) in MeOH (4 mL) was stirred at room temperature for 5 h which resulted in the formation of pale yellow colour solid. It was filtered through filter paper, washed with toluene and acetonitrile mixture (1:1) and air dried. Yield: 32 mg (51%). Calcd for $C_{24}H_{33}N_3O_{11}Co$ (MW 598.46): C, 48.17; H, 5.56; N, 7.02. Found: C, 48.10; H, 6.92; N, 8.01. Selected FTIR peaks (KBr, cm^{-1}): 3483 (br), 1686 (s), 1606 (s), 1440 (m), 1228 (s), 753 (m).

{[Zn_2(diab)]·$5H_2O$}$_n$ (68) To a mixture of H_4diab (23.2 mg, 0.05 mmol) in 4 mL methanol, NaOH (8 mg, 0.2 mmol) was added followed by addition of $Zn(OAc)_2·2H_2O$ (22 mg, 0.1

mmol) and the resultant reaction mixture was stirred for another 5 h at room temperature. A yellow-white color precipitate were formed. The resulting precipitate was filtered through filter paper, washed with MeOH and dried in air affording a yellow solid. Yield: 30 mg (88%). Anal. Calcd for $C_{24}H_{26}N_2O_{13}Zn_2$ (MW 681.22): C, 42.31; H, 3.85; N, 4.11. Found: C, 42.99; H, 4.08; N, 5.95. Selected FTIR peaks (KBr, cm^{-1}): 3428 (br), 2860 (m), 1636 (m), 1569 (s), 1418 (s), 1375 (m), 775 (m).

$\{[Zn_2(bipy)_2(diab)]\cdot 3H_2O\}_n$ (69) To a mixture of H_4diab (23.2 mg, 0.05 mmol) and bipy (31 mg, 0.2 mmol) in 4 mL methanol, NaOH (8 mg, 0.2 mmol) was added followed by addition of $Zn(OAc)_2\cdot 2H_2O$ (22 mg, 0.1 mmol) and the resultant reaction mixture was stirred for another 5 h at room temperature.The resulting pale white color precipitate were filtered through filter paper, washed with MeOH and dried in air affording a pale white solid. Yield: 69 mg (71%). Anal. Calcd for $C_{44}H_{38}N_6O_{11}Zn_2$ (MW 957.56): C, 55.19; H, 4.00; N, 8.78. Found: C, 56.99; H, 3.98; N, 7.20. Selected FTIR peaks (KBr, cm^{-1}): 3400 (br), 1575 (s), 1419 (s), 1363 (s), 1221 (w), 1071 (m), 779 (m).

$\{[Cd_2(diab)]\cdot CH_3OH\cdot 6H_2O\}_n$ (70) To a mixture of H_4diab (23.2 mg, 0.05 mmol) in 4 mL methanol, NaOH (8 mg, 0.2 mmol) was added followed by addition of $Cd(OAc)_2\cdot 2H_2O$ (26 mg, 0.1 mmol) and the resultant reaction mixture was stirred for another 5 h at room temperature. The resulting precipitate was filtered through filter paper, washed with MeOH and dried in air affording a yellow-white solid. Yield: 29 mg (72%). Anal. Calcd for $C_{25}H_{32}N_2O_{15}Cd_2$ (MW 825.34): C, 36.38; H, 3.91; N, 3.39. Found: C, 36.30; H, 4.50; N, 3.30. Selected FTIR peaks (KBr, cm^{-1}): 3361 (br), 1560 (s), 1414 (s), 1373 (s), 1126 (m), 1020 (w), 780 (m), 773 (m).

$\{[Cd_2(bipy)_2(diab)]\cdot 3H_2O\}_n$ (71) To a mixture of H_4diab (23.2 mg, 0.05 mmol) and bipy (31 mg, 0.2 mmol) in 4 mL methanol, NaOH (8 mg, 0.2 mmol) was added followed by addition of $Cd(OAc)_2\cdot 2H_2O$ (43 mg, 0.2 mmol) and the resultant reaction mixture was stirred for another 5 h at room temperature.. The resulting yellow color precipitate were filtered through filter paper, washed with MeOH and dried in air affording a yellow solid. Yield: 35 mg (68%). Anal. Calcd for $C_{44}H_{38}N_6O_{11}Cd_2$ (MW 1051.62): C, 50.25; H, 3.64; N, 7.99. Found: C, 48.35; H, 4.02; N, 7.90. Selected FTIR peaks (KBr, cm^{-1}): 3360 (br), 1602 (s), 1558 (s), 1414 (s), 1373 (s), 1069 (w), 807 (m), 779 (m), 732 (m), 627 (w).

$\{[Zn_2(bdiab)]\cdot 3H_2O\}_n$ (72) To a mixture of H_4bdiab (32 mg, 0.05 mmol) in 4 mL methanol, NaOH (8 mg, 0.2 mmol) was added followed by addition of $Zn(OAc)_2\cdot 2H_2O$ (22 mg, 0.1 mmol) and the resultant reaction mixture was stirred for another 5 h at room temperature. The resulting precipitate was filtered through filter paper, washed with MeOH and dried in

air affording a yellow solid. Yield: 35 mg (85%). Anal. Calcd for $C_{36}H_{32}N_4O_{11}Zn_2$ (MW 827.41): C, 52,26; H, 3.90; N, 6.77. Found: C, 50.99; H, 3.59; N, 6.65. Selected FTIR peaks (KBr, cm^{-1}): 3446 (br), 1573 (s), 1419 (s), 1436 (s), 1365 (s), 1260 (m), 779 (m), 735 (w).

{[Cd_2(bdiab)]·5H_2O}$_n$ (73) To a mixture of H_4bdiab (32 mg, 0.05 mmol) in 4 mL methanol, NaOH (8 mg, 0.2 mmol) was added followed by addition of $Cd(OAc)_2{\cdot}2H_2O$ (26 mg, 0.1 mmol) and the resultant reaction mixture was stirred for another 5 h at room temperature. The resulting precipitate was filtered through filter paper, washed with MeOH and dried in air affording a yellow-white solid. Yield: 38 mg (80%). Anal. Calcd for $C_{36}H_{36}N_4O_{13}Cd_2$ (MW 957.51): C, 45.16; H, 3.79; N, 5.85. Found: C, 45.09; H, 4.95; N, 5.68. Selected FTIR peaks (KBr, cm^{-1}): 3419 (br), 1550 (s), 1558 (s), 1375 (s), 1260 (m), 1025 (w), 777 (m), 687 (w).

{[Cu_2(bdiab)]·2CH_3OH·5H_2O}$_n$ (74) To a mixture of H_4bdiab (32 mg, 0.05 mmol) in 4 mL methanol, NaOH (8 mg, 0.2 mmol) was added followed by addition of $Cu(OAc)_2{\cdot}H_2O$ (20 mg, 0.1 mmol) and the resultant reaction mixture was stirred for another 5 h at room temperature. The resulting precipitate was filtered through filter paper, washed with MeOH and dried in air affording a green solid. Yield: 33 mg (72%). Anal. Calcd for $C_{38}H_{44}N_4O_{15}Cu_2$ (MW 923.86): C, 49.40; H, 4.80; N, 6.06. Found: C, 51.00; H, 4.87; N, 6.12. Selected FTIR peaks (KBr, cm^{-1}): 3422 (br), 1624 (s), 1560 (s), 1431 (s), 1364 (s), 1259 (m), 776 (m), 686 (w).

{[Ni_2(bdiab)]·4H_2O}$_n$ (75) To a mixture of H_4bdiab (32 mg, 0.05 mmol) in 4 mL methanol, NaOH (8 mg, 0.2 mmol) was added followed by addition of $Ni(OAc)_2{\cdot}4H_2O$ (25 mg, 0.1 mmol) and the resultant reaction mixture was stirred for another 5 h at room temperature. The resulting precipitate was filtered through filter paper, washed with MeOH and dried in air affording a light green solid. Yield: 27 mg (64%). Anal. Calcd for $C_{36}H_{34}N_4O_{12}Ni_2$ (MW 832.06): C, 51.97; H, 4.12; N, 6.73. Found: C, 51.32; H, 5.73; N, 6.70. Selected FTIR peaks (KBr, cm^{-1}): 3383 (br), 1608 (s), 1567 (s), 1557 (s), 1445 (s), 1417 (s), 1372 (s), 1258 (m), 774 (m), 720 (s).

{[Co_2(bdiab)]·3CH_3OH·5H_2O}$_n$ (76) To a mixture of H_4bdiab (32 mg, 0.05 mmol) in 4 mL methanol, NaOH (8 mg, 0.2 mmol) was added followed by addition of $Co(OAc)_2{\cdot}4H_2O$ (25 mg, 0.1 mmol) and the resultant reaction mixture was stirred for another 5 h at room temperature. The resulting precipitate was filtered through filter paper, washed with MeOH and dried in air affording a pink solid. Yield: 37 mg (78%). Anal. Calcd for $C_{39}H_{48}N_4O_{16}Co$ (MW 946.68): C, 49.48; H, 5.11; N, 5.92. Found: C, 50.95; H, 5.09; N, 6.87. Selected FTIR peaks (KBr, cm^{-1}): 3385 (br), 1557 (s), 1373 (s), 1250 (w), 777 (m), 670 (m).

CHAPTER III

Results and Discussion

This chapter contains two major sections: (a) coordination architectures derived from three components and (b) coordination architectures derived from two components. Both sections are further divided into different subsections depending on the ligand system used. A judicious choice of a metal center along with ligand/linker provides structural and functional diversity in the formation of metal organic coordination networks.[151–156] Various polypyridyl-based ligands have been synthesized by Schiff-base condensation reaction followed by reduction and further substitution reactions.[157] Synthesis and characterization of all new ligands are discussed prior to the major sections. Considering the three-component systems, a combination of these polypyridyl ligands with different di/tricarboxylates and metal center results in the formation of various coordination architectures with different dimensionality and structures. In addition to strong metal-O/N coordinate bonds, supramolecular interactions, like π–π stacking[158] and hydrogen bonding, provide additional stability to the formation of different supramolecular assemblies.[159–162] With respect to the two-component systems, new mixed ligands have been designed and synthesized for making various neutral and ionic coordination architectures. For their characterization, various techniques, like UV-Vis, FTIR, Raman and fluorescence spectroscopy, single crystal and powder X-ray diffraction, and thermogravimetric analysis have been used. Many of these coordination architectures have been utilized in four key applications mentioned in Chapter 1.

Synthesis of Ligands. Both **6-Mebpea** and **6-Mebpta** were synthesized by condensation reaction between 6-methyl-pyridine-2-carboxaldehyde and the corresponding amine (in a 1:1 ratio) followed by reduction using $NaBH_4$ at room temperature. Further reaction of the reduced Schiff base with picolylchloride provided the desired product (Scheme 3.1). On the other hand, **6,6′-Me$_2$bpta** ligand was prepared in a one-step reaction between 6-methyl-pyridine-2-carboxaldehyde and tert-butylamine (in a 2:1 ratio) using sodium triacetoxyborohydride in dry dichloroethane (DCE) solvent under inert conditions at room temperature (Scheme 3.1). These ligands were thoroughly characterized by ^{1}H NMR

spectroscopy and HRMS and used for making their metal complexes without further purification.

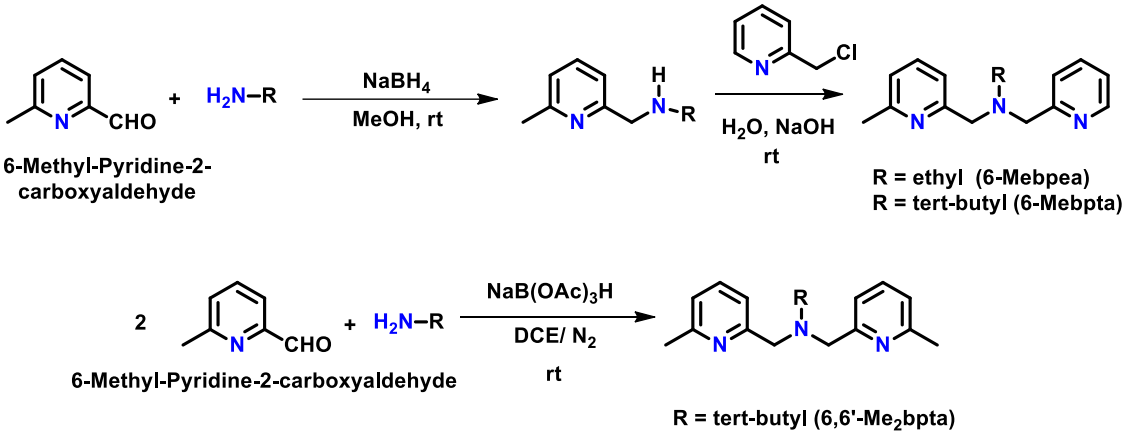

Scheme 3.1. Synthesis of 6-Mebpea, 6-Mebpta and 6,6′-Me_2bpta.

Functionalized polypyridyl based ligands (**2,2′-terpyBA** and **4,4′-terpyBA**) have been synthesized in two steps. In the first step, 4-hydroxy benzaldehyde was reacted with propargyl bromide to insert the acetylene functionality. In in the second step, the resulting aldehyde in the first step was reacted with two equivalents of acetyl pyridine (2-acetylpyridine for **2,2′-terpyBA** and 4-acetylpyridine for **4,4′-terpyBA**) to get the desired product (Scheme 3.2).

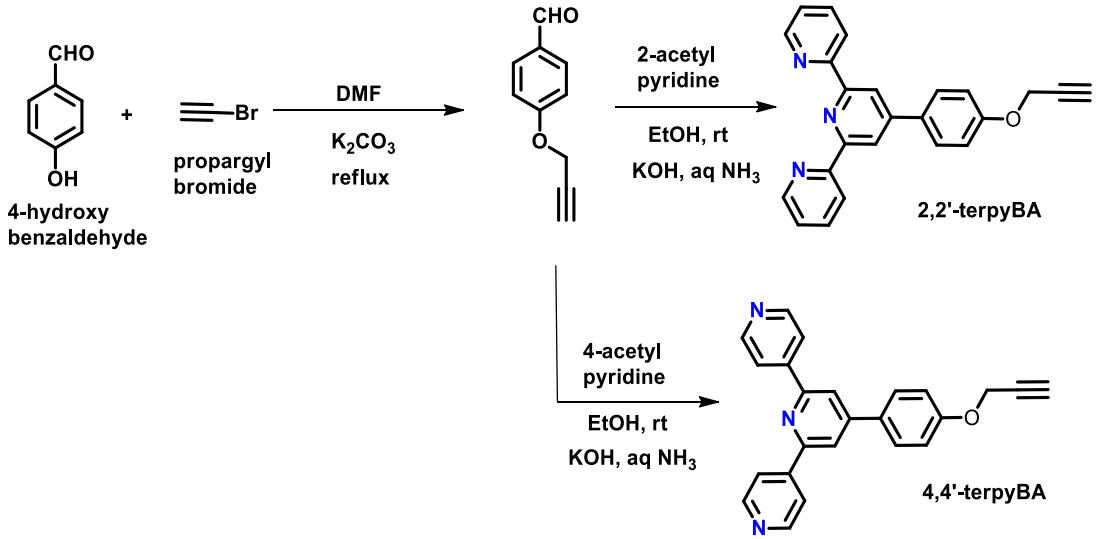

Scheme 3.2. Synthesis of 2,2′-terpyBA and 4,4′-terpyBA.

Synthesis of mixed pyridyl-carboxylate based ligands has been achieved in two steps. For the synthesis of **H_2bpaipa**, 5-amino isophthalic acid was reacted with pyridyl-2-carboxaldehyde followed by reduction using $NaBH_4$. The resulting reduced Schiff base was reacted with 2-picolyl chloride to get the final product. In a similar fashion, **2,4-H_2bpaipa** was synthesized where pyridyl-4-carboxaldehyde was used instead of pyridyl-2-

carboxaldehyde, while **H_3pbaipa** required 4-formyl benzoic acid as the aldehyde (Scheme 3.3).

For the synthesis of tetracarboxylate ligands **H_4daib** and its derivative **H_4bdaib**, a procedure similar to that for H_3pbaipa was followed except isophthalaldehyde was used instead of 4-formyl benzoic acid (Scheme 3.4).

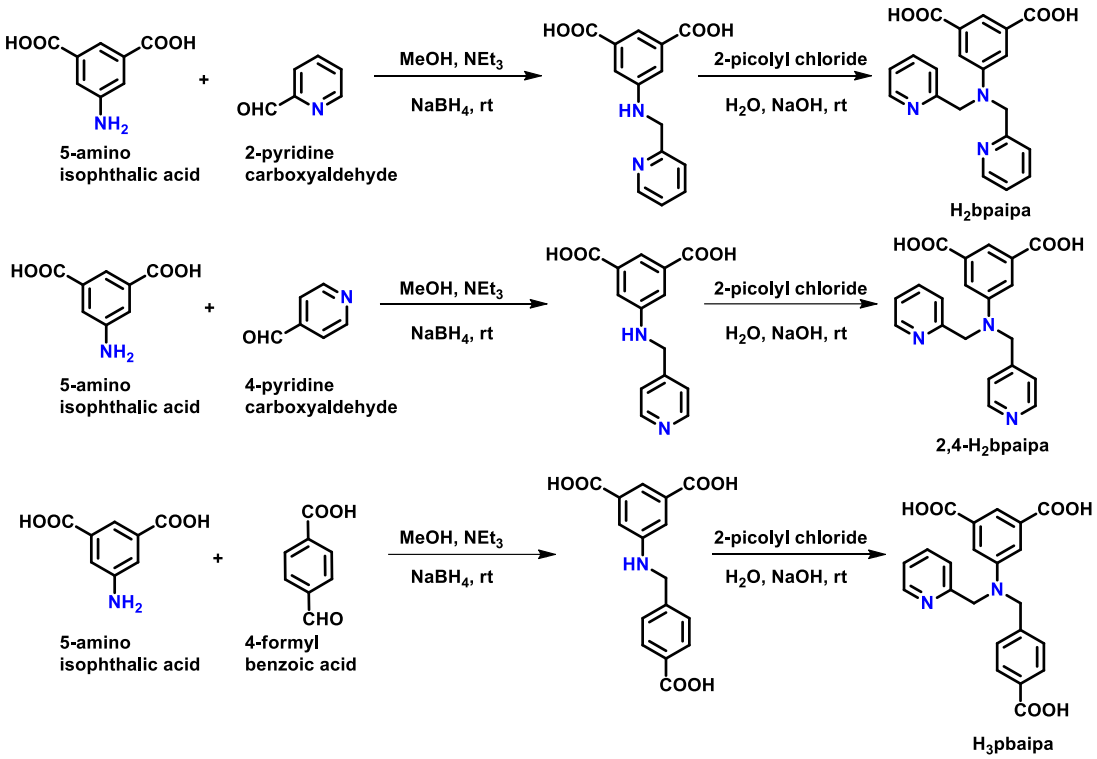

Scheme 3.3. Synthesis of H_2-bpaipa, 2,4-H_2bpaipa and H_3-pbaipa.

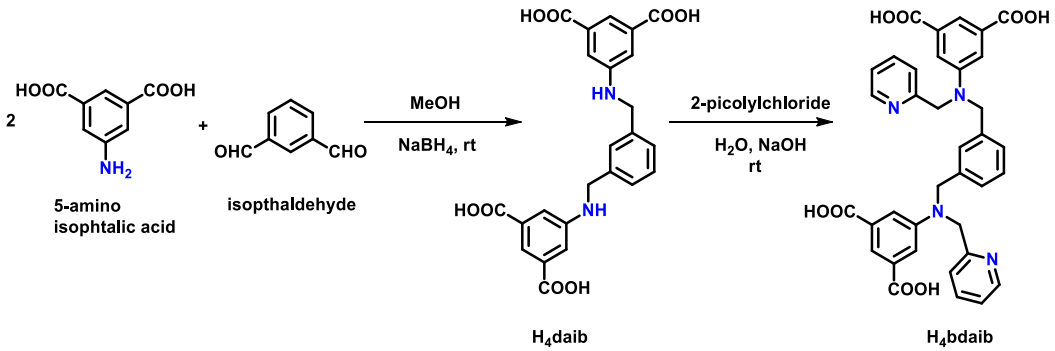

Scheme 3.4. Synthesis of H_4daib and H_4bdaib.

3.1 COORDINATION ARCHITECTURES DERIVED FROM THREE COMPONENTS

In this section, we have explored the syntheses, characterization and applications of metal organic coordination architectures formed by three components, namely a metal ion, an ancillary ligand (tridentate pyridyl based), and a linker (dicarboxylate/tricarboxylate). A proper ratio of these components is the key for deciding the final architecture, in addition to the other factors such as synthetic method, temperature and pH of the reaction.[163,164] In doing so, coordination architectures with different dimensionality are obtained.[76] The various possibilities which can be achieved through such combinations are shown in Figure 3.1. Examples of those reported from this group are: a dinuclear compound (type a),[76] a mononuclear compound having one side of the dicarboxylate uncoordinated (type b)[63], a molecular square (type c),[75] a dinuclear compound with a bridging carboxylate as well as a free dicarboxylate as an anion to neutralize the charge (type d)[63] and a 1D coordination polymer (type f).[76] Interestingly, the structure type e is not reported with a tridentate ligand.

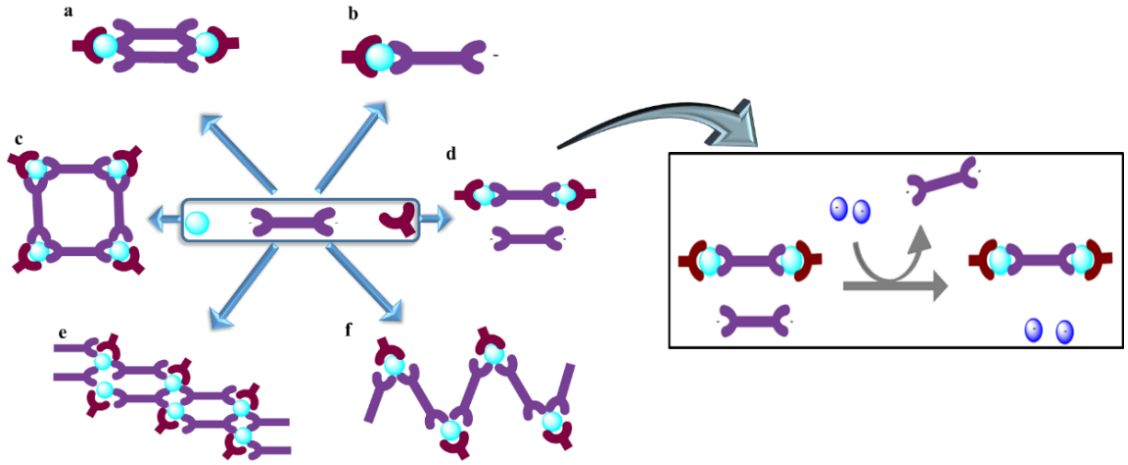

Figure 3.1. Schematic representation of possible coordination architectures formed in three-component systems (a) a dinuclear compound, (b) mononuclear compound having one side of carboxylate free, (c) a square, (d) a dinuclear compound having one free anion, and (e and f) 1D coordination polymers; only with type d, an anion exchange is possible (right).

On the other hand, type d is a good candidate for anion exchange applications. A dicarboxylate can be replaced by another anion to give compounds having different properties and can affect the overall structure of the architecture by affecting the encapsulated solvent molecules.[74,111]

3.1.1 Pyridyl-based ligands and dicarboxylates

Three different polypyridyl ligands (6-Mebpea, 6-Mebpta and 6,6'-Me_2bpta) have been chosen for the construction of coordination architectures where a dicarboxylate (flexible or rigid) is used as a linker. For Ni(II) coordination complexes synthesized using the same ligand with different dicarboxylates, both neutral and cationic dinuclear coordination architectures are formed. In the case of cationic coordination compounds, the presence of free anion helps in the neutralization of charge on the metal center and provides stability to the overall supramolecular architecture. Similarly, Zn(II) and Cd(II) complexes are also made. Synthesis of these complexes was attained by three component self-assembly of a metal salt, a linker and a ligand in a 1:1:1 ratio in methanol at ambient conditions or by solvothermal reaction in a mixture of solvents like, a 1:1 mixture of water and methanol, at 120 °C for 48 h followed by cooling in 24 h. In all the cases, an acetate salt of various metals was used and acetic acid formed as the side product was removed by treating the compound with an acetonitrile and toluene mixture (1:1) several times. Crystallization of various compounds was successfully achieved by using either slow evaporation or direct layering of reactants in suitable solvents.

Chemistry with 6-Mebpta

With the 6-Mebpta ligand, twelve compounds were prepared as shown in Schemes 3.5-3.7. There is a variation of lattice water molecules in these compounds. For this reason, different types of supramolecular assemblies are formed along with the encapsulation of water clusters having different shapes and arrangements. Furthermore, compounds having free carboxylates (type d structure in Figure 3.1) were employed for anion exchange to observe the effect on water clusters.

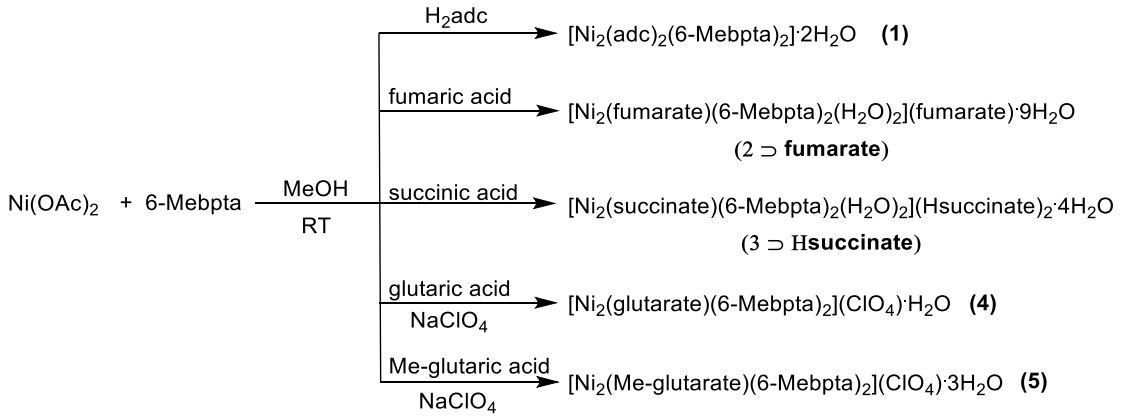

Scheme 3.5. Synthesis of **1-5**.

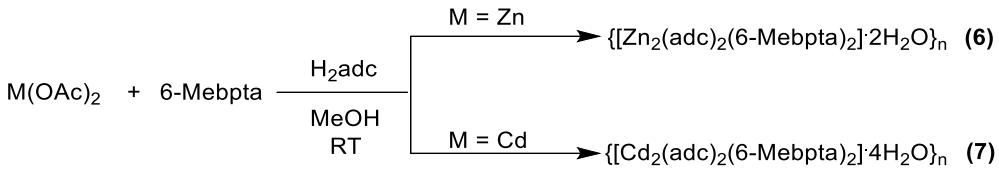

Scheme 3.6. Synthesis of **6-7**.

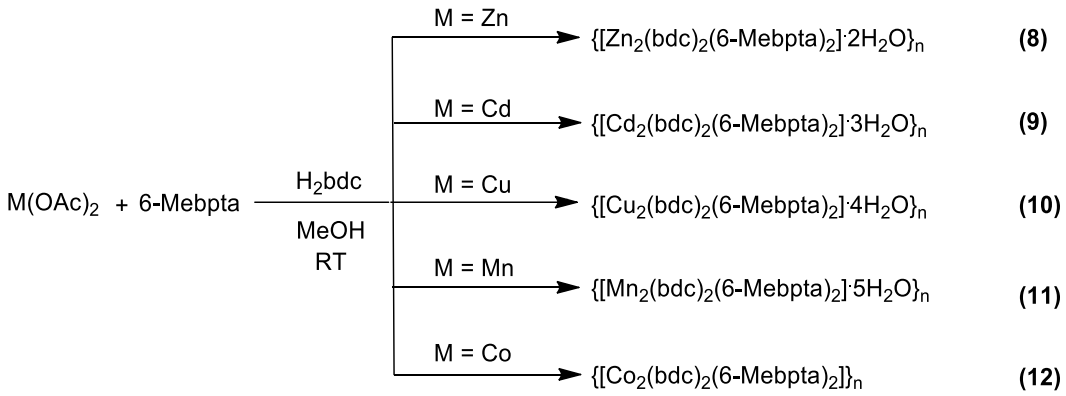

Scheme 3.7. Synthesis of **8-12**.

FTIR and Raman spectroscopic studies. Various functional groups and their modes of binding to the divalent metal ions in the coordination architectures can be well deduced from the FTIR stretching frequencies. In these coordination architectures, the binding mode of carboxylates plays a very important role in deciding the overall structure of the framework. The carboxylate binding to the metal centers in the architectures can be well predicted from the difference between the asymmetric (ν_1) and symmetric (ν_2) stretching frequencies (the $\Delta\nu$ value). When the $\Delta\nu$ value is greater than 210 cm^{-1}, a monodentate binding mode is observed, whereas a value below 200 cm^{-1} suggests a bidentate mode of carboxylate. Along with functional groups, we can easily identify the presence of lattice solvents, for example, a peak around 1650-1680 cm^{-1} corresponds to DMF molecules and a peak around 3400-3500 cm^{-1}, 3300-3400 cm^{-1} and 3200-3300 cm^{-1} stands for –OH of lattice and coordinated water molecules, respectively. There are many functionalities which are FTIR inactive like an alkyne group. Therefore, compound **1** was studied with the help of Raman spectroscopy.

For compound **1**, a broad band centered at 3408 cm^{-1} corresponds to lattice water molecules. A series of bands between 1610 cm^{-1} and 1310 cm^{-1} are associated with the 6-Mebpta ligand, while bands at 1624 cm^{-1} and 1352 cm^{-1} are due to asymmetric and symmetric stretching modes of carboxylate groups of adc, respectively (Figure 3.2). The $\Delta\nu$ value of 272 cm^{-1} indicates a monodentate binding of the carboxylate group of adc to Ni(II) as found

in the crystal structure of **1** (Figure 3.8, *vide infra*). On the other hand, the Raman spectrum of **1** shows a peak at 2203 cm^{-1} for the C-C triple bond. The observed value for the C-C triple bond is very close to those (2239 cm^{-1} and 2220 cm^{-1}) found in the other Ni(II) complexes.[165,166]

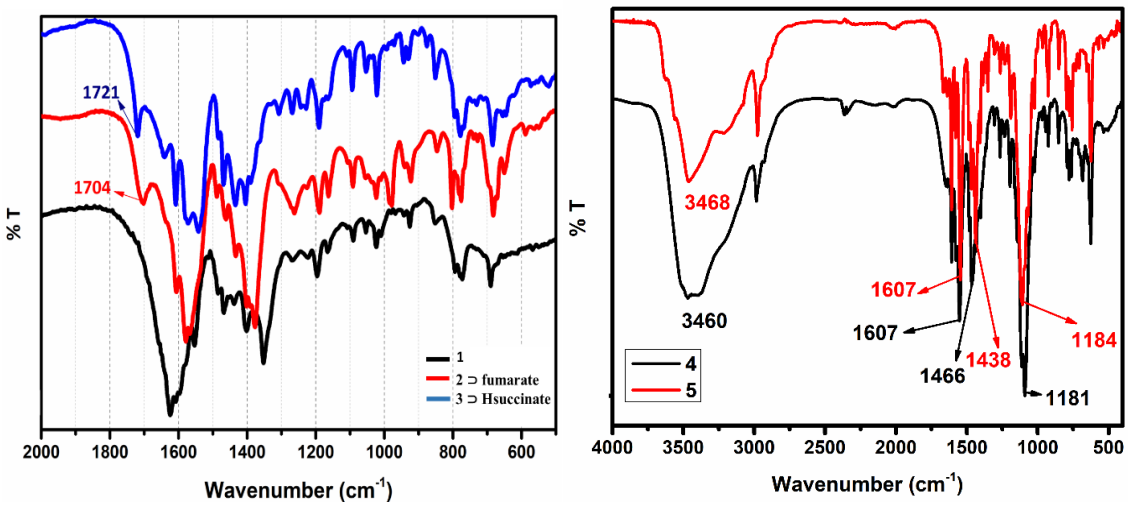

Figure 3.2. FTIR spectra of **1**-**5**.

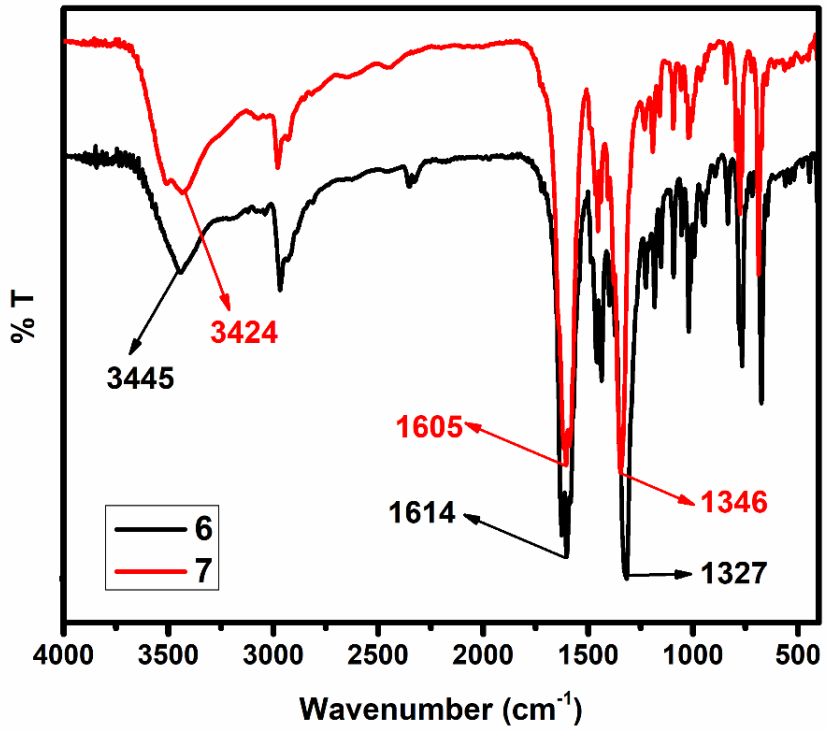

Figure 3.3. FTIR spectra of **6** and **7**.

The FTIR spectrum of **2⊃fumarate** (Figure 3.2) shows two broad bands around 3406 cm^{-1} and 3274 cm^{-1} corresponding to two types of water (coordinated and lattice water, respectively) while the band at 1704 cm^{-1} is due to the free carboxylate groups of the

fumarate anion. The bands at 1581 cm^{-1} and 1385 cm^{-1} are due to asymmetric and symmetric stretching modes of the carboxylate group of the coordinated fumarate, respectively. The $\Delta\nu$ value of 196 cm^{-1} indicates a bidentate (chelated) type binding of carboxylate groups of fumarate to Ni(II) as found in the structure of **2⊃fumarate** (Figure 3.10, *vide infra*). In case of **3⊃Hsuccinate**, the IR spectrum (Figure 3.2) shows two broad peaks around 3412 cm^{-1} and 3221 cm^{-1} corresponding to two types of water molecules as in **2⊃fumarate**. Similarly, a peak at 1718 cm^{-1} is due to the deprotonated free carboxylate group of succinate and a difference of 182 cm^{-1} between asymmetric (1570 cm^{-1}) and symmetric (1388 cm^{-1}) stretching frequencies indicates a bidentate chelated mode of carboxylate to Ni(II).

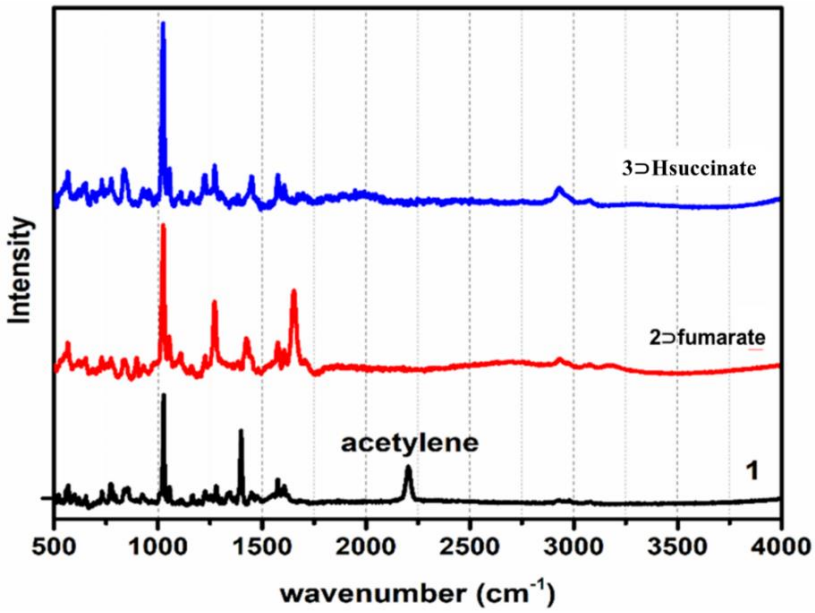

Figure 3.4. Raman spectra of **1-3**.

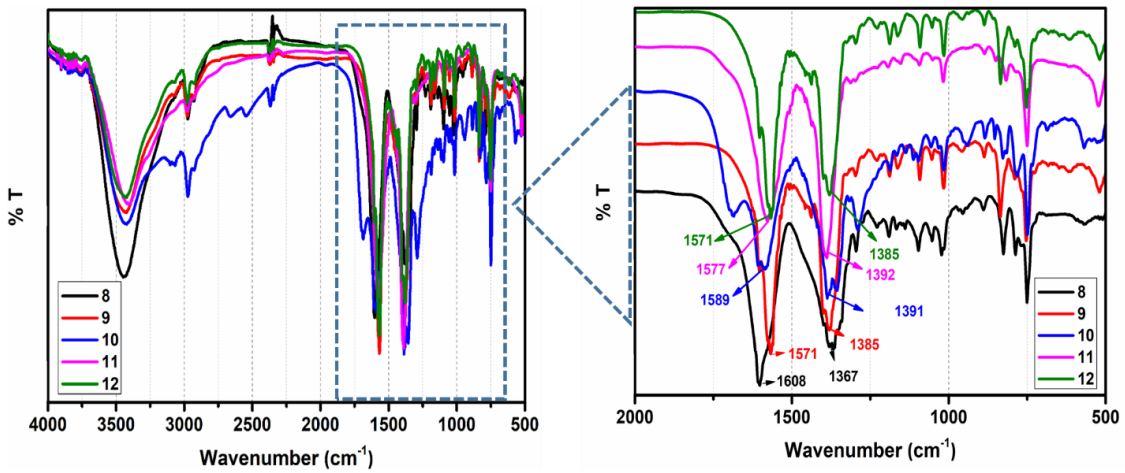

Figure 3.5. FTIR spectra of **8-12**.

The FTIR spectra of compounds **4** and **5** are similar (Figure 3.2) with a difference in the asymmetric and symmetric frequencies ($\Delta\nu$) corresponding to 141 cm^{-1} and 169 cm^{-1}, respectively, indicating a bidentate mode of carboxylate binding to the metal center. For compounds **6**, **7** and **8** the observed $\Delta\nu$ values of 268 cm^{-1}, 259 cm^{-1} and 241 cm^{-1}, respectively, (Figure 3.3) indicate the monodentate mode of carboxylate binding to the metal center. On the other hand, compounds **9-12** have smaller values of $\Delta\nu$: 186 cm^{-1}, 198 cm^{-1}, 185 cm^{-1} and 186 cm^{-1}, respectively, confirming a bidentate mode of carboxylate binding to the metal center (Figure 3.5). For **1-12**, the FTIR data for the carboxylate groups are listed in Table 3.1.

Table 3.1. Asymmetric and symmetric stretching frequencies and their respective binding modes of carboxylates in **1-12**.

Compound	Asymmetric (υ_1) cm^{-1}	Symmetric (υ_2) cm^{-1}	$\Delta\upsilon = \upsilon_1 - \upsilon_2$ cm^{-1}	Binding mode
1	1624	1352	272	Monodentate
2⊃fumarate	1581	1385	196	Bidentate (chelated)
3⊃Hsuccinate	1570	1388	182	Bidentate (chelated)
4	1607	1466	141	Bidentate (chelated)
5	1607	1438	169	Bidentate (chelated)
6	1614	1327	268	Monodentate
7	1605	1346	259	Monodentate
8	1608	1367	241	Monodentate
9	1571	1385	186	Bidentate (chelated)
10	1589	1391	198	Bidentate (chelated)
11	1577	1392	185	Bidentate (chelated)
12	1571	1385	186	Bidentate (chelated)

Thermogravimetric analyses. Thermal stabilities of **1-3** and **5-12** were studied as a function of temperature in the range of 25-500 °C (Figures 3.6 and 3.7). Compounds **4** and **5** were excluded because of the explosive nature of the perchlorate anions present in them. All compounds under consideration are found to be stable up to 200 °C with an initial loss of both lattice as well as coordinated solvent molecules at around 100 °C. In case of **1**, a loss of 7.56% (ca. 6.61%) corresponds to the loss of four lattice water molecules. Further decomposition of **1** was evident by a continuous loss of the weight. Compound **2⊃fumarate** shows a loss of 18.30% (ca. 18.02%) corresponding to the loss of eleven water molecules followed by its decomposition. Compound **3⊃Hsuccinate** exhibits a loss of 10.84% corresponding to the loss of six water molecules (ca. 11.87%) (Figure 3.6).

Compound **6** has the first loss of about 3.87% (ca. 4.05%) corresponding to the loss of two water molecules followed by its decomposition. In case of compound **7**, first weight loss of 6.79% corresponds to the loss of four lattice water molecules (ca. 7.06%) followed by its decomposition. Compounds **8**-**10** having similar nature with different metals exhibit the first weight loss of 3.48% (ca. 3.90%), 4.71% (ca. 4.48%) and 6.75% (ca. 6.71%), respectively, corresponding to the loss of two, three and four lattice water molecules, respectively. Compounds **11** and **12** exhibit the first weight loss of 23.82% (ca. 24.69%) and 14.68% (ca. 14.95%), respectively, corresponding to the loss of five water molecules and one bdc in **11** and the loss of one bdc in case of **12**. Compounds **9** and **11** are more stable after losing the lattice solvent molecules as compared to other related compounds (see Figure 3.7).

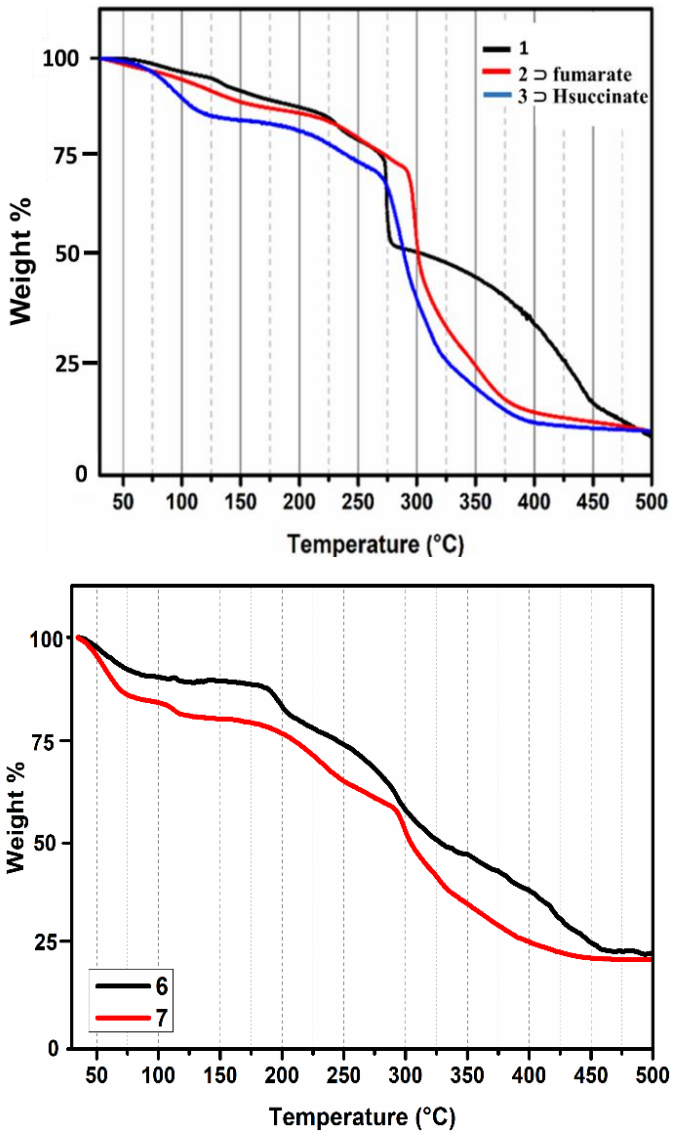

Figure 3.6. TGA scans of **1**-**3** and **6**-**7**.

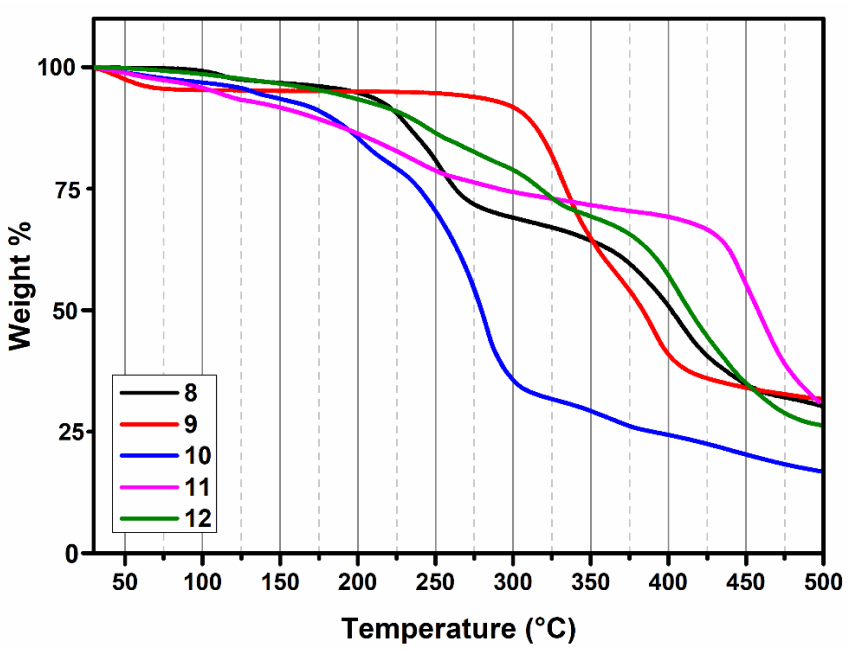

Figure 3.7. TGA scans of **8-12**.

Single crystal structure analyses. Crystals of **1-4** were grown by the slow evaporation of their clear solutions in a mixture of water and acetonitrile. For anion exchange, two methods have been used for getting the daughter crystals: one is the SC-SC transformation (solid to solid) and the other is the slow evaporation of an aqueous solution of the compound and new salt of the anion (liquid to solid).

Structural description of **1**. It crystallizes in the $P2_1/n$ space group. It has a dinuclear unit consisting of two Ni(II) centers bridged by two adc groups, which bind in both monodentate and bidentate fashion. Its asymmetric unit consists of a metal, one ligand, one linker

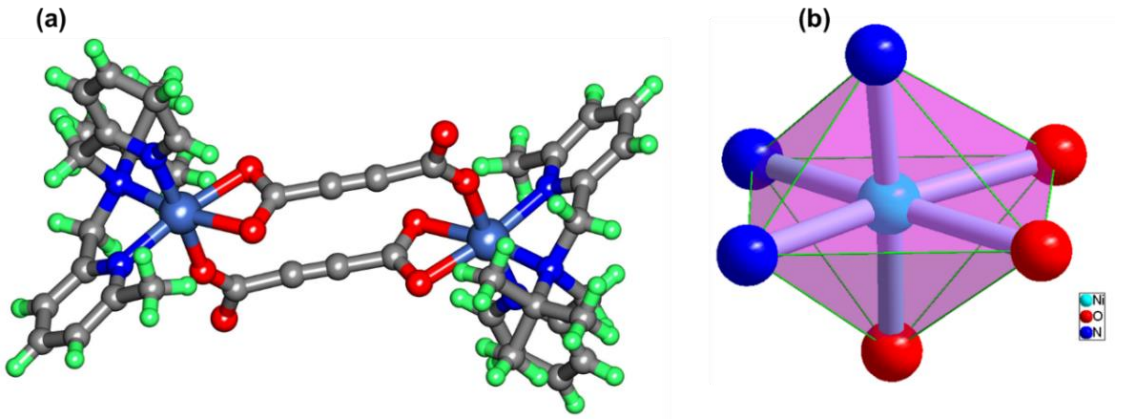

Figure 3.8. (a) Formation of a *bis*(adc) dinuclear core and (b) distorted octahedron having N_3O_3 type surrounding in **1**.

and one lattice water molecule. The Ni(II) centers are crystallographically equivalent. The geometry around each Ni(II) center is distorted octahedral and is surrounded by three

nitrogens of the ligand (6-Mebpta) with Ni-N_{Py} (2.048 Å and 2.079 Å) and Ni-N_{alkyl} (2.131 Å) bonds, two oxygens of one adc (unsymmetrical chelated, having bond distances of 2.107 Å and 2.213 Å) and one oxygen of other adc (monodentate, having a bond distance of 2.053 Å) molecule. A 14-membered ring with dimensions 4.952 Å x 3.273 Å (Figure 3.8) is formed by two Ni(II) centers, four oxygens and eight carbons (from both adc). To the best of our knowledge, it is the first example with a Ni(II) *bis*(adc) core. Selected bond lengths and angles around the metal center are comparable as reported in the literature.

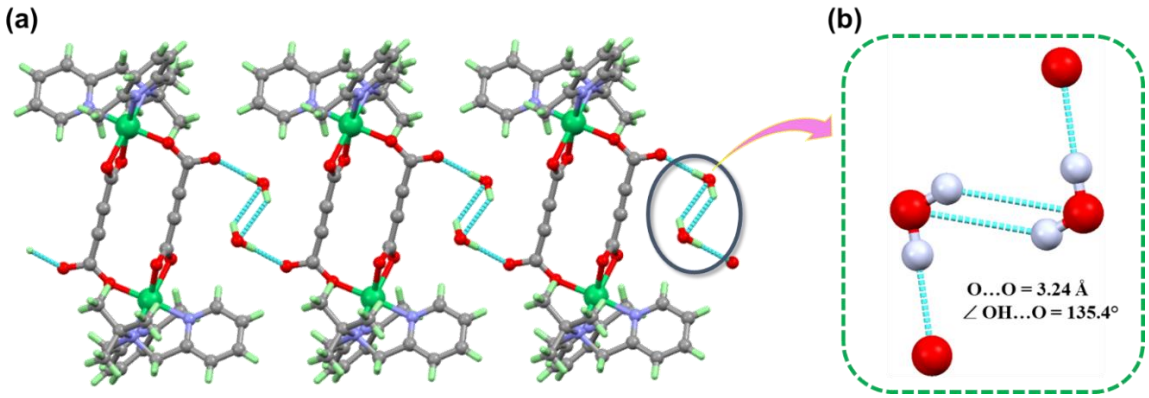

Figure 3.9. (a) Formation of 1D Supramolecular assembly and (b) doubly hydrogen-bonded cyclic water cluster in **1**.

There are two lattice water molecules in **1**, which are involved in the formation of a linear supramolecular assembly. These two lattice water molecules form a doubly hydrogen-bonded cyclic water dimer, which acts as a bridge between two Ni(II) *bis*(adc) units (Figure 3.9). A water dimer with a double hydrogen bond to form a cyclic cluster is very rare.

Table 3.2. Hydrogen bonding parameters in **1.**

D---H…A (Å)	r(D-H) (Å)	r(H…A) (Å)	r(D…A) (Å)	∠D-H…A (deg)	Symmetry
O5 -H5A...O4	0.8500	1.900	2.7453	177	-x,-y,1-z
O5 -H5B...O5	0.8500	2.6000	3.2436	133	-x,-y,1-z
C2 -H2A...O1	0.9000	2.4800	3.3049	152	-
C3 -H3...O3	0.8700	2.5600	3.2970	143	x,y,-1+z
C7 -H7A…O5	1.0000	2.3300	3.3110	169	1/2+x,1/2-y,-1/2+z
C7 -H7B...O3	0.9300	2.4900	3.0105	116	1-x,-y,1-z
C9 -H9B...O2	1.0600	2.4000	3.3046	143	-
C11 -H11C...O2	1.0500	2.4800	3.4015	145	-
C16 -H16...O4	0.9400	2.3600	3.2180	153	-x,-y,1-z

To the best of our knowledge, there is only one example reported in the literature which described a water dimer with O···O distance is 2.93(5) Å in the solid state and characterized by X-ray structure.[167] Thus, we can claim that this is the second example of a cyclic water dimer. The O···O distance between O5 and O5' involved in the cyclic water dimer is 3.243 Å, while the O-H···O distance is 2.600 Å with an angle of 135.40° (∠O-H···O). All hydrogen bonding parameters are listed in Table 3.2.

Structural description of **2⊃fumarate**. Compound **2⊃fumarate** crystallizes in the $P2_1/c$ space group consisting of a dinuclear unit bridged by a fumarate linker. The asymmetric unit consists of two metal center, two ligands and two linkers. Both Ni(II) centers have a distorted octahedral geometry and are surrounded by three nitrogens of the ligand with Ni-N bond distances 2.082(2) Å and 2.079(3) Å (Ni(II)-N_{py}) and 2.144(3) Å (Ni(II)-N_{alkyl}), two oxygens of the fumarate linker (chelated, OCO angle: 120° and Ni-O bond distances: 2.144(2) Å, 2.171(2) Å) and one coordinated water (bond distance: 2.041(2) Å) as shown in Figure 3.10. The bond distances and angles in **2⊃fumarate** are listed in Table A23 and A34 (Appendix). To neutralize the charge on both the Ni(II) centers, an additional fumarate is also present but is in the free state (Figure 3.10).

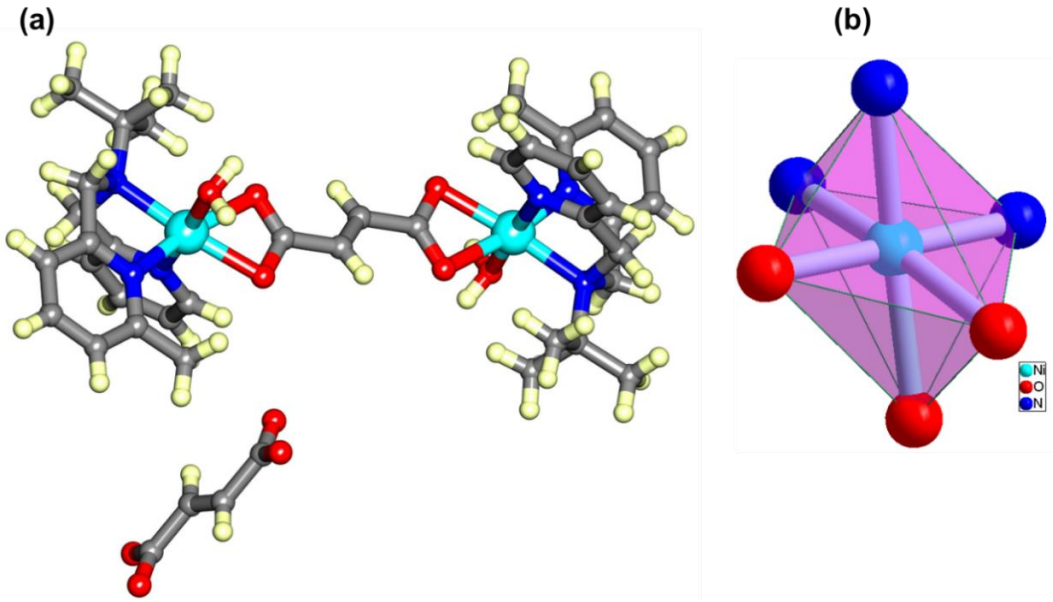

Figure 3.10. (a) Formation of a dinuclear complex having free fumarate anion and (b) distorted octahedral geometry having N3O3 type surrounding around the metal center in **2⊃fumarate**.

In the crystal structure of **2⊃fumarate** there are nine lattice water molecules (O11, O12, O13, O14, O15, O16, O17, O18, and O19). These lattice water molecules and fumarate anions form a strong hydrogen bonding network to generate a 3D supramolecular assembly (Figure 3.11). Ten different types of motifs are formed via hydrogen bonding. Motif 1 is a

hexagonal motif ($R_5^5(6)$); this is formed by hydrogen bonding between one coordinated water molecule (O3), two oxygen atoms (O8···O7) of the counter anion fumarate, and two lattice water molecules (O11···O16) with distances: 2.687 Å, 2.653 Å, 2.685 Å and 2.763 Å. Motif 2 is a hexagonal motif, ($R_6^6(6)$), consisting of two oxygens of two counter fumarate anions (O8···O10) and four lattice water molecules (O18···O13···O19···O16); distances: 2.763 Å, 2.804 Å, 2.839 Å, 2.824 Å, 2.697 Å, and 2.769 Å. Motif 3, ($R_5^5(5)$), consists of five lattice water molecules (O18···O19···O15···O12···O17) resulting in the formation of a pentamer of water cluster (Figure 3.11 and 3.12); distances: 2.839 Å, 2.769 Å, 2.783 Å, 2.850 Å, and 2.653 Å. Motif 4, ($R_5^5(5)$), consists of three lattice water molecules (O17, O14 and O12), one coordinated water molecule (O6) and one oxygen (O9) from counter fumarate (distances: 2.850 Å, 2.687 Å, 2.807 Å, 2.657 Å and 2.732 Å).

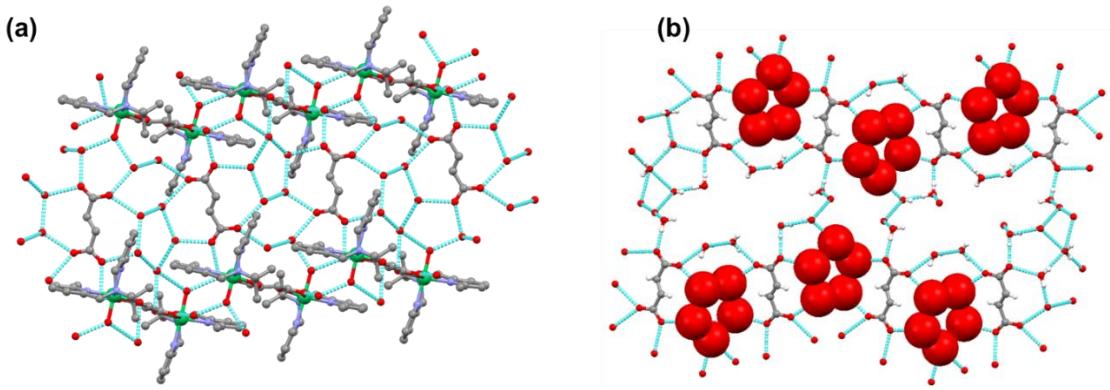

Figure 3.11. (a) Formation of supramolecular assembly and (b) cyclic pentamer of water cluster in **2⊃fumarate**.

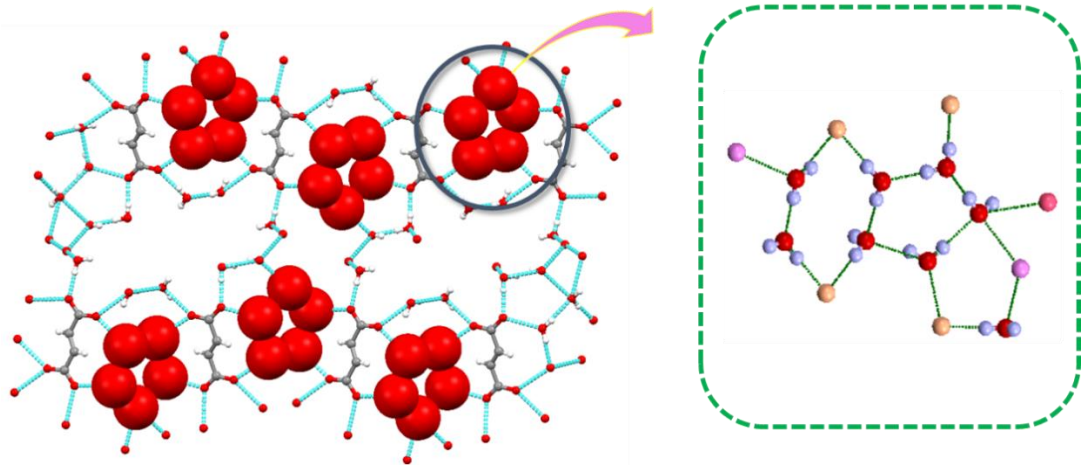

Figure 3.12. Closer view of a quasi-planar cyclic pentamer of water cluster formed in **2⊃fumarate**.

Motif 5, ($R_3^3(4)$), is a tetragonal motif consisting of one lattice water molecule (O17), one oxygen of the coordinated fumarate (O4), one coordinated (O6) water molecule (distances:

2.972 Å and 2.807 Å) and one Ni(II) center. Motif 6, ($R_5^5(10)$), is a decamer consisting of three lattice water molecules (O15···O11···O17), two oxygens from coordinated fumarate (O5···O4), one oxygen (O7) from counter anion fumarate (distances: 2.685 Å, 2.777 Å, 2.872 Å, 2.857 Å and 2.652 Å); four carbon atoms of fumarate also involved in the formation of this decameric motif. Motif 7, ($R_4^4(8)$), consists of two oxygens from counter fumarate (O8···O7), and two lattice water (O18···O15) molecules (distances: 2.777 Å, 2.804 Å and 2.783 Å). Motif 8, ($R_4^4(8)$), is same as Motif 7 except that different oxygen atoms from lattice water (O19···O12) and two oxygens (O9···O10) from counter fumarate (distances: 2.769 Å, 2.824 Å and 2.722 Å) are involved.

Table 3.3. Hydrogen bonding parameters for **2⊃fumarate**.

D---H…A (Å)	r(D-H) (Å)	r(H…A) (Å)	r(D…A) (Å)	∠D-H…A (deg)	Symmetry
O3 -H3A...O19	0.88	1.89	2.6873	149	x,1/2-y,-1/2+z
O3 -H3B...O11	0.88	2	2.6534	130	x,1/2-y,-1/2+z
O6 -H6A...O14	0.87	1.88	2.6392	145	-
O11 -H11E...O7	0.85	1.87	2.6853	161	-
O12 -H12C...O13	0.85	2.02	2.8506	164	-
O12 -H12D...O15	0.85	2.03	2.7675	144	-
O13 -H13A...O4	0.85	2.29	2.9722	137	1-x,1/2+y,1/2-z
O13 -H13B…O16	0.85	1.8	2.6499	177	-
O14 -H14A...O9	0.85	1.84	2.6873	173	-
O14 -H14B...O1	0.85	1.97	2.8073	169	1-x,-1/2+y,1/2-z
O17 -H17B...O10	0.85	1.86	2.6968	167	-
O18 -H18A…O15	0.85	1.99	2.8392	174	x,1/2-y,-1/2+z
O18 -H18B...O8	0.85	1.96	2.8044	174	-
O19 -H19A...O8	0.85	1.95	2.7616	159	-
O19 -H19B...O17	0.85	1.92	2.7687	175	-
C7 -H7A...O18	0.99	2.45	3.4272	167	-
C9 -H9C...O2	0.98	2.57	3.4405	149	-
C11 -H11B...O2	0.98	2.59	3.4567	148	-
C28 -H28A...O4	0.98	2.47	3.3182	145	-
C29 -H29A...O4	0.98	2.39	3.247	146	-
C38 -H38...O11	0.95	2.51	3.4391	168	1+x,y,z

Motif 9, ($R_7^7(13)$), consists of three lattice water molecules (O19···O13···O14), two oxygens from counter fumarate (O9···O10), one oxygens from coordinated water (O3) and one oxygen (O1) of the bonded fumarate (distances: 2.687 Å, 2.769 Å, 2.697 Å, 2.687 Å and

2.807 Å). Motif 10, ($R_6^6(8)$), formed by hydrogen bonding network between two lattice water molecules (O11···O14), two oxygens from coordinated water molecules (from two different unit) (O6···O3) and two oxygens from the coordinated fumarate (from different unit) (O1···O5); distances: 2.807 Å, 2.639 Å, 2.663 Å and 2.857 Å. Motif 1 connects one dinuclear synthon with counter anion fumarate through coordinated water and two lattice water molecules. Motif 3 is present in the center and surrounded by six different motifs. Motif 10 connects two dinuclear synthons with each other and forms a 3D supramolecular assembly (Figures 3.11 and 3.12). Hydrogen bonding parameters for **2⊃fumarate** are listed in Table 3.3.

Structural description of **3⊃Hsuccinate**. Compound **3⊃Hsuccinate** is isostructural with compound **2⊃fumarate**. It crystallizes in the monoclinic $P2_1/c$ space group consisting of a dinuclear Ni(II) synthon. The asymmetric unit consists of one Ni(II) center, one ligand, half of the bridging succinate and one Hsuccinate as a counter anion. Like the fumarate in **2⊃fumarate**, the succinate acts as a bridging ligand as well as a counter anion (Figure 3.13). However, the arrangement of anion and water clusters is different in the supramolecular assembly of **3⊃Hsuccinate**. This could be due to the main difference in the anions: there are two molecule of Hsuccinate as it is monodeprotonated in **3⊃Hsuccinate** compared to fully deprotonated fumarate in case of **2⊃fumarate**.

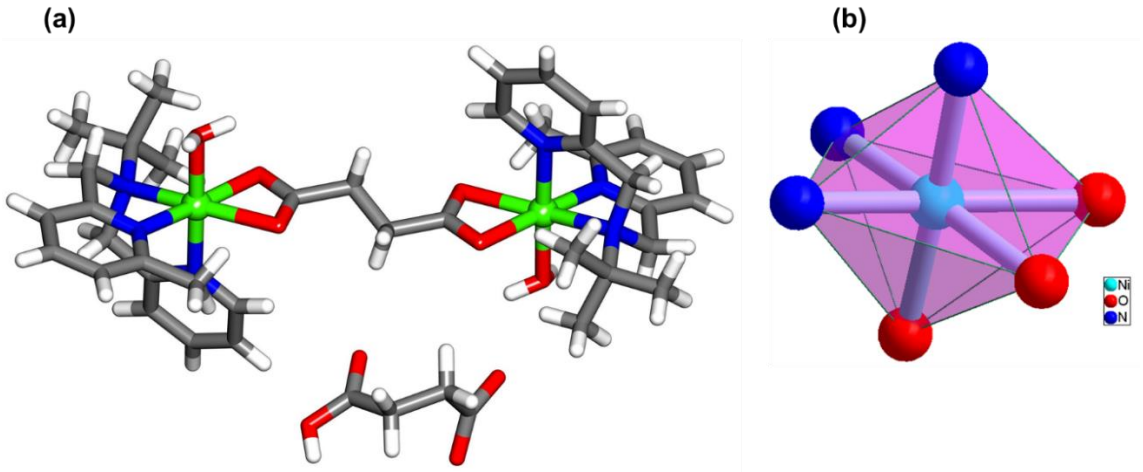

Figure 3.13. (a) Dinuclear unit along with free Hsuccinate anion and (b) distorted octahedral geometry around the Ni(II) having N3O3 in **3⊃Hsuccinate**.

The Ni(II) metal centers have distorted octahedral geometry with three nitrogens from ligand having bond distances: 2.104(11) Å and 2.102(11) (Ni(II)-N_{py}) and 2.164(11) Å (Ni(II)-N_{alkyl}), two oxygens of the succinate linker (chelated, OCO angle: 120°; bond distances: 2.230(9) Å and 2.068(9) Å) and one coordinated water oxygen (bond distance:

2.106(9) Å). Selected bond distances and angles are listed in Table A24 and A35 (Appendix). There are four lattice water molecules present in the compound which helps in the formation of a supramolecular assembly through strong hydrogen bonding. Two dinuclear synthons are connected with each other through hydrogen bonding between two coordinated water molecules (O3…O3'), two lattice water molecules (O9…O9') and two oxygens of the bridged succinate (O2…O2') resulting in the formation of an octameric motif ($R_6^6(8)$) to form a linear 2D supramolecular assembly.

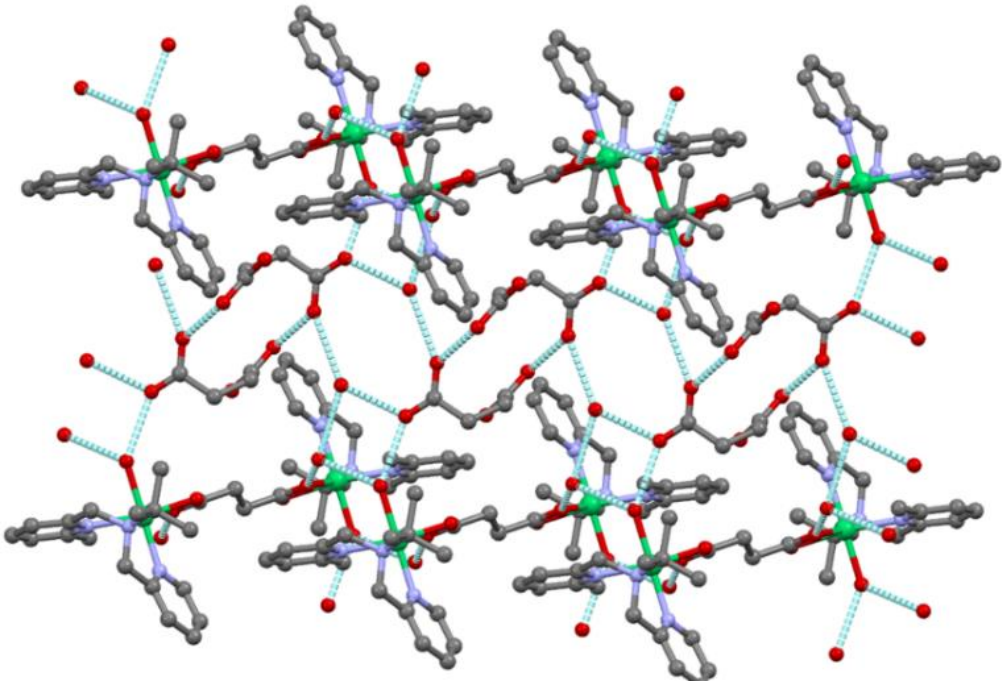

Figure 3.14. Formation of a 3D supramolecular assembly in **3⊃Hsuccinate**.

Two such layers are connected with each other through hydrogen bonding between lattice water molecules and Hsuccinate anions (uncoordinated) to form a 3D supramolecular assembly (Figure 3.14) consisting of three different types of motifs. Motif 1 is an octagonal motif ($R_6^6(8)$), which is formed by two lattice water molecules (O8…O8') and four oxygens of the two Hsuccinate anions (O4…O4'…O5…O5'); distances 2.923 Å and 2.734 Å. Motif 2 is tetragonal ($R_4^4(4)$) consisting of two lattice water oxygens (O8…O9), one coordinated water molecule (O3) and one oxygen (O5) of the counter Hsuccinate anion. In addition to this, both Hsuccinate are formed a dimer through hydrogen bonding with each other between the carboxylic acid group of one and the carboxylate group of the other molecule with a distance of 2.54 Å. Hydrogen bonding parameters for **3⊃Hsuccinate** are listed in Table 3.4.

Table 3.4. Hydrogen bonding parameters in **3⊃Hsuccinate**.

D---H…A (Å)	r(D-H) (Å)	r(H…A) (Å)	r(D…A) (Å)	∠D-H…A (deg)	Symmetry
O3 –H3A…O9	0.8600	2.0000	2.8136	157.00	1-x,1/2+y,1/2-z
O3 –H3B…O5	0.8600	2.1600	2.7160	122.00	1-x,1/2+y,1/2-z
O6 –H6…O4	0.8400	1.7900	2.5423	148.00	-x,1-y,-z
O8 -H8A…O5	0.8500	2.0200	2.7534	145.00	.
O8 –H8B…O9	0.8500	2.1000	2.9140	161.00	.
O9 -H9E…O8	0.8500	2.1000	2.9140	159.00	.
C3 –H3…O7	0.9500	2.5400	3.4392	158.00	x,1/2-y,1/2+z
C9 -H19C…O1	0.9800	2.5000	3.3215	141.00	.
C10 -H10A…O1	0.9800	2.4800	3.3288	145.00	.
C14 -H14…O8	0.9500	2.5300	3.4263	158.00	.
C16 -H16…O6	0.9500	2.5100	3.1940	129.00	1+x,1/2-y,1/2+z
C17 –H17…O2	0.9500	2.5900	3.1415	117.00	.

Structural description of **4.** To crystallize compound **4**, a perchlorate salt was used. Crystals were grown by the slow evaporation of its aqueous solution. It crystallizes in the monoclinic *C*2/*c* space group. In addition to a coordinated glutarate, two free perchlorate ions are also present in the crystal structure to neutralize the overall charge on the metal centers. The asymmetric unit consists of a Ni(II) center, one ligand, half of the glutarate linker, half lattice water molecule and one perchlorate ion. After expanding the asymmetric unit, a dinuclear synthon has been formed (Figure 3.15).

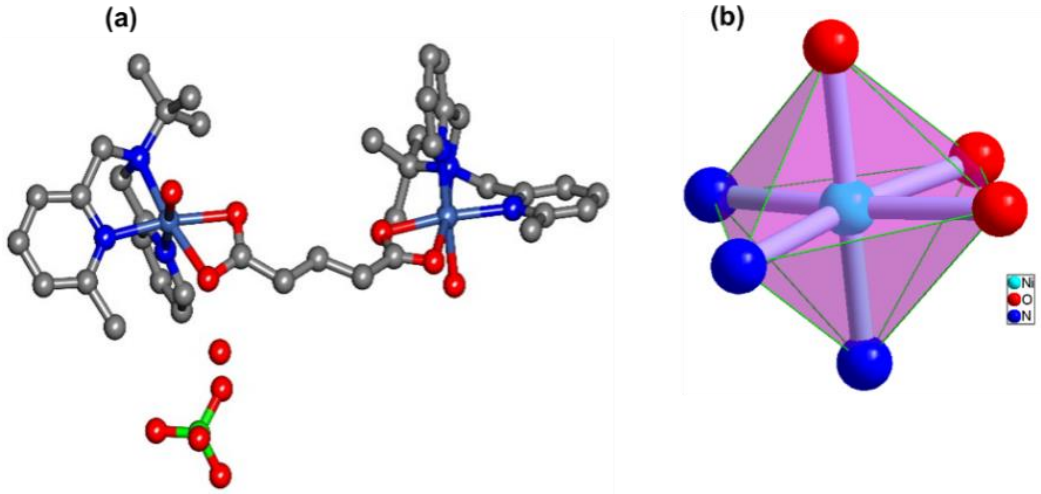

Figure 3.15. (a) Formation of a dinuclear complex having free perchlorate anion and (b) distorted octahedral geometry having N3O3 type surrounding around the metal center in **4**.

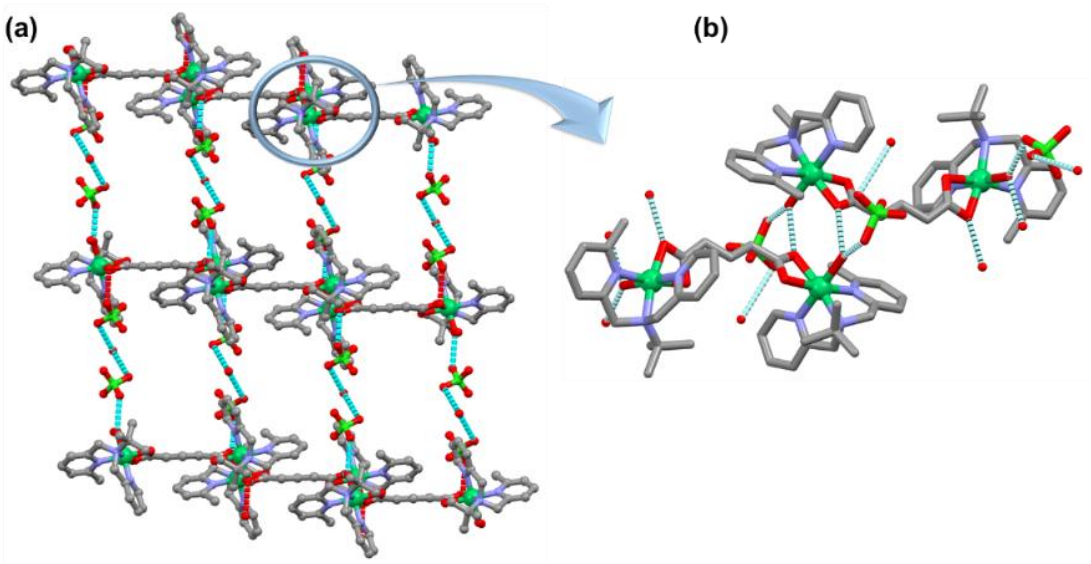

Figure 3.16. (a) Formation of a 3D supramolecular network and (b) hydrogen bonding between two dinuclear synthons in **4**.

The Ni(II) is hexacoordinated consisting of three nitrogen atoms from the ligand with bond distances: 2.075(3) Å and 2.052(3) (Ni(II)-N_{py}) and 2.145(3) Å (Ni(II)-N_{alkyl}), two oxygens of the glutarate linker (chelated, bond distances: 2.121(2) Å and 2.132(2) Å) and one coordinated water oxygen (bond distance: 2.099(2) Å). Due to the presence of one lattice water molecule, a 3D supramolecular assembly is formed by the presence of strong hydrogen bonding between lattice water, coordinated water and perchlorate ions (Figure 3.16). Two dinuclear units are connected by strong hydrogen bonding between coordinated water molecules (O3···O3') and two oxygens from two different fumarates (O1···O1') to generate a hexagonal motif ($R_2^2(6)$), having a distance of 2.726 Å. In other direction, this coordinated water molecule (O3) shows further hydrogen bonding with the oxygen (O4) of the perchlorate molecule having a distance of 2.835 Å.

Table 3.5. Hydrogen bonding parameters in **4**.

D---H…A (Å)	r(D-H) (Å)	r(H…A) (Å)	r(D…A) (Å)	∠D-H…A (deg)	Symmetry
O3 -H3B…O1	0.8600	1.8700	2.7258	173.00	1/2-x,1/2-y,1-z
O8 -H8D…O6	0.8500	2.4300	3.0223	128.00	1/2+x,1/2-y,-1/2+z
O8 -H8E…O6	0.8500	2.4000	3.0223	130.00	1/2-x,1/2-y,1-z
C1 -H1…O5	0.9300	2.3700	3.2384	155.00	1/2-x,1/2-y,1-z
C6 -H6A…O4	0.9700	2.5300	3.4015	150.00	x,-y,-1/2+z
C8 -H8C…O2	0.9600	2.5200	3.3803	149.00	.
C13 -H13…O7	0.9300	2.4900	3.2858	144.00	x,-y,-1/2+z

Furthermore, one oxygen of perchlorate (O6) molecule forms hydrogen bonding with the lattice water molecule (O8). This water molecule (O8) further connects with the oxygen of perchlorate (O6) and oxygen of same perchlorate (O4) connects with the coordinated water molecule (O3) making a linear thread which connects two different one-dimensional supramolecular networks. Hydrogen bonding parameters are listed in Table 3.5.

Powder X-ray diffraction studies. The crystalline nature of **1-12** was confirmed by powder X-ray diffraction studies. This has also allowed to check purity of the bulk sample with respect to single crystal by comparing the respective simulated pattern with the experimental pattern.

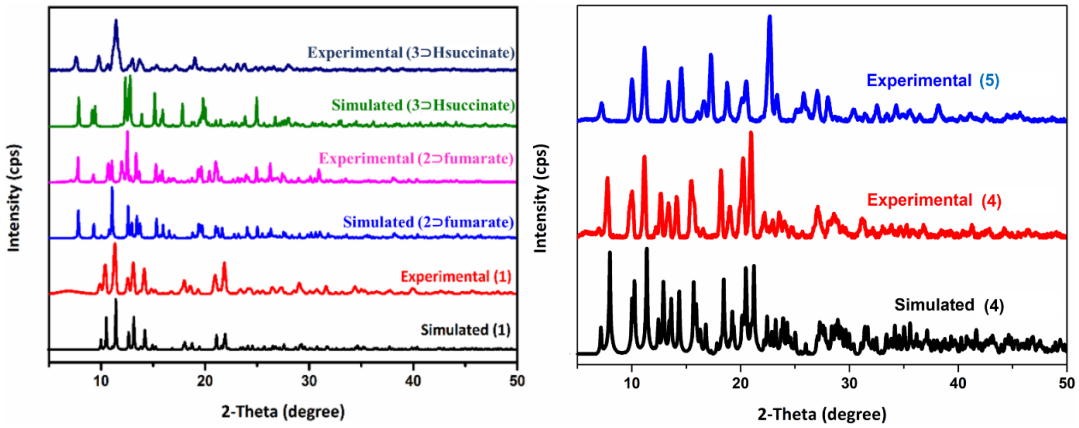

Figure 3.17. PXRD patterns of **1-5**.

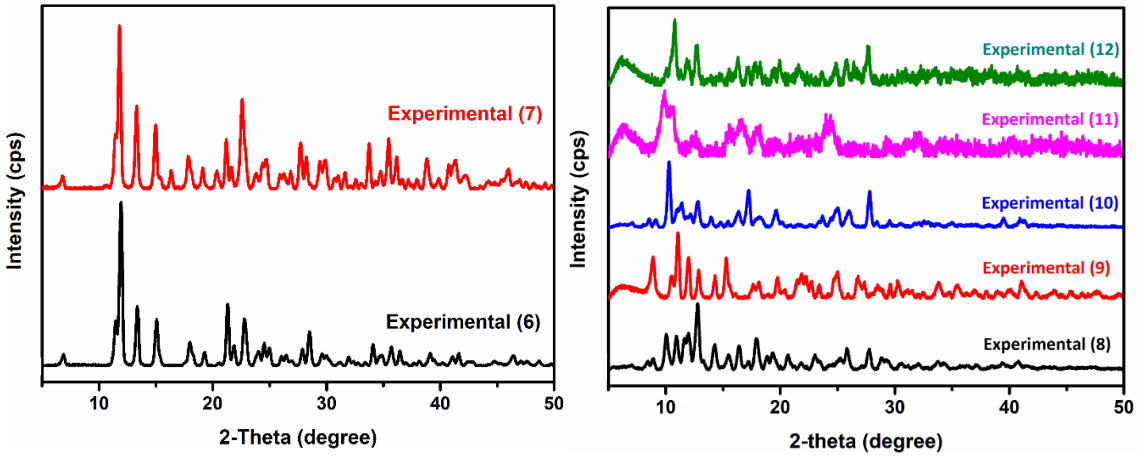

Figure 3.18. PXRD patterns of **6-12**.

For compounds **1-4**, the simulated and experimental patterns match very well while comparing the experimental pattern of **5** with that of **4** indicates these are isostructural (see Figure 3.17). Similarly, compounds **6** and **7** are isostructural; compounds **8-12** are also isostructural (see Figure 3.18).

Encapsulation of water clusters

Water clusters can play an important role in the stabilization of supramolecular systems both in solution as well as in the solid state. Thus, there is clearly a need for better understanding of how such water aggregations are influenced by the overall structure of their surroundings. There are various types of water clusters reported in the literature on the basis of SCXRD analysis and theoretical computational studies.[168–171] These clusters can be linear chains, cyclic or branched with numbers varying between 2-10 or more (Figure 3.19). Considering the cyclic water cluster, there are many arrangements of cyclic water clusters like dimer, trimer, tetramer, pentamer, hexamer, heptamer and octamer, which are reported in the literature.[66,172–175]

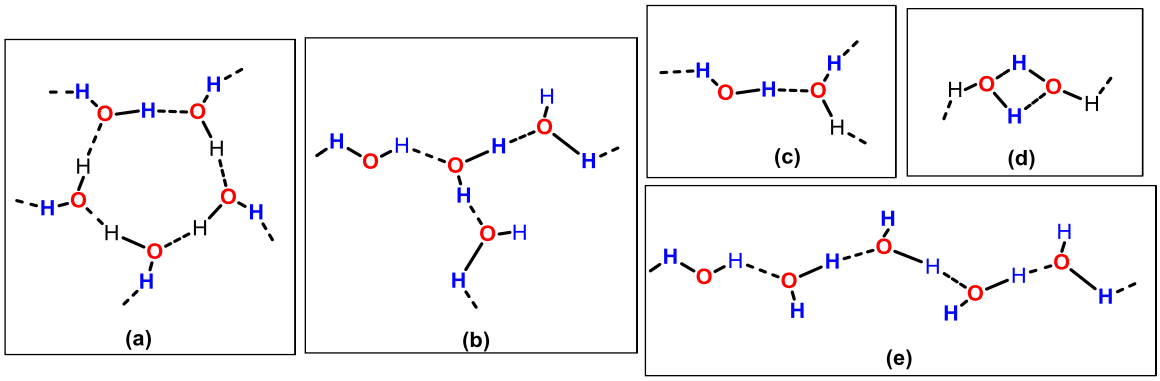

Figure 3.19. Some of the possible arrangement of water clusters like (a) cyclic pentamer, (b) branched, (c) linear dimer, (d) cyclic dimer (e) linear chain observed in this study.

From all these, few are very rare and not much explored experimentally as well as theoretically. For example, double hydrogen-bonded cyclic water dimer is not much explored. Only one example of such type of water cluster, which is characterized in the solid-state, is reported in the literature.[167] Previously, we have contributed to the water clusters like cyclic hexamer[66] and octamer[295] of water clusters in supramolecular coordination architectures.

To illustrate further, both modification in the ligands and change in metal ions were done to generate various types of supramolecular synthons. These supramolecular coordination architectures show diversification in water clusters.[176–181] Along with this, the use of different anions also plays an important role in diversifying the structure and in the arrangement of water cluster. The anions in coordinated or uncoordinated forms (trapped in solvent molecules) or both, support the aggregation of water clusters and are helpful in the construction of supramolecular architectures. Compounds **1**-**3** are the Ni(II) compounds with 6-Mebpta having different dicarboxylate linkers (adc, fumarate and Hsuccinate,

respectively). These different anions affect the formation of coordination architecture as well as water arrangement. In compound **1,** a *bis*(adc) dinuclear network has been formed which have two lattice water molecules. These water molecules form a double hydrogen-bonded cyclic water cluster. This type of cyclic dimer of water cluster having double hydrogen bonding is very rare (Figure 3.20).

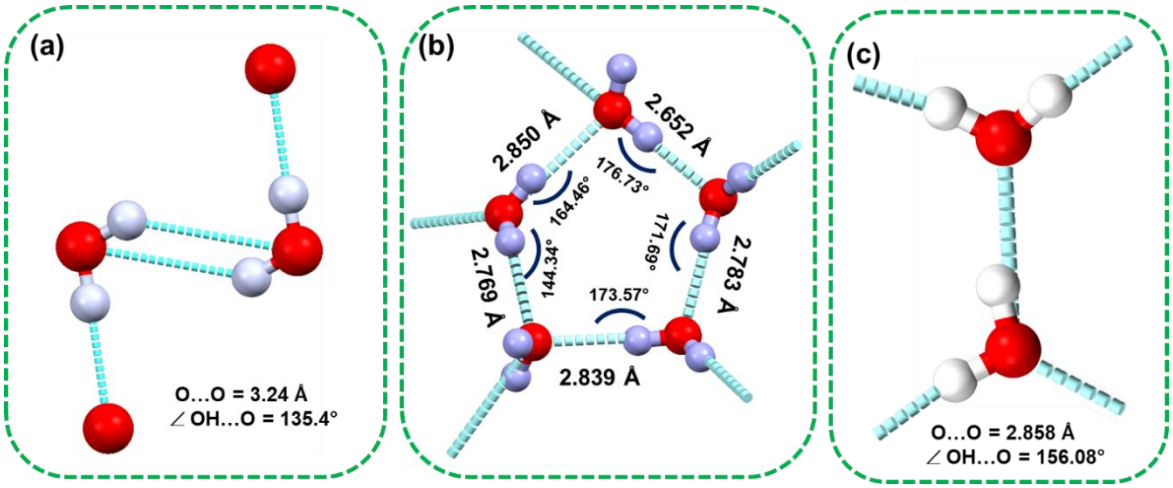

Figure 3.20. Different arrangement of water clusters observed in this study (a) cyclic dimer in **1**, (b) cyclic pentamer in **2⊃fumarate** and (c) linear dimer in **3⊃Hsuccinate**.

On the other hand, **2⊃fumarate**, which has fumarate ion in the place of adc, forms a different structure as well as shows different arrangement of water cluster as compared to **1**. Compound **2⊃fumarate** has a dinuclear synthon in which one fumarate acts as a bridge between two metal centers while the other fumarate is free. The free fumarate forms hydrogen bonding with the lattice water molecules *via* four oxygen atoms. There are nine lattice water molecules present in compound **2⊃fumarate**. Out of these nine lattice water molecules, five form an unusual cyclic pentamer of water cluster. All the five lattice water molecules involved in the formation of cyclic water cluster are in the same plane to make this a quasi-planar cyclic pentamer of water cluster (Figure 3.21). Compound **3⊃Hsuccinate** has the same type of dinuclear synthon as **2⊃fumarate** with a free succinate anion.

Compound **3⊃Hsuccinate** has four lattice water molecules, where two water molecules show the formation of a linear dimer of water cluster (Figure 3.19). Other compounds with Ni(II) and Mn(II) have the same type of coordination architecture, but the formation of different supramolecular assemblies has been formed. In Compound **4** there is only one lattice water molecule, thus no such type of unusual water cluster has been formed, though different water-anion cluster formation is observed.

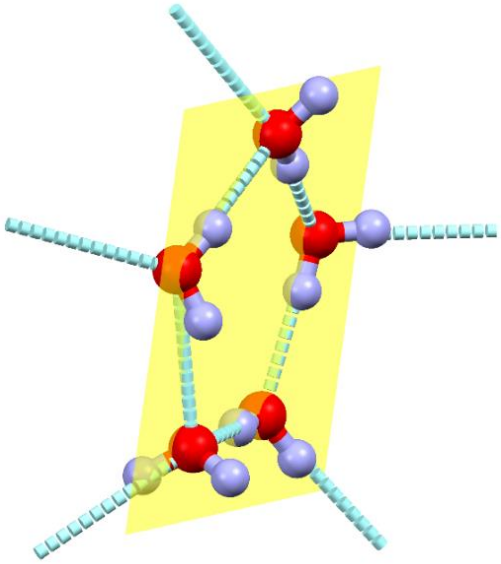

Figure 3.21. Quasi-planar pentamer of water formed in **2⊃fumarate**.

Effect of anion exchange on encapsulated water clusters

It is evident that the free anion can be exchanged with other anions under favorable conditions, resulting in the change in arrangement of water clusters and supramolecular architectures as well.[182] Among the various possibilities for three-component systems shown in Figure 3.1 (*vide supra*), the structural type d has a free anion which is available for exchange with other anions.[18,183–187] Both **2⊃fumarate** and **3⊃Hsuccinate** have free anions and are good candidates for anion exchange.

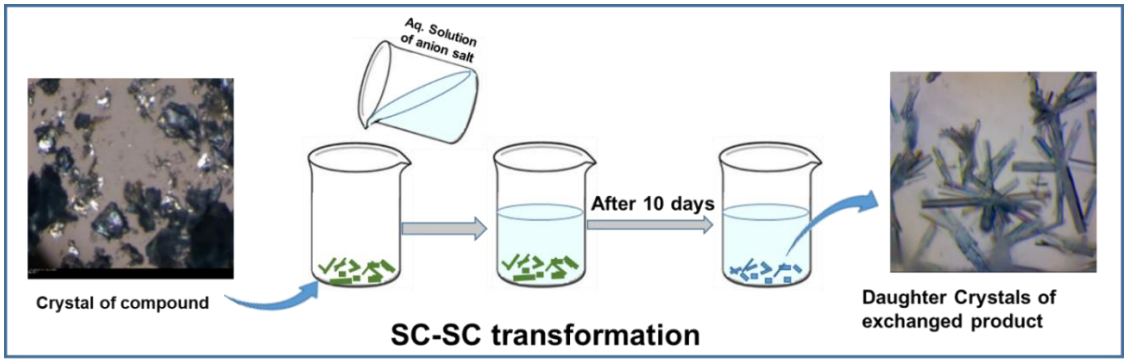

Figure 3.22. Schematic representation of the formation of anion exchanged product via SC-SC transformation (solid-liquid post-synthetic anion exchange).

Two different approaches have been used for the anion exchange process. Out of these two methods, one is the SC-SC transformation (solid-liquid post-synthetic anion exchange) by which crystals of the as-synthesized compound were immersed into the aqueous solution of different anions. After a few days, a change in the color of the crystal was observed and then these crystals were isolated and used for single crystal structure analysis (Figure 3.22).

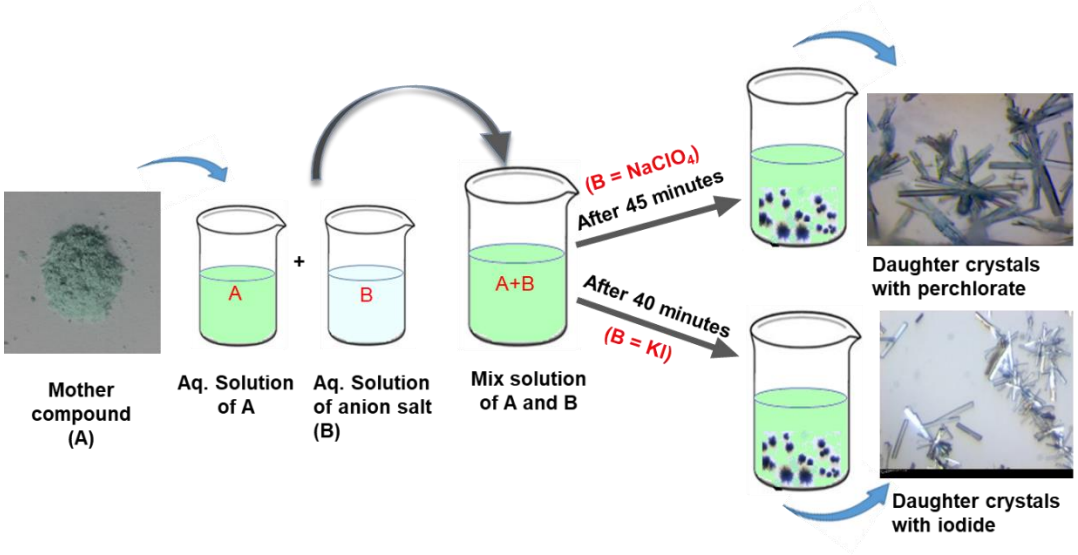

Figure 3.23. Schematic representation of anion exchange in **2⊃ClO_4^-** and **2⊃I^-** from **2⊃fumarate** by liquid-liquid post-synthetic anion exchange method.

The second method is the wet method (liquid-liquid post-synthetic anion exchange) in which reformation of the crystals takes place. In this method, a solution of the compound was prepared in water and was poured into other solutions of different anions in water. After evaporation of this solution, crystals have been formed, which were suitable for the single crystal study. The growth of crystals from this method was fast as monitored by microscopy (Figure 3.23).

***Anion exchange in* 2⊃fumarate.** Its aquesous solution was treated with different anions like perchlorate, iodide, chloride, bromide, sulfate and nitrate in water. The products were isolated and characterized (Scheme 3.8) by various techniques like FTIR, TGA, SCXRD and PXRD.

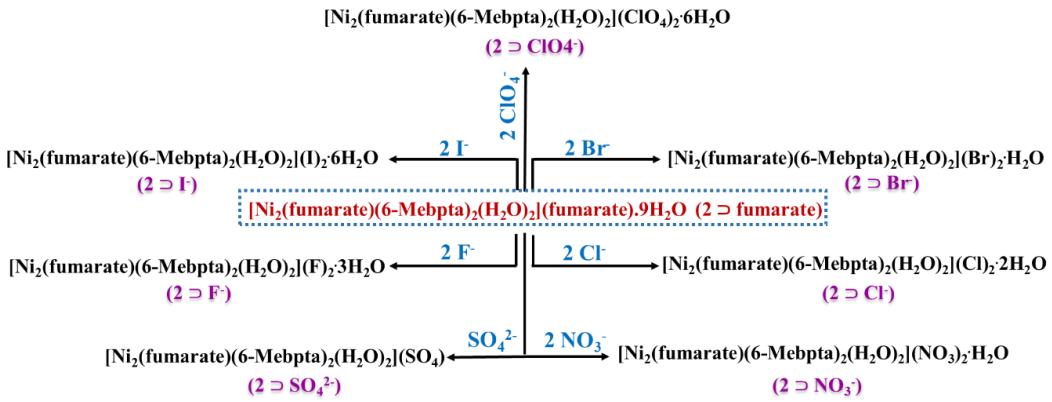

Scheme 3.8. Exchange of fumarate anion with different anions in **2⊃fumarate**.

Formation and structural description of **2⊃ClO_4^-** . In case of **2⊃ClO_4^-**, sodium perchlorate (2 eq.) was added to a solution of **2⊃fumarate** (10 mg dissolved in 0.5 mL of water). The formation of the exchanged product was examined by careful microscopic study (Figure 3.24). Very interestingly, the rod-shaped greenish-blue crystals of the exchanged product was obtained in few minutes. It was found that after adding sodium or potassium perchlorate solution to the aqueous solution of **2⊃fumarate**, within two minutes, crystals started appearing and with an increase in the time, size and quantity of the crystals also enhanced. It crystallizes in triclinic *P*-1 space group, different from mother compound (as synthesized) but the dinuclear synthon was the same as **2⊃fumarate**. The counter anion fumarate (trapped in the water clusters) got exchanged with two perchlorate anions. It was also found that during the anion exchange process three lattice water molecules also came out with the fumarate anion. This exchange of anion resulted in the formation of a new supramolecular assembly. The asymmetric unit consists of two metal centers, two ligands, one coordinate fumarate and two free perchlorate anions. Along with this, six lattice water molecules are present. The metal center was coordinated by three nitrogens of the ligand (bond distances: Ni-N_{Py} (2.052(9) Å and 2.073(8) Å) and Ni-N_{alkyl} (2.151(8) Å), two oxygens of fumarate (bond distances: 2.105(7) Å and 2.187(7)Å) and one oxygen from the coordinated water molecule with a bond distance of 2.087(7) Å (Figure 3.25).

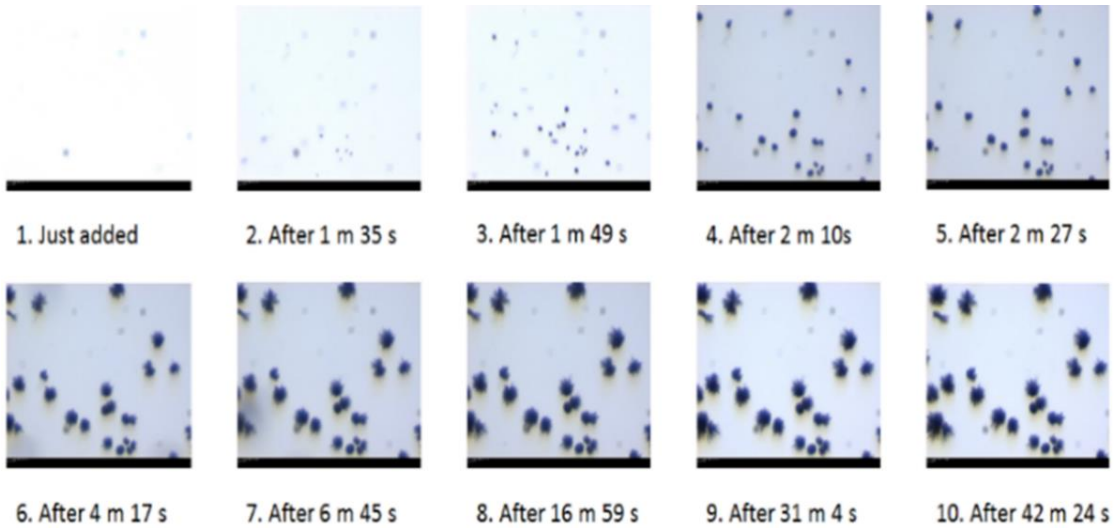

Figure 3.24. Growth of **2⊃ClO_4^-** crystals from **2⊃fumarate** and perchlorate anion solution monitored by microscopy.

The six water molecules and two perchlorate anions show strong hydrogen bonding resulting in the formation of a 3D supramolecular assembly (Figure 3.26) having three different type of motifs. Motif 1, ($R_4^4(8)$), is an octamer formed by two lattice water

molecules (O18···O19) and two oxygens of fumarate (one from both sides of the same molecule) (O1···O2); distances: 2.935 Å, 2.905 Å and 2.979 Å. Four carbon atoms of fumarate are also involved in the formation of this octamer. Motif 2, ($R_6^6(8)$), is formed by two lattice water (O19···O20) molecules, two coordinated water molecules (O6···O3), two oxygens from fumarate anion (from different synthons) (O4···O2) and two Ni(II) centers; distances: 2.979 Å, 2.650 Å, 2.827 Å and 2.740 Å.

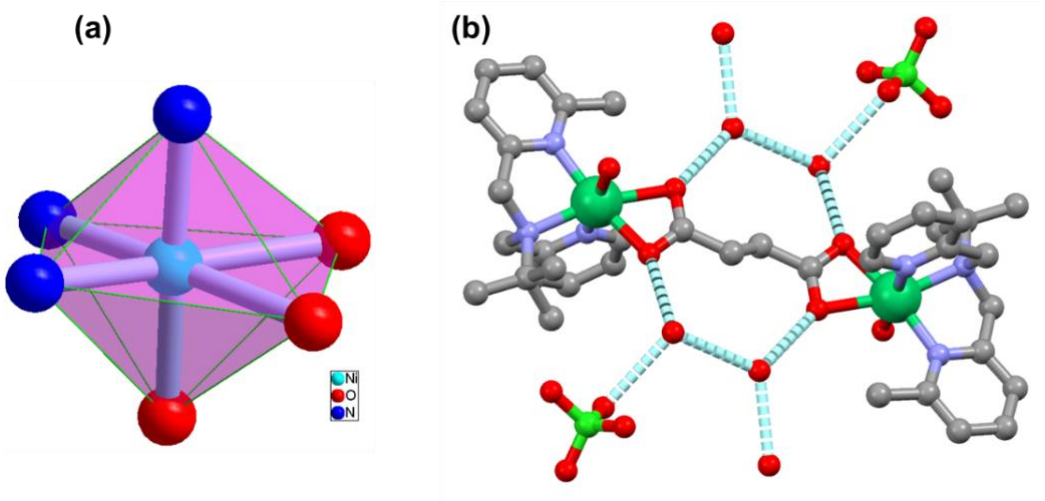

Figure 3.25. (a) Distorted octahedral geometry having N3O3 type surrounding around the metal center and (b) formation of dinuclear synthon having free perchlorate anion and lattice water in **2⊃ClO_4^-**.

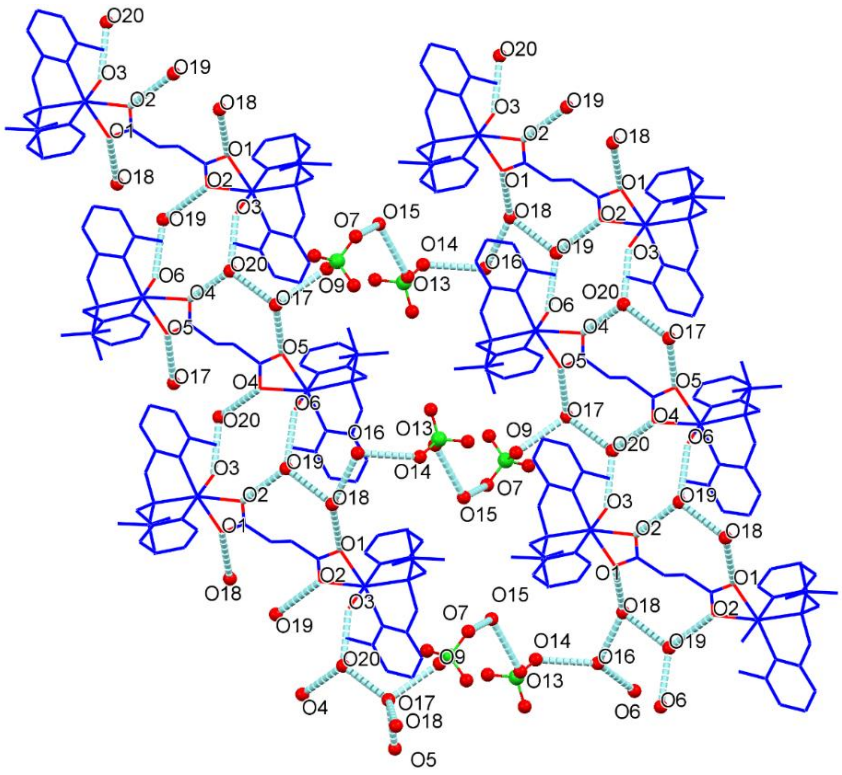

Figure 3.26. Supramolecular assembly showing three types of motifs in **2⊃ClO_4^-**.

This motif connects two synthons and forms a linear chain type of 1D supramolecular assembly. This linear chain is connected to the other similar chain by Motif 3, ($R_{21}^{21}(27)$). which involves two Ni(II) centers, four chlorine atoms (from perchlorate), eight oxygens of four perchlorate anions (O7…O9…O13…O14…O7'…O9'…O13'…O14'), ten lattice water molecules (O18…O19…O16...O17...O15...O18'...O19'...O16'...O17'...O15'), two oxygen atoms of the coordinated fumarate (O5…O5') and two oxygens from two coordinated water molecules (O6…O6'), distances: 2.91 Å, 2.965 Å, 2.836 Å, 2.861 Å, 2.815 Å, 2.924 Å, 2.905 Å and 2.740 Å as shown in Figure 3.26. All hydrogen bonding parameters are listed in Table 3.6.

Table 3.6. Hydrogen bonding parameters in **2⊃ClO_4^-**.

D---H…A (Å)	r(D-H) (Å)	r(H…A) (Å)	r(D…A) (Å)	∠D-H…A (deg)	Symmetry
O3 -H3B...O20	0.85	1.92	2.6506	143	.
O6 -H6A...O16	0.86	1.99	2.8	157	1-x,1-y,-z
O6 -H6B...O19	0.86	1.91	2.7324	160	.
O16 -H16A...O6	0.85	2.53	2.8	100	1-x,1-y,-z
O16 -H16B...O14	0.85	2.23	2.9298	140	1-x,1-y,1-z
O17 -H17A...O9	0.85	2.22	2.8749	134	.
O17 -H17B...O5	0.85	2	2.8151	160	1-x,1-y,-z
O18 -H18B…O1	0.85	2.12	2.9517	167	.
O19 -H19D…O2	0.85	2.14	2.9848	177	.
O20 -H20B…O4	0.85	2.13	2.8336	140	.
C8 -H8…O4	0.93	2.49	3.0799	122	.
C14 -H14...O13	0.93	2.55	3.3753	149	1-x,1-y,1-z
C19 -H19A…O8	0.96	2.42	3.376	173	1-x,1-y,1-z
C19 -H19B…O4	0.96	2.59	3.208	122	.
C21 -H21A…O11	0.96	2.51	3.3783	151	1-x,1-y,1-z
C22 -H22A…O5	0.96	2.56	3.3756	142	.
C22 -H22A…O6	0.96	2.59	3.2558	127	.
C23 -H23A…O9	0.96	2.47	3.3466	152	1-x,1-y,-z
C23 -H23C…O5	0.96	2.41	3.2587	147	.
C37 -H37B…O15	0.97	2.52	3.4843	175	x,-1+y,z
C39 -H39…O9	0.93	2.56	3.1654	123	x,-1+y,z
C46 -H46C…O1	0.96	2.57	3.3952	145	.
C46 -H46C…O3	0.96	2.5	3.1299	123	.
C47 -H47B…O1	0.96	2.43	3.2985	150	.
C47 -H47C...O15	0.96	2.47	3.3106	147	-x,1-y,1-z

Formation and structural description of **2⊃I**$^{-}$. In order to form **2⊃I**$^{-}$ from **2⊃fumarate** both solid-solid and liquid-solid methods described above were used. For the first method, some of **2⊃fumarate** crystals were soaked in a saturated solution of potassium iodide and after 10 days greenish-blue color of the crystals changed to light green color. On the other hand, growth of the crystals by the second method was monitored by microscopy as shown in Figure 3.27.

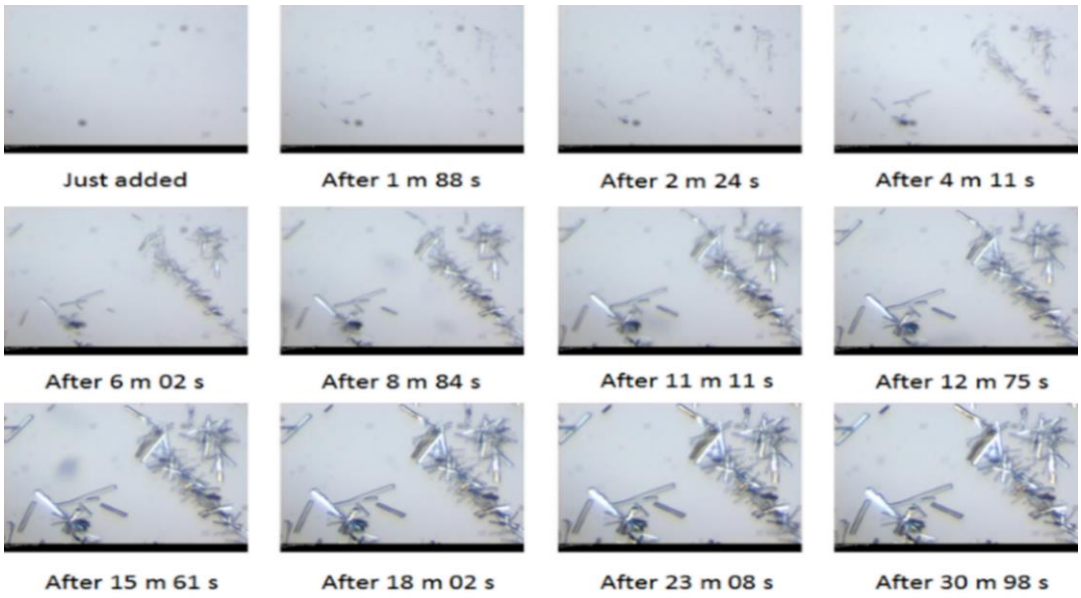

Figure 3.27. Growth of **2⊃I**$^{-}$ crystals from **2⊃fumarate** and iodide anion solution monitored by microscopy.

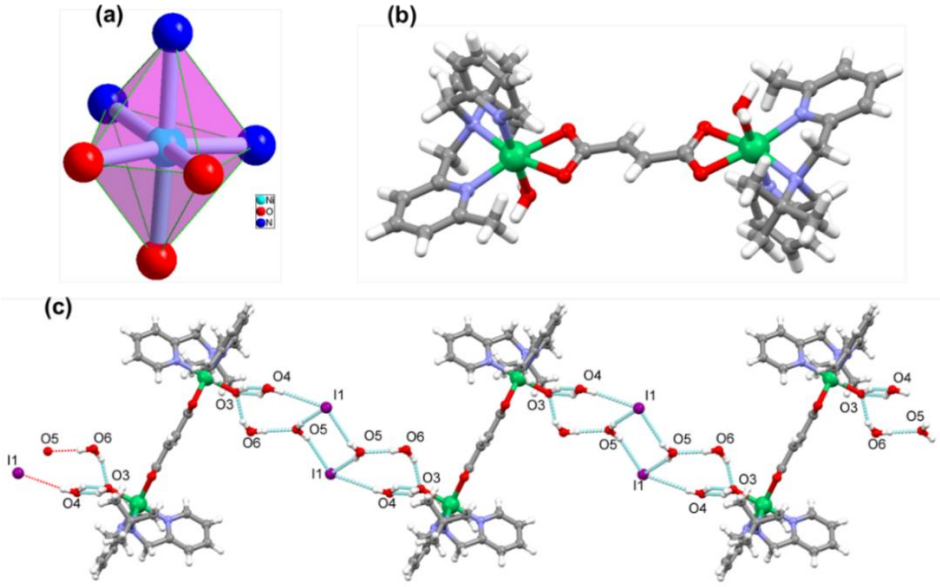

Figure 3.28. (a) Distorted trigonal octahedral geometry having N3O2 type surrounding around the metal center, (b) formation of a dinuclear complex and (c) supramolecular assembly showing two types of motifs in **2⊃I**$^{-}$.

Based on the single crystal X-ray diffraction, it crystallizes in the same space group $P2_1/n$. In its structure, two iodide ions replaced the uncoordinated fumarate ion while three lattice water molecules were also lost (similar to **2⊃ClO$_4^-$**). This anion exchange has also altered the pentamer of water cluster and thus a new supramolecular assembly has formed as shown in Figure 3.28. The asymmetric unit consists of a metal center, one ligand, half of the coordinate fumarate, one free iodide ion, and one coordinated and three lattice water molecules. The coordination environment (N3O3) around the metal center is completed by three nitrogen atoms of the ligand (distances: Ni-N_{Py} (2.051(8) Å and 2.078(8) Å) and Ni-N_{alkyl} (2.178(7) Å), two oxygens of fumarate (distances: 2.101(6) Å and 2.215(6) Å) and one oxygen from the coordinated water molecule with a distance of 2.067(6) Å (Figure 3.28). All bond distances and angles are listed in Table A23 and A34 (Appendix). All hydrogen bonding parameters are listed in Table 3.7.

Table 3.7. Hydrogen bonding parameters in **2⊃I$^-$**.

D---H…A (Å)	r(D-H) (Å)	r(H…A) (Å)	r(D…A) (Å)	∠D-H…A (deg)	Symmetry
O3 -H3B...O4	0.91	1.88	2.7456	159	1/2+x,1/2-y,-1/2+z
O4 -H4A...I1	0.87	2.94	3.7959	166	1/2-x,1/2+y,1/2-z
O4 -H4B…O3	0.87	1.97	2.7456	147	-1/2+x,1/2-y,1/2+z
O5 -H5A…I1	0.87	2.79	3.6304	162	.
O5 -H5B…I1	0.87	2.95	3.8008	167	1-x,-y,1-z
O6 -H6A…O3	0.87	1.95	2.7701	157	1/2+x,1/2-y,1/2+z
O6 -H6B…O5	0.87	1.96	2.8272	171	1/2+x,1/2-y,-1/2+z
C10 -H10…I1	0.95	3.03	3.8768	150	1/2-x,1/2+y,1/2-z
C13 -H13…O2	0.95	2.55	3.1292	120	.
C15 -H15B…O1	0.98	2.54	3.3833	144	.
C17 -H17C…O1	0.98	2.53	3.3885	147	.
C19 -H19…O4	0.95	2.47	3.4023	166	-1/2+x,1/2-y,-1/2+z

Due to the presence of lattice water molecules and iodide anions, one synthon is connected with the other through strong hydrogen bonding resulting in the formation of a 1D zig-zag chain having three different motifs. Motif 1, ($R_4^4(4)$), involves two iodide anion (I1···I1′), two oxygens of lattice water molecule (O5···O5′) with distances of 3.630 Å and 3.801 Å (one iodide with both water). Motif 2, ($R_4^5(5)$), is formed by two oxygens of two lattice water molecules (O4···O6), one oxygen from coordinated water molecule (O1) and one iodide (I1) anion with distances: 2.770 Å, 2.827 Å and 2.746 Å (O···O) and 3.796 Å and 3.801Å (O···I). Motif 3, ($R_2^2(2)$), is a dimer of lattice water (O4) and coordinated water (O1) with a distance of 2.746 Å.

By comparing all three structures, it is observed that diversification in the water clusters has taken place by the anion exchange. A pentamer of water cluster in **2⊃fumarate** loses its identity due to the exchange of fumarate with perchlorate (Figures 3.29 and 3.30). Instead a linear chain of water clusters is formed in **2⊃ClO_4^-**. By exchanging the fumarate with iodide anion, a square of two water and two iodides was formed. Furthermore, a cyclic dimer of water cluster is also formed with a coordinated water molecule and lattice water molecule. It should be noted that the hydrogen bonding distance between water and iodide anion is longer than the common hydrogen bonding distance between water molecules.

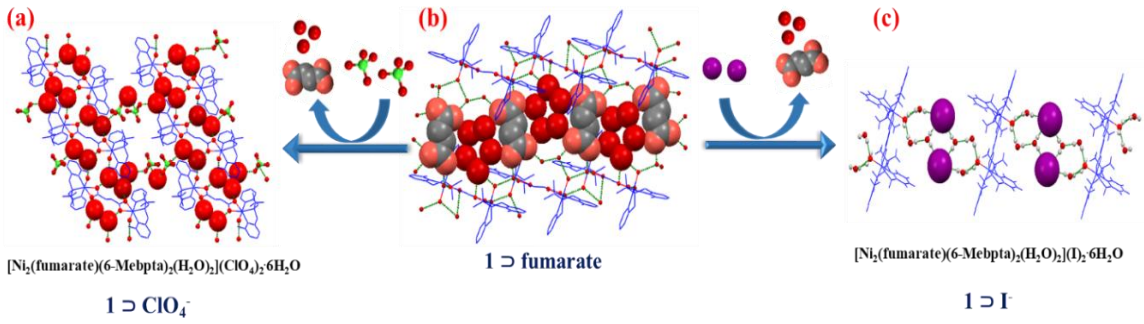

Figure 3.29. Change in the water cluster and supramolecular assembly (a) Supramolecular assembly formed in **2⊃ClO4$^-$** (b) Supramolecular assembly formed in **2⊃fumarate** and (c) Supramolecular assembly formed in **2⊃I^-**.

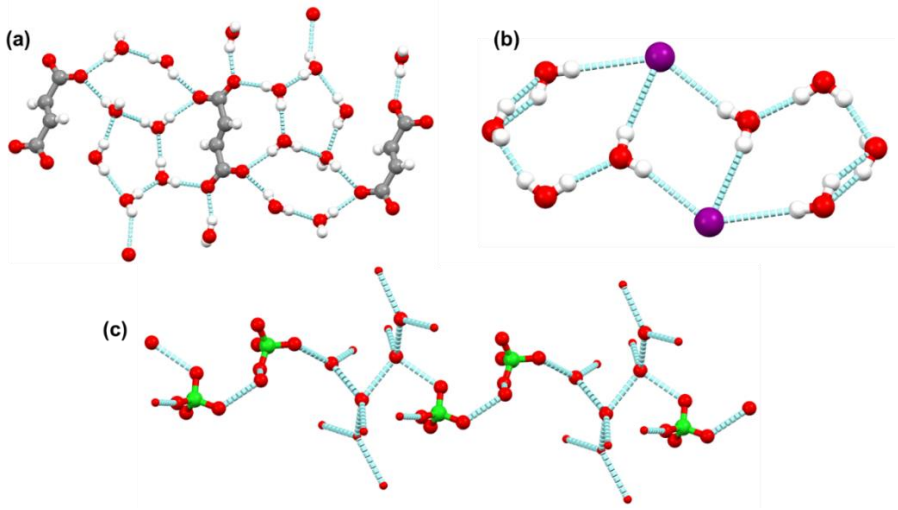

Figure 3.30. Arrangement of water cluster and anion in **2⊃fumarate** (a), **2⊃I^-** (b) and **2⊃ClO_4^-** (c).

After studying the effect of anion exchange on the shape of water clusters by comparing their structures, we have confirmed the anion exchange by other techniques also like FTIR, and PXRD. By comparing the PXRD patterns of all exchanged products with different anions, it is found that there is a change in the patterns confirming the formation of new compounds (Figure 3.31). However, all exchanged compounds retain their crystallinity.

Furthermore, both **2⊃ClO$_4^-$** and **2⊃I$^-$** having single crystal structures show good agreement with the simulated and the experimental data confirming their phase purity.

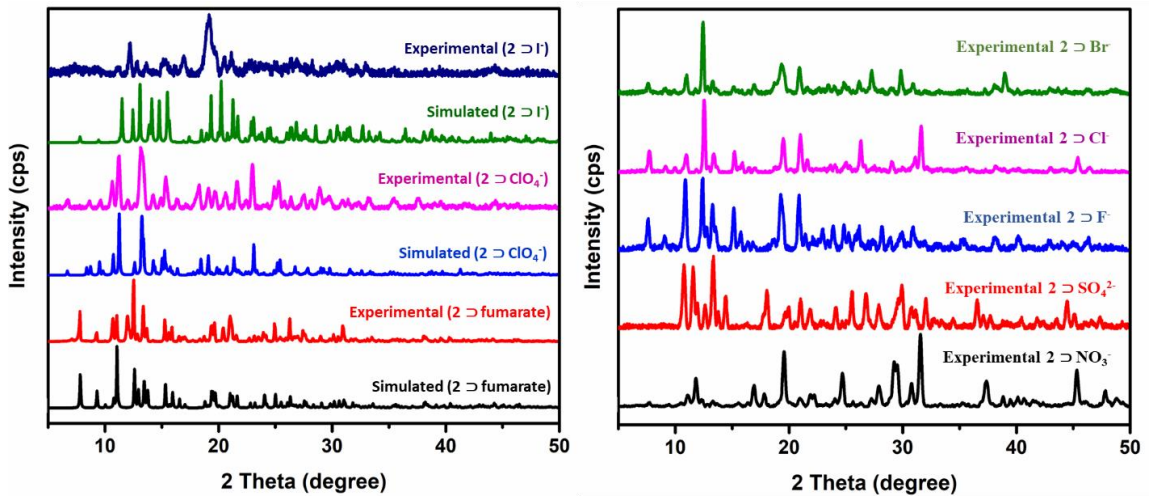

Figure 3.31. Change in powder patterns of **2⊃fumarate** upon anion exchange.

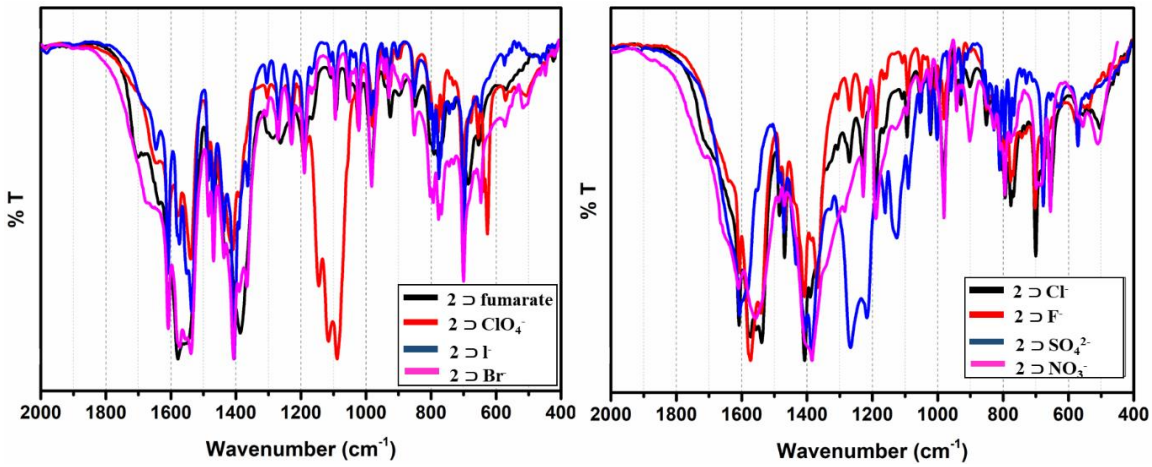

Figure 3.32. Change in FTIR spectra of **2⊃fumarate** due to anion exchange.

Most anions have signature peaks in the FTIR and their presence in a compound can be confirmed. In case of exchanging fumarate anion by other anions, the peak of free fumarate around 1702 cm^{-1} disappeared and new peaks of a particular anion appeared in the spectrum. For example, peaks at 1084 cm^{-1}, 1254 cm^{-1} and 1384 cm^{-1} correspond to the perchlorate ion, sulfate ion and nitrate ion, respectively (Figure 3.32).

***Anion exchange in* 3⊃Hsuccinate**. After getting the successful exchange of fumarate anion in **2⊃fumarate** with numerous anions, a similar study was carried out for the exchange of succinate in **3⊃Hsuccinate** with other anions (Scheme 3.9).

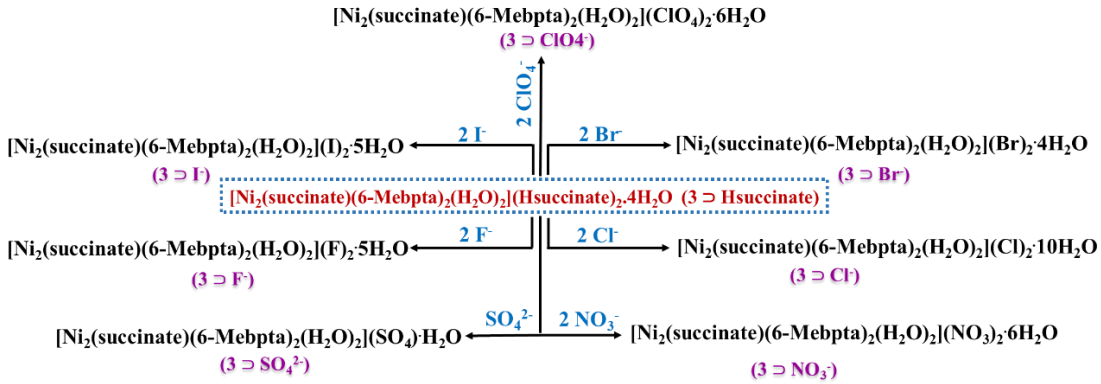

Scheme 3.9. Exchange of succinate anion with different anions in **3⊃Hsuccinate**.

Formation and structural description of **3⊃ClO$_4^-$**. As shown in Scheme 3.9, upon exchange of both Hsuccinate with two molecules of perchlorate the resulting crystals were found to crystallize in the monoclinic $P2_1/n$ space group. The asymmetric unit consists of one nickel, one ligand, half of the coordinate succinate and one free iodide molecules as well as three lattice water molecules (O8, O9 and O10), which helps in the formation of a supramolecular assembly via hydrogen bonding.

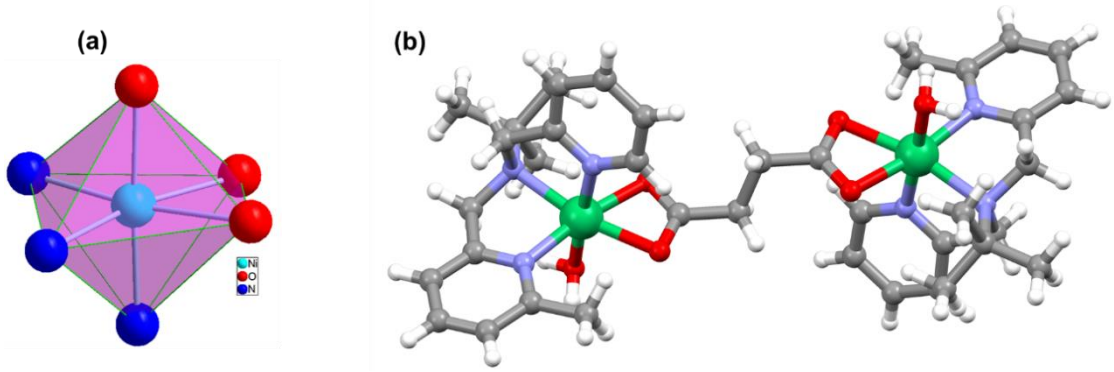

Figure 3.33. (a) Distorted octahedral geometry having N3O3 type surrounding around the metal center and (b) formation of dinuclear synthon in **3⊃ClO$_4^-$**.

A N3O3 type of surrounding around metal center was formed using three nitrogens of the ligand (distances: Ni-N_{Py} (2.064(6) Å and 2.058(7) Å) and Ni-N_{alkyl} (2.133(7) Å), two oxygens of succinate (distances: 2.133(5) Å and 2.144(6) Å) and one oxygen from the coordinated water molecule with distance 2.072(5) Å (Figure 3.33). Due to the presence of two perchlorate and five lattice water molecules, the resultant compound has a supramolecular assembly consisting of five different types of motifs (Figure 3.34) formed by strong hydrogen bonding. Motif 1, ($R_6^6(8)$) consists of two lattice water molecules (O8···O8'), two oxygens of two succinates from different synthons (O1···O1'), two coordinated water (O3···O3'), distances: 2.674 Å, 2.780 Å and two Ni(II) centers. This motif

connects two dinuclear synthons to generate a supramolecular network. Motif 2, ($R_4^4(8)$), consists of two lattice water molecules (O8···O9), two oxygens of the same succinate from both side (O1···O2), distances: 2.780 Å, 2.800 Å, 2.766 Å and four carbon atoms of succinate. Motif 3, ($R_5^5(7)$), consists of one coordinated water (O3), one fumarate oxygen (O2), one lattice water oxygen (O9), two oxygens from one perchlorate anion (O12···O10), distances: 2.800 Å, 2.874 Å, 2.919 Å, one Ni(II) center and one chloride atom also involved in this. Motif 4, ($R_6^6(8)$), consists of four oxygens of two perchlorate anions (O4···O5···O4'···O5'), two lattice water molecules (O10···O10'), distances: 2.619 Å, 2.889 Å and two chloride atoms.

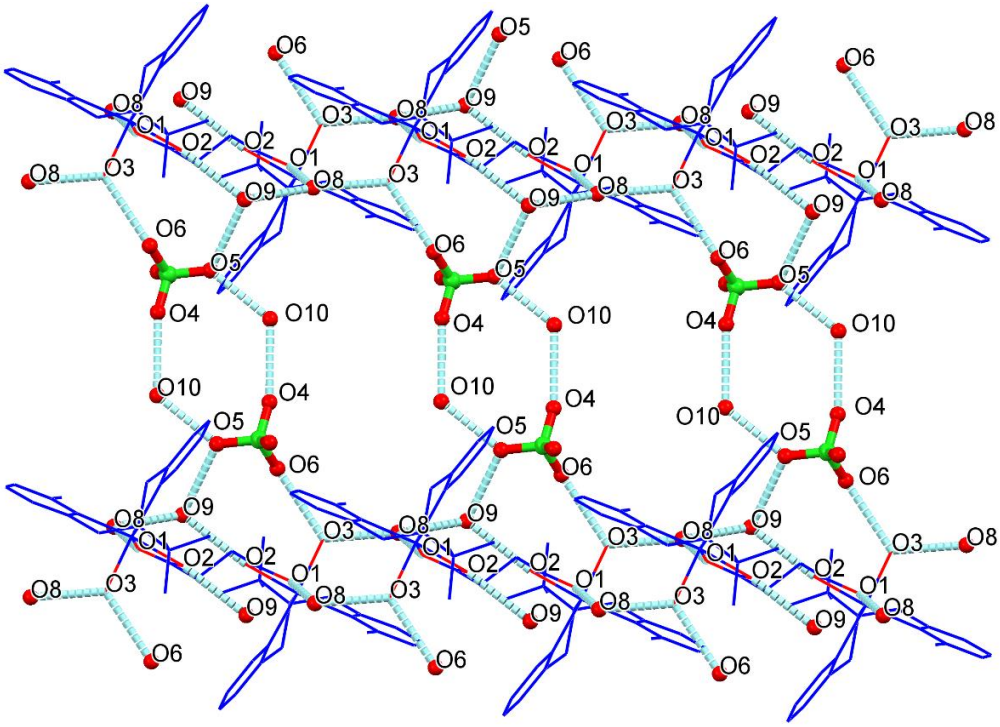

Figure 3.34. Supramolecular assembly showing five types of motifs in **3⊃ClO_4^-**.

Motif 5, ($R_{14}^{14}(16)$), consists of four lattice water molecules (O8···O9···O8'···O9'), two coordinated water molecules (O3···O3'), six oxygens from perchlorate (O4···O5···O6···O4'···O5'···O6'), distances: 2.889 Å, 2.619 Å, 2.874 Å, 2.766 Å, 2.671 Å, 2.919 Å and two chloride atoms. In the formation of this motif, out of four perchlorate ions, two perchlorate show hydrogen bonding through two oxygen atoms and other two perchlorate shows hydrogen bonding through one oxygen atom only. The supramolecular assembly is shown in Figure 3.34, while all the hydrogen bonding parameters are listed in Table 3.8.

Table 3.8. Hydrogen bonding parameters in **3⊃ClO$_4^-$**.

D---H…A (Å)	r(D-H) (Å)	r(H…A) (Å)	r(D…A) (Å)	∠D-H…A (deg)	Symmetry
O3 -H3B…O8	0.86	1.87	2.7124	165	3/2-x,-1/2+y,1/2-z
O8 -H8C…O3	0.85	2.14	2.7124	124	3/2-x,1/2+y,1/2-z
O9 -H9B…O8	0.85	1.95	2.7685	161	.
O10 -H10A…O5	0.85	2.1	2.6461	122	.
C1 -H1B…O7	0.98	2.54	3.485	162	1/2+x,1/2-y,1/2+z
C11 -H11…O9	0.95	2.55	3.3248	139	-1+x,y,z
C12 -H12…O7	0.95	2.56	3.3533	141	-1/2+x,1/2-y,1/2+z
C13 -H13…O1	0.95	2.54	3.0942	117	.
C15 -H15B…O2	0.98	2.51	3.3756	147	.
C17 -H17B…O2	0.98	2.52	3.3899	148	.

Formation and structural description of **3⊃Cl$^-$**. In case of **3⊃Cl$^-$** (exchanged with chloride) crystals were formed by following the same procedure as previous. It crystalizes in monoclinic $P2_1/c$ space group. The asymmetric unit consists of a metal center, one ligand, half of the coordinate succinate and one free chloride ion. Along with this, five lattice water molecules are also present. A N3O3 type of surrounding around metal center was formed using three nitrogen of the ligand (distances: Ni-N_{Py} (2.063(12) Å and 2.094(11) Å) and Ni-N_{alkyl} (2.135(11) Å), two oxygens of succinate (distances: 2.133(9)Å and 2.160(9) Å) and one oxygen from the coordinated water molecule with distance 2.056(10) Å (Figure 3.35).

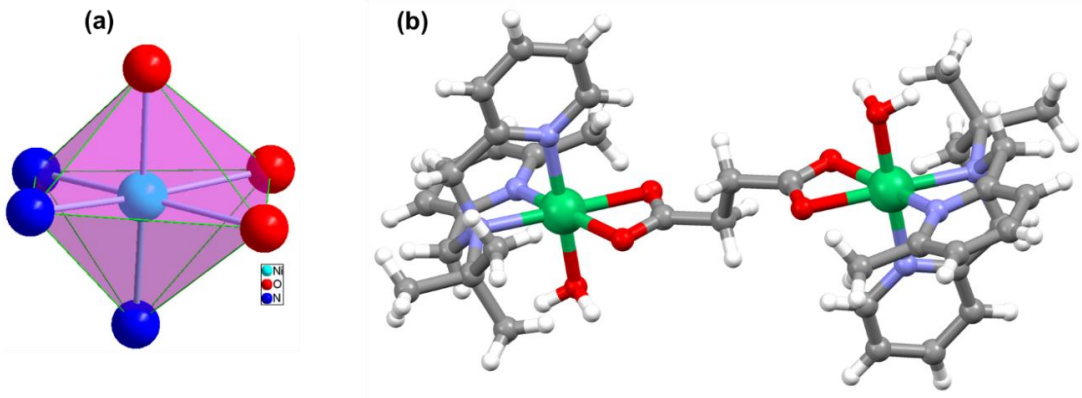

Figure 3.35. (a) Distorted octahedral geometry having N3O3 type surrounding around the metal center and (b) formation of dinuclear synthon in **3⊃Cl$^-$**.

In this case, two Hsuccinate molecule were exchanged with two chloride ions. Due to the presence of the five lattice water molecules (O4, O5, O6, O7 and O8), a 1D supramolecular assembly was formed which consist of five different type of motifs (Figure 3.36). Motif 1, ($R_4^4(8)$), consists of two lattice water molecules (O4···O6), two oxygens of the bridging

succinate (O1···O2), (distances: 2.816 Å, 2.764 Å, 2.718 Å) and four carbons of succinate. Motif 2, ($R_4^5(5)$), consists of four lattice water molecules (O4···O6···O8···O7), one chloride ion; distances: 2.734 Å, 2.937 Å, 2.840 Å, 3.239 Å (Cl···O8), 3.222 Å (Cl···O6).

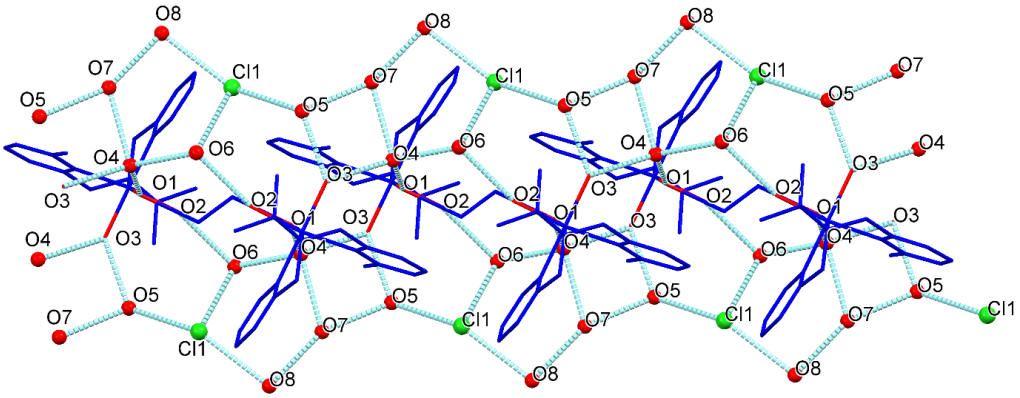

Figure 3.36. Supramolecular assembly showing five types of motifs in **3⊃Cl**$^-$.

Motif 3, ($R_4^5(6)$), consists of two lattice water molecules (O5···O6), one coordinated water oxygen (O3), one oxygen from succinate (O2), one chloride ion, distances: 2.816 Å, 2.682 Å, 3.109 Å (Cl···O5), 3.222 Å (Cl···O6) and one Ni(II) center. Motif 4, ($R_4^4(4)$), consists of three lattice water molecules (O4···O5···O7) and one coordinated water molecule (O3), distances: 2.937 Å, 2.818 Å, 2.682 Å, 2.731 Å.

Table 3.9. Hydrogen bonding parameters in **3⊃Cl**$^-$.

D---H…A (Å)	**r(D-H) (Å)**	**r(H…A) (Å)**	**r(D…A) (Å)**	**∠D-H…A (deg)**	**Symmetry**
O3 -H3B...O5	0.88	1.92	2.6838	144	1-x,1/2+y,1/2-z
O4 -H4D...O6	0.85	2.33	2.7399	110	.
O4 -H4E…O1	0.85	1.89	2.7339	171	x,1/2-y,-1/2+z
O5 -H5A…Cl1	0.85	2.29	3.116	164	x,1/2-y,-1/2+z
O5 -H5B…O7	0.85	2	2.8122	160	.
O6 -H6A…O4	0.85	2.09	2.7399	133	.
O6 -H6B…O2	0.85	2.03	2.833	156	2-x,-1/2+y,1/2-z
O7 -H7B…O4	0.85	2.36	2.9339	126	.
O8 -H8B…O7	0.85	2.35	2.8744	120	1-x,1-y,-z
C4 -H4A…O1	0.96	2.56	3.4302	152	1-x,1-y,1-z
C4 -H4B…O1	0.96	2.54	3.0896	116	.
C10 -H10A…O7	0.97	2.59	3.4292	144	.
C10 -H10B…O5	0.97	2.51	3.19	127	.
C13 -H13…Cl1	0.93	2.74	3.5387	144	1+x,y,z
C17 -H17A…O2	0.96	2.53	3.3715	147	.
C19 -H19A…O3	0.96	2.53	3.1108	119	.

Motif 5, ($R_6^6(8)$), consists of two lattice water molecule (O4···O4'), two coordinated water molecules (O3···O3'), two oxygen from succinate (O1···O1'), distances: 2.718 Å, 2.731 Å and two Ni(II) center from two different synthons. Motif 5 connects two different synthons to each other. In this case, O5, O7, O8 and chloride molecules formed a linear chain of the water and anion shown in the Figure 3.36. All the bond lenths, bond angles and hydrogen bonding parameters are listed in Table A24, A35 (Appendix) and Table 3.9, respectively.

Structural description of **3⊃NO$_3^-$**. In case of **3⊃NO$_3^-$** (exchanged with nitrate), the compound crystallizes in the $P2_1/n$ space group. The asymmetric unit consists of a metal center, one ligand, half of the coordinate succinate and one free nitrate ion. Along with this, three lattice water molecules are also present. A N3O3 type of surrounding around metal center was formed using three nitrogens of the ligand (distances: Ni-N_{Py} (2.164(2) Å and 2.070(2) Å) and Ni-N_{alkyl}(2.087(3) Å), two oxygens of succinate (distances: 2.079(3) Å and 2.214(2) Å) and one oxygen from the coordinated water molecule with distance 2.072(2) Å (Figure 3.37).

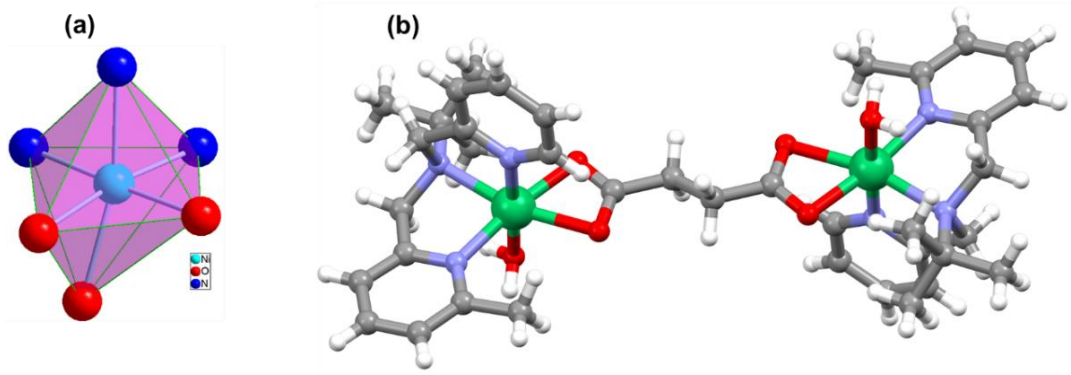

Figure 3.37. (a) Distorted octahedral geometry having N3O3 type surrounding around the metal center and (b) formation of dinuclear synthon in **3⊃NO$_3^-$**.

Due to the presence of six lattice water molecules, resulting supramolecular assembly consists of five different type of the motifs. Motif 1, ($R_3^6(13)$), consists of two lattice water molecule (O8···O7), one coordinated water molecule (O3), one oxygen of succinate (O2), two oxygens of the nitrate (O4···O5), distances: 2.756 Å, 2.818 Å, 2.929 Å, 3.022 Å, one nitrogen of nitrate, two Ni(II) centers, four carbon atom of succinate and one oxygen of the succinate (non hydrogen bonded). Motif 2, ($R_6^6(8)$), consists of the two lattice water molecules (O7···O7'), two coordinated water molecules (O3···O3'), two oxygen of succinate (O2···O2'), distances: 2.714 Å, 2.818 Å and two Ni(II) centers (from different synthons). Motif 3, ($R_4^5(5)$), consists of three lattice water molecules (O7···O8···O9), one coordinated

water molecule (O3) and one oxygen of the nitrate (O4), having distances: 2.714 Å, 2.756 Å, 2.868 Å, 2.852 Å and 2.929 Å.

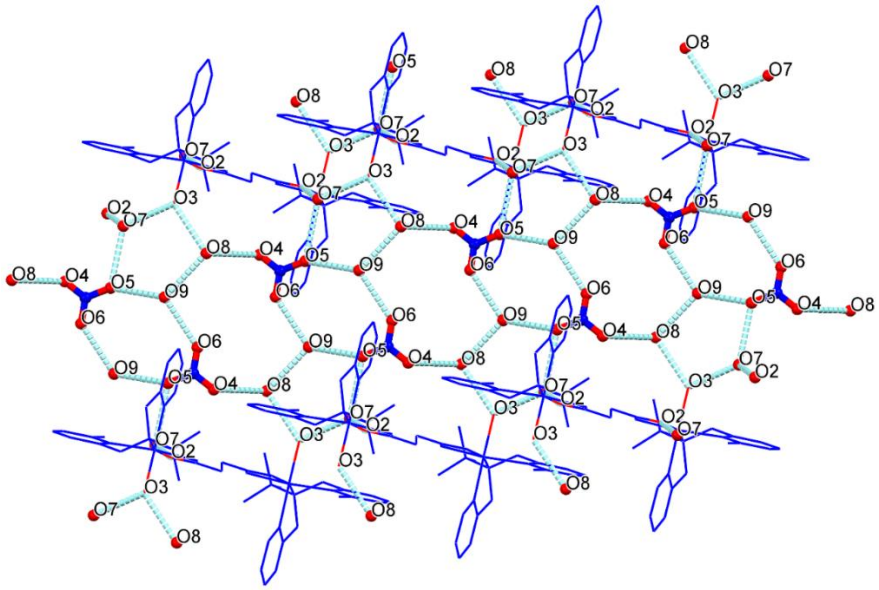

Figure 3.38. Supramolecular assembly formed in **3⊃NO_3^-**.

Motif 4, ($R_2^6(8)$), consists of two lattice water molecules (O9···O9'), four oxygens from two different nitrate molecules (O6···O4···O6'···O4'), distances: 2.852 Å, 2.801 Å and two nitrogen atoms from two nitrate molecules. Motif 5, ($R_4^8(10)$), consists of four lattice water molecules (O8···O9···O8'···O9'), four oxygens from two different nitrate molecules (O6···O5···O6'···O5'); distances: 2.801 Å, 2.868 Å, 3.022 Å and two nitrogens of two nitrate ions (Figure 3.38). Motif 2 connect two synthons with each other (Figure 3.38). All the bond lenths, bond angles and hydrogen bonding parameters are listed in Table A24, A35 (Appendix) and Table 3.10, respectively.

Table 3.10. Hydrogen bonding parameters in **3⊃NO_3^-**.

D---H…A (Å)	r(D-H) (Å)	r(H…A) (Å)	r(D…A) (Å)	∠D-H…A (deg)	Symmetry
O3 -H3A...O7	0.86	1.89	2.712	160	1/2+x,1/2-y,-1/2+z
O7 -H7A...O2	0.85	1.98	2.8235	170	1/2-x,1/2+y,1/2-z
O7 -H7B…O5	0.85	2.09	2.9342	172	1/2-x,1/2+y,1/2-z
O8 -H8A…O4	0.85	2.23	3.0353	158	1/2-x,1/2+y,1/2-z
O9 -H9D…O5	0.85	2.05	2.8701	163	1-x,-y,1-z
C1 -H1B…O4	0.97	2.51	3.4651	168	-x,-y,-z
C11 -H11A…O1	0.96	2.43	3.2864	148	.
C13 -H13C…O1	0.96	2.53	3.3615	145	.
C14 -H14A…O8	0.97	2.58	3.3255	134	.
C19 -H19…O2	0.93	2.55	3.1277	120	.

By comparing all the four structures, it was observed that by anion exchange, diversification in the water cluster formation takes place, like in **2⊃fumarate**. In **3⊃Hsuccinate**, lattice water molecules form hydrogen bonding with the free succinate anion resulting in the formation of a 3D supramolecular assembly while when exchanged with perchlorate, a change in the water clusters arrangement was observed. Along with this, due to hydrogen bonding between lattice water molecules and perchlorate anion, a 3D supramolecular assembly was formed. By exchanging with chloride ions, a pentamer of one chloride and four water molecules are formed while, in case of nitrate, a different arrangement of water molecules have been observed (Figure 3.39 and 3.40). After studying the effect of anion exchange on the shape of water clusters by comparing their structure, we have confirmed the anion exchange by other techniques like FTIR, PXRD and thermogravimetric analysis as like compound **2⊃fumarate**.

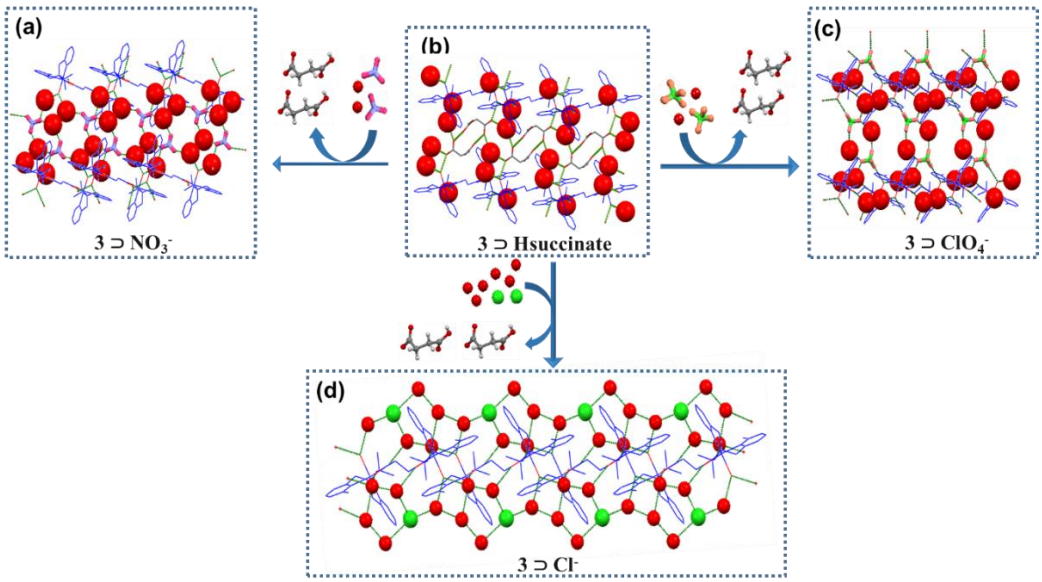

Figure 3.39. Anion exchange in **3⊃Hsuccinate** (a) Supramolecular assembly and formation of water cluster in **3⊃NO_3^-**, (b) Supramolecular assembly and formation of water cluster in **3⊃Hsuccinate**, (c) Supramolecular assembly and formation of water clusters in **3⊃ClO_4^-**, (d) Supramolecular assembly and formation of water cluster in **3⊃Cl^-**.

By comparing the PXRD patterns of all the exchanged product with different anions, it was found that there is a change in the powder pattern confirming the diversity in the formation of coordination architecture (Figure 3.41). Moreover, compounds having the single crystal structure show a good agreement between the simulated and experimental data, hence confirming the phase purity of the compounds.

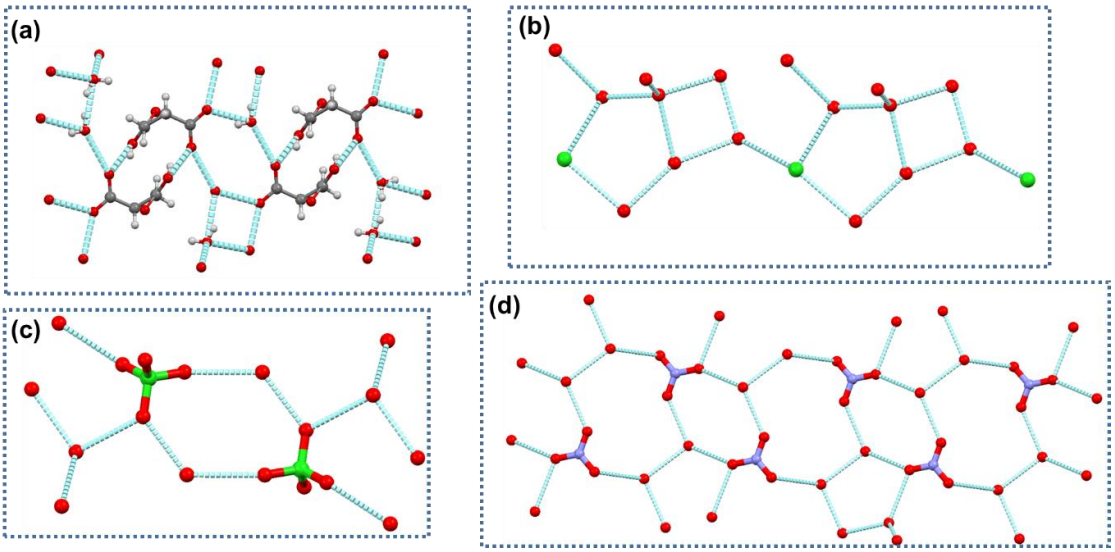

Figure 3.40. Arrangement of water cluster and anion in **3⊃fumarate** (a), **3⊃Cl**$^-$ (b), **3⊃ClO$_4$**$^-$ (c), and **3⊃NO$_3$**$^-$ (d).

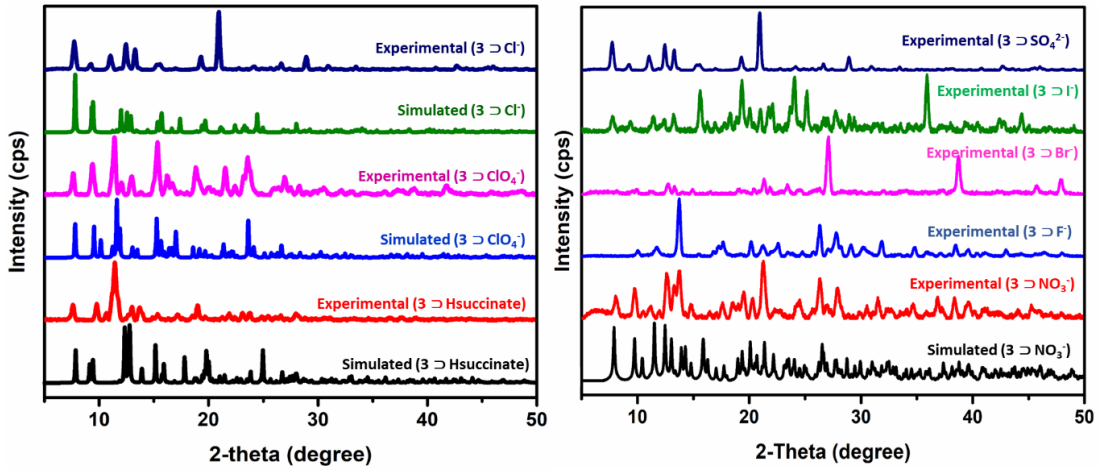

Figure 3.41. Change in powder patterns of **3⊃Hsuccinate** upon anion exchange.

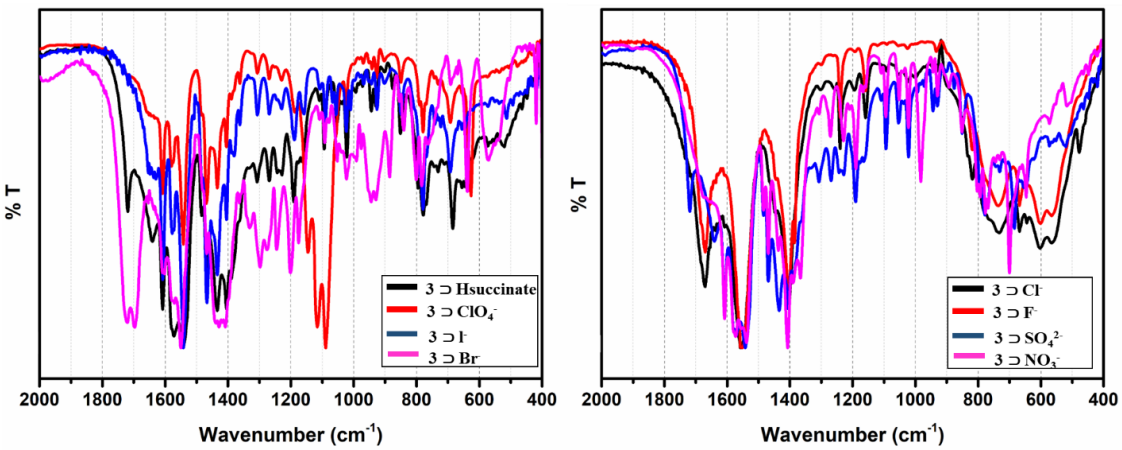

Figure 3.42. Change in FTIR spectra of **3⊃Hsuccinate** upon anion exchange.

Exchane of fumarate with other anions was further confirmed by FTIR. technique.. As Every anion has a significant peak in FTIR, therefore exchange of fumarate with different anions can be monitered by disappearence of the chararctersticpeak of fumarate anion, followed by appearence of a new peak correcponding to the anion exchanged.. After exchange of fumarate anions in **3,** peak at 1702 cm^{-1} was disappeared and new peaks were appeared based on the anion exchanged.. For example, theappearance of a peak at 1084 cm^{-1} corresponded to the perchlorate ions, a peak around 1254 cm^{-1} corresponded to sulfate ions and a peak at 1384 cm^{-1} confirmed the exchange of fumarate with the nitrate anion. (Figure 3.42).

Chemistry with 6-Mebpea

This ligand is a derivative of 6-Mebpta, in which tertiary butyl group is replaced by an ethyl group. Using 6-Mebpea, several MOCNs have been synthesized with Ni(II), Zn(II) and Cd(II) in combination with different dicarboxylates as shown in the Schemes 3.10-3.11.

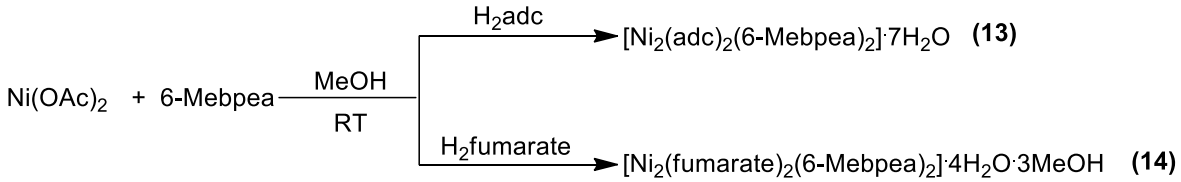

Scheme 3.10. Synthesis of **13** and **14**.

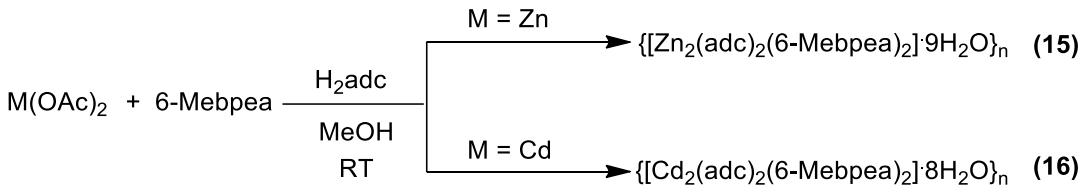

Scheme 3.11. Synthesis of **15** and **16**.

FTIR spectroscopic studies. For **13** and **14**, a $\Delta\nu$ value of 235 cm^{-1} and 156 cm^{-1}, respectively, confirms the monodentate and bidentate binding mode of the carboxylate to the metal center (Figure 3.43). Similarly, in **15** and **16**, a $\Delta\nu$ value of 257 cm^{-1} and 291 cm^{-1}, respectively, confirms the monodentate mode of carboxylate binding to the metal center. The asymmetric and symmetric stretching frequencies of **13-16** are listed in Table 3.11.

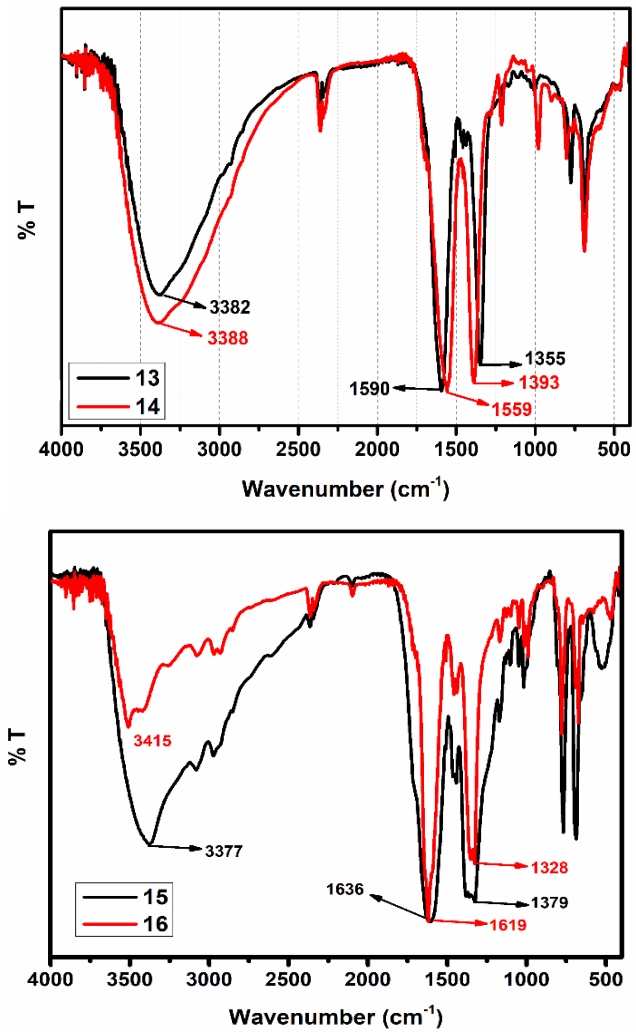

Figure 3.43. FTIR spectra of **13-16**.

Thermogravimetric analyses. Thermal stabilities of **13-16** were studied as a function of temperature in the range of 25-500 °C (Figures 3.44). The coordination polymers show thermal stabilities up to 200 °C with an initial loss of the lattice solvent molecules at around 100 °C, followed by the loss of coordinated water molecues around 150 °C

Table 3.11. Asymmetric and symmetric stretching frequencies and their respective binding modes of carboxylates in **13-16**.

Compound	**Asymmetric (υ_1) cm^{-1}**	**Symmetric (υ_2) cm^{-1}**	**$\Delta\upsilon = \upsilon_1 - \upsilon_2$ cm^{-1}**	**Binding mode**
13	1590	1355	235	Monodentate
14	1620	1464	156	Bidentate (chelated)
15	1636	1379	257	Monodentate
16	1619	1328	291	Monodentate

For **13**, the first loss of 25.05% corresponds to the loss of seven water molecules (ca. 24.45%), while the same (16.87%) for **14** corresponds to the loss of four lattice water and three methanol (ca. 17.08%). Similarly, compound **15** and **16** exhibiting a weight loss of 14.68% (ca. 14.95) and 14.82% (cal. 13.22%), respectively, correspond to the loss of eight water molecules.

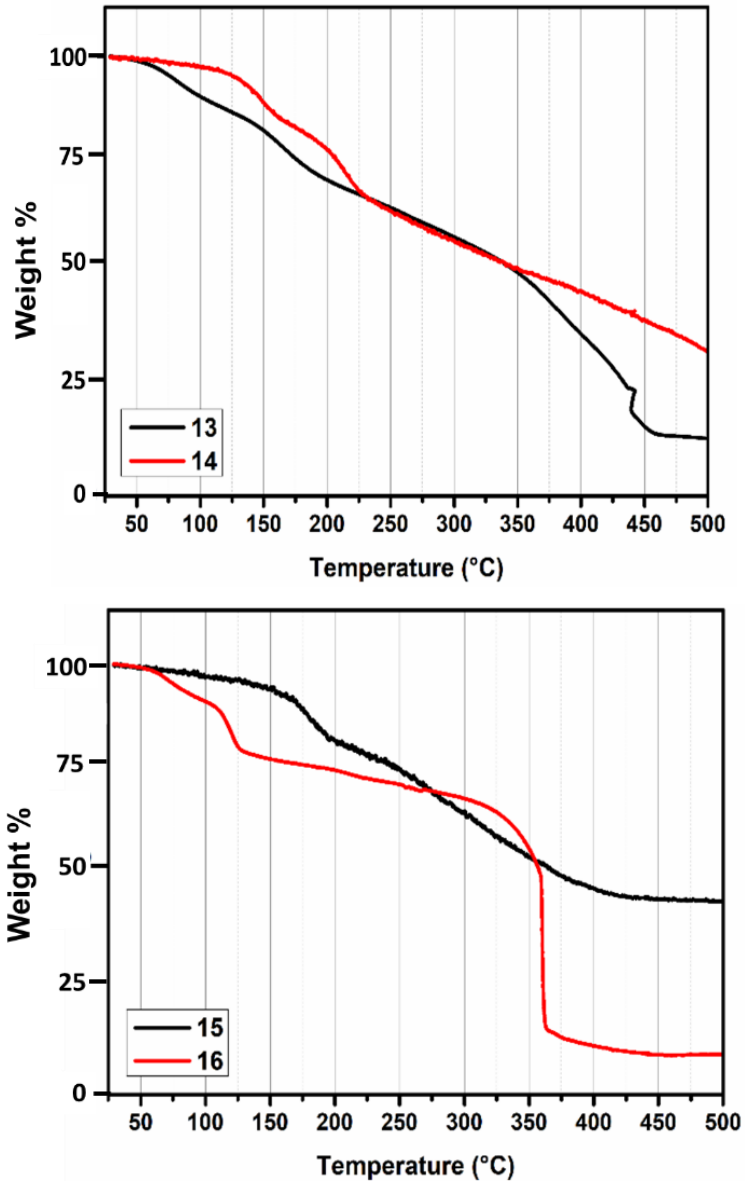

Figure 3.44. TGA scans of **13-16**.

Powder X-ray diffraction studies. The crystalline nature of **13-16** was confirmed by powder X-ray diffraction studies and found that all these compounds have different type of framework as they show different type of powder pattern (see Figure 3.45).

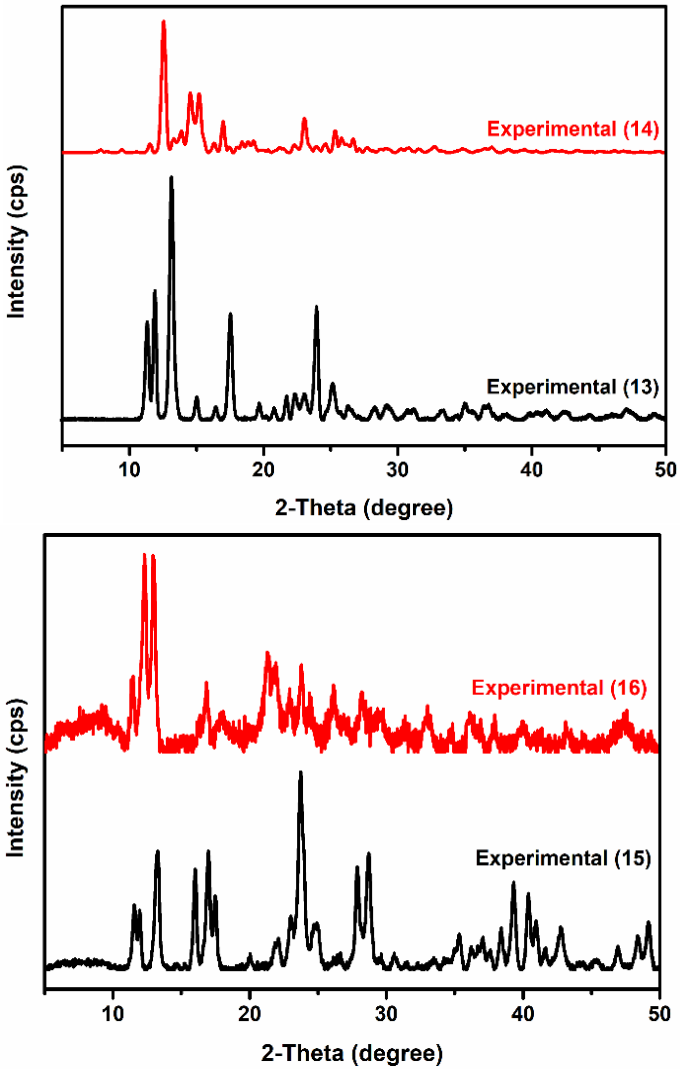

Figure 3.45. PXRD patterns of **13-16**.

Chemistry with 6,6′-Me_2bpta

Using the 6,6′-Me_2bpta ligand, seven MOCNs of Ni(II), Zn(II), Mn(II) and Cd(II) have been synthesized in combination with different dicarboxylates as shown in the Schemes 3.12-3.14.

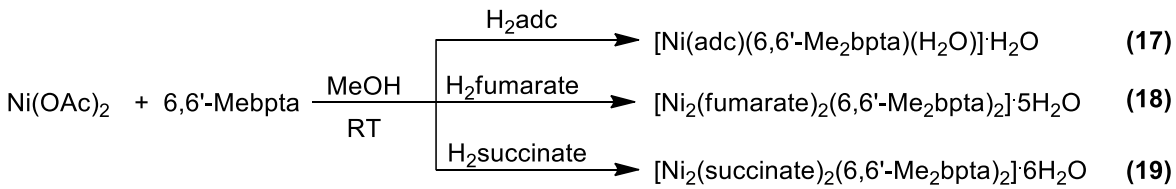

Scheme 3.12. Synthesis of **17-19**.

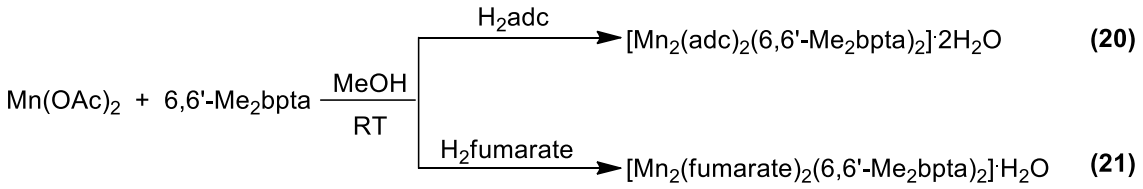

Scheme 3.13. Synthesis of **20** and **21**.

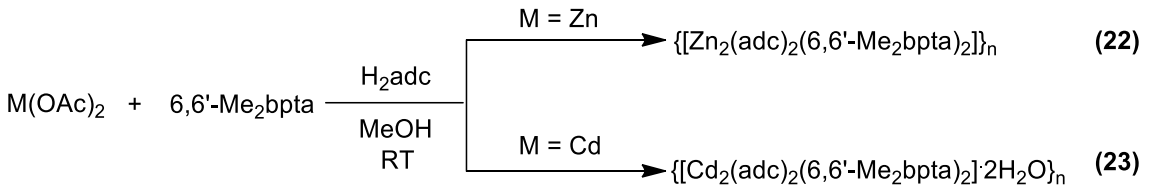

Scheme 3.14. Synthesis of **22** and **23**.

FTIR spectroscopic studies. Compound **17** having a Δν value of 183 cm^{-1} indicates the bidentate mode of carboxylate binding to the Ni(II). A peak around 1704 cm^{-1} confirmed the presence of non-bonded deprotonated carboxylate group of adc.

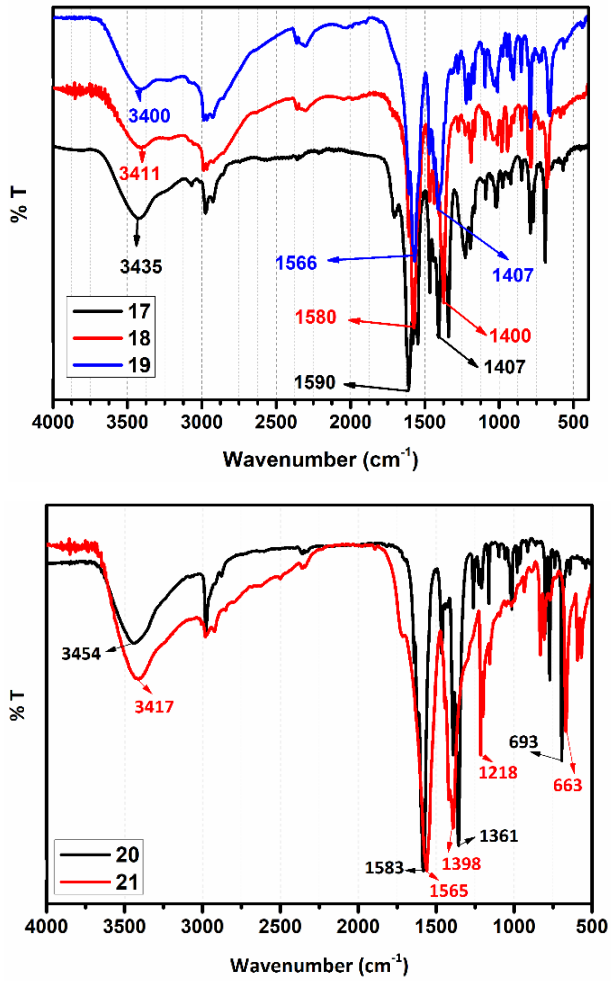

Figure 3.46. FTIR spectra of **17-21**.

Presence of coordinated water molecule in **17** was confirmed by the presence of peak around 3200 cm^{-1}. (Figure 3.46). In case of compounds **18** and **19**, Δν values are 180 cm^{-1} and 159 cm^{-1}, respectively, indicating a bidentate mode of carboxylate binding to the Ni(II). Similarly, compounds **20** and **21** have a Δν value of 222 cm^{-1} and 167 cm^{-1}, respectively, indicating the monodentate and the bidentate mode of carboxylate binding to the Mn(II) center (Figure 3.46).

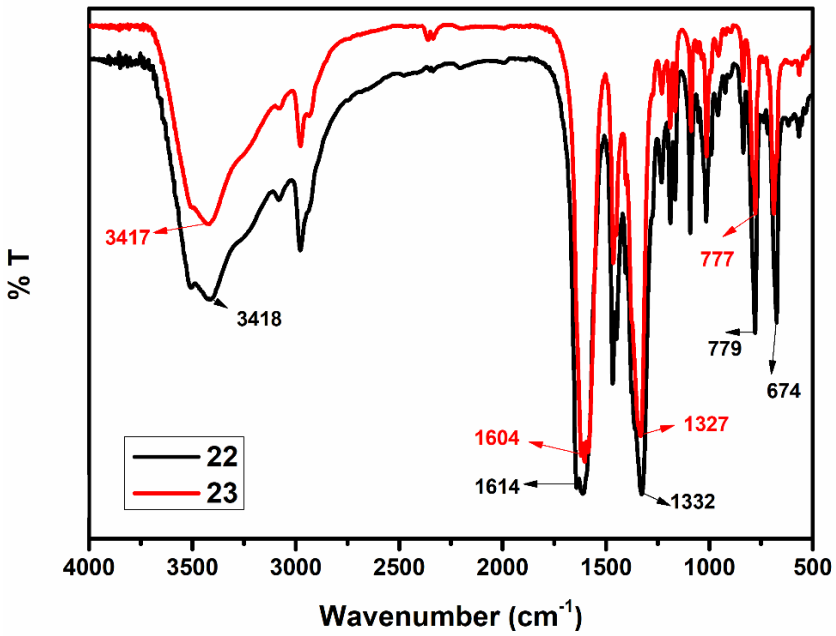

Figure 3.47. FTIR spectra of **22** and **23**.

22 and **23** exhibit a Δν value of 282 cm^{-1} and 277 cm^{-1}, respectively, confirming the monodentate mode of carboxylate binding to the metal center (Figure 3.47). The asymmetric and symmetric stretching frequencies are listed in Table 3.12.

Table 3.12. Asymmetric and symmetric stretching frequencies and their respective binding modes of carboxylates of **17-23**.

Compound	**Asymmetric (υ_1) cm^{-1}**	**Symmetric (υ_2) cm^{-1}**	**$\Delta\upsilon = \upsilon_1 - \upsilon_2$ cm^{-1}**	**Binding mode**
17	1590	1407	183	Bidentate (chelated)
18	1580	1400	180	Bidentate (chelated)
19	1566	1407	159	Bidentate (chelated)
20	1583	1361	222	Monodentate
21	1565	1398	167	Bidentate (chelated)
22	1614	1332	282	Monodentate
23	1604	1327	277	Monodentate

Thermogravimetric analyses. Thermal stabilities of **17-23** were studied as a function of temperature in the range of 25-500 °C (Figures 3.48).

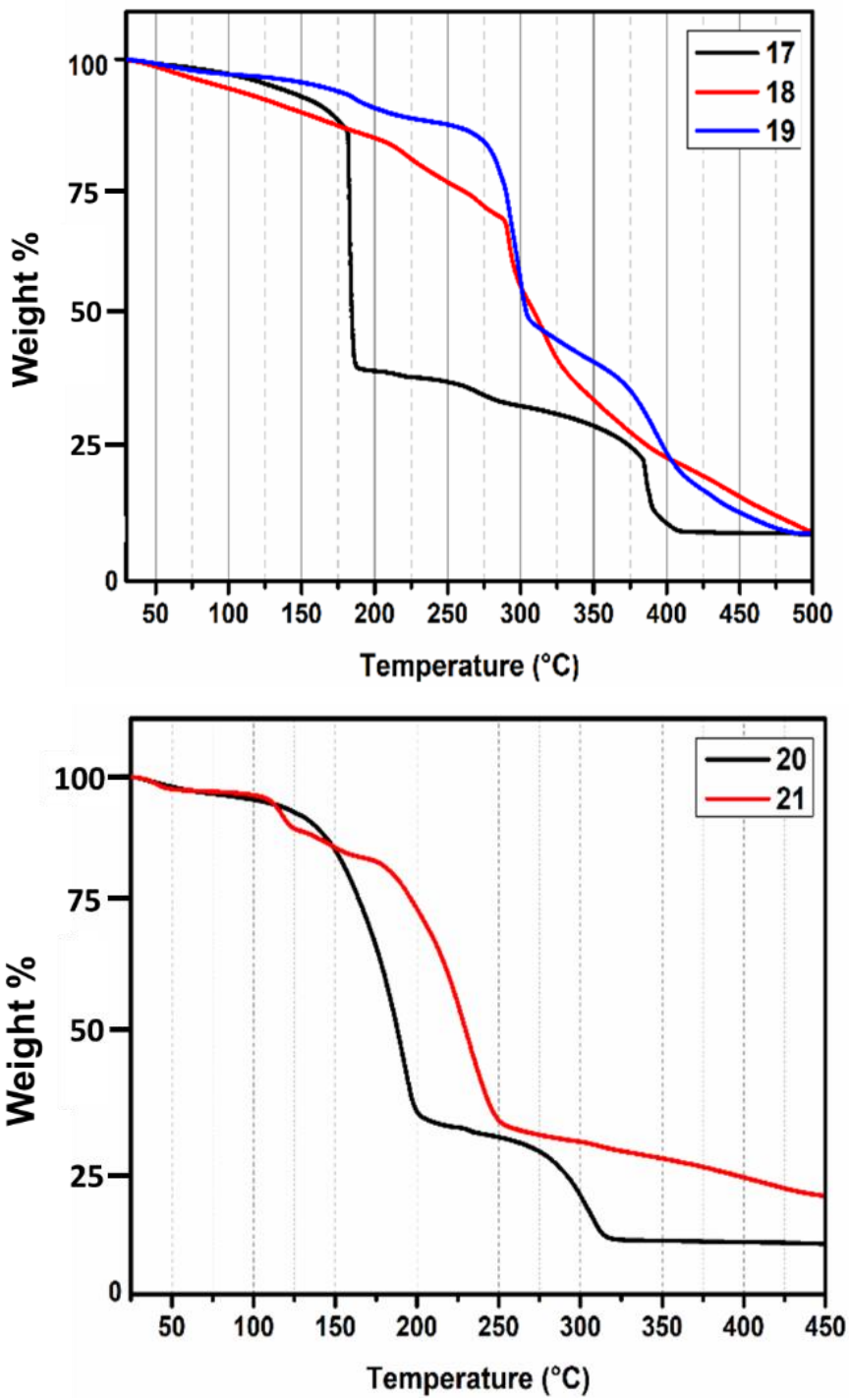

Figure 3.48. TGA scans of **17-21**.

In **17**, the first weight loss of 4.55% corresponding to the loss of two water (one coordinated and one lattice) molecules (ca. 5.01%), while for compound **18** the weight loss of 9% was observed for the loss of five lattice water molecules followed by decomposition of the network.

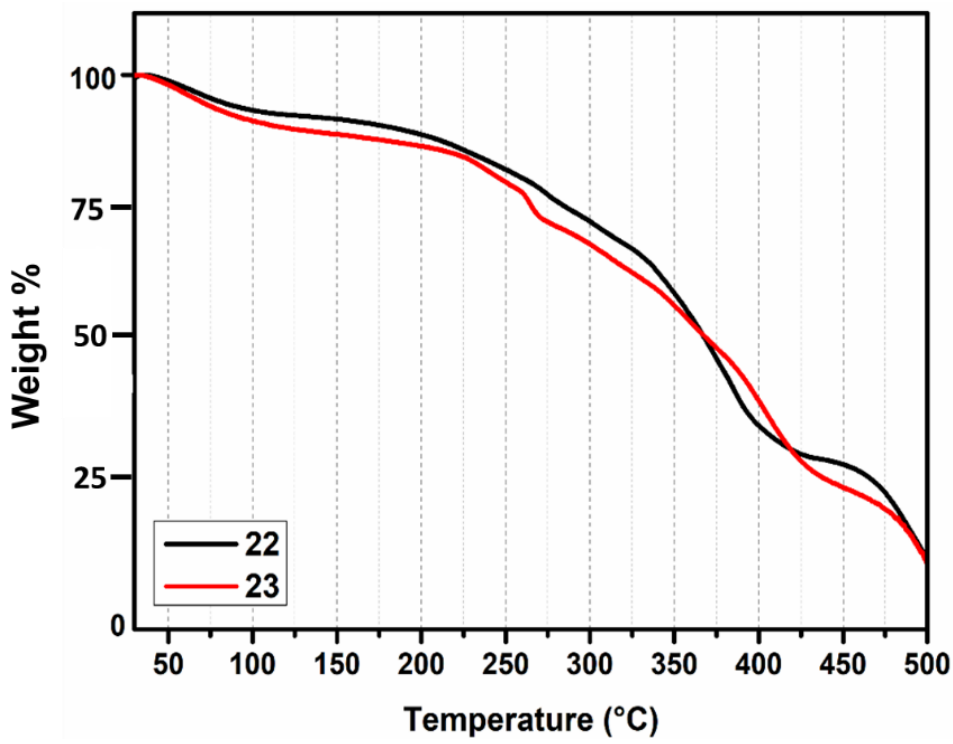

Figure 3.49. TGA profiles of **22** and **23**.

For **19**, a weight loss of 10.54% was observed for the loss of six water molecules (ca. 9.26%). In **20**, loss of two lattice water molecules was observed around 75 °C (ca. 9.26%), while **21** exhibits a weight loss of 14.31% corresponds to the loss of one lattice water molecule (cal. 14.68%). As shown in the Figure 3.48, **20** and **21** show the same type of thermal stability. Similarly, for 23, loss of two lattice water molecules was observed around 100 °C.

Single crystal structure analyses. Crystals of compound **17** were grown using liquid diffusion mehod. Linker and ligand were dissolved in methanol and layered over aqueous solution of metal salt separated by a buffer layer (a mixture of water and methanol in a 1:1 ratio) for slow diffusion of two liquids.

Structural description of **17**. Compound **17** crystallizes in the $P2_1/n$ space group and consists of a discrete mononuclear unit Ni(II) center has an octahedral geometry and is surrounded by three nitrogens of the ligand (bond distances: Ni-N_{Py} (2.0474(14) Å and 2.1317(14) Å) and Ni-N_{alkyl} (2.1108(14) Å), two oxygens of the adc (unsymmetrical chelated having bond distances: 2.1675(12) Å and 2.1217(11) Å) and one coordinated water molecule having a distance of 2.0828(12) Å.

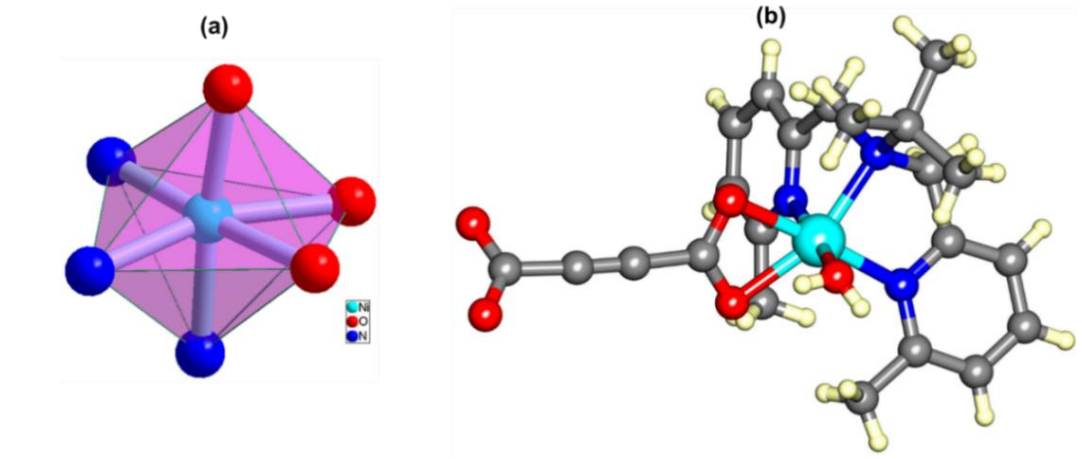

Figure 3.50. (a) Distorted octahedral geometry having N3O3 type surrounding around the metal center and (b) a mononuclear complex formed in **17**.

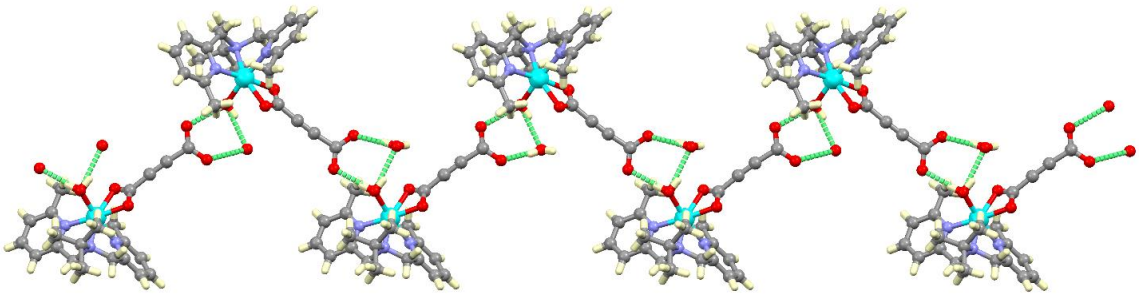

Figure 3.51. Supramolecular assembly formed in **17**.

The selected bond distances and angles are listed in Table A25 and A36 (Appendix). Interestingly, one side of the adc is binding with Ni(II) center in a chelated fashion and another side is free and presentin deprotonated form (Figure 3.50). The two discrete units are connected through hydrogen bonding between coordinated water, one lattice water molecule and two oxygen atoms of uncoordinated adc to form a pentagonal motif ($R_4^4(5)$) resulting in the formation of a zig-zag shaped supramolecular assembly as shown in Figure 3.51. All hydrogen bonding parameters are listed in Table 3.13.

Table 3.13. Hydrogen bonding parameters in **17**.

D---H…A (Å)	r(D-H) (Å)	r(H…A) (Å)	r(D…A) (Å)	∠D-H…A (deg)	Symmetry
O5 -H5A...O2	0.82	1.87	2.6791	172	3/2-x,1/2+y,1/2-z
O5 -H5B...O6	0.81	2.08	2.863	163	.
O6 -H6A...O1	0.82	1.88	2.6908	169	3/2-x,1/2+y,1/2-z

Structural description of **22**. It crystallizes in the monoclinic $P2_1/n$ space group and forms a 1D spiral coordination network. The asymmetric unit consists of two metal centers, two ligands and two linkers. The Zn(II) center is penta-coordinated consisting of three nitrogen atoms from the ligand and two oxygen atoms from two different dicarboxylate linkers (Figure 3.52). Their bond distances are: Zn-N_{Py} (2.320(8) Å and 2.349(9) Å) and Zn-N_{alkyl} (2.431(7) Å), Zn-O_{carb} (distances: 2.250(8) Å and 2.251(9) Å) and Zn-O_{water} (2.072(5) Å). All distances and angles are listed in Tables A25 and A36 (Appendix).

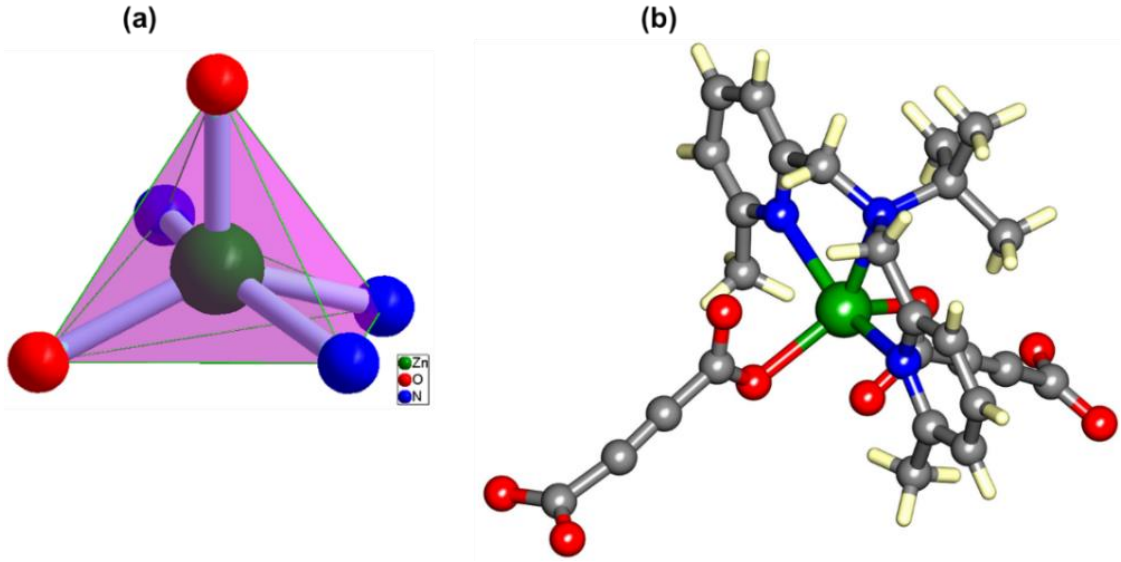

Figure 3.52. (a) Distorted trigonal bipyramidal geometry having N3O2 type surrounding around the metal center and (b) coordination environment around the metal center in **22**.

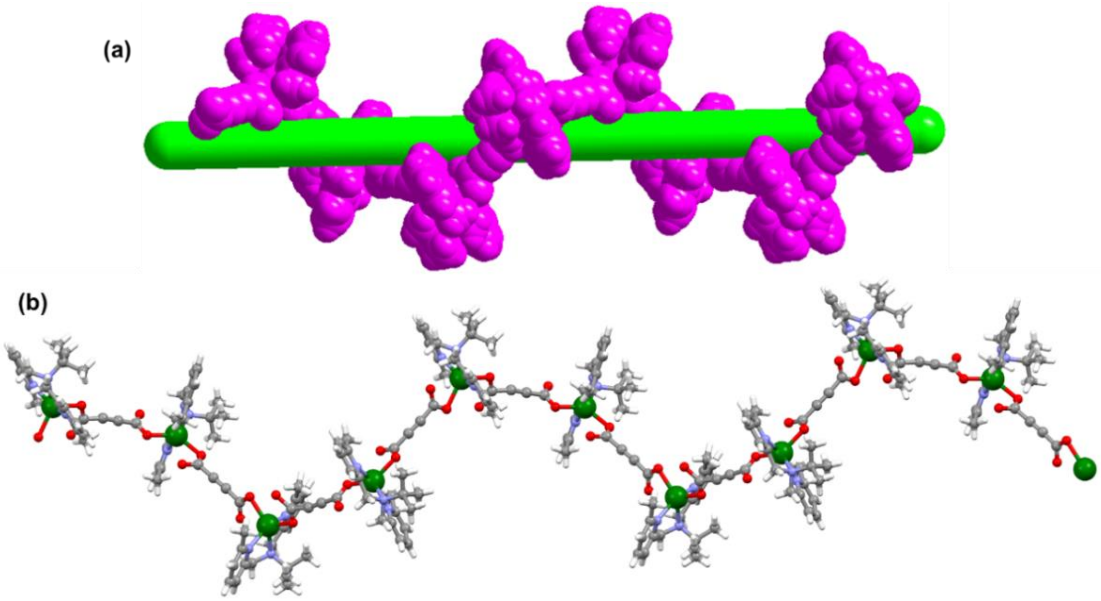

Figure 3.53. (a) Spiral helical type of geometry and (b) spiral chain of coordination polymer of **22** in ball and stick representation.

A perfect spiral coordination polymer was generated by expanding the asymmetric unit (Figure 3.53). In the close packing, two layers are stacked in AA fashion as shown in Figure 3.54. The interlayer distance between two adjacent layers is in the range of 8.542 Å to 9.00 Å. A perfect packing between these zig-zag layersis clearly seen along the *a*-axis (Figure 3.54).

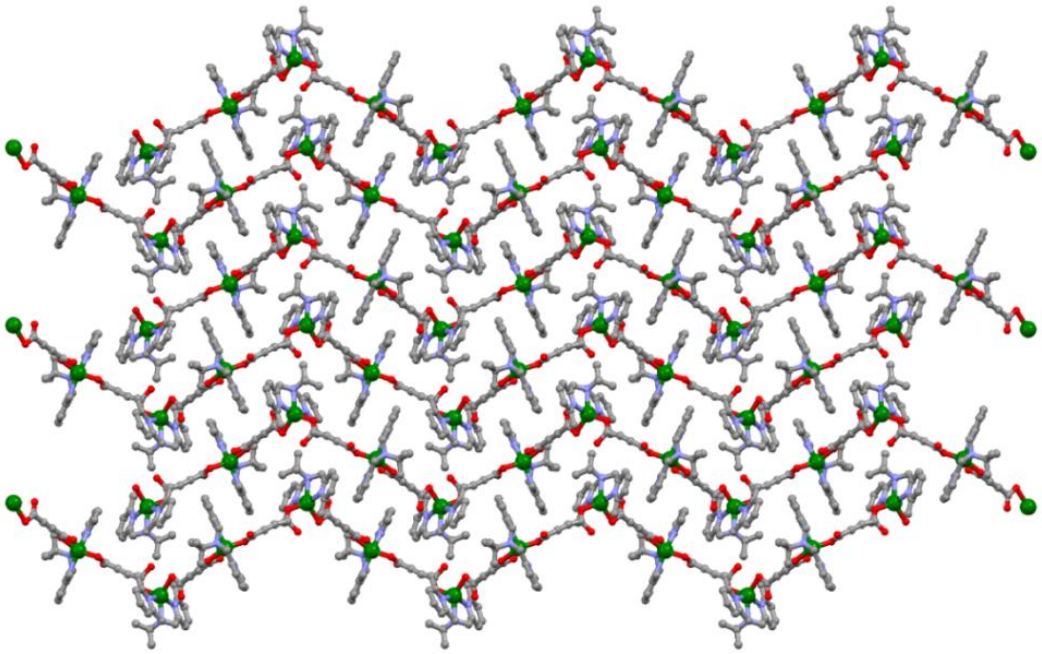

Figure 3.54. Formation of AA type packing in **22**.

Powder X-ray diffraction studies. Crystalline nature of all synthesized complexes (17-23) was confirmed by powder X-ray diffraction studies. In addition to this, bulk phase purity of **17** and **22**, was further confirmed by comparison of experimental data with the simulated data . (Figure 3.55 and 3.56).

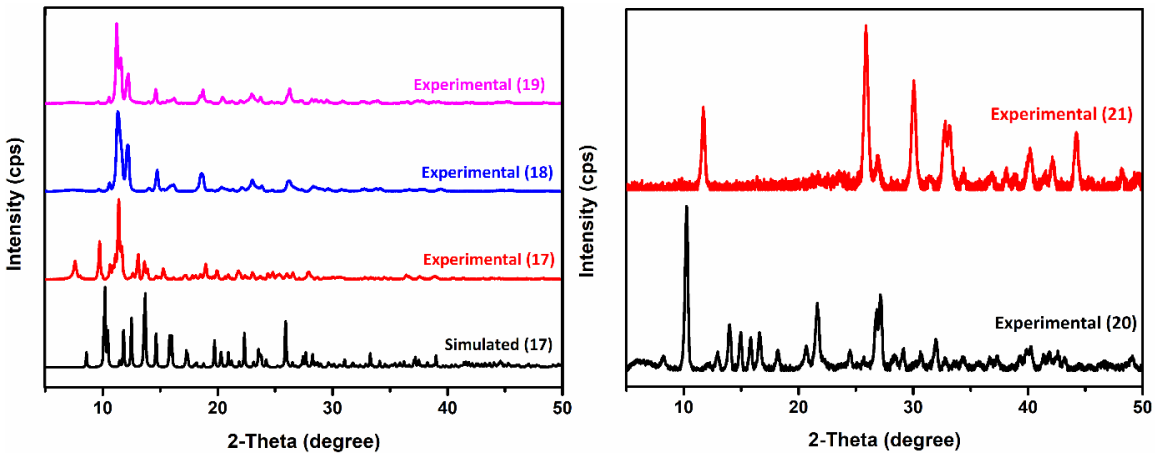

Figure 3.55. PXRD patterns of **17**-**21**.

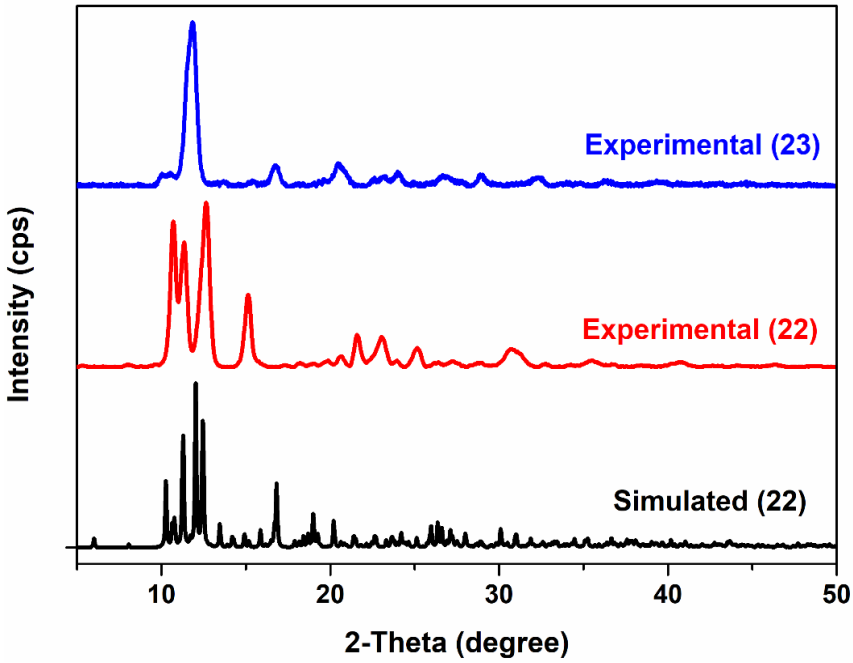

Figure 3.56. PXRD patterns of **22** and **23**.

Effect of metal, ancillary ligand, or linker on the coordination architecture: A change or modification of any component (metal, ancillary ligand, or linker) led to the formation of different coordination architectures with respect to stability, dimensionality, supramolecular assembly and applications. The metal centers or metal clusters provide different coordination sites to build various coordination networks. On the other hand, the selection of ancillary ligands and the organic linkers is very crucial in making such assemblies with varied dimensionalities. The ancillary ligands (polypyridyl) surround the metal center and provide particular open sites for the binding of organic linkers which results in making such pre-designed metal organic coordination networks. For our interest to explore and identify the factors governing the formation of supramolecular assemblies *vs*. discrete polygons, such as squares and rectangles, and their further association through supramolecular interactions, a systematic study has been carried using multidentate polypyridyl ancillary ligands and multitopic carboxylate linkers with the metal centers. All the coordination architectures were synthesized at ambient temperature and crystals were grown by either slow evaporation method or by the direct layering of the components in particular solvents.

Effect of an ancillary ligand on the coordination architectures: Both **1** and **17** are Ni(II) adc compounds. howeverdiffer from each other by the presence of one extra methyl group in the ancillary ligand, 6-Mebpta and 6,6′-Me_2bpta respectively, which led to a tremendous

change in the resulting supramolecular architecture and coordination sphere. A close view of d **1** shows that it is a dinuclear compound having Ni(II) *bis*(adc) units. One dimensional linear chain type of supramolecular architecture was formed due to the presence of two lattice water molecules in **1**. These two lattice water molecules form a doubly hydrogen-bonded cyclic dimeric of water cluster which acts as a bridge between two Ni(II) *bis*(adc) units as shown in the Figure 3.57. While compound **17** is a mononuclear complex having one tridentate ligand, and an acetylene dicarboxylate bonded to the Ni(II) center from one side only in monodentate fashion while another side of the adc is uncoordinated and freely present in deprotonated form.

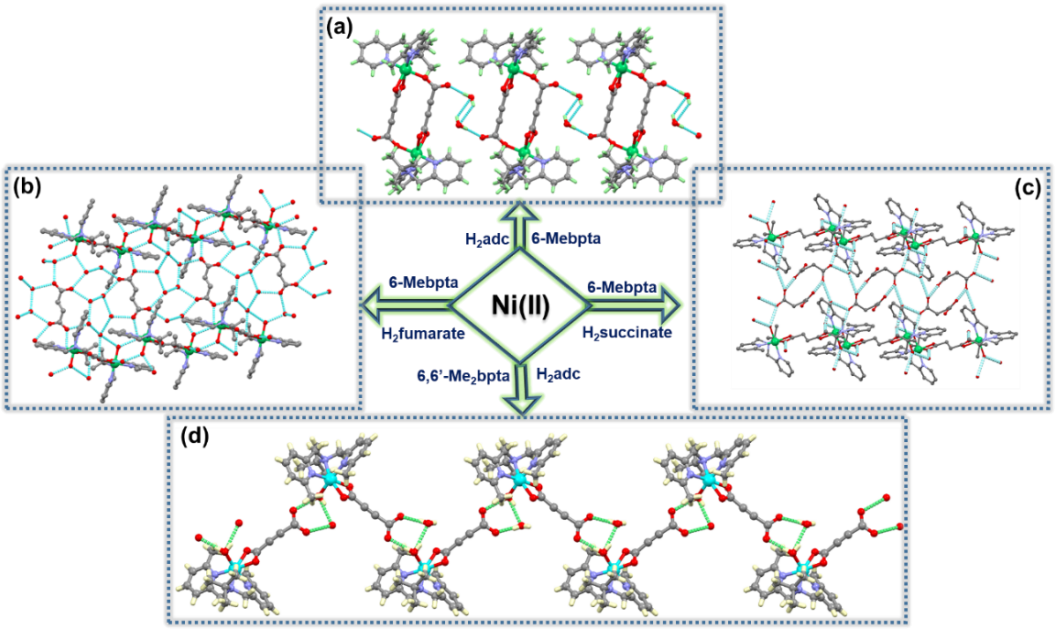

Figure 3.57. Diversification in coordination architectures due to change in the linker and ancillary ligand and formation of supramolecular assemblies in (a) **1**, (b) **2⊃fumarate**, (c) **3⊃Hsuccinate** and (d) **17**.

Along with this, one lattice water molecule is also present which helps in the formation of 1D zig-zag chain through hydrogen bonding with the coordinated water molecule and uncoordinated carboxylate. Interestingly, this type of change in the supramolecular architecture and water cluster is observed due to a small variation in the ligand (adding extra methyl group). In case of **13**, which has 6-Mebpea (three methyl group less) as the ancillary ligand, the resultant compound is different from both **1** and **17** with respect to its binding of carboxylate to the metal center, as confirmed by FTIR. It is evident that carboxylate shows bidentate mode of binding with metal unlike **1**, where it is monodentate in nature and in **17** carboxylate binds in bidentate mode. From TGA analysis it was found that the thermal stability of **13** is less in comparison to **1** and **17**.

On comparison of Ni(II)-fumarate compounds having 6-Mebpta, 6-Mebpea, and 6,6′-Me_2bpta as ancillary ligand, it was found that show a slight change in the ancillary ligand leads to great diversity in the coordination architecture. All three coordination networks, **2⊃fumarate** (6-Mebpta), **14** (6-Mebpea) and **18** (6,6′-Me_2bpta) have different architectures which has been confirmed by the comparison of their PXRD pattern, thermal stabilities (TGA)and FTIR spectra. Complex **18** is thermally less stable than **2⊃fumarate**, **and 14**. Along with this, all exhibit bidentate mode of carboxylate binding except **2⊃fumarate,** which shows bidentate mode and also contain a free free carboxylate group, making it a cationic coordination compound with free anion to neutralize overall assembly, this was further supported by SCXRD analysis. Comparison of Ni(II)-succinate compound with 6-Mebpta **(3⊃Hsuccinate**) and 6,6′-Me_2bpta **(19)** shows different architecture which was confirmed by PXRD and thermogravimetric analysis. From the FTIR spectra, it was observed thatboth have bidentate mode of carboxylate binding, but **3⊃Hsuccinate** has both bidentate modes as well as free carboxylate like **2⊃fumarate** and generate a cationic architecture stabilized by free anions, corroborating well with their SCXRD structures.

Comparison of Zn(II) and Cd(II) compounds of adc with 6-Mebpta (**6** and **7**), 6-Mebpea (**15** and **16**) and 6,6′-Me_2bpta (**22** and **23**) have shown the formation of different architectures by changing the ligand, keeping metal constant, as confirmed by the PXRD and thermal analysis.

Effect of organic linker on the coordination architectures: After the effect of change in metal or ancillary ligand on the coordination architecture, it is worth to discuss the effect of change in the organic linker on the coordination architecture. From SCXD analysis it was found that,**1** consists of Ni(II) metal, 6-Mebpta ligand and a rigid dicarboxylate (adc) forming a dinuclear neutral Ni(II) *bis*(adc) units with two lattice water molecules resulting in the formation of a 1D supramolecular assembly. Carboxylate binds with the metal center in both mono and bidentate modes. There is no coordinated water molecule present although the metal center is hexacoordinated. A change from a rigid dicarboxylate to a flexible or semi-flexible dicarboxylate (succinate or fumarate) led to a tremendous change in the coordination environment as well as supramolecular network. Compounds, **2⊃fumarate** and **3⊃Hsuccinate** were synthesized using fumarate and succinate, respectively, having metal and ligand constant. Both compounds consist of cationic dinuclear synthon in which Ni(II) is hexacoordinated and the carboxylate binds with the metal in a bidentate mode. A coordinated water molecule is also present. Different

lattice water molecules are present in both the compounds. For example, there are nine lattice water molecules in **2⊃fumarate** and four lattice water molecules in **3⊃Hsuccinate**. These water molecules form a supramolecular network having a free anion to neutralize the charge on metal center resulting in the formation of a neutral supramolecular architecture. In both the cases, a 3D supramolecular assembly is formed by strong hydrogen bonding between lattice waters and carboxylates.

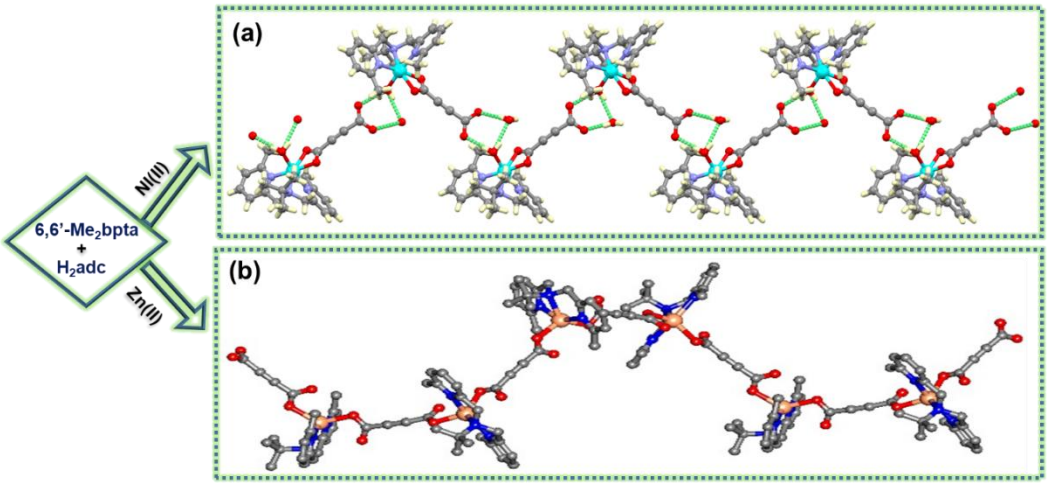

Figure 3.58. Diversification in coordination architectures due to change in the metal center (a) formation of 1D zig-zag chain in **17** and (b) formation of 1D coordination polymer in **22**.

Furthermore, diversification in the arrrangment of water clusters is also observed due to the change in the dicarboxylates. In case of adc (**1**), a double hydrogen-bonded cyclic water dimer was observed which is very rare. On the other hand, in case of fumarate (**2⊃fumarate**), a cyclic pentamer of water cluster was formed whereas, such type of unusual water cluster was not observed in case of succinate (**3⊃Hsuccinate**). In case of combination of Ni(II), 6,6′-Me_2bpta with adc (**17**), fumarate (**18**) and succinate (**19**), it is found that former two compounds are different from the first one as confirmed by PXRD, CHN and FTIR. In **17** a mononuclear synthon with one water molecule was formed to generate a zig-zag supramolecular assembly. Furthermore, it was observed that combination of Mn(II), 6,6′-Me_2bpta with adc (**20**) and fumarate (**21**) also have different architectures due to change in the linker. In FTIR, it was observed that **20** has a monodentate mode of carboxylate binding while **21** has a bidentate mode of binding with metal center. For **4** and **5**, which have combination of Ni(II), 6-Mebpta, with glutarate and 3-Me-glutarate, respectively, same type of assembly was formed, as confirmed by their PXRD analysis. They have similar characteristics like **2⊃fumarate** and **3⊃Hsuccinate** as discussed before in the same section.

Effect of metal center on the coordination architectures: As discussed above by changing the ancillary ligand, change in the supramolecular and coordination architecture was observed. Further to investigate the effect of change in the metal center having the same ligand and linkerfew more studies have been done.. Comparison of **17** and **22**, highlights the effect of change in metal center on the coordination architectures. It was observed that in compound **17,** a hexacoordinate Ni(II) complex which has a mononuclear synthon with one lattice water molecule resulted in the formation of a zig-zag type of supramolecular assembly. On the other hand, by using Zn(II) in **22** in the place of Ni(II), a spiral coordination polymer was formed in which Zn(II) is penta-coordinated and adc binds with the metal center in a monodentate fashion (Figure 3.58). By replacing Zn(II) with Cd(II), it was observed that Cd(II) shows resemblance with the Zn(II) complexes by comparing their PXRD and FTIR spectra.

3.1.2 Pyridyl-based ligands and tricarboxylate

In the previous section, we have discussed that the variation in the ligand, metal center and dicarboxylate results in the diversification of structural aesthetics of coordination architectures. In literature, there are many reports for Cd(II) and btc, but still there is lot of scope to explore in this field.[188–195] We also observed that the formation of either discrete units or polymers of low dimensionality took place. To break the monotony of getting discrete units, a dicarboxylate was changed by a tricarboxyle. Two coordination architectures of Cd(II) were sythesized under hydrothermal conditions with a ratio of Cd(II), 6-Mebpta and H_3btc 3:3:2 (Scheme 3.15).

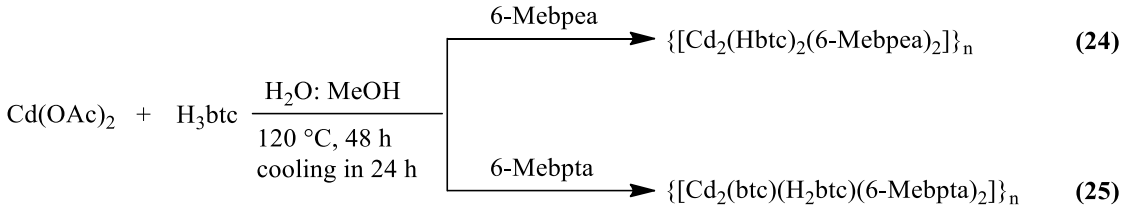

Scheme 3.15. Synthesis of **24** and **25**.

FTIR spectroscopic studies. In compound **24,** two different type of peaks are observed with respect to two different carboxylic acid groups. The difference in asymmetric (1575 cm^{-1}) and symmetric (1368 cm^{-1}) stretching frequencies is around 189 cm^{-1} reflecting a bidentate mode of carboxylate binding with a Cd(II) center. On the other hand, a peak around 1683 cm^{-1} indicates the presence of the free acid group. In case of compound **25,** three different types of peaks were observed primarily due to the presence of different binding modes of carboxylate groups with a Cd(II) center. The difference between asymmetric and symmetric stretching frequencies is 196 cm^{-1} and 209 cm^{-1} which further confirms the bidentate and monodentate mode of carboxylate binding.

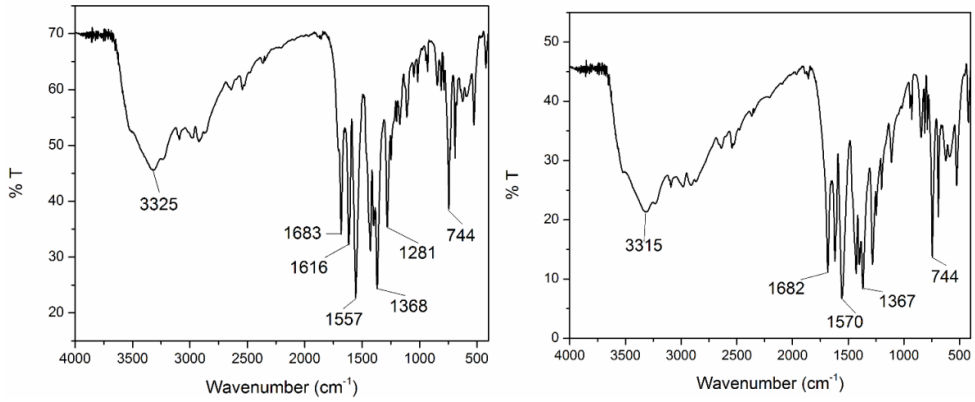

Figure 3.59. FTIR spectra for **24** and **25**.

Table 3.14. Asymmetric and symmetric stretching frequencies and binding mode of carboxylates in **24** and **25**.

Compound	Asymmetric (υ_1) cm^{-1}	Symmetric (υ_2) cm^{-1}	$\Delta\upsilon = \Delta\upsilon_1 - \Delta\upsilon_2$ cm^{-1}	Binding mode
24	1575	1368	189	Bidentate (chelated)
	1683		Free carboxylic acid	
25	1570	1367	196	Bidentate (chelated)
	1610	1401	209	Monodentate
	1682		Free carboxylic acid	

A peak around 1682 cm^{-1} stands for the free carboxylic acid group. FTIR spectra of both the synthesized compounds (**24** and **25**) are shown in Figure 3.59 and difference in the asymmetric and symmetric stretching frequencies are listed in the Table 3.14.

Thermogravimetric analysis. From the thermogravimetric analysis, it was confirmed that **24** is more stable than **25**. Both the compounds do not show any weight loss up to 150 °C which indicates the absence of lattice solvent molecules (Figure 3.60). The weight loss corresponds to ligand was observed between 150 °C to 300 °C followed by decomposition of the compound. TGA scans of **24** and **25**are shown in Figure 3.60.

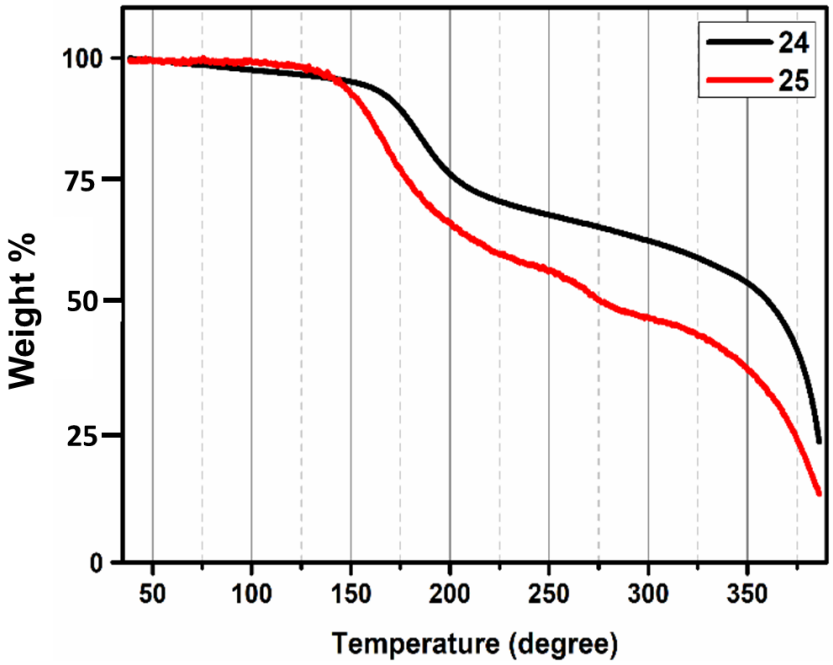

Figure 3.60. Thermogravimetric analysis of **24** and **25**.

Single crystal structure analysis. Crystals of **24** and **25**, suitable for the single crystal X-ray studies were grown by using the solvothermal method. In both the cases, colorless

crystals were obtained which were directly taken out from the mother liquor and used for the single crystal analysis.

Structural description of **24**. Compound **24** crystallizes in monoclinic $P2_1/c$ space group. The asymmetric unit of **24** consists of a Cd(II) center, one ligand and one linker (btc). In **24**, Cd(II) center which adopts a hepta-coordinated geometry in which it is surrounded by three nitrogens of the ligand (distances: Cd-N_{py}, 2.290(2) Å, 2.350(2) Å and Cd-N_{alkyl}, 2.420(2) Å) and four oxygens from two different carboxylates of two different H_3btc linkers (distances: 2.333(17) Å, 2.442(15) Å, 2.24(2) Å and 2.482(17) Å) to generate an N3O4 environment around Cd(II0 center. It is very interesting to notice that out of three carboxylic acid group of trimesic acid (H_3btc), two show the bidentate mode of binding with two Cd(II) centers, and the remaining one is present in a protonated form, which is not involved in any type of bonding with the metal center resulting on the formation of 1D coordination polymer (Figure 3.61). All the free carboxylates are situated on the same side of the 1D chain and ancillary ligand situated diagonally opposite to the free carboxylate. After packing in three dimensions, these one dimensional layers pack in such a manner that the free carboxylate group point towards another free carboxylate of another layer (Figure 3.62).

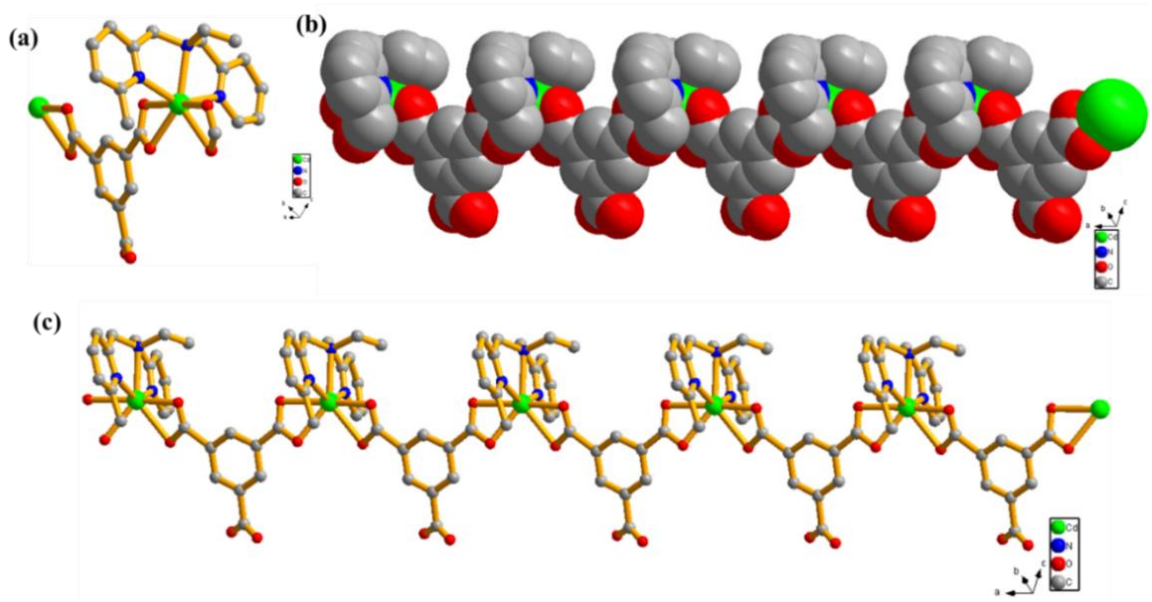

Figure 3.61. (a) Coordination environment around the Cd(II), (b) space-filling representation, and (c) 1D chain formed in **24**.

Furthermore, this linear chain is connected to another layer through interlayer hydrogen bonding between bonded carboxylate group and a carboxylic acid group of another layer,

and form a 1D ladder-shaped supramolecular assembly as shown in Figure 3.63. Due to this hydrogen bonding, by a combination of two half ladder chains two different types of motifs were generated, one is fourteen membered ($R_2^2(14)$) and the other is eighteen membered ($R_2^2(18)$). These two motifs include hydrogen bonding between carboxylic acid and carboxylate groups. All the bond angles and distances are listed in the Table A26 and A37 (Appendix). All the hydrogen bonding parameters are listed in the Table 3.15 which confirms the strength of H-bonding. Furthermore, packing of this compound (**24**) in different directions generate a 3D supramolecular assembly in which both the free carboxylic acids are pointed towards each other (Figure 3.62).

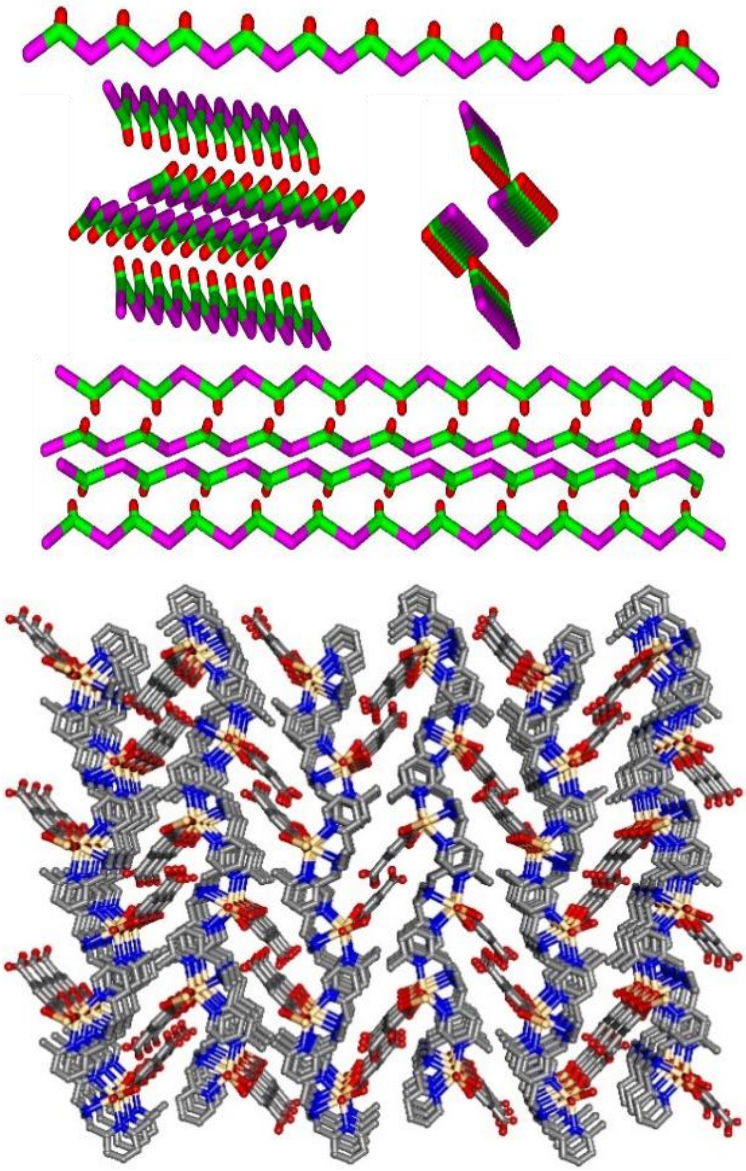

Figure 3.62. Topological view in three different directions and packing diagram of **24**.

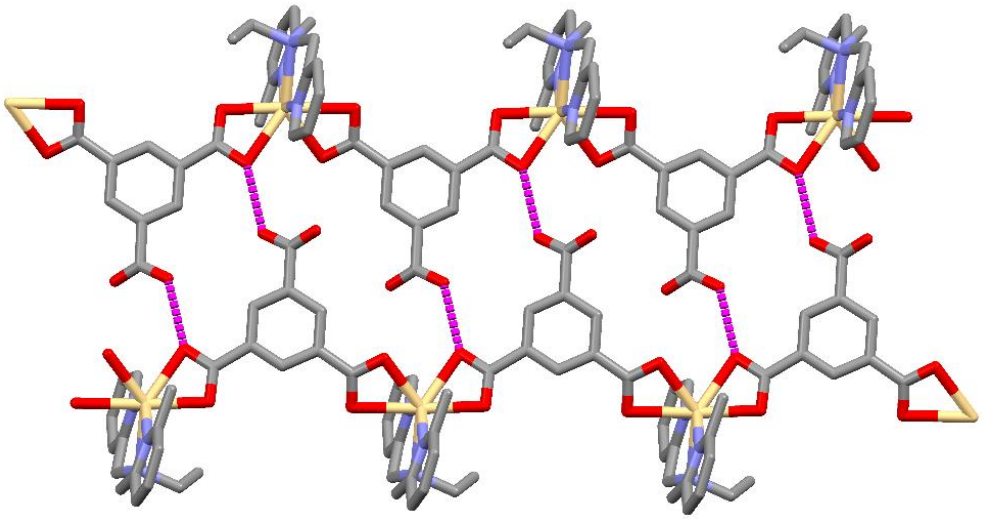

Figure 3.63. Formation of hydrogen bonding between two layers in **24**.

Table 3.15. Hydrogen bonding parameters in **24**.

D---H···A (Å)	r(D-H) (Å)	r(H···A) (Å)	r(D···A) (Å)	∠D-H···A (deg)	Symmetry
C14 –H14...O3	0.93	2.58	3.30	135	1-x,1/2+y,1/2-z
C23 –H23...O5	0.93	2.45	3.30	153	2-x,1-y,1-z

Structural description of **25**. Compound **25** crystallizes in an orthorhombic *Pn*a2_1 space group. In the asymmetric unit, two types of Cd(II) centers are present with two ligands (6-Mebpta) and two linkers (H_3btc). Out of these two linkers, one has all three carboxylic group in deprotonated form and binds with a metal center, while another one has only one carboxylic group in deprotonated form and connected with a metal center. On the other hand, remaining two are in a protonated carboxylic acid do not participate in any type of covalent bonding. One of the Cd(II) centers adopts a distorted octahedral geometry while another one adopts a pentacoordinated geometry to generate a N3O3 and N3O2 type of surrounding respectively around metal center. Considering the Cd1, which is surrounded by three nitrogens of the ligand (distances: Cd-N_{py}, 2.363(10) Å, 2.355(9)Å and Cd-N_{alkyl}, 2.458(9) Å), two oxygens from the bidentate carboxylate group (distances: 2.374(7) Å and 2.373(7) Å) and one oxygen atom from carboxylate of another H_2btc, which show monodentate binding with Cd(II) center having distance 2.260(9) Å. All the bond angles and distances are listed in Table A26 and A37 (Appendix).

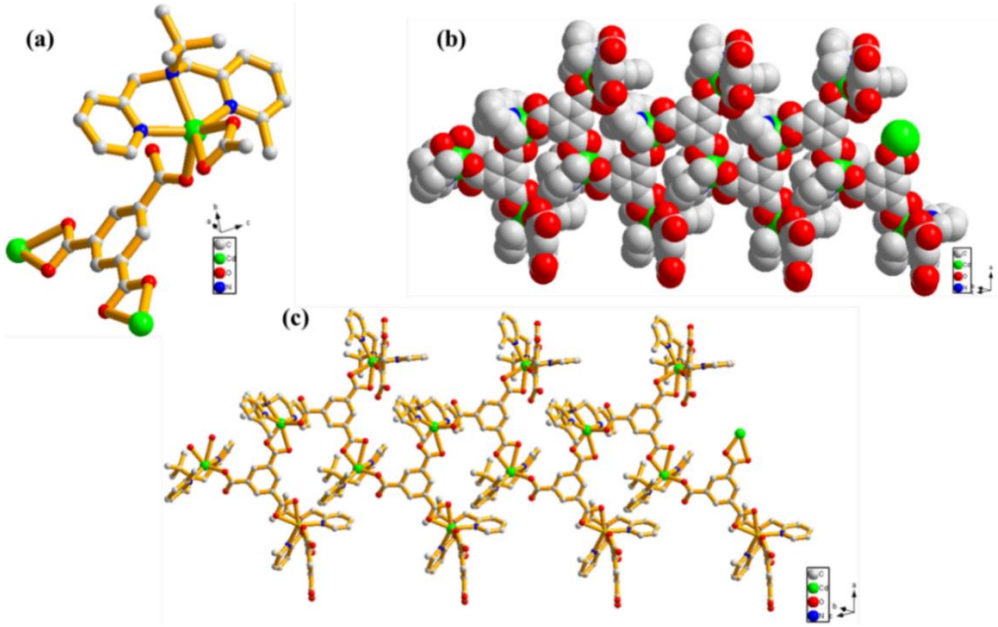

Figure 3.64. (a) Coordination environment around the Cd(II) center, (b) space fill representation and (c) 1D spiral chain formed by **25**.

The Cd2 has pentacoordinated geometry surrounded by three nitrogens of the ligand (distances: Cd-N_{Py}, 2.298(10) Å, 2.303(10) Å and Cd-N_{alkyl}, 2.506(8) Å) and two oxygen atoms from the bidentate carboxylate group of btc (distances 2.231(8) Å and 2.229(8) Å). Both the linkers (1,3,5-benzene tricarboxylate) present in the asymmetric unit are different from each other w.r.t the bonding with the metal center as well as deprotonation of carboxylic groups. One linker has all three carboxylic groups in a deprotonated form, bonded with the Cd(II) (one bidentate and two monodentate), while the other linker exhibits one deprotonated carboxylic acid group having a monodentate binding mode with the metal center and the remaining two groups are present in free carboxylic acid form (Figure 3.64). A 1D coordination polymer with helical chain is formed after expansion of the asymmetric unit. Packing of compound **25** in different directions forms a 3D network in which two 1D layers are located perpendicular to each other (Figure 3.65).

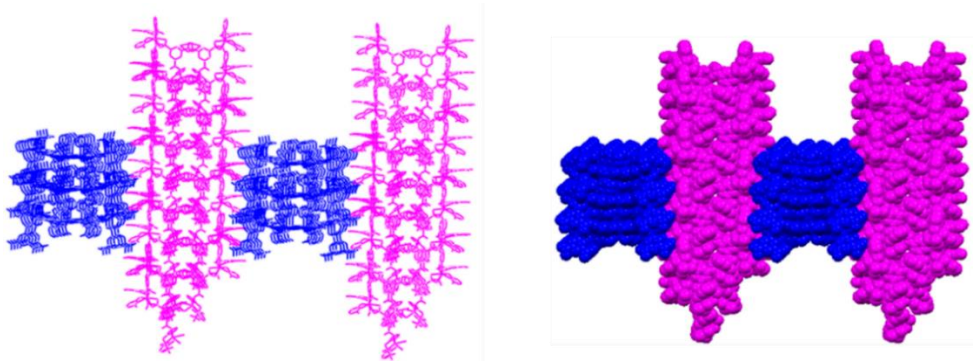

Figure 3.65. Perpendicular packing of different 1D layers in **25**.

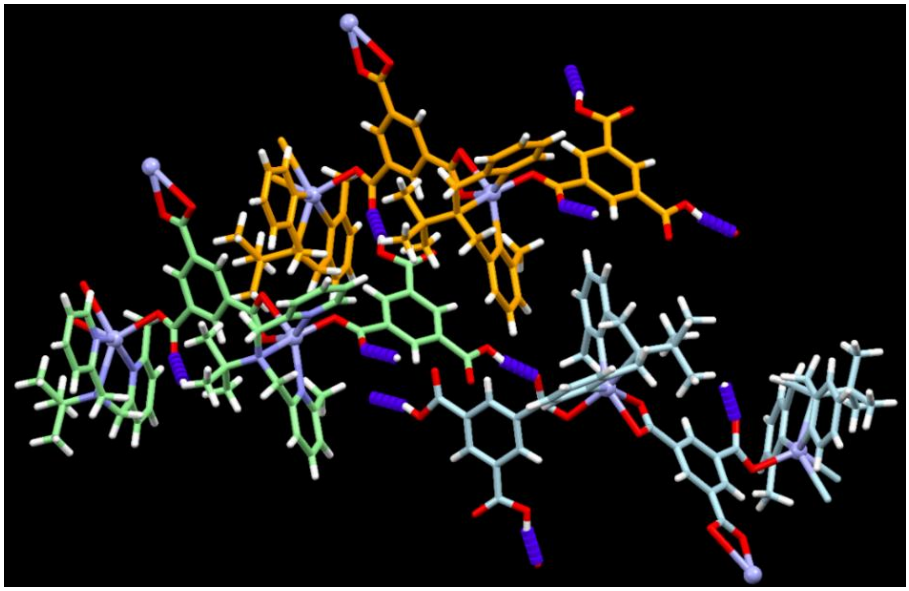

Figure 3.66. Formation of hydrogen bonding to generate 3D supramolecular assembly in **25**.

This 1D coordination polymer connects further with the other layers through hydrogen bonding to generate a 3D supramolecular assembly. These two layers are connected with each other through strong hydrogen bonding between carboxylic acid and carboxylate groups.

Table 3.16. Hydrogen bonding parameters in **25**.

D---H…A (Å)	r(D-H) (Å)	r(H…A) (Å)	r(D…A) (Å)	∠D-H…A (deg)	Symmetry
C1 -H1...O15	0.93	2.42	3.0129	122	1/2-x,-1/2+y,1/2+z
C3 -H3...O15	0.93	2.59	3.1908	123	x,-1+y,z
C12 -H12...O10	0.93	2.49	3.3504	154	x,-1+y,1+z
C16 -H16A...O14	0.96	2.52	3.4287	157	1/2-x,-1/2+y,1/2+z
C21 -H21B...O11	0.97	2.24	3.1964	169	x,-1+y,-1+z
C28 -H28A...O11	0.96	2.56	3.491	163	x,-1+y,-1+z
C29 -H29C...O4	0.96	2.52	3.4538	166	-
C30 -H30C...O3	0.96	2.5	3.423	161	-
C33 -H33A...O3	0.96	2.53	3.4374	158	-
C36 -H36...O13	0.93	2.6	3.3369	137	-x,3-y,-1/2+z
C38 -H38...O13	0.93	2.33	2.6706	101	-
C41 -H41...O8	0.93	2.39	2.7137	100	-
C43 -H43...O4	0.93	2.52	2.835	100	-
C72 -H72...O11	0.93	2.48	3.409	173	x,-1+y,z
C73 -H73...O1	0.93	2.39	2.7163	100	-
C73 -H73...O14	0.93	2.43	2.7472	100	-

As shown in the Figure 3.66, the free oxygen of the carboxylate group shows monodentate mode of binding and forms a hydrogen bonding with the hydrogen of the carboxylic acid group of H_2btc. Both the carboxylic acid group and free oxygen of the carboxylate group (bonded with metal in monodentate fashion) of H_2btc are involved in hydrogen bonding. On the other hand, only the free oxygen of the carboxylate (bonded with metal in monodentate fashion) of another btc participates in the H-bonding as shown in the Figure 3.66. All the hydrogen bonding parameters are listed in the Table 3.16.**Powder X-ray diffraction studies**. Crystalline nature of both **24** and **25** was confirmed by powder X-ray diffraction studies. To confirm whether the single crystal structure corresponds to the bulk material or not, powder X-ray diffraction patterns were recorded for both the compounds **24** and **25** at room temperature. It was observed that the experimental and simulated (from the SCXRD data) patterns are similar to each other, although some change in the intensity of the peaks was observed (Figure 3.67). The PXRD patterns obtained confirmed that the single crystal and bulk material properties are in good agreement with each other which confirms the phase purity of the bulk sample.

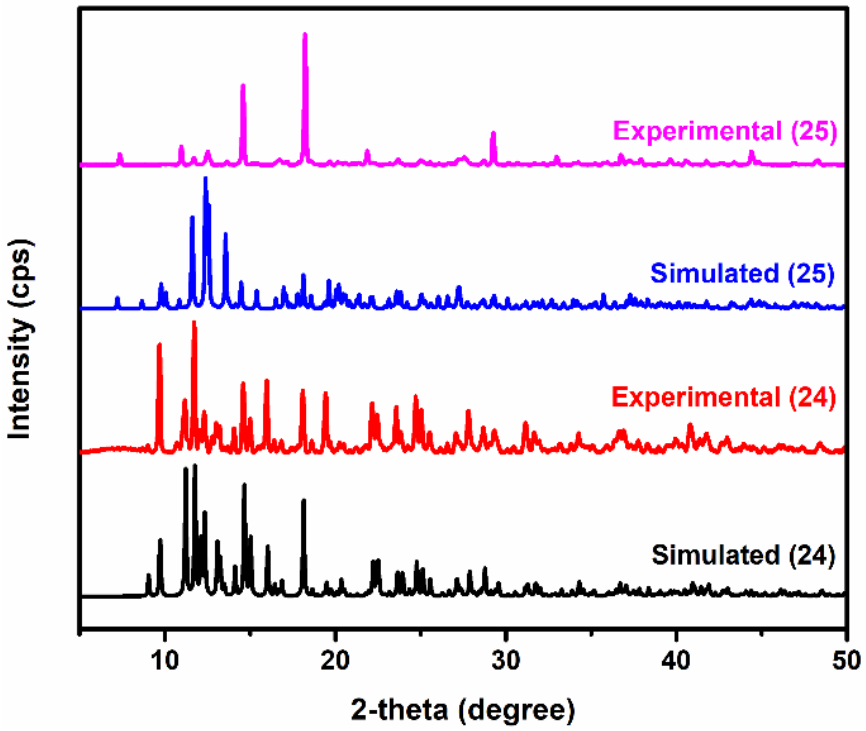

Figure 3.67. PXRD patterns of **24** and **25**.

In the previous section (**3.1.1)**, we have discussed that by using dicarboxylates as linkers, discrete molecules or supramolecular architecture having di/tri-nuclear synthon with lattice solvent molecules have been formed. After using tricarboxylates, a change in the

dimensionality and coordination architecture was observed. In case of tricarboxylates, the formation of coordination polymers was preferred over discrete molecules. Both the compounds synthesized by using tricarboxylate are 1D coordination polymers having no lattice solvent molecules. Along with this, different modes of carboxylate binding have been observed in the coordination architectures which were synthesized by using tricarboxylic acid as the linker.

Effect of ancillary ligand on the structure of 24 and 25. Both the compounds (**24** and **25**) were synthesized by using the same synthetic method. In **24**, 6-Mebpea was used as an ancillary ligand, while in **25**, 6-Mebpta was used as an ancillary ligand. In **24**, formation of a a 1D zig-zag type coordination polymer is obderved where Cd(II) metal center is heptacoordinated. On the other hand, 1D spiral type coordination polymer is formed in **25** in which Cd(II) metal center is hexacoordinated (Figure 3.68).

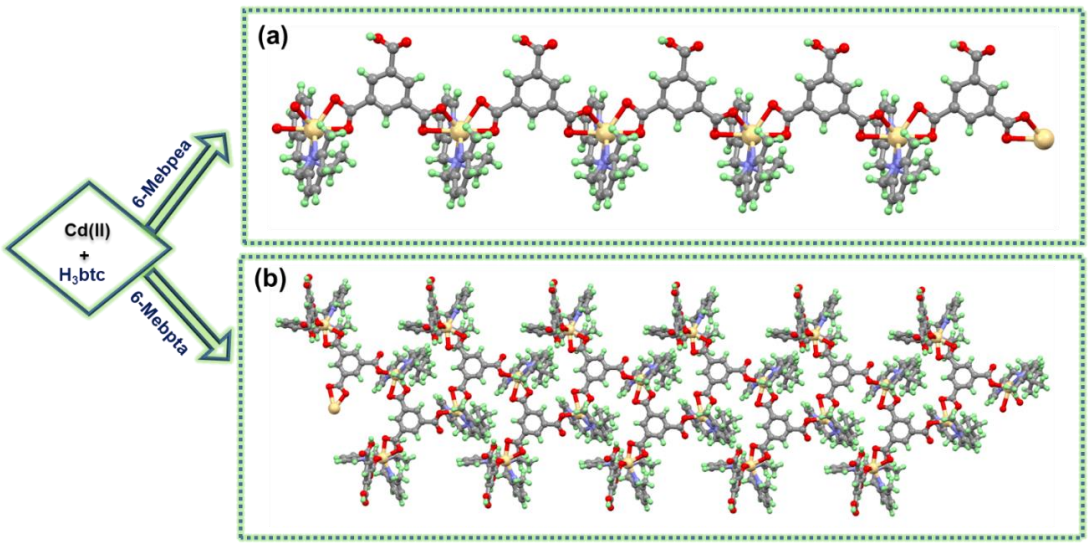

Figure 3.68. Diversification in coordination architectures due to change in the ligand (a) coordination architecture formed in **24** and (b) coordination architecture formed in **25**.

In compound **24**, two 1D layers (half ladder) are connected to each other through strong hydrogen bonding generating a 1D ladder-shaped supramolecular assembly while in compound **25**, a 1D coordination architecture having a spiral chain was formed in which variations in the binding of carboxylates were observed. Although there is no solvent molecule present in **24** and **25**, these complexes form a 3D supramolecular assembly by interlayer H-bonding between carboxylic acid and carboxylates groups present.

3.1.3 Functionalized-Pyridyl ligands and dicarboxylates

With the new functionalized pyridyl-based tridentate ligands, the main purpose was to synthesize coordination networks for target based applications like catalysis and guest encapsulation. In this section, we have used two tridentate ligands 2,2'-terpyBA and 4,4'-terpyBA having free acetylene group tosynthesize various architectures with different transition metals and rigid dicarboxylates (H_2bdc and NH_2bdc). The NH_2bdc provides an extra functionality (primary amine) to the architecture which enhances the guest encapsulation properties through interaction with incoming guest species via hydrogen bonding. Most of the compounds have been synthesized under ambient conditions using a mixture of DMF, water and ethanol in a 1:1:1 ratio.

Chemistry with 2,2'-terpyBA

Using 2,2'-terpyBA, five compounds (**26-30**) containing H_2bdc and six compounds (**31-36**) containing NH_2bdc have been synthesized (Schemes 3.16 and 3.17).

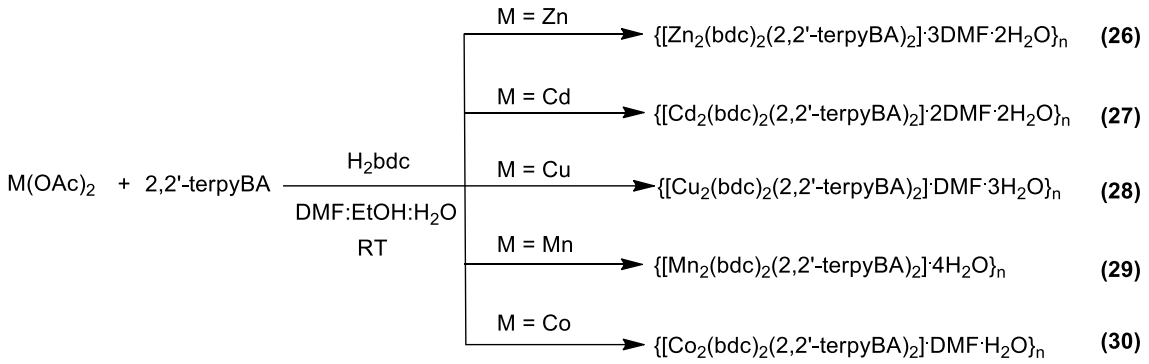

Scheme 3.16. Synthesis of **26-30**.

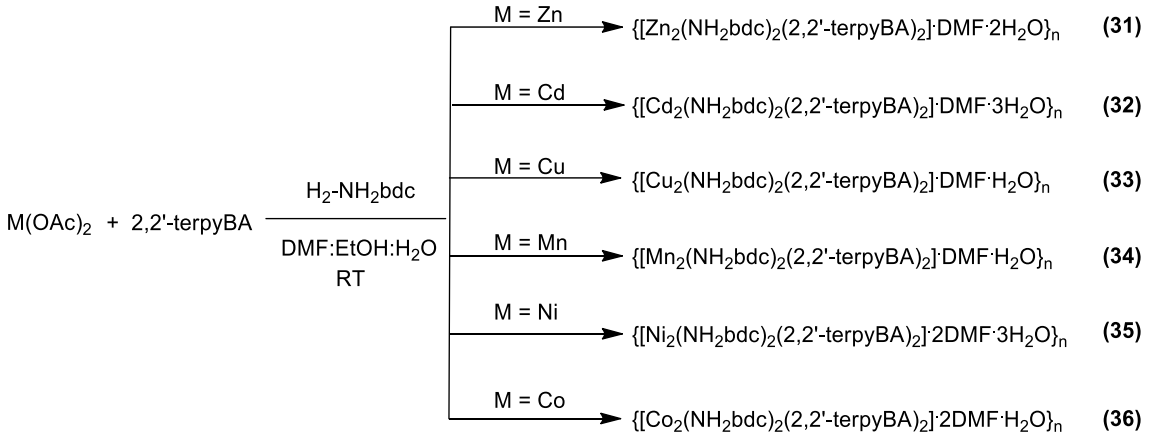

Scheme 3.17. Synthesis of **31-36**.

FTIR spectroscopic studies. For the synthesis of these compounds, the ligand was used in which terminal acetylene functionality was introduced and this functionality shows a characteristic peak around 2118-2120 cm^{-1}. Apart from this, primary amine shows two peaks around 3300 cm^{-1} and 3200 cm^{-1}. Furthermore, binding of carboxylates were determined by calculating the difference between asymmetric and symmetric stretching frequencies. Presence of lattice solvents is also confirmed by this technique; for example, peaks around 3400 cm^{-1} and 3200 cm^{-1} corresponds to the -OH stretching from the water and peak at 1664 cm^{-1} corresponds to the DMF molecules. FTIR comparison of these five compounds (**26-30**) reveals the monodentate mode of carboxylate binding with the central metal atom (Figure 3.69). The difference between the asymmetric and symmetric stretching frequencies falls in the range of 220 cm^{-1} to 245 cm^{-1}, confirming the monodentate mode of carboxylate binding with metal center. Except for compound **29**, remaining four compounds **26-28** and **30** exhibiting a peak around 1664 cm^{-1} shows the presence of DMF solvent molecules in the porous networks (Figure 3.69).

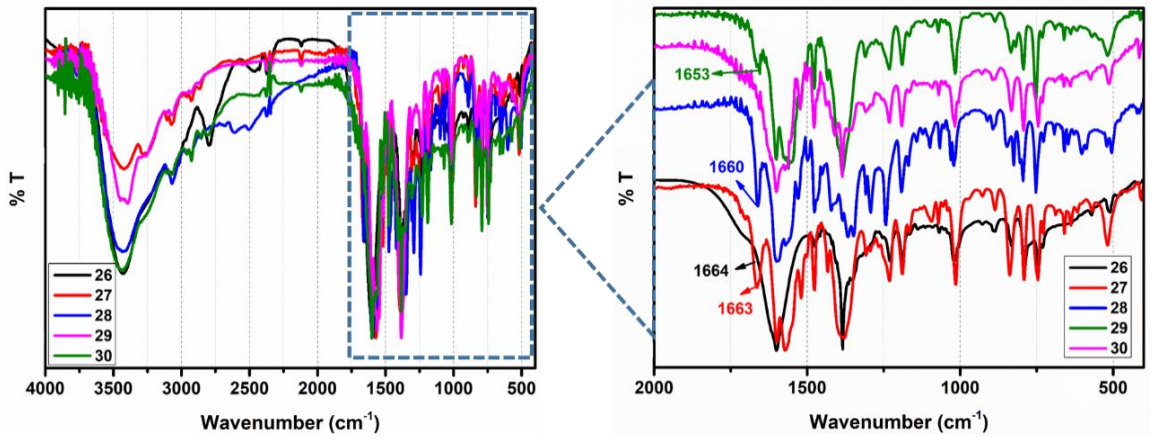

Figure 3.69. FTIR spectra of **26-30**.

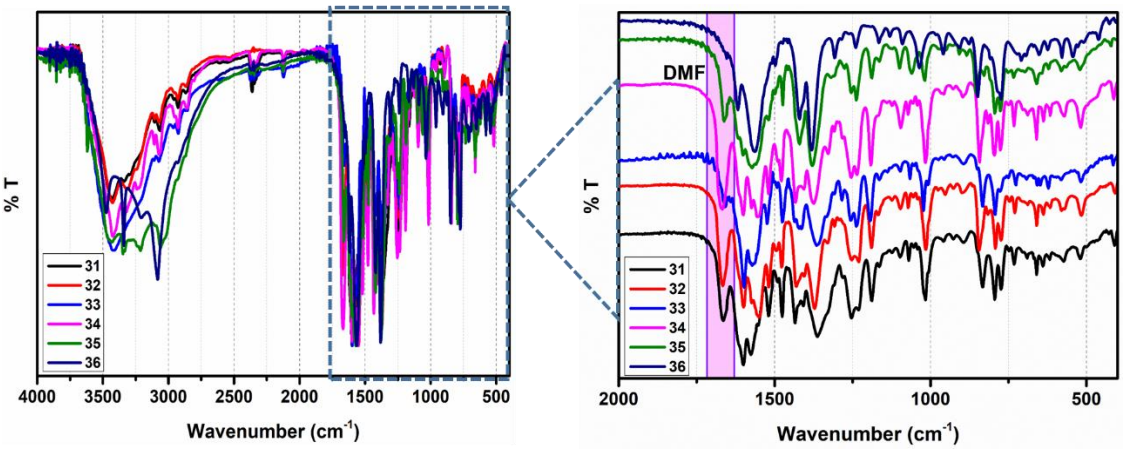

Figure 3.70. FTIR spectra of **31-36**.

Compounds **31-36** are similar type of compounds with different metals having 2,2'-terpyBA ligand with NH_2bdc used in the place of H_2bdc. All these compounds show two broad peaks in the region of 3400cm^{-1}-3200 cm^{-1} confirming the presence of a primary amine group. All other features of ligand obtained in FTIR spectrum were same as found in previous compounds of this section. All these compounds have DMF in the lattice space confirmed by FTIR analysis (Figure 3.70). All the binding mode are summarised in Table 3.17.

Table 3.17. Asymmetric and symmetric stretching frequencies and their respective binding modes of carboxylates of **26-36**.

Compound	Asymmetric (υ_1) cm^{-1}	Symmetric (υ_2) cm^{-1}	$\Delta\upsilon = \upsilon_1 - \upsilon_2$ cm^{-1}	Binding mode
26	1599	1356	243	Monodentate
27	1598	1378	220	Monodentate
28	1599	1366	233	Monodentate
29	1600	1384	216	Monodentate
30	1600	1381	219	Monodentate
31	1600	1362	238	Monodentate
32	1599	1430	169	Bidentate (chelated)
33	1598	1360	238	Monodentate
34	1600	1433	167	Bidentate (chelated)
35	1603	1420	183	Bidentate (chelated)
36	1563	1381	182	Bidentate (chelated)

Thermogravimetric analyses. It was found that a loss of lattice solvents like DMF and water has taken place up to 200 °C, followed by the decomposition of the metal complex. In all the complexes an unusual behavior was observed after 300 °C, which may be due to the removal of CO_2 molecules. Compound **26** exhibits a loss of 17.71% corresponding to the loss of three DMF and two lattice water molecules (ca. 16.26%), while, compound **27** exhibits a first weight loss of 12.46% corresponding to the loss of two DMF and two lattice water molecules (ca.11.83%). Compound **28** exhibits a loss of 9.70% corresponding to loss of one DMF and three lattice water molecules (ca.10.52%), while in case of **29**, first weight loss is around 2.99% corresponding to the loss of only two water molecules (ca. 2.72%).

In case of compound **30**, a loss of 7.19% corresponds to the loss of one DMF and one water molecule up to 200 °C followed by the decomposition of the complex. Compound **31** exhibits a weight loss of 8.23% up to 200 °C corresponding to loss of one DMF and two

lattice water molecules (ca. 8.49%), while, compound **32** exhibits a weight loss of 8.84% which corresponds to the loss of one DMF and three lattice water molecules (ca. 9.31%). Compound **33** exhibits the first weight loss of about 6.98% corresponding to the loss of one DMF and one lattice water molecule (ca. 9.71%), while compound **34** shows a loss of 20.99% corresponding to the loss of one DMF, one water and four CO_2 molecules (ca. 19.00%). After the loss of these solvent molecules, decomposition of the framework takes place. In case of compound **35** and **36**, first weight loss of 14.27% and 11.99% respectively, corresponds to the loss of two DMF and three water molecules in case of **35** (ca. 15.04%), while the loss of two DMF and one water molecule in case of **36** (ca. 12.39%). All the TGA scans have been shown in the Figure 3.71.

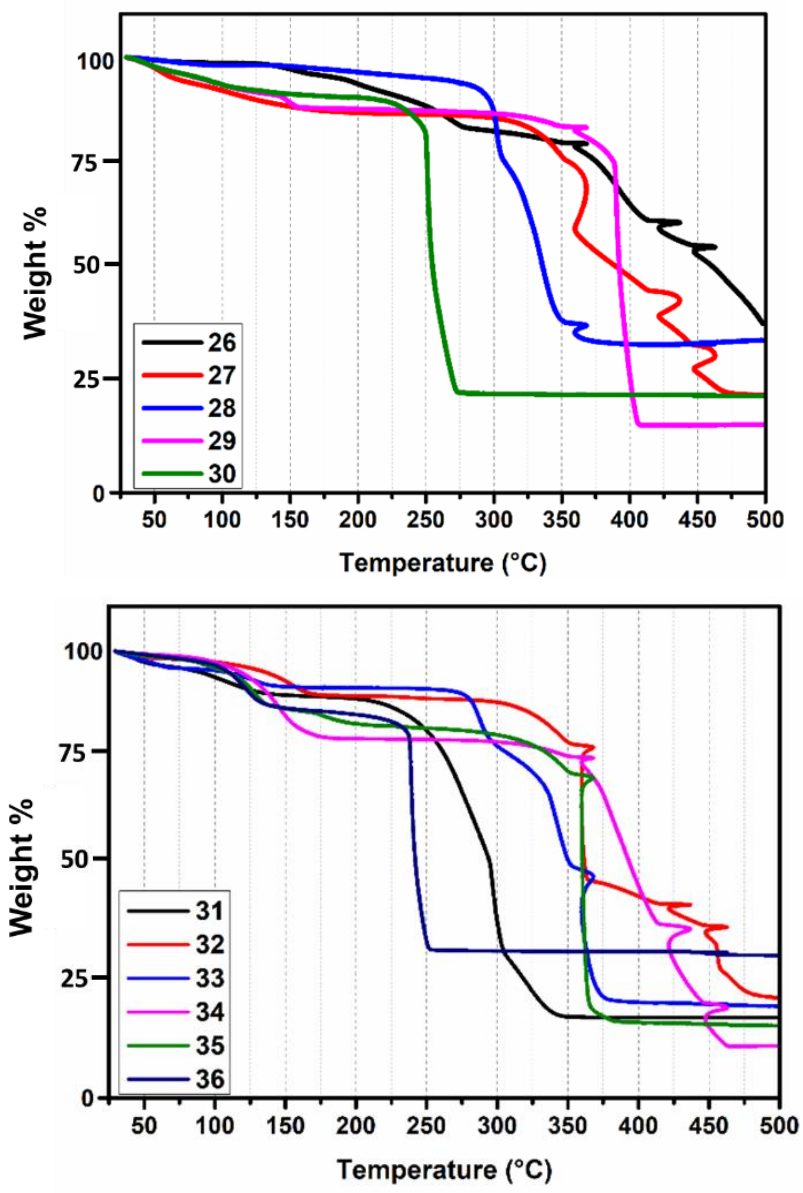

Figure 3.71. TGA scans of **26-36**.

Single crystal structure analyses. Crystals of compounds **33** and **34** were grown by the layering method. A 1:1 ethanol and water solution of metal salt was layered over the DMF solution of the ligand having a buffer solution of water and ethanol (1:2) between two layers. The crystals were directly taken out from the layering tube and used for single crystal diffraction analysis.

Structural description of **33**. Compound **33** crystallizes in the triclinic *P*-1 space group. The asymmetric unit consists of two ligands (2,2'-terpyBA), two linkers (NH_2bdc) and a two Cu(II) metal centers . Along with this, two lattice water molecules are also present in the asymmetric unit. The central metal is surrounded by three nitrogens of the ligand (distances: Cu-N_{py}, 1.831(10) Å, 1.942(11) Å and 1.890(7) Å) and two oxygens from two different 2-aminoterephthalate (distances: 1.872(9) Å and 2.015(10) Å) to form a pentacoordinated environment with N3O2 type surrounding as shown in Figure 3.72a. Both the metal centers have the same type of coordination environment although both are different from each other with only slight changes in the distance between the metal and donor atoms. All the distances and angles are listed in Table A27 and A38 (Appendix). After expanding the asymmetric unit, a zig-zag type of 1D coordination polymer is formed which have free acetylene moieties hanging in both the direction (Figure 3.72c). The other functionality present in the system is the primary amine group from the NH_2bdc counterpart. The arrangement of two different linkers to the metal center is such that the two NH_2 groups from different linkers face towards each other near the metal center (Figure 3.72c).

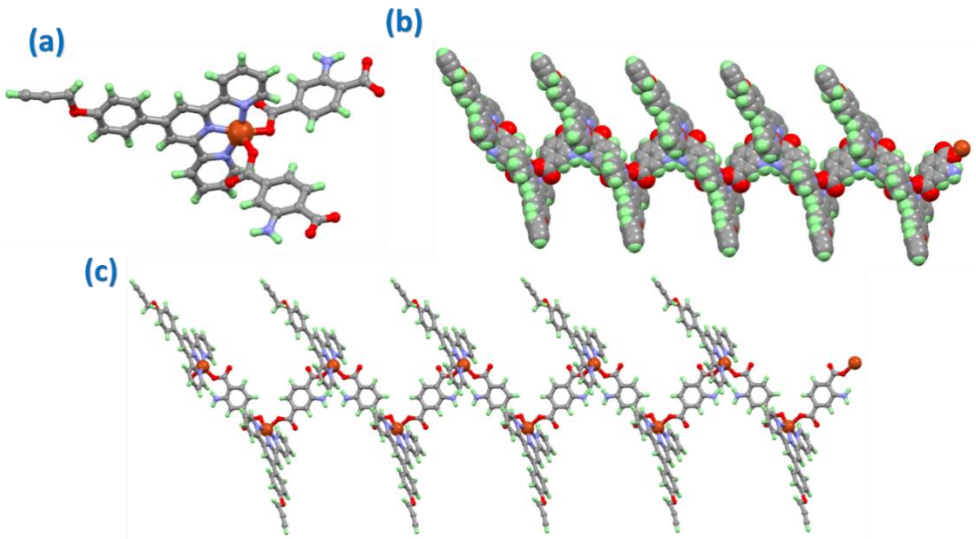

Figure 3.72. (a) Coordination environment around Cu(II), (b) space fill representation and (c) ball and stick model forming 1D zig-zag chain in **33**.

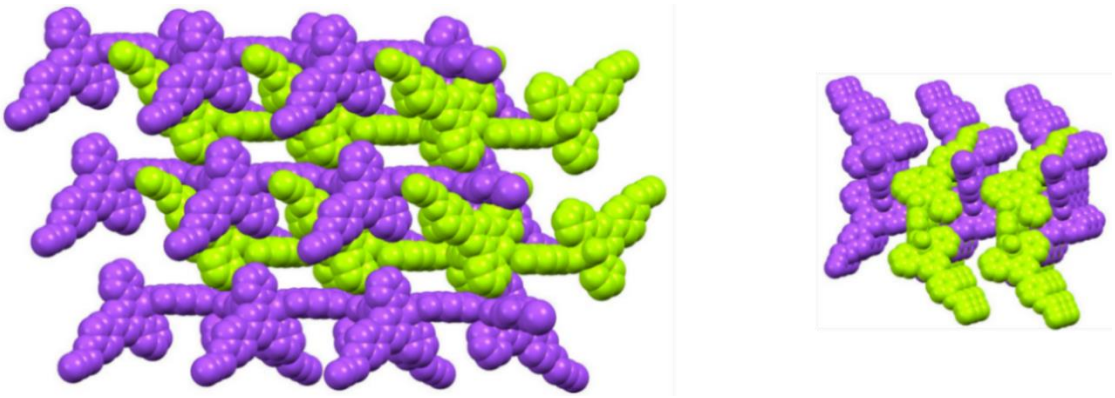

Figure 3.73. Packing of different 1D zig-zag chains of **33** in two different directions.

By the overall packing of this molecule in three dimensions, a 3D supramolecular assembly has been formed (Figure 3.73). In the formation of this 3D supramolecular assembly, weak interactions like π–π stacking, hydrogen bonding and van der Waals interactions play a very important role. Hydrogen bonding is present between lattice water and NH_2 groups in this compound which does not play any role in extending the dimensionality of the structure.

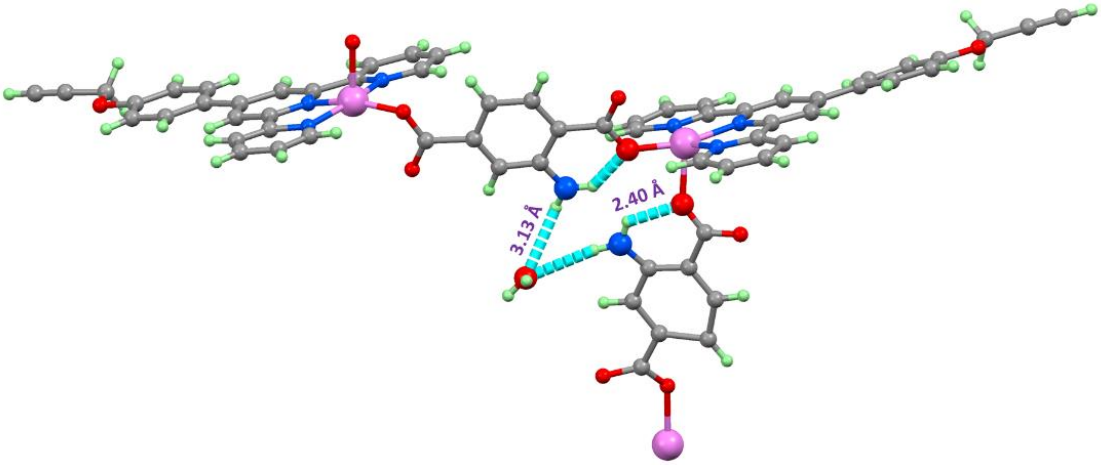

Figure 3.74. Hydrogen bonding formation between lattice water and 1D chain in **33**.

As shown in Figure 3.75, there are two lattice water molecules present which show strong hydrogen bonding with the same 1D layer. One water molecule formed hydrogen bonding with the uncoordinated oxygen of the carboxylate using one hydrogen, while the second hydrogen of these water molecule does not show any type of bonding with any other molecule or atom while other water molecules show hydrogen bonding with two primary amine groups of NH_2bdc (see Figure 3.74).

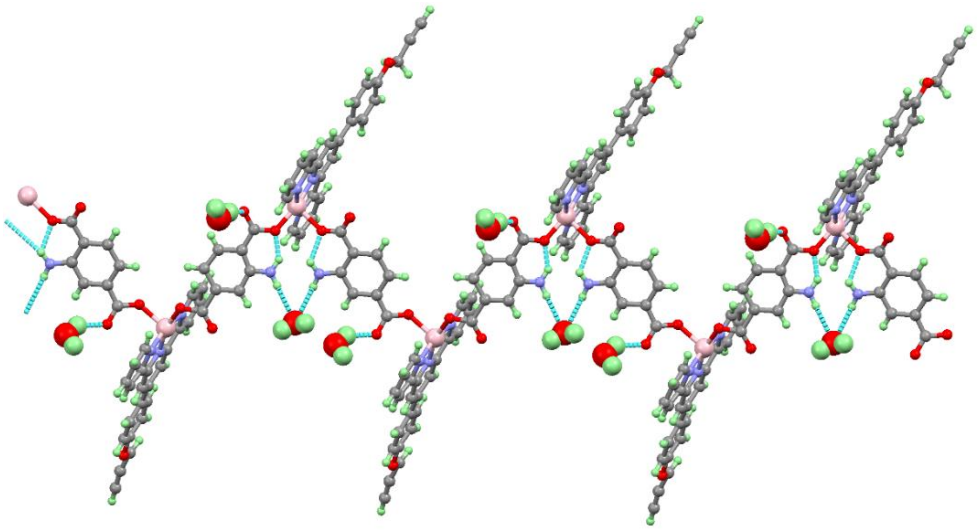

Figure 3.75. Hydrogen bonding formation between lattice water and 1D chain in **33**.

Both the amine functionalities point towards each other because both primary amines are involved in the formation of strong hydrogen bonding with lattice water molecule from one side as well as with the coordinated oxygen of carboxylate from another side. These two amines, one water molecule and two coordinated oxygens from different carboxylates form a six-member ($R_3^2(6)$) motif. Due to the presence of this type of hydrogen bonding with the primary amines, peaks corresponding to primary amines are strangle altered in which a single peak for the primary amine is observed in the FTIR spectrum. As shown in the FTIR spectrum of this compound, there are no primary amine peaks in the range of 3200 cm^{-1} and 3400 cm^{-1} depicting the presence of strong hydrogen bonding.

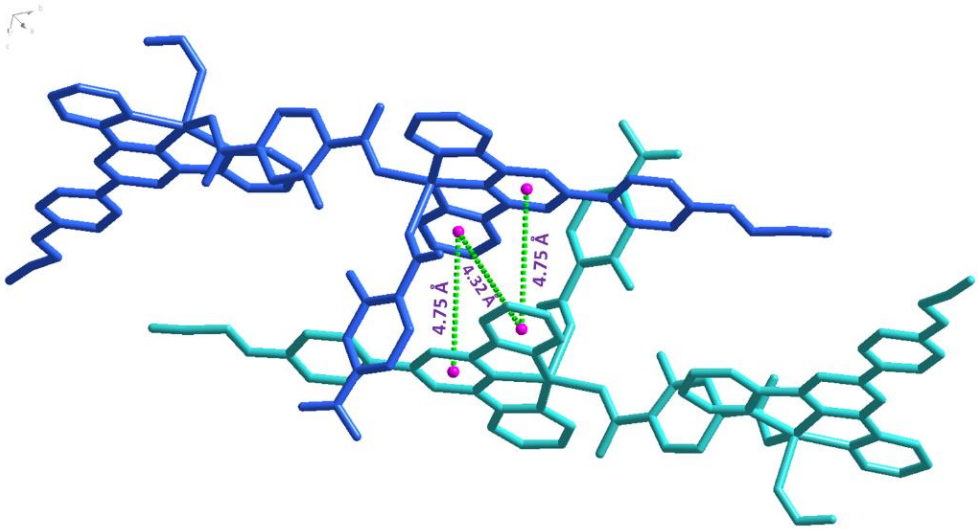

Figure 3.76. Depiction of π–π (edge to centroid) stacking between pyridine moieties in **33**.

Along with the hydrogen bonding, π–π interactions are also present in **33**.. It was observed that a strong π–π interaction is present between pyridine moieties of two different layers which are the driving force to combine two layers and generate a 3D supramolecular assembly as shown in the Figure 3.76. A pyridine ring (peripheral) of one layer is connected to the metal center showing π–π interaction with two pyridine rings of another layer; one is a central ring (distance: 4.75Å) and the second is peripheral pyridine ring having a distance of 4.32 Å (Figure 3.76). All the hydrogen bonding parameters are listed in Table 3.18.

Table 3.18. Hydrogen bonding parameters in **33**.

D---H…A (Å)	r(D-H) (Å)	r(H…A) (Å)	r(D…A) (Å)	∠D-H…A (deg)	Symmetry
O11 -H11A...O12	0.85	2.12	2.7349	129	x,-1+y,z
O12 -H7AA...O11	0.85	2.2	2.7349	121	x,1+y,z
O12 -H8AA...O8	0.85	1.89	2.6742	152	1-x,2-y,-z
N4 -H3BA...O1	0.86	1.73	2.4324	137	.
N4 -H3BA...N5	0.86	2.33	2.6835	105	.
N4 -H4BA...O11	0.86	2.29	3.0975	157	1-x,1-y,-z
N5 -H5BA...O10	0.86	1.91	2.4947	124	.
N5 -H5BA...N4	0.86	2.29	2.6835	108	.
N5 -H6BA...O11	0.86	2.45	3.1389	138	1-x,1-y,-z
O13 -H9BA...O2	0.85	2.31	3.121	160	-1+x,y,z
C21 -HC...O3	0.93	2.41	3.3228	168	x,-1+y,z
C9 -HJ...O3	0.93	2.2	3.0719	156	x,-1+y,z
C1 -HP...O1	0.93	2.55	3.0453	113	.
C41 -HQ …O2	0.93	2.32	3.1804	154	x,1+y,z
C44 -HS...O2	0.93	2.46	3.2651	146	x,1+y,z
C36 -HT...O7	0.93	2.41	3.1747	139	1-x,2-y,-z
C35 -HU...O8	0.93	2.48	3.1575	130	1-x,2-y,-z
C53 -HZ...O2	0.93	2.52	3.3879	155	x,1+y,z
C14 -H1AA...O10	0.93	2.45	3.3628	167	2-x,1-y,-z
C12 -H3AA...O3	0.93	2.27	3.1093	150	x,-1+y,z
C24 -H4AA...O9	0.93	2.05	2.9707	170	1-x,1-y,-z
C3 -H5AA...O9	0.93	2.59	3.425	149	1-x,1-y,-z
C56 -H7BA...O12	0.93	2.4	3.1444	137	x,1+y,z
C56 -H7BA...O8	0.93	2.54	3.4033	155	1-x,3-y,-z

Structural description of **34**. Compound **34** crystallizes in the monoclinic $C2_1/c$ space group. The metal center is heptacoordinated and forms an N3O4 type of surrounding. The asymmetric unit consists of a Mn(II) center, a ligand, and a linker. Mn(II) is surrounded by three nitrogen atoms from the ligand (distances: Mn-N_{py}, 2.193(7) Å, 2.193(7) Å, and

2.209(5) Å) and four oxygen atoms from two different linkers (2-aminoterephthalate) with distances: 2.240(5) Å, 2.240(5) Å, 2.209(5) Å and 2.209(5) Å). Overall, by expanding the asymmetric unit, a 1D coordination architecture is formed in a zig-zag fashion as shown in Figure 3.77. It contains two functional groups -NH_2 and acetylene group which are free to interact with the guest molecules. Two -NH_2 groups are far away from each other, and hence there is no interaction between them. Along with this, there is a lattice water molecule which forms hydrogen bonding with the primary amine. The overall packing of the molecule generates a 3D supramolecular assembly due to the presence of weak interactions like π–π stacking, Hydrogen bonding, and van der Waals interactions. Presence of these interactions helps in the formation of a 3D supramolecular assembly with stacked and fused layers as shown in the Figure 3.78.

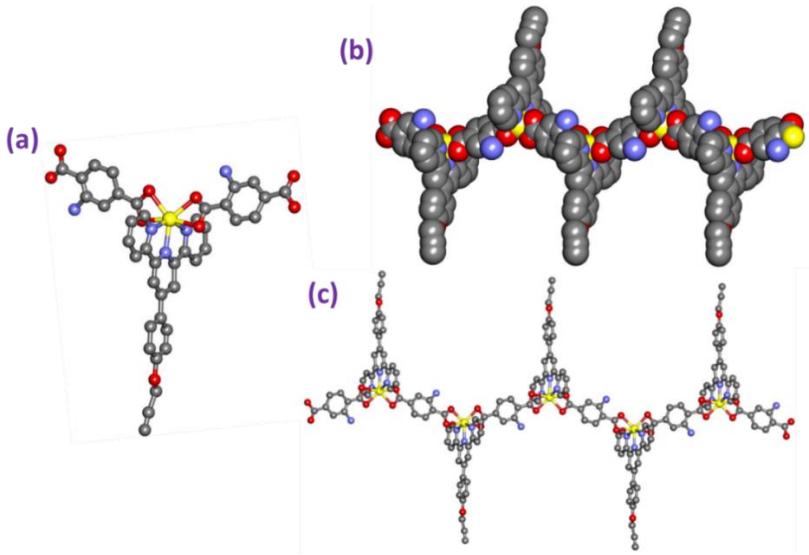

Figure 3.77. (a) Coordination environment around the metal center, (b) space fill representation, and (c) formation of 1D coordination polymer in **34**.

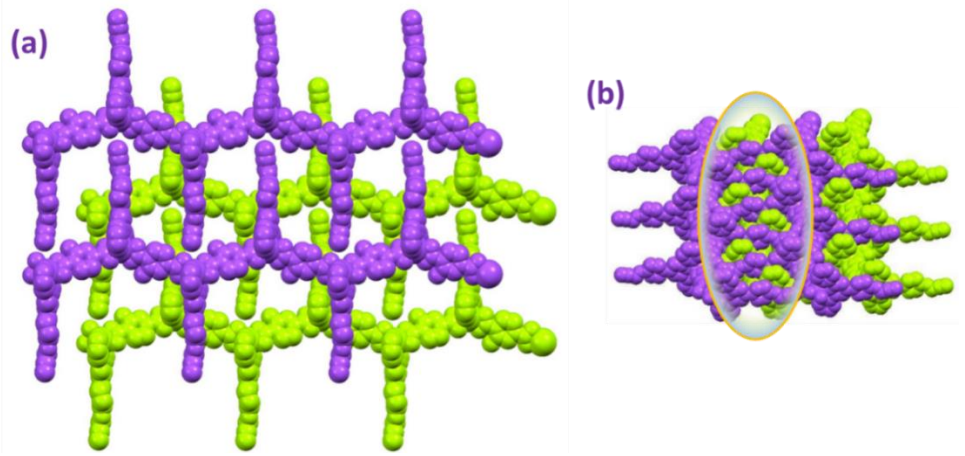

Figure 3.78. Packing of **34** in two different directions (a) view along a direction, and (b) view along c direction.

All the acetylene moieties are situated only in two directions to generate the functionalized surface. Packing of layers is such that the acetylene moieties are close to the metal center of another layer. There is one lattice water molecule present which shows strong hydrogen bonding between the hydrogen of the amine group while another hydrogen of the amine group forms hydrogen bonding with the carboxylate oxygen which shows the chelated mode of binding with the metal center (Figure 3.79).

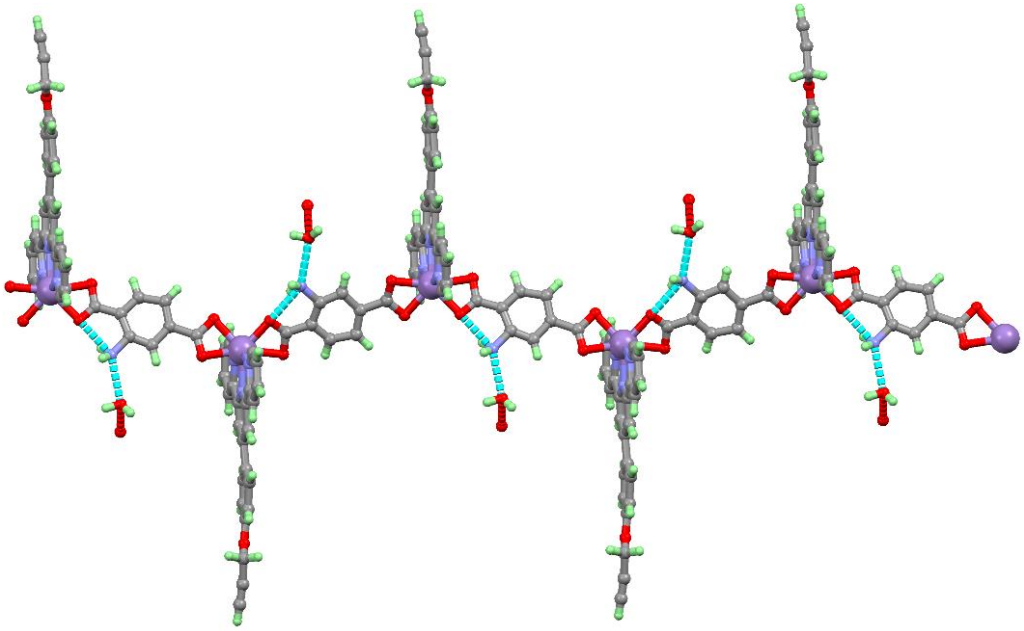

Figure 3.79. Formation of hydrogen bonding between lattice water, amine and coordinated carboxylate oxygen in **34**.

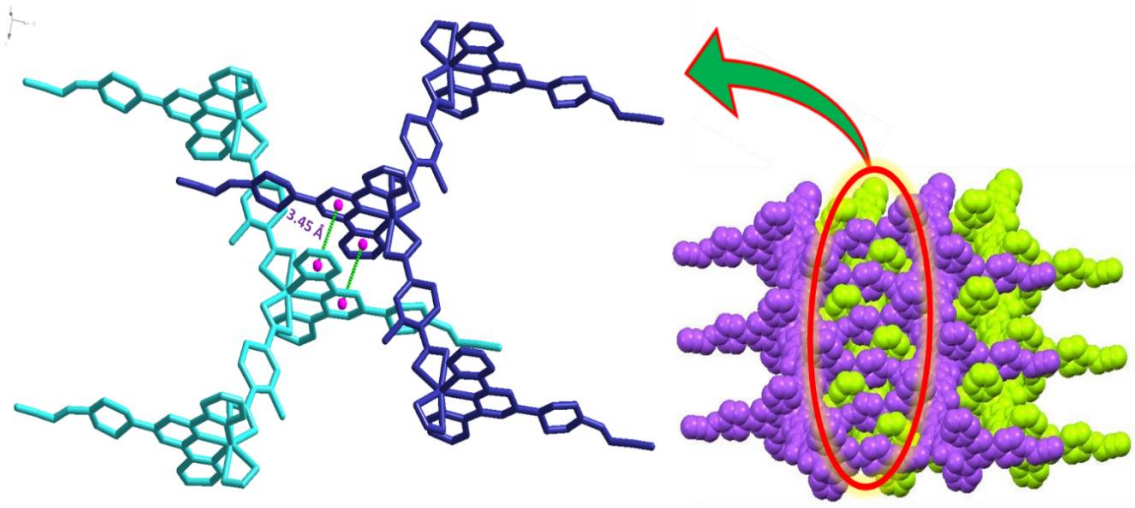

Figure 3.80. Formation of a strong π–π (edge to centroid) stacking between two 1D layers.

A strong π–π interaction between pyridyl groups has been observed which plays a very important role in the formation of 3D supramolecular assembly. As shown in the Figure

3.80, one 1D layer connects with another 1D layer via a strong edge to centroid π–π interaction with distance: 3.45 Å. The central pyridyl ring shows interaction with the peripheral pyridyl to generate this fused layer.

Powder X-ray diffraction studies. Crystalline nature for **26-30** were examined using powder X-ray diffractiontechnique. It was found that Compound **26-30**, are crystalline in nature with similar kind of powder patterns attributing to similar kind of structural asthetics as shown in the Figure 3.81. Furthermore, in the case of **31-36** change in the powder pattern has been observed.

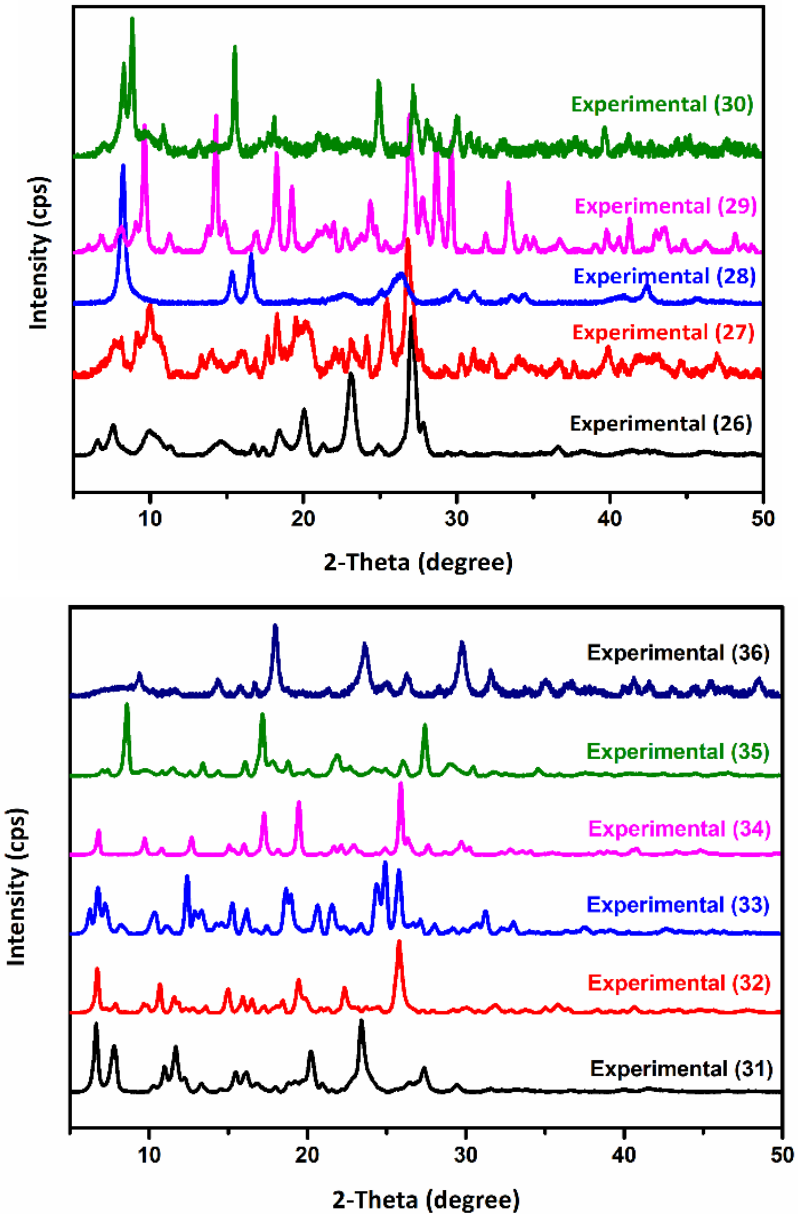

Figure 3.81. PXRD patterns for **26-36.**

Luminescence properties of MOCNs containing terpyridine ligands. Luminescence properties of terpyridine based MOCNs arises due to charge transfer within the ligand. When this type of ligand binds with a metal by a dative bond, one part of ligand becomes electron deficient, and the other part remains electron rich.

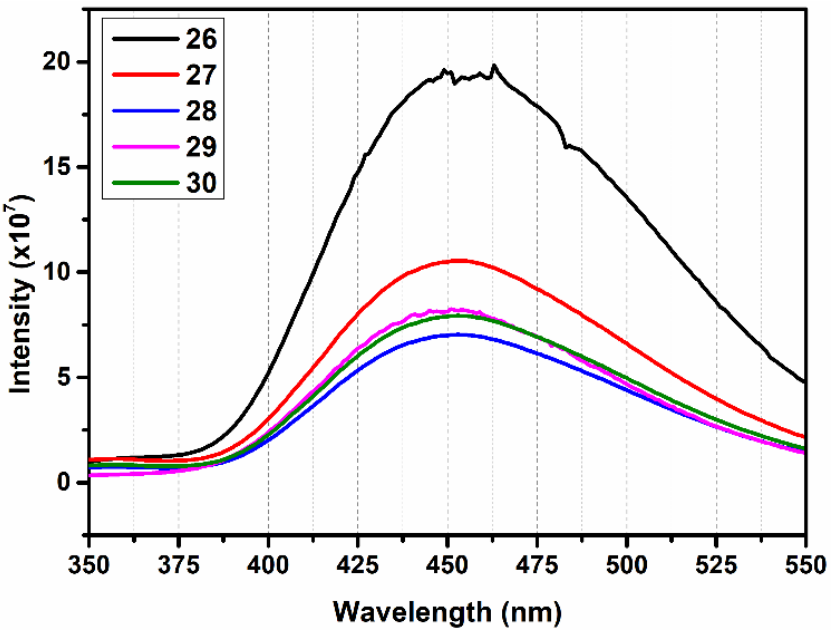

Figure 3.82. Fluorescence spectra of **26**-**30**.

Furthermore, fluorescent nature gets enhanced due to n-π* and π– π* transition. Moreover, a ligand to metal charge transfer is also involved in imparting fluorescent nature to the system. Some of the MOCNs synthesized using these terpyridine ligands have been used for the metal ion sensing due to their good fluorescent nature as well as having an interaction site for the incoming metal ions. Luminescence spectra of compound **26**-**30** have been collected by taking 1 mg of compound in 2 mL of water. An excitation wavelength of 285 nm was used for the excitation resulting in an emission peak around 430 nm and 460 nm by using entrance and exit slit widths of 3 nm each. (see Figure 3.82). Along with this compound, **31**-**36** are showing the same type of features in fluorescence.

Sensing of metal ions

Sensing of metal ions is one of the very important concerning issue with respect to the toxic nature of some of metal ions as well as their contribution in biological systems. By using fluorescent-tagged molecules, we can detect/sense the various metals ion due to the presence of various interaction sites in coordination compounds. Ligands (substituted terpyridine) used in this section have a strong ability to produce strong luminescence when

it binds with a metal center. Due to the ligand to metal charge transfer, one moiety of this ligand becomes electron deficient, and another part becomes electron rich. This electron rich moiety transfers the electrons to the electron deficient moiety by n-π* and π– π* transition which makes these compounds fluorescent in nature. The ligand is designed in such a manner that there should be two different interaction sites present; one is electron deficient moiety and another towards the electron rich moiety. In case of 2,2'-terpyBA, all three nitrogens bind with the metal center leaving no interaction sites available for the incoming metal ions in the electron deficient moiety. Therefore, to make another interaction site towards electron deficient moiety, another component (2-aminoteraphthalic acid) has been used which has two amine groups. When incoming metal ions interact with the electron-deficient site, it makes it more electron deficient thereby increasing n-π* and π-π* transition of electrons exhibiting an enhancement in fluorescence intensity (turn-on). While interaction at electron rich moiety decreases, the n-π* and π-π* transition of electrons, results in quenching in fluorescence (turn-off). Lead (Pb^{2+}) is one of the soft-metal ions which is highly toxic in nature. It causes an adverse effect on human health as well as on the environment even at low concenteration. Therefore, sensing of Pb^{2+} is an important concern to overcome the adverse effects of these ions on human health. Fe^{3+} is an another important metal ion present in biological system. Both deficiency as well as excess, will lead to metabolic disorders. Therefore, efficient methods have to be developed for detection of Fe^{3+} even at very low concentrations.[138,196–200]

Sensing of Metal Ions by **33**. Before performing the metal ion sensing, we checked the fluorescence intensity of these compounds in different organic solvents. In case of compound **33,** we carried out the photoluminescence study by taking 1 mg of compound in 2 mL of different solvents like methanol, ethanol, acetone, acetonitrile, dimethyl sulfoxide and water. From this experiment, it was found that compound **33** (Cu(II) compound) quenching in fluoresence intensity on addition of acetone, while maximum intensity was observed in case of water (Figure 3.83). Motivated from thesewe further tried to investigate the sensing ability for metal ions in aqueous solutions. For this, 2 mL solution of different metal ions was prepared in water having concentration 0.1 mmol/L. In every case, 1 mg of the compound was added to the solution and was stirred for 15 min to make a uniform slurry, which was then used for the fluorescence. For this experiment, entrance and exit slits were kept at 3 nm and 3 nm, respectively with the excitation wavelength of 285 nm and resulting emission band (λ_{max}) around 440 nm. The results obtained from this study

indicate that different cations show different behavior with the fluorescence of compounds due to a different type of interactions with the framework. This interaction can be at the different positions of the framework by which a change in the behavior of luminescence intensity of the compound was observed.

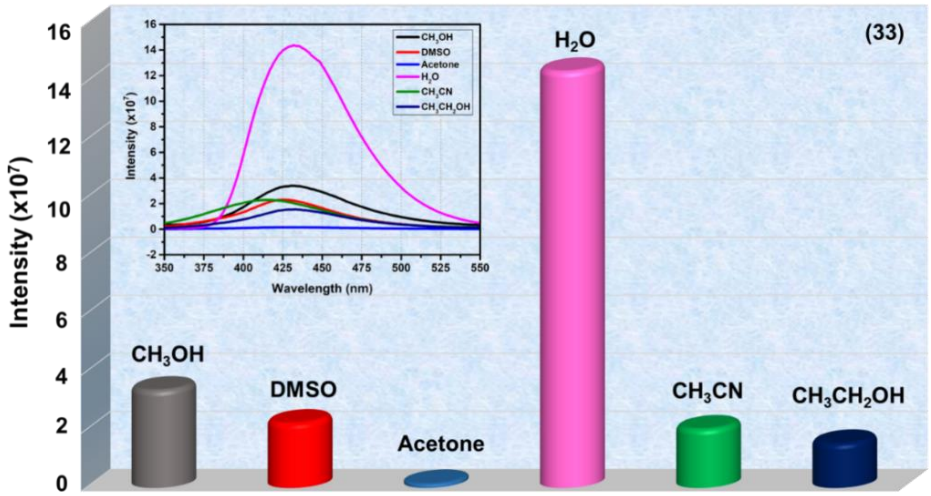

Figure 3.83. Change in the emission intensity of **Cu-MOF** (**33**) with respect to different solvents.

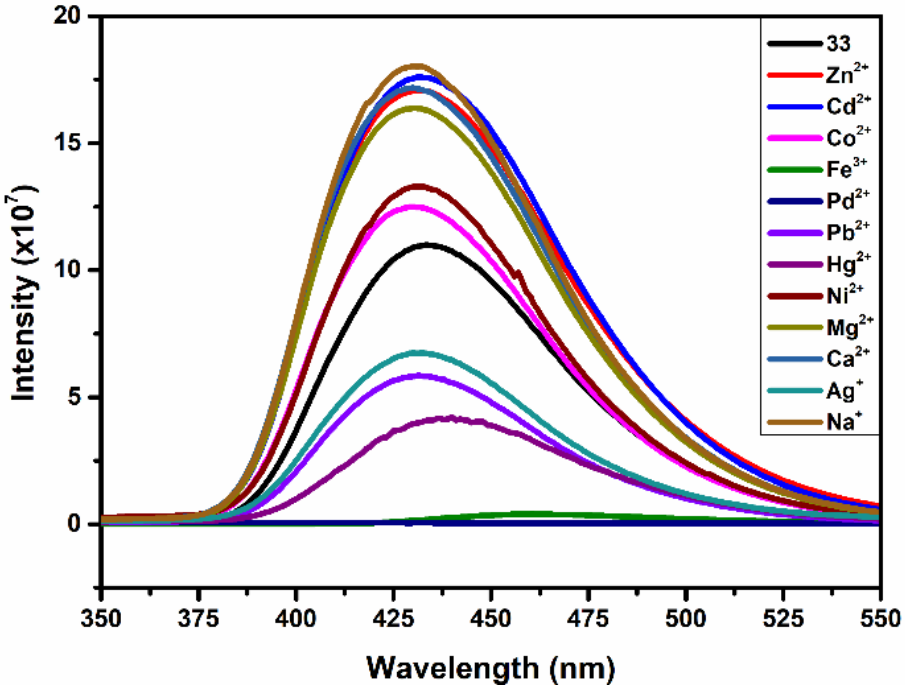

Figure 3.84. Change in the emission intensity of **Cu-MOF** (**33**) upon addition of different cations in water.

The change in the fluorescence intensity with respect to different cations is shown in Figure 3.84. It was found that metal ions like Na^{+}, Ca^{2+}, Co^{2+}, Cd^{2+}, Ni^{2+}, Zn^{2+}, Mg^{2+}, show enhancement in the fluorescence intensity with respect to the probe. While other metal ions

like Ag^{2+}, Pb^{2+}, Hg^{2+}, Fe^{3+}, Pb^{2+}, Pd^{2+} shows quenching in the fluorescence intensity of the probe (Figure 3.85). Due to the presence of different binding sites in the framework, variation in the lumnisecnce behaiviour was observed.

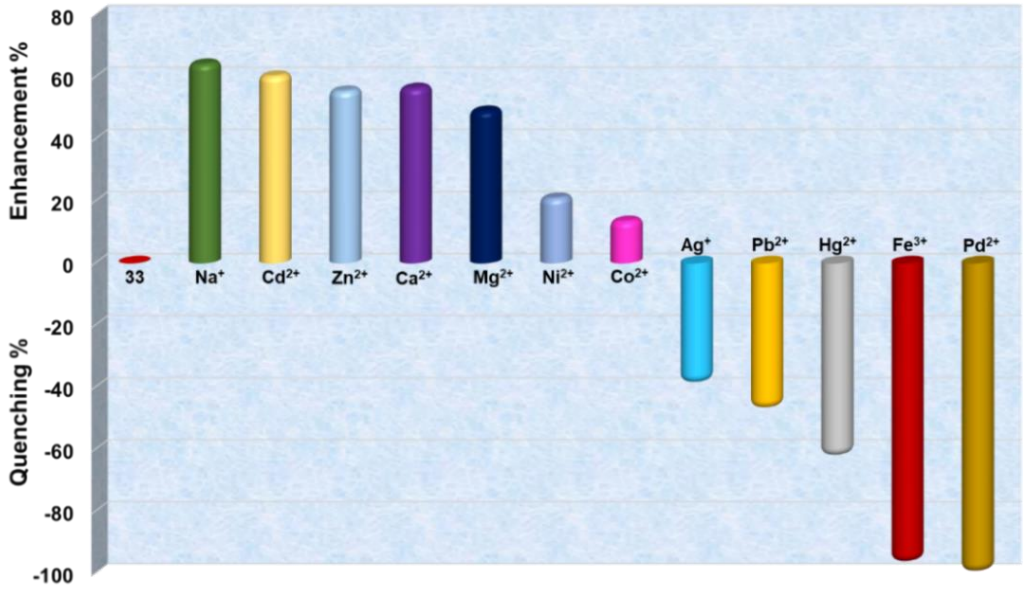

Figure 3.85. Change in the emission intensity of **Cu-MOF** (**33**) upon addition of different cations.

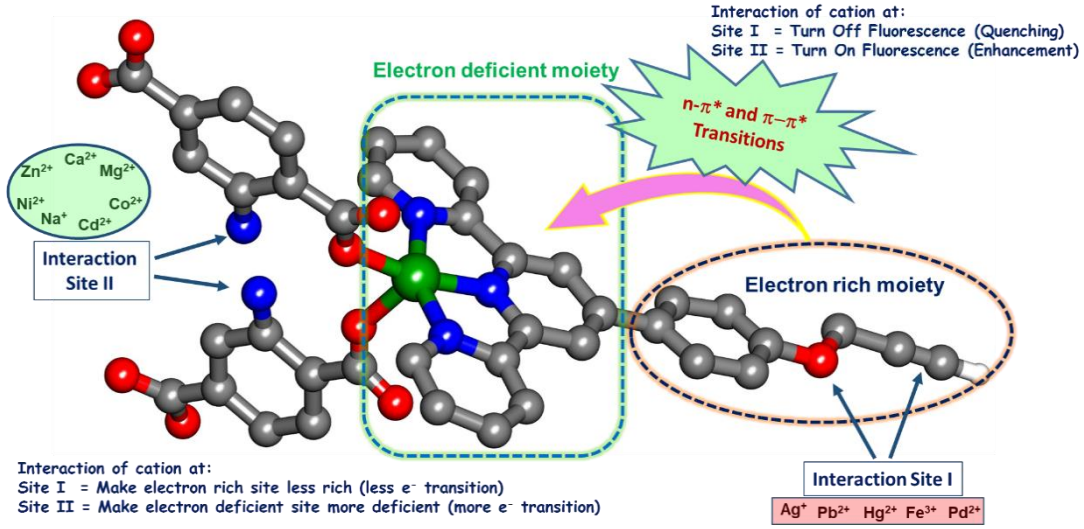

Figure 3.86. Possible interaction of the metal ion with the complex in **33**.

Single crystal structure of compound **33** reveals that there are two interaction sites present (Figure 3.86). Interaction site I is a free acetylene moiety with oxygen near it providing additional support. While interaction site II is a free amine group of two different NH_2bdc linkers. This interactive site is formed due to the conformational arrangement of two amine groups which are pointing towards each other such that they can easily interact with the incoming metal ions. After binding of the terpyridine ligand with Cu(II), one part of the

ligand becomes more electron deficient due to the ligand to metal electron transfer, while another part which is an electron-rich part transfers charge to the electron deficient part (Figure 3.86).

Possibly, cations like Ag^{+}, Pb^{2+}, Hg^{2+}, Fe^{3+}, Pb^{2+}, Pd^{2+} interact with site I due to which a charge transfer from electron rich to electron deficient site decreases, as a result of which quenching in the fluorescence intensity is observed. While, other cations like Na^{+}, Ca^{2+}, Co^{2+}, Cd^{2+}, Ni^{2+}, Zn^{2+}, Mg^{2+} interact at interaction site II, making the electron-deficient site more electron deficient and enhance the charge transfer from electron rich site to the deficient site, resulting in enhancement in the fluorescence intensity of the **33**.

Sensing of Metal Ions by **34**. Inspired by the sensing results of **33** for detection of metal ion***s***, **34** is also used for sensing of metal ions. It is a Mn(II) compound and shows fluorescent behavior due to terpyridine moiety. This compound is more fluorescent than **33**. In this case also before doing the metal ion sensing, we have checked the fluorescence intensity of this compound in different organic solvents. It was found that, **34** exhibits a strong and broad emission spectrum with λ_{max} = 445 nm when excited at 285 nm using slit widths of 1 nm and 1 nm, respectively (entrance and exit slit). In case of **34**, fluorescence studies have been performed by taking 1 mg of compound in different solvents like methanol, ethanol, acetonitrile, water, dimethyl sulfoxide, and acetone. From this experiment, it was found that compound **34** shows fluorescent nature in water, as observed in **33.** Quenching in the fluorescence spectrum was observed in acetone (Figure 3.87). Water was choosen as solvent for metal ion sensing experiments.

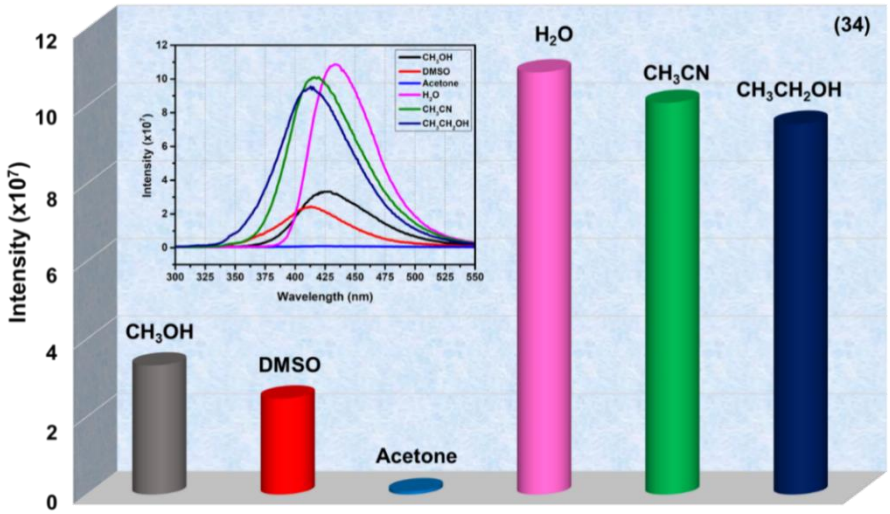

Figure 3.87. Change in the emission intensity of Mn-MOF (**34**) with respect to different solvents.

For this, a 2 mL solution of different metal ions was prepared in water having a concentration of 0.1 mmol/L. In every case, 1 mg of the compound has been added to the solution and was stirred for 15 min to make a uniform slurry, which was then used for the fluorescence study. Results obtained from this study show that different cations show different interaction with **34** towards. Due to the different type of interaction of cations with the framework, variation in the fluorescence behaiviour was obsereved. some cations have shown enhancement in the fluorescence intensity while some havequenched the fluorescence intensity on interaction with . On the other hand, few cations show a change in the λ_{max} towards higher or lower wavelength along with enhancement and quenching.

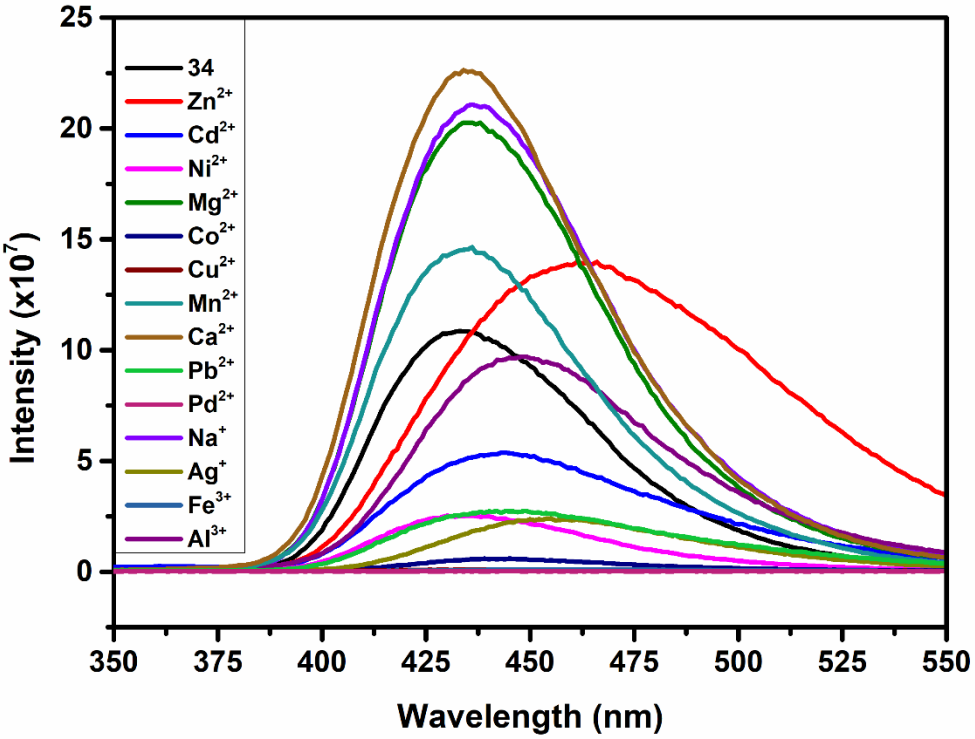

Figure 3.88. Change in the emission intensity of Mn-MOF (**34**) upon addition of different cations.

From the result, it was found that metal ions like Na^{+}, Ca^{2+}, Zn^{2+}, Mg^{2+} have shownenhancement in the fluorescence intensity. While on addition of other metal ions like Ag^{2+}, Pb^{2+}, Al^{3+}, Fe^{3+}, Pd^{2+}, Cd^{2+}, Ni^{2+}, Co^{2+} and, Cu^{2+} quenching of the fluorescence intensity was observed. (Figure 3.89). It was also observed that on addition of Zn^{2+} ions red shift in the wavelength was observed (see Figure 3.88).

Single crystal structure of compound **34** reveals that there are two interaction sites present (Figure 3.90). Interaction site I is a free acetylene moiety with oxygen near it providing additional support. While interaction site II is a free amine group of two different bdc

linkers. This interaction site is formed due to the conformational arrangement of two amine groups which are pointing towards each other such that they can easily interact with the incoming metal ions. After binding of the terpyridine based ligand with Mn(II), one part of the ligand becomes more electron deficient due to the ligand to metal electron transfer, while another part which is an electron-rich part transfers charge to the electron deficient part (Figure 3.90).

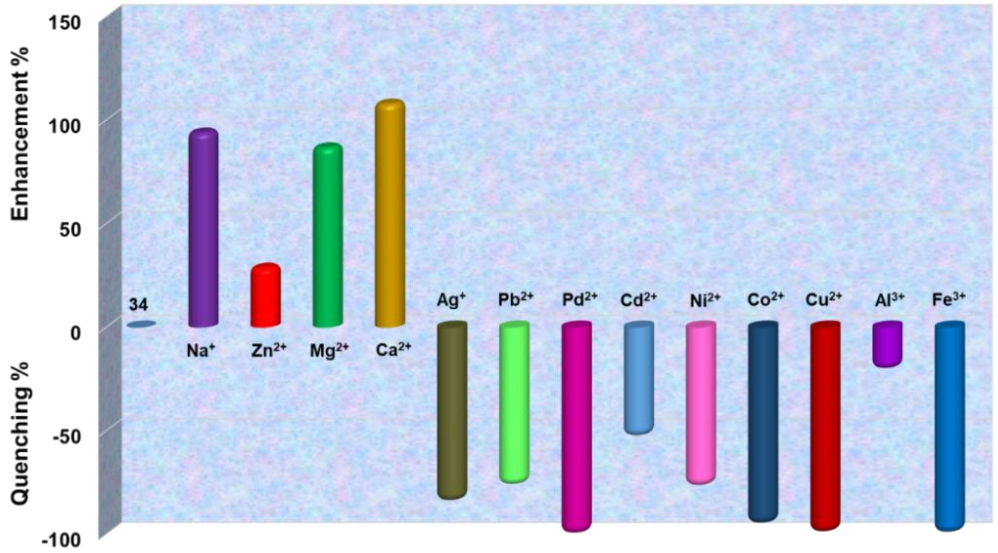

Figure 3.89. Change in the emission intensity of Mn-MOF (**34**) upon addition of different cations.

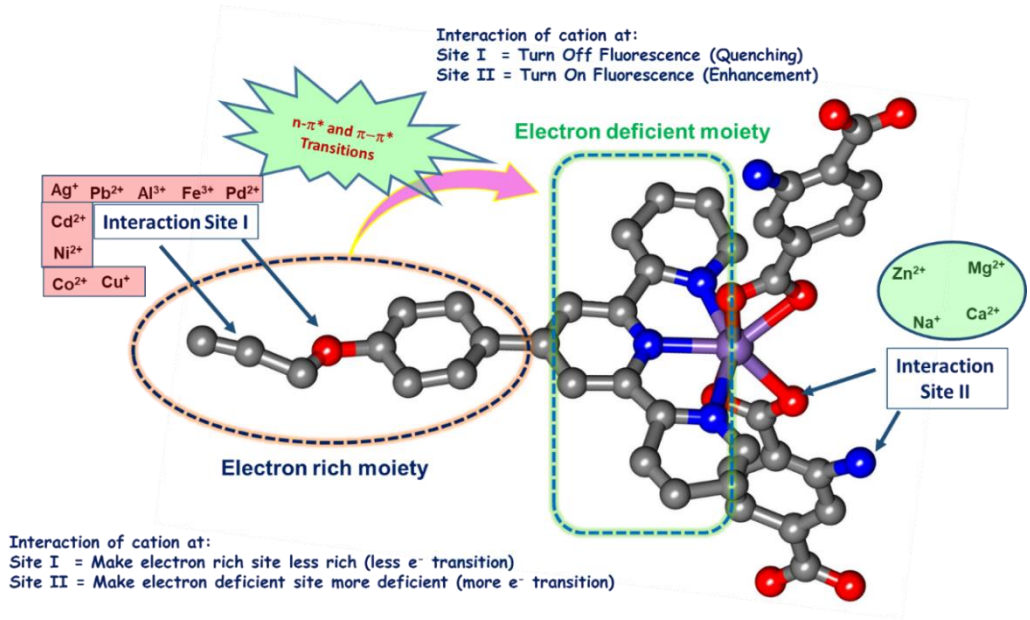

Figure 3.90. Possible interaction of the metal ion with the complex in **34**.

Possibly, cations likeAg^{2+}, Pb^{2+}, Al^{3+}, Fe^{3+}, Pd^{2+}, Cd^{2+}, Ni^{2+}, Co^{2+} and, Cu^{2+} interact with the site I as the result, charge transfer from electron rich to electron deficient site decreases and quenching in the fluorescence intensity is observed. For cations like Na^{+}, Ca^{2+}, Zn^{2+}, Mg^{2+},interaction take place site II, making the electron-deficient site more electron deficient enhance the charge transfer from electron rich site to the deficient site, resulting in enhancement in the fluorescence intensity of the **34**.

Chemistry with 4,4′-terpyBA

After exploring 2,2′-terpyBA, another terpyBA ligand was designed by changing the nitrogen atom from *ortho* to *para* position. This change in the position of nitrogen atom in the ring resulted in dramatic change in the nature of the ligand from a capping type ligand to a spacer linker, where only two pyridyl nitrogens were involved in bonding. The synthesis of all these metal complexes is shown in Scheme 3.18 and 3.19.

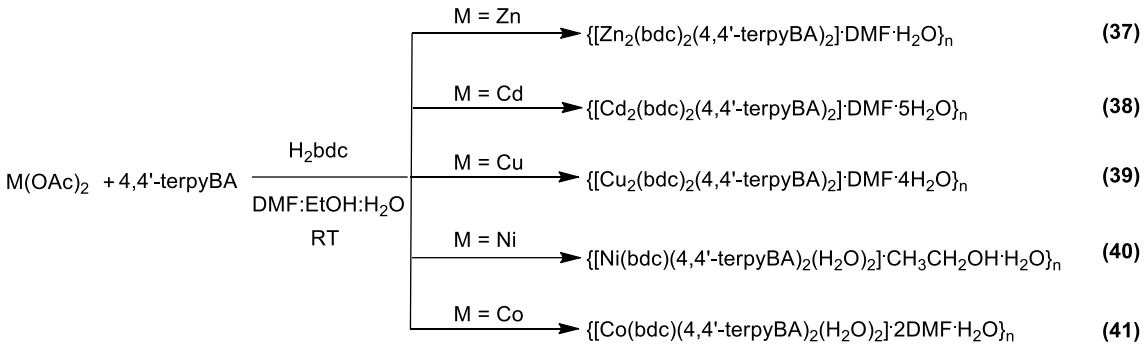

Scheme 3.18. Synthesis of **37-41**.

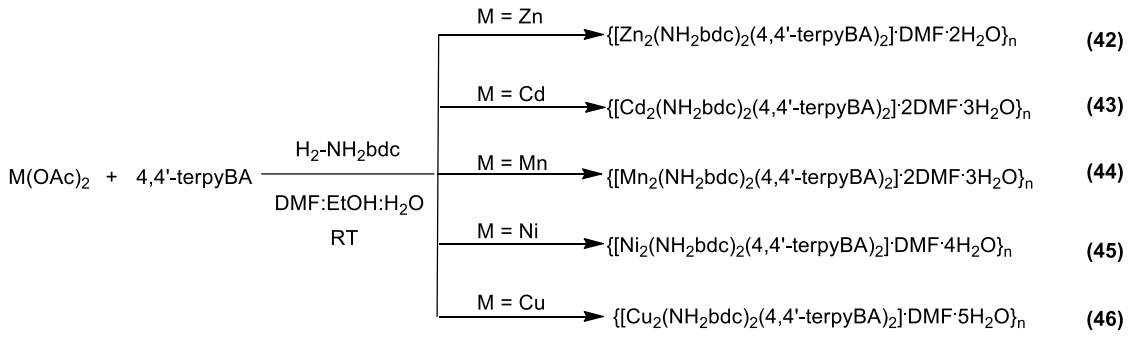

Scheme 3.19. Synthesis of **42-46**.

FTIR spectroscopic studies. Compounds **37-41** show the monodentate mode of carboxylate binding with the metal center as the difference between asymmetric and symmetric stretching is between 200 cm^{-1} to 240 cm^{-1}.

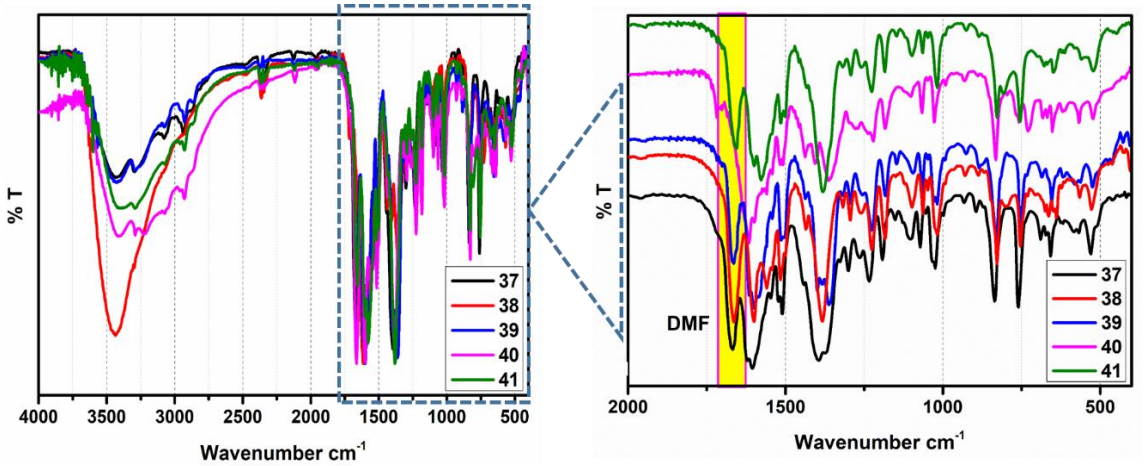

Figure 3.91. FTIR spectra of **37-41**.

Presence of lattice DMF was confirmed by the peak around 1661 cm^{-1} in **37**, **39**, and **41**. (Figure 3.91). All these compounds show monodentate mode of carboxylate binding with respective metal center as the difference between asymmetric and symmetric stretching is between 200 cm^{-1} to 240 cm^{-1}. All these compounds have a peak at 1662 cm^{-1} corresponding to the DMF solvent molecules (Figure 3.92). Along with this, all the binding modes and change in the stretching frequencies are summarised in the Table 3.19.

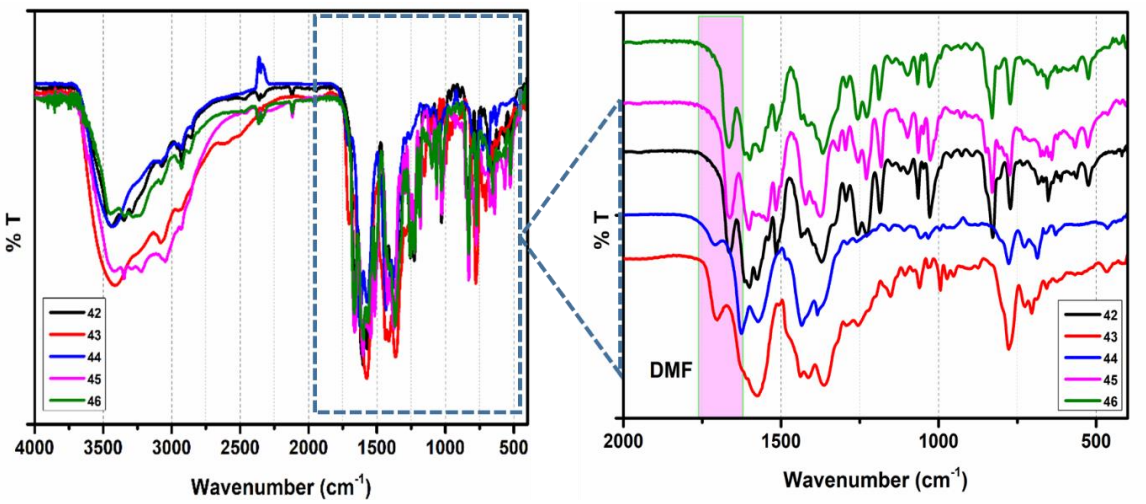

Figure 3.92. FTIR spectra of **37-46**.

Table 3.19. Asymmetric and symmetric stretching frequencies and their respective binding modes of carboxylates in **37-46**.

Compound	Asymmetric (υ_1) cm^{-1}	Symmetric (υ_2) cm^{-1}	$\Delta\upsilon = \upsilon_1 - \upsilon_2$ cm^{-1}	Binding mode
37	1599	1386	213	Monodentate
38	1614	1410	204	Monodentate
39	1599	1395	204	Monodentate
40	1600	1382	218	Monodentate
41	1599	1375	224	Monodentate
42	1597	1367	230	Monodentate
43	1598	1378	220	Monodentate
44	1600	1384	216	Monodentate
45	1600	1375	225	Monodentate
46	1598	1367	231	Monodentate

Thermogravimetric analyses. After the loss of the lattice solvents molecules, these compounds show stability up to 300 °C followed by decomposition of the framework. Forcompounds **37-46**, a two-step loss was observed, in which the first step shows the loss of solvent molecules and the second loss confirms the decomposition of the frameworks (Figure 3.93). Compound **37** exhibits a weight loss of 7.12% corresponding to the loss of one DMF and one water molecule (ca. 5.66%), while compound **38** shows a first weight loss of 11.29% corresponding to the loss of one DMF and five lattice water molecules (ca. 11.34%). In **39**, first weight loss of 10.92% corresponds to the loss of one DMF and four lattice water molecules (ca. 11.59%).

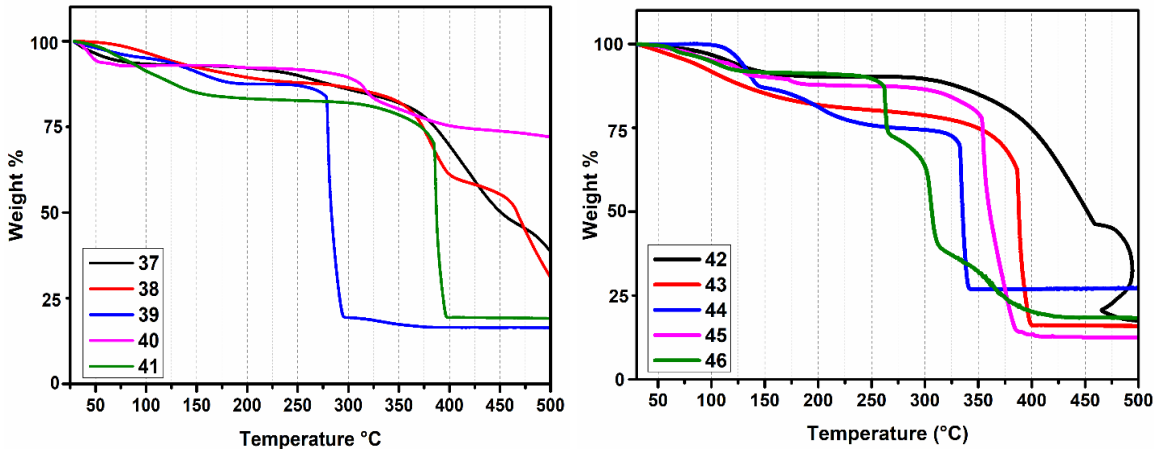

Figure 3.93. TGA scans of **37-46**.

In**40**, first weight loss of 6.31% corresponding to the loss of one methanol and one lattice water molecule (ca. 6.21%) was observed. For **41**, loss of two DMF and two water molecules is observed.. A loss of 16.07% is due to the loss of these solvent molecules up to 200 °C (ca. 15.45%). Further a two step loss profile was observed for **42-46.**. For **42**, first weight loss of 8.23% was calculated corresponding to the loss of one DMF, followed by the loss of two lattice water molecules (ca. 8.95). A weight loss of 13.24% corresponding to the loss of two DMF and three water molecules (ca. 13.89%) was observed in **43**. For **44** a weight loss of 8.25% corresponding to the loss of one DMF and two water molecules (ca. 8.41%) was calculated, while **45**, shows a weight loss of 10.76% corresponding to loss of one DMF and four water molecules (ca. 11.88%). Similarly**46** exhibits a weight loss of 11.93% corresponding to the loss of one DMF and five lattice water molecules (ca. 12.46%) followed by the decomposition of the architecture.

Single crystal structure analyses. Crystals of **37** were grown by a solvothermal method using a mixed solution of DMF and water in 1:1 ratio. Furthermore, crystals of **40** and **41** were grown by the direct layering of the reactants.

Structural description of **37**. Single crystal structure of this **37** shows that it crystalizes in the monoclinic *C*2/*c* space group. The asymmetric unit consists of a metal center, one bdc, and one ligand. In this, (Zn(II)) is tetra coordinated in N2O2 fashion, surrounded by two nitrogen atoms of two different ligands (distances: 2.030(4) Å and 2.036(3) Å) and two oxygen atoms from two different dicarboxylates (distances: 1.937(3) Å and 1.935(4) Å).

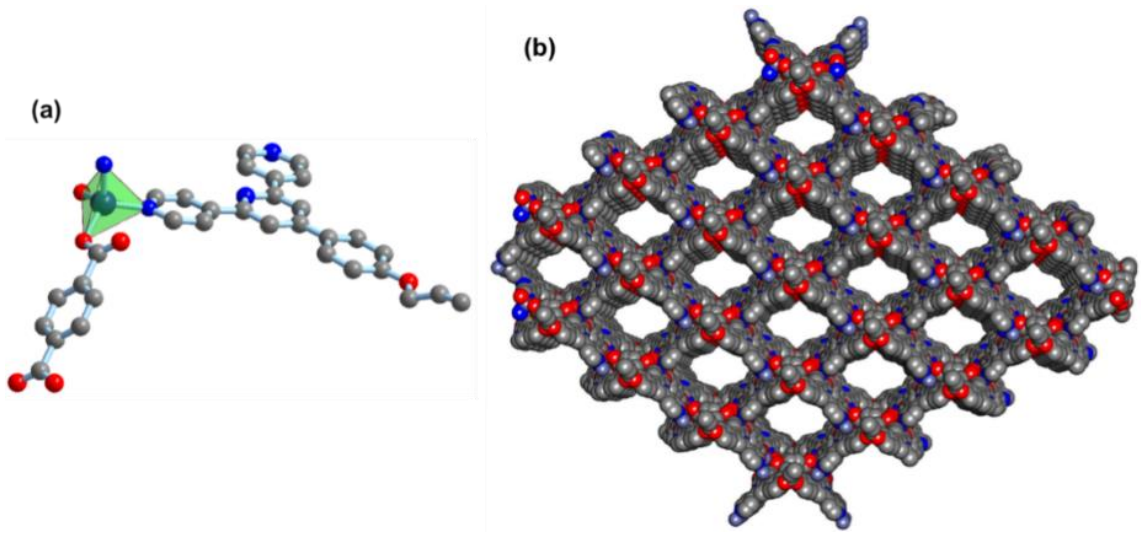

Figure 3.94. (a) Asymmetric unit having N2O2 surrounding and (B) 3D network down to c axis in **37**.

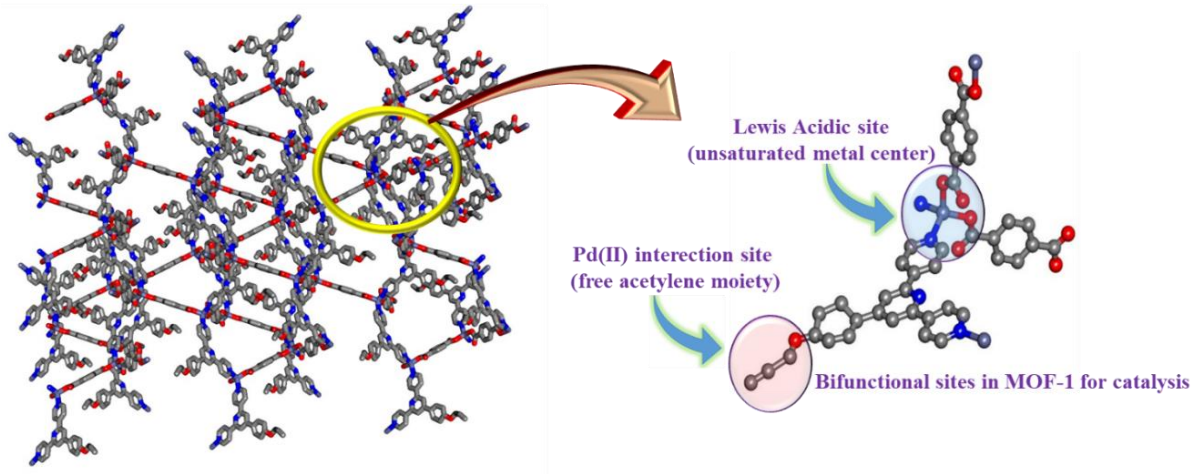

Figure 3.95. Bifunctional site present in **37** to interact with the guest for catalysis.

On polymer expansion, a 3D structure is generated which is having pores of dimensions: 16.794 x 14.164 $Å^2$. Free acetylene group of the ligand is hanging inside the pores. Coordination environment and the 3D network formed is shown in the Figure 3.94. Along with this, the solvents of crystallization, DMF and water, are also present in the lattice. Due to the disordered nature of the solvent molecules, it was removed by using Squeeze method.

As this compound is porous having free acetylene moiety inside the pores, it can be used for different applications like guest encapsulation and catalysis. By using this free acetylene functionality, various metal precursors can be encapsulated inside the pore, which can be further reduced to form metal nanoparticles. These nanoparticles can be used for various organic transformations. Along with this, metal is tetra coordinated which provides a Lewis acidic site that also is very useful for organic transformations. Presence of these two functionalities makes this compound a dual catalyst which can perform two different catalytical reactions as shown in Figure 3.95.

Structural description of **40**. It crystallizes in monoclinic *C*2/*c* space group. The central metal Ni(II) is hexacoordinated surrounded with the N2O4 environment to form an octahedral geometry. Two oxygens of two different linker (monodentate carboxylate), two nitrogen atoms from two different ligands and two oxygens from the coordinated water molecules participate in the formation of distorted octahedral geometry. Two nitrogen from the ligand (anti to each other) and two oxygen from linker (anti to each other) makes a plane with four equatorial bonds connected to the metal center with distances 2.099(3) Å and 2.109(2) Å respectively.

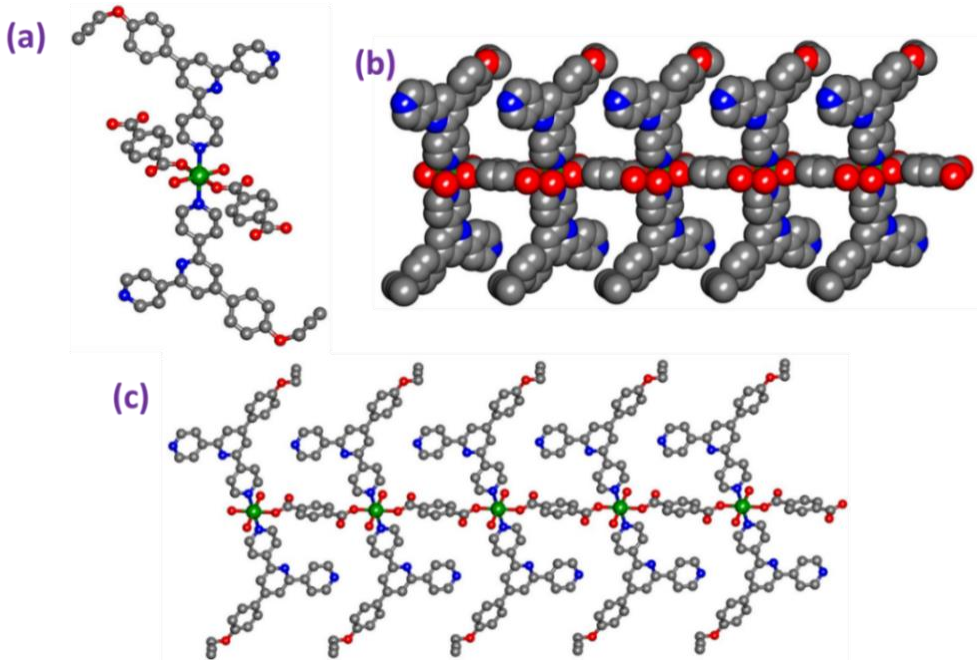

Figure 3.96. (a) Coordination environment around metal center, (b) space fill representation and (c) formation of a 1D coordination polymer in **40**.

Furthermore, the axial position is acquired by coordinated water molecules with smaller bond distance (2.059(3) Å) than the axial bonds. All the angles around the metal center are in the range of 88.02° - 180° to form a distorted octahedral geometry. The central pyridine nitrogen is not connected to any metal because the position is not appropriate to form a bond with a metal center. The interesting thing to notice in this structure is that the one peripheral pyridyl nitrogen also does not participate in the formation of a coordination bond with any metal as shown in Figure 3.96.

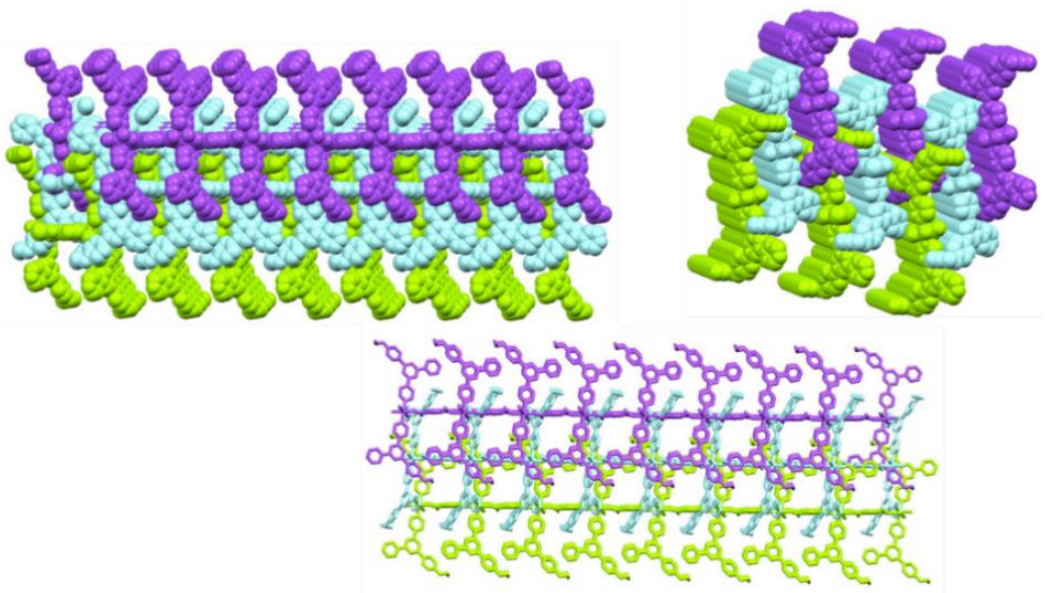

Figure 3.97. Packing of **40** in two different directions.

The asymmetric unit consists of a metal center, a ligand, and a linker to form overall a neutral complex. After polymer expansion, a flexible ladder (with central base) shaped 1D coordination polymer is formed. Due to the presence of flexibility of C-O bond, acetylene moieties are hanging outside the structure. Overall packing of the molecule generates a 3D supramolecular assembly due to the presence of weak interactions like π–π stacking, Hydrogen bonding and van der Waals interactions (Figure 3.97).

Structural description of **41**. The crystal structure is similar to the previous one however, it is crystalized in monoclinic *C*2/*c* space group. The asymmetric unit consists of one ligand, metal center, half of the linker, one coordinated water, one lattice methanol, and one lattice water molecule. Central metal is Co(II), which is hexacoordinated surrounds with the N2O4 environment to form octahedral geometry. Two oxygens of two different linkers (monodentate carboxylate), two nitrogen atoms from two different ligands and two oxygens from the coordinated water molecules participate in the formation of distorted octahedral geometry. Two nitrogens from the ligand (anti to each other) and two oxygens from the linker (anti to each other) make a plane with four equatorial bonds connected to the metal center with distances 2.154 Å and 2.078 Å respectively.

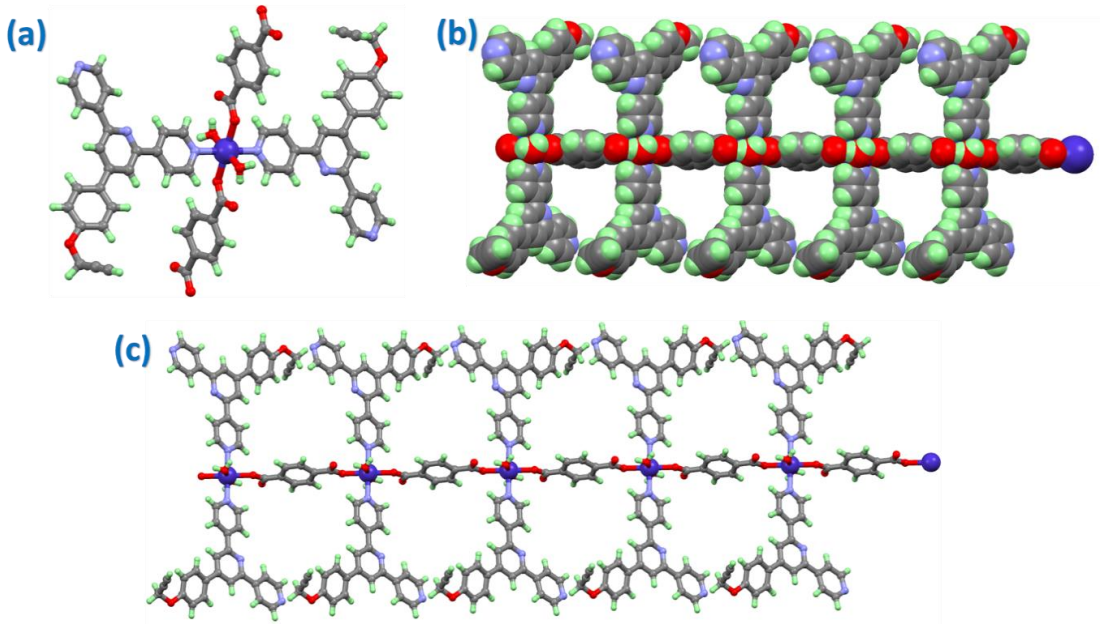

Figure 3.98. (a) Coordination environment around metal center, (b) space fill diagram and (c) formation of a 1D coordination polymer in **41**.

Furthermore, the axial position is occupied by coordinated water molecules with smaller bond distance (2.1451(18) Å) than the axial bonds while the bond distance of carboxylate oxygen to the metal center is around 2.078(2) Å. All the angles around the metal center are

in the range of 88.02° - 180° to form a distorted octahedral geometry. The central pyridine nitrogen is not connected to any metal because of the absence of chelation for binding. The interesting thing to notice in this structure is that the peripheral pyridyl nitrogen does not participate in the formation of a coordination bond with any metal as shown in Figure 3.98 and 3.99. All the bond angles and distances are listed in Table A28 and A39 (Appendix).

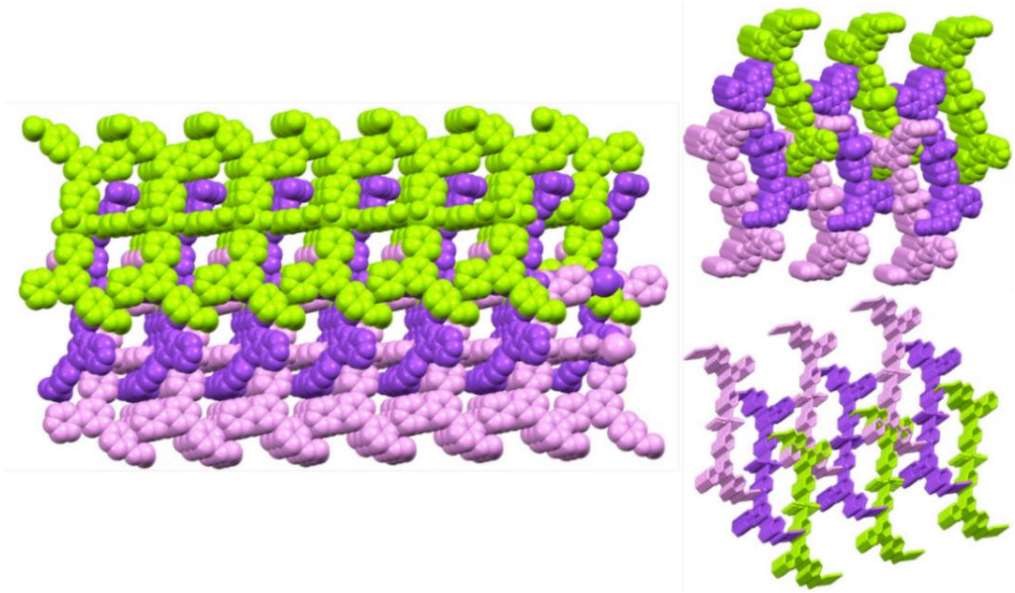

Figure 3.99. Packing of **41** in two different directions.

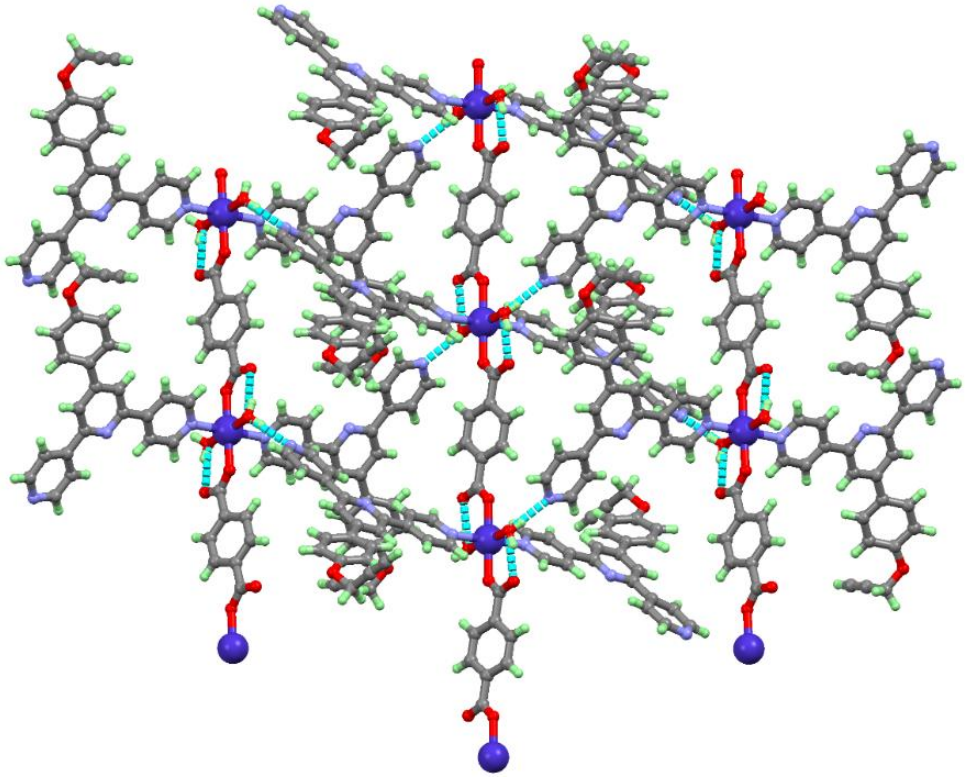

Figure 3.100. Formation of H-bonding between two layers in **41**.

In this case, the asymmetric unit consists of a metal center, a ligand, and a linker to form a neutral complex like **40**. After polymer expansion, a flexible ladder (with central base) shaped 1D coordination polymer is formed. Due to the presence of flexibility of C-O bond, acetylene moieties are folded towards the central atom. The overall packing of the molecule generates a 3D supramolecular assembly due to the presence of weak interactions like π–π stacking, hydrogen bonding and van der Waals interactions (Figure 3.100).

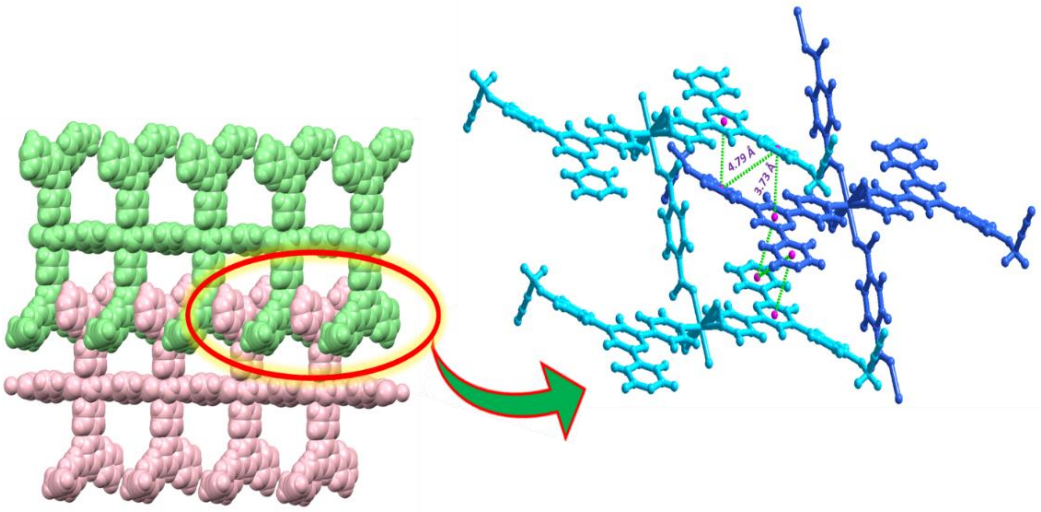

Figure 3.101. Formation of a strong π–π (edge to centroid) stacking between two 1D layers in **41**.

The presence of these interactions helps in the formation of a 3D supramolecular assembly with stacked layers as shown in the Figure 3.101. A strong hydrogen bonding plays very important role in growing the structure in three dimensions. Both the coordinated water molecules, uncoordinated oxygen from the linker and non-bonded nitrogen atom from the peripheral pyridyl ring of the ligand participate in the hydrogen bonding. One hydrogen of the coordinated water molecule forms strong hydrogen bonding with the free nitrogen of the ligand and other hydrogen forms bonding with the uncoordinated oxygen of the carboxylic group (monodentate) of the linker.

Powder X-ray diffraction studies. Crystalline nature of all the synthesized complexes was confirmed by powder X-ray diffraction studies. For **37-46** a similar type of powder patterns indicate the formation of similar compounds as shown in the Figure 3.102. Furthermore, in the case of **42-46**, all show different powder pattern. PXRD pattern of **42**, is different from all others, however, **43**, **44** , **44**, **45**, **46** show similar type of powder patterns.

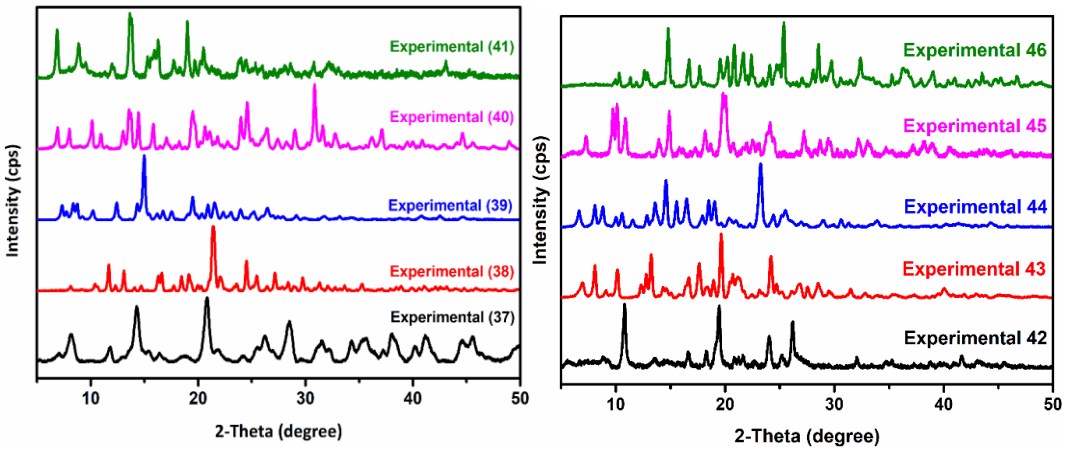

Figure 3.102. PXRD patterns for **37-46**.

Gas adsorption study. To evaluate the porosity of **37**, N_2 adsorption measurement was done at 77 K, showing a classic type II adsorption isotherm (see Figure 3.103) revealing the mesoporous nature of the MOF. Gas sorption studies of this compound reveal the pore size distribution (based on N_2 adsorption isotherm) of different size range which is persistent with the single crystal structure. The uptake amounts are 62 cm^3 g^{-1}, corresponding to a BET surface of 60 m^2 g^{-1}. The permanent porosity of **37** was confirmed by N_2 adsorption.

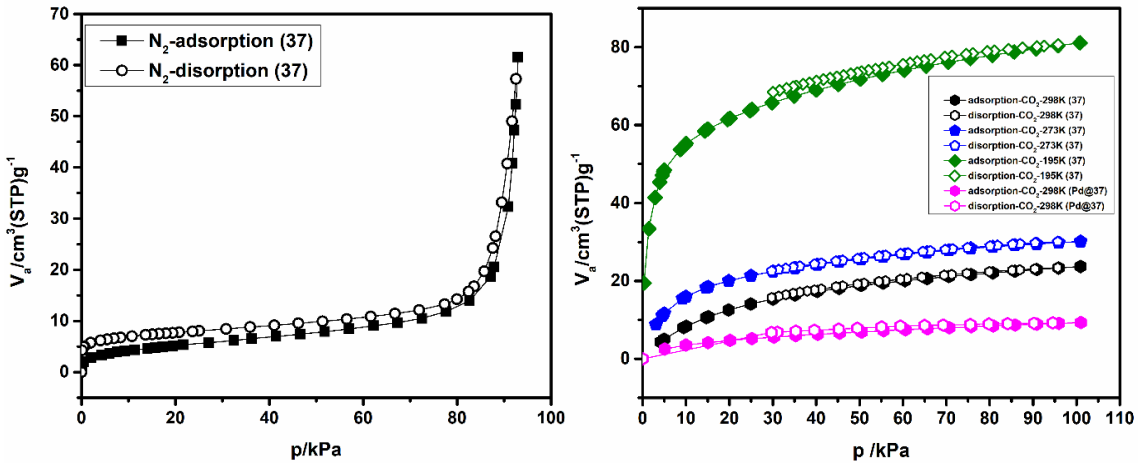

Figure 3.103. N_2 adsorption isotherms of **Zn-MOF** (**37**) at 77 K and CO_2 adsorption isotherms of **Zn-MOF** at variable temperature and CO_2 adsorption isotherm of **Pd@Zn-MOF** at 298 K.

Further, it was used for CO_2 adsorption studies. Low-pressure CO_2 adsorption measurements of **37** were performed at variable temperatures as shown in Figure 3.103. At different temperatures, different amount of CO_2 was adsorbed like 17 cm^3 g^{-1}, 27 cm^3 g^{-1} and 80 cm^3 g^{-1} at 298 K, 273 K and 195K, respectively. CO_2 adsorption was also performed after implementation of nanoparticles inside **37**. After loading of Pd(0)-nanoparticles inside the MOF, less amount of CO_2 was adsorbed indicating the unavailability of pore space.

More than 90% of space was occupied by Pd(0) nanoparticles which is confirmed by the adsorbed value of CO_2.

Zn-MOF (37) as a heterogeneous catalyst. MOFs are widely used in various organic transformations. The main reason is that these are heterogeneous in nature and can be reused further for a number of catalytic cycles. Considering catalytic applications, both inorganic and organic components of the framework can be involved in the transformative reaction.[103,107,201–206] Indeed, the inorganic nodes composed of coordinatively unsaturated metal sites can act as Lewis and Brønsted acids for the subsequent organic transformation of substrates.[105,207–211] Moreover, the incorporation of functional linkers like amino based linkers and its derivatives in MOFs makes it a heterogeneous catalyst which behaves like organocatalysts. These functional linkers are used because these are well known for accelerating a variety of enantioselective organic reactions.[212–218] This functionalization of the linker in the MOFs can be achieved either by using functional linker for synthesis or by post-synthetic modification in the linker. The modification based on coordination chemistry allows incorporating functionalities either on the unsaturated metal sites or on the organic linkers.[219] Another case is to modify the surface either by incorporating the different metal inside the pores or by fabrication of metal nanoparticles (Figure 3.104).[202,220–224]

As discussed before, MOFs can show catalytic activity because of the open sites present in metals, catalytically active organic linkers and integration of host matrixes such as metal nanoparticles. A proper design of ligand helps in the incorporation of metal precursor or direct metal nanoparticles inside the pores. Uptake of precursors for the nanoparticles formation can be enhanced or accelerated by incorporation of certain functionality inside the pores. After implantation of metal nanoparticles, the catalytic performance depends on size, shape, composition and loading amount which strongly depends on the size and nature of the pores. This implementation of metal NPs can generate new functionalities which can be used for various organic transformations. In literature, various reports are available which indicate different methods to achieve this task.[225–227]

So, keeping all these things in mind, we have designed few metal-based 3D MOFs which have free acetylene functionality associated with the organic linker. With the help of this functionality, first Pd(II) metal was incorporated into the framework, followed by its reduction to Pd(0) nanoparticles to make NPs@MOF.[228] Thus the introduction of nanoparticles is achieved inside the MOF, then this catalyst is employed for cascade reaction in the presence of reducing agent in one pot. As far as the synthesis is concerned,

the formation of Schiff base from aldehyde and amine is well explored in the literature. On the other hand, Schiff base formation from nitro derivatives and aldehyde in one pot is not much explored. To perform this reaction, the presence of Pd(0) nanoparticles along with a reducing agent is essential. Along with this in most of the literature reports hydrogen gas was used as a hydrogen source, while sodium borohydride is not reported as a hydrogen source. Moreover, this also provides an unsaturated metal site which makes it a bifunctional catalyst.

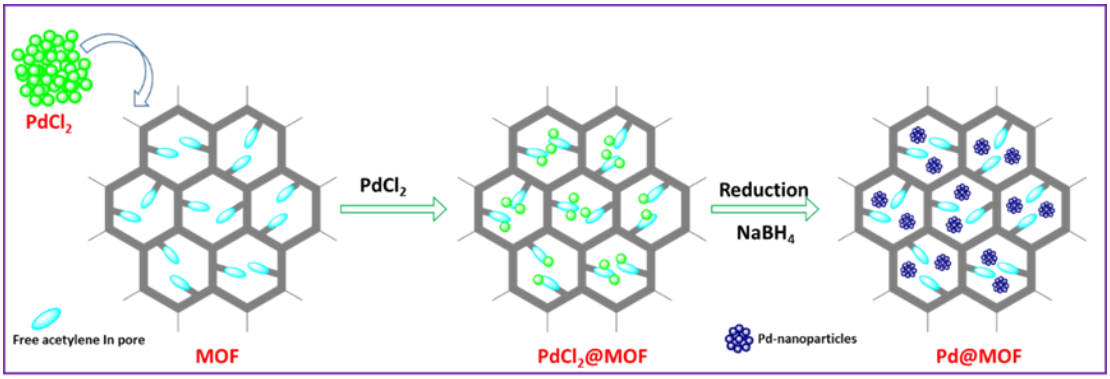

Figure 3.104. Schematic representation of the formation of Pd(0) nanoparticles inside the **Zn-MOF (37)** by two-step solvent infiltration method.

The Knoevenagel condensation reaction is one of the important reaction performed in the presence of a catalyst which provides a Lewis acidic site. In literature, it is well explored with the MOFs which has coordinated water molecules.[229–232] So, to achieve this, first, the coordinated water has to be removed by heating at a certain temperature to generate an unsaturated coordination site on the metal atom. Herein, we are reporting a catalyst which already has an unsaturated metal center which can provide a platform to achieve this type of reaction.

Loading of Pd(0) Nanoparticles inside MOF. Herein, we have followed a solvent infiltration method to load metal NPs into MOFs. This took place in a stepwise manner (two steps) which was started from corresponding metal ion precursors. First, adsorption of $PdCl_2$ into **Zn-MOF**(**37**) was achieved and secondly, a wet chemical reduction method is used to reduce $PdCl_2$ by $NaBH_4$ in methanol to form the corresponding NPs@MOF.[233,234] Initially, MOF was activated at 140 °C to remove all the solvent molecules entangled inside the pores. This activated **Zn-MOF**(**37**) is immersed into the $PdCl_2$ solution in methanol. The bright orange color of the $PdCl_2$ solution disappears gradually within 1 h, and colorless **Zn-MOF** (**37**) turned into a yellow color which indicates the adsorption of Pd^{2+} ions into the **Zn-MOF** (**37**) (see Figure 3.105 and 3.106). The adsorption of metal ions was promoted

by the interaction of Pd-alkyne inside the pores which provides stability to the adsorptive metal ions. PXRD analysis of **$PdCl_2$@Zn-MOF** indicates that there is no change in the framework even after encapsulation of $PdCl_2$ in the MOF. The presence of $PdCl_2$ is also confirmed by PXRD analysis because peaks corresponding to the Pd(0) is observed after $2\theta = 38°$ (see Figure 3.109 *vide-infra*).

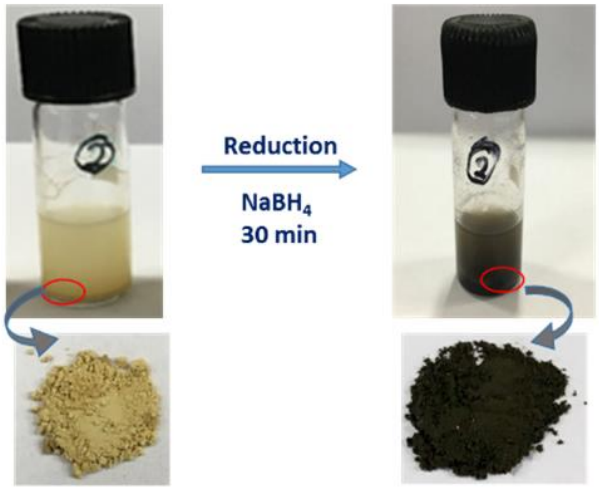

Figure 3.105. Change in the color of **Zn-MOF**(**37**) after fabrication of nanoparticles (reduction of Pd(II) to Pd(0) using sodium borohydride).

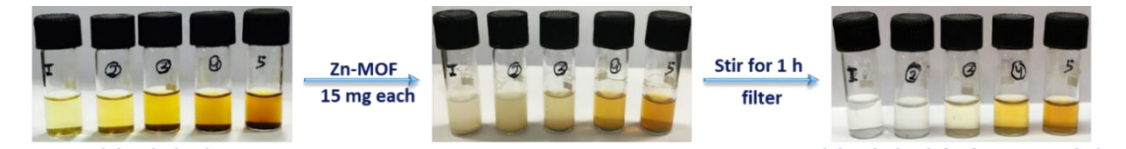

Figure 3.106. Encapsulation of $PdCl_2$ inside the **Zn-MOF** (**37**) followed by a change in the color of the solution.

Further reduction of Pd(II) into Pd(0) nanoparticles was successfully achieved by using $NaBH_4$ in methanolic suspension of the **$PdCl_2$@Zn-MOF**. After addition of $NaBH_4$, yellow color of the compound turns into dark brown indicating the formation of nanoparticles. This dark brown compound was filtered and washed with methanol 5-6 times to remove the excess $NaBH_4$ and dried in air. Finally, implementation of Pd(0) nanoparticles inside the **Zn-MOF**(**37**) was confirmed by various techniques like PXRD, FESEM, and TEM and was used for catalysis applications as is without further purification. To find out the exact amount of $PdCl_2$ incorporated inside Zn-MOF (**37**), solutions of different concentration of $PdCl_2$ were prepared, and UV-Vis spectra were recorded before and after the adsorption (Figure 3.107). From the calculation, it was found that around 16 wt% of palladium was incorporated inside the **Zn-MOF** (**37**). Furthermore, it was reduced

to Pd(0), which was confirmed by various techniques. FESEM images of **Zn-MOF** (**37**) shows a rod type of morphology, and after addition of $PdCl_2$, the morphology of the compound remains intact. However, after the reduction of Pd(II) to Pd(0), the morphology of the compounds changes to flower-like structures (Figure 3.108).

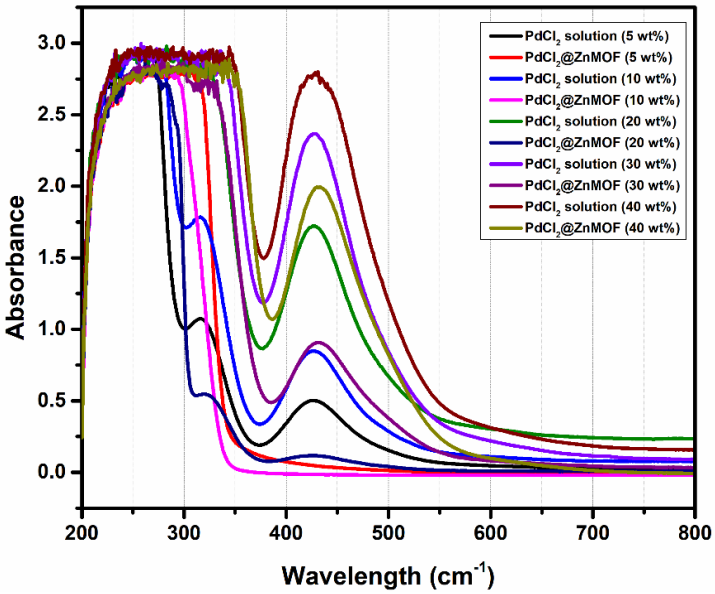

Figure 3.107. UV-Vis Spectra of different weight% of $PdCl_2$ solution before and after addition of **Zn-MOF** (**37**).

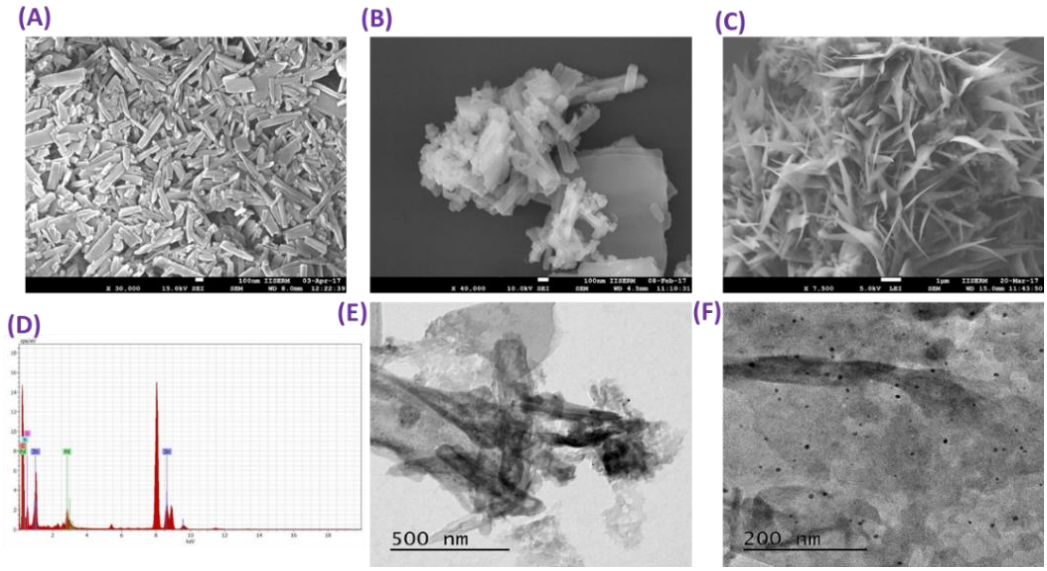

Figure 3.108. FESEM images of (A) Zn-MOF (**37**), (B) **$PdCl_2$@Zn-MOF**, (C) **Pd@Zn-MOF**, (D) EDX of **Pd@Zn-MOF** and TEM images (E and F) of **Pd@Zn-MOF**.

EDX analysis of these compounds confirmed the presence of both zinc and Pd. The formation and presence of Pd(0) nanoparticles were finally confirmed by TEM analysis, in which appearance of black dots confirmed the presence of Pd(0) nanoparticles.

Furthermore, TEM analysis reveals that the size of the nanoparticles is in the range of 2-20 nm (Figure 3.108).

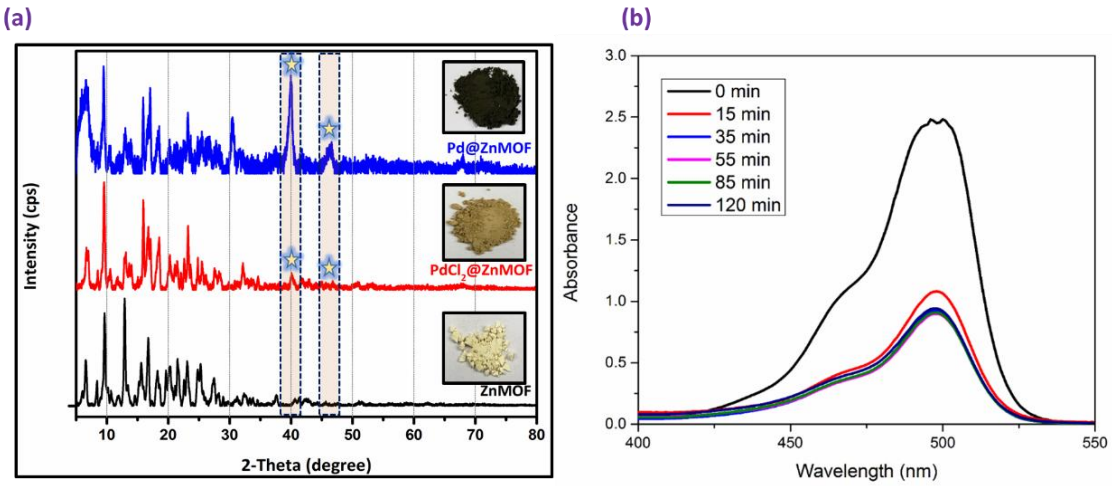

Figure 3.109. (a) Comparison of PXRD patterns of **Zn-MOF**(**37**) before and after encapsulation of nanoparticles, and (b) UV-Vis spectra of $PdCl_2$ at different interval of time after adding **Zn-MOF** (**37**).

The retention of crystalline nature or framework was confirmed by the powder X-ray diffraction analysis. Comparing the PXRD patterns of both **Zn-MOF** (**37**) and **$PdCl_2$@Zn-MOF** with the **Pd@Zn-MOF** clearly indicates the retention of the framework before and after incorporation of nanoparticles (Figure 3.109). On the other hand, the appearance of the peaks corresponding to the Pd(0) along with the framework peaks, confirms the presence or formation of palladium nanoparticles. For the encapsulation of $PdCl_2$ up to saturation, **Zn-MOF** (**37**) was poured into the methanolic solution of the $PdCl_2$ solution and stirred for 1 h. During stirring, the reaction mixture was observed by the UV-Vis analysis, which showed that after 35 minutes there was no change in the spectrum, indicating the saturation of MOF with $PdCl_2$ (see Figure 3.109). After successful implementation of the nanoparticles in 3D Zn-MOF (**37**), this compound was used as a heterogeneous catalyst in the reduction of nitrophenols, Knoevenagel condensation reaction and one-pot cascade N-alkylation reaction (tandem reaction).

Catalysis Studies with Pd@Zn-MOF (37). The metal organic coordination networks (MOCNs) have recently been applied in heterogeneous catalysis and catalyst for several organic reactions. Coordination polymers can work as catalysts through two different components, viz. the metal center, which either provide the coordinatively unsaturated nodes and/or form the active metal sites or by integrated functionality with organic

linker/ligands. Depending on the nature of the ligands and its binding to metal ions, coordination polymers can act as Lewis acid or base in the catalytic medium.[222,235–242]

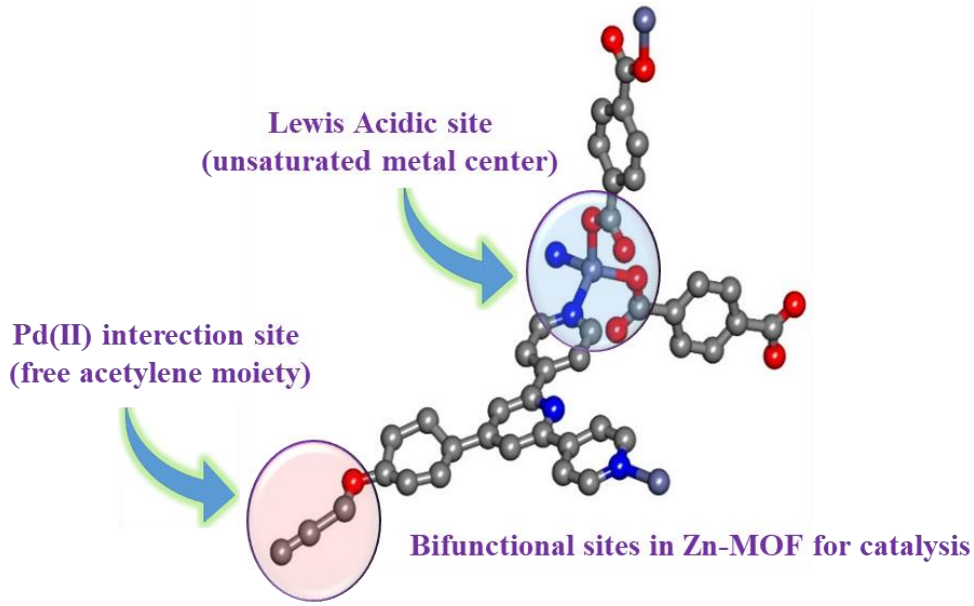

Figure 3.110. Two different sites present in **Zn-MOF** (**37**) for catalysis.

After nanoparticles fabrication, **37**, a Zn(II) based 3D MOF, has been employed for catalytic application. This MOF was designed in such a manner that it can be used as a bifunctional catalyst, so that it can be employed for different organic transformations. After crystal structure analysis, it was confirmed that this compound is a 3D porous compound having free acetylene functionality inside the pores. This predesigned strategy provides us the way to go forward to make it a bifunctional catalyst. As shown in Figure 3.110, metal has an unsaturated Lewis acidic site which helps in forwarding the Knoevengal reaction towards the product side with good efficiency. Along with this, by the successful implementation of Pd(0) nanoparticles inside the **Zn-MOF** (**37**), various palladium-catalyzed reactions can be achieved.

Reduction of nitrophenol. Reduction of nitrophenol was monitored by UV-Vis spectroscopy. In UV-Vis spectrum, nitrophenol gives a peak around 400 nm, on the other hand, there is no peak for aminophenol is observed in the visible region .[243] To confirm the conversion of nitrophenol to aminophenol, the UV-Vis spectrum of nitrophenol solution in methanol was recorded, which gives a peak around 400 nm. Furthermore, catalyst and sodium borohydride were added and stirred for 15 min; after filtration, UV-Vis spectrum of the filtrate was recorded again. The disappearance of the peak corresponding to the nitrophenol confirmed the formation of amino phenol as shown in Figure 3.111.

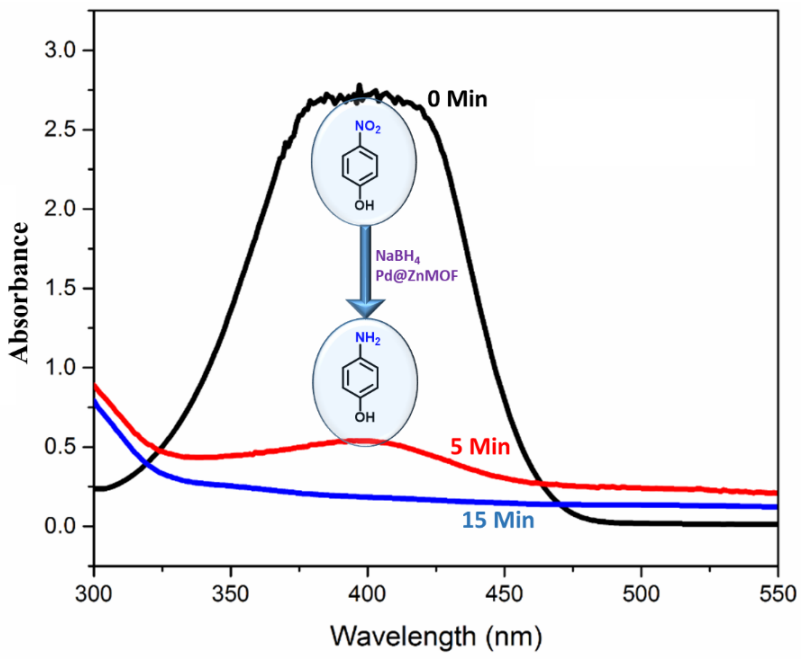

Figure 3.111. Reduction of nitrophenols using a **Pd@Zn-MOF** catalyst followed by UV-Vis spectroscopy.

This exciting result encouraged us to go forward to perform cascade reaction to synthesize reduced Schiff base in one step from nitro compound and aldehydes. First, it goes through in-situ reduction of the nitro group in the presence of catalyst and sodium borohydride, followed by Schiff base condensation and finally gets reduced to the final product. In the literature, these type of reactions are mainly reported using H_2 gas as a reducing agent, while it is rarely reported in the literature to use sodium borohydride as a hydride source. So, we have employed sodium borohydride as a reducing agent in the presence of a catalyst for the Tandem reaction (cascade reaction).

Cascade one pot Reductive N-alkylation reactions. The reductive N-alkylation of nitrobenzene with aldehyde was carried out at room temperature. Typically, an aldehyde (0.5 mmol), nitrobenzene (0.55 mmol) and $NaBH_4$ (6 mmol) were added in MeOH followed by addition of **Pd@Zn-MOF** (2 mg) in a screw-capped glass vial. The reaction mixture was stirred at room temperature for 2 h. After completion of the reaction, catalyst (**Pd@Zn-MOF)** was filtrated off through a filter paper and washed with water (2.0 mL). In the filtrate, 2 mL ethyl acetate was added, and the product was extracted with ethyl acetate, which was further dried over anhydrous sodium sulfate and after filtration, the solvent was evaporated under reduced pressure to get a slurry of the product which was further used for the ^{1}H NMR analysis without any purification. ^{1}H NMR technique is used for the calculation of conversion% as well as the purity of the product. Some control

experiments have been carried out to find out the proper reaction conditions because many factors like temperature, solvents and amount of catalyst affect the formation of the product.

Table 3.20. Cascade condensation reaction between benzaldehyde and nitrobenzene derivatives with **Pd@Zn-MOF** at room temperature (27 °C).

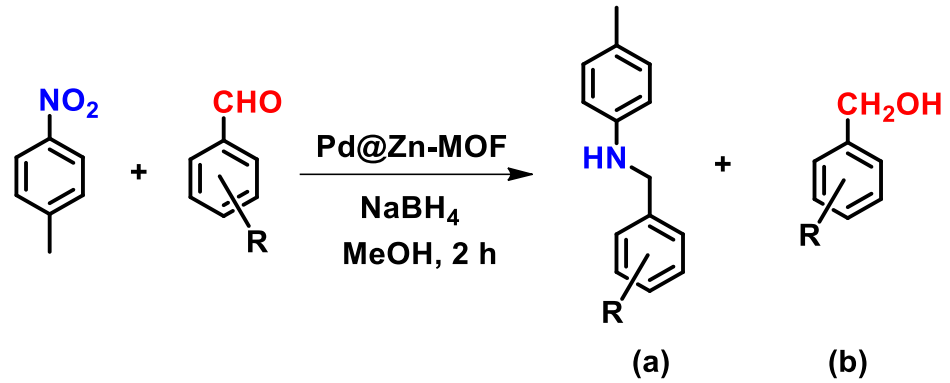

Entry	-R	Product	Conversion (%)
1	H	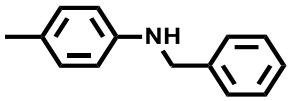	>99
2	3-Cl	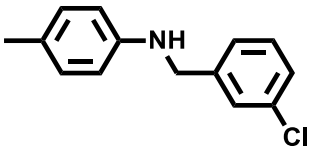	>99
3	4-F	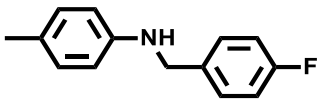	>99
4	4-CH_3	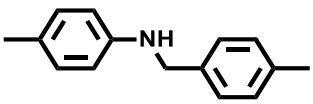	>99
5	Ph	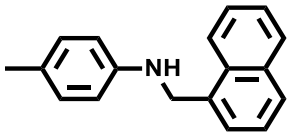	>99

Conversion was calculated by ^{1}H NMR.

From the control experiment, by changing the solvent and amount of catalyst, it was found that in methanol having 2 mg of catalyst, the reaction ends up with >99% conversion with good purity. Along with this, to check the substrate scope, different derivatives of aldehyde have been used. The results obtained from these experiments indicate >99% conversion in

all cases with good purity. Furthermore, this result indicates the excellent capability of this catalyst in the formation of different products (Table 3.20).

Knoevenagel condensation reaction. Lewis acidic or basic nature of the catalyst is responsible for the Knoevenagel condensation reaction. Various homogeneous, as well as heterogeneous catalysts, are reported in the literature to achieve this condensation reaction.[75,244] To explore more, we have used the same **Pd@Zn-MOF** catalyst for this condensation reaction. As we have discussed, Zn(II) has an unsaturated site which acts as Lewis acid to perform this type of reaction. This reaction was performed by using benzaldehyde (0.1 mmol) and malononitrile (0.15 mmol) by stirring for 2 h in methanol and water (1:1) by adding 2 mg of the catalyst. The mixture was then centrifuged and filtered to remove the solid catalyst; the filtrate was evaporated under reduced pressure to give the crude product. The product was extracted with ethyl acetate, and the resulting slurry was used for the ^{1}H NMR analysis without any further treatment. The conversion and purity of the product were confirmed by ^{1}HNMR and GC analysis. A systematic investigation was done to find out the proper reaction condition by changing the solvent (Table 3.21).

After optimization of reaction conditios, that is, stirring at room temperature using water and methanol (1:1) mixture as a solvent for 2 h, substrate scope using different derivatives of aldehydes was demonstrated. For the GC analysis, crude sample dissolved in ethyl acetate was injected to injector port of GC having temperature 300 °C. In the starting, column temperature was kept 60 °C, while it was increased to 120 °C by a heating rate of 30 °C/min. After that, it was heated to 170 °C at a rate of 2 °C/min, further, in the end, it was heated up to 300 °C with a heating rate of 50 °C/min. Conversion% was then calculated by integrating the area of the product and reactant peaks in the gas chromatogram. The peak of aldehyde was used as a reference in both GC and ^{1}H NMR analysis to calculate conversion%.

Table 3.21. Effect of different solvents on conversion% of the reaction.

S. No	Time	Solvent	Conversion%
1.	2 h	MeOH	>99
2.	2 h	H_2O	95
3.	2 h	H_2O: MeOH	>99

As we have discussed that this type of condensation reaction is dependent on the Lewis acidic site present in the MOF, we have explored the same reaction with the **Pd@Zn-MOF**

as well as with the **Zn-MOF** (**37**) under the same reaction conditions. It was observed that both the catalysts, behave similarly with respect to the conversion of reactant to the product. Both the results are compared in the Table 3.22 (below) which gives almost similar behavior.

Table 3.22. Knoevenagel reaction between benzaldehyde and nitrobenzene derivatives with **Pd@Zn-MOF** and **Zn-MOF** (**37**) at room temperature (27 °C).

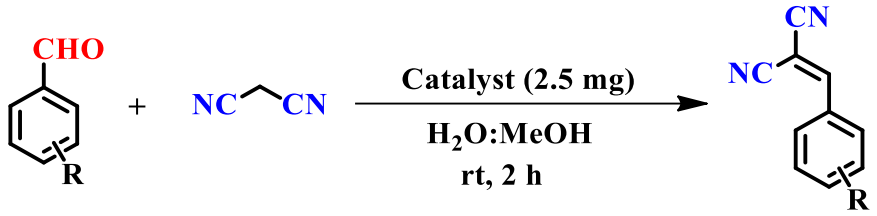

Entry	-R	Product	Conversion (%) (Pd@Zn-MOF)	Conversion (%) (Zn-MOF)(37)
1	H	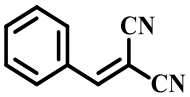	97	>99
2	3-NO_2	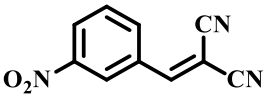	97	98
3	4-NO_2	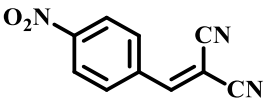	98	91
4	3-OH	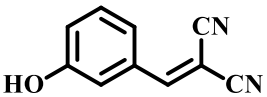	94	95
5	3-Cl	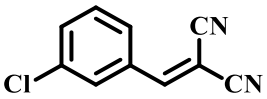	98	>99
6	4-F	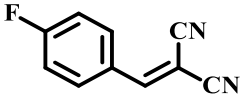	>99	>99
7	4-OMe	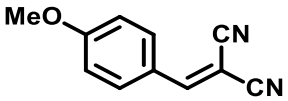	>99	>99
8	4-CH_3	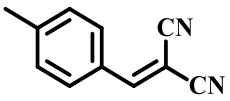	99	>99

Conversion% was calculated by GC analysis.

This result clearly reflects that Pd nanoparticles is not playing any role, while the Lewis acidic site (unsaturated metal node) is playing a crucial role in this conversion. We can use

both the compounds with and without nanoparticles for getting this condensed product in good yield. Therefore, we can use nanoparticle loaded catalyst s for both the reaction like cascade N-alkylation as well as Knoevenagel condensation reactions. This result proves that this catalyst acts as a bifunctional catalyst in which two different active sites are present, and both the sites are used for different type of organic transformations as per the requirement of the catalytic reaction.

Hot filtration test (leaching experiment). To confirm the heterogeneity of the catalyst, hot filtration experiment was conducted. An experiment was set up in which the catalyst was removed from the reaction mixture after 20 min by filtration. From the analysis of the reaction mixture, it was observed that a 65% conversion was achieved up to this time (calculated by GC). After that, the reaction mixture (without catalyst) was kept for further stirring at same reaction conditions and every 25 min, an aliquot from the reaction mixture was taken out and used for GC analysis. This was further stirred for 160 min after removing the catalyst. As shown in Figure 3.112, after removal of the solid catalyst, there is no significant change in the conversion% of the product, demonstrating that the catalysis is heterogeneous in nature and there is no leaching taking place into the solution during the reaction.

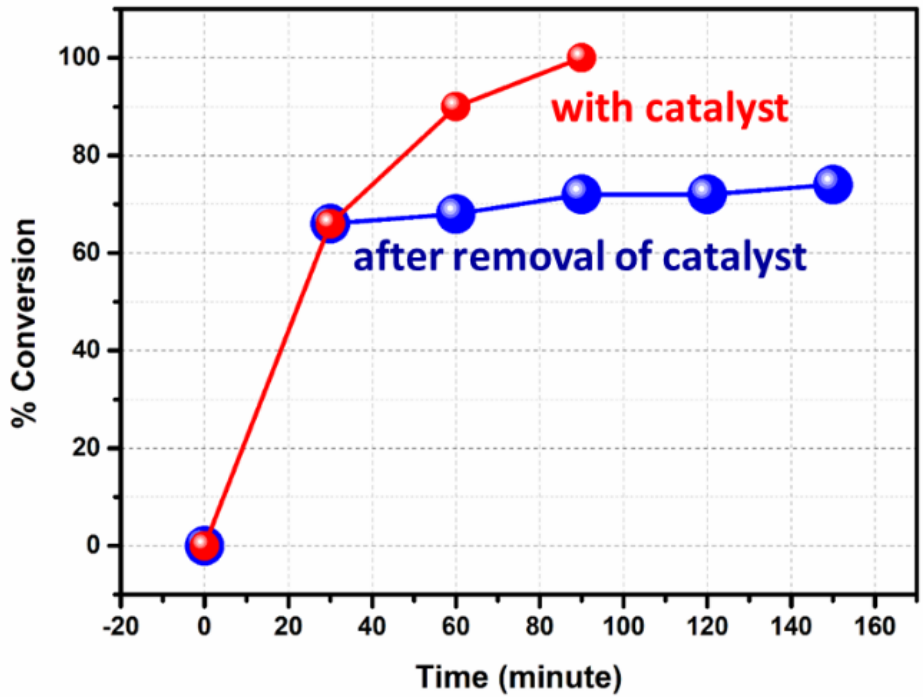

Figure 3.112. Plot between %conversion and time of the reaction without catalyst confirming the heterogenicity of the catalyst (**Pd@Zn-MOF**).

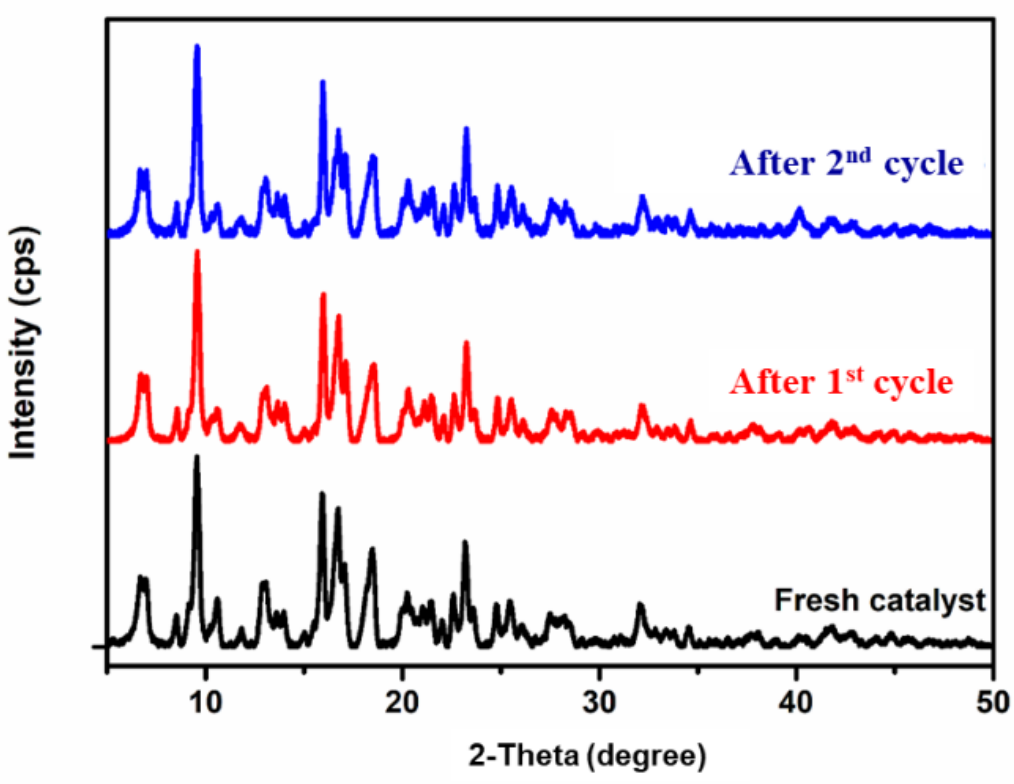

Figure 3.113. Comparision of PXRD patterns of fresh catalyst and catalyst left first and second catalytic cycles confirm the stability of the catalyst.

Reusability of the **Pd@ZnMOF**. The catalyst **Pd@Zn-MOF** is easily recoverable by filtration and can be reused further for another catalytic cycle without any significant loss of catalytic activity. After the completion of the first reaction cycle, the catalyst was recovered by centrifugation and then washed thoroughly with methanol and water (1:1), followed by drying in air. Furthermore, the stability of the recovered catalyst after the first and second cycle was confirmed by PXRD analysis (Figure 3.113).

3.1.4 Functionalized pyridyl ligand and tricarboxylates

Two tridentate ligands 2,2′-terpyBA and 4,4′-terpyBA were used in the previous section to synthesize various coordination architectures in combination with different dicarboxylates. In this section, we have replaced the dicarboxylates with tricarboxylates to enhance the dimensionality and nature of pores.

Chemistry with 2,2′-terpyBA

Using 2,2′-terpyBA, four coordination architectures have been synthesized using 1,3,5-benzenetricarboxylate (H_3btc) under ambient conditions in a mixed solution of DMF, H_2O and EtOH (1:1:1 ratio) using metal, ligand, and linker in a 3:3:2 ratio as shown in Scheme 3.20. Crystals of some of these compounds have been grown by the slow diffusion of the reactants dissolved in different solvents.

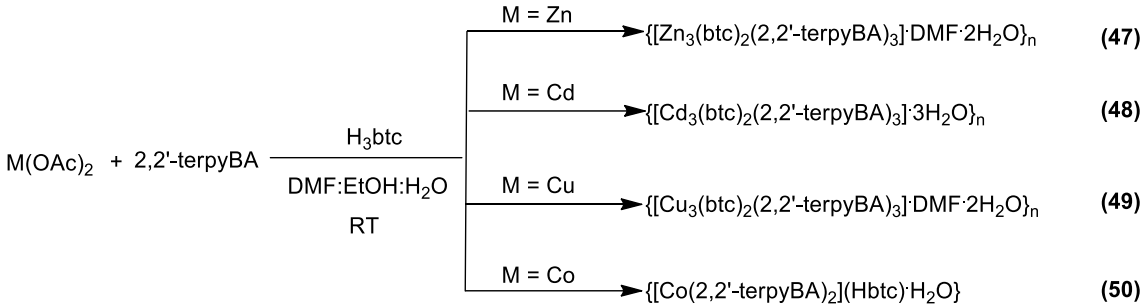

Scheme 3.20. Synthesis of **47**-**50**.

FTIR Spectroscopic studies. All the compounds clearly show a peak for the free acetylene group around 2108 cm^{-1}-2118 cm^{-1}.. In FTIR spectra od **47-49** monodentate mode of binding ofor the carboxylate was observed(Figure 3.114), with a difference between asymmetric and symmetric stretching greater than 230 cm^{-1} (Table 3.23). For compound **50,** along with the monodentate mode of binding of the carboxylate, a peak around 1660 cm^{-1} confirms the presence of free carboxylate.

Table 3.23. Asymmetric and symmetric stretching frequencies and their respective binding modes of carboxylates of **47**-**50**.

Compound	Asymmetric (υ_1) cm^{-1}	Symmetric (υ_2) cm^{-1}	$\Delta\upsilon = \upsilon_1 - \upsilon_2$ cm^{-1}	Binding mode
47	1618	1362	256	Monodentate
48	1610	1369	241	Monodentate
49	1602	1361	241	Monodentate
50	1625	1371	254	Monodentate
		1660	Free carboxylate	

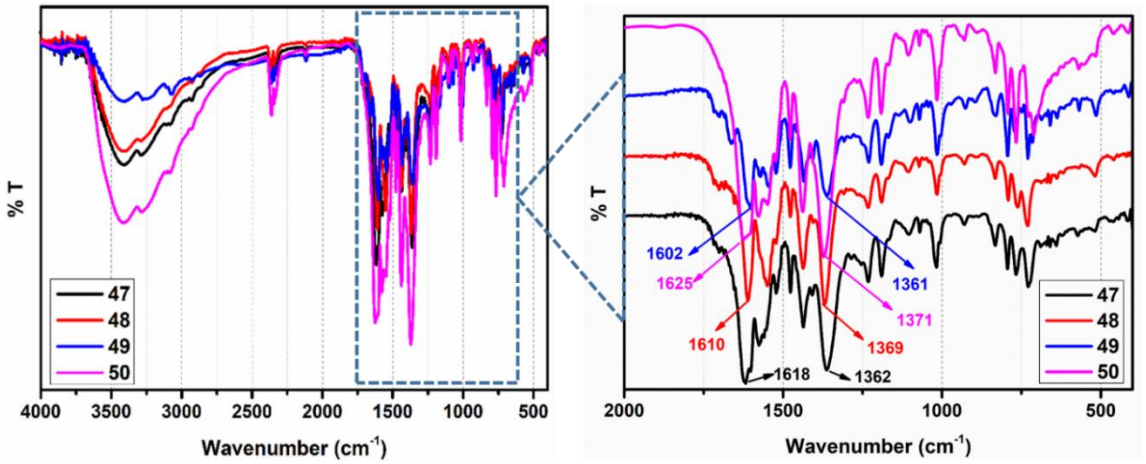

Figure 3.114. FTIR spectra of **47-50**.

Thermogravimetric analyses. Thermal stabilities of **47-50** were studied as a function of temperature in the range of 25-450 °C. Except **48**, other compounds exhibit a two-step weight loss. The first weight loss is up to 200 °C due to the loss of lattice solvent molecules followed by a sharp weight loss after 350 °C corresponding to the decomposition of framework. TGA scan of **47**, exhibits a loss of 6.02% corresponding to the loss of one DMF and two water molecules (ca. 6.35%) followed by decomposition of metal complex, while **48** exhibits the first loss of 24.48% corresponding to the loss of two btc and three water molecules (ca. 25.95%).

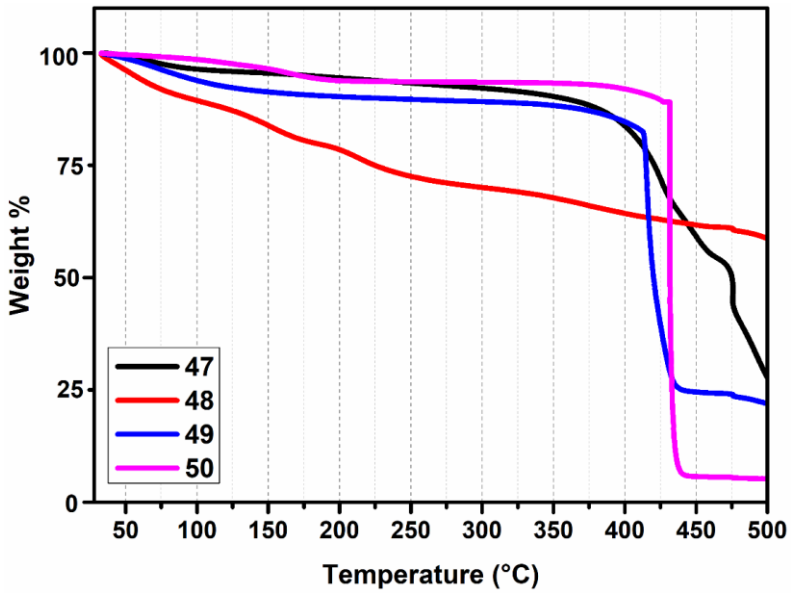

Figure 3.115. TGA scans of **47-50**.

Further, **49** shows a loss of 9.71% corresponding to the loss of two DMF and two water molecules (ca. 9.16%), while **50** exhibiting a loss of 2.77% corresponds to the loss of one

water molecule (ca. 2.08%). After comparing the thermal stabilities of these compounds, it was found that **48**, shows less thermal stability than other compounds (Figure 3.115).

Single crystal structure analyses. Crystals suitable for single crystal analysis of some compounds were grown by the direct layering of reactants dissolved in different solvents (water, EtOH and DMF). For this, two solutions of reactants are layered very carefully in thin glass tubes by putting a buffer solution (water and EtOH 1:3) between two reactants. After few days at the junction of two solutions, crystals was observedwere formed, which were used for SCXRD analysis.

Structural description of **50**. This compound crystallizes in the triclinic *P*-1 space group. The Co(II) metal has a perfect octahedral geometry and generates aN6 type of surrounding environment around the metal center. As shown in the Figure 3.116, metal is hexacoordinated, and all the binding sites are occupied by the six nitrogen atoms from the two ligands with distances (Co-N_{alkyl}: 1.712(4) Å and 1.696(4) Å; Co-N_{py}: 1.795(4) Å, 1.781(4) Å, 1.799(4) Å, and 1.789(4) Å). All the bond distances and angles are listed in Table A29 and A40 (Appendix). The ligand has a strong capping tendency to bind with the metal, thereby leaving little (negligible) scope for the linker (carboxylate) to approach the metal center. As a result, a cationic complex is formed, and a free linker acts as anion to neutralize the overall structure. Asymmetric unit consists of a metal, two ligands and one Hbtc linker as shown in the Figure 3.116. As the metal carries a two-positive charge, in order to neutralize it, two carboxylic acid get deprotonated, while the third one remains in carboxylic acid form.

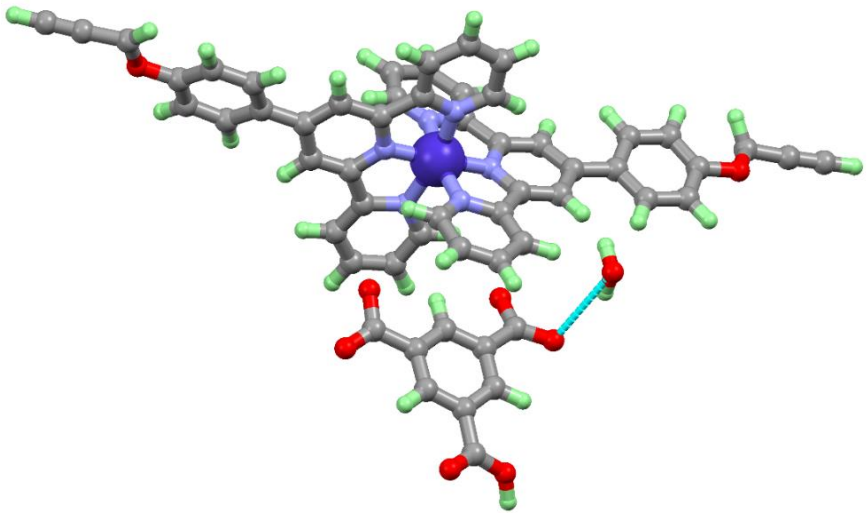

Figure 3.116. Coordination environment around the metal center in **50**.

In addition to this, a lattice water molecule is also present which forms hydrogen bonding with the deprotonated carboxylic acid of the linker. This water molecule does not help in the formation of 3D supramolecular structure although it forms H-bonding, with the carboxylate group using only one hydrogen, while the other hydrogen and oxygen do not participate in the H-bonding. In the formation of a 3D supramolecular network, weak interactions like π–π stacking and H-bonding play a very important role. As we have discussed, there is no role of H-bonding in the formation of 3D supramolecular assembly, although one lattice water molecule is present. A strong π–π slipped centroid to centroid interaction between aromatic rings plays a very important role to generate a 3D supramolecular assembly.

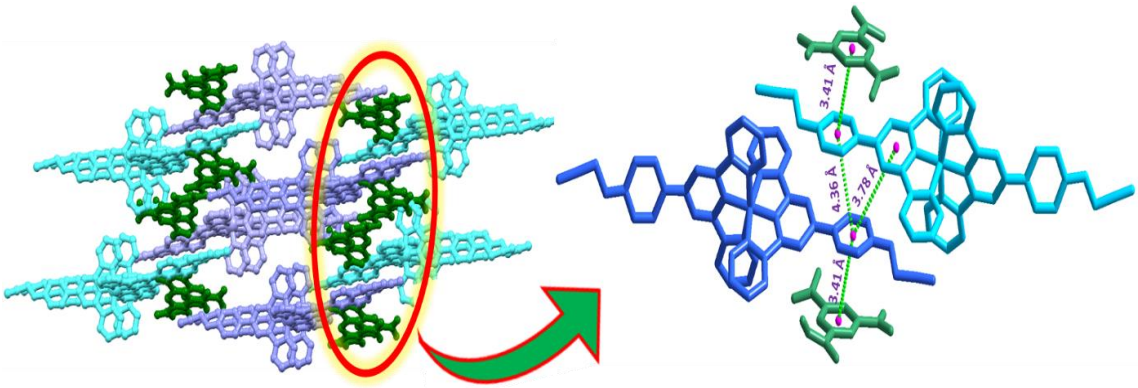

Figure 3.117. Depiction of π–π bonding and formation of 3D supramolecular assembly in **50**.

As shown in the Figure 3.117, benzene ring of Hbtc exhibits a strong π–π interaction with the benzene ring of the ligand having a distance of 3.41 Å. Furthermore, the benzene ring of the ligand forms strong π–π interaction with the benzene (4.36 Å) and pyridyl (3.78 Å) ring of another corresponding ligand and *vice-versa*. A network of this π–π interaction in different direction helps in generating a supramolecular three dimensional assembly.

Powder X-ray diffraction studies. Crystalline nature of all the synthesized coordination networks was confirmed by powder X-ray diffraction studies. As shown in figure 3.118, similarity in the powder patterns of **47-49** indicates the formation of similar compounds. Furthermore, PXRD patters of **50** is different compared to other compounds of this series. Powder patterns also indicate the phase purity of the compounds as simulated powder pattern of compounds shows good agreement with the experimental pattern.

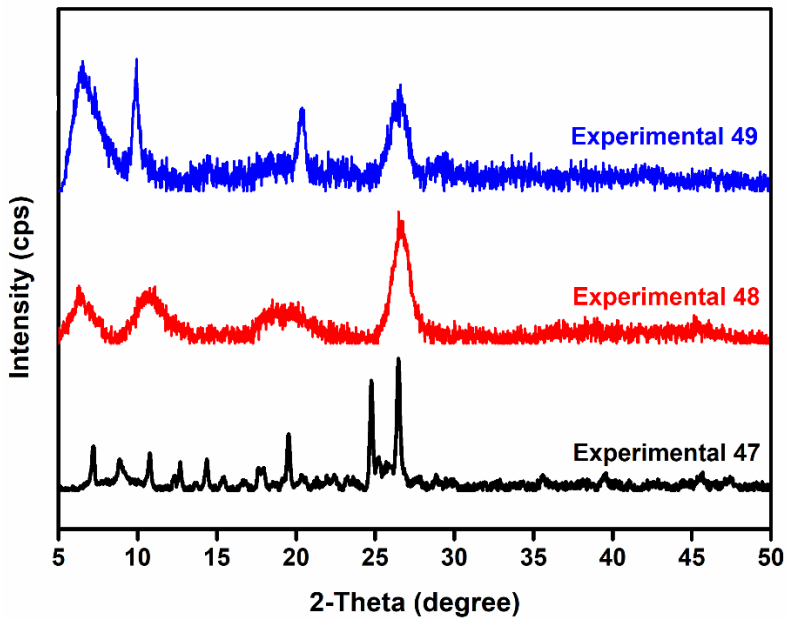

Figure 3.118. PXRD patterns of **47-50**.

Luminescence properties of 47-50. As shown previously, terpyridine based MOFs have shown good fluorescence upon interaction with the metal center. These compounds (**47-50**) are synthesized by using tricarboxylate instead of dicarboxylate and similar to fluorsence properties of compounds dicussed above, the spectra of these MOCNs were also obtained in a water slurry. Luminescent nature of terpyridine based MOCNs is due to charge transfer within the ligand. Somehow, a ligand to metal charge transfer is also involved in imparting fluorescent nature to the compound. From the results obtained, it was found that Zn(II) exhibits fluorescence of higher intensity than other compounds having different metal centers (see Figure 3.119).

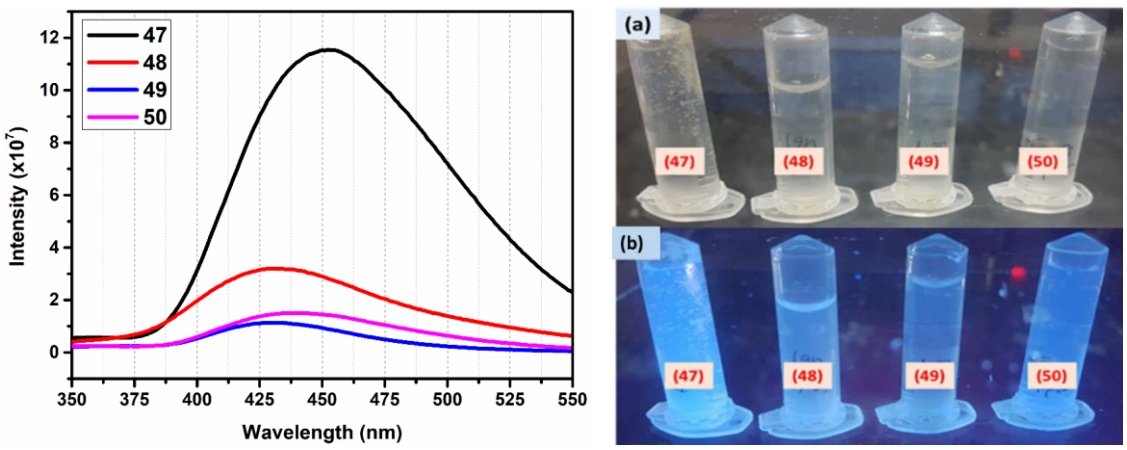

Figure 3.119. Fluorescence spectra of **47-50** and change in color in visible (a) and UV-light (b).

Chemistry with 4,4′-terpyBA ligand

Compared to 2,2′-terpyBA, the position of the nitrogen atoms have been changed from *ortho* to *para* position in 4,4′-terpyBA. This change in ligand break the monotony of the capping ligand and acts as a linker using only two pyridyl nitrogens. In this case, we have chosen a tricarboxylate linker instead of dicarboxylates. The synthesis of all these metal complexes is shown in Scheme 3.21.

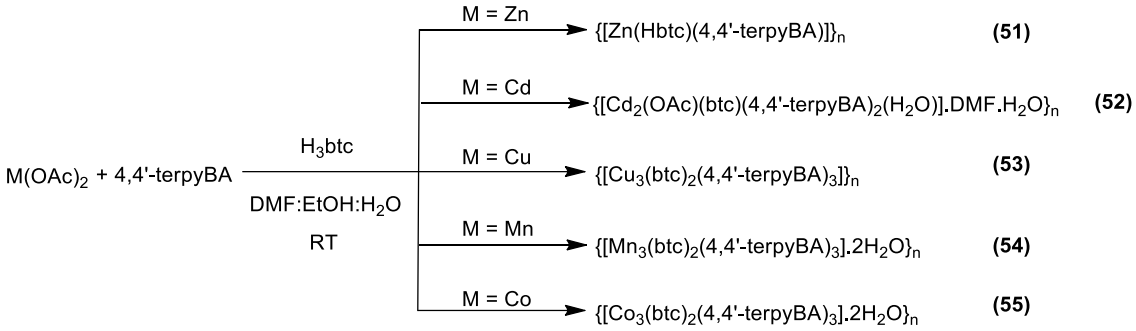

Scheme 3.21. Synthesis of **51-55**.

FTIR Spectroscopic studies. All the compounds clearly show the peak of free acetylene group around 2108 cm^{-1} and 2118 cm^{-1} indicating the presence of the terminal acetylene moiety in all the compounds.. From FTIR analysis, it was found that **51-55**, show monodentate binding mode of carboxylate except for one additional feature in **52**, which confirms the bidentate mode of carboxylate as well (Table 3.24). A peak around 1662 cm^{-1} in **52**, corresponding to the presence of lattice DMF molecules (Figure 3.120).

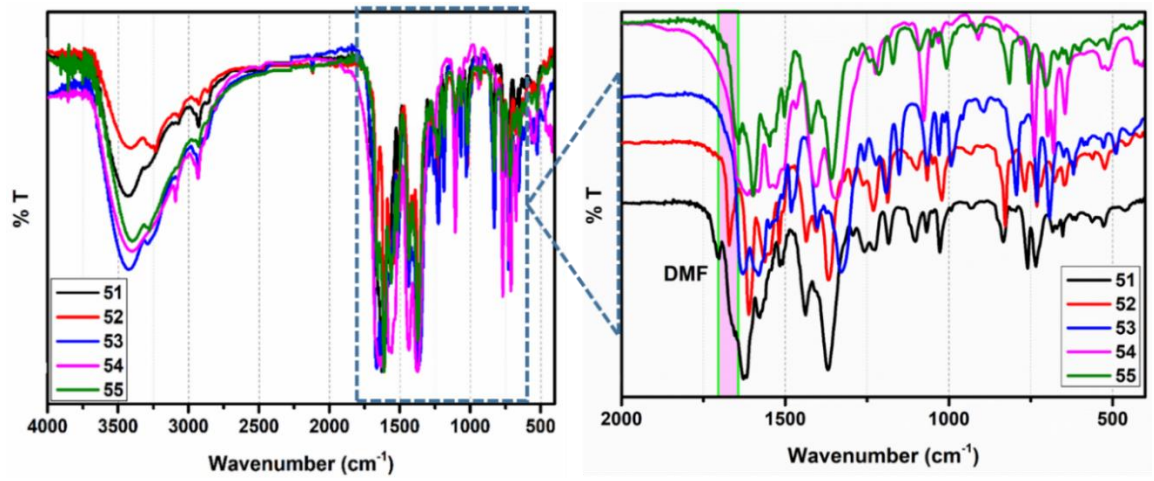

Figure 3.120. FTIR spectra of **51-55**.

Table 3.24. Asymmetric and symmetric stretching frequencies and their respective binding modes of carboxylates of **51-55**.

Compound	Asymmetric (υ_1) cm^{-1}	Symmetric (υ_2) cm^{-1}	$\Delta\upsilon = \upsilon_1 - \upsilon_2$ cm^{-1}	Binding mode
51	1627	1369	258	Monodentate
52	1609 1561	1366 1434	243 127	Monodentate Bidentate bridging
53	1616	1363	253	Monodentate
54	1628	1374	254	Monodentate
55	1610	1372	238	Monodentate

Thermogravimetric analyses. In TGA analysis of **51**, a two-step profile of weight loss was observed. First loss of 16.23% in **51** between 50 °C to 220 °C corresponds to the loss of one btc molecule (ca. 16.42%). After this, decomposition of the compound takes place. Similarly for **52**, weight loss of 9.44% between 50 °C to 200 °C corresponding to the loss of three water molecules and one DMF molecule (ca. 8.29%). Apart from this, **53**, exhibits a three-step profile of weight loss. The first loss about 24.42% corresponds to the loss of one btc molecule (ca. 23.55%).

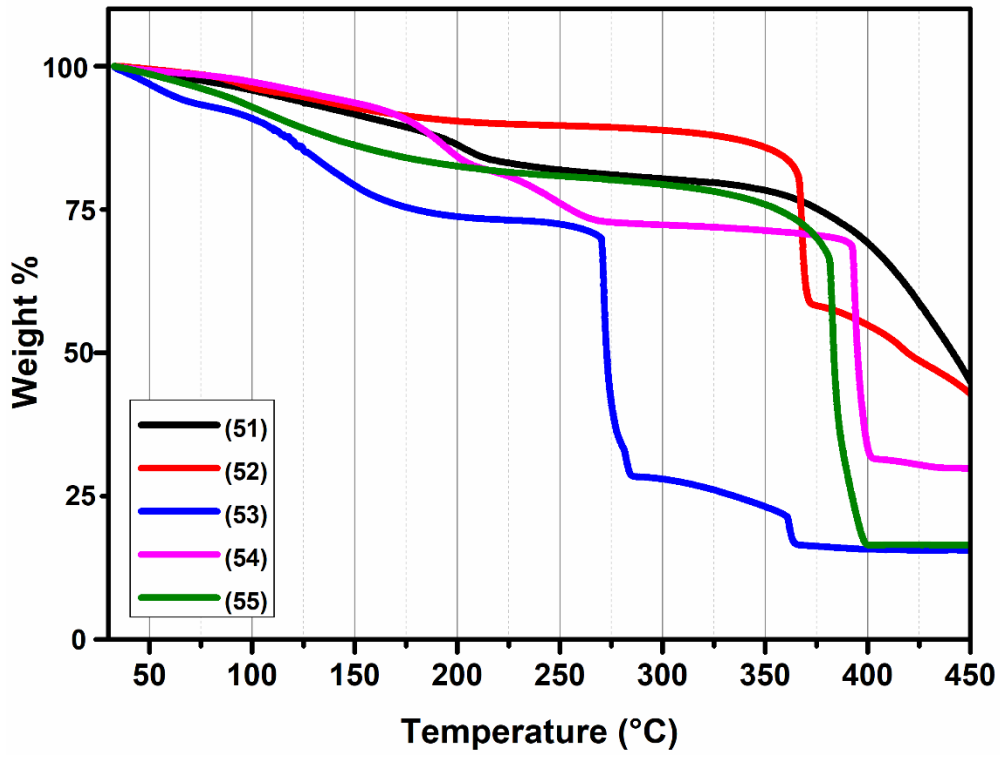

Figure 3.121. TGA scans of **51-55**.

Further in two steps, decomposition of the framework takes place. Compound **54** exhibits a weight loss of 26.39% corresponding to the loss of two btc and two water molecules (ca.

26.57%). Compound **55** exhibits a weight loss of 14.15% corresponding to the loss of two water molecules (ca. 15.45%) followed by the decomposition of metal complexes. After losing the solvent molecules, all the compounds are stable up to 300 °C, except **53**, which shows thermal stability up to 250 °C (Figure 3.121).

Single crystal structure analyses. Crystals suitable for single crystal analysis of **51** and **52** were grown by the direct layering of the reactants dissolved in different solvents (water, EtOH and DMF). For this, two solutions of reactants are layered very carefully in the thin glass tubes putting a buffer solution (water and EtOH 1: 3) between the two. After a few days, at the junction of the two solutions, the formation of crystals takes place and directly used for single crystal analysis.

Structural description of **51**. It crystallizes in triclinic $P2_1/n$ space group. The asymmetric unit consists of a central metal atom (Zn(II)), one ligand (4,4-terpyBA) and one Hbtc linker. Central metal accommodates a distorted octahedral geometry surrounded by four oxygens of two different Hbtc (distances: 2.022(5) Å, 2.457(5) Å, 2.386(4) Å, and 2.066(4) Å) and two nitrogens of the two different ligands (distances: 2.070(4) Å and 2.076(4) Å) which results in an N2O4 type surrounding around metal center.

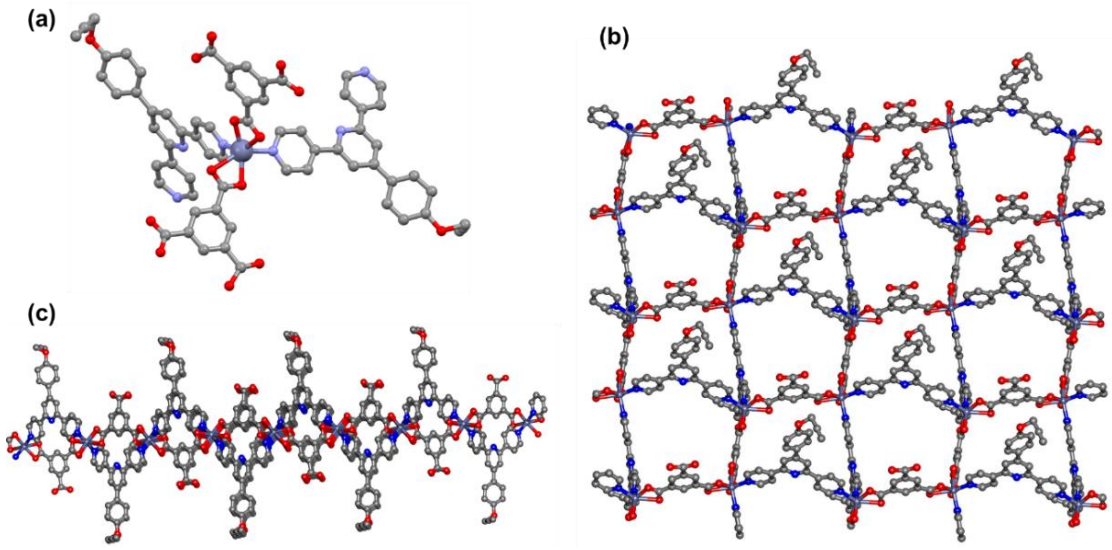

Figure 3.122. (a) Coordination environment around metal center, (b) formation of a 2D coordination network and (c) view along a-axis showing the presence of functionalities in an alternative fashion in **51**.

Two out of three carboxylic groups of benzene tricarboxylic acid show the bidentate chelated mode of carboxylate binding with a metal center while the remaining one is in protonated carboxylic acid form. After expansion of the asymmetric unit, a 2D network is formed. Both the surfaces of this compound have two functionalities: one is free acetylene,

and another one is a carboxylic acid. These functionalities are present in an alternation fashion and are opposite to each other (Figure 3.122). Both the organic parts act as a linker in the formation of this 2D coordination network. A rectangular pore has been generated using four metal centers, two ligands and two Hbtc having dimensions 15.617 x 15.964 $Å^2$.

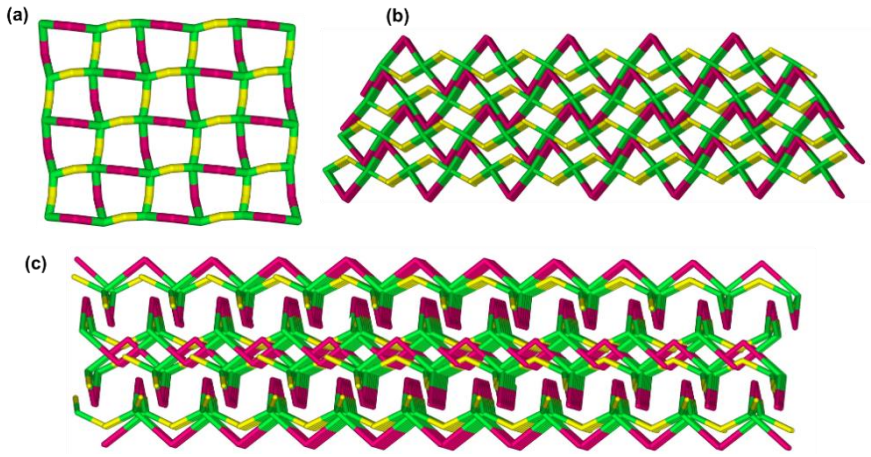

Figure 3.123. Topological view of **51** in three different directions.

As functionality is present on the surface, so it can be used for various surface applications like catalysis, sensing, and post-synthetic modification. A 4-c net; uninodal net (sql/Shubnikov tetragonal plane net) topology is generated having a point symbol $\{4^4.6^2\}$ for the net (Figure 3.123).

Structural description of **52**. Single crystal structure analysis reveals that **52** crystallizes in the monoclinic $P2_1/n$ space group. It contains two different types of Cd(II) centers: one is hexacoordinated with N2O4 surrounding, and the other is heptacoordinated with the N2O5 type of surrounding environment. In the asymmetric unit along with these two Cd(II) centers, two ligands, one btc, one coordinated acetate group, and two lattice molecules (one water and one DMF) are present (Figure 3.124). The distance between the two metal centers is around 3.793 Å. Both the metals have two nitrogen atoms from the different ligands which are anti (axial) to each other. The Cd1 which is hexacoordinated has two nitrogens from two different ligands (distances 2.299(4) Å and 2.305(4) Å), one oxygen from the btc carboxylate (monodentate) with distance 2.271(4) Å, one coordination water (distance 2.308(4) Å), one bridging oxygen from acetate (distance 2.292(3) Å) and one oxygen from the bridging carboxylate of btc (2.420(3) Å). Cd2 is heptacoordinated surrounded by two nitrogen from two different ligands (anti to each other) with distances 2.315(4) Å and 2.349(4) Å, one oxygen from btc carboxylate (monodentate) with distance 2.270(3) Å, two oxygen atoms from the acetate (having distances 2.555(3) Å and 2.479(3) Å) which shows

bidentate chelating mode of binding and two oxygens from another btc carboxylate (having distances 2.481 Å and 2.553 Å) showing bidentate chelation as well as bridging mode of binding.

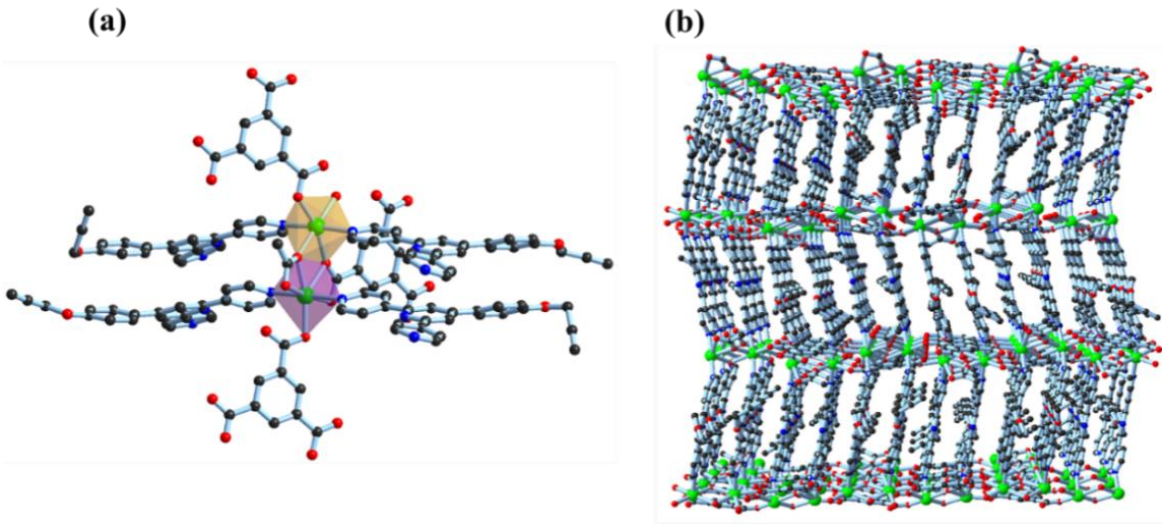

Figure 3.124. (a) Coordination environment around the metal center and (b) formation of a 3D coordination architecture in **52**.

In this complex, acetate shows the bidentate chelating mode of binding with one metal as well as one oxygen of the same acetate is bridging with another metal. Along with this, one carboxylate from btc shows the bidentate chelated type of binding with one metal as well as one oxygen of the same chelated carboxylate is bridging with the other metal. Considering the btc molecule in which two carboxylates show the monodentate mode of binding and the remaining one shows bidentate chelated as well as bridging mode. The bond length and bond angles have been listed in Table A29 and A40, respectively.

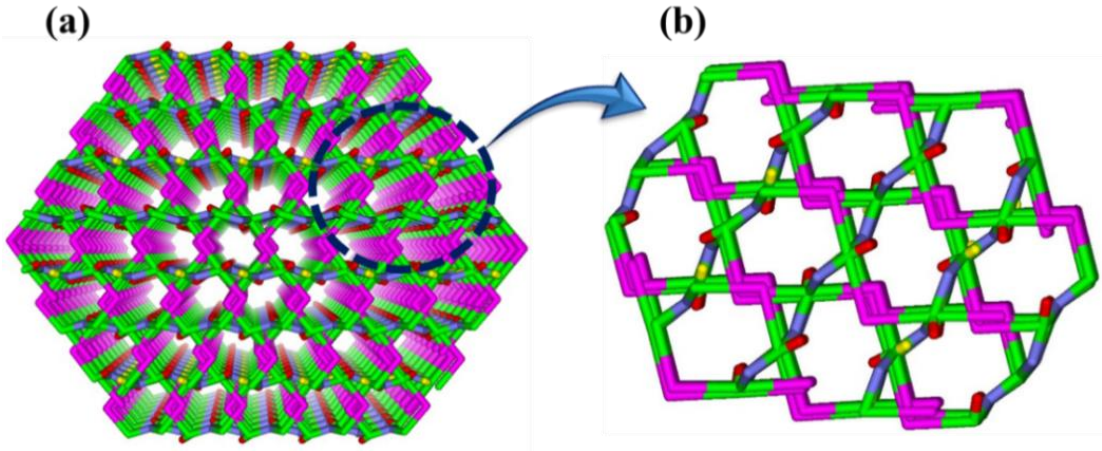

Figure 3.125. A topological view of **52**.

Overall by expanding the asymmetric unit, formation of a porous 3D network takes place. The dimensions of the pores are 13.452 x 8.542 $Å^2$. This compound shows an 8-c; uninodal net topology with the point symbol for the net: $\{3^6.4^{10}.5^{10}.6^2\}$ (Figure 3.125).

We have designed this ligand with acetylene functionality so that after formation of the metal complex the functionality remains free, thus can be used for various applications. As predicted, the free acetylene functionality is found to be situated inside the pores as confirmed by the single crystal structure analysis. Two different types of pores are present in which one of them have one free acetylene functionality, while the other has two.

Powder X-ray diffraction studies. Crystalline nature of all the synthesized complexes was confirmed by powder X-ray diffraction studies. A similar trend in the patterns obtained for **52-55**, wherease, **51** shows difference in paxrd patters, indicationg differenet type structural aspects compared to **52-55**. Powder pattern of **52,** is in good agreement with the simulated patterns, further confirming bulk phase purity of the compound (Figure 3.126).

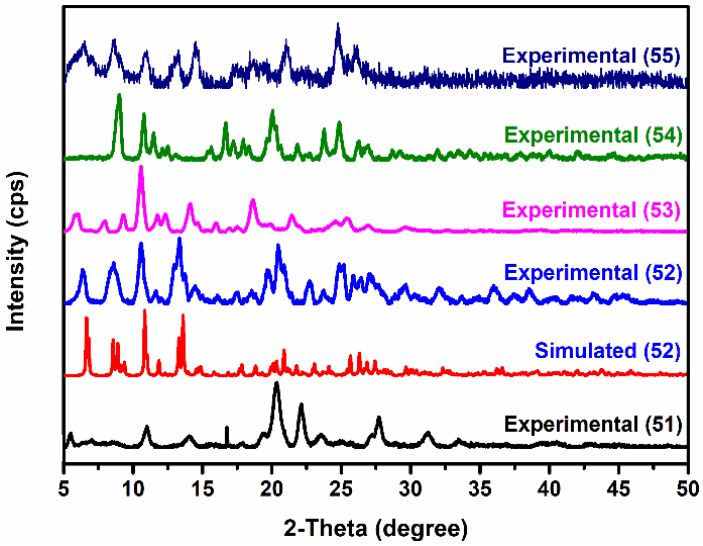

Figure 3.126. PXRD patterns of **51**-**55**.

Positional effect of the donor atoms in the ligand on the MOF structures. The powder X-ray diffraction studies of the synthesized compounds using 2,2′-terpyBA show similar patterns indicating the formation of similar type of frameworks. As 2,2′-terpyBA forms the same type of architecture with every metal center, so the position of donor nitrogen atom was changed from *ortho* to the para position of the ring and complexes were synthesized.. Due to the change in the position, 4,4′-terpyBA can also act as a linker or spacer also. This modification in the ligand leads to a tremendous change in the formation of architectures. As both cobalt(II) and cadmium(II) centers prefer six coordination,in both the cases, metal

is hexacoordinated but due to change in the position of nitrogen atom from two to four, the capping chelation site is not present, and the ligand acts as a linker between the two metal centers. Due to this capping chelation site, a cationic discrete complex having free anion was formed, on the other hand in the latter case, a porous coordination network has been formed (Figure 3.127).

A discrete unit of mononuclear compound was formed in **50**, which further forms a 3D supramolecular assembly due to the presence of π–π interaction between aromatic rings, while **51**, is a 2D coordination compound having a net-like structure. On the other hand, **52** is a 3D coordination network having different sizes of pores. In the prior case, the carboxylic group is not bonded to any metal and out of three groups in linker (btc), two are in deprotonated form while third remain same in protonated carboxylic acid form. In **51**, btc acts as a bidentate linker in which two carboxylic groups forms the coordinated bond with two different metal centers in bidentate chelated mode, while the third carboxylic group remains same in protonated carboxylic acid form.

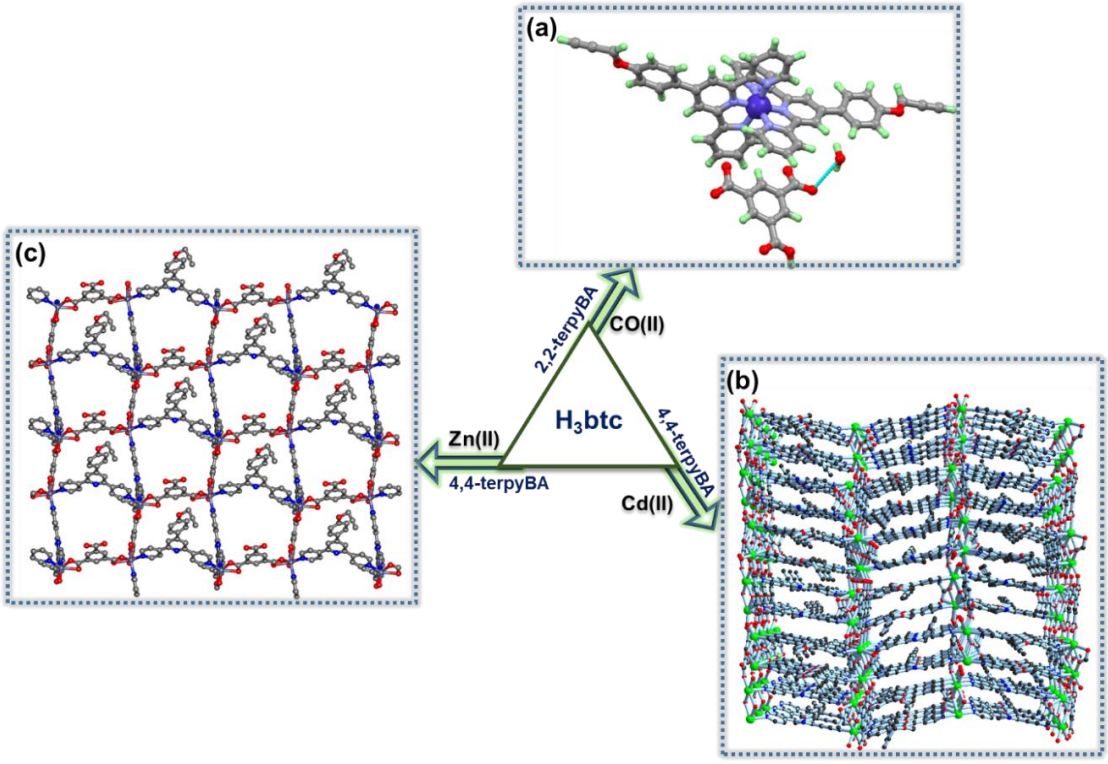

Figure 3.127. Diversification of the structure due to change in the ligand and metal center having tricarboxylate as a linker.

In addition to this, both the organic components act as a linker between two metal centers and result in the formation of a 2D network structure. The protonated non-bonded carboxylate and free acetylene moiety are the functional groups present on the surface of

this 2D network and make it a functionalized surface. Both the functionalities are present in an alternative fashion and are opposite to each other. While in case of **52**, carboxylate groups are bonded with the metal in both monodentate, bidentate as a well monodentate bridging mode. Unlike **50** and **51**, there is no free carboxylic acid group in **52**. Furthemore, an acetate group is also present which shows a bidentate as well as monodentate bridging mode between the two metal centers. The presence of free acetylene group and highly porous nature make **52**, a highly desirable material forapplications like guest encapsulation; hence this has been used for encapsulation of nanoparticles which was further used for various applications.

Sensing of Metal Ions by **Cd-MOF (52)**. Before performing metal ion sensing, the fluorescence intensity of **52** was analyzed in different organic solvents. In case of **Cd-MOF (52)**, 1 mg of compound was dispersed in different solvents like methanol, ethanol, acetonitrile, water, acetone and dimethyl sulfoxide (Figure 3.128).

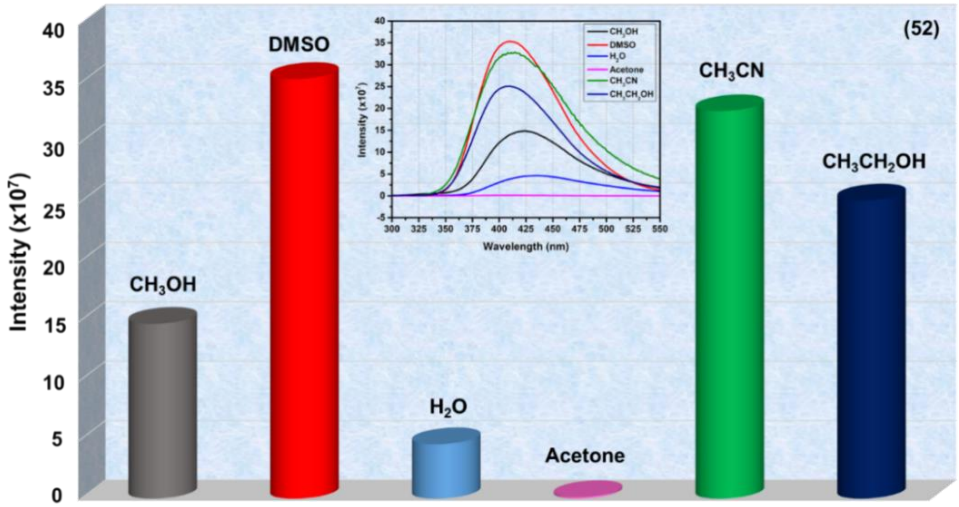

Figure 3.128. Emission intensity of **Cd-MOF** (**52**) in different solvents.

From this experiment, it was found that **52** (**Cd-MOF**) has shown fluorescence in water, therefore it was choosen as the solvent for further sensing experiments. To investigate the effect of addition of metal ions on fluorescence intensity of **52**, 1mg of the compound was dispersed in water. To this uniform dispersion, different metal ion (Na^{+}, Ag^{2+}, Ca^{2+}, Co^{2+}, Cd^{2+}, Ni^{2+}, Zn^{2+}, Mn^{2+}, Cr^{3+}, Fe^{3+}, Pb^{2+}, Pd^{2+}, Mg^{2+}) solutions (1mM, 190 μL) were added and suspension was stirred for 5 minutes and fluorescence spectrum was recorded. From the screening experiment, it was observed that, based on the nature cations, different kind

of interactions has taken place as the result both quenching and enhancement in the fluorescence intensity was observed (Figure 3.129).

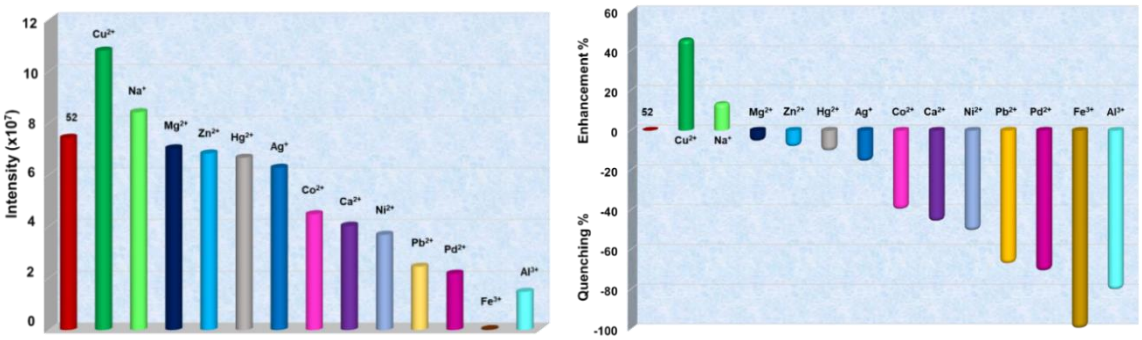

Figure 3.129. Change in the emission intensity of **Cd-MOF** (**52)** due to the influence of different cations in water (left) and quenching and enhancement percent with respect to different cations (right).

From the result, it was found that only metal ions like Na^{+} and Cu^{2+} show an enhancement in the fluorescence intensity, while other metal ions like Ca^{2+}, Co^{2+}, Cd^{2+}, Ni^{2+}, Zn^{2+}, Mg^{2+}, Ag^{2+}, Pb^{2+}, Hg^{2+}, Fe^{3+}, Pb^{2+}, $Pd^{2+}$and Al^{3+} have shown quenching in the fluorescence intensity of **52**. Among the cations showing quenching phenomenon, Fe^{3+}, quenches more than 99% of the fluorescence intensity.

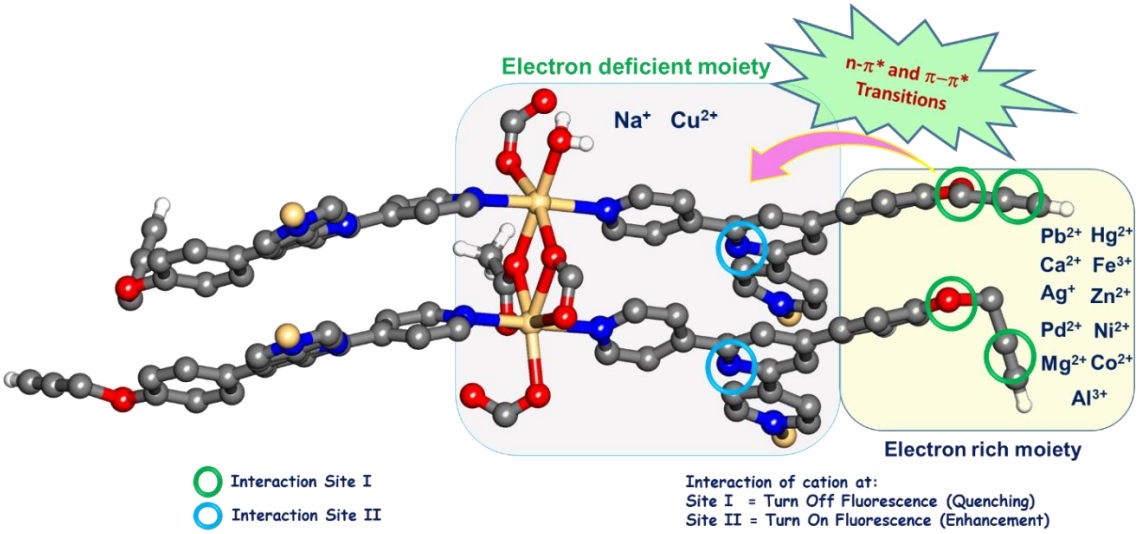

Figure 3.130. Possible interaction of the metal ion with the complex in **52**.

Single crystal structure of **Cd-MOF** (**52)** reveals that there are two interaction sites present (Figure 3.130). Interaction site I is a free acetylene moiety with oxygen near it providing additional support. While interaction site II is a free amine group of two different bdc linkers. This interactive site is formed due to the conformational arrangement of two amine

groups which are pointing towards each other such that they can easily interact with the incoming metal ions.

After binding of the terpyridine based ligand with Cd(II), one part of the ligand becomes more electron deficient due to the ligand to metal electron transfer, while another part which is an electron-rich part transfers charge to the electron deficient part. Possibly, cations like Ag^{2+}, Pb^{2+}, Hg^{2+}, Fe^{3+}, Pb^{2+}, Pd^{2+}, Ca^{2+}, Co^{2+}, Cd^{2+}, Ni^{2+}, Zn^{2+}, $Mg^{2+}$and Al^{3+} interact with the site I due to which a charge transfer from electron rich to electron deficient site decreases as a result of which a quenching in the fluorescence intensity is observed.

While, other cations like Na^{+}, Cu^{2+} interact with interaction site II, making the electron-deficient site more electron deficient, hence enhance the charge transfer from electron rich site to the deficient site, resulting in enhancement of fluorescence intensity of the compound. Since Fe^{3+} exhibits maximum quenching as compared to other metal ions, fluorescence titration experiment was performed to get a deeper insight into the quenching process. As shown in Figure 3.131, a gradual decrease in the luminescence intensity of **52** is observed upon incremental addition of Fe^{3+} ions. Upon addition of 190 μL of 1.0 mM Fe^{3+} solution, more than 95% quenching is observed.

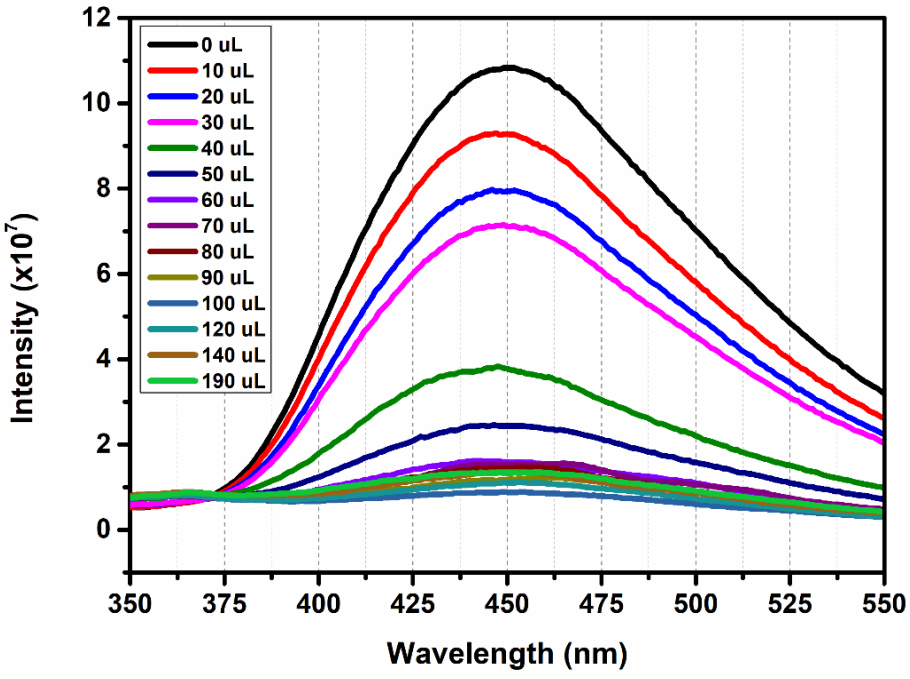

Figure 3.131. Change in the fluorescence intensity of **52** after incremental addition of an aqueous Fe^{3+} solution (1 mM).

***Fabrication of Pd(0) nanoparticles inside Cd-MOF* (52)**. From the fluorescence spectra, it was confirmed that Pd^{2+} interact with the framework as the result, decrease the fluorescence intensity intensity was observed. Compound **52** has been used for the encapsulation of $PdCl_2$ and further reduced it to form Pd(0) nanoparticles, which can be further used for catalysis.[245] As compound **52** is a porous material with free acetylene moieties inside the pores, this is used for encapsulation/formation of Pd(0) nanoparticles. These nanoparticles are very important for various organic transformation reactions. Formation of nano-size nanoparticles is still a difficult but achievable task. Despite of the diversity in application, the performance of all nanoparticle technology is defined by the same physical properties, including particle size, size distribution, shape, and surface features. Size of nanoparticles formation strongly depends on the pore size and pore environment. So, we have used this porous compound for nanoparticle formation. To achieve this task, we used the solvent infiltration wet method as described further (Figure 3.132).

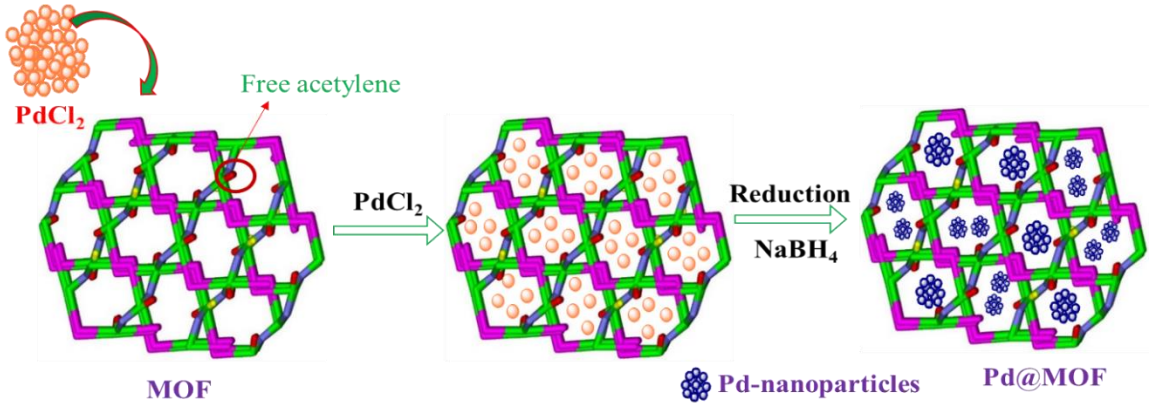

Figure 3.132. Schematic representation for the formation of Pd nanoparticles inside the **Cd-MOF** (**52**).

***Loading of Pd Nanoparticles in* Cd-MOF (52)**. We have followed a solvent infiltration method to load MNPs into MOFs. This took place in a stepwise manner (two steps) which was started from corresponding metal ion precursors. First, adsorption of $PdCl_2$ into **Cd-MOF** (**52**) and in the second step, wet chemical reduction method was used to reduce $PdCl_2$ to Pd(0) NPs by $NaBH_4$ in methanol. Initially, MOF was activated at 140 °C to remove all the solvent molecules present inside the pores. This activated **Cd-MOF** (**52**) is immersed into the $PdCl_2$ solution in methanol. The bright orange color of the $PdCl_2$ solution disappeared gradually within 1 h, as a result, colorless MOF turned to yellow solid which indicated the sorption of $PdCl_2$ in **Cd-MOF** (**52**) (Figure 3.133). The adsorption of metal

ions was promoted by the interaction of Pd(II) with free acetylene group hanging inside the pores, which provide stability to the adsorptive metal ions. PXRD analysis of **$PdCl_2$@Cd-MOF(52)** indicates that there is no change in the framework even after encapsulation. In addition to this, the appearance of some new peaks at higher angles confirms the presence of $PdCl_2$.

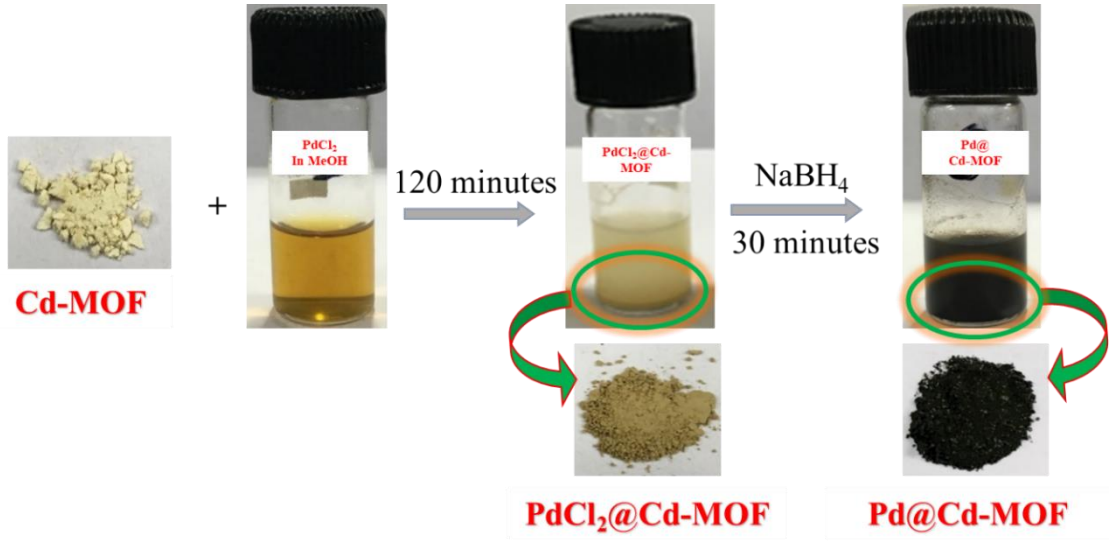

Figure 3.133. Monitoring the encapsulation of $PdCl_2$ and formation of Pd(0) nanoparticles inside the **Cd-MOF (52)**.

Further reduction of Pd(II) into Pd(0) nanoparticles was successfully achieved by using $NaBH_4$ in methanolic suspension of the **$PdCl_2$@Cd-MOF(52)**. After addition of $NaBH_4$, yellow color of the compound turns to dark brown indicating the formation of Pd(0) nanoparticles. This dark brown compound was filtered and washed with methanol 5-6 times to remove the excess of $NaBH_4$ and dried in air. Finally, implementation of Pd(0) nanoparticles inside the **Cd-MOF** (**52**) was confirmed by various techniques like PXRD, FESEM,and TEM and was further used for catalytic applications. Loading amount was calculated by UV-Vis absorption spectra. Using the absorbance values before and after adsorption, the loading of $PdCl_2$ was calculated; hence the absorbed amount was found to be 16% (by weight) of $PdCl_2$. Furthermore, from the PXRD analysis, it was confirmed that the framework is intact during this process, as the appearance of additional peaks represented the presence of Pd-nanoparticles (Figure 3.134).

Compound **52 (Cd-MOF)** shows a good affinity towards adsorption of CO_2 at 273 K, while, **Pd@Cd-MOF** shows very less affinity to adsorb CO_2 compared to the parental compound. This decrease in the CO_2 adsorption indicates a decrease in the pore space due

to occupancy of this space by nanoparticles. Around 73% decrease in the pore space was observed due to the presence of nanoparticles (Figure 3.135). This happens because Pd(0) nanoparticles occupy the pore space resulting in the decrease in the available area for incoming gas molecules.

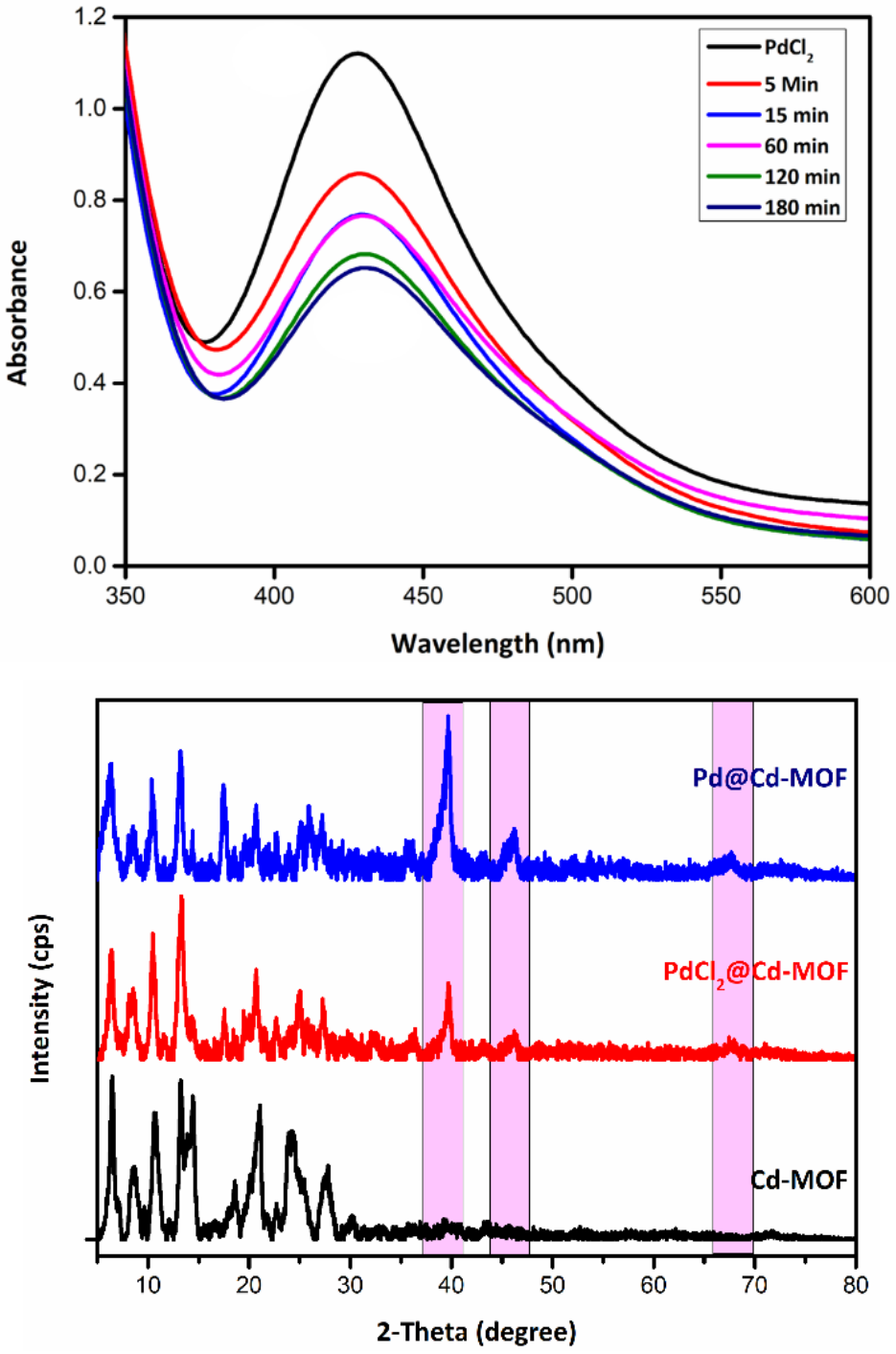

Figure 3.134. Monitoring of encapsulation of $PdCl_2$ in **52(Cd-MOF)** by UV-vis spectroscopy and Change in the PXRD by fermentation of Pd(0) nanoparticles.

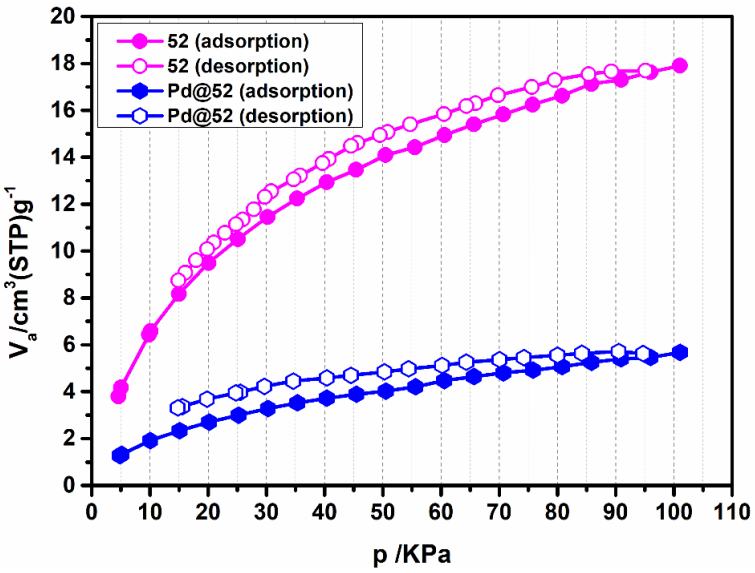

Figure 3.135. CO_2 adsorption isotherm of **52 (Cd-MOF)** and **Pd@52(Cd-MOF)** at 273 K.

FESEM and TEM analysis. FESEM and TEM are very useful techniques to observe the morphological changes during the process. FESEM images clearly indicate the change in the morphology of the compound after the implementation of nanoparticles. To confirm this further, EDX analysis was performed, and the appearance of peaks corresponding to both the metals indicated the presence of both the metals. FESEM and EDX are shown in the Figure 3.136 below. The EDX shows the presence of only Cd metal in the parental (as synthesized) compound (**52**), while EDX Figure 1.336d shows the presence of both the metals (cadmium and palladium) in **Pd@Cd-MOF**.

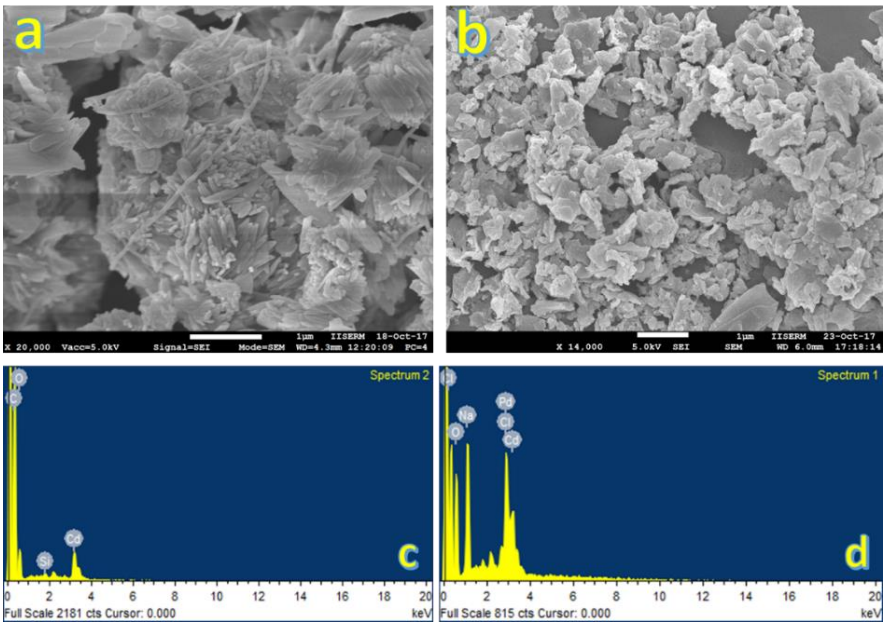

Figure 3.136. FESEM images and EDX of **Cd-MOF** (a and c) and **Pd@Cd-MOF** (b and d).

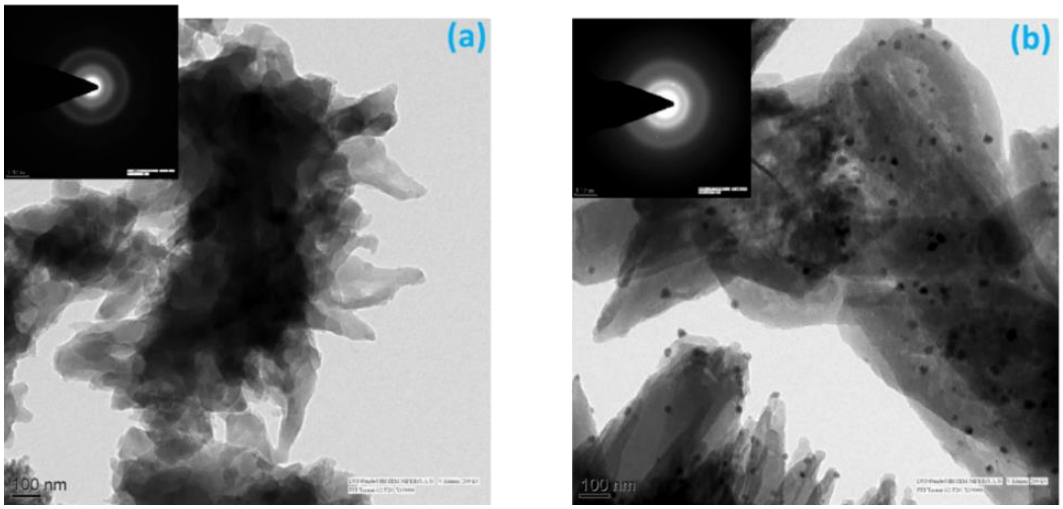

Figure 3.137. TEM images of **Cd-MOF** (a) and **Pd@Cd-MOF** (b).

To confirm the size and presence of nanoparticles, HRTEM was used. Due to the small size of particles and low loading of metal nanoparticles inside the MOFs, TEM is often the only possible method for determination of particle size. We have to be very careful to measure and interpret the TEM analysis because sometimes TEM irradiation might decompose the MOF and charge in the material may also create an obstacle in the analysis. After all these, HRTEM can directly image the metal particles within the framework without causing structural changes in the particles themselves.

For this HRTEM analysis of both the compounds was done and after analysis, it was found that in **Pd@Cd-MOF**, black spots of the nanoparticles appear (Figure 3.137). Although all the particles are not the equal size, they are in the range of 2-20 nm depending upon the pore size and agglomeration of particles.

3.2 COORDINATION ARCHITECTURES DERIVED FROM TWO COMPONENTS

In this section, we have explored the two-component system for the synthesis of coordination architectures with new ligands consisting of both linker and ancillary moieties. Compared to the three-component systems, only 2D and 3D coordination polymers are formed. These are categorized into two subsections.

3.2.1 Mixed pyridyl-carboxylate ligands

Three different ligands with a variation in the position of N-donor atom of the pyridyl moiety are used. Two ligands are dicarboxylates (2,2′-H_2bpaipa and 2,4-H_2bpaipa) while the third one is a tricarboxylate (H_3pbaipa).

Chemistry with 2,2'-H_2bpaipa ligand

Using 2,2'-H_2bpaipa, four MOCNs of Zn(II) and Cd(II) with a 1:1 ratio were synthesized at solvothermal as well as ambient conditions (Scheme 3.22). Due to the change in the reaction condition, formula of the compounds differ in lattice solvent molecules. For both metals, one DMF and two lattice water molecules are present under solvothermal conditions, while only lattice water molecules are present when the compounds are synthesized under ambient conditions.

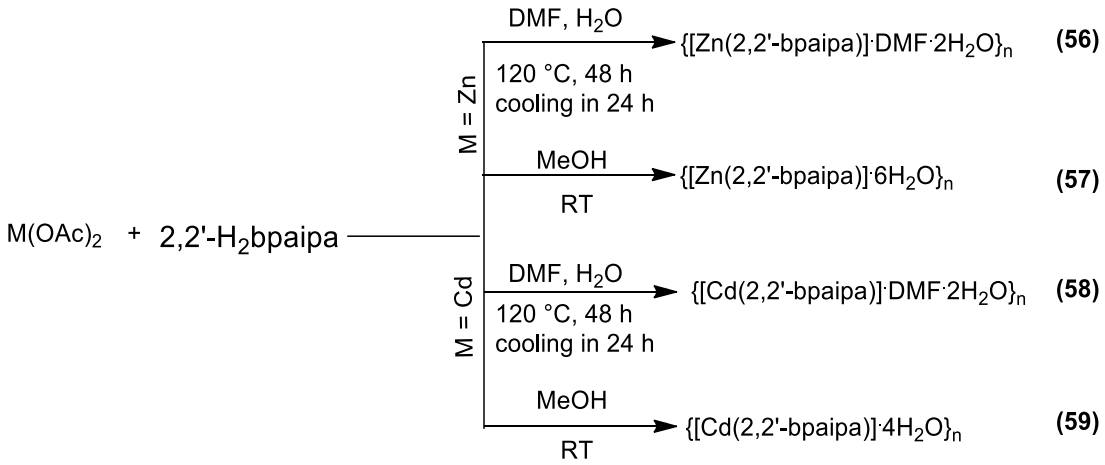

Scheme 3.22. Synthesis of **56-59**.

FTIR spectroscopic studies. The FTIR spectra of **56-59** are compared in Figure 3.138. For **56,** a broad band centered at 3408 cm^{-1} and a peak at 1662 cm^{-1} corresponds to lattice water and DMF molecules, respectively. Other two important peaks at 1633 cm^{-1} and 1345 cm^{-1} are due to asymmetric and symmetric stretching modes of the carboxylate groups,

respectively, with a value of $\Delta\nu$ = 288 cm^{-1}, which indicates the monodentate mode of carboxylate binding with metal center (Table 3.25).

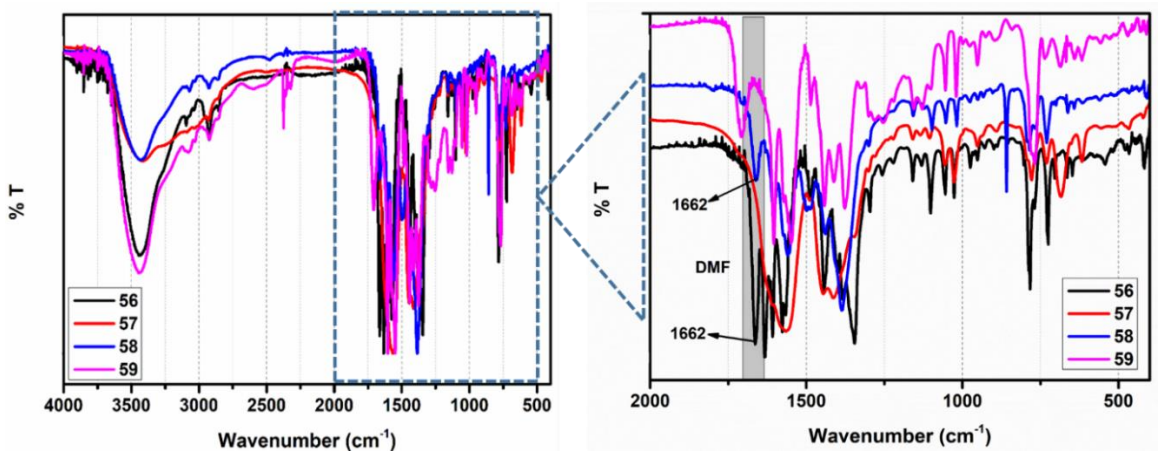

Figure 3.138. FTIR spectra of **56-59**.

As expected, there is no peak due to lattice DMF molecules in **57,** while other features are same as those in **56** with a monodentate fashion of carboxylate binding with the metal center because of difference in the asymmetric (1608 cm^{-1}) and symmetric (1398 cm^{-1}) stretching frequencies, which is found to be 210 cm^{-1}. Both the Cd(II) compounds, **58** and **59** show the same bidentate mode of binding of carboxylates with the metal center having $\Delta\nu$ values 174 cm^{-1} and 162 cm^{-1} respectively. The difference of both the compounds is only presence of DMF peak at 1665 cm^{-1} in compound **58**, while in compound **59** it is absent.

Table 3.25. Asymmetric and symmetric stretching frequencies and binding modes of carboxylates in **56-59**.

Compound	**Asymmetric (υ_1) cm^{-1}**	**Symmetric (υ_2) cm^{-1}**	**$\Delta\upsilon = \upsilon_1 - \upsilon_2$ cm^{-1}**	**Binding mode**
56	1633	1345	288	Monodentate
57	1608	1398	210	Monodentate
58	1560	1386	174	Bidentate (chelated)
59	1604	1442	162	Bidentate (chelated)

Thermogravimetric analyses. **56** exhibits first weight loss up to 200 °C (16.52%) corresponding to the loss of lattice solvents (one DMF and two water molecules, ca. 15.91%). In case of **57**, the first weight loss is 13.6% corresponding to the loss of four

lattice water molecules (ca. 13.48%); however, its single crystal structure contains six water molecules.

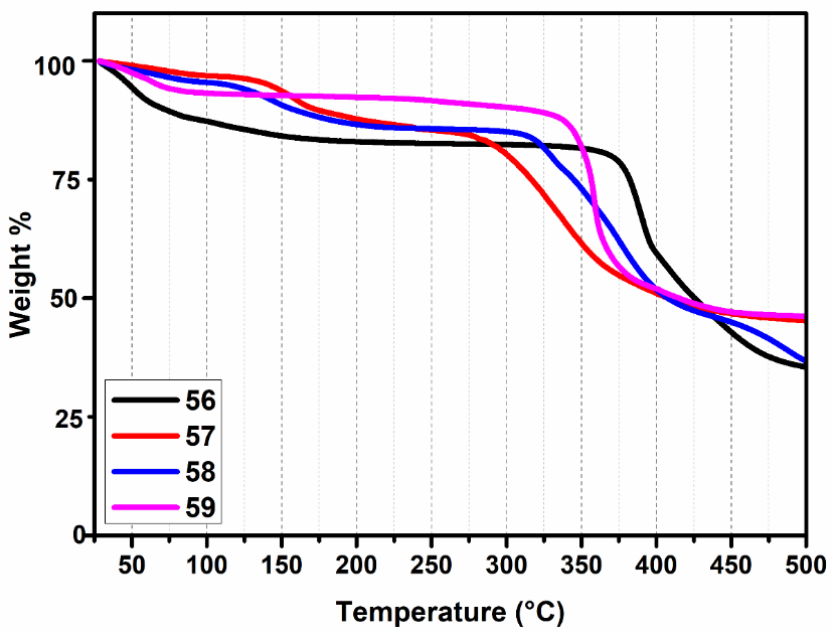

Figure 3.139. TGA scans of **56**-**59**.

Similarly, **58** exhibits its first weight loss of 7.92% corresponding to the loss of two water molecules (ca. 8.49%); its single crystal structure has one DMF and two water molecules. In case of **59**, the first loss is 6.68% corresponding to the loss of two lattice water molecules (ca. 6.60%). The second loss for **56**-**59** indicates their decomposition (Figure 3.139).

Single crystal structure analyses. Crystals of **56** and **58** were grown by solvothermal methods, while crystals of **57** were grown by slow evaporation of its aqueous solution over a period of ten days.

Structural description of **56**. It crystallizes in the monoclinic $P2_1/n$ space group. The asymmetric unit consists of a Zn(II) center, a bpaipa ligand, and solvent molecules as shown in Figure 3.140. Each Zn(II) is surrounded by three nitrogens and two oxygens of the ligand resulting in a distorted square-pyramidal geometry ($\tau = 0.22$). Both the carboxylate groups bind in a monodentate mode with Zn(II) (distances: 2.059(2) Å and 1.989(2) Å). Zn-N_{py} distances (2.088(3) Å, and 2.059(3) Å) are much shorter than the Zn-N_{alkyl} distance (2.399(3) Å).

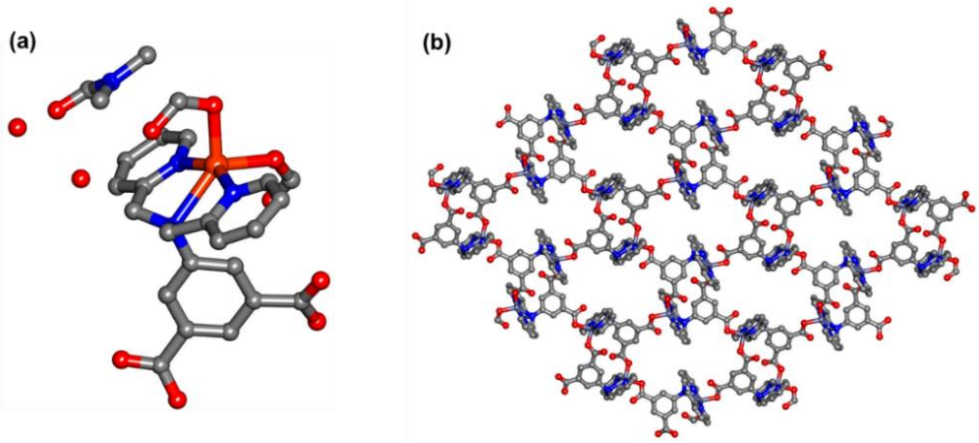

Figure 3.140. (a) Coordination environment around Zn(II) center in **56** and (b) 2D coordination network formed with two different types of pores in **56**.

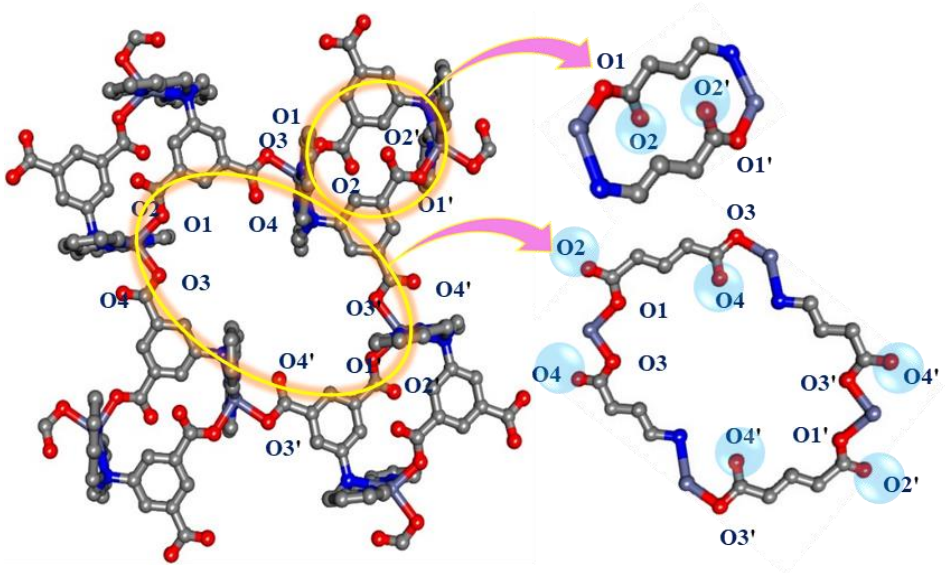

Figure 3.141. (a) Segment of **56** showing small and large pore and (b) nature of large and small pores with respect to the atoms present inside the pore.

Its 2D framework consists of a sheet-like structure having two different types of pores as shown in Figure 3.141. Large and small pore dimensions are 14.715(2) × 9.586(2) $Å^2$ (defined by the distance between corners Zn^{2+} centers) and 3.652(2) × 7.5613(2) $Å^2$ (defined by the distance between corners Zn^{2+} centers and uncoordinated oxygen to oxygen), respectively. Inside the small pore, there are two nonbonded oxygens (from monodentate carboxylate) present which generate a 14-membered ring including two metal centers. While the large pore forms a thirty-membered cyclic ring, which has two nonbonded oxygens (inside the pore) of the coordinated carboxylates and four metal centers (Figure 3.141).

Structural description of **57**. **57** crystallizes in the same space group as **56**, monoclinic $P2_1/n$. The coordination environment around the Zn(II) centre is N3O2 type, where the ligand 'bpaipa' blocks the three coordination sites of the metal with two pyridyl nitrogen atoms (distances: $Zn–N_{py}$, 2.057(7) Å and 2.057(11) Å; $Zn–N_{alkyl}$, 2.313(8) Å) as shown in Figure 3.142. The remaining two coordination sites are occupied by the oxygen atoms of the carboxylate from two different ligands with distances: 2.009(7) Å and 1.998(7) Å. Both the carboxylates bind with the metal center in a monodentate fashion. The τ parameter is found to be 0.413, which indicates that its geometry is close to square-pyramidal.

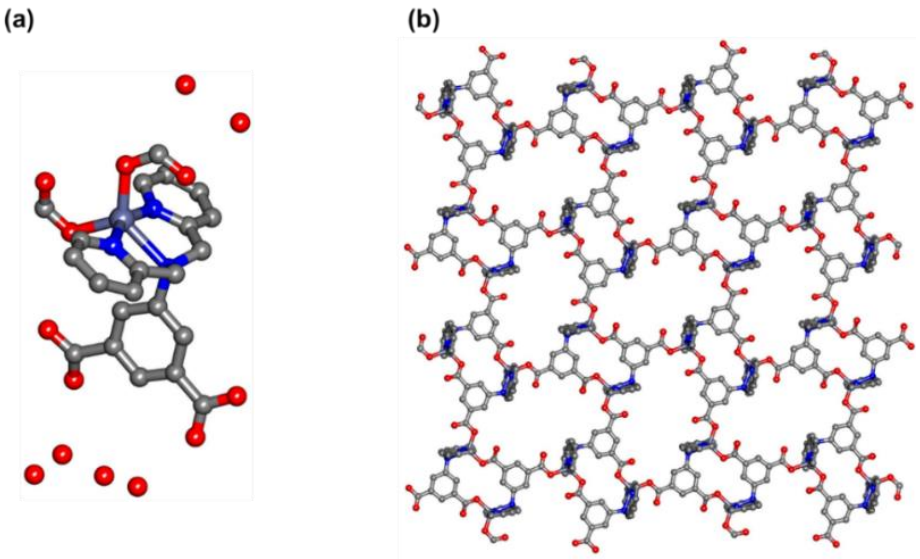

Figure 3.142. (a) Coordination environment of Zn(II) center in **57** and (b) 2D coordination network with two different types of pores in **57**. (hydrogens are omitted for clarity).

Selected bond angles and distances are listed in table A31 and A42 (Appendix). Furthermore, 2D sheet-type network shown in the Figure 3.142 contains two different type of pores: one small and one large pore with dimensions 8.216(2) × 3.775(2) $Å^2$ (defined by the distance between corners of Zn^{2+} centers) and 16.026(2) × 10.350(1) $Å^2$ (defined by the distance between corners of Zn^{2+} centers and coordinated oxygen to oxygen), respectively.

Although both **56** and **57** crystallizes in same space group, same topology, and the same type of 2D network, the environment around the metal centers is different because of the difference in the pore environment (Figure 3.143).

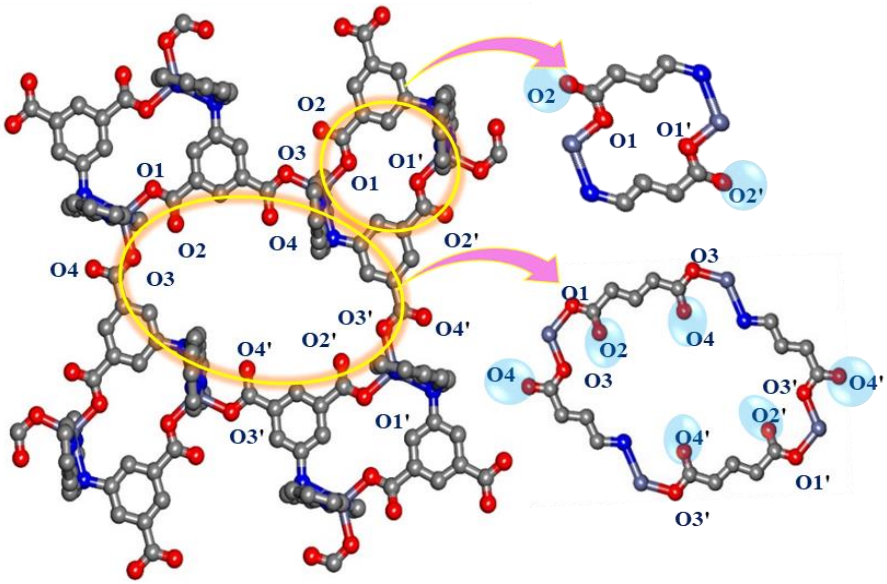

Figure 3.143. (a) Segment of **57** showing small and large pore and (b) nature of large and small pores with respect to the atoms present inside the pore.

Structural description of **58**. It crystallizes in monoclinic $P2_1/n$ space group. The coordination environment around the metal center is N3O4 type including three nitrogens from the ligand and four oxygens from two different carboxylates of the different ligands. Both the carboxylates bind with Cd(II) center in bidentate chelation mode with distances: 2.640(4) Å, 2.264(4) Å, 2.609(4) Å and 2.248(3) Å.

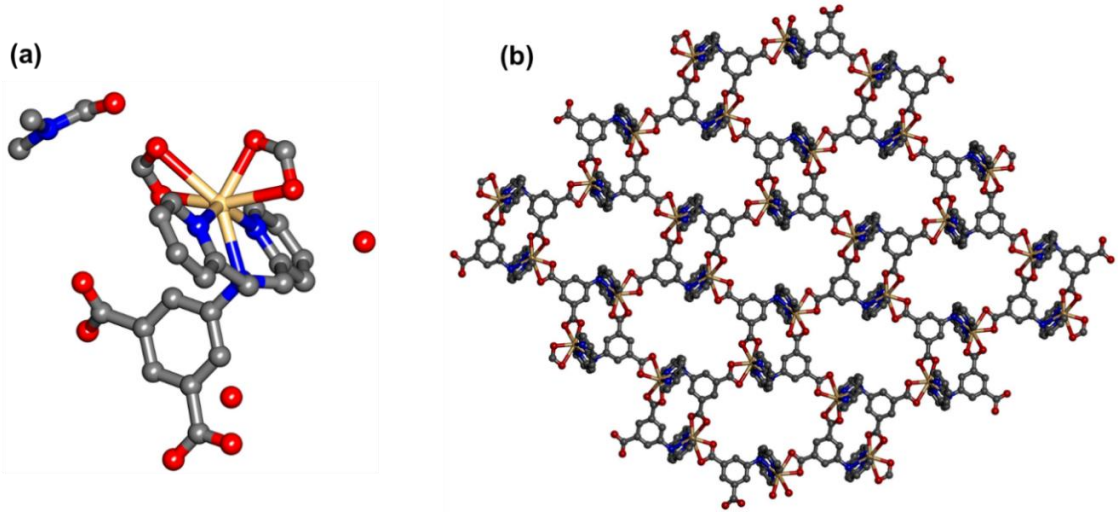

Figure 3.144. (a) Coordination environment of Cd(II) center in **58** and (b) 2D framework in **58**. (hydrogens are omitted for clarity).

Along with this, two pyridyl nitrogens (distances: 2.315(4) Å and 2.337(4) Å) and one alkyl nitrogen (distance: 2.487(3) Å) are also bound to the metal center (Figure 3.144). **58** shows two different types of pores as observed in **56** and **57**, having dimensions 6.984 × 3.635 $Å^2$ (defined by the distance between two Cd(II) centers)

and 15.669 × 11.906 $Å^2$ (defined by the distance between two Cd(II) centers and two carboxylate oxygens). Similar to Zn(II) compounds, the small pore consists of a fourteen membered ring, while the large pore consists of a thirty membered ring. All the carboxylates are bonded to the metal in a bidentate mode. Thus, there is no possibility to have non-bonded oxygens inside the pores as observed in Zn(II) compounds.

Powder X-ray diffraction studies. The crystalline nature of **56**-**59** has been confirmed by powder X-ray diffraction studies. In addition to this, the purity of the bulk sample with respect to single crystal is confirmed by comparison of the simulated patterns with experimental powder patterns. **56**-**58** have similar PXRD patterns, while the PXRD pattern of **59** is different (Figure 3.145).

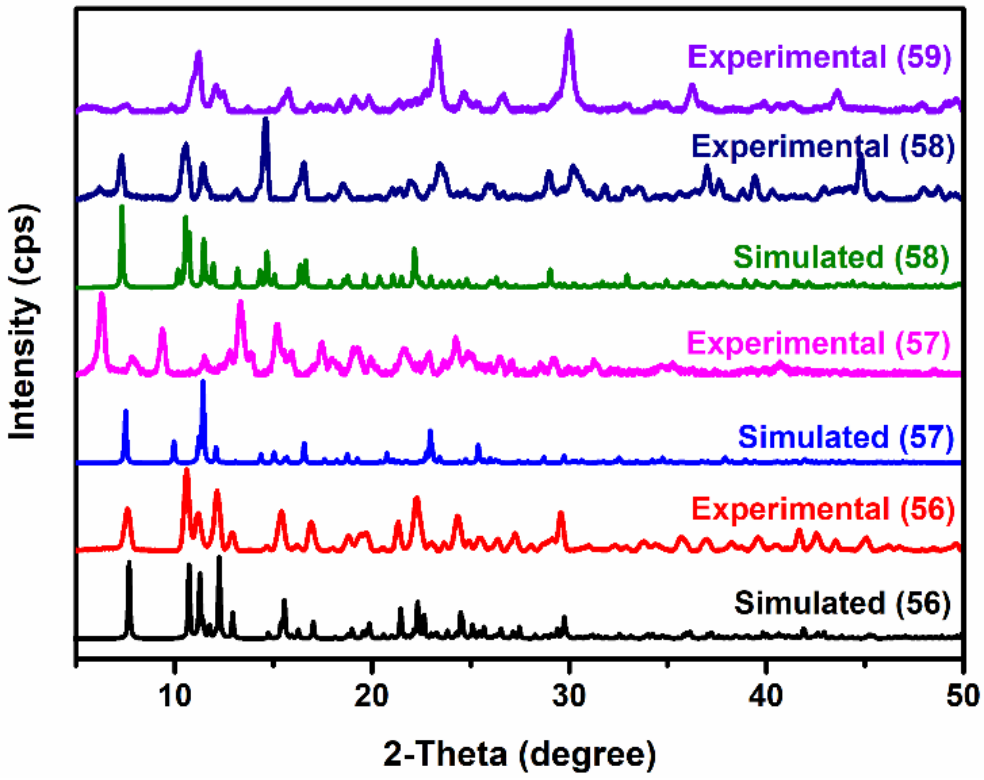

Figure 3.145. Simulated and experimental PXRD patterns of **56**-**59**.

Gas and vapor sorption study. Due to the presence of different types of pores, these compounds were treated for gas and vapor adsorption studies. The porosity or porous nature of the compounds can be easily confirmed by the gas adsorption studies. Adsorption of nitrogen at 77 K is used primarily to find out the porosity. The pore distribution calculated from the N_2 adsorption provides a good agreement with the single crystal structure of the compound.

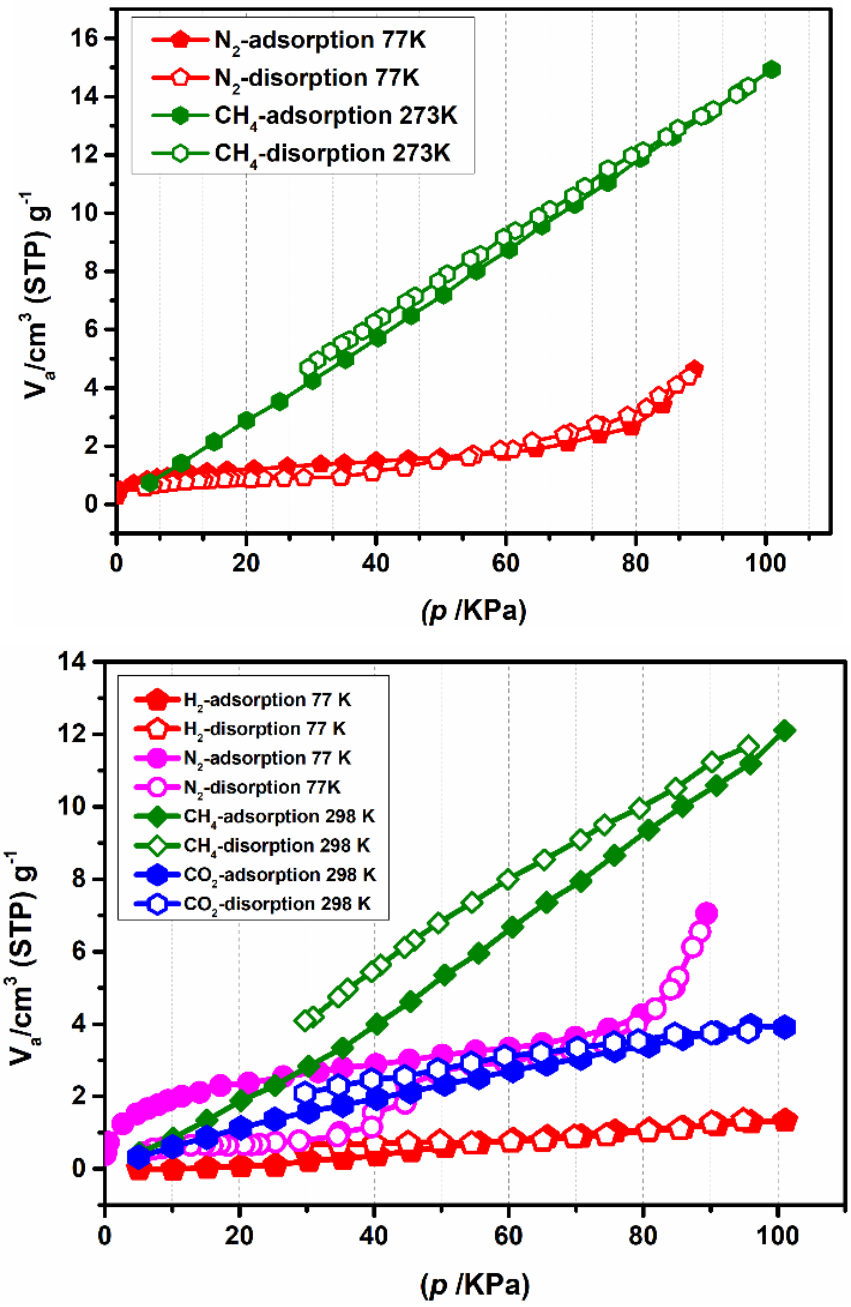

Figure 3.146. Gas adsorption isotherms for **56** and **57**.

In this context, we have also used other gases like H_2, CO_2, and CH_4 for some of these compounds. For the porous materials, porosity is the main factor to check the capacity of gravimetric gas storage and related to its BET surface area and pore volume. Methane and hydrogen have been widely used for the gas adsorption studies in MOFs because these are the alternative fuel for the vehicles. Along with this, methane and carbon dioxide are the greenhouse gases, which has adverse effects on human health as well environment.

56-**59** have been used for gas adsorption studies. For **56**, adsorption of N_2 at 77 K and CH_4 at 273 K has been performed after pretreatment of the sample at 140 °C for 24 h under

vacuum. From this study, it was found that an amount of 4.63 cm^3/g of N_2 has been adsorbed at 77 K and the BET surface area calculated was found to be 4.5 m^2/g. Furthermore, the same compound has been used for the adsorption of methane gas and it was found that an amount of 15 cm^3/g of methane was adsorbed at 273 K. So, it was found that this compound is selective for methane compared to nitrogen (Figure 3.146 (*above*)). **57**, which is an analog of **56**, has also been used for the gas adsorption studies and it is found that an amount of 7.05 cm^3/g of N_2 was adsorbed at 77 K and the BET surface area was found to be 9 m^2/g. **57** has double surface area in comparison to **56**.

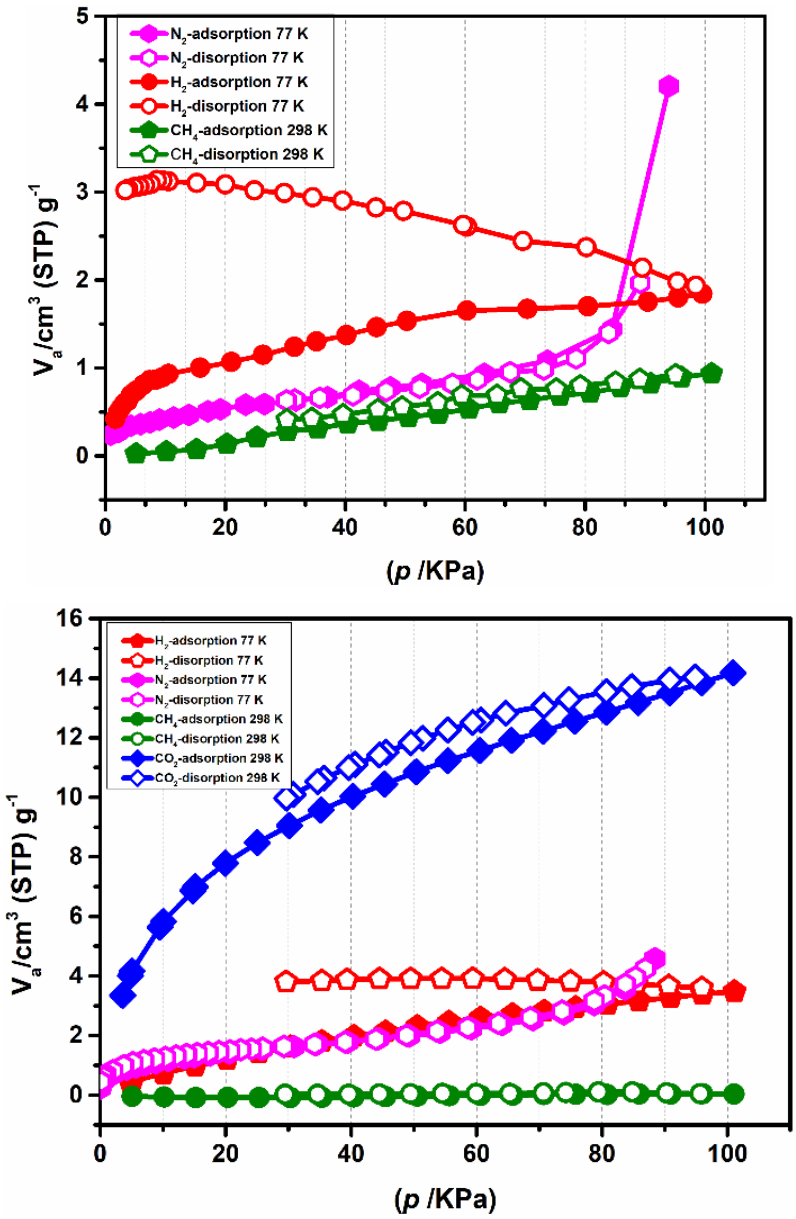

Figure 3.147. Gas adsorption isotherm for **58** and **59**.

So further it was used for adsorption of other gases like hydrogen, methane, and carbon dioxide. The amount of methane gas adsorbed in **57** was found to be 12.10 cm^3/g at 298 K;

for hydrogen, it was 1.5 cm^3/g at 77 K; and for CO_2, 3 cm^3/g of gas was adsorbed at 298 K (Figure 3.146 (*below*)). **58** and **59** have also been used for the gas adsorption studies . For **58**, N_2, H_2, and CH_4 gases have been used for the studies and amount of gas adsorbed was found to be 4.45 cm^3/g, 2 cm^3/g, and 1 cm^3/g, respectively. From the nitrogen adsorption studies, BET surface area has been calculated which was found to be 2 m^2/g. For **59**, N_2, H_2, CO_2, and CH_4 gases have been used for the gas adsorption studies, and amount of gas adsorbed was 4.58 cm^3/g at 77 K (N_2), 2 cm^3/g at 77 K (H_2), 14.1 cm^3/g at 298 K (CO_2), and 1 cm^3/g 298 K (CH_4), respectively. The BET surface area for **59** was calculated to be 5.3 m^2/g by the nitrogen adsorption isotherm at 77 K (Figure 3.147).

From the above results, it was found that the observed adsorption of gases is very less compared to the expected values of compounds having similar type of 2D sheets. Thus, it was necessary to check what is happening at the molecular level. Before doing the gas adsorption, we have to pretreat the sample at a certain temperature under vacuum to remove the already present lattice solvents to make the pores available for the gas adsorption. In order to achieve this, the thermal stability of these compounds were checked, and then the effect of desolvation on the molecular structure of the compound via SC-SC transformation was studied.

Structural change due to desolvation process via SC-SC transformation. This section will give an insight to the question highlighted in the previous section as in why these compounds show less adsorption of gases although they have a 2D porous structure with good pore volume and stability after desolvation and resolvation process. SC-SC transformation is a process by which a single crystal of the compound can be used to convert it into another useful compound which is not possible by the common procedures.[57,58,246–253] It is fascinating because in some cases it leads to the formation of unusual products which otherwise cannot be designed by routine synthetic routes. This transformation is very helpful to find the change in molecular structure during the transformation process. SC-SC transformation is also used to expose a single crystal of particular compound to solvent, solvent vapors, heat, light and mechanical forces which results in the formation of structurally transformed products.[57] Although there are many challenges to achieve this transformation like loss of crystallinity, cracking in crystals and decomposition of compounds. On the other hand, if a crystal sustained the crystallinity during the transformation then any change in physical properties such as color, magnetism, porosity, luminescence, chirality, etc. as well as a change in coordination number,

geometry, and dimensionality also observed which leads to the formation of a new product.[55,254–260] Another interesting factor is the removal or encapsulation of guest molecules inside the porous materials. The main problem in this is that a porous network gets collapsed during the desolvation process. As we have discussed in the previous section that in porous networks, encapsulation of any guest molecule can easily take place. However, to achieve this, the sample has to be pretreated by washing with particular solvent followed by heating in vacuum at a particular temperature (depending on the nature of solvent) to remove the traces of solvent molecules already present. Compounds **56-59** have been employed for this desolvation and resolvation process. Gas adsorption studies reveal that the amount of gases adsorbed is less than the expected value. So, to understand this, we wanted to understand what is actually happening to the network during the desolvation at the molecular level. Before going for SC-SC transformation, we have checked the thermal stability of this compound at variable temperature which was followed by using different techniques like FTIR, VT-PXRD, and TGA.

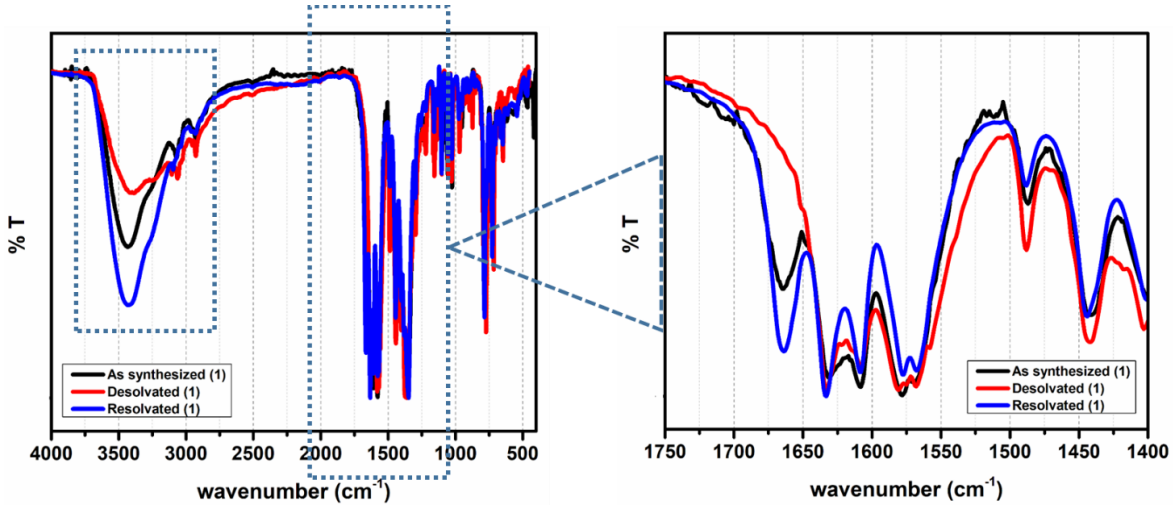

Figure 3.148. Change in the FTIR spectra due to de/re-solvation in **56**.

For the desolvation process, as-synthesized compounds were first washed with methanol followed by heating at 140 °C in a vacuum oven. This pretreated sample was cooled down at room temperature and all the characterization techniques were performed. Considering **56** and **58**, DMF and water as lattice solvents in the pores can be observed by FTIR spectroscopy as they show a characteristic peak in FTIR, for example, a peak around 1662 cm^{-1} is due to the presence of free DMF molecules.

After heating, disappearance of this peak indicates the removal of guest solvents (DMF) from the pores while other peaks remain same, as shown in the Figure 3.148. For

resolvation, the compound was placed in the same solvent as **56** in DMF, and again the appearance of the DMF peak in FTIR indicate the formation of the mother compound (as synthesized) again.

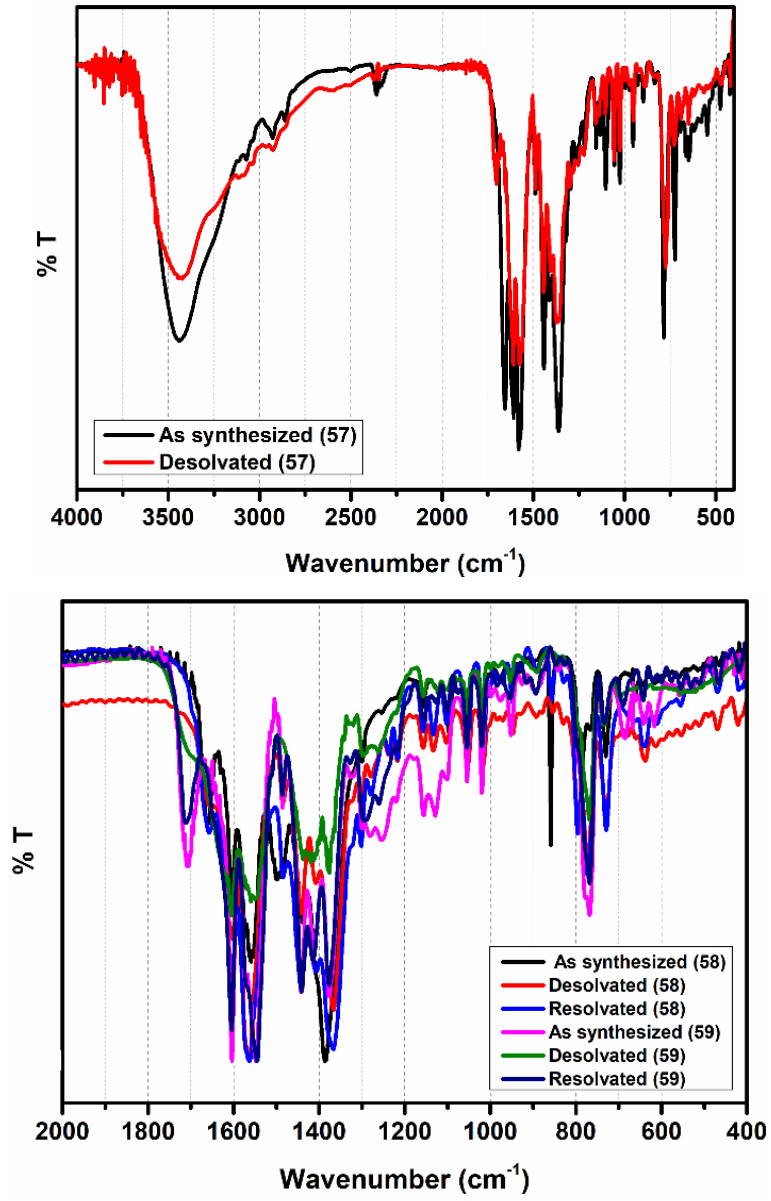

Figure 3.149. Change in the FTIR spectra due to de/re-solvation in **57-59**.

For **56**, a peak in FTIR around 1662 cm^{-1} corresponds to the DMF and after desolvation by heating in a vacuum this peak got disappeared indicating the removal of DMF molecule, while reduction of a peak around 3400 cm^{-1} is due to the loss of some lattice water molecules. Again after keeping the same air dried desolvated compound into the mixture of DMF and water for one day, regeneration of the peak of DMF molecules confirms the resolvation of the compound hence, proving the reversibility of the process. Also, it was found that peak corresponding to the lattice water molecule got stronger as compared to the

as-synthesized compound indicating absorption of more water than the as-synthesized compound **56** (Figure 3.149).

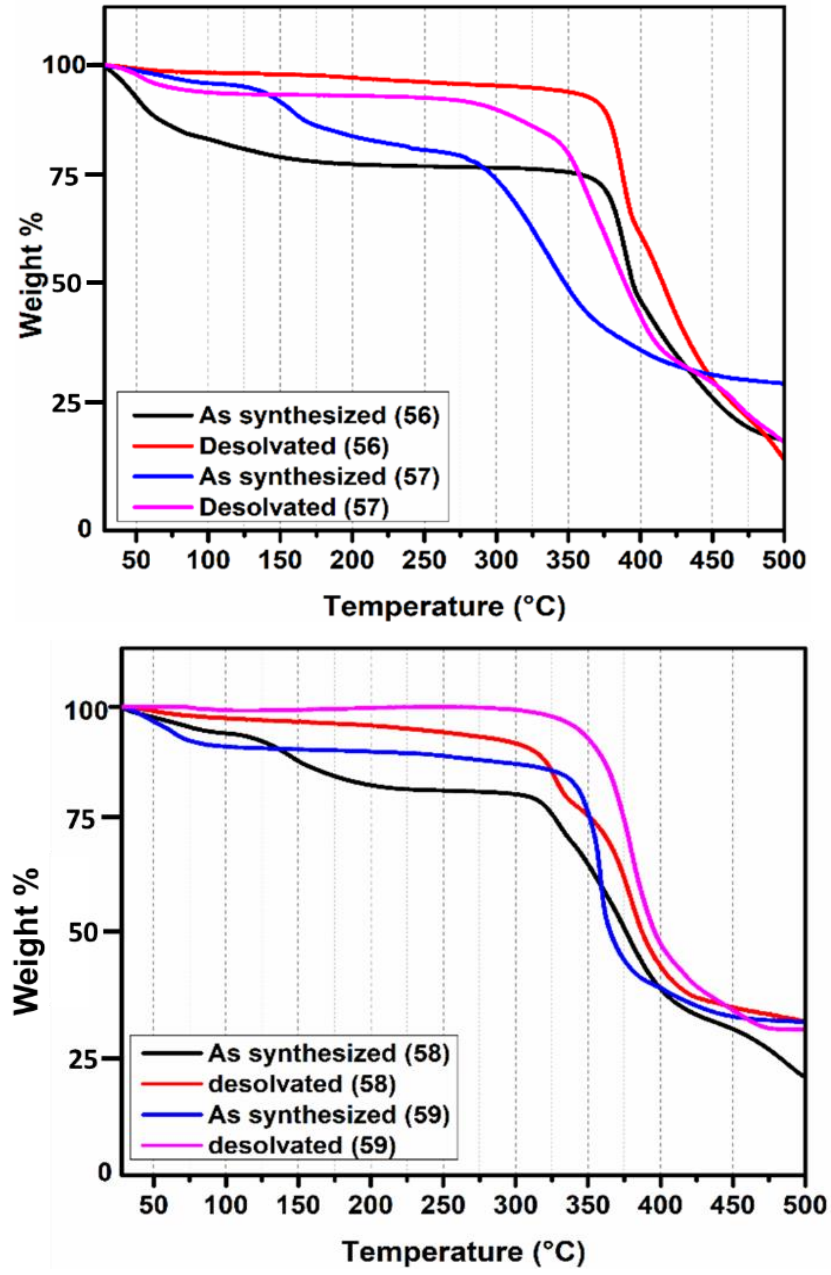

Figure 3.150. TGA scans of as-synthesized and desolvated samples of **56**-**59**.

Like **56,** other compounds, **57**, **58**, and **59** were also used for desolvation process. In **57** and **59**, since no DMF was present, therefore, a change in the peak intensity corresponding to the lattice water molecule has been observed (Figure 3.149). As observed in compound **56**, **58** also has a DMF peak which disappeared during the desolvation process.

After the FTIR studies of desolvation and resolvation process of these compounds, TGA was also performed to prove the desolvation process for some of these compounds.

Consider **56**, it is stable up to 350 °C and shows the first weight loss of DMF and two water molecules up to 200 °C. After comparing both as-synthesized and desolvated species, it was found that in the desolvated counterpart, there was no weight loss due to the lattice solvent molecules up to 200 °C, indicating the removal of solvent molecules from the lattice of compound (Figure 3.150). Like **56**, the other three compounds, **57-59** were also treated for thermal analysis and found that after desolvation there was no weight loss corresponding to any lattice solvent (Figure 3.150). This experiment confirms the stability of the compound after heating and desolvation under high temperature and vacuum.

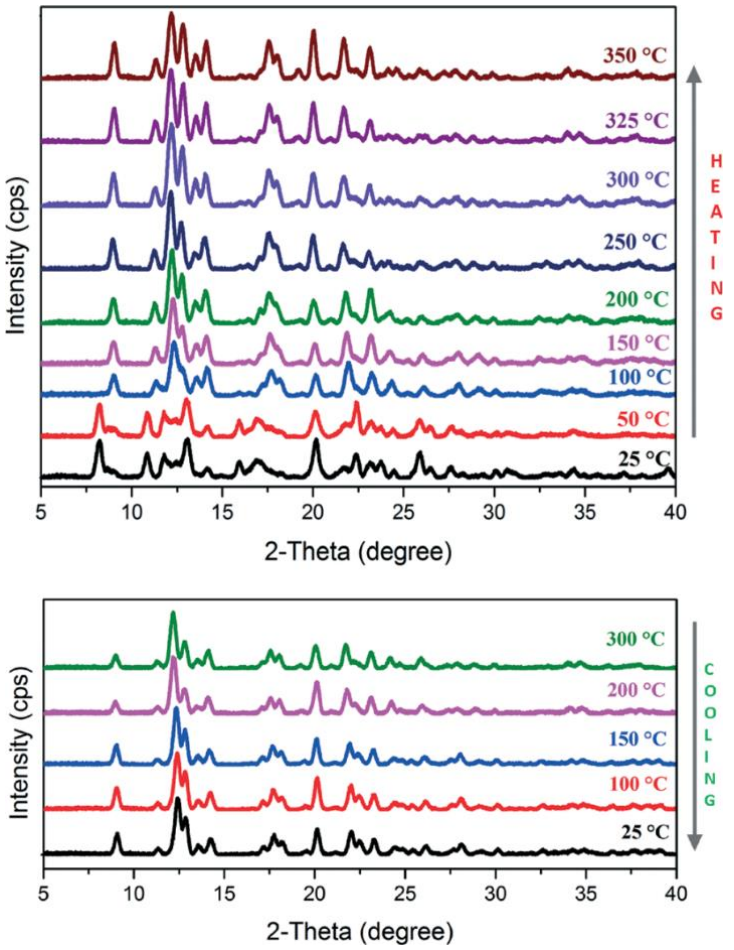

Figure 3.151. VT-PXRD for **56**.

After that, the retention of crystallinity was confirmed by the PXRD analysis. It was found that all **57-59** retain their crystalline nature even after removal of the solvents from the pore which indicates the intactness of the framework. Choosing one of these compounds, **56**, VT-PXRD has been performed and found that there is a slight shift in the peaks at lower region due to loss of solvent molecules, while other peaks remain intact up to 350 °C. Along with heating, cooling profile was also performed to check for the maintenance of

crystallinity and it was found that **56** is thermally very stable under heating as well cooling conditions (Figure 3.151). Although there is intactness in crystallinity of the compound during solvation and desolvation process, when it comes to SC-SC transformation at the molecular level, **56**-**59** behave differently. Except for compound **56**, crystals of other compounds were not suitable for SC-SC transformation. It is because cracking in the crystals take place when heated at a higher temperature. Therefore, such crystals cannot be used for the single crystal studies. So, for this transformation, crystals of **56** were heated in a beaker by placing in a vacuum oven at 140 °C for 12 h. After this, a crystal was taken out and used for the single crystal study.

Structural description of **56**'. Upon desolvation of **56**, no change in the space group was observed. The coordination environment around the Zn(II) centre is same as **56,** that is, N3O2 type, wherethe ligand 'bpaipa' block the three coordination sites of metal with two pyridyl nitrogen atoms (distances: Zn–N_{py}, 2.065(8) Å and 2.116(8) Å), one alkyl nitrogen (distance: 2.340(8) Å) as shown in Figure 3.152. The remaining two coordination sites are occupied by the oxygen atoms of carboxylate from two different ligands with distances: 2.007(7) Å and 1.938(7) Å.

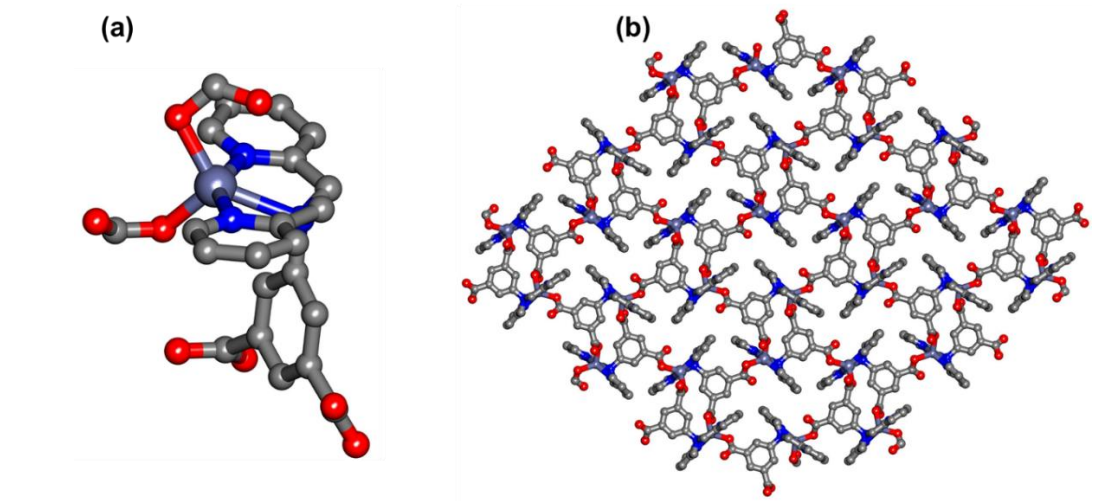

Figure 3.152. (a) Coordination environment of Zn(II) center in **56**' and (b) 2D coordination network formed by expansion of asymmetric unit (hydrogens are omitted for clarity).

Both the carboxylates bind with the metal center in monodentate fashion. The τ parameter is found to be 0.15 which indicates more character of square-pyramidal geometry. Selected bond angles and distances are listed in table A30 and A41 (Appendix). Furthermore, by expanding the asymmetric unit, a 2D sheet-type network was generated as shown in the Figure 3.152 after expanding the asymmetric unit which contains two different type of pores: small as well as large with dimension

7.292 × 4.918 Å^2 (defined by the distance between corners Zn^{2+} centers) and 15.575 x 8.725 Å^2 (defined by the distance between corners Zn^{2+} centers and two carboxylate oxygens) respectively.

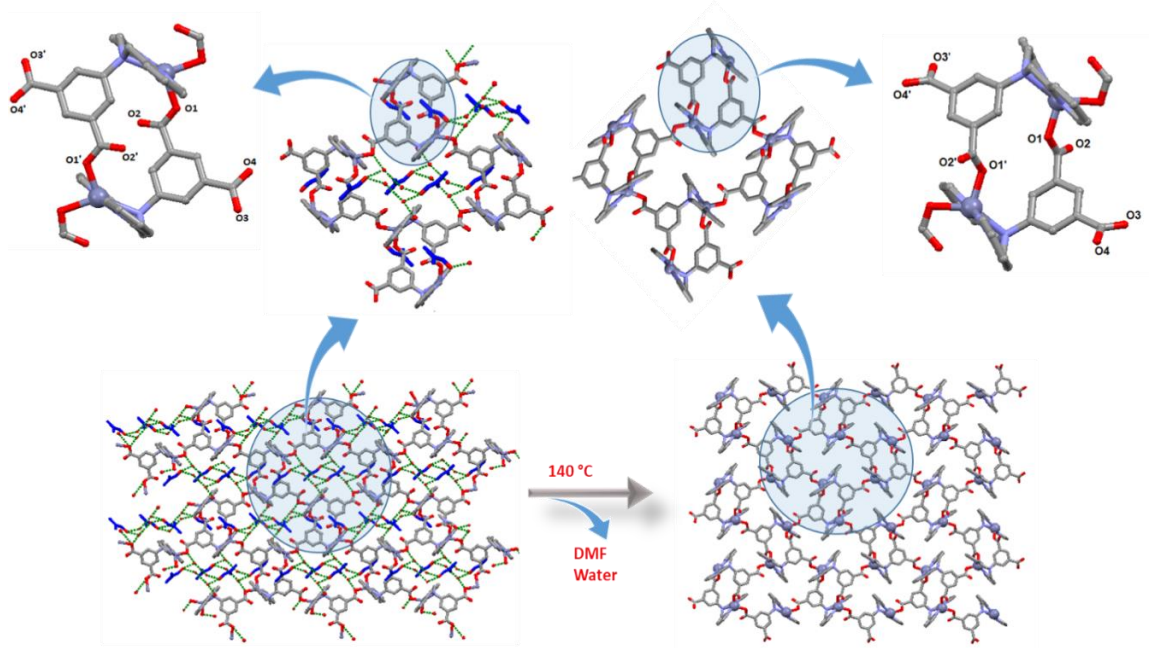

Figure 3.153. Single-crystal-to-single-crystal transformation in **56**.

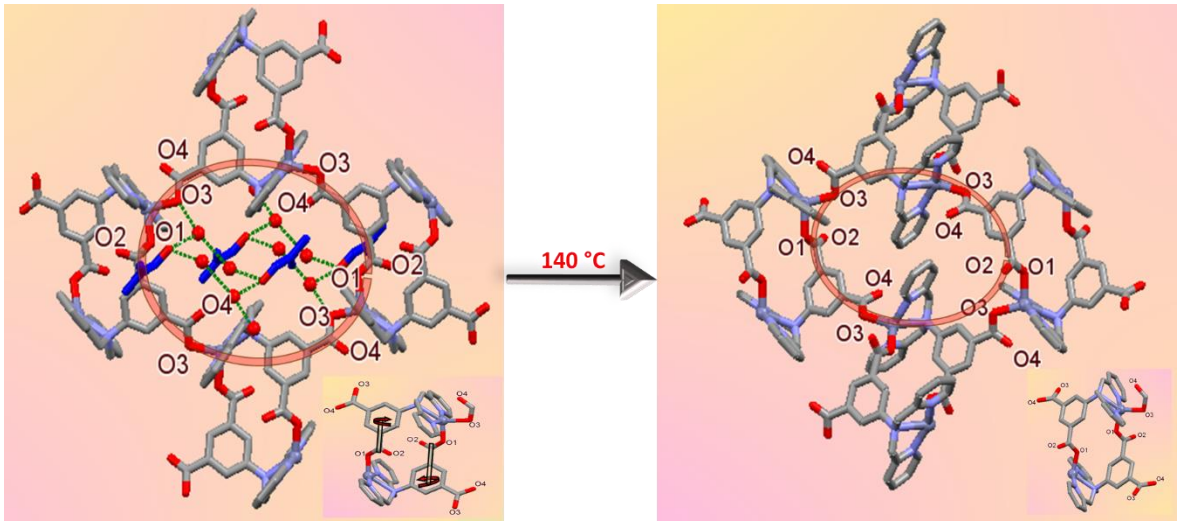

Figure 3.154. Closer view of **56** and its desolvated compound **56**'.

The topology of this compound is same as **56** and **57**. Due to desolvation, environment of large and small got changed hence create a different nature of pores than that of as-synthesized compound **56**. Comparing the small pore of the as-synthesized and desolvated **56**, it is clear that rotation of the carboxylate takes place due to desolvation of the compound by heating under vacuum. In the small pore of the as-synthesized compound **56**, two non-

bonded oxygens named O2 are inside the pore, while in the desolvated **56**', these non-bonded oxygen named O2 got rotated to other side emptying the small pore (Figure 3.153). This is possible due to the free rotation of carboxylate which is bonded with the metal center in a monodentate fashion. Because of this rotation, the non-bonded oxygens and the pyridyl group which were inside the small pore rotate into the large pore. Because of this transformation, there is less space available for gas molecules, thereby eaxplaining less absorption of gases (Figure 3.154). This SC-SC transformation studies explained the reason why this compound accommodates lesser amount of gases as compared to other 2D MOFs.

Comparison of 56 and 57 and desolvated 56 (56'). Consider the large pores, which show a difference in their dimensions as well as a different number of atoms inside and outside the pore. The ratio of total no. of uncoordinated oxygen of carboxylate to the total no. of coordinated oxygen inside the large pore is different in both the cases. For **56**, it is 2/4; for desolvated **56**', it is 4/2; and for **57**, it is 4/2, as shown in Figure 3.155. In **56**, both the uncoordinated oxygens are inside the small pore. On the other hand, in **56'** and **57**, both are outside. In **56**, large pore has two uncoordinated oxygen atoms and in **56'** and **57**, four oxygen atoms are inside the large pore. The flexible rotation of the carboxylate group is confirmed by the change in the angle between the two planes drawn using both the carboxylate and metal center (see Figure 3.155).

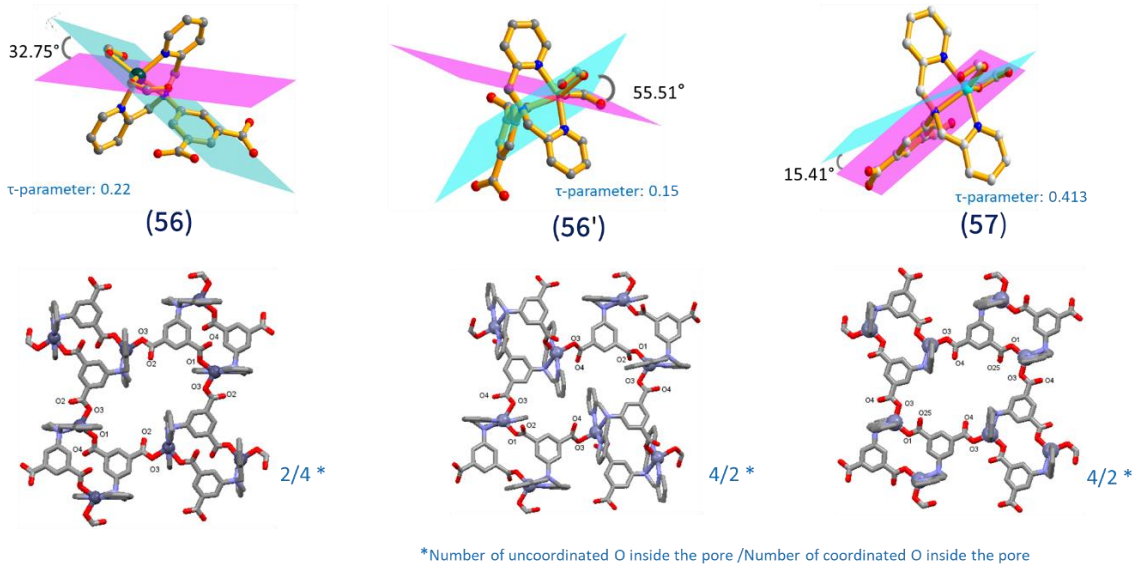

Figure 3.155. Comparison of the single crystal structures of **56**, desolvated **56**' and **57**.

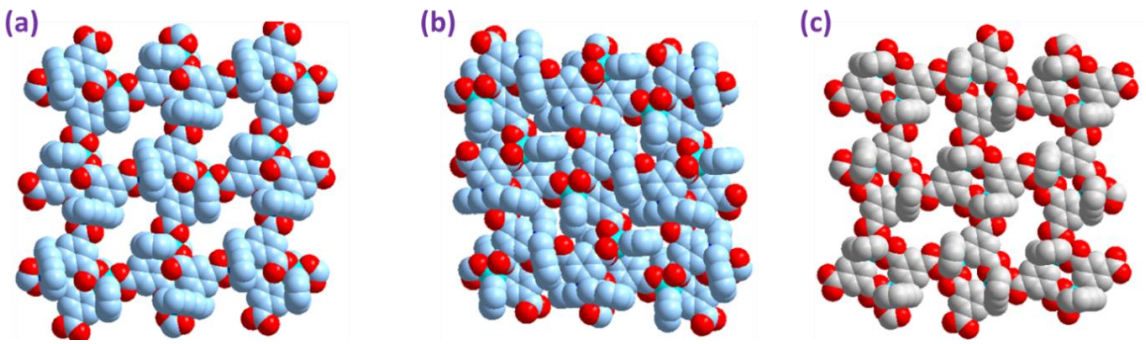

Figure 3.156. Comparison of available pore space for gas adsorption studies in **56**, desolvated **56'** and **57**.

In case of **56**, the angle is 32.75°, for **56'** it is 55.51°, while **57** shows 15.41° angle. These differences in the pores affect the various application based on the pores. Furthermore, both the compounds have a different value of τ parameter, which represents the deviation from regular geometry (Figure 3.156). The τ parameter was calculated for **56** (0.22), for **56'** (0.15), and for **57** it was 0.413, indicating the deviation in the regular geometry by desolvation or because of synthesis under different conditions. Considering the single crystal study of daughter compound (desolvated **56'**), it is found that its overall geometry and topology is same as the mother compound (**56**). In this, the metal center is pentacoordinated similar to the previous one having the N3O2 environment.

Both the carboxylates bind with the metal center in a monodentate fashion. This change in the τ parameter is a sign of change in the geometry of the metal center coordination, which confirms the free rotation of the carboxylate group around the metal center after the addition/removal of solvents. The FTIR spectra of all the compounds were recorded in solid state using KBr pellet. In case of **56**, peak at 1662 cm^{-1} indicates the presence of DMF molecules. The difference between the symmetric and asymmetric stretch indicates the monodentate binding mode of the carboxylate. Comparison of the space fill diagram of these three compounds, it was found shows that there is no available space in the desolvated compounds, explaining less amount of gas uptake by these MOFs (Figure 3.156).

Solvent encapsulation. For the study of solvent encapsulation, first, the as-synthesized compounds were pretreated by heating them at 120 °C in a vacuum oven for 8 h. We have followed the second method to encapsulate the solvent molecule as described before (Figure 3.157). These pretreated samples were dispersed in the different solvents for 2 days, then filtered, dried in air and used for further characterization, which prove the

encapsulation. This solvent encapsulation also confirms the stability of coordination compounds in different solvents as well. To prove this phenomenon of guest encapsulation, samples having encapsulated guests were characterized by various methods like FTIR, TGA, and PXRD. Before doing this, thermal stabilities of these complexes were investigated. Sometimes the framework gets collapsed due to the removal of guest molecules already present. In this case, different solvents were used as guests. The removal of solvent already present was confirmed by thermogravimetric analysis and the retention of crystallinity of the framework upon thermal treatment and exposure to different solvents was confirmed by PXRD analysis. Four compounds, **56-59** were used for this solvent encapsulation study.

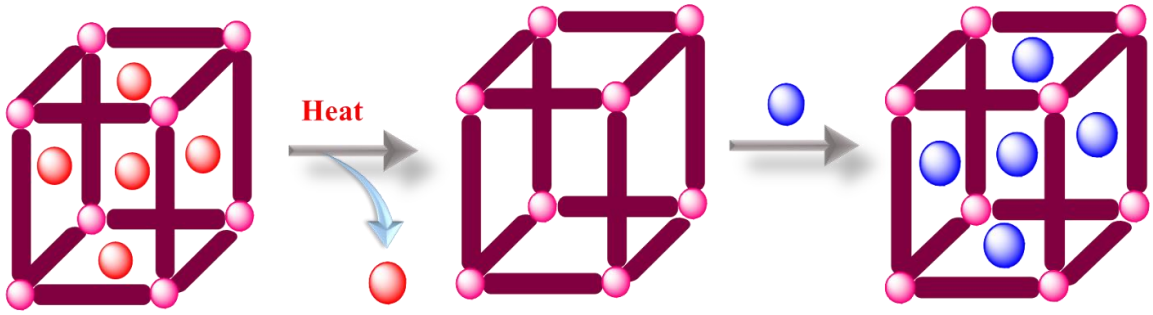

Figure 3.157. Schematic representation showing the strategy of encapsulation of guest molecules inside the coordination polymers.

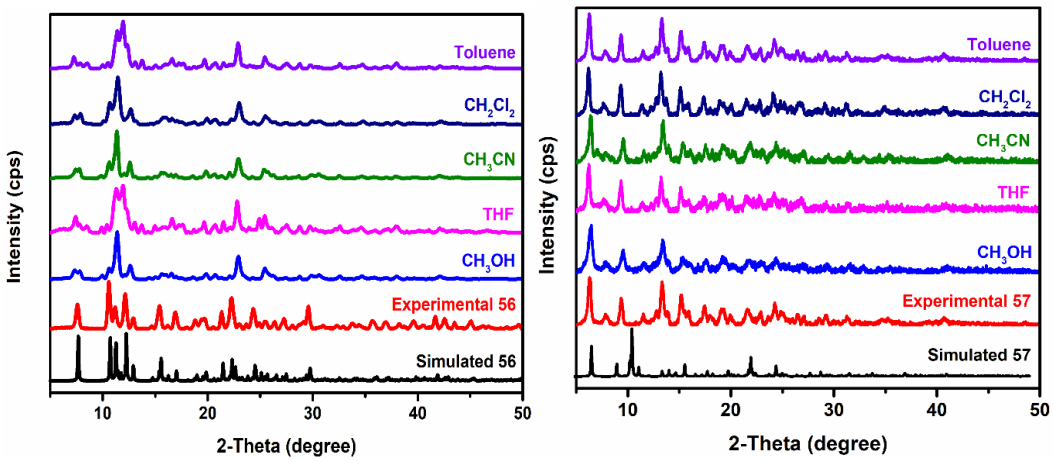

Figure 3.158. Retention of crystallinity of **56** and **57** in different solvents**.**

From the structural comparison, we found that the solvent plays an important role in the structural change of MOFs. All this is because of the different interaction of solvent molecules with the framework. PXRD patterns of these four compounds indicate the retention of crystallinity of all four compounds **56-59** (Figure 3.158 and 3.159).

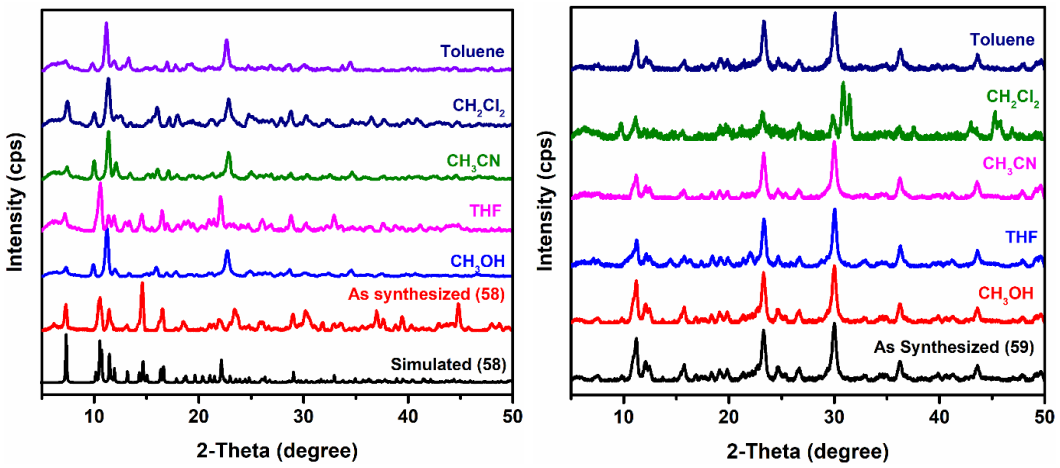

Figure 3.159. Retention of crystallinity of **58** and **59** in different solvents**.**

56 consists of one DMF and two lattice water molecules present in the pores, which was confirmed by TGA, CHN and single crystal structure analysis. **57**, which is an analogue of **56 and** was synthesized at room temperature contains only six lattice water molecules. **58** consists of one DMF and two water molecules like **56,** and **59** consists of only six lattice water molecules.

Thermogravimetric analysis of all these compounds (having solvent molecules) has been done from 25 °C to 500 °C to check for the thermal stability of the compounds as well as to find out the number of guests (solvent) molecules encapsulated inside their respective pores. For all desolvated compounds of **56**-**59**, there was no appreciable weight loss up to 200 °C. However, after immersing in different solvents, an appreciable weight loss was observed corresponding to the encapsulated solvent molecules inside the pores of the respective compounds (Figure 3.160 and 3.161). From the thermogravimetric analysis, the number of molecules encapsulated per unit formula were calculated and found that a different number of molecules were encapsulated in different compounds. For example, in case of compound **56**, methanol (3 molecules), THF (1 molecule), toluene (0.2 molecules) and DCM (0.6 molecules) were encapsulated per unit formula weight.

In case of **57**, 1, 0.5, 0.25 and 0.5 molecules of methanol, THF, toluene, and DCM, respectively, got encapsulated. On the other hand, it was observed that **58** can accommodate methanol, THF, toluene, and DCM up to 2, 0.5, 0.8 and 0.1 molecules per unit formula weight, respectively. Similarly, **59** shows encapsulation of THF, toluene, DCM, and acetonitrile up to 0.5, 0.1, 0.3 and 1 molecules per unit formula weight.

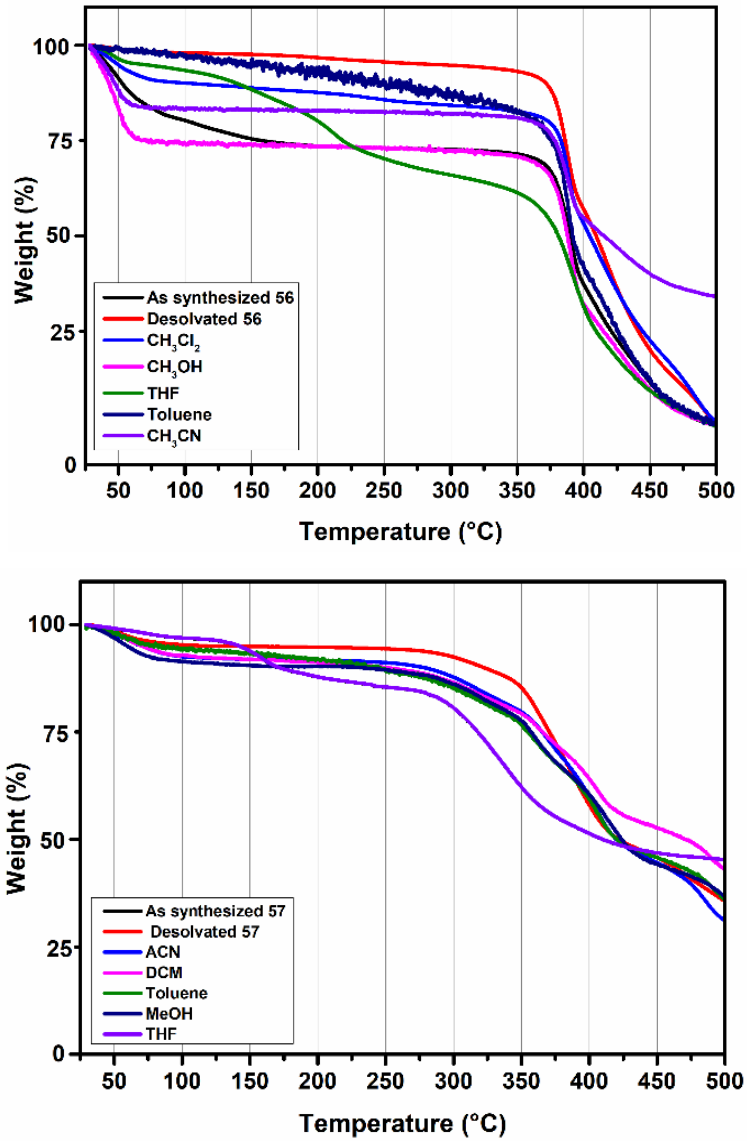

Figure 3.160. Change in the TGA scans of **56** and **57** in different solvents.

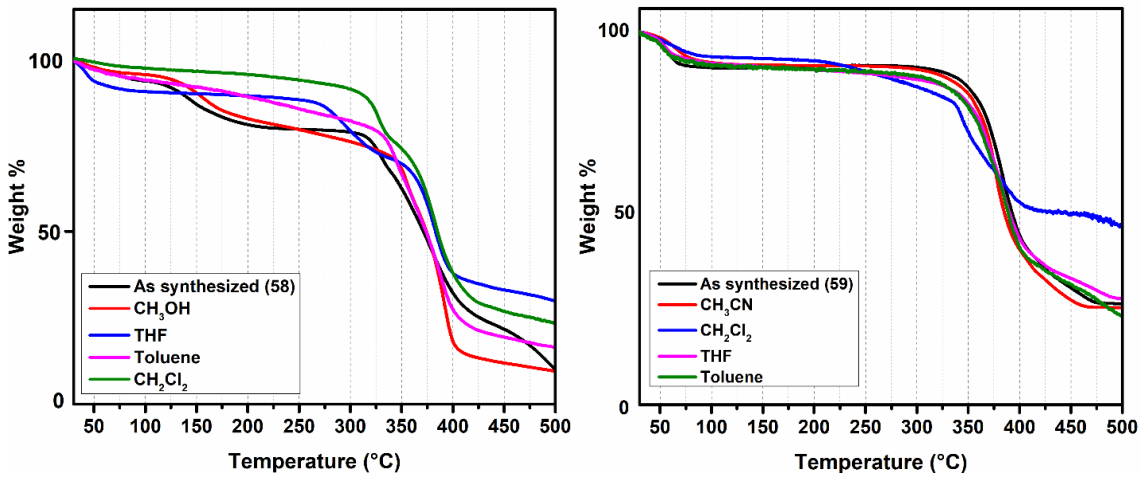

Figure 3.161. Change in the TGA scans of **58** and **59** in different solvents.

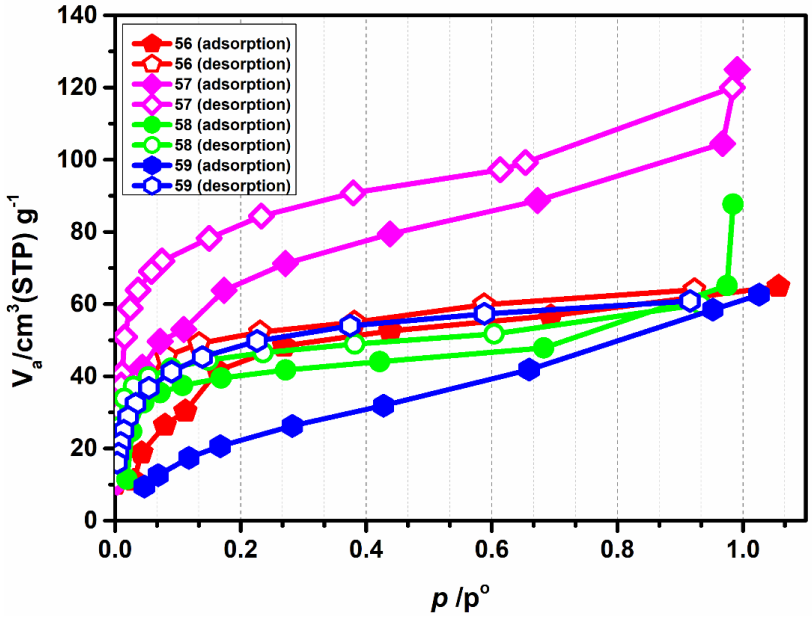

Figure 3.162. Methanol adsorption isotherm for **56**-**59**.

From the thermal analysis, it was found that all these compounds show a good affinity towards adsorption of methanol. Therefore, **56**-**59** were used for methanol sorption studies. From the adsorption isotherm, it was found that **57** shows a better affinity for methanol adsorption compared to **56**, **58**, and **59**. For compound **56**, the amount of methanol adsorbed was 60 cm^3/g; for **57**, it was 125 cm^3/g; for **58**, it was 80 cm^3/g; and for **59**, it was around 50 cm^3/g (see Figure 3.162).

Photophysical properties. The Zn(II) and Cd(II) compounds having d^{10} electronic configuration can exhibit ligand to metal charge transfer or metal to ligand charge transfer and hence exhibit luminescence properties. Luminescence behavior of these Zn-MOFs (**56** and **57**) was recorded in the solid state as well as in a slurry and used for sensing of various analytes like small molecules, explosives, vapors of amines and phenolic compounds. Upon excitation at 285 nm, these compounds show an emission peak around 430-460 nm with good intensity. The emission intensity of **56** and **57** was observed different solvents and was found to be maximum in case of methanol. On the basis of these results, the sensing experiment of vapors and nitro compounds with **56** and **57** was done in a methanolic slurry of these compounds.

Sensing of small organic molecules. To explore the sensing of small organic molecule (solvents), 3 mg of the activated compound (**56** and **57**) was soaked in 3 mL of different solvents like methanol, ethanol, tert. butyl alcohol, acetonitrile,

acetone, toluene, and THF respectively. After stirring for 30 minutes, this slurry was transferred to the cuvette for fluorescence studies.

In both the cases, **56** and **57**, it was observed that these compounds exhibit different luminescent intensities in different solvents. **56** shows maximum intensity in acetonitrile, while **57** exhibits maximum intensity in ethanol. Interestingly, the luminescence intensity of both the compounds got completely quenched in case of acetone. In literature, this type of behavior is reported mostly in case of lanthanides based coordination architectures.[261] A very few examples of transition metals-based frameworks are reported which show this type of behavior.[262,263] In case of **56**, the observed trend of fluorescence intensity with respect to different solvents is in the following order: ACN > MeOH > THF > EtOH > tBuOH > Toluene > acetone, while in case of **57,** it is MeOH > EtOH > ACN > Toluene > THF > tBuOH > acetone as shown in Figure 3.163. This is possibly due to different type of interactions with different solvents. The results obtained from these studies indicate that these compounds can be excellent candidates for the sensing of small organic molecules, especially, acetone compared to other solvent molecules(Figure 3.164). Motivated from these exciting results, we investigated the detection of acetone in other solvents like MeOH, EtOH, and THF.

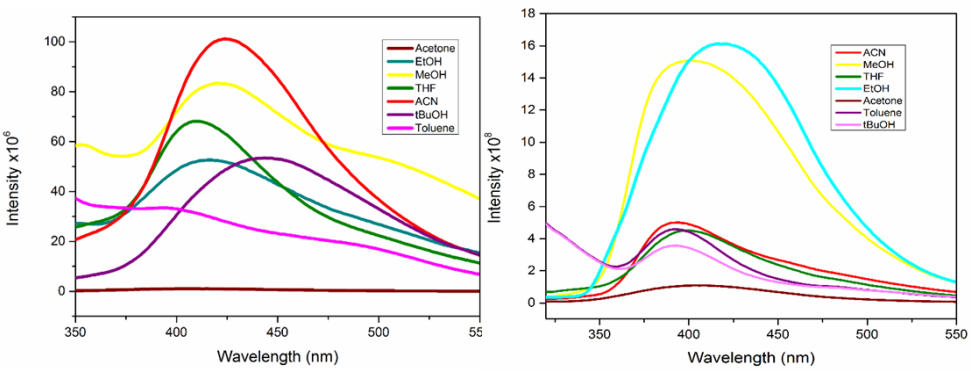

Figure 3.163. Selective sensing of acetone compared to other small molecules by **56** (left) and **57** (right).

For this purpose, compound **56** and **57** were immersed in different concentrations of acetone in MeOH and EtOH followed by recording the fluorescence response. First, different v/v% (10%, 25%, 50%, and 75%) solutions of acetone in methanol and ethanol were prepared. To 3 mL of each solution, 3 mg of compound was added, and after stirring for 15 minutes, their emission spectra were recorded. The same experiment was performed in 100% acetone also. As shown in the Figure 3.165, at

10% acetone concentration (v/v) in methanol, **56** shows more than 90% decrease in its fluorescence intensity, while in case of ethanol it shows 89% decrease in the fluorescence intensity.

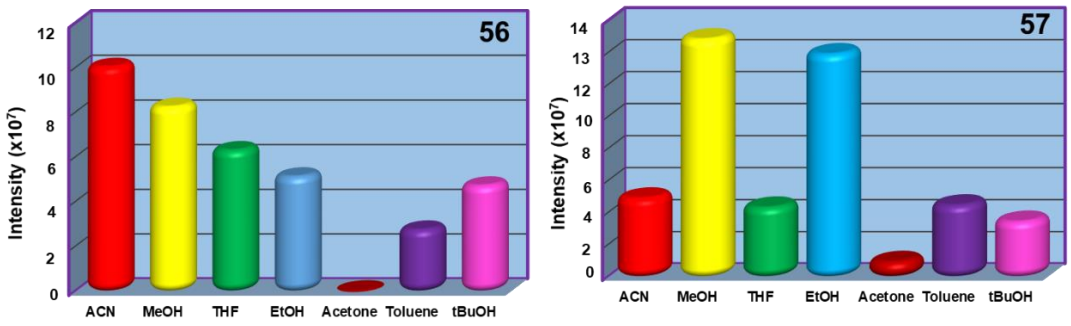

Figure 3.164. Selective sensing of acetone compared to other small molecules by **56** (left) and **57** (right).

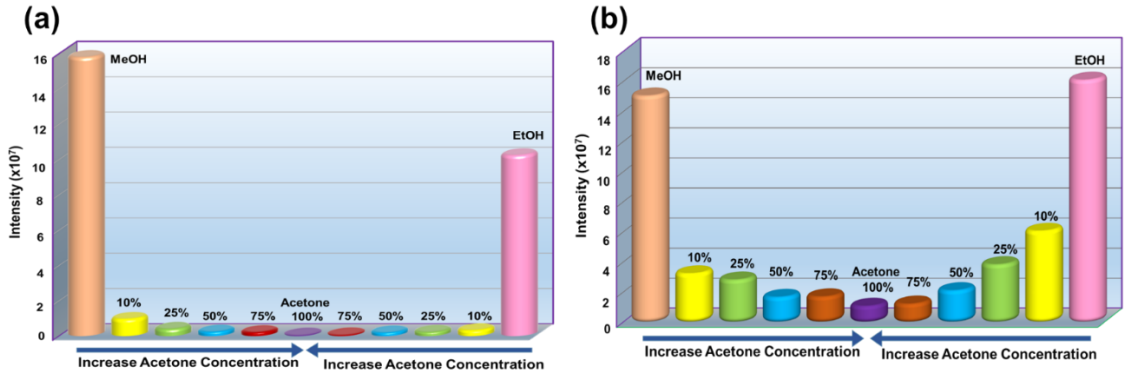

Figure 3.165. Comparison of change in the emission intensity of various concentration of acetone in methanol and ethanol by **56** (a) and **57** (b).

The same experiment was performed for compound **57** and it was found that a 60% decrease in the emission intensity was observed at 10% volume concentration of acetone in ethanol, while in methanol the decrease was around 80%. From the comparison of these results, it was found that **56** is more efficient towards detection of acetone compared to **57** (Figure 3.165).

To investigate the sensitivity of acetone detection in different solvents like methanol, ethanol, and THF, we have performed the same experiment taking 3 mg of compound in 3 mL of different solvents and sequentially adding acetone from 10 μL to 500 μL. The fluorescence spectra of the slurry were recorded upon stirring it for an interval of 5 minutes after each sequential addition of the acetone solution. From this result, it was observed that a 2 v/v% of acetone is sufficient to quench the intensity of compound **56** to approximately 70% in ethanol, methanol, and THF.

(Figure 3.166). At 6 v/v % of acetone, a decrease of 89.8%, 91.5% and 76% in the fluorescence intensity was observed in ethanol, methanol, and THF, respectively.

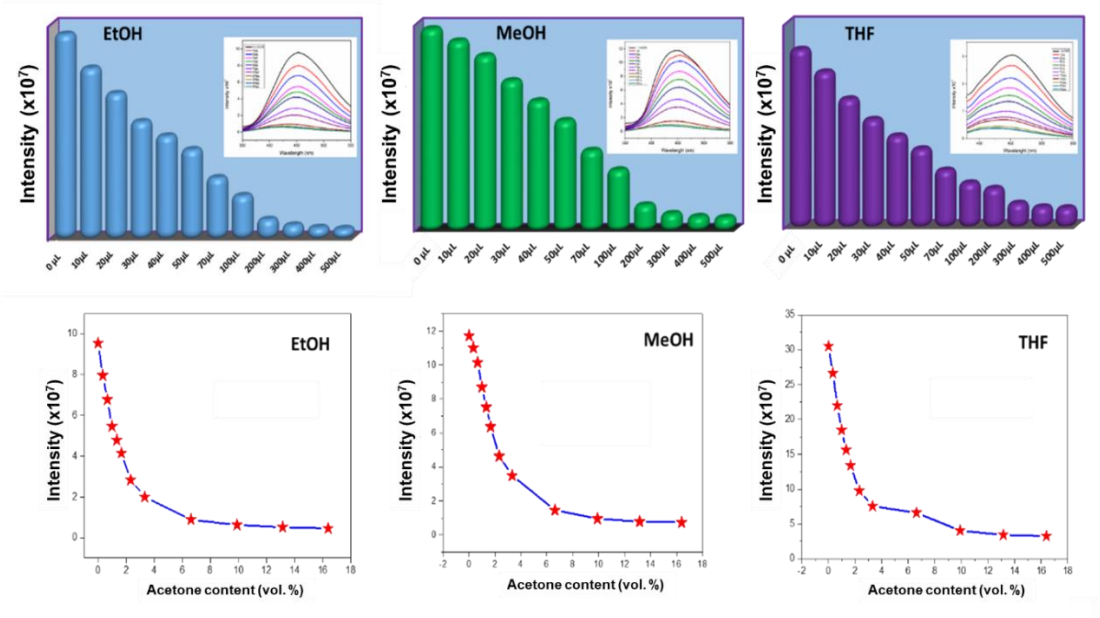

Figure 3.166. Sensitive detection of acetone in MeOH, THF, and EtOH by **56**.

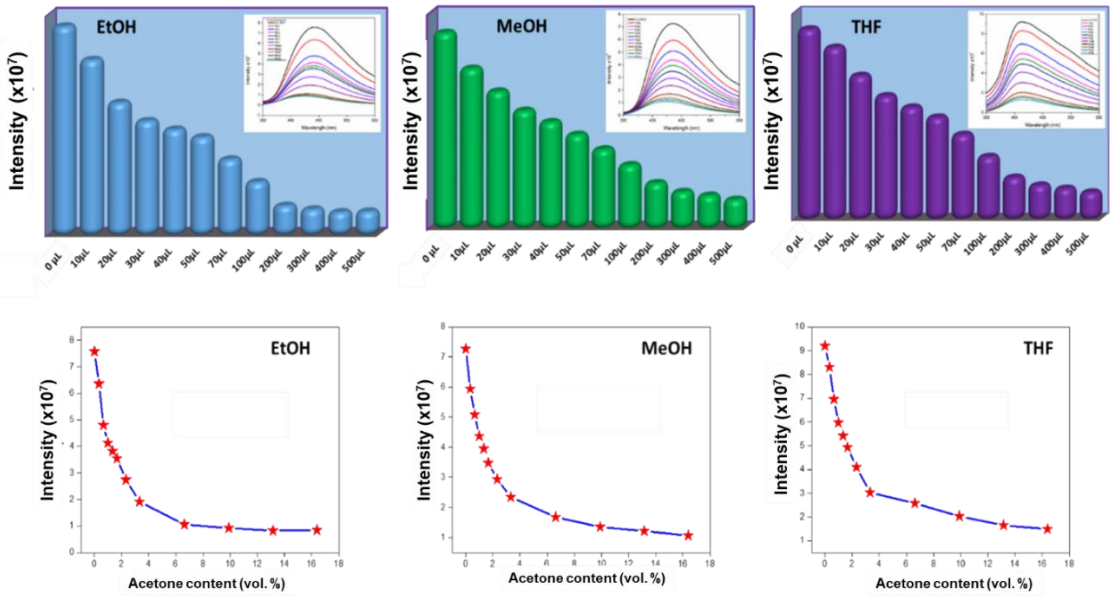

Figure 3.167. Sensing of acetone in MeOH, THF, and EtOH by **57**.

A similar fluorescence titration experiment was performed for **57** and comparable results were obtained in this case.(Figure 3.167). It was observed that at 2 v/v% solution of acetone is sufficient to decrease the fluorescence intensity by more than 70% in methanol, ethanol, and THF. At 6 v/v% of acetone, a decrease of 87%, 76% and 73% in the fluorescence intensity was observed in ethanol, methanol, and THF,

respectively. So, we can say that **56** and **57** are good candidates for detection of minute quantities of acetone. By comparing the result obtained from this study with literature, it was found that only two or three reports are there in the literature which show sensitive detection of acetone.[126,127,263,264] It was found that all these are the lanthanide metal-based coordination polymers; only a few transition metals have been used for this study.

Inspired by these results, we moved towards the sensing of different ketones (aliphatic, cyclic and aromatic) by using **56** and **57**.

Sensing of ketones. As dicussed above, we carried out the sensing experiment of ketones for **56** and **57** in suspension media. For this purpose, we have selected various ketones like acetophenone, butanone, cyclopentanone, mesityl oxide, acetylacetone, cyclohexanone, cycloheptanone, butanone, and acetone. To examine the sensing selectivity of these ketones, a suspension of the compound in MeOH was placed in a cuvette, and upon adding different quantities of ketones, the fluorescence spectra were recorded. A graph between the quenching percent versus concentration of all ketones was plotted and it was found that **56** and **57** behave similarly with respect to acetophenone and acetylacetone (Figure 3.168), while showing different behavior with other ketones.

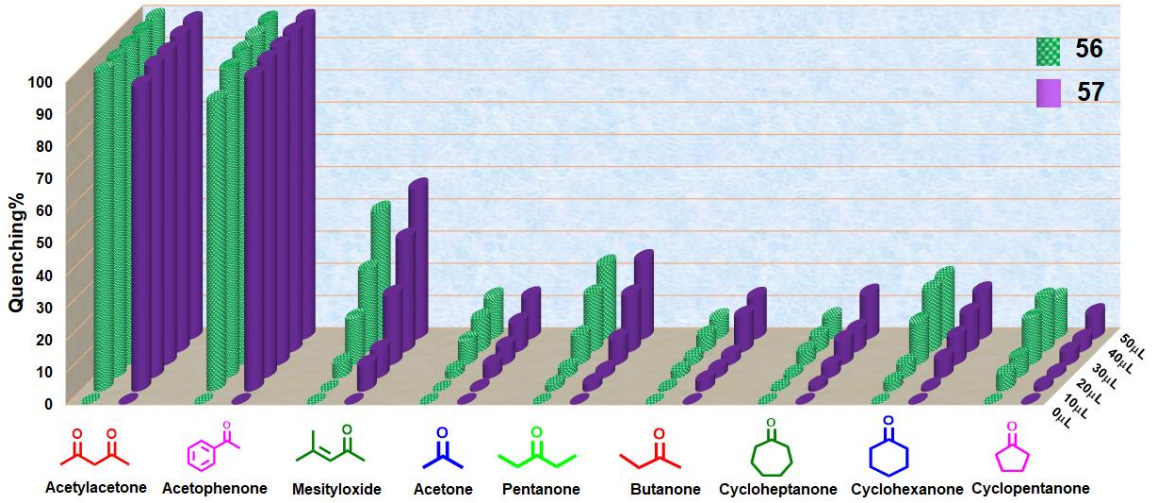

Figure 3.168. Comparison of sensing of ketone derivatives by **56** and **57**.

In case of acetone, compound **56** is more efficient compared to **57**. The general trend of detection of ketones shows the order as follows: aromatic and diketones show maximum quenching followed by cyclic ketones and then aliphatic ketones. In both

cases, sensing of acetophenone and acetylacetone is shows more than 99% quenching after just 20 μL addition to the slurry of **56** and **57**, respectively in methanol. This type of extensive sensing of ketones (acetophenone and acetylacetone) is not reported in the literature (only acetone and cyclohexanone have been studied). Moreover, the detection of cyclohexanone is getting a lot of importance because of its importance in indirect sensing of RDX.[262,265,266]

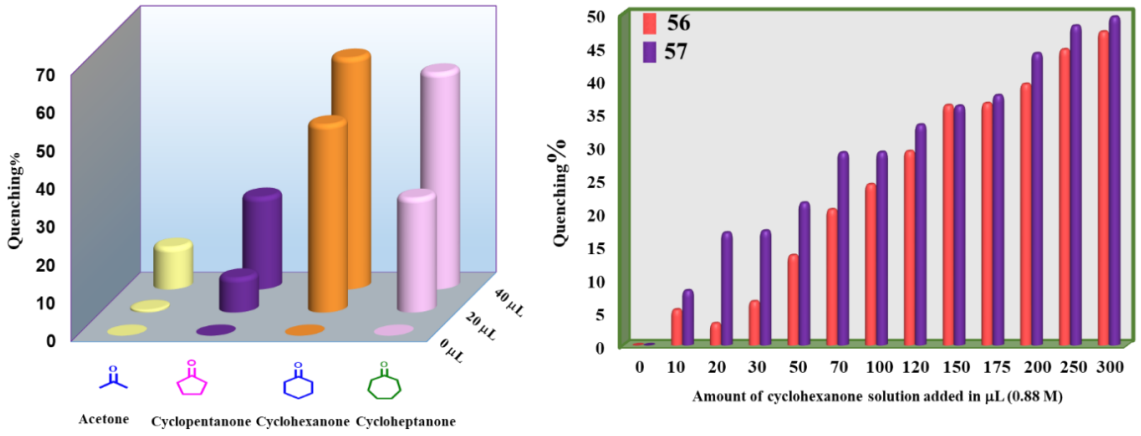

Figure 3.169. Comparison of selective sensing of cyclohexanone over other cyclic ketone and acetone by compound **57** (left) and comparison of detection of cyclohexanone by both the compounds **56** and **57** (right).

Detection of explosives chemical agents has the potential importance because they are frequently used by terrorist activities.[138,265,267–271] Cyclotrimethylenetrinitramine (RDX) was the second most produced explosive during World War II and is still widely used today. Due to the explosive nature and low vapor pressure, it is difficult to detect the RDX directly. An alternative approach to direct detection of RDX is the detection of cyclohexanone, a chemical used to recrystallize RDX. Therefore, inspired by the results obtained form the sensing of acetone, we focused on the sensing of cyclohexanone among other ketones. By comparing the sensing of cyclic ketones with acetone as shown in the Figure 3.169, it was found that cyclohexanone shows maximum sensitivity among all other ketones. More than 65% decrease in the fluorescence intensity was observed in the case of cyclohexanone. For cycloheptanone, 55% quenching in the fluorescence intensity was observed, while in cyclopentanone it was 30% and acetone showed 20% quenching in the fluorescence intensity of **57**. After comparing these results, it was found that as these compounds show excellent sensitivity towards detection of acetone, while in case of cyclohexanone it is much higher than acetone. Furthermore, sensing sensitivity of cyclohexanone was examined by

performing an experiment by incremental addition of cyclohexanone from 10 μL-300 μL (0.88 M). The result obtained from this study strongly indicates that **57** is more efficient towards sensing cyclohexanone compared to **56** as shown in Figure 3.169.

Vapor sensing of volatile amines. From the past few decades, detection of volatile organic amines (VOAs) have been getting great importance because of their important roles in the fields of quality control, medical diagnosis, industrial and environmental concern.[272–282] For this purpose, GC-MS and electrochemical devices are used frequently. However, these detection methods are very expensive in terms of instruments and accessories. Therefore, the use of photoluminescent materials is preferred which is a much easier and cost-effective method for the detection and sensing of amines in vapor as well as in solution phase.[130,132,140–143] Herein, we have demonstrated the sensing of various amines in the vapor phase by using two analogs of Zn(II) metal-organic frameworks. These two compounds (**56** and **57**) were synthesized at two different conditions, by which they adopted different properties and pore environment.

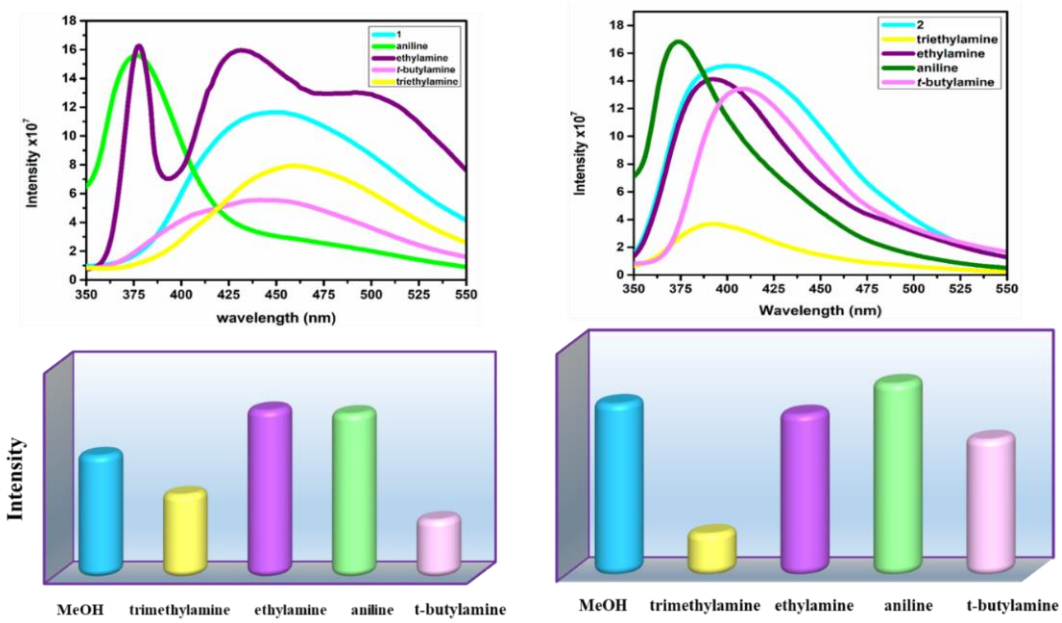

Figure 3.170. Comparison of Sensing of volatile amines by **56** and **57**.

Sensing of amine vapors has been employed for both the compounds **56** and **57**. For this purpose, different volatile amines like triethylamine, ethylamine, aniline, and tertiary butyl amine have been used owing to their low boiling points (Figure 3.170). **56** and **57** being analogous to each other having different properties also show a variation in their sensing properties. For the detection of amine vapors, **56** or **57** (2

mg) was placed in a small glass tube and was kept in the eppendorf having 0.2 mL amine and was tightly sealed. After 18 h it was taken out and poured in 2 mL methanol and covered tightly. Furthermore, it was sonicated for 15 min to make a uniform slurry and then immediately transferred into aquartz cuvette to carry out the fluorescence experiment.

The results obtained from this study indicate the different response of both the compounds towards different volatile amines. As shown in the Figure 3.170, along with the quenching and enhancement of the fluorescence intensity, a shift in the λ_{max} was also observed. The results obtained indicate aniline and ethylamine show enhancement and t-butyl amine show maximum quenching in the intensity in case of compound **56**. While in case of **57**, only aniline shows enhancement and trimethylamine shows maximum quenching. This is due to different type of interactions of amines with the framework of **56** and **57**. Compound **57** shows a good selectivity for trimethylamine among other amines.

Sensing of aromatic amines in solution. After the sensing of volatile amines, we move towards the sensing of aromatic amines in the solution state. For this purpose, different aromatic amines were used which are shown in the Figure 3.171.

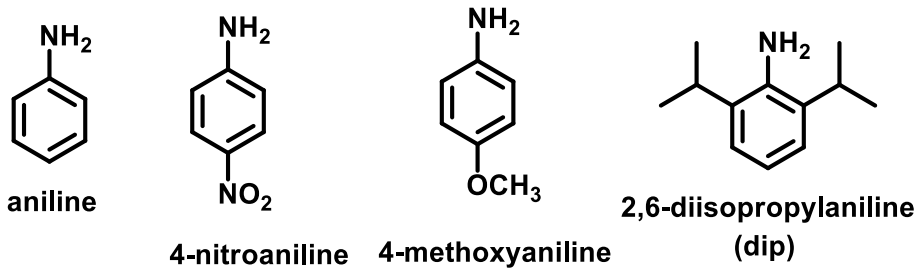

Figure 3.171. Structure of different amines used for sensing in the solid state (slurry) by **57**.

57 was chosen amon the two compounds for sensing experiment because it was synthesized at room temperature which is a green method. For the sensing of aromatic amines, a slurry of compound **57** in methanol was prepared using 2 mg of the compound. To make a uniform suspension, compound was first stirred in the methanol for 30 min and then sonicated for 5 min. After transferring this slurry into the cuvette, fluorescence spectra were recorded for the pristine sample. After this 30 μL amine solution having a concentration of 0.023 M (in methanol) was added , stirred for 5 min and the emission spectrum was recorded. A series of amines have been employed for this study using the same protocol. These different aromatic amines have different groups associated with them, which may be electron

donating or/and electron withdrawing groups, attached at different positions of the phenyl ring. Because of this, we have found that both turn-on and turn-off behavior in luminescence takes place with respect to different analytes (Figure 3.172). Along with the quenching and enhancement, red and blue shift in the λ_{max} also takes place.

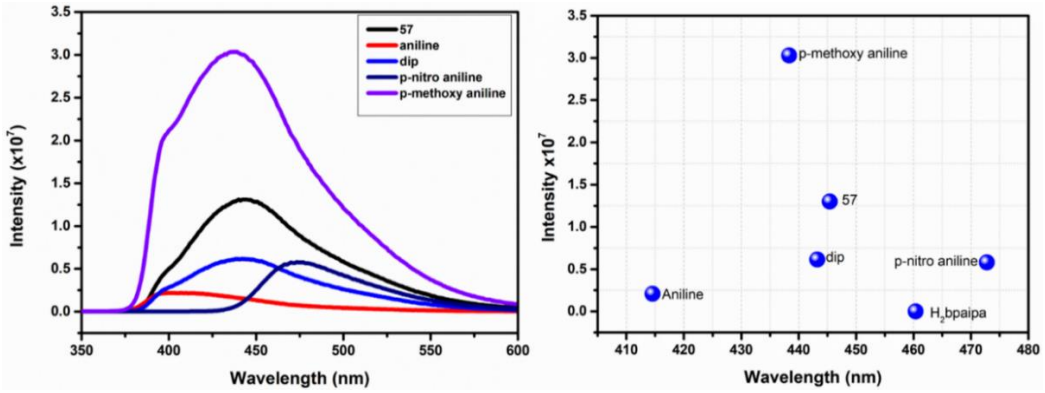

Figure 3.172. Sensing of aromatic amines (a) Response of **57** dispersed in methanol towards sensing of different aromatic amines (30 μL, 0.023 M) and (b) 2D decoded map of intensity *vs* wavelength for different aromatic amines in **57**.

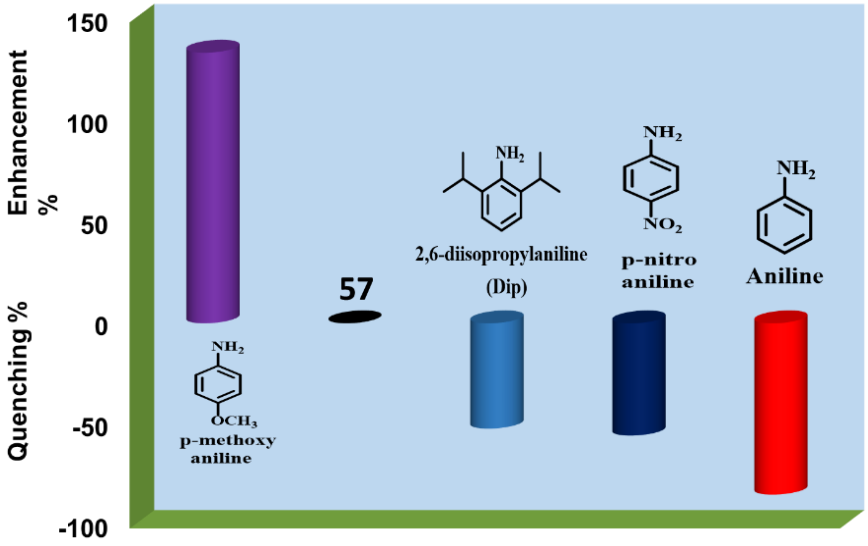

Figure 3.173. Sensing of aromatic amines (a) Response of **57** dispersed in methanol towards sensing of different aromatic amines.

As shown in the Figure 3.173, p-methoxyaniline shows turn-on fluorescence, while others like p-nitroaniline, aniline, and 2,6-diisopropyl aniline show a turn-off behavior. If we consider the quenching percentage, it is maximum in case of aniline (more than 90%), while 2,6-diisopropylaniline and p-nitro aniline show around 50% quenching. From this experiment, it was observed that aniline derivatives show a decrease in the fluorescence intensity, while the presence of electron donating group enhances the intensity.

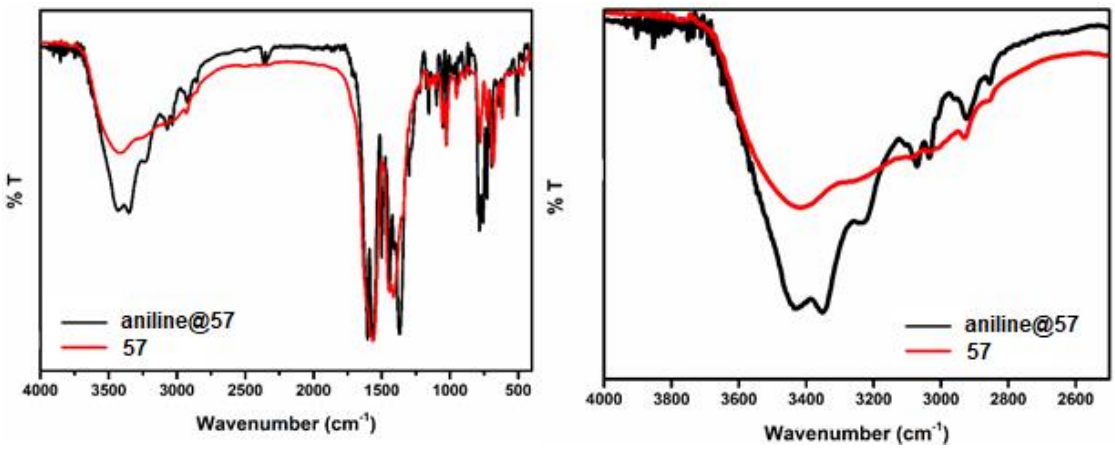

Figure 3.174. Change in FTIR spectrum after aniline encapsulation inside **57**.

This change in fluorescence is due to the interaction of amines with the framework by which these amines can enter inside the pores. Interaction of aniline takes place at different interaction sites of the framework which is responsible for the change in the fluorescence intensity as well shift in the λ_{max} value. To check for the presence of amines inside the framework or interaction of amines, different techniques have been used. For this purpose, the compound having aniline was filtered off from the solution after fluorescence and dried in air. Using this compound, FTIR, PXRD and thermogravimetric analysis have been performed.

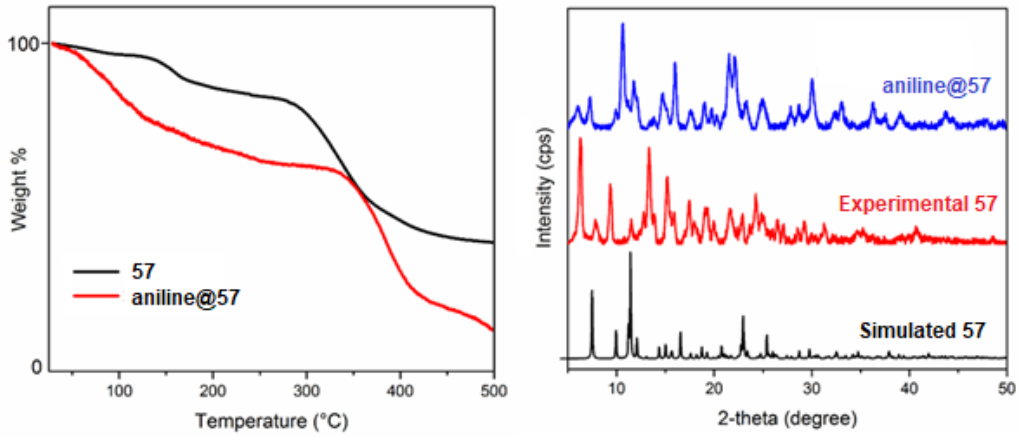

Figure 3.175. TGA scans (left) and PXRD patterns (right) before and after aniline encapsulation in **57**.

By comparing the FTIR of the fresh compound with a compound having aniline it is confirmed that aniline is present in the framework. As shown in the Figure 3.174, appearance of two peaks in between 3100 cm^{-1} to 3500 cm^{-1} is a strong evidence for the same. Furthermore, a slight change in the PXRD pattern as well as a change in the thermal stabilityconfirms the presence of amine within the metal-organic framework. An

appreciable weight loss in the TGA scan of **57** after aniline encapsulation confirms the encapsulation of aniline within the framework (Figure 3.175).

Sensing of nitroaromatic compounds (NACs) in solution. Compound **57** was further employed for the sensing of nitroaromatic compounds (NACs). Nitroaromatic compounds consist of the major ingredients which are used in common explosives. Because of environment and human health concern, it is very important to sense these chemical compounds.[112,121,283] A fast and efficient detection of explosives is one of the concerns for a variety of reasons which make these sensors more efficient and reliable. We have discussed that due to the presence of analyte, a change in the fluorescent behavior of the compound occurs. The change in the fluorescence behavior is due to the interaction of the analyte with the framework.[281]

For this study, 2 mg of **57** was taken in 2 mL methanol after activation at 120 °C in a vacuum oven. It was stirred for 30 min followed by sonication for 15 min to make a proper slurry. This was then transferred to the cuvette, and fluorescence spectrum was recorded. This was excited at 285 nm and scanned for a range of 310 nm-550 nm using slit width 3 nm and 3 nm (entrance and exit slit). A broad spectrum was obtained having λ_{max} between 400 nm to 450 nm as shown in Figure 3.176.

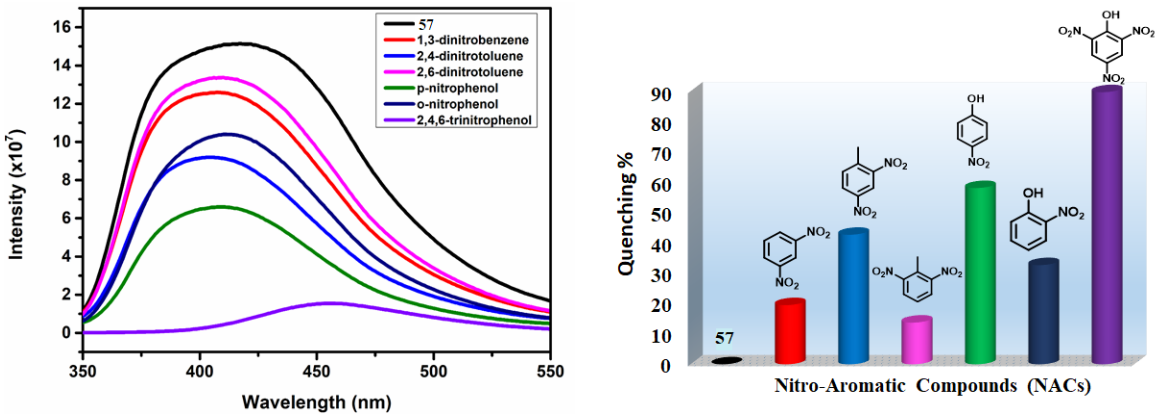

Figure 3.176. Change in emission intensity after addition of different analytes (left) and quenching with respect to the different analyte in **57** (right).

A series of nitroaromatic have been employed for this study mainly toluene and phenolic nitro-aromatic compounds. A 1 mM solution of all these analytes was prepared, and 50 μL of each was added to a well-dispersed slurry of **57** taken in methanol, and the fluorescence spectrum was recorded. The results obtained from this study indicate that in all the cases quenching in the fluorescence intensity takes place. No enhancement in the fluorescence intensity was observed like aromatic

amines. A slight shift in the λ_{max} was observed in some cases in addition to the quenching in intensity. Considering the trend of quenching, it was found that nitrophenols show maximum quenching compared to other nitro aromatic derivatives (Figure 3.176). Out of all nitroaromatics, 2,4,6-trinitrophenol (TNP) shows maximum quenching around 90% followed by *p*-nitrophenol (60%) and *o*-nitrophenol (30%). *o*-nitrophenol shows less quenching effect than the 2,4-dinitrotoluene (45%). Further, 1,3-dinitrobenzene (20%) shows higher quenching efficiency than 2,6-dinitrotoluene (15%).

The quenching effect of 2,4,6-trinitrophenol (TNP or picric acid) inspired us to investigate further the detection limit and K_{sv} constant which can further explain the extent of interaction between TNP and **57**. As we know, compound **57** is soluble in water, therefore, detection of TNP (picric acid) has been done in water and as per the literature survey it is rare to sense the picric acid in the aqueous medium.[284] So, we have chosen the aqueous medium for sensing of picric acid. We have taken 1 mg of compound, dissolved in 3 mL of water and fluorescence spectra was recorded.

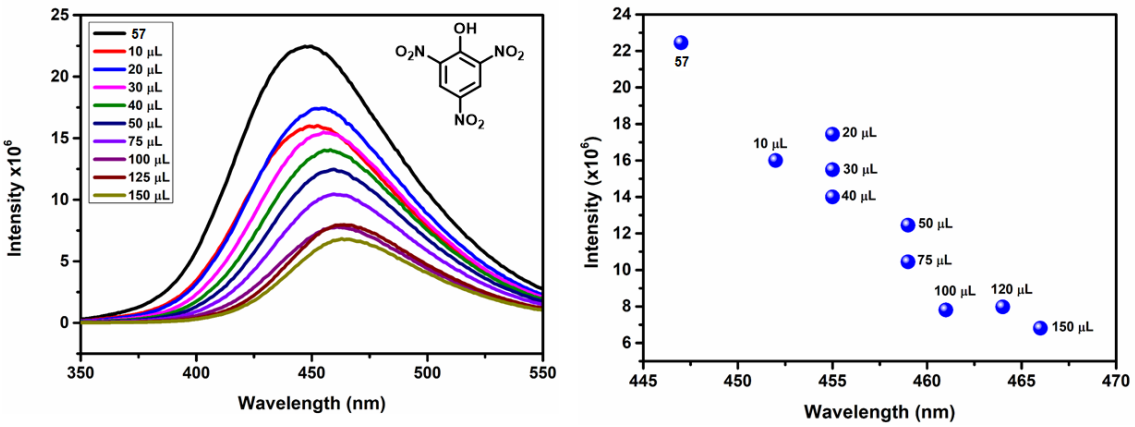

Figure 3.177. Change in emission intensity after addition of picric acid (left) and shift in λmax with respect to the incremental addition of picric acid in a solution of **57** (right).

Furthermore, after an incremental addition of TNP solution (1 mM), fluorescence spectra were recorded. After plotting a graph between intensity versus wavelength for every addition, a sequential quenching in the fluorescence intensity was observed (Figure 3.177). Upon closer investigation of the fluorescence spectra, we have found that the fluorescence spectrum of **57** in presence of TNP is red shifted by 20 nm. The extent of interaction of TNP with **57** i.e. the K_{sv} value is found to be 1.98 x 10^4 M^{-1} and has been calculated from the linear fitting of the graph between concentration verses I_o/I. This K_{sv} value indicates the presence of strong interaction

of TNP with the framework. Furthermore, the detection limit was calculated by linear fitting of intensity versus concentration. A detection limit of 0.16 ppm was calculated which is good for the detection of TNP in water.

Transmetalation in 56 and 58. Transmetalation is the process by which one metal is exchanged with another metal to form a new compound.[285] In case of MOFs, it is convenient to swap their constituent with a surrounding medium via post-synthetic modification to create a novel structure. These compounds formed by post-synthetic approach have different properties when compared with the starting compounds. Sometimes, if it is not possible to make the compound by the common methods then post-synthetic modification plays a very important in the formation of these new compounds.[285–288] In MOFs, exchange of ion (cation and anion), coordinated water molecules, ligands, linkers and modification of ligands having functionality is a way to design new materials. However, it is not possible to get the desired product always; sometimes MOFs lose their identity or a collapse of the framework can occur during the process. In the transmetalation process, cleavage of all the bonds of donor atom and metal takes place followed by the formation of new bonds with the new metal. This process can only happen when the bond between the ligand and the metal is not strong enough. This post-synthetic modification can cause a change in the topology of the starting compound, or it may remain intact. For this purpose, we have chosen two different compounds which have been synthesized by solvothermal conditions using two different metals Zn(II) (**56**) and Cd(II) (**58**) and a common mixed ligand. The exchange of metal already present in MOF with another metal was achieved by the post-synthetic modification process. Zn(II) or Cd(II) was replaced by Cu(II) metal center by following the reported procedure in literature (Figure 3.178).

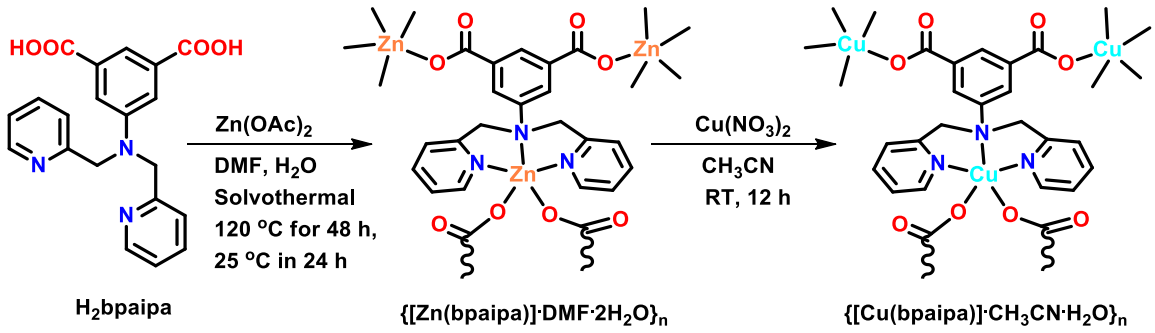

Figure 3.178. Schematic representation showing the synthesis of **56** and transmetalation to **56Cu.**

At room temperature, freshly prepared crystals of **56** and **58** were immersed in acetonitrile solutions of $Cu(NO_3)_2$ (5 mg in 25 mL). After 12 h, a change in the color was observed which indicates the exchange of Zn(II) and Cd(II), respectively, with copper in the primary stage (Figure 3.179).

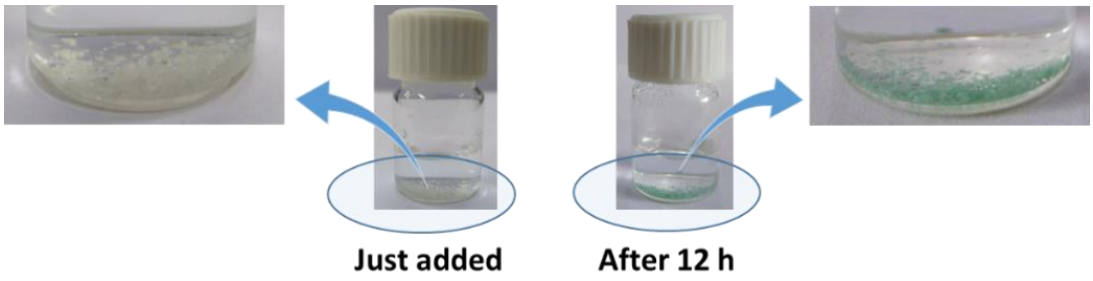

Figure 3.179. Change in the color of crystals of **56** after transmetalation.

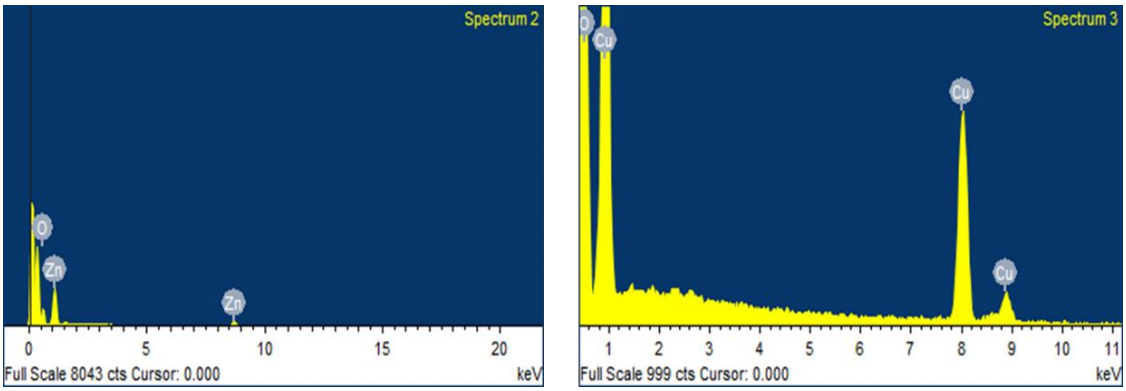

Figure 3.180. EDX spectrum of **56** (left) and corresponding exchanged product with Cu (right) is that **56Cu**.

Compound **56** is a Zn(II) complex with a mixed ligand; forms whitecrystals which turns greenish after transmetalation as shown in the Figure 3.179. After keeping the crystals in the same solution of $Cu(NO_3)_2$ for 15 days, the resulting product was filtered-off and washed with acetonitrile followed by drying in air. These green crystals were further used for other characterizations like elemental analysis, FTIR, absorption spectroscopy, energy-dispersive X-ray spectrometry (EDX), and powder XRD analysis. To confirm the presence of exchanged metal, EDX analysis was performed. From the EDX studies, we can easily find out which metal is present in the compound. The appearance of the peak for only copper in the EDX spectrum indicates complete exchange of Zn(II) and Cd(II) with the incoming Cu(II) metal, as shown in Figure 3.180. For compound **56**, crystals were good

enough for single crystal studies. So, after washing the crystals with fresh acetonitrile, these were used for single crystal analysis.

Single crystals analysis of compound **56Cu** indicates that this compound crystallizes in the monoclinic *C*2/*c* space group which is different from the mother Zn(II) compound ($P2_1/n$). However, the coordination environment around the metal center is same, surrounded by three nitrogens and two oxygens of the ligand, resulting in a distorted square-pyramidal geometry. The asymmetric unit consists of a Cu(II) center, a bpaipa ligand, and solvent molecules as shown in Figure 3.181. After transmetalation, no change in the overall topology of the compound was observed, although due to the flexible rotation of the carboxylate, a slight change in the arrangement of the carboxylate was observed. In this case, DMF also gets replaced by the acetonitrile molecule which are situated in the pores of the framework.

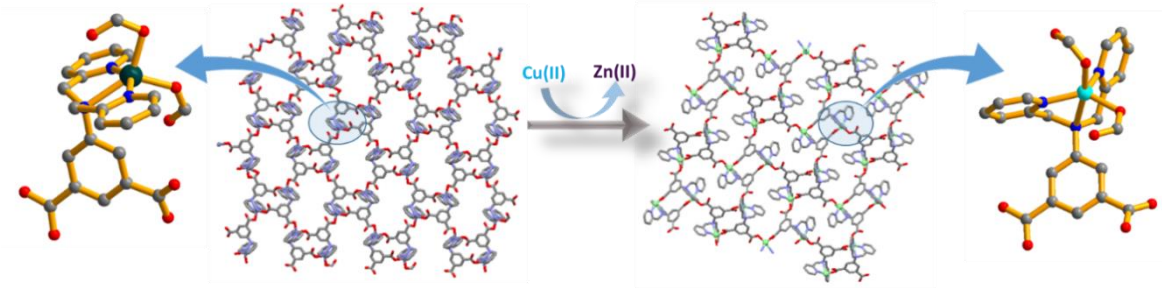

Figure 3.181. Change in the crystal structure after transmetalation in **56**.

Both the carboxylates bind in a monodentate fashion with Cu(II) center (distances: 1.995(2) Å and 1.958(2) Å), and the pyridyl nitrogens bind with the metal (distances: Cu–N_{py}, 2.074(3) Å, and 2.046(3) Å) and one alkyl nitrogen (distance: Cu–N_{alkyl}, 2.321(3) Å). There is not much difference in the distances between the donor atom and the metal in both mother and daughter complexes. The τ parameter found to be 0.22, which indicates the geometry is close to square-pyramidal. Similar to the mother Zn-MOF (**56**), a 2D MOF was generated by expanding this asymmetric unit which consists of a sheet-like structure having two different types of pores as shown in Figure 3.182. Large and small pore dimensions are 14.825 (2) × 8.675 (2) $Å^2$ (defined by the distance between two Cu^{2+} centers) and 3.653 (2) × 7.444 (2) $Å^2$ (defined by the distance between corners Cu^{2+} centers and an oxygen atom).

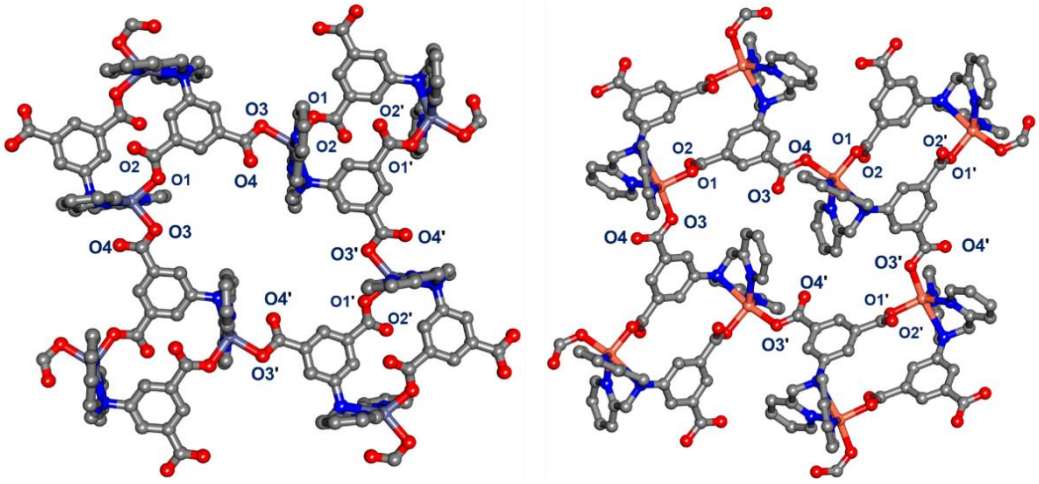

Figure 3.182. Change in the small and large pore after transmetalation in **56**.

After transmetalation, no change in the overall topology took place, although a slight change in the orientation of the carboxylates was observed as shown in the Figure 3.183. As in **56**, both the carboxylates are situated in the same plane, while in **56Cu** both the carboxylates are not in the same plane and are oriented in different directions.

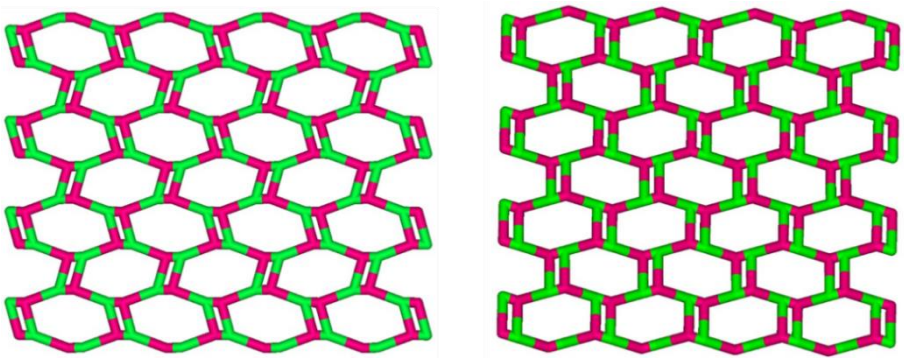

Figure 3.183. Topological view of **56** (left) and **56Cu** (right).

Due to this flexible rotation of carboxylates, the pyridyl group gets situated more inside the pores which result in a change of the τ parameter as well as pore volume. Considering the lattice solvent, in **56,** it has one DMF and two water molecules, while in **56Cu**, one water molecule and two acetonitrile molecules are present in the pores. After investigating very carefully both the structures, it was found that the available pore volume and nature inside the pores is different. Compound **56** shows more available pore space than compound **56Cu**.

In every case, it is not easy to exchange metals with a 100% conversion rate, however, by increasing the time we can achieve this. It is reported in the literature that conversion starts from the surface and goes towards the bulk. This can be easily confirmed by removing the

crystals after some time and breaking the crystal into two halves. The difference in the color of surface and bulk is the proof for this partial conversion. There are some methods by which we can calculate the kinetics of exchange. In our study, we have used EDX spectroscopic technique to find out the time taken by a crystal for 100% conversion or exchange. To do so, we took out some crystals from the solution of $Cu(NO_3)_2$ every day and used for EDX studies. The percent of both the metal atoms was plotted against the number of days. From this, a conclusion can be drawn that 100% conversion of Zn(II) with copper(II) takes place in sixteen days, as shown in Figure 3.184.

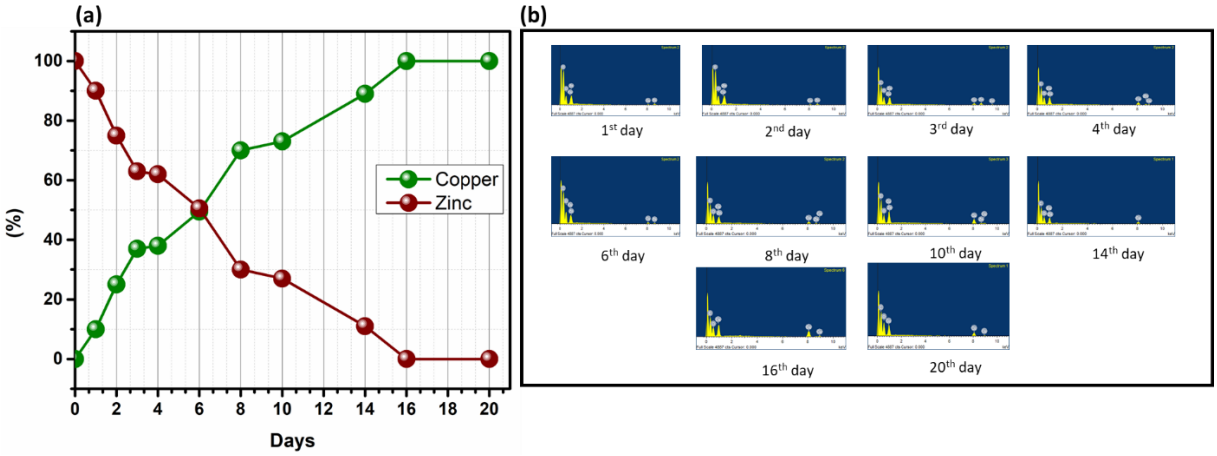

Figure 3.184. Kinetics of replacement of Zn(II) with Cu(II) followed by EDX in **56**.

Furthermore, this exchange of metal via post-synthetic modification was confirmed by other techniques like UV-Vis spectroscopy and powder X-ray diffraction analysis. As shown in the Figure 3.185, the PXRD patterns of both **56** and **56Cu** are slightly different, while they show good agreement with their respective simulated powder pattern obtained from their single crystal structures.

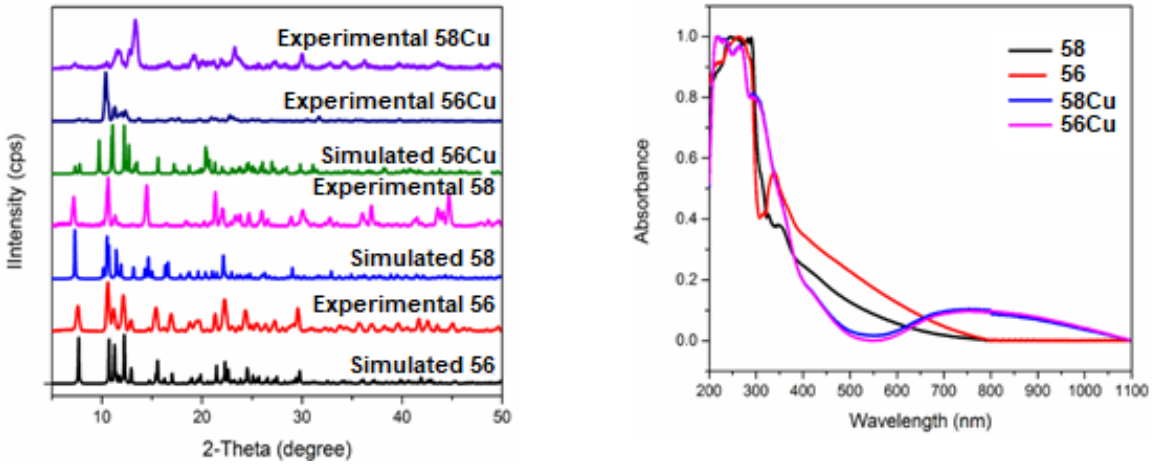

Figure 3.185. Simulated and experimental powder patterns of **56, 58, 56Cu and 58Cu** (left) and solid state reflactance spectra of **56**, **56Cu, 58** and **58Cu** (right).

Along with this, the bulk phase purity of the resulting compounds was also confirmed by their respective PXRD patterns. Furthermore, UV-Vis spectra of both the Zinc and Copper compounds have been done in the solid state, where the appearance of a peak around 700-800 nm in the **56Cu** confirms the presence of copper instead of Zn(II) (see Figure 3.185).

To explore further, we moved towards the Cd(II) compound (**58**). Similar protocol for the transmetalation in compound **58** was followed (Figure 3.186). Even after using similar protocols and going for several attempts, we could not get crystals good enough for SCXRD as the crystals got cracked after the process. So, we have used other analytical techniques like TGA, FTIR, CHN, and PXRD to prove this cation exchange via post-synthetic modification.

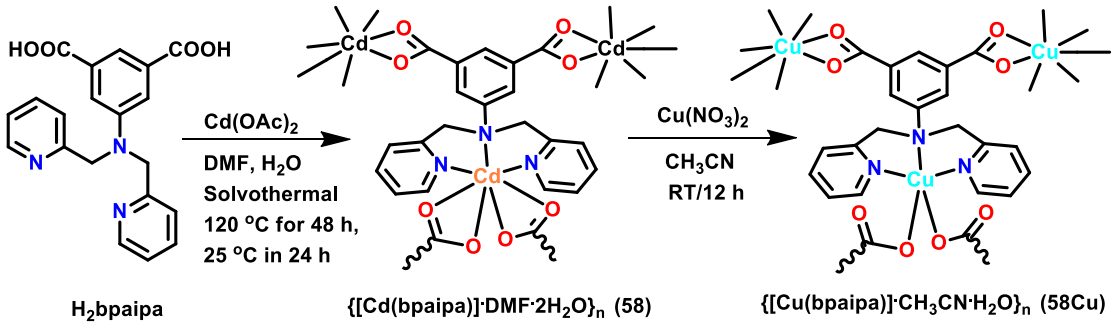

Figure 3.186. Schematic representation showing the synthesis of **58** and transmetalation to **58Cu**.

This compound had light yellow color crystals which were used for the transmetalation study. The crystals were dipped in a solution of $Cu(NO_3)_2$ in acetonitrile for 15 days. After few days, color of these crystals started changing to light green color and at the end total compound turned into green color, as shown in Figure 3.187.

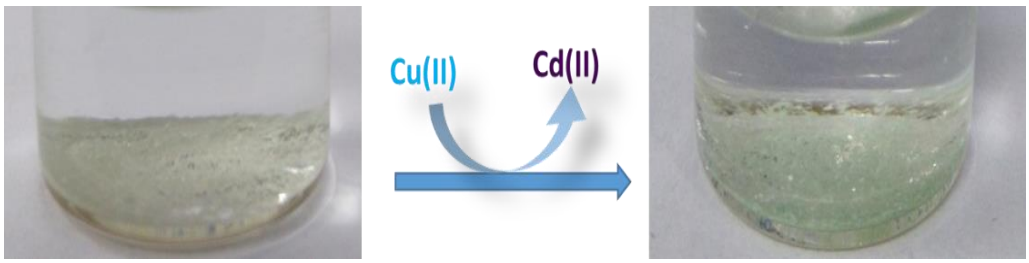

Figure 3.187. Change in the color of crystals of **58** after transmetalation.

A strong evidence for the metal exchange is the appearance of the copper peak and disappearance of cadmium peak in the EDX spectrum. Furthermore, a change in the PXRD pattern of **58** after transmetalation is another evidence of change in the structure. By comparing the PXRD patterns of **56Cu** and **58Cu** which shows similar nature confirming

the formation of similar compound as formed in **56**. The appearance of a broad peak around 700-800 nm in the solid state reflectance spectra of **58Cu** confirms the transmetalation in **58**. To check the percent exchange of Cd(II) with Cu(II), kinetics was done similar to that in compound **56**. From this study, it was confirmed that 100% conversion takes place in 15 days like in **56**. From this study, it also confirmed that exchange of Cd(II) with Cu(II) takes place with slower speed compared to Zn(II) compound, as shown in Figure 3.188.

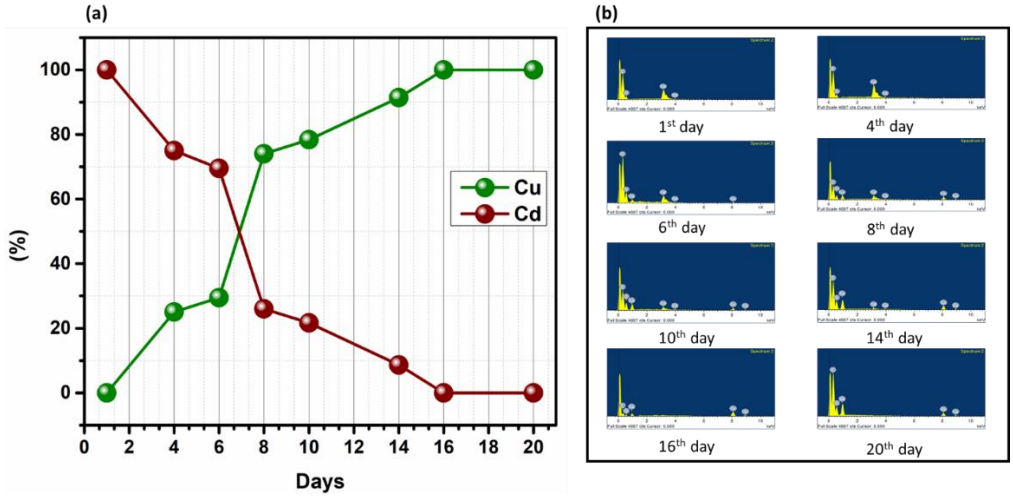

Figure 3.188. Kinetics of transmetalation in **58**.

Chemistry with 2,4-H_2bpaipa ligand

Under hydrothermal conditions, four MOFs, **60-63**, were synthesized (Scheme 3.23) utilizing 2,4-H_2bpaipa by heating the reaction mixture in a mixed solvent (DMF, methanol, and water in 1:1:1 ratio) at 120 °C for 48 h, followed by cooling over a period of 24 h.

$$M(OAc)_2 + \text{2,4-}H_2\text{bpaipa} \xrightarrow[\text{120 °C, 48 h; cooling in 24 h}]{\text{DMF:}H_2\text{O:MeOH}} \begin{cases} M = Zn \rightarrow \{[Zn(2,4\text{-bpaipa})]\cdot CH_3OH\cdot 2H_2O\}_n & (60) \\ M = Cd \rightarrow \{[Cd(2,4\text{-bpaipa})]\cdot 3H_2O\}_n & (61) \\ M = Ni \rightarrow \{[Ni(2,4\text{-bpaipa})]\}_n & (62) \\ M = Co \rightarrow \{[Co(2,4\text{-bpaipa})]\}_n & (63) \end{cases}$$

Scheme 3.23. Synthesis of **60-63**.

FTIR spectroscopic studies. The carboxylate in 2,4-H_2bpaipa in **60** and **61** show monodentate binding mode with Zn(II) and Cd(II), respectively, while it shows bidentate binding mode in **62** and **63** with Ni(II) and Co(II), respectively. (Figure 3.189 and Table 3.26).

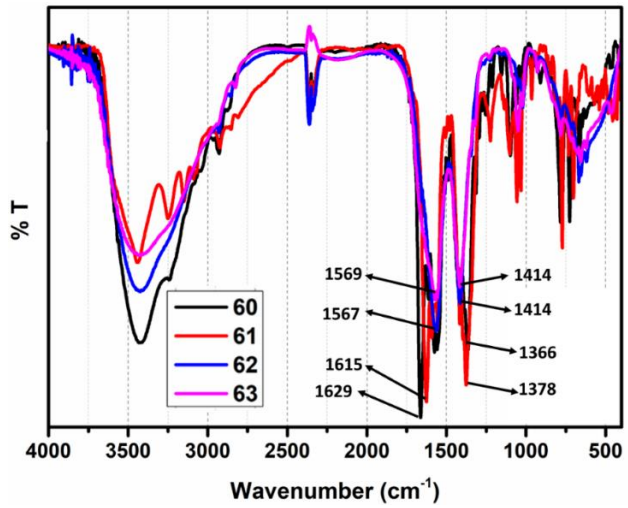

Figure 3.189. FTIR spectra of **60**-**63**.

Table 3.26.Asymmetric and symmetric stretching frequencies and their respective binding modes of carboxylates in **60**-**63**.

Compound	Asymmetric (υ_1) cm^{-1}	Symmetric (υ_2) cm^{-1}	$\Delta\upsilon = \upsilon_1 - \upsilon_2$ cm^{-1}	Binding mode
60	1629	1366	263	Monodentate
61	1615	1378	237	Monodentate
62	1567	1414	153	Bidentate
63	1569	1414	155	Bidentate

Thermogravimetric analyses. Thermal stability of **60**-**63** were studied as a function of temperature in the range of 25-500 °C (Figure 3.190).

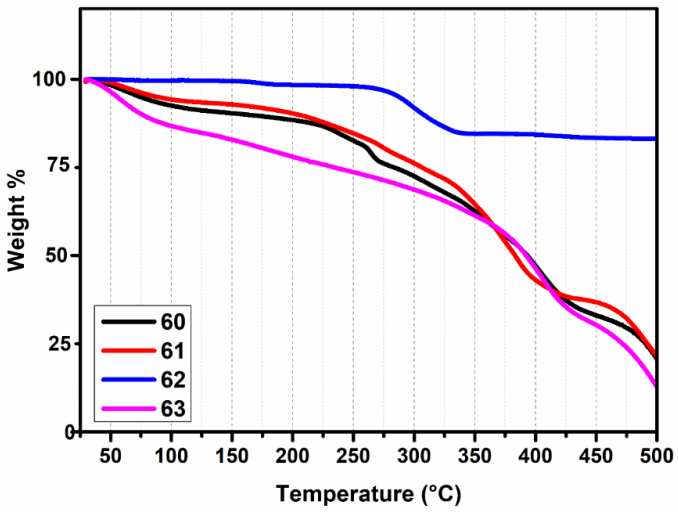

Figure 3.190. TGA scans of **60**-**63**.

60 is stable up to 250 °C after loss of one lattice water molecules corresponding to 3.86% (ca. 3.54%). **61** is more stable up to 300 °C with the first weight loss of 10.13% corresponding to the loss of one water molecule (ca. 10.23%). Compound **62** showed

negligible weight loss up to 200 °C, indicating the absence of lattice solvent molecules, while **63** shows a gradual weight loss.

Single crystal structure analyses. 60 crystallizes in the $P2_1/n$ space group. In this structure, Zn(II) is tetracoordinated and is surrounded by two oxygen atoms from the carboxylate groups and two nitrogen atoms of the pyridyl groups from four different ligands forming an N2O2 type coordination environment.

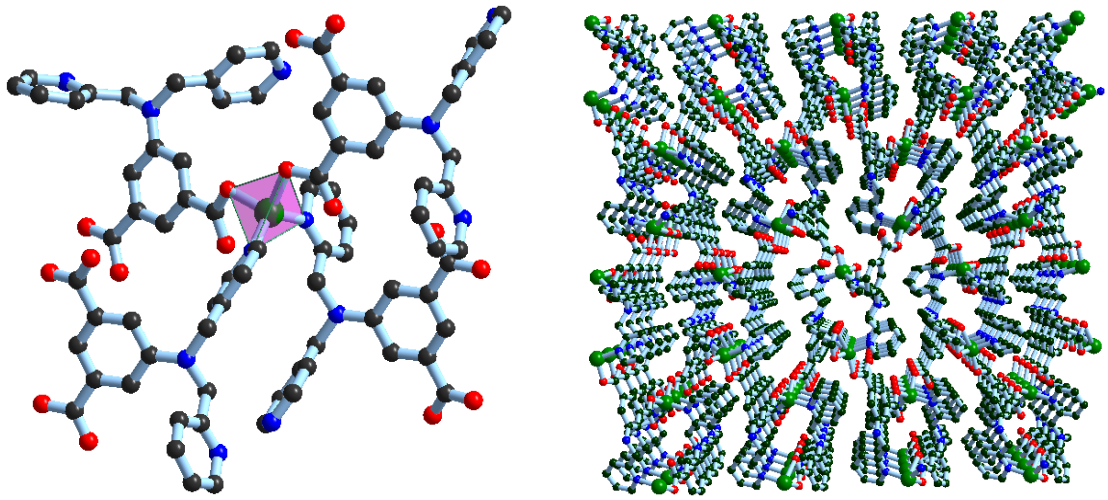

Figure 3.191. Coordination environment around the metal centers (left), Formation of 3D porous structures (right) in **60**.

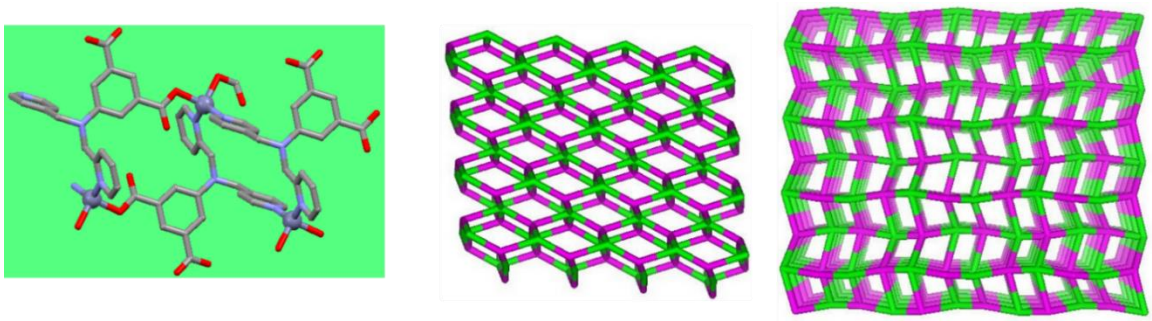

Figure 3.192. Topological view of **60** in two different directions.

All the carboxylates bind with Zn(II) center in a monodentate fashion, with Zn-O distances of 1.957(6) Å and 1.986(6) Å. On the other hand, Zn-N distances are 2.061(7) Å and 2.003(7) Å. Both the carboxylate and the pyridyl groups are *cis* to each other (Figure 3.191). A 3D porous coordination polymer is generated after expanding the structure in all directions, with four different types of pores in which two pores are small with dimensions, 9.33 x 7.51 $Å^2$ and 9.06 x 8.692 $Å^2$, and other two pores are large with dimensions 15.46 x 8.31 $Å^2$ and 14.12 x 10.12 $Å^2$. This compound exhibits a 7-connected; uninodal net

topology (new topology), as shown in Figure 3.192. All the bond distances and angles are listed in Appendix (Table A32 and A43).

Adsorption of dyes in 60. **60** was pretreated for adsorption of dyes by washing with methanol and heated at 120 °C in a vacuum oven for 8 h. Both cationic and anionic dyes were screened using this compound. Three different dyes congo red (CR), rhodamine B (RB) and methylene blue (MB) have been employed for the dye adsorption studies. A 2 μM concentration of these dyes was used, and the UV-Vis spectrum was recorded; 15 mg of **60** was added to the solution of dye and after every 10 min, the UV-Vis spectrum was recorded.

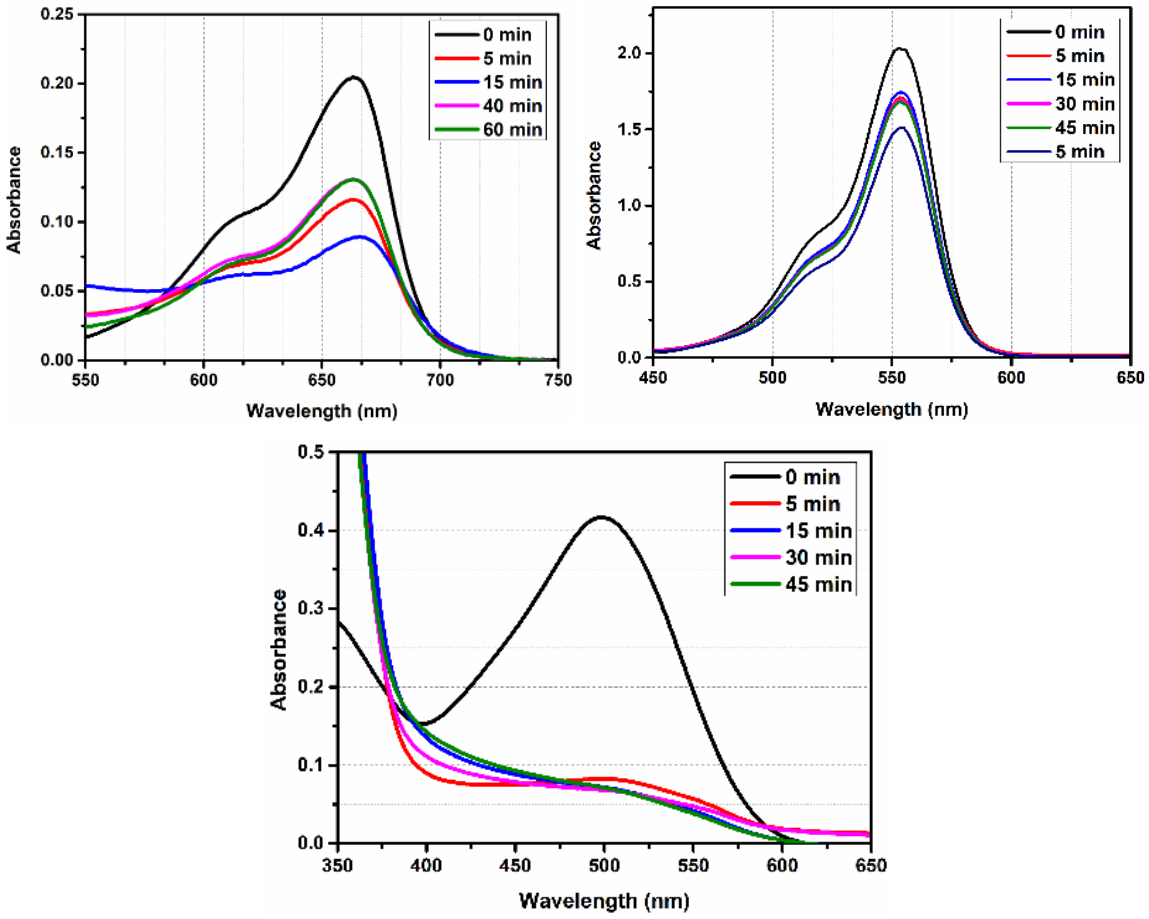

Figure 3.193. Response of **60** towards methylene blue (left), rhodamine B (right) and congo red (bottom).

With time, a decrease in the concentration of the dye was observed due to adsorption inside the MOF. It was found that congo red (CR) showed the maximum absorbtion by **60** compared to the other two dyes. Although **60** is a neutral MOF, it exhibited good efficiency to absorb CR which is an anionic dye. However, adsorption of other cationic dyes also took

place although to a lesser extent (Figure 3.193). A variation in the adsorbed amount of the anionic and cationic dyes was observed due to the variable size of the dyes.

Chemistry with H_3pbaipa ligand

Using H_3pbaipa, four metal-organic coordination networks (**64-67**) were synthesized under solvothermal conditions by heating the reaction mixture in a teflon reactor at 120 °C for 48 h in a mixed solvent mixture, i.e. water and DMF (1:1), followed by cooling in 24 h to 25 °C, as shown in Scheme 3.24. In case of **65**, the metal to ligand ratio is 3:2. On the other hand, all other compounds are 1:1 product with an overall negative charge, which is balanced by the dimethyl ammonium cation formed from the DMF solvent at high temperature.

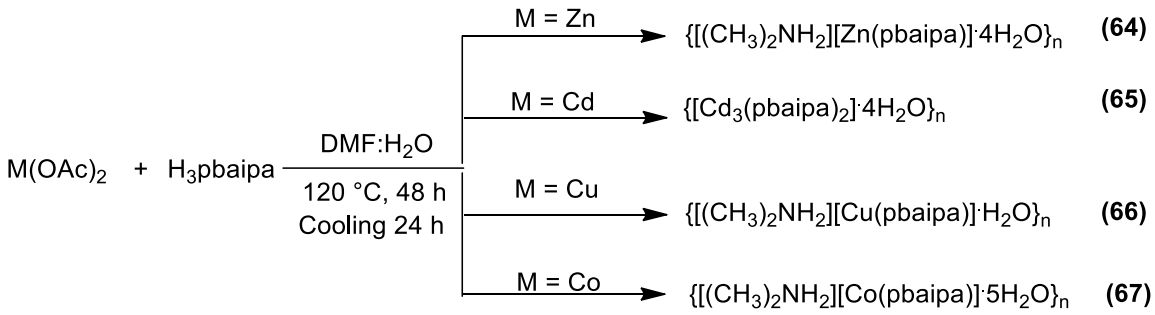

Scheme 3.24. Synthesis of **64-67**.

FTIR spectroscopic studies. In the FTIR spectra of **64**, **66** and **67**, a peak around 1680-1690 cm^{-1} confirms the presence of the dimethyl ammonium cation, while other features are same for all the compounds.

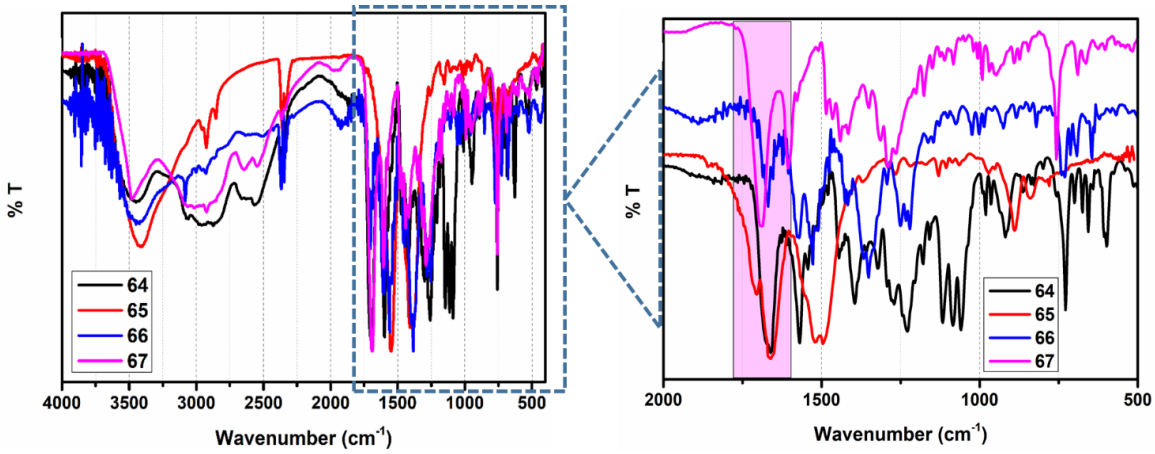

Figure 3.194. FTIR spectra of **64-67**.

Table 3.27. Asymmetric and symmetric stretching frequencies and respective binding modes of carboxylates of **64-67**.

Compound	Asymmetric (υ_1) cm^{-1}	Symmetric (υ_2) cm^{-1}	$\Delta\upsilon = \upsilon_1 - \upsilon_2$ cm^{-1}	Binding mode
64	1598	1300	298	Monodentate
65	1594	1385	209	Bidentate (chelated)
66	1570	1386	184	Bidentate (chelated)
67	1606	1440	166	Bidentate (chelated)

On the other hand, compounds **65**, **66** and **67** exhibit a bidentate mode of carboxylate binding, while **64** shows a monodentate mode of carboxylate binding with the metal center (Figure 3.194). A comparison of their carboxylate binding modes is shown in Table 3.27.

Thermogravimetric analyses. The thermal stability of **64-67** were studied as a function of temperature in the range of 25-500 °C. **64** is stable up to 250 °C after losing four lattice water molecules (loss of 11.48% vs. ca. 12.25%). Similarly, in case of **65** the first weight loss of 6.47% was observed, corresponding to four lattice water molecules (ca. 5.92%).

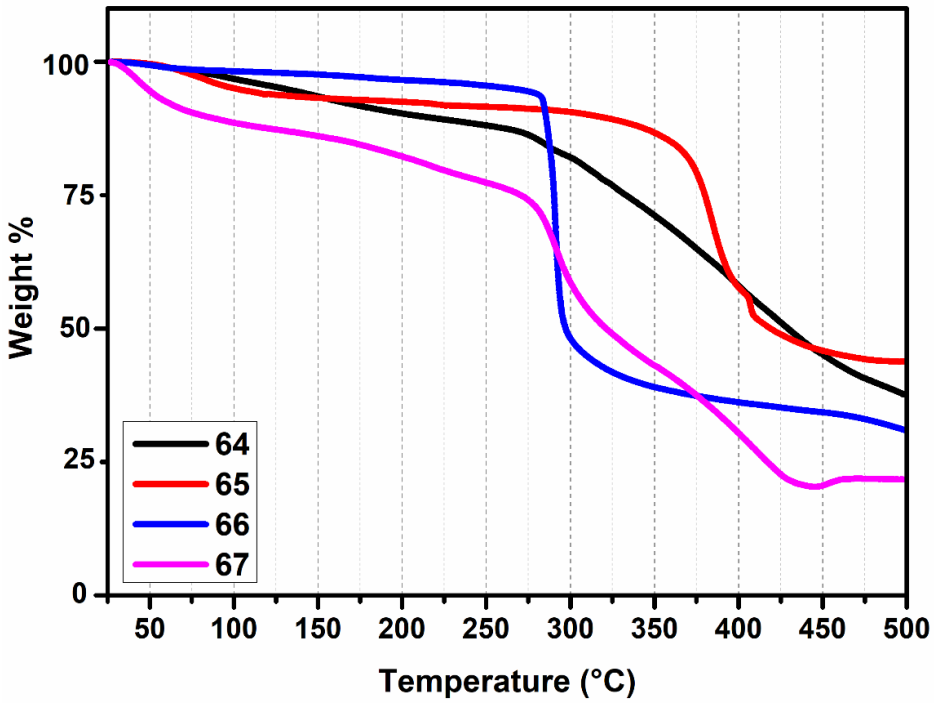

Figure 3.195. TGA scans for **64-67**.

66 exhibits a first weight loss of 4.21% corresponding to one lattice water molecule (ca. 3.38%). In case of compound **67,** the first loss of 14.42% corresponds to five lattice water

molecules (ca. 15.05%). From the comparison, it was found that compound **65**, after losing the lattice solvent molecules, is more stable comapred to other in the series (Figure 3.195).

Single crystal structure analyses. **64** crystallizes in the triclinic *P*-1 space group in which Zn(II) center is tetracoordinated and is surrounded by three oxygens from the carboxylate group of three different ligands and one nitrogen from the fourth ligand making it NO3 type surrounding. The asymmetric unit consists of two Zn(II) centers having the same type of surrounding environment, two ligands, two dimethyl ammonium cation, and three water molecules. These two metal centers and ligands form a circular loop in the asymmetric unit. The Zn-N_{py} distance is 2.045(4) Å, while Zn-O distances are 1.954(3) Å, 1.955(3) Å and 1.926(3) Å, respectively. The aliphatic nitrogen atom is in the non-bonded form (Figure 3.196).

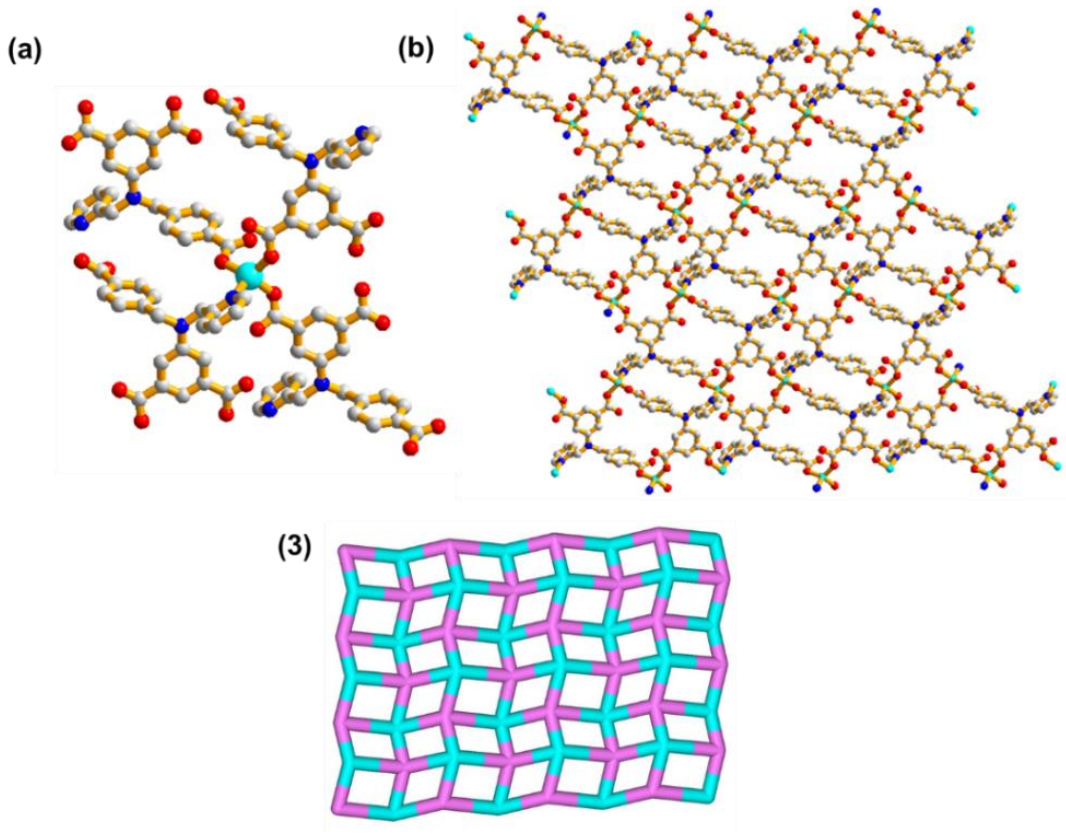

Figure 3.196. (a) Coordination environment around metal center, (b) formation of a 2D sheet and (c) topological view of **64** (solvent molecules are removed for clarity).

All the carboxylates bind to the metal center in monodentate fashion. It contains four different pores, two small and two large pores (Figure 3.197) in which solvent molecules as well cation can be trapped. These cations can be easily exchanged with other cations and make them potential candidates for different applications (separation and absorption of dyes for purification of industrial wastewater) based on anion exchange.

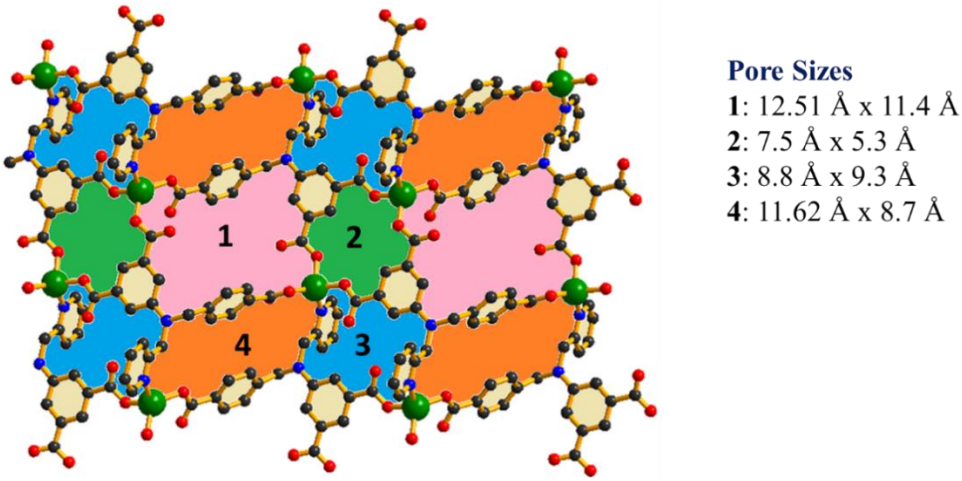

Figure 3.197. Formation of four different type of pores and their respective diameter in **64**.

Adsorption and separation of dyes/water purification: Dyes have been used for coloring the textile from ancient time. Although in the previous years natural dyes were used, from the past few decades, synthetic dyes have been widely used in the paper, pharmaceutical, food, and textile industries. A large number of dyes are being synthesized every day all over the world. In the dye production process, nitration, sulfonation, diazotization, and salting-out processes take place which can produce large amounts of dye-containing wastewater.[289–294] This enormous amount of wastewater is difficult to clean up for a variety of reasons. Along with this, some carcinogenic and mutagenic chemicals such as benzene, naphthalene, and benzoquinone are widely used in the dye production. Because of these reasons, removal of dyes from wastewater is necessary to improve human health and make a suitable environment for living systems. This is also an important step in the purification of the waste water coming out of the industries. Among the removal methods reported to date, adsorption removal has received a large amount of attention because it has many advantages like the low operating cost, easy handling, easy regeneration of material used for purification and no side effect to the environment. To explore this adsorption technique, many porous MOFs have been reported and used for adsorption and separation of dyes. Mostly anionic and cationic frameworks are more efficient for separation of dyes because of anion exchange. Herein, we have synthesized an anionic framework (**64**) having solvent molecules and cation in their lattice space. Different cationic dyes can be easily entrapped inside these MOFs by anion exchange. The properties and porosity of these porous materials can be tuned by using specific organic linker and the metal centers. Adsorption of dyes in these porous materials basically depends on the size of the pores and nature of

the porous material. The dyes having comparable size with the pores can be easily adsorbed inside the MOFs. Some of the common dyes are shown in the Figures 3.198.

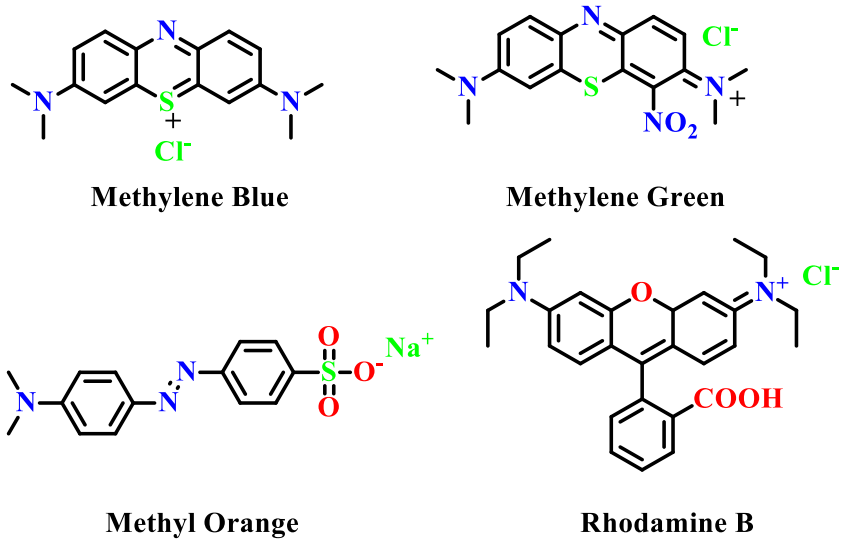

Figure 3.198. Structure of common dyes present in the industrial wastewater.

In case of separation of dyes, there are basically two methods which are reported, one is size selective, and another one is the ion-exchanged based. MOFs having small pores can be used to adsorb small size dyes leaving bigger size dyes in the solution. Therefore, we can easily separate the small dyes from the mixture of different size dyes. The second method is based on the nature of the MOFs. Anionic and cationic dyes are mostly used in industries, hence, on the basis of charge we can easily separate. Anionic MOFs can adsorb cationic dyes by ion exchange process and *vice versa*. By using this type of ionic materials, we can easily separate ionic dyes from their respective mixture. After successfully synthesizing 2D anionic MOF by using different metal and a tricarboxylate based mixed ligand (H_3pbaipa) in DMF and water under solvothermal conditions, it was used for separation of various dyes.

Before doing the adsorption experiment, this material was washed with methanol followed by pre-treatment at 120 °C for 8 h in a vacuum oven. An aqueous solution of various dyes (cationic and anionic) having a know concentration (2 μM) was prepared and used for this study. We know that dyes have their own color and a characteristic peak corresponding to them appears in the visible region. For example, methyl orange is an anionic dye of yellow color having a characteristic peak at 465 cm^{-1}. On the other hand, methylene blue which is a cationic dye shows a peak at 660 cm^{-1}. Along with this, a shoulder peak around 610 cm^{-1} also appears due to quenching by self-aggregation of the molecules. Like methylene blue,

two other cationic dyes like methylene green and rhodamine B also show two peaks at 650 cm^{-1}, 610 $cm^{-1,}$ and 560 cm^{-1}, 520 cm^{-1} respectively. An activated sample of **64** was dipped in an aqueous solution (2μM) of particular dyes. The absorbance intensity of dyes decreases as time increases which indicates the encapsulation of dyes inside the MOF. It was observed that **64** behaves differently with cationic and anionic dyes. It was observed that this compound showed no change in the absorbance intensity in case of anionic dye, for example, methyl orange (Figure 3.199). On the other hand, all the cationic dyes like RB, MB, and MO have shown change (decrease) in the absorbance intensity (Figure 3.199 and 3.200).

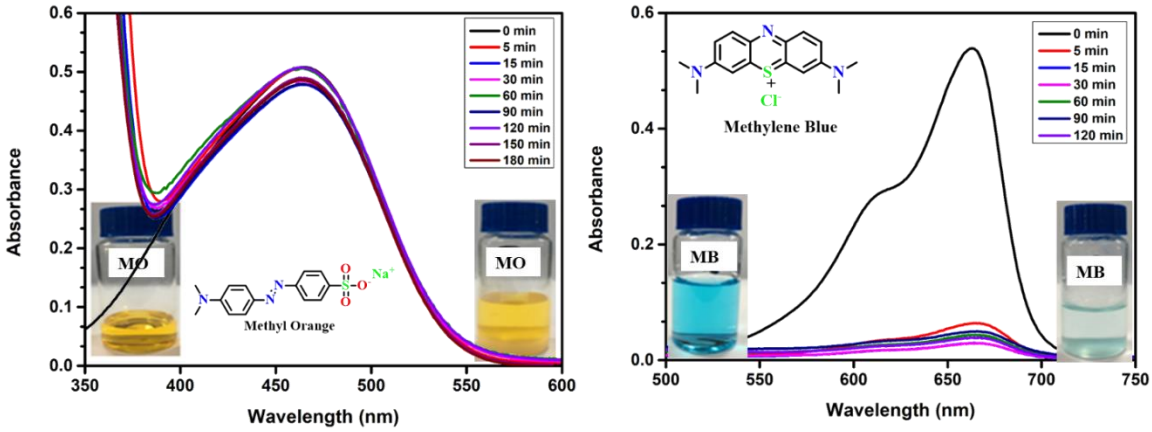

Figure 3.199. Response of anionic MOF(**64**) towards methyl orange and methylene blue.

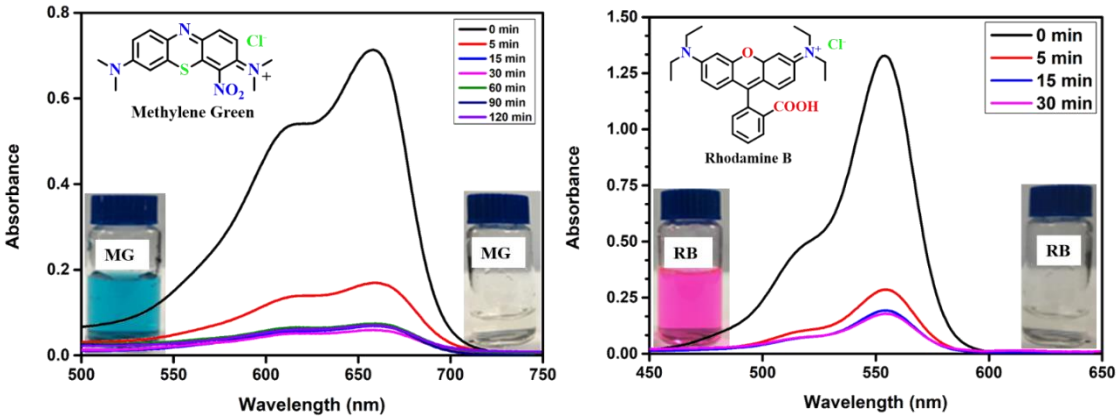

Figure 3.200. Response of anionic MOF(**64**) towards methylene green and rhodamine B.

The amount of methyl orange (MO) absorbed in the **64** is negligible, while 94% methylene blue (MB) got absorbed inside the MOF. Methylene green (MG) about 92% and rhodamine B (RB) about 88% got adsorbed by **64**. This amount is calculated by the UV-Vis spectrum of the particular dye before and after adsorption. With the change in concentration of the solution by adsorption of dyes by MOF, absorbance also changed as these two are directly

related to each other. After elimination of the left-over concentration obtained after the adsorption of dye from the stock solution of dye, the amount of dye absorbed inside the MOF was calculated. This concentration was calculated with respect to the change in the λ_{max}. From this result, it was observed that using **64**, cationic dyes can be easily separated from a mixture of anionic and cationic dyes.

Separation of dyes: **64** is an anionic compound, which is capable of separating the cationic dyes from a mixture of cationic and anionic dyes. We found that with increasing time, cationic dyes like MB, RB, and MG get trapped within the pores of **64**, while MO was not trapped. As a result, it was demonstrated that anionic dyes could be easily separated from cationic dyes in an aqueous solution. So, for the separation process, a mixture of MB and MO was prepared in same concentration in water. After mixing these dyes, a greenish color solution was formed which gave two peaks corresponding to both MO and MB as shown in the Figure 3.201. To this mixture, anionic MOF was dispersed and stirred. At every interval of time (0, 5, 10, 15 minutes), an aliquot was taken out and after centrifugation the UV-Vis spectrum was recorded. From the result obtained, the peak corresponding to MB gets suppressed, and there was no change in the absorbance intensity corresponding to MO (Figure 3.201). Along with this, green solution from the mixture was separated, compound got blue in color and solution color remains yellow. After decanting and evaporating the solvent MO was recovered. So, from this result, we can say that this is a good candidate for separation of cationic dye from the mixture of cationic and anionic dyes.

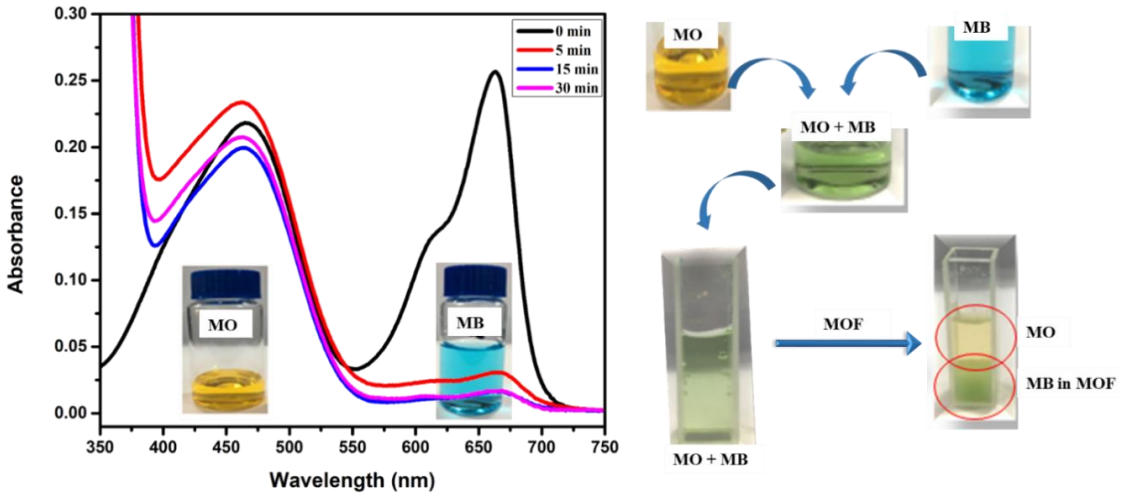

Figure 3.201. Separation of methyl orange and methylene blue by using an anionic MOF (**64**).

Effect of reaction conditions on the structures. As we know that **56** and **57** were synthesized under different conditions, a structural change was observed in both the

structure. Both the compounds have the same molecular formula except the lattice solvent molecules. In **56,** one DMF and two water molecules are present, while in **57** only six water molecules are present in the lattice. Both the compounds show the same type of topology and two different types of pores, in which one is smaller than the other. Along with these properties, both the compounds are different from each other with respect to lattice solvent molecules as well as in dimension and nature of pores. In **56**, dimensions of both large and small pores is 14.715(2) × 9.586(2) $Å^2$ (from corner Zn(II)) and 15.565(2) × 8.72(2) $Å^2$ (from corner Zn(II)), while in case of **57**, it is 16.026 x 10.350 $Å^2$ (from corner Zn(II)) and 8.216 (Zn(II) to Zn(II)) x 3.775 $Å^2$ (coordinated oxygen to oxygen) respectively. This indicates that **57** has larger pore size than **56**.

Effect of change in the metal center on the structures. As we have discussed in the section above that by changing the synthetic procedures, structural changes can take place. To explore it further, the metal center was changed, and both the compounds were compared. As we know that **56** is a Zn(II) compound while **58** is a Cd(II) compound which has been synthesized under the similar solvothermal conditions. The crystal structures indicated that both the compounds have the same type of coordination architecture as well as topology, but the coordination environment around the metal center is different. In **56**, Zn(II) preferred a pentacoordination geometry, while Cd(II) in **58** preferred heptacoordination geometry. Both the carboxylates in **56** binds with the metal center in monodentate mode, while in **58**, both the carboxylates adopt a bidentate chelation mode of binding. Pore dimensions in **58** (6.984 (Cd to Cd) x 3.635 $Å^2$ (coordinated oxygen to oxygen) and 15.669 x 11.906 $Å^2$ (from corner Zn)) is larger than that of **56**.

Positional effect of ligands on the structures. Compound **56** and **57** are the 2D complexes with bpaipa and Zn(II). Both the compounds have the same type of topology. To explore further, the position of donor atom (nitrogen) in the ligand was changed from *ortho* to *para* resulting in a formation of a new ligand, 2,4-H_2bpaipa. By using this ligand, metal complexes with Zn(II) have been synthesized and compared with the Zn(II) complex of 2,2′-H_2bpaipa. The change in the donor atom position resulted in a tremendous change in the structures. As shown in the Figure 3.202, **57** forms a 2D coordination polymer while **60** is a 3D metal-organic framework. Furthermore, this is also confirmed by gas adsorption studies. **60** shows a higher amount of nitrogen adsorption than **57** which further confirms the change in the dimensionality of the products.

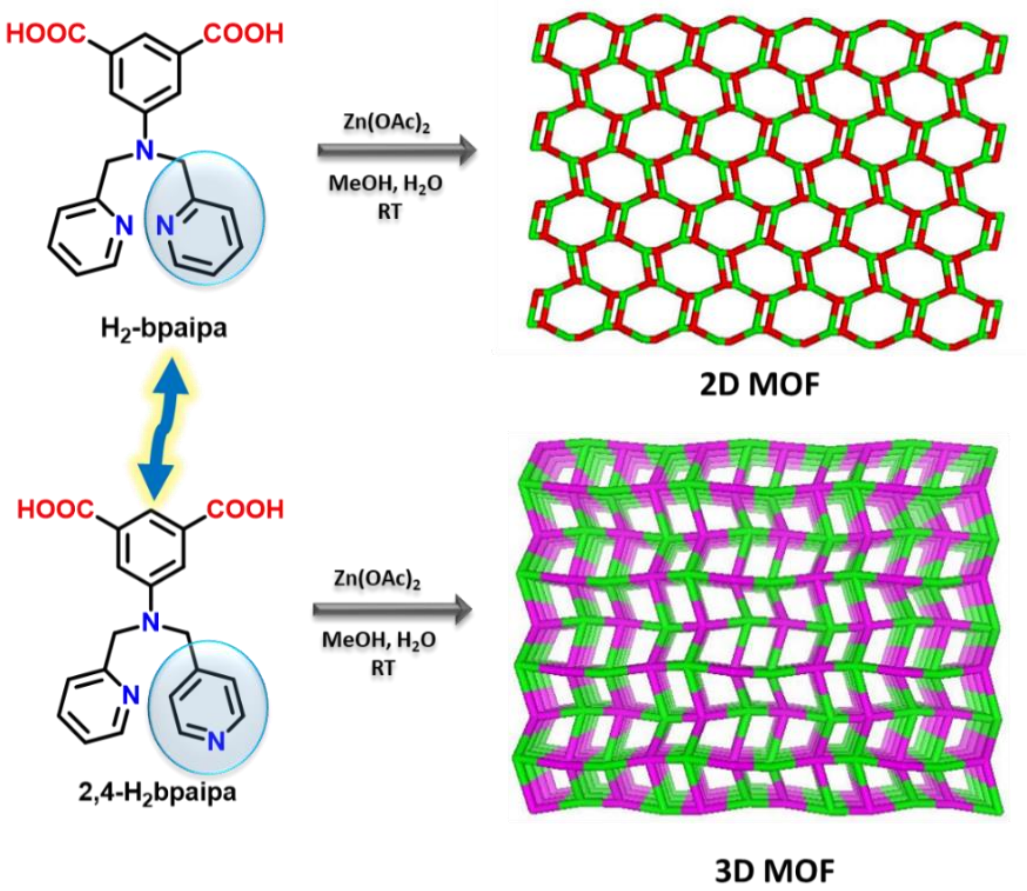

Figure 3.202. Effect of change in the position of donor atom in ligand resulting in change in the dimensionality of the MOF.

Effect of donor atoms on the structures. After exploring the effect of the change in the position of donor atom in the ligand in the construction of metal-organic frameworks, we step forward to check the effect of a change in the donor moiety at the same position of the ligand in the formation of MOFs. For this purpose, a new mixed ligand was designed which is a tricarboxylate pyridyl-based ligand, H_3pbaipa. On comparing **60** with **64**, it was observed that by replacing nitrogen with the flexible carboxylate group at the same position in the ligand, a 2D MOF was formed while in the former case, it was a 3D MOF. As **64** is formed by using a tricarboxylate, it resulted in the formation of an anionic 2D MOF. On the other hand, the former compound is a neutral 3D compound (Figure 3.203). **64** has free cation which is a dimethyl ammonium cation located in the pores with the solvent molecules. From this study, it was confirmed that by using different donor groups at the same position of the ligand also affects the final architecture.

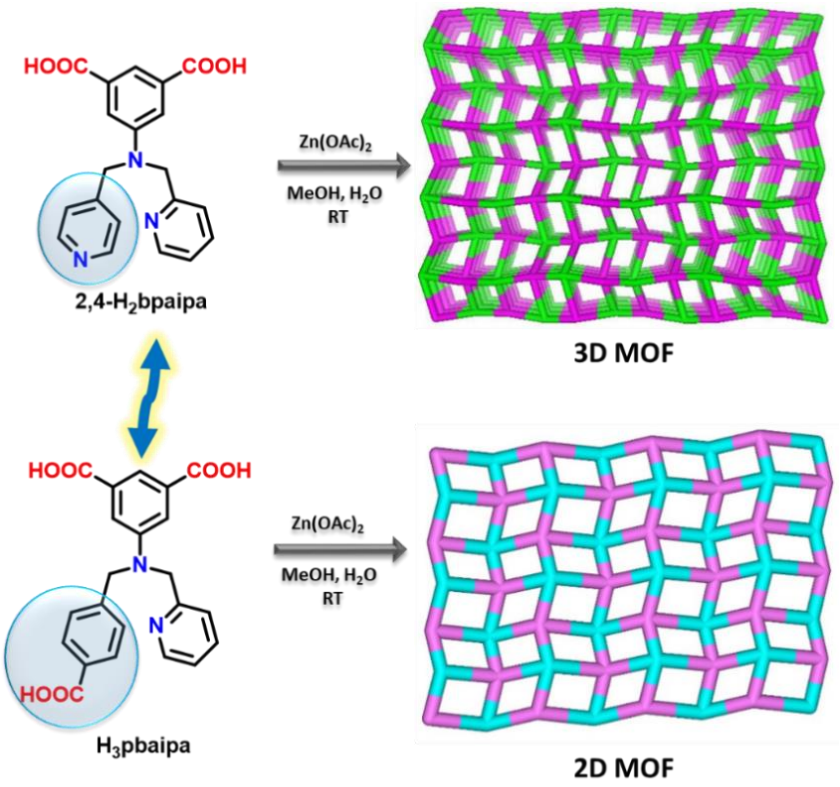

Figure 3.203. Effect of change in the donor moiety in ligand on the dimensionality of the MOF.

3.2.2 Functionalized tetracarboxylate ligands

In this section, two functional tetracarboxylates having secondary and tertiary amines and a xylyl spacer were utilized for making a series of porous materials to study their physiochemical properties. In case of H_4diab, the 4,4′-bypy linker was also used to compare the effect on the structure and properties with those having no linker. All compounds were obtained in high yields and purity under ambient conditions (Schemes 3.25 and 3.26). Unfortunately, no single crystal of all these compounds could be obtained even after multiple attempts.

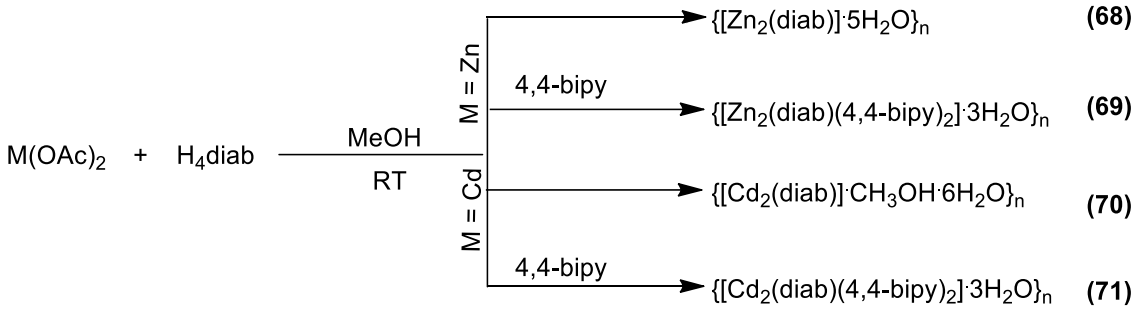

Scheme 3.25. Synthesis of **68-71**.

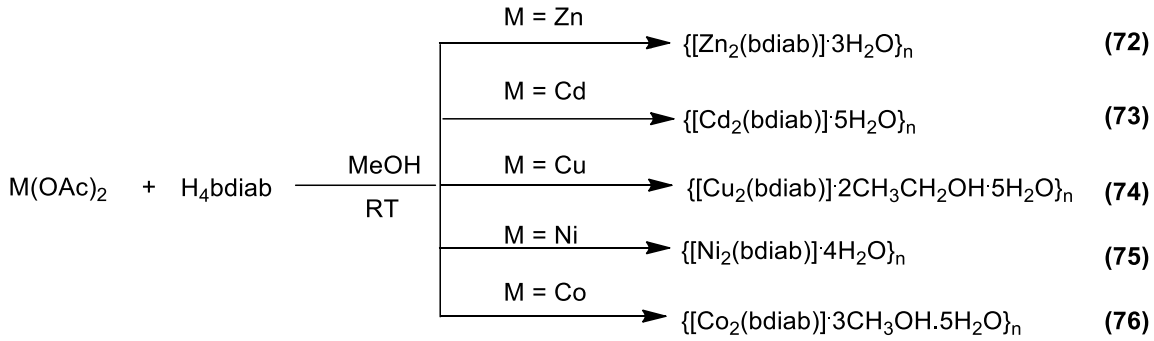

Scheme 3.26. Synthesis of **72-76**.

FTIR spectroscopic studies. In all cases, the difference between asymmetric and symmetric stretching frequency for the carboxylate groups is either below or close to 200 cm^{-1}, which indicates their bidentate mode with the metal center (Figure 3.204 and Table 3.28).

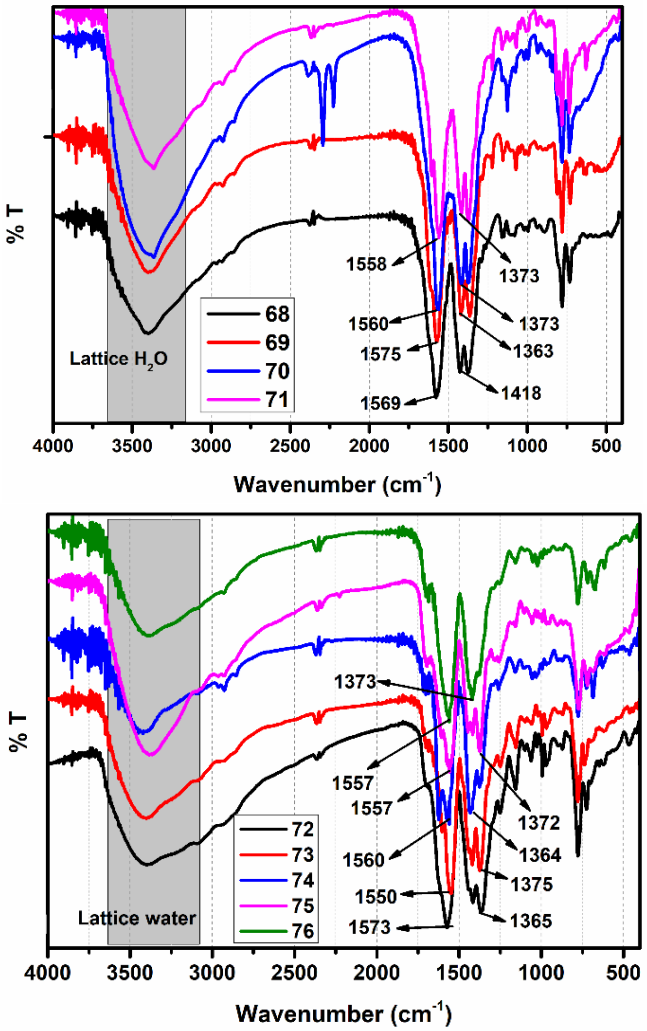

Figure 3.204. FTIR spectra of **68-76**.

Table 3.28. Asymmetric and symmetric stretching frequencies and their respective binding modes of carboxylates **68-76**.

Compound	Asymmetric (υ_1) cm^{-1}	Symmetric (υ_2) cm^{-1}	$\Delta\upsilon = \upsilon_1 - \upsilon_2$ cm^{-1}	Binding mode
68	1569	1418	151	Bidentate (chelated)
69	1575	1363	212	Bidentate (chelated)
70	1560	1373	187	Bidentate (chelated)
71	1558	1373	185	Bidentate (chelated)
72	1573	1365	208	Bidentate (chelated)
73	1550	1375	175	Bidentate (chelated)
74	1560	1364	196	Bidentate (chelated)
75	1557	1372	185	Bidentate (chelated)
76	1557	1373	184	Bidentate (chelated)

Thermogravimetric analyses. **68** shows a two-step weight loss profile, where the first weight loss of 12.06% between 50-130 °C corresponds to the loss of five lattice water molecules (ca. 13.21%). **69** shows first weight loss of 6.23% between 25-150 °C corresponding to the loss of three water molecules (ca. 5.64%). In case of **70**, the first weight loss of 17.34% corresponds to one methanol and six lattice water molecules (ca. 16.9%), while for **71**, the first loss of 5.66% corresponds to the loss of three water molecules (ca. 5.12%). **72** shows a loss of 5.94% between 25-150 °C corresponding to the loss of three water molecules (ca. 6.52%) followed by its decomposition.

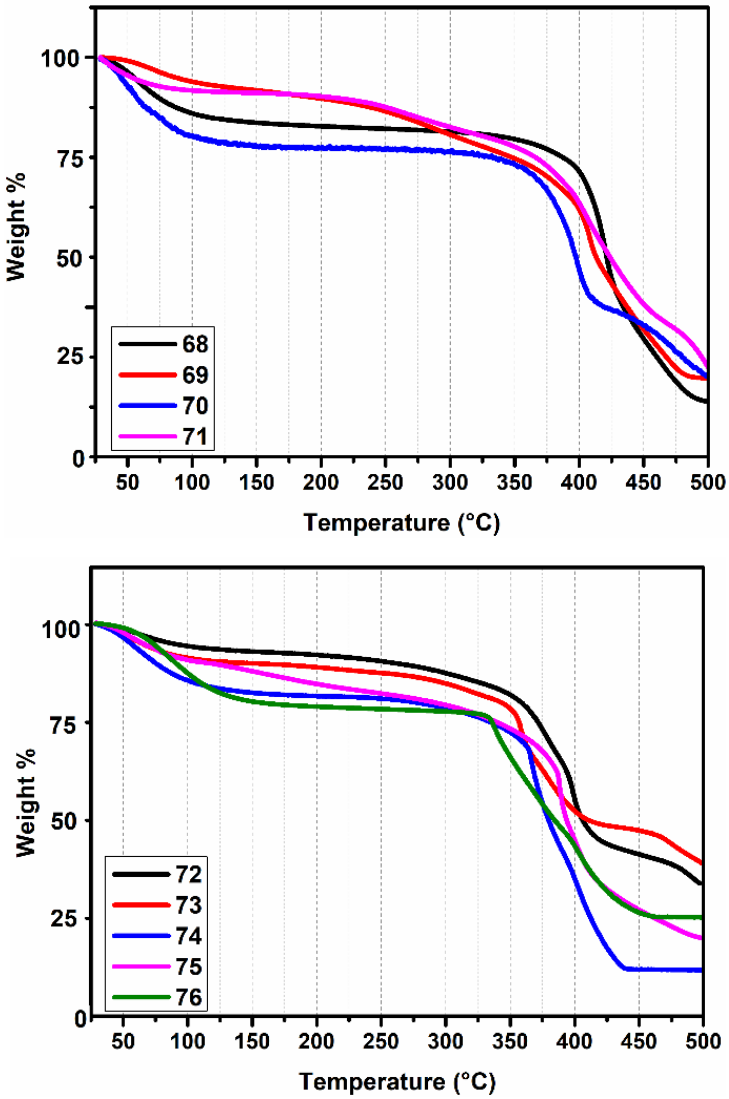

Figure 3.205. TGA scans of **68-76**.

For compound **73**, the first loss of 8.85% corresponds to five water molecules (ca. 9.39%), while for **74** the first weight loss of 16.14% corresponds to five water molecules and two methanol (ca. 16.68%). For **75**, the first loss of 9.32% corresponds to the four water molecules (ca. 8.65), while in case of **76**, the first weight loss of 20.18% corresponds to

five water and three methanol molecules (ca. 19.68%). After the first weight loss, **72-76** are stable up to 300 °C after which these decompose to their respective metal oxides(Figure 3.205).

Photoluminescence properties. UV-vis spectra of **68-76** compounds have been recorded in the solid state using KBr as a dispersion medium, which shows two maxima peaks around 250 nm and 350 nm (Figure 3.206). **74** shows an additional peak around 710 nm in the visible region corresponds to Cu(II) center, while the same peak for Ni(II) in **75** and Co(II) in **76** is observed at 700 nm and 550 nm, respectively.

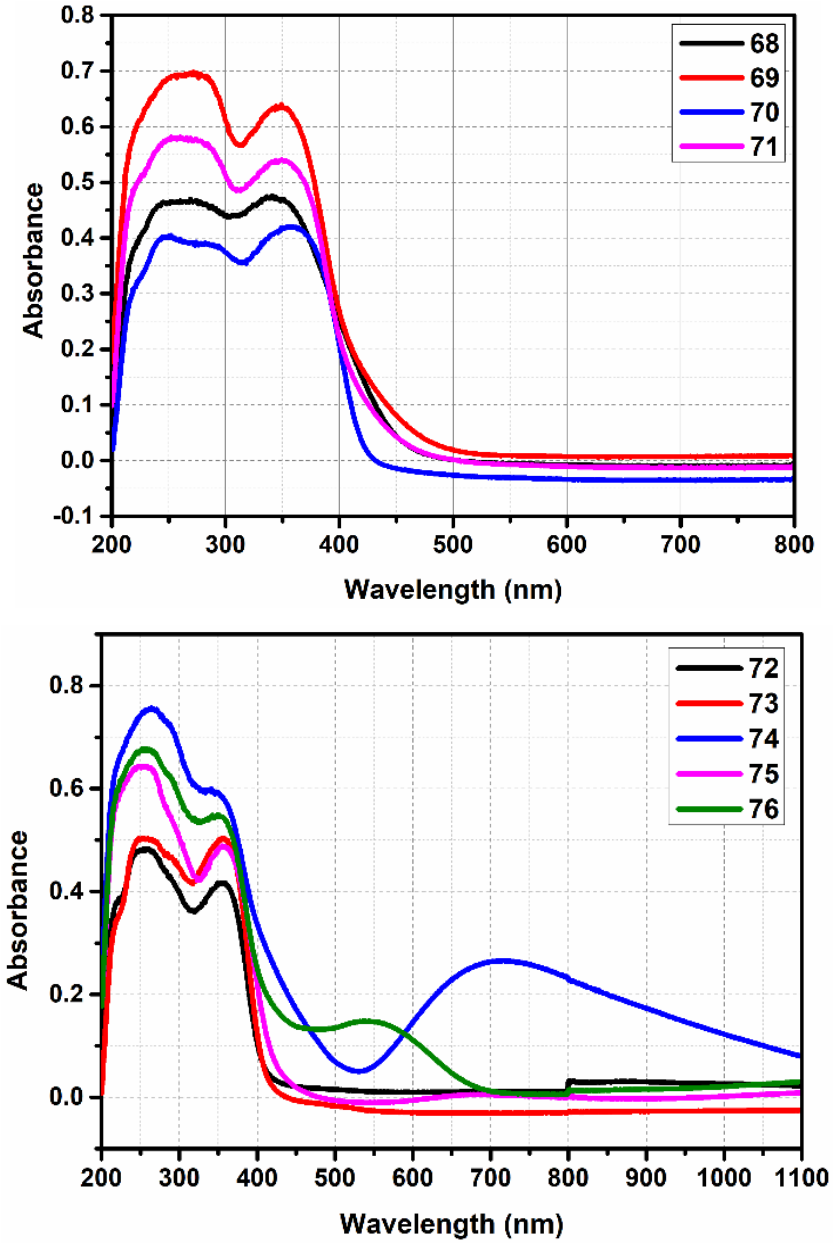

Figure 3.206. UV-Vis spectra of **68-76**.

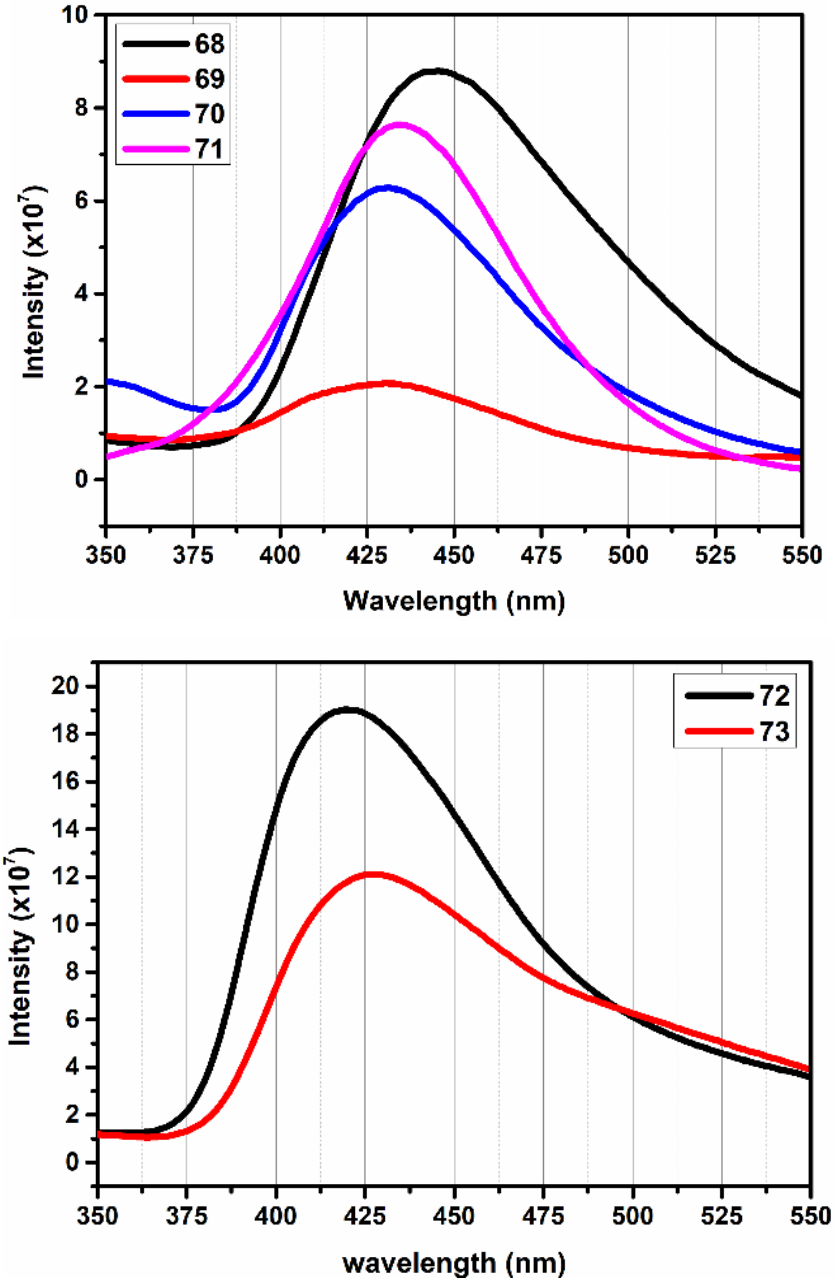

Figure 3.207. Fluorescence spectra of **68**-**73**.

This difference in the position of peaks in the UV-Vis spectra is mainly attributed to their characteristic electronic configuration. Further, we have explored emission properties of these compounds (**68**-**73**), for which the fluorescence experiments were carried out in slurry mode by dispersing 1 mg of compounds in 2 mL MeOH with excitation wavelength of 310 nm for each compound. These compounds have shown excellent fluroscence properties and λ_{emi} was observed at 430 nm, 427 nm, 430 nm and 435 nm for **68**-**71**, respectively. On the other hand for **72** and **73**, it was observed around 425 nm and 415 nm, respectively (Figure 3.207).

Gas adsorption studies. From the nitrogen adsorption isotherms, it was observed that these compounds have permanent porosity. **68** and **70** have adsorption of N_2 upto 30 and 25 cm^3(STP)/g at 77 K with the BET, Langumir surface are 23, 42.72 m^2g^{-1} and 5.9, 8.9 m^2g^{-1}, respectively. By insertion of a rigid pillar linker (4,4-bpy), porosity of these compounds was drastically increased, which was reflected in the higher N_2 uptake in **69** up to 200 cm^3 (STP)/g at 77 K with BET and Langumir surface area of 69.1 m^2g^{-1} and 131.28 m^2g^{-1} compared to **68** .

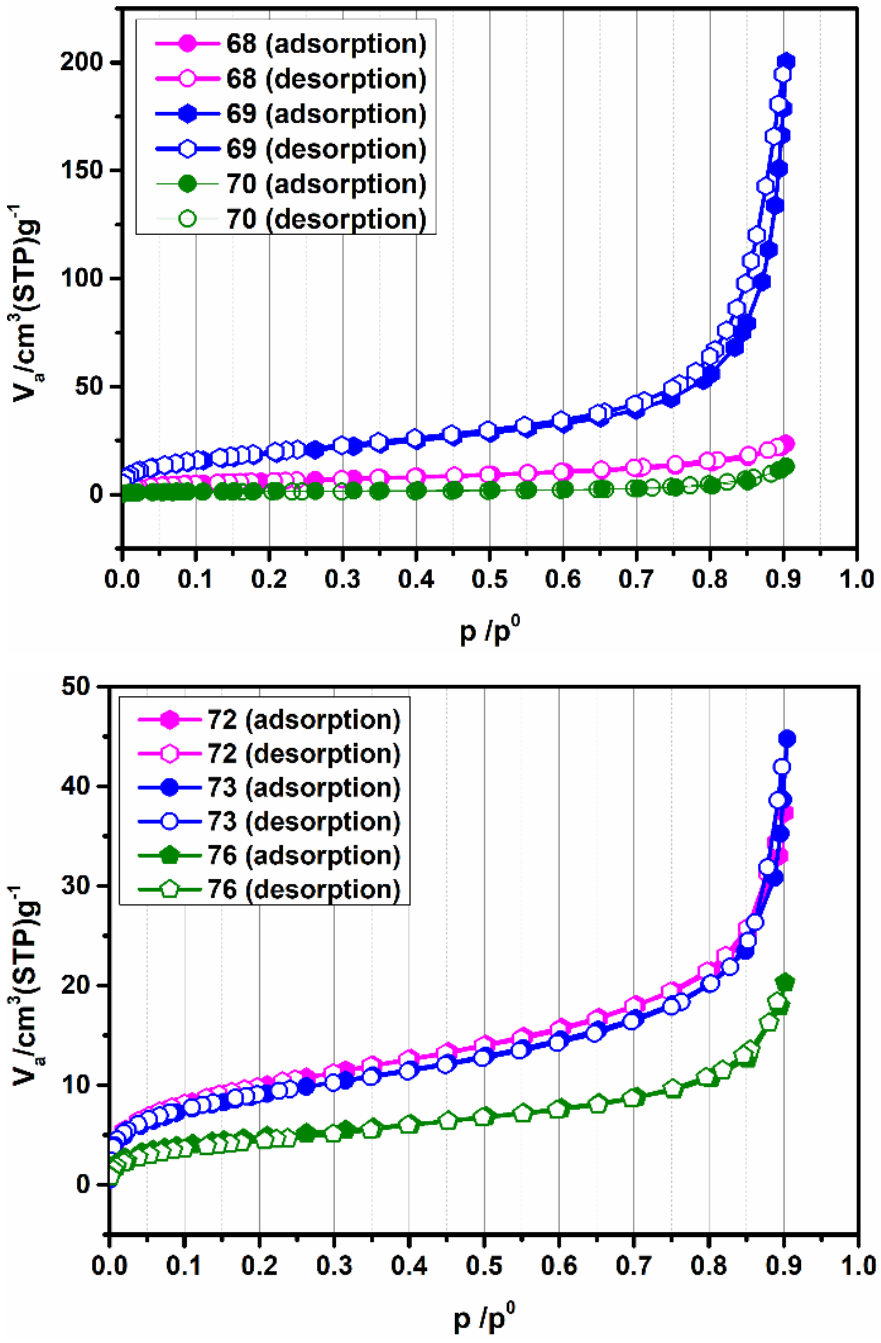

Figure 3.208. N_2 adsorption isotherm for **68-76**.

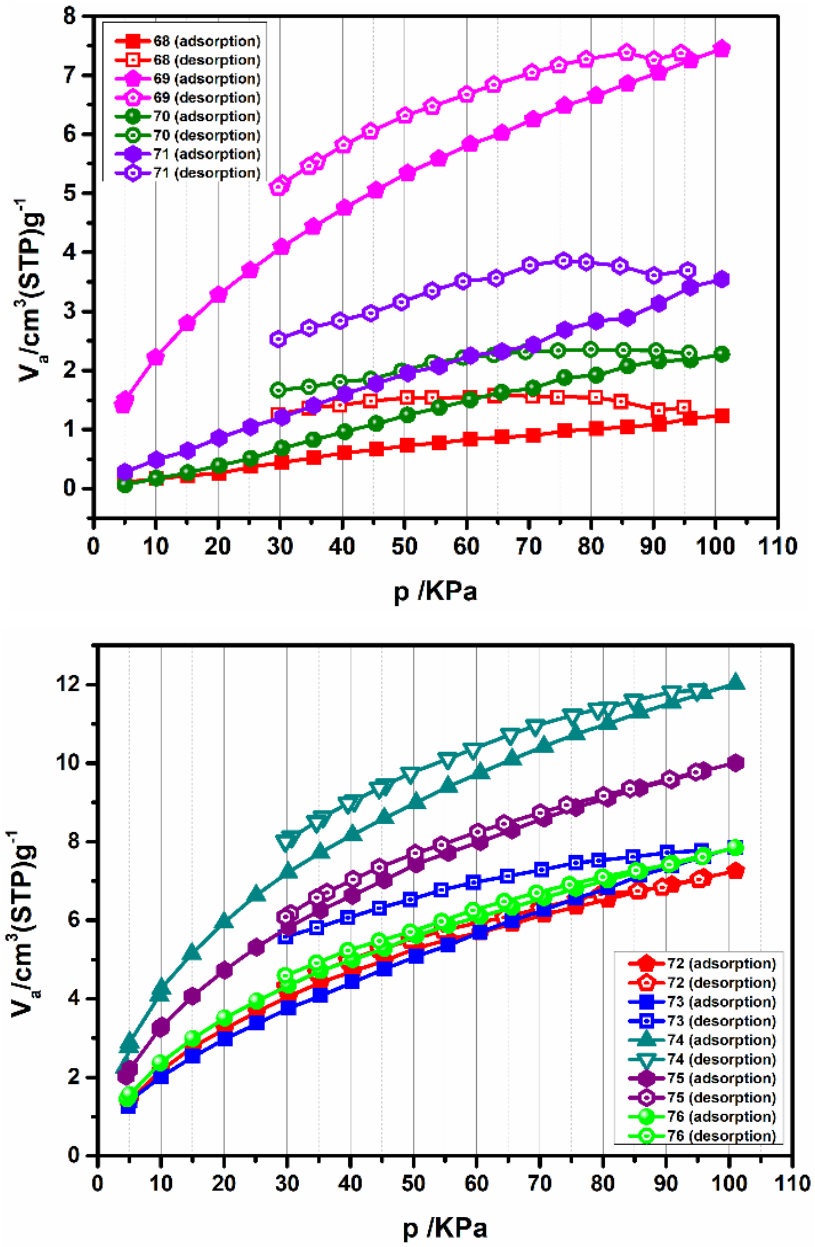

Figure 3.209. CO_2 adsorption isotherm for **68-76**.

Apart from using rigid pillar linker, porosity has also been enhanced by incorporating an additional pyridyl functionality in H_4bdaib. **72** and **73** show adsorption of N_2 upto 40 and 45 cm^3(STP)/g at 77 K with BET, Langumir surface area of 33.3, 54.1 m^2g^{-1} and 36.1, 68.1 m^2g^{-1}, respectively. In addition to this, compound **76** shows 15 cm^3(STP)/g of N_2 adsorption at 77 K (Figure 3.208) with the BET and Langumir surface area of 17 and 31 m^2g^{-1}. After N_2 adsorption studies, these compounds have been used for CO_2 adsorption studies. Due to high emission of CO_2 in the environment, mankind is facing challenges like global warming, hence CO_2 sequestration has become essential. From the results, it was observed that **69** and **71**

synthesized using rigid pillar linker (4,4-bipy) show better CO_2 adsorption (7.5 and 2.5 cm^3(STP)/g at 298 K) compared to **68** and **70** (1 and 1.5 cm^3(STP)/g at 298 K). While compound **72-76** show 6, 6.5, 12, 9 and 6 cm^3(STP)/g of CO_2 uptake at 298 K. From the above discussed results, it is clear that by inserting a pillar linker porosity of coordination architectures can be enhanced.

CHAPTER IV

Conclusions

1. For this work, the design and synthesis of various organic ligands (neutral and anionic) was the first step. These include pyridyl and mixed pyridyl-carboxylate ligands. In addition to these, few ligands with bare acetylene functionality were also utilized in various applications. All these ligands have been isolated in good-to-excellent yields and extensively characterized by various spectroscopic methods.
2. Using the new organic ligands and other readily available carboxylates and 4,4'-bpy, two different strategies (three-component and two-component) have been successfully employed for the synthesis of various metal organic coordination networks (MOCNs) or architectures in good yields and purity.
3. First of all, for the three-component systems (metal centers, ancillary ligands and dicarboxylates) a number of supramolecular assemblies of different dimensions was obtained. For Ni(II) as a metal center and 6-Mebpta, 6-Mebpea or 6,6'-Me_2bpta as a tridentate ancillary ligand, neutral or cationic dinuclear synthons bridged by one or more dicaroxylates have been formed to associate with a variable number of lattice water molecules in them. This led to a systematic study of various type of water clusters. For the combination of 6-Mebpta and acetylene dicarboxylate, the formation of a neutral *bis(*adc*)* dinuclear compound, $[Ni_2(adc)_2(6\text{-Mebpta})_2]\cdot 2H_2O$ (**1**), resulted into encapsulating dimer of water. On the other hand, for fumarate and succinate, cationic dinuclear synthons are formed with free carboxylates as anions in the supramolecular network of $[Ni_2(fumarate)(6\text{-Mebpta})_2(H_2O)_2](fumarate)\cdot 9H_2O$ (**2**), and $[Ni_2(succinate)(6\text{-Mebpta})_2(H_2O)_2](Hsuccinate)_2\cdot 4H_2O$ (**3**). In **2**, out of nine lattice water molecules, five form a rare quasi-planar cyclic pentamer of water cluster.Using the concept of host-guest interactions, an effect of anion exchange on the water clusters present in cationic coordination networks of **2** and **3** has been shown via single-crystal-to-single-crystal transformation without a change in the dinuclear synthons.In changing the ancillary ligand from 6-Mebpta to 6,6'-Me_2bpta, further diversification in the supramolecular network takes place with a change in the metal synthon. In this case, a mononuclear complex (**17**) has been formed having one side

of the dicarboxylate uncoordinated but strongly hydrogen bonded to the coordinated water of the second metal synthon. Interestingly, a change in the metal ion to Zn(II) with the same ligand and linker results in a 1D coordination polymer.

4. By using a tricarboxylate instead of a dicarboxylate, an increase in the dimensionality of the coordination network of Cd(II) has also been demonstrated through examples of **24** and **25**.
5. For the functional tridentate ligand (2,2-terpyBA), MOCNs of different metal ions and dicarboxylates have been synthesized. These form either mononuclear complexes or ladder/zig-zag shaped 1D coordination polymers. Further association of these units through supramolecular interactions forms 3D supramolecular assemblies.
6. For solvent sensing and site selective sensing (detection) of various metal ions, it is observed that due to the interaction of metal ions at different positions turn-on and turn-off fluorescence take place.
7. With a change in the position of nitrogen donor atoms, 4,4'-terpyBA ligand in combination with H_2bdc and Zn(II) provides a 3D MOF, $\{[Zn_2(bdc)_2(4,4\text{-terpyBA})_2]\cdot DMF\cdot H_2O\}_n$ (**37**). On the other hand, with Ni(II) and Co(II), 1D coordination polymers (ladder-shaped) $\{[Ni(bdc)(4,4\text{-terpyBA})(H_2O)]\cdot CH_3CH_2OH\cdot H_2O\}_n$ (**40**) and $\{[Co(bdc)(4,4\text{-terpyBA})(H_2O)]\cdot 2DMF\cdot H_2O\}_n$ (**41**), respectively, have been isolated. Similarly, with Cd(II) and Cu(II), 3D coordination polymers have been formed $\{[Cd_2(bdc)_2(4,4'\text{-terpyBA})_2]\cdot DMF\cdot 5H_2O\}_n$ (**38**) and $\{[Cu_2(bdc)_2(4,4'\text{-terpyBA})_2]\cdot DMF\cdot 4H_2O\}_n$ (**39**), respectively.
8. Using $\{[Zn_2(bdc)_2(4,4'\text{-terpyBA})_2]\cdot DMF\cdot H_2O\}_n$ (**37**), the fabrication of Pd nanoparticles inside its pores provided a new multifunctional catalyst **NPs@Zn-MOF**, which was a platform for various organic transformations. Both cascade one-pot N-alkylation and Knoevenagel condensation reactions have been performed with good efficiency using NPs@MOFs catalyst was fully characterized by various techniques like FESEM, TEM, UV-Vis sepctroscopy, gas adsorption and PXRD analysis.
9. Replacement of the dicarboxylate with a tricarboxylate in case of functional tridentate ligands has shown a tremendous effect on the coordination architectures formed. Using the H_3btc tricarboxylate, a mononuclear complex $[Co(2,2\text{-terpyBA})_2](Hbtc)\cdot H_2O$ (**50**) was formed with 2,2'-terpyBA, while porous 2D

$\{[Zn_2(Hbtc)_2(4,4\text{-terpyBA})_2]\}_n$ (**51**) and 3D $\{[Cd_2(OAc)(btc)(4,4\text{-terpyBA})_2(btc)_2]\cdot DMF\cdot H_2O_n$ (**51**) MOFs were formed with 4,4'-terpyBA. Utilizing the bare acetylene functionality in $\{[Cd_2(OAc)(btc)(4,4\text{-terpyBA})_2(btc)_2]\cdot DMF\cdot H_2O\}_n$ (**51**), sensing of metal ions was explored, where quenching (turn-off fluorescence) was observed in case of Ca^{2+}, Co^{2+}, Cd^{2+}, Ni^{2+}, Zn^{2+}, Mg^{2+}, Ag^{2+}, Pb^{2+}, Hg^{2+}, Fe^{3+}, Pb^{2+}, Pd^{2+} and Al^{3+}, and enhancing (turn-on fluorescence) was observed for Cu(II) and Na(I). Based on the data, detection of Fe(III) was found to be selective over other metal ions.

10. For the two-component systems, a mixed ligand (H_2bpaipa) was selected to explore the effect of reaction conditions for making Zn(II) and Cd(II) MOFs. An example of such outcome is the pair $\{[Zn(bpaipa)]\cdot DMF\cdot 2H_2O\}_n$ (**56**) and $\{[Zn(bpaipa)]\cdot 6H_2O\}_n$ (**57**), where these only differ in their lattice solvent, however, have different structures and properties. Through single-crystal-to-single-crystal transformation, the desolvation-resolvation of **56** was studied. Based on this extraordinary experimentation, it was possible to explain the reduced pore space upon desolvation for gas adsorption due to flexible rotation of the carboxylate group bonded with the metal center.
11. Along with **56** and **57**, the Cd(II) analogs $\{[Cd(bpaipa)]\cdot DMF\cdot 2H_2O\}_n$ (**58**) and $\{[Cd(bpaipa)]\cdot 4H_2O\}_n$ (**59**) were used for solvent encapsulation studies. All these four MOFs are good candidates for the adsorption of methanol.
12. Complete transmetalation of Zn(II) and Cd(II) in $\{[Zn(bpaipa)]\cdot DMF\cdot 2H_2O\}_n$ (**56**) and $\{[Cd(bpaipa)]\cdot DMF\cdot 2H_2O\}_n$ (**58**) with Cu(II), respectively, have been demonstrated successfully along with kinetic parameters for such exchange.
13. Both **56** and **57** were found to be good fluorescent sensors for ketones, specifically, cyclohexanone and amines. These were also used for sensing nitroaromatic compounds with a detection limit of 0.16 ppm for trinitrophenol.
14. Using a tricarboxylate based mixed ligand, anionic MOFs like $\{[(CH_3)_2NH_2][Zn(bpaipa)]\cdot 4H_2O\}_n$ (**64**)) have been synthesized for the absorption-induced separation of dyes from water.
15. Both tetracarboxylates and mixed tetracarboxylates based ligands, with or without 4,4'-bpy linker have provided various amorphous MOFs (**69**-**76**). The effect of linker has been explored with respect to their sorption of different gases and luminescence properties.

REFERENCES

(1) Yoon, M.; Srirambalaji, R.; Kim, K. Homochiral Metal-Organic Frameworks for Asymmetric Heterogeneous Catalysis. *Chem. Rev.* **2012**, *112*, 1196–1231.

(2) Xu, W.; Thapa, K. B.; Ju, Q.; Fang, Z.; Huang, W. Heterogeneous Catalysts Based on Mesoporous Metal–organic Frameworks. *Coord. Chem. Rev.* **2018**, *373*, 199–232.

(3) Wang, P.; Liu, H.; Niu, J.; Li, R.; Ma, J. Entangled Pd Complexes over Fe_3O_4@SiO_2 as Supported Catalysts for Hydrogenation and Suzuki Reactions. *Catal. Sci. Technol.* **2014**, *4*, 1333–1339.

(4) Corma, A.; García, H.; Llabrés i Xamena, F. X. Engineering Metal Organic Frameworks for Heterogeneous Catalysis. *Chem. Rev.* **2010**, *110*, 4606–4655.

(5) Li, B.; Wen, H.-M.; Zhou, W.; Chen, B. Porous Metal-Organic Frameworks for Gas Storage and Separation: What, How, and Why? *J. Phys. Chem. Lett.* **2014**, *5*, 3468–3479.

(6) Li, J.-R.; Sculley, J.; Zhou, H.-C. Metal–Organic Frameworks for Separations. *Chem. Rev.* **2012**, *112*, 869–932.

(7) Campbell, M. G.; Dincă, M. Metal–organic Frameworks as Active Materials in Electronic Sensor Devices. *Sensors* **2017**, *17*, 1–11.

(8) Ma, D.; Li, B.; Zhou, X.; Zhou, Q.; Liu, K.; Zeng, G.; Li, G.; Shi, Z.; Feng, S. A Dual Functional MOF as a Luminescent Sensor for Quantitatively Detecting the Concentration of Nitrobenzene and Temperature. *Chem. Commun.* **2013**, *49*, 8964–8966.

(9) Nagarkar, S. S.; Joarder, B.; Chaudhari, A. K.; Mukherjee, S.; Ghosh, S. K. Highly Selective Detection of Nitro Explosives by a Luminescent Metal-Organic Framework. *Angew. Chemie - Int. Ed.* **2013**, *52*, 2881–2885.

(10) Yang, X.; Xu, Q. Bimetallic Metal-Organic Frameworks for Gas Storage and Separation. *Cryst. Growth Des.* **2017**, *17*, 1450–1455.

(11) Li, B.; Wang, H.; Chen, B. Microporous Metal-Organic Frameworks for Gas

Separation. *Chem. - An Asian J.* **2014**, *9*, 1474–1498.

(12) Getman, R. B.; Bae, Y.-S.; Wilmer, C. E.; Snurr, R. Q. Review and Analysis of Molecular Simulations of Methane, Hydrogen, and Acetylene Storage in Metal–Organic Frameworks. *Chem. Rev.* **2012**, *112*, 703–723.

(13) Germain, M. E.; Knapp, M. J. Optical Explosives Detection: From Color Changes to Fluorescence Turn-On. *Chem. Soc. Rev.* **2009**, *38*, 2543–2555.

(14) Salinas, Y.; Martínez-Máñez, R.; Marcos, M. D.; Sancenón, F.; Costero, A. M.; Parra, M.; Gil, S. Optical Chemosensors and Reagents to Detect Explosives. *Chem. Soc. Rev.* **2012**, *41*, 1261–1296.

(15) Chakraborty, G.; Mandal, S. K. Neutral Luminescent Metal-Organic Frameworks: Structural Diversification, Photophysical Properties, and Sensing Applications. *Inorg. Chem.* **2017**, *56*, 14556–14566.

(16) Lustig, W. P.; Mukherjee, S.; Rudd, N. D.; Desai, A. V.; Li, J.; Ghosh, S. K. Metal–organic Frameworks: Functional Luminescent and Photonic Materials for Sensing Applications. *Chem. Soc. Rev.* **2017**, *46*, 3242–3285.

(17) Li, C. P.; Liu, B. L.; Wang, L.; Liu, Y.; Tian, J. Y.; Liu, C. Sen; Du, M. Tracking the Superefficient Anion Exchange of a Dynamic Porous Material Constructed by Ag(I) Nitrate and Tripyridyltriazole via Multistep Single-Crystal to Single-Crystal Transformations. *ACS Appl. Mater. Interfaces* **2017**, *9*, 7202–7208.

(18) Chu, W.-J.; Yao, H.-C.; Fan, Y.-T.; Hou, H.-W. Anion Exchange Induced Tunable Catalysis Properties of an Uncommon Butterfly-like Tetranuclear Copper(II) Cluster and Magnetic Characterization. *Dalt. Trans.* **2011**, *40*, 2555–2561.

(19) Noori, Y.; Akhbari, K. Post-Synthetic Ion-Exchange Process in Nanoporous Metal-Organic Frameworks; an Effective Way for Modulating Their Structures and Properties. *RSC Adv.* **2017**, *7*, 1782–1808.

(20) Coghlan, C. J.; Sumby, C. J.; Doonan, C. J. Utilising Hinged Ligands in MOF Synthesis: A Covalent Linking Strategy for Forming 3D MOFs. *CrystEngComm* **2014**, *16*, 6364–6371.

(21) Kurmoo, M. Magnetic Metal-Organic Frameworks. *Chem. Soc. Rev.* **2009**, *38*, 1353–1379.

(22) Zhao, X.; Liu, S.; Tang, Z.; Niu, H.; Cai, Y.; Meng, W.; Wu, F.; Giesy, J. P. Synthesis of Magnetic Metal-Organic Framework (MOF) for Efficient Removal of Organic Dyes from Water. *Sci. Rep.* **2015**, *5*, 1–10.

(23) Rozhkov, A. V.; Novikov, A. S.; Ivanov, D. M.; Bolotin, D. S.; Bokach, N. A.; Kukushkin, V. Y. Structure-Directing Weak Interactions with 1,4-Diiodotetrafluorobenzene Convert One-Dimensional Arrays of $[M^{II}(Acac)_2]$ Species into Three-Dimensional Networks. *Cryst. Growth Des.* **2018**, *18*, 3626–3636.

(24) Amani, A.; Derikvand, Z.; Dusek, M.; Eigner, V.; Azadbakht, A. A New One-Dimensional 3D Supramolecular Coordination Polymer of Cd(II) Based on Pyrazine and 3-Nitropththalic Acid: Synthesis, Characterization, Crystal Structure, Thermal Analysis. *Inorg. Nano-Metal Chem.* **2018**, *48*, 74–79.

(25) Yong, B. G.; Wang, X.; Anokhina, E. V.; Jacobson, A. J. Influence of the Reaction Temperature and PH on the Coordination Modes of the 1,4-Benzenedicarboxylate (BDC) Ligand: A Case Study of the Ni^{2+}(BDC)/2,2-Bipyridine System. *Inorg. Chem.* **2005**, *44*, 8265–8271.

(26) Datta, D. On Pearson's HSAB Principle. *Inorg. Chem.* **1992**, *31*, 2797–2800.

(27) Stock, N.; Biswas, S. Synthesis of Metal-Organic Frameworks (MOFs): Routes to Various MOF Topologies, Morphologies, and Composites. *Chem. Rev.* **2012**, *112*, 933–969.

(28) Melnic, E.; Coropceanu, E. B.; Forni, A.; Cariati, E.; Kulikova, O. V.; Siminel, A. V.; Kravtsov, V. C.; Fonari, M. S. Discrete Complexes and One-Dimensional Coordination Polymers with $[Cu(II)(2,2'\text{-Bpy})]^{2+}$ and $[Cu(II)(Phen)]^{2+}$ Corner Fragments: Insight into Supramolecular Structure and Optical Properties. *Cryst. Growth Des.* **2016**, *16*, 6275–6285.

(29) Chen, Z.; Li, Y.; Jiang, C.; Liang, F.; Song, Y. Metal Complexes with N-(2-Pyridylmethyl)Iminodiacetate: From Discrete Polynuclear Compounds to 1D Coordination Polymers. *Dalt. Trans.* **2009**, 27, 5290.

(30) Kumar, N.; Khullar, S.; Singh, Y.; Mandal, S. K. Hierarchical Importance of Coordination and Hydrogen Bonds in the Formation of Homochiral 2D Coordination Polymers and 2D Supramolecular Assemblies. *CrystEngComm* **2014**, *16*, 6730–

6744.

(31) Agarwal, R. A. One Dimensional Coordination Polymer of Zn(II) for Developing Multifunctional Nanoparticles. *Sci. Rep.* **2017**, *7*, 1–9.

(32) Madhu, V.; Das, S. K. Neutral Coordination Polymers Based on a Metal–mono(Dithiolene) Complex: Synthesis, Crystal Structure and Supramolecular Chemistry of $[Zn(Dmit)(4,4'\text{-Bpy})]_n$, $[Zn(Dmit)(4,4'\text{-Bpe})]_n$ and $[Zn(Dmit)(Bix)]_n$ (4,4′-Bpy = 4,4′-Bipyridine, 4,4′-Bpe = trans-1,2-bis(4-pyridyl)ethene, bix = 1,4-bis(imidazole-1-ylmethyl)-benzene. *Dalt. Trans.* **2011**, *40*, 12901.

(33) Kutasi, A. M.; Batten, S. R.; Harris, A. R.; Moubaraki, B.; Murray, K. S. Structure and Magnetism of the Ladder-like Coordination Polymer $Co_3(Dca)_2(Nic)_4(H_2O)_8 \cdot 2H_2O$ [Dca = Dicyanamide Anion, $N(CN)_2^-$; Nic = Nicotinate Anion]. *CrystEngComm* **2002**, *4*, 202–204.

(34) Zhou, H. C. J.; Kitagawa, S. Metal-Organic Frameworks (MOFs). *Chem. Soc. Rev.* **2014**, *43*, 5415–5418.

(35) Lin, Z.-J.; Lü, J.; Hong, M.; Cao, R. Metal–organic Frameworks Based on Flexible Ligands (FL-MOFs): Structures and Applications. *Chem. Soc. Rev.* **2014**, *43*, 5867–5895.

(36) Cook, T. R.; Zheng, Y. R.; Stang, P. J. Metal-Organic Frameworks and Self-Assembled Supramolecular Coordination Complexes: Comparing and Contrasting the Design, Synthesis, and Functionality of Metal-Organic Materials. *Chem. Rev.* **2013**, *113*, 734–777.

(37) Lee, Y.-R.; Kim, J.; Ahn, W.-S. Synthesis of Metal-Organic Frameworks: A Mini Review. *Korean J. Chem. Eng.* **2013**, *30*, 1667–1680.

(38) Almeida Paz, F. A.; Klinowski, J.; Vilela, S. M. F.; Tomé, J. P. C.; Cavaleiro, J. A. S.; Rocha, J. Ligand Design for Functional Metal–organic Frameworks. *Chem. Soc. Rev.* **2012**, *41*, 1088–1110.

(39) Tranchemontagne, D. J.; Mendoza-Cortés, J. L.; O'Keeffe, M.; Yaghi, O. M. Secondary Building Units, Nets and Bonding in the Chemistry of Metal–organic Frameworks. *Chem. Soc. Rev.* **2009**, *38*, 1257–1283.

(40) Schoedel, A.; Li, M.; Li, D.; O'Keeffe, M.; Yaghi, O. M. Structures of Metal–

Organic Frameworks with Rod Secondary Building Units. *Chem. Rev.* **2016**, *116*, 12466–12535.

(41) Chen, L.; Luque, R.; Li, Y. Controllable Design of Tunable Nanostructures inside Metal-Organic Frameworks. *Chem. Soc. Rev.* **2017**, *46*, 4614–4630.

(42) Wu, M. X.; Yang, Y. W. Metal–Organic Framework (MOF)-Based Drug/Cargo Delivery and Cancer Therapy. *Adv. Mater.* **2017**, *29*, 1–20.

(43) Feng, D.; Liu, T.-F.; Su, J.; Bosch, M.; Wei, Z.; Wan, W.; Yuan, D.; Chen, Y.-P.; Wang, X.; Wang, K.; et al. Stable Metal-Organic Frameworks Containing Single-Molecule Traps for Enzyme Encapsulation. *Nat. Commun.* **2015**, *6*, 5979.

(44) Dias, E. M.; Petit, C. Towards the Use of Metal-Organic Frameworks for Water Reuse: A Review of the Recent Advances in the Field of Organic Pollutants Removal and Degradation and the next Steps in the Field. *J. Mater. Chem. A* **2015**, *3*, 22484–22506.

(45) Rojas, S.; Carmona, F. J.; Maldonado, C. R.; Horcajada, P.; Hidalgo, T.; Serre, C.; Navarro, J. A. R.; Barea, E. Nanoscaled Zinc Pyrazolate Metal-Organic Frameworks as Drug-Delivery Systems. *Inorg. Chem.* **2016**, *55*, 2650–2663.

(46) Bobbitt, N. S.; Mendonca, M. L.; Howarth, A. J.; Islamoglu, T.; Hupp, J. T.; Farha, O. K.; Snurr, R. Q. Metal–organic Frameworks for the Removal of Toxic Industrial Chemicals and Chemical Warfare Agents. *Chem. Soc. Rev.* **2017**, *46*, 3357–3385.

(47) Barea, E.; Montoro, C.; Navarro, J. A. R. Toxic Gas Removal – Metal–organic Frameworks for the Capture and Degradation of Toxic Gases and Vapours. *Chem. Soc. Rev.* **2014**, *43*, 5419–5430.

(48) Teo, H. W. B.; Chakraborty, A. Water Adsorption on Various Metal Organic Framework. *IOP Conf. Ser. Mater. Sci. Eng.* **2017**, *272*, 012019.

(49) Zhang, Y.-Z.; He, T.; Kong, X.-J.; Lv, X.-L.; Wu, X.-Q.; Li, J.-R. Tuning Water Sorption in Highly Stable Zr(IV)-Metal–Organic Frameworks through Local Functionalization of Metal Clusters. *ACS Appl. Mater. Interfaces* **2018**, No. IV, acsami.8b09333.

(50) Qiao, C.; Sun, L.; Zhang, S.; Liu, P.; Chang, L.; Zhou, C.; Wei, Q.; Chen, S.; Gao, S. Pore-Size-Tuned Host-Guest Interactions in Co-MOFs via in Situ

Microcalorimetry: Adsorption and Magnetism. *J. Mater. Chem. C* **2017**, *5*, 1064–1073.

(51) Amirjalayer, S.; Schmid, R. Influence of Pore Dimension on the Host-Guest Interaction in Metal-Organic Frameworks. *J. Phys. Chem. C* **2016**, *120*, 27319–27327.

(52) Shi, R. B.; Pi, M.; Jiang, S. S.; Wang, Y. Y.; Jin, C. M. Encapsulated Discrete Octameric Water Cluster, 1D Water Tape, and 3D Water Aggregate Network in Diverse MOFs Based on Bisimidazolium Ligands. *J. Mol. Struct.* **2014**, *1071*, 23–33.

(53) Duan, C.; Wei, M.; Guo, D.; He, C.; Meng, Q. Crystal Structures and Properties of Large Protonated Water Clusters Encapsulated by Metal-Organic Frameworks. *J. Am. Chem. Soc.* **2010**, *132*, 3321–3330.

(54) Zhang, J.-P.; Zhou, H.-L.; Zhou, D.-D.; Liao, P.-Q.; Chen, X.-M. Controlling Flexibility of Metal–organic Frameworks. *Natl. Sci. Rev.* **2017**, 1–13.

(55) Neogi, S.; Sen, S.; Bharadwaj, P. K. Substitution at the Metal Center of Coordination Polymers in Single-Crystal-to-Single-Crystal (SC-SC) Transformation. *CrystEngComm* **2013**, *15*, 9239–9248.

(56) Li, J.; Huang, P.; Wu, X. R.; Tao, J.; Huang, R. Bin; Zheng, L. S. Metal-Organic Frameworks Displaying Single Crystal-to-Single Crystal Transformation through Postsynthetic Uptake of Metal Clusters. *Chem. Sci.* **2013**, *4*, 3232–3238.

(57) Wen, L.; Cheng, P.; Lin, W. Solvent-Induced Single-Crystal to Single-Crystal Transformation of a 2D Coordination Network to a 3D Metal-Organic Framework Greatly Enhances Porosity and Hydrogen Uptake. *Chem. Commun.* **2012**, *48*, 2846–2848.

(58) Suh, M. P.; Ko, J. W.; Choi, H. J. A Metal-Organic Bilayer Open Framework with a Dynamic Component: Single-Crystal-to-Single-Crystal Transformations. *J. Am. Chem. Soc.* **2002**, *124*, 10976–10977.

(59) Naumov, P.; Bharadwaj, P. K. Single-Crystal-to-Single-Crystal Transformations. *CrystEngComm* **2015**, *17*, 8775.

(60) Sun, J.; Dai, F.; Yuan, W.; Bi, W.; Zhao, X.; Sun, W.; Sun, D. Dimerization of a

Metal Complex through Thermally Induced Single-Crystal-to-Single-Crystal Transformation or Mechanochemical Reaction. *Angew. Chemie - Int. Ed.* **2011**, *50*, 7061–7064.

(61) Xue, D.-X.; Zhang, W.-X.; Chen, X.-M.; Wang, H.-Z. Single-Crystal-to-Single-Crystal Transformation Involving Release of Bridging Water Molecules and Conversion of Chain Helicity in a Chiral Three-Dimensional Metal-Organic Framework. *Chem. Commun.* **2008**, 13, 1551–1553.

(62) Zhao, C.; Dai, X.; Yao, T.; Chen, W.; Wang, X.; Wang, J.; Yang, J.; Wei, S.; Wu, Y.; Li, Y. Ionic Exchange of Metal-Organic Frameworks to Access Single Nickel Sites for Efficient Electroreduction of CO_2. *J. Am. Chem. Soc.* **2017**, *139*, 8078–8081.

(63) Khullar, S.; Mandal, S. K. Supramolecular Assemblies of Dimanganese Subunits and Water Clusters Organized by Strong Hydrogen Bonding Interactions: Single Crystal to Single Crystal Transformation by Thermal De-/Rehydration Processes. *Cryst. Growth Des.* **2012**, *12*, 5329–5337.

(64) Mukhopadhyay, U.; Bernal, I. A Self-Assembled, Decameric Water Cluster Stabilized by a Cyano-Bridged Copper(II) Complex. *Cryst. Growth Des.* **2006**, *6*, 363–365.

(65) Sun, X.; Li, B.; Xia, C.; Zhou, X.; Zhang, H. "Liquid-like" Type $(COO^{-})_2(H_2O)_{10}$ Anion Water Clusters in Three-Dimensional Supramolecular Structure of Cucurbit[6]Uril. *CrystEngComm* **2012**, *14*, 8525–8529.

(66) Khullar, S.; Mandal, S. K. Structural Diversity of the Encapsulated Water Clusters in the 3D Supramolecular Assemblies: A Cyclic Quasi-Planar Hexamer of Water Constructed through Strong Hydrogen Bonding Interactions. *CrystEngComm* **2013**, *15*, 6652–6662.

(67) Saykally, R. J.; Wales, D. J. Pinning Down the Water Hexamer. *Science* **2012**, *336*, 814–815.

(68) Manna, P.; Seth, S. K.; Bauzá, A.; Mitra, M.; Ray Choudhury, S.; Frontera, A.; Mukhopadhyay, S. PH Dependent Formation of Unprecedented Water–Bromide Cluster in the Bromide Salts of PTP Assisted by Anion−π Interactions: Synthesis,

Structure, and DFT Study. *Cryst. Growth Des.* **2014**, *14*, 747–755.

(69) Ghosh, A. K.; Ghoshal, D.; Ribas, J.; Mostafa, G.; Chaudhuri, N. R. Hydrogen-Bonded Assembly of Water and Chloride in a 3D Supramolecular Host. *Cryst. Growth Des.* **2006**, *6*, 36–39.

(70) Dąbrowa, K.; Ceborska, M.; Jurczak, J. Solid-State Entrapment of Water Clusters by 26-Membered Pentamide Unclosed Cryptands–probing the Para-Substituent Effect. *Supramol. Chem.* **2018**, *30*, 464–472.

(71) Carballo, R.; Covelo, B.; Fernández-Hermida, N.; García-Martínez, E.; Lago, A. B.; Vázquez, M.; Vázquez-López, E. M. Supramolecular Aggregation of Hexameric Water Clusters into a 2D Water Polymer Containing $(H_2O)_{18}$ Holes. *Cryst. Growth Des.* **2006**, *6*, 629–631.

(72) Tabatabaee, M. Supramolecular Assembled of Hexameric Water Clusters into a 1D Chain Containing $(H_2O)_6$ and $[(H_2O)_4O_2]$ Stabilized by Hydrogen Bonding in a Copper Complex. *Chem. Cent. J.* **2012**, *6*, 5.

(73) Gupta, V.; Khullar, S.; Kumar, S.; Mandal, S. K. Construction of a Robust Pillared-Layer Framework Based on the Rare Paddlewheel Subunit $[Mn^{II}_2(\mu\text{-}O_2CR)_4L_2]$: Synthesis, Crystal Structure and Magnetic Properties. *Dalt. Trans.* **2015**, *44*, 16778–16784.

(74) Khullar, S.; Gupta, V.; Mandal, S. K. Tuning the Formation of Dicarboxylate Linker-Assisted Supramolecular 1D Chains and Squares of Ni(II) Using Coordination and Hydrogen Bonds. *CrystEngComm* **2014**, *16*, 5705–5715.

(75) Gupta, V.; Mandal, S. K. Coordination Driven Self-Assembly of [2 + 2 + 2] Molecular Squares: Synthesis, Crystal Structures, Catalytic and Luminescence Properties. *Dalt. Trans.* **2018**, *47*, 9742–9754.

(76) Khullar, S.; Mandal, S. K. Non-Hydrothermal Synthesis, Structural Characterization and Thermochemistry of Water Soluble and Neutral Coordination Polymers of Zn(Ii) and Cd(Ii): Precursors for the Submicron-Sized Crystalline ZnO/CdO. *RSC Adv.* **2014**, *4*, 39204–39213.

(77) Lee, E.; Ju, H.; Kim, S.; Park, K. M.; Lee, S. S. Anion-Directed Coordination Networks of a Flexible S-Pivot Ligand and Anion Exchange in the Solid State. *Cryst.*

Growth Des. **2015**, *15*, 5427–5436.

(78) Aijaz, A.; Lama, P.; Bharadwaj, P. K. Two-Dimensional Coordination Polymer with a Non-Interpenetrated (4,4) Net Showing Anion Exchange and Structural Transformation in Single-Crystal-to- Single-Crystal Fashion. *Inorg. Chem.* **2010**, *49*, 5883–5889.

(79) Song, Y.; Fan, R.-Q.; Xing, K.; Du, X.; Su, T.; Wang, P.; Yang, Y.-L. Insight into the Controllable Synthesis of Cu(I)/Cu(II) Metal–Organic Complexes: Size-Exclusive Selective Dye Adsorption and Semiconductor Properties. *Cryst. Growth Des.* **2017**, *17*, 2549–2559.

(80) Yagub, M. T.; Sen, T. K.; Afroze, S.; Ang, H. M. Dye and Its Removal from Aqueous Solution by Adsorption: A Review. *Adv. Colloid Interface Sci.* **2014**, *209*, 172–184.

(81) Abbasi, A. R.; Karimi, M.; Daasbjerg, K. Efficient Removal of Crystal Violet and Methylene Blue from Wastewater by Ultrasound Nanoparticles Cu-MOF in Comparison with Mechanosynthesis Method. *Ultrason. Sonochem.* **2017**, *37*, 182–191.

(82) Sahoo, A.; Tripathy, S. K.; Dehury, N.; Patra, S. A Porous Trimetallic Au@Pd@Ru Nanoparticle System: Synthesis, Characterisation and Efficient Dye Degradation and Removal. *J. Mater. Chem. A* **2015**, *3*, 19376–19383.

(83) Du, P. Y.; Gu, W.; Liu, X. Multifunctional Three-Dimensional Europium Metal-Organic Framework for Luminescence Sensing of Benzaldehyde and Cu^{2+} and Selective Capture of Dye Molecules. *Inorg. Chem.* **2016**, *55*, 7826–7828.

(84) Zhao, N.; Sun, F.; Zhang, N.; Zhu, G. Novel Pyrene-Based Anionic Metal-Organic Framework for Efficient Organic Dye Elimination. *Cryst. Growth Des.* **2017**, *17*, 2453–2457.

(85) Dey, A.; Konavarapu, S. K.; Sasmal, H. S.; Biradha, K. Porous Coordination Polymers Containing Pyridine-3,5-Bis(5-Azabenzimidazole): Exploration of Water Sorption, Selective Dye Adsorption, and Luminescent Properties. *Cryst. Growth Des.* **2016**, *16*, 5976–5984.

(86) Jia, Y. Y.; Ren, G. J.; Li, A. L.; Zhang, L. Z.; Feng, R.; Zhang, Y. H.; Bu, X. H.

Temperature-Related Synthesis of Two Anionic Metal-Organic Frameworks with Distinct Performance in Organic Dye Adsorption. *Cryst. Growth Des.* **2016**, *16*, 5593–5597.

(87) Han, Y.; Sheng, S.; Yang, F.; Xie, Y.; Zhao, M.; Li, J. R. Size-Exclusive and Coordination-Induced Selective Dye Adsorption in a Nanotubular Metal-Organic Framework. *J. Mater. Chem. A* **2015**, *3*, 12804–12809.

(88) Song, T.; Yu, J.; Cui, Y.; Yang, Y.; Qian, G. Encapsulation of Dyes in Metal-Organic Frameworks and Their Tunable Nonlinear Optical Properties. *Dalt. Trans.* **2016**, *45*, 4218–4223.

(89) García, E. R.; Medina, R. L.; Lozano, M. M.; Pérez, I. H.; Valero, M. J.; Maubert Franco, A. M. Adsorption of Azo-Dye Orange II from Aqueous Solutions Using a Metal-Organic Framework Material: Iron- Benzenetricarboxylate. *Materials* **2014**, *7*, 8037–8057.

(90) Loera-Serna, S.; Solis, H.; Ortiz, E.; Martínez-Hernandéz, A. L.; Noreña, L. Elimination of Methylene Blue and Reactive Black 5 from Aqueous Solution Using HKUST-1. *Int. J. Environ. Sci. Dev.* **2017**, *8*, 241–246.

(91) Lee, J.; Farha, O. K.; Roberts, J.; Scheidt, K. A.; Nguyen, S. T.; Hupp, J. T. Metal–organic Framework Materials as Catalysts. *Chem. Soc. Rev.* **2009**, *38*, 1450–1459.

(92) Mo, K.; Yang, Y.; Cui, Y. A Homochiral Metal–Organic Framework as an Effective Asymmetric Catalyst for Cyanohydrin Synthesis. *J. Am. Chem. Soc.* **2014**, *136*, 1746–1749.

(93) Corma, A.; García, H.; Llabrés i Xamena, F. X. Engineering Metal Organic Frameworks for Heterogeneous Catalysis. *Chem. Rev.* **2010**, *110*, 4606–4655.

(94) Markad, D.; Mandal, S. K. Synthesis and Structural Characterization of a Novel Dinuclear Cu(II) Complex: An Efficient and Recyclable Bifunctional Heterogeneous Catalyst for the Diastereoselective Henry Reaction. *Dalt. Trans.* **2018**, *47*, 5928–5932.

(95) Zhu, L.; Liu, X.-Q.; Jiang, H.-L.; Sun, L.-B. Metal–Organic Frameworks for Heterogeneous Basic Catalysis. *Chem. Rev.* **2017**, *117*, 8129–8176.

(96) Almáši, M.; Zeleňák, V.; Opanasenko, M.; Čejka, J. A Novel Nickel Metal–organic

Framework with Fluorite-like Structure: Gas Adsorption Properties and Catalytic Activity in Knoevenagel Condensation. *Dalt. Trans.* **2014**, *43*, 3730–3738.

(97) Ogiwara, Y.; Takahashi, K.; Kitazawa, T.; Sakai, N. Indium(III)-Catalyzed Knoevenagel Condensation of Aldehydes and Activated Methylenes Using Acetic Anhydride as a Promoter. *J. Org. Chem.* **2015**, *80*, 3101–3110.

(98) Sharma, M. K.; Singh, P. P.; Bharadwaj, P. K. Two-Dimensional Rhombus Grid Coordination Polymer Showing Heterogeneous Catalytic Activities. *J. Mol. Catal. A Chem.* **2011**, *342*, 6–10.

(99) Tan, Y.; Fu, Z.; Zhang, J. A Layered Amino-Functionalized Zinc-Terephthalate Metal Organic Framework: Structure, Characterization and Catalytic Performance for Knoevenagel Condensation. *Inorg. Chem. Commun.* **2011**, *14*, 1966–1970.

(100) Isaeva, V. I.; Kustov, L. M. The Application of Metal-Organic Frameworks in Catalysis (Review). *Pet. Chem.* **2010**, *50*, 167–180.

(101) Dhakshinamoorthy, A.; Li, Z.; Garcia, H. Catalysis and Photocatalysis by Metal Organic Frameworks. *Chem. Soc. Rev.* **2018**, *7*.

(102) Huang, Y. B.; Liang, J.; Wang, X. S.; Cao, R. Multifunctional Metal-Organic Framework Catalysts: Synergistic Catalysis and Tandem Reactions. *Chem. Soc. Rev.* **2017**, *46*, 126–157.

(103) Rossin, A.; Tuci, G.; Luconi, L.; Giambastiani, G. Metal-Organic Frameworks as Heterogeneous Catalysts in Hydrogen Production from Lightweight Inorganic Hydrides. *ACS Catal.* **2017**, *7*, 5035–5045.

(104) Sabale, S.; Zheng, J.; Vemuri, R. S.; Yu, X.-Y.; Mcgrail, P.; Motkuri, R. K. Synthesis and Catalysis: Open Access Recent Advances in Metal-Organic Frameworks for Heterogeneous Catalyzed Organic Transformations. *Synth. Catal. Open Access* **2016**, *1*, 1–8.

(105) Chughtai, A. H.; Ahmad, N.; Younus, H. A.; Laypkov, A.; Verpoort, F. Metal-Organic Frameworks: Versatile Heterogeneous Catalysts for Efficient Catalytic Organic Transformations. *Chem. Soc. Rev.* **2015**, *44*, 6804–6849.

(106) Yang, Q.; Xu, Q.; Jiang, H. L. Metal-Organic Frameworks Meet Metal Nanoparticles: Synergistic Effect for Enhanced Catalysis. *Chem. Soc. Rev.* **2017**, *46*,

4774–4808.

(107) Kalbasi, R. J.; Mazaheri, O. Facile One-Pot Tandem Reductive Amination of Aldehydes from Nitroarenes over a Hierarchical ZSM-5 Zeolite Containing Palladium Nanoparticles. *New J. Chem.* **2016**, *40*, 9627–9637.

(108) Joarder, B.; Desai, A. V.; Samanta, P.; Mukherjee, S.; Ghosh, S. K. Selective and Sensitive Aqueous-Phase Detection of 2,4,6-Trinitrophenol (TNP) by an Amine-Functionalized Metal-Organic Framework. *Chem. - A Eur. J.* **2015**, *21*, 965–969.

(109) Wang, B.; Lv, X. L.; Feng, D.; Xie, L. H.; Zhang, J.; Li, M.; Xie, Y.; Li, J. R.; Zhou, H. C. Highly Stable Zr(IV)-Based Metal-Organic Frameworks for the Detection and Removal of Antibiotics and Organic Explosives in Water. *J. Am. Chem. Soc.* **2016**, *138*, 6204–6216.

(110) Karmakar, A.; Kumar, N.; Samanta, P.; Desai, A. V.; Ghosh, S. K. A Post-Synthetically Modified MOF for Selective and Sensitive Aqueous-Phase Detection of Highly Toxic Cyanide Ions. *Chem. - A Eur. J.* **2016**, *22*, 864–868.

(111) Karmakar, A.; Joarder, B.; Mallick, A.; Samanta, P.; Desai, A. V.; Basu, S.; Ghosh, S. K. Aqueous Phase Sensing of Cyanide Ions Using a Hydrolytically Stable Metal-Organic Framework. *Chem. Commun.* **2017**, *53*, 1253–1256.

(112) Kreno, L. E.; Leong, K.; Farha, O. K.; Allendorf, M.; Van Richard P., D.; Hupp, J. T.; Van Duyne, R. P.; Hupp, J. T. Metal–Organic Framework Materials as Chemical Sensors. *Chem. Rev.* **2012**, *112*, 1105–1125.

(113) Nagarkar, S. S.; Desai, A. V.; Ghosh, S. K. A Fluorescent Metal-Organic Framework for Highly Selective Detection of Nitro Explosives in the Aqueous Phase. *Chem. Commun.* **2014**, *50*, 8915–8918.

(114) Qi, X. L.; Lin, R. B.; Chen, Q.; Lin, J. Bin; Zhang, J. P.; Chen, X. M. A Flexible Metal Azolate Framework with Drastic Luminescence Response toward Solvent Vapors and Carbon Dioxide. *Chem. Sci.* **2011**, *2*, 2214–2218.

(115) Chen, L.; Ye, J. W.; Wang, H. P.; Pan, M.; Yin, S. Y.; Wei, Z. W.; Zhang, L. Y.; Wu, K.; Fan, Y. N.; Su, C. Y. Ultrafast Water Sensing and Thermal Imaging by a Metal-Organic Framework with Switchable Luminescence. *Nat. Commun.* **2017**, *8*, 1–10.

(116) Kumar, N.; Khullar, S.; Mandal, S. K. Solvent Effect on Neutral Chiral Supramolecular Assemblies and Their Distinct Receptor Behaviour towards Anions. *Dalt. Trans.* **2015**, *44*, 1520–1525.

(117) Kumar, N.; Khullar, S.; Mandal, S. K. Controlling the Self-Assembly of Homochiral Coordination Architectures of CuIIby Substitution in Amino Acid Based Ligands: Synthesis, Crystal Structures and Physicochemical Properties. *Dalt. Trans.* **2015**, *44*, 5672–5687.

(118) Kumar, N.; Khullar, S.; Mandal, S. K. A Homochiral Luminescent Compound with Four-Fold Symmetry as a Potential Chemosensor for Nitroanilines. *RSC Adv.* **2014**, *4*, 47249–47253.

(119) Das, P.; Mandal, S. K. Strategic Design and Functionalization of an Amine-Decorated Luminescent Metal Organic Framework for Selective Gas/Vapor Sorption and Nanomolar Sensing of 2,4,6-Trinitrophenol in Water. *ACS Appl. Mater. Interfaces* **2018**, *10*, 25360–25371.

(120) Chakraborty, G.; Mandal, S. K. Design and Development of Fluorescent Sensors with Mixed Aromatic Bicyclic Fused Rings and Pyridyl Groups: Solid Mediated Selective Detection of 2,4,6-Trinitrophenol in Water. *ACS Omega* **2018**, *3*, 3248–3256.

(121) Tian, D.; Chen, R.-Y.; Xu, J.; Li, Y.-W.; Bu, X.-H. A Three-Dimensional Metal–organic Framework for Selective Sensing of Nitroaromatic Compounds. *APL Mater.* **2014**, *2*, 124111.

(122) Wu, Y.; Yang, G.-P.; Zhang, Y.; Shi, N.; Han, J.; Wang, Y.-Y. A New Luminescent Cd(II)-MOF as a Highly Selective Chemical Probe for Fe^{3+} in Aqueous Solution with Mixed Metal Ions. *RSC Adv.* **2015**, *5*, 90772–90777.

(123) Lu, Y.; Yan, B. A Ratiometric Fluorescent PH Sensor Based on Nanoscale Metal-Organic Frameworks (MOFs) Modified by Europium(III) Complexes. *Chem. Commun.* **2014**, *50*, 13323–13326.

(124) Hu, Z.; Deibert, B. J.; Li, J. Luminescent Metal–organic Frameworks for Chemical Sensing and Explosive Detection. *Chem. Soc. Rev.* **2014**, *43*, 5815–5840.

(125) Zhou, J. M.; Shi, W.; Xu, N.; Cheng, P. Highly Selective Luminescent Sensing of

Fluoride and Organic Small-Molecule Pollutants Based on Novel Lanthanide Metal-Organic Frameworks. *Inorg. Chem.* **2013**, *52*, 8082–8090.

(126) Chen, B.; Yang, Y.; Zapata, F.; Lin, G.; Qian, G.; Lobkovsky, E. B. Luminescent Open Metal Sites within a Metal-Organic Framework for Sensing Small Molecules. *Adv. Mater.* **2007**, *19*, 1693–1696.

(127) Wang, H.; Jiang, S.; Lu, Q.; Zhou, Z.; Zhuo, S.; Shan, G.; Su, Z. A Pillar-Layer MOF for Detection of Small Molecule Acetone and Metal Ions in Dilute Solution. *RSC Adv.* **2015**, *5*, 48881–48884.

(128) Yi, F.-Y.; Yang, W.; Sun, Z.-M. Highly Selective Acetone Fluorescent Sensors Based on Microporous Cd(II) Metal–organic Frameworks. *J. Mater. Chem.* **2012**, *22*, 23201.

(129) Cui, Y.; Xu, H.; Yue, Y.; Guo, Z.; Yu, J.; Chen, Z.; Gao, J.; Yang, Y.; Qian, G.; Chen, B. A Luminescent Mixed-Lanthanide Metal-Organic Framework Thermometer. *J. Am. Chem. Soc.* **2012**, *134*, 3979–3982.

(130) Yan, B. Lanthanide-Functionalized Metal-Organic Framework Hybrid Systems to Create Multiple Luminescent Centers for Chemical Sensing. *Acc. Chem. Res.* **2017**, *50*, 2789–2798.

(131) Wang, H. S.; Li, J.; Li, J. Y.; Wang, K.; Ding, Y.; Xia, X. H. Lanthanide-Based Metal-Organic Framework Nanosheets with Unique Fluorescence Quenching Properties for Two-Color Intracellular Adenosine Imaging in Living Cells. *NPG Asia Mater.* **2017**, *9*, 1–9.

(132) Gao, Y.; Jing, P.; Yan, N.; Hilbers, M.; Zhang, H.; Rothenberg, G.; Tanase, S. Dual-Mode Humidity Detection Using a Lanthanide-Based Metal-Organic Framework: Towards Multifunctional Humidity Sensors. *Chem. Commun.* **2017**, *53*, 4465–4468.

(133) Wang, K. M.; Du, L.; Ma, Y. L.; Zhao, J. S.; Wang, Q.; Yan, T.; Zhao, Q. H. Multifunctional Chemical Sensors and Luminescent Thermometers Based on Lanthanide Metal-Organic Framework Materials. *CrystEngComm* **2016**, *18*, 2690–2700.

(134) Du, P. Y.; Liao, S. Y.; Gu, W.; Liu, X. A Multifunctional Chemical Sensor Based on a Three-Dimensional Lanthanide Metal-Organic Framework. *J. Solid State*

Chem. **2016**, *244*, 31–34.

(135) Yang, D.; Tian, Y.; Xu, W.; Cao, X.; Zheng, S.; Ju, Q.; Huang, W.; Fang, Z. A Series of Lanthanide-Based Metal-Organic Frameworks: Synthesis, Structures, and Multicolor Tuning of Single Component. *Inorg. Chem.* **2017**, *56*, 2345–2353.

(136) Wang, J.; Wang, J.; Li, Y.; Jiang, M.; Zhang, L.; Wu, P. A Europium(III)-Based Metal–organic Framework as a Naked-Eye and Fast Response Luminescence Sensor for Acetone and Ferric Iron. *New J. Chem.* **2016**, *40*, 8600–8606.

(137) Letzel, S.; Göen, T.; Bader, M.; Angerer, J.; Kraus, T. Exposure to Nitroaromatic Explosives and Health Effects during Disposal of Military Waste. *Occup. Environ. Med.* **2003**, *60*, 483–488.

(138) Zhao, S. S.; Yang, J.; Liu, Y. Y.; Ma, J. F. Fluorescent Aromatic Tag-Functionalized Mofs for Highly Selective Sensing of Metal Ions and Small Organic Molecules. *Inorg. Chem.* **2016**, *55*, 2261–2273.

(139) Zhang, H.; Yang, J.; Liu, Y.-Y.; Song, S.; Ma, J.-F. A Family of Metal–Organic Frameworks with a New Chair-Conformation Resorcin[4]Arene-Based Ligand: Selective Luminescent Sensing of Amine and Aldehyde Vapors, and Solvent-Mediated Structural Transformations. *Cryst. Growth Des.* **2016**, *16*, 3244–3255.

(140) Lu, G.; Farha, O. K.; Kreno, L. E.; Schoenecker, P. M.; Walton, K. S.; Van Duyne, R. P.; Hupp, J. T. Fabrication of Metal-Organic Framework-Containing Silica-Colloidal Crystals for Vapor Sensing. *Adv. Mater.* **2011**, *23*, 4449–4452.

(141) Cui, C.; Liu, Y.; Xu, H.; Li, S.; Zhang, W.; Cui, P.; Huo, F. Self-Assembled Metal-Organic Frameworks Crystals for Chemical Vapor Sensing. *Small* **2014**, *10*, 3672–3676.

(142) Assen, A. H.; Yassine, O.; Shekhah, O.; Eddaoudi, M.; Salama, K. N. MOFs for the Sensitive Detection of Ammonia: Deployment of Fcu-MOF Thin Films as Effective Chemical Capacitive Sensors. *ACS Sensors* **2017**, *2*, 1294–1301.

(143) Wales, D. J.; Grand, J.; Ting, V. P.; Burke, R. D.; Edler, K. J.; Bowen, C. R.; Mintova, S.; Burrows, A. D. Gas Sensing Using Porous Materials for Automotive Applications. *Chem. Soc. Rev.* **2015**, *44*, 4290–4321.

(144) *APEX2, SADABS and SAINT*; Bruker AXS Inc, Madison, WI, USA, 2008.

(145) Dolomanov, O. V.; Bourhis, L. J.; Gildea, R. J.; Howard, J. A. K.; Puschmann, H. OLEX2 : A Complete Structure Solution, Refinement and Analysis Program. *J. Appl. Crystallogr.* **2009**, *42*, 339–341.

(146) Sheldrick, G. M. SHELXT – Integrated Space-Group and Crystal-Structure Determination. *Acta Crystallogr. Sect. A Found. Adv.* **2015**, *71*, 3–8.

(147) Sheldrick, G. M. Crystal Structure Refinement with SHELXL. *Acta Crystallogr. Sect. C Struct. Chem.* **2015**, *71*, 3–8.

(148) Macrae, C. F.; Bruno, I. J.; Chisholm, J. A.; Edgington, P. R.; McCabe, P.; Pidcock, E.; Rodriguez-Monge, L.; Taylor, R.; van de Streek, J.; Wood, P. A. Mercury CSD 2.0 – New Features for the Visualization and Investigation of Crystal Structures. *J. Appl. Crystallogr.* **2008**, *41*, 466–470.

(149) Spek, A. L. *PLATON, Version 1.62*; University of Utrecht, 1999.

(150) Spek, A. L. Single-Crystal Structure Validation with the Program PLATON. *J. Appl. Crystallogr.* **2003**, *36*, 7–13.

(151) Lu, W.; Wei, Z.; Gu, Z. Y.; Liu, T. F.; Park, J.; Park, J.; Tian, J.; Zhang, M.; Zhang, Q.; Gentle, T.; et al. Tuning the Structure and Function of Metal-Organic Frameworks via Linker Design. *Chem. Soc. Rev.* **2014**, *43*, 5561–5593.

(152) Zhao, M.; Huang, Y.; Peng, Y.; Huang, Z.; Ma, Q.; Zhang, H. Two-Dimensional Metal–organic Framework Nanosheets: Synthesis and Applications. *Chem. Soc. Rev.* **2018**, *47*, 6267–6295.

(153) Bai, Y.; Dou, Y.; Xie, L.-H.; Rutledge, W.; Li, J.-R.; Zhou, H.-C. Zr-Based Metal–organic Frameworks: Design, Synthesis, Structure, and Applications. *Chem. Soc. Rev.* **2016**, *45*, 2327–2367.

(154) Jiang, H. L.; Xu, Q. Porous Metal-Organic Frameworks as Platforms for Functional Applications. *Chem. Commun.* **2011**, *47*, 3351–3370.

(155) McGuire, C. V.; Forgan, R. S. The Surface Chemistry of Metal-Organic Frameworks. *Chem. Commun.* **2015**, *51*, 5199–5217.

(156) Liu, X. W.; Sun, T. J.; Hu, J. L.; Wang, S. D. Composites of Metal-Organic Frameworks and Carbon-Based Materials: Preparations, Functionalities and

Applications. *J. Mater. Chem. A* **2016**, *4*, 3584–3616.

(157) Markad, D.; Mandal, S. K. An Exploration into the Amide-Pseudo Amide Hydrogen Bonding Synthon between a New Coformer with Two Primary Amide Groups and Theophylline. *CrystEngComm* **2017**, *19*, 7112–7124.

(158) Janiak, C. A Critical Account on Π–π Stacking in Metal Complexes with Aromatic Nitrogen-Containing Ligands †. *J. Chem. Soc. Dalt. Trans.* **2000**, *0*, 3885–3896.

(159) Hu, Y.; Hu, H.; Li, Y.; Chen, R.; Yang, Y.; Wang, L. Supramolecular Assemblies of Tetrafluoroterephthalic Acid and N-Heterocycles via Various Strong Hydrogen Bonds and Weak C-H...F Interactions: Synthons Cooperation, Robust Motifs and Structural Diversity. *J. Mol. Struct.* **2016**, *1122*, 256–267.

(160) Bowers, J. R.; Hopkins, G. W.; Yap, G. P. A.; Wheeler, K. A. Structural Consequences of Strong and Weak Interactions to Binary Benzoic Acid/Bipyridine Supramolecular Assemblies. *Cryst. Growth Des.* **2005**, *5*, 727–736.

(161) Wang, W. H.; Xi, P. H.; Su, X. Y.; Lan, J. B.; Mao, Z. H.; You, J. S.; Xie, R. G. Supramolecular Assemblies of Multifunctional Diimidazole and Dicarboxylic Acids via Various Hydrogen Bonds and X···π (X = π, CH) Interactions. *Cryst. Growth Des.* **2007**, *7*, 741–746.

(162) Seth, S. K.; Sarkar, D.; Roy, A.; Kar, T. Insight into Supramolecular Self-Assembly Directed by Weak Interactions in Acetophenone Derivatives: Crystal Structures and Hirshfeld Surface Analyses. *CrystEngComm* **2011**, *13*, 6728–6741.

(163) Silva, P.; Vilela, S. M. F.; Tomé, J. P. C.; Almeida Paz, F. A. Multifunctional Metal-Organic Frameworks: From Academia to Industrial Applications. *Chem. Soc. Rev.* **2015**, *44*, 6774–6803.

(164) Chen, B.; Wang, X.; Zhang, Q.; Xi, X.; Cai, J.; Qi, H.; Shi, S.; Wang, J.; Yuan, D.; Fang, M. Synthesis and Characterization of the Interpenetrated MOF-5. *J. Mater. Chem.* **2010**, *20*, 3758–3767.

(165) Maniam, P.; Stock, N. Investigation of Porous Ni-Based Metal–Organic Frameworks Containing Paddle-Wheel Type Inorganic Building Units via High-Throughput Methods. *Inorg. Chem.* **2011**, *50*, 5085–5097.

(166) Gholipour-Ranjbar, H.; Soleimani, M.; Naderi, H. R. Application of Ni/Co-Based

Metal–organic Frameworks (MOFs) as an Advanced Electrode Material for Supercapacitors. *New J. Chem.* **2016**, *40*, 9187–9193.

(167) Biswas, A.; Saha, R.; Ghosh, A. Two Unusual Mixed-Valent Trinuclear CuII2CuI Complexes Containing Copper(I) Tribromide Dianion as Bridging Ligand: Identification of an Unprecedented Doubly Hydrogen-Bonded Water Dimer. *CrystEngComm* **2011**, *13*, 5342–5347.

(168) Jian, F. F.; Liu, E.; Ma, J. Y. Interesting Fluorine Anion Water Clusters [$F^{-}\cdot(H_2O)_n$] in Metal Complex Crystals. *CrystEngComm* **2018**, *20*, 3849–3857.

(169) Rakshit, A.; Yamaguchi, T.; Asada, T.; Bandyopadhyay, P. Understanding the Structure and Hydrogen Bonding Network of $(H_2O)_{32}$ and $(H_2O)_{33}$: An Improved Monte Carlo Temperature Basin Paving (MCTBP) Method and Quantum Theory of Atoms in Molecules (QTAIM) Analysis. *RSC Adv.* **2017**, *7*, 18401–18417.

(170) Jassal, A. K.; Rana, L. K.; Hundal, G. Structure Directing Role of Amines and Water Molecules in the Self-Assembly of Polyoxomolybdates. *CrystEngComm* **2017**, *19*, 2021–2035.

(171) Li, X.; Xu, X.; Yuan, D.; Weng, X. Hexagonal Prismatic Dodecameric Water Cluster: A Building Unit of the Five-Fold Interpenetrating Six-Connected Supramolecular Network. *Chem. Commun.* **2012**, *48*, 9014–9016.

(172) Albertí, F. M.; Mihály, T.; Lippert, B.; Miguel, P. J. S. Unsupported Single-Walled Water Cluster Nanotube: A Novel Hydrogen Bonding Pattern for Water Organization. *CrystEngComm* **2012**, *14*, 6178–6181.

(173) Yuan, D.; Shen, X.; Li, W.; Li, S. Are Fragment-Based Quantum Chemistry Methods Applicable to Medium-Sized Water Clusters? *Phys. Chem. Chem. Phys.* **2016**, *18*, 16491–16500.

(174) Fu, K.; Ren, C.-X.; Chen, C.; Cai, L.-X.; Tan, B.; Zhang, J. Auxiliary Ligand-Controlled Photochromism and Decolourization of Two Bipyridinium-Based Metal–organic Hybrid Materials with Various Water Clusters. *CrystEngComm* **2014**, *16*, 5134–5141.

(175) Debnarova, A.; Techert, S.; Schmatz, S. Limitations of High-Intensity Soft X-Ray Laser Fields for the Characterisation of Water Chemistry: Coulomb Explosion of the

Octamer Water Cluster. *Phys. Chem. Chem. Phys.* **2012**, *14*, 9606–9614.

(176) Xu, Z.; Li, X.; Zhang, X. A Novel Water Cluster Held Up by a Tungstotellurate of the $[Ni(2,2'\text{-}Bipy)_3]^{2+}$ Cations: Synthesis and Characterization of $[Ni(2,2'\text{-}Bipy)_3]_2[H_2(TeW_6O_{24})]\cdot 28H_2O$. *Synth. React. Inorganic, Met. Nano-Metal Chem.* **2012**, *42*, 140–144.

(177) Zhang, L.; Li, Z. J.; Lin, Q. P.; Zhang, J.; Yin, P. X.; Qin, Y. Y.; Cheng, J. K.; Yao, Y. G. Novel (3,6)-Connected Network and (4,6)-Connected Framework in Two Copper(II) and Cadmium(II) Complexes of Flexible (2S,3S,4R,5R)-Tetrahydrofurantetracarboxylic Acid: Synthesis, Structure, Thermostability, and Luminescence Studies. *CrystEngComm* **2009**, *11*, 1934–1939.

(178) Jin, Y.; Che, Y. X.; Zheng, J. M. Supramolecularly Assembled Decameric Water Cluster Stabilized by Dichromate Anions in Complex of Ni(II). *Inorg. Chem. Commun.* **2007**, *10*, 514–516.

(179) Covelo, B.; Carballo, R.; Vázquez-López, E. M.; Lago, A. B. Stabilization of Discrete (H2O)14 Water Clusters in the Supramolecular Crystal Host of $[Ni(Phen)_3](HB)_2\cdot 7H_2O$ (HB^-=benzilate). *Synth. React. Inorganic, Met. Nano-Metal Chem.* **2008**, *38*, 49–54.

(180) Infantes, L.; Chisholm, J.; Motherwell, S. Extended Motifs from Water and Chemical Functional Groups in Organic Molecular Crystals. *CrystEngComm* **2003**, *5*, 480–486.

(181) Shi, R.; Pi, M,; Jiang, S,; Wang, Y,; Jin, C-M. Encapsulated Discrete Octameric Water Cluster, 1D Water Tape, and 3D Water Aggregate Network in Diverse MOFs based on Bisimidazolium Ligands. *journal of molecular structure.* **2014**, *1071*, 23–33.

(182) Liu, D.; Li, H.-X.; Ren, Z.-G.; Chen, Y.; Zhang, Y.; Lang, J.-P. Encapsulation of Unusual Nitrate−Water Cluster $[(NO_3)_4(H_2O)_6]_4^-$Anions into Cages of a Three-Dimensional Cationic Coordination Polymer. *Cryst. Growth Des.* **2009**, *9*, 4562–4566.

(183) Takaoka, K.; Kawano, M.; Tominaga, M.; Fujita, M. In Situ Observation of a Reversible Single-Crystal-to-Single-Crystal Apical-Ligand-Exchange Reaction in a Hydrogen-Bonded 2D Coordination Network. *Angew. Chemie - Int. Ed.* **2005**, *44*,

2151–2154.

(184) Gabriel, C.; Raptopoulou, C. P.; Psycharis, V.; Terzis, A.; Zervou, M.; Mateescu, C.; Salifoglou, A. 1D-3D Metal - Organic Lattice Assemblies through Chemical Reactivity and Metal-Assisted Ligand Transformations in Ternary Pb(II)-Phenanthroline-(Hydroxy) Dicarboxylic Acid Systems. *Cryst. Growth Des.* **2011**, *11*, 382–395.

(185) Li, G.-B.; He, J.-R.; Liu, J.-M.; Su, C.-Y. Anion Effect on the Structural Diversity of Three 1D Coordination Polymers Based on a Pyridyl Diimide Ligand. *CrystEngComm* **2012**, *14*, 2152–2158.

(186) Manna, B.; Desai, A. V.; Ghosh, S. K. Neutral N-Donor Ligand Based Flexible Metal–organic Frameworks. *Dalt. Trans.* **2016**, *45*, 4060–4072.

(187) Zhu, L.; Xiao, C.; Dai, X.; Li, J.; Gui, D.; Sheng, D.; Chen, L.; Zhou, R.; Chai, Z.; Albrecht-Schmitt, T. E.; et al. Exceptional Perrhenate/Pertechnetate Uptake and Subsequent Immobilization by a Low-Dimensional Cationic Coordination Polymer: Overcoming the Hofmeister Bias Selectivity. *Environ. Sci. Technol. Lett.* **2017**, *4*, 316–322.

(188) Lei, X. P.; Lian, T. T.; Chen, S. M.; Zhang, J. Tuning the Formations of Metal-1,3,5-Benzenetricarboxylate Frameworks via the Assistance of Amino Acids. *J. Solid State Chem.* **2015**, *223*, 44–52.

(189) Xia, C. K.; Wu, F.; Yang, K.; Sun, W.; Min, Y. Y.; Wu, Y. L.; Lu, X. J. Zn(II) and Cd(II) Complexes Assembled from Versatile 1,2,3,5-Benzenetetracarboxylic Acid and Chelating N-Donor Auxiliary Coligands. *Polyhedron* **2016**, *117*, 637–643.

(190) Tomar, K. Assembly of an Eight Connected Porous Cd(II) Framework with Octahedral and Cubo-Octahedral Cages: Sorption and Luminescent Properties. *Inorg. Chem. Commun.* **2013**, *37*, 127–131.

(191) Wang, X. W.; Sun, J. W.; Zhang, H.; Hou, G. F.; Li, G. M. Building Block Controlled Cd(II) Coordination Polymers from One Dimension Chain to Three Dimension Network. *J. Inorg. Organomet. Polym. Mater.* **2015**, *25*, 1218–1225.

(192) Habib, H. A.; Sanchiz, J.; Janiak, C. Magnetic and Luminescence Properties of Cu(II), Cu(II)4O4core, and Cd(II) Mixed-Ligand Metal-Organic Frameworks Constructed from 1,2-Bis(1,2,4-Triazol-4-Yl)Ethane and Benzene-1,3,5-Tricarboxylate. *Inorganica Chim. Acta* **2009**, *362*, 2452–2460.

(193) Burrows, A. D.; Frost, C. G.; Kandiah, M.; Keenan, L. L.; Mahon, M. F.; Savarese, T. L.; Warren, J. E. The Effect of Reaction Conditions on the Nature of Cadmium

1,3,5-Benzenetricarboxylate Metal-Organic Frameworks. *Inorganica Chim. Acta* **2011**, *366*, 303–309.

(194) Chen, Z. H.; Zhao, Y.; Chen, S. S.; Wang, P.; Sun, W. Y. Synthesis and Characterization of D10metal Complexes with Mixed 1,3-Di(1H-Imidazol-4-Yl)Benzene and Multicarboxylate Ligands. *J. Solid State Chem.* **2013**, *202*, 215–226.

(195) Rachuri, Y.; Bisht, K. K.; Parmar, B.; Suresh, E. Luminescent MOFs Comprising Mixed Tritopic Linkers and Cd(II)/Zn(II) Nodes for Selective Detection of Organic Nitro Compounds and Iodine Capture. *J. Solid State Chem.* **2015**, *223*, 23–31.

(196) Chen, C. H.; Wang, X. S.; Li, L.; Huang, Y. B.; Cao, R. Highly Selective Sensing of Fe^{3+} by an Anionic Metal-Organic Framework Containing Uncoordinated Nitrogen and Carboxylate Oxygen Sites. *Dalt. Trans.* **2018**, *47*, 3452–3458.

(197) Li, H.; Han, Y.; Shao, Z.; Li, N.; Huang, C.; Hou, H. Water-Stable Eu-MOF Fluorescent Sensors for Trivalent Metal Ions and Nitrobenzene. *Dalt. Trans.* **2017**, *46*, 12201–12208.

(198) Han, L. J.; Yan, W.; Chen, S. G.; Shi, Z. Z.; Zheng, H. G. Exploring the Detection of Metal Ions by Tailoring the Coordination Mode of V-Shaped Thienylpyridyl Ligand in Three MOFs. *Inorg. Chem.* **2017**, *56*, 2936–2940.

(199) Jana, A. K.; Natarajan, S. Fluorescent Metal-Organic Frameworks for Selective Sensing of Toxic Cations (Tl^{3+}, Hg^{2+}) and Highly Oxidizing Anions ($(CrO_4)^{2-}$, $(Cr_2O_7)^{2-}$, $(MnO_4)^{-}$). *Chempluschem* **2017**, *82*, 1153–1163.

(200) Tang, Q.; Liu, S.; Liu, Y.; Miao, J.; Li, S.; Zhang, L.; Shi, Z.; Zheng, Z. Cation Sensing by a Luminescent Metal-Organic Framework with Multiple Lewis Basic Sites. *Inorg. Chem.* **2013**, *52*, 2799–2801.

(201) Liu, J.; Chen, L.; Cui, H.; Zhang, J.; Zhang, L.; Su, C.-Y. Applications of Metal–organic Frameworks in Heterogeneous Supramolecular Catalysis. *Chem. Soc. Rev.* **2014**, *43*, 6011–6061.

(202) Li, X.; Van Zeeland, R.; Maligal-Ganesh, R. V.; Pei, Y.; Power, G.; Stanley, L.; Huang, W. Impact of Linker Engineering on the Catalytic Activity of Metal-Organic Frameworks Containing Pd(II)-Bipyridine Complexes. *ACS Catal.* **2016**, *6*, 6324–6328.

(203) Chen, H.; Shen, K.; Mao, Q.; Chen, J.; Li, Y. Nanoreactor of MOF-Derived Yolk-Shell Co@C-N: Precisely Controllable Structure and Enhanced Catalytic Activity. *ACS Catal.* **2018**, *8*, 1417–1426.

(204) Stavila, V.; Parthasarathi, R.; Davis, R. W.; El Gabaly, F.; Sale, K. L.; Simmons, B. A.; Singh, S.; Allendorf, M. D. MOF-Based Catalysts for Selective Hydrogenolysis of Carbon-Oxygen Ether Bonds. *ACS Catal.* **2016**, *6*, 55–59.

(205) Huang, C.; Liu, R.; Yang, W.; Li, Y.; Huang, J.; Zhu, H. Enhanced Catalytic Activity of MnCo-MOF-74 for Highly Selective Aerobic Oxidation of Substituted Toluene. *Inorg. Chem. Front.* **2018**, *5*, 1923–1932.

(206) Rani, P.; Srivastava, R. Tailoring the Catalytic Activity of Metal Organic Frameworks by Tuning the Metal Center and Basic Functional Sites. *New J. Chem.* **2017**, *41*, 8166–8177.

(207) Zhu, C.; Xia, Q.; Chen, X.; Liu, Y.; Du, X.; Cui, Y. Chiral Metal−Organic Framework as a Platform for Cooperative Catalysis in Asymmetric Cyanosilylation of Aldehydes. *ACS Catal.* **2016**, *6*, 7590–7596.

(208) Gascon, J.; Corma, A.; Kapteijn, F.; Llabrés I Xamena, F. X. Metal Organic Framework Catalysis: Quo Vadis? *ACS Catal.* **2014**, *4*, 361–378.

(209) Hall, E. A.; Redfern, L. R.; Wang, M. H.; Scheidt, K. A. Lewis Acid Activation of a Hydrogen Bond Donor Metal-Organic Framework for Catalysis. *ACS Catal.* **2016**, *6*, 3248–3252.

(210) Kurisingal, J. F.; Babu, R.; Kim, S. H.; Li, Y. X.; Chang, J. S.; Cho, S. J.; Park, D. W. Microwave-Induced Synthesis of a Bimetallic Charge-Transfer Metal Organic Framework: A Promising Host for the Chemical Fixation of CO_2. *Catal. Sci. Technol.* **2018**, *8*, 591–600.

(211) Maina, J. W.; Pozo-Gonzalo, C.; Kong, L.; Schütz, J.; Hill, M.; Dumée, L. F. Metal Organic Framework Based Catalysts for CO_2 Conversion. *Mater. Horiz.* **2017**, *4*, 345–361.

(212) Yamashita, Y.; Yasukawa, T.; Yoo, W.-J.; Kitanosono, T.; Kobayashi, S. Catalytic Enantioselective Aldol Reactions. *Chem. Soc. Rev.* **2018**, *47*, 4388–4480.

(213) Nguyen, K. D.; Kutzscher, C.; Drache, F.; Senkovska, I.; Kaskel, S. Chiral Functionalization of a Zirconium Metal-Organic Framework (DUT-67) as a Heterogeneous Catalyst in Asymmetric Michael Addition Reaction. *Inorg. Chem.* **2018**, *57*, 1483–1489.

(214) Li, Z.; Liu, Y.; Kang, X.; Cui, Y. Chiral Metal–Organic Framework Decorated with TEMPO Radicals for Sequential Oxidation/Asymmetric Cyanation Catalysis. *Inorg. Chem.* **2018**, *57*, 9786–9789.

(215) Cao, S. L.; Yue, D. M.; Li, X. H.; Smith, T. J.; Li, N.; Zong, M. H.; Wu, H.; Ma, Y.

Z.; Lou, W. Y. Novel Nano-/Micro-Biocatalyst: Soybean Epoxide Hydrolase Immobilized on UiO-66-NH_2MOF for Efficient Biosynthesis of Enantiopure (R)-1, 2-Octanediol in Deep Eutectic Solvents. *ACS Sustain. Chem. Eng.* **2016**, *4*, 3586–3595.

(216) Chołuj, A.; Zieliński, A.; Grela, K.; Chmielewski, M. J. Metathesis@MOF: Simple and Robust Immobilization of Olefin Metathesis Catalysts inside (Al)MIL-101-NH_2. *ACS Catal.* **2016**, *6*, 6343–6349.

(217) Liu, J.; Wang, F.; Ding, Q. R.; Zhang, J. Synthesis of an Enantipure Tetrazole-Based Homochiral CuI,II-MOF for Enantioselective Separation. *Inorg. Chem.* **2016**, *55*, 12520–12522.

(218) Moghadam, P. Z.; Düren, T. Origin of Enantioselectivity in a Chiral Metal-Organic Framework: A Molecular Simulation Study. *J. Phys. Chem. C* **2012**, *116*, 20874–20881.

(219) Meilikhov, M.; Yusenko, K.; Esken, D.; Turner, S.; Van Tendeloo, G.; Fischer, R. A. Metals@MOFs - Loading MOFs with Metal Nanoparticles for Hybrid Functions. *Eur. J. Inorg. Chem.* **2010**, 24, 3701–3714.

(220) Li, K.; Zeng, Y.; Neuenswander, B.; Tunge, J. A. Sequential Pd(II)-Pd(0) Catalysis for the Rapid Synthesis of Coumarins. *J. Org. Chem.* **2005**, *70*, 6515–6518.

(221) Rogers, S. M.; Catlow, C. R. A.; Chan-Thaw, C. E.; Chutia, A.; Jian, N.; Palmer, R. E.; Perdjon, M.; Thetford, A.; Dimitratos, N.; Villa, A.; et al. Tandem Site- and Size-Controlled Pd Nanoparticles for the Directed Hydrogenation of Furfural. *ACS Catal.* **2017**, *7*, 2266–2274.

(222) Li, X.; Goh, T. W.; Li, L.; Xiao, C.; Guo, Z.; Zeng, X. C.; Huang, W. Controlling Catalytic Properties of Pd Nanoclusters through Their Chemical Environment at the Atomic Level Using Isoreticular Metal-Organic Frameworks. *ACS Catal.* **2016**, *6*, 3461–3468.

(223) Mondal, J.; Trinh, Q. T.; Jana, A.; Ng, W. K. H.; Borah, P.; Hirao, H.; Zhao, Y. Size-Dependent Catalytic Activity of Palladium Nanoparticles Fabricated in Porous Organic Polymers for Alkene Hydrogenation at Room Temperature. *ACS Appl. Mater. Interfaces* **2016**, *8*, 15307–15319.

(224) Zhang, D.; Zhaorigetu, B.; Bao, Y.-S. Supported Palladium Nanoparticles Catalyzed Ortho -Directed C–C Coupling Reaction via a Pd 0 /Pd II /Pd IV Catalytic Cycle. *J. Phys. Chem. C* **2015**, *119*, 20426–20432.

(225) Llabrés i Xamena, F. X.; Abad, A.; Corma, A.; Garcia, H. MOFs as Catalysts:

Activity, Reusability and Shape-Selectivity of a Pd-Containing MOF. *J. Catal.* **2007**, *250*, 294–298.

(226) Dong, W.; Feng, C.; Zhang, L.; Shang, N.; Gao, S.; Wang, C.; Wang, Z. Pd@UiO-66: An Efficient Catalyst for Suzuki-Miyaura Coupling Reaction at Mild Condition. *Catal. Letters* **2016**, *146*, 117–125.

(227) Lu, G.; Li, S.; Guo, Z.; Farha, O. K.; Hauser, B. G.; Qi, X.; Wang, Y.; Wang, X.; Han, S.; Liu, X.; et al. Imparting Functionality to a Metal-Organic Framework Material by Controlled Nanoparticle Encapsulation. *Nat. Chem.* **2012**, *4*, 310–316.

(228) Gole, B.; Sanyal, U.; Banerjee, R.; Mukherjee, P. S. High Loading of Pd Nanoparticles by Interior Functionalization of MOFs for Heterogeneous Catalysis. *Inorg. Chem.* **2016**, *55*, 2345–2354.

(229) Wang, J.; Wang, X.; Xu, H.; Zhao, X.; Zheng, Z.; Xu, Z. L. A Zinc(II) Porous Metal–Organic Framework and Its Morphologically Controlled Catalytic Properties in the Knoevenagel Condensation Reaction. *Chempluschem* **2017**, *82*, 1182–1187.

(230) Taher, A.; Lee, D.-J.; Lee, B.-K.; Lee, I.-M. Amine-Functionalized Metal-Organic Frameworks: An Efficient and Recyclable Heterogeneous Catalyst for the Knoevenagel Condensation Reaction. *Synlett* **2016**, *27*, 1433–1437.

(231) Neogi, S.; Sharma, M. K.; Bharadwaj, P. K. Knoevenagel Condensation and Cyanosilylation Reactions Catalyzed by a MOF Containing Coordinatively Unsaturated Zn(II) Centers. *J. Mol. Catal. A Chem.* **2009**, *299*, 1–4.

(232) Dhakshinamoorthy, A.; Heidenreich, N.; Lenzen, D.; Stock, N. Knoevenagel Condensation Reaction Catalysed by Al-MOFs with CAU-1 and CAU-10-Type Structures. *CrystEngComm* **2017**, *19*, 4187–4193.

(233) Xiang, W.; Zhang, Y.; Lin, H.; Liu, C. Nanoparticle/Metal–Organic Framework Composites for Catalytic Applications: Current Status and Perspective. *Molecules* **2017**, *22*, 2103.

(234) Chen, L.; Chen, H.; Luque, R.; Li, Y. Metal−organic Framework Encapsulated Pd Nanoparticles: Towards Advanced Heterogeneous Catalysts. *Chem. Sci.* **2014**, *5*, 3708–3714.

(235) Ma, H. C.; Kan, J. L.; Chen, G. J.; Chen, C. X.; Dong, Y. Bin. Pd NPs-Loaded Homochiral Covalent Organic Framework for Heterogeneous Asymmetric Catalysis. *Chem. Mater.* **2017**, *29*, 6518–6524.

(236) Li, B.; Chrzanowski, M.; Zhang, Y.; Ma, S. Applications of Metal-Organic Frameworks Featuring Multi-Functional Sites. *Coord. Chem. Rev.* **2016**, *307*, 106–

129.

(237) Hu, Y. H.; Wang, J. C.; Yang, S.; Li, Y. A.; Dong, Y. Bin. CuI@UiO-67-IM: A MOF-Based Bifunctional Composite Triphase-Transfer Catalyst for Sequential One-Pot Azide-Alkyne Cycloaddition in Water. *Inorg. Chem.* **2017**, *56*, 8341–8347.

(238) Sun, D.; Li, Z. Double-Solvent Method to Pd Nanoclusters Encapsulated inside the Cavity of NH_2-Uio-66(Zr) for Efficient Visible-Light-Promoted Suzuki Coupling Reaction. *J. Phys. Chem. C* **2016**, *120*, 19744–19750.

(239) Dhakshinamoorthy, A.; Asiri, A. M.; Garcia, H. Metal Organic Frameworks as Versatile Hosts of Au Nanoparticles in Heterogeneous Catalysis. *ACS Catal.* **2017**, *7*, 2896–2919.

(240) Cirujano, F. G.; Leyva-Pérez, A.; Corma, A.; Llabrés i Xamena, F. X. MOFs as Multifunctional Catalysts: Synthesis of Secondary Arylamines, Quinolines, Pyrroles, and Arylpyrrolidines over Bifunctional MIL-101. *ChemCatChem* **2013**, *5*, 538–549.

(241) Chen, Y. Z.; Zhou, Y. X.; Wang, H.; Lu, J.; Uchida, T.; Xu, Q.; Yu, S. H.; Jiang, H. L. Multifunctional PdAg@MIL-101 for One-Pot Cascade Reactions: Combination of Host-Guest Cooperation and Bimetallic Synergy in Catalysis. *ACS Catal.* **2015**, *5*, 2062–2069.

(242) Dhakshinamoorthy, A.; Garcia, H. Cascade Reactions Catalyzed by Metal Organic Frameworks. *ChemSusChem* **2014**, *7*, 2392–2410.

(243) Sadeghzadeh, S. M.; Zhiani, R.; Emrani, S. The Reduction of 4-Nitrophenol and 2-Nitroaniline by the Incorporation of Ni@Pd MNPs into Modified UiO-66-NH_2 metal-Organic Frameworks (MOFs) with Tetrathia-Azacyclopentadecane. *New J. Chem.* **2018**, *42*, 988–994.

(244) Hu, Z.; Zhao, D. Metal-Organic Frameworks with Lewis Acidity: Synthesis, Characterization, and Catalytic Applications. *CrystEngComm* **2017**, *19*, 4066–4081.

(245) Gole, B.; Sanyal, U.; Banerjee, R.; Mukherjee, P. S. High Loading of Pd Nanoparticles by Interior Functionalization of MOFs for Heterogeneous Catalysis. *Inorg. Chem.* **2016**, *55*, 2345–2354.

(246) Noori, Y.; Akhbari, K. Post-Synthetic Ion-Exchange Process in Nanoporous Metal–organic Frameworks; an Effective Way for Modulating Their Structures and Properties. *RSC Adv.* **2017**, *7*, 1782–1808.

(247) Kim, M.; Cahill, J. F.; Fei, H.; Prather, K. A.; Cohen, S. M. Postsynthetic Ligand and Cation Exchange in Robust Metal–Organic Frameworks. *J. Am. Chem. Soc.*

2012, *134*, 18082–18088.

(248) Wu, Y.; Breeze, M. I.; Clarkson, G. J.; Millange, F.; O'Hare, D.; Walton, R. I. Exchange of Coordinated Solvent During Crystallization of a Metal-Organic Framework Observed by In Situ High-Energy X-Ray Diffraction. *Angew. Chemie Int. Ed.* **2016**, *55*, 4992–4996.

(249) Fei, H.; Bresler, M. R.; Oliver, S. R. J. A New Paradigm for Anion Trapping in High Capacity and Selectivity: Crystal-to-Crystal Transformation of Cationic Materials. *J. Am. Chem. Soc.* **2011**, *133*, 11110–11113.

(250) Karagiaridi, O.; Bury, W.; Mondloch, J. E.; Hupp, J. T.; Farha, O. K. Solvent-Assisted Linker Exchange: An Alternative to the De Novo Synthesis of Unattainable Metal-Organic Frameworks. *Angew. Chemie Int. Ed.* **2014**, *53*, 4530–4540.

(251) Kumar, S.; Mandal, S. K. Capturing the Structural Diversification upon Thermal Desolvation of a Robust Metal Organic Framework via a Single-Crystal-to-Single-Crystal Transformation. *CrystEngComm* **2015**, *17*, 8801–8806.

(252) Wu, C. De; Lin, W. Highly Porous, Homochiral Metal-Organic Frameworks: Solvent-Exchange- Induced Single-Crystal to Single-Crystal Transformations. *Angew. Chemie - Int. Ed.* **2005**, *44*, 1958–1961.

(253) Bradshaw, D.; Warren, J. E.; Rosseinsky, M. J. Reversible Concerted Ligand Substitution at Alternating Metal Sites in an Extended Solid. *Science* **2007**, *315*, 977–980.

(254) Manna, B.; Desai, A. V.; Kumar, N.; Karmakar, A.; Ghosh, S. K. Single-Crystal-to-Single-Crystal Transformation of an Anion Exchangeable Dynamic Metal-Organic Framework. *CrystEngComm* **2015**, *17*, 8796–8800.

(255) Lee, J. H.; Kim, T. K.; Suh, M. P.; Moon, H. R. Solvent-Induced Single-Crystal to Single-Crystal Transformation of a Zn_4O-Containing Doubly Interpenetrated Metal-Organic Framework with a Pcu Net. *CrystEngComm* **2015**, *17*, 8807–8811.

(256) Zakharov, B. A.; Marchuk, A. S.; Boldyreva, E. V. A Single-Crystal to Single-Crystal Phase Transition in $[Co(NH_3)_5NO_2]Br_2$ at High Pressure: A Step towards Understanding Linkage Photo-Isomerisation. *CrystEngComm* **2015**, *17*, 8812–8816.

(257) Ke, S. Y.; Wang, C. C. Water-Induced Reversible SCSC or Solid-State Structural Transformation in Coordination Polymers. *CrystEngComm* **2015**, *17*, 8776–8785.

(258) Lee, J. H.; Park, S.; Jeoung, S.; Moon, H. R. Single-Crystal-to-Single-Crystal Transformation of a Coordination Polymer from 2D to 3D by [2 + 2] Photodimerization Assisted by a Coexisting Flexible Ligand. *CrystEngComm* **2017**,

19, 3719–3722.

(259) Khorasani, S.; Botes, D. S.; Fernandes, M. A.; Levendis, D. C. A Single-Crystal-to-Single-Crystal Diels-Alder Reaction with Mixed Topochemical and Topotactic Behaviour. *CrystEngComm* **2015**, *17*, 8933–8945.

(260) Alen, J.; Van Meervelt, L.; Dehaen, W.; Dobrzańska, L. Solvent Diffusion through a Non-Porous Crystal "caught in the Act" and Related Single-Crystal-to-Single-Crystal Transformations in a Cationic Dinuclear Ag(I) Complex. *CrystEngComm* **2015**, *17*, 8957–8964.

(261) Manna, B.; Desai, A. V.; Ghosh, S. K. Neutral N-Donor Ligand Based Flexible Metal-Organic Frameworks. *Dalt. Trans.* **2016**, *45* (10), 4060–4072.

(262) Shi, Y.-X.; Hu, F.-L.; Zhang, W.-H.; Lang, J.-P. A Unique Zn(II)-Based MOF Fluorescent Probe for the Dual Detection of Nitroaromatics and Ketones in Water. *CrystEngComm* **2015**, *17*, 9404–9412.

(263) Liu, S.; Xiang, Z.; Hu, Z.; Zheng, X.; Cao, D. Zeolitic Imidazolate Framework-8 as a Luminescent Material for the Sensing of Metal Ions and Small Molecules. *J. Mater. Chem.* **2011**, *21*, 6649.

(264) Liu, F.-H.; Qin, C.; Ding, Y.; Wu, H.; Shao, K.-Z.; Su, Z.-M. Pillared Metal Organic Frameworks for the Luminescence Sensing of Small Molecules and Metal Ions in Aqueous Solutions. *Dalt. Trans.* **2015**, *44*, 1754–1760.

(265) Hu, Z.; Tan, K.; Lustig, W. P.; Wang, H.; Zhao, Y.; Zheng, C.; Banerjee, D.; Emge, T. J.; Chabal, Y. J.; Li, J. Effective Sensing of RDX via Instant and Selective Detection of Ketone Vapors. *Chem. Sci.* **2014**, *5*, 4873–4877.

(266) Zhao, F.; Guo, X.-Y.; Dong, Z.-P.; Liu, Z.-L.; Wang, Y.-Q. 3D Ln III -MOFs: Slow Magnetic Relaxation and Highly Sensitive Luminescence Detection of Fe^{3+} and Ketones. *Dalt. Trans.* **2018**, *47*, 8972–8982.

(267) Shi, Y. X.; Hu, F. L.; Zhang, W. H.; Lang, J. P. A Unique Zn(II)-Based MOF Fluorescent Probe for the Dual Detection of Nitroaromatics and Ketones in Water. *CrystEngComm* **2015**, *17*, 9404–9412.

(268) Liu, C.; Yan, B. Luminescent Zinc Metal-Organic Framework (ZIF-90) for Sensing Metal Ions, Anions and Small Molecules. *Photochem. Photobiol. Sci.* **2015**, *14*, 1644–1650.

(269) Liu, Y. L.; Tseng, M. C.; Chu, Y. H. Sensing Ionic Liquids for Chemoselective Detection of Acyclic and Cyclic Ketone Gases. *Chem. Commun.* **2013**, *49*, 2560–2562.

(270) Guo, Z.; Xu, H.; Su, S.; Cai, J.; Dang, S.; Xiang, S.; Qian, G.; Zhang, H.; O'Keeffe, M.; Chen, B. A Robust near Infrared Luminescent Ytterbium Metal-Organic Framework for Sensing of Small Molecules. *Chem. Commun.* **2011**, *47*, 5551–5553.

(271) Frazier, K. M.; Swager, T. M. Robust Cyclohexanone Selective Chemiresistors Based on Single-Walled Carbon Nanotubes. *Anal. Chem.* **2013**, *85*, 7154–7158.

(272) Liu, J. J.; Shan, Y. Bin; Fan, C. R.; Lin, M. J.; Huang, C. C.; Dai, W. X. Encapsulating Naphthalene in an Electron-Deficient MOF to Enhance Fluorescence for Organic Amines Sensing. *Inorg. Chem.* **2016**, *55*, 3680–3684.

(273) Mani, P.; Ojha, A. A.; Reddy, V. S.; Mandal, S. "turn-on" Fluorescence Sensing and Discriminative Detection of Aliphatic Amines Using a 5-Fold-Interpenetrated Coordination Polymer. *Inorg. Chem.* **2017**, *56*, 6772–6775.

(274) Chen, J.; Yi, F. Y.; Yu, H.; Jiao, S.; Pang, G.; Sun, Z. M. Fast Response and Highly Selective Sensing of Amine Vapors Using a Luminescent Coordination Polymer. *Chem. Commun.* **2014**, *50*, 10506–10509.

(275) Mallick, A.; Garai, B.; Addicoat, M. A.; Petkov, P. S.; Heine, T.; Banerjee, R. Solid State Organic Amine Detection in a Photochromic Porous Metal Organic Framework. *Chem. Sci.* **2015**, *6*, 1420–1425.

(276) Shen, X.; Yan, B. A Novel Fluorescence Probe for Sensing Organic Amine Vapors from a Eu^{3+} β-Diketonate Functionalized Bio-MOF-1 Hybrid System. *J. Mater. Chem. C* **2015**, *3*, 7038–7044.

(277) Bünzli, J. C. G. Lanthanide Luminescence for Biomedical Analyses and Imaging. *Chem. Rev.* **2010**, *110*, 2729–2755.

(278) Mertz, E.; Zimmerman, S. C. Cross-Linked Dendrimer Hosts Containing Reporter Groups for Amine Guests. *J. Am. Chem. Soc.* **2003**, *125*, 3424–3425.

(279) Longstreet, A. R.; Jo, M.; Chandler, R. R.; Hanson, K.; Zhan, N.; Hrudka, J. J.; Mattoussi, H.; Shatruk, M.; McQuade, D. T. Ylidenemalononitrile Enamines as Fluorescent "Turn-on" Indicators for Primary Amines. *J. Am. Chem. Soc.* **2014**, *136*, 15493–15496.

(280) Yi, F.-Y.; Chen, D.; Wu, M.-K.; Han, L.; Jiang, H.-L. Chemical Sensors Based on Metal-Organic Frameworks. *Chempluschem* **2016**, *81*, 675–690.

(281) Zhang, Y.; Yuan, S.; Day, G.; Wang, X.; Yang, X.; Zhou, H.-C. Luminescent Sensors Based on Metal-Organic Frameworks. *Coord. Chem. Rev.* **2018**, *354*, 28–45.

(282) Gao, M.; Li, S.; Lin, Y.; Geng, Y.; Ling, X.; Wang, L.; Qin, A.; Tang, B. Z.

Fluorescent Light-Up Detection of Amine Vapors Based on Aggregation-Induced Emission. *ACS Sensors* **2016**, *1*, 179–184.

(283) Parmar, B.; Rachuri, Y.; Bisht, K. K.; Laiya, R.; Suresh, E. Mechanochemical and Conventional Synthesis of Zn(II)/Cd(II) Luminescent Coordination Polymers: Dual Sensing Probe for Selective Detection of Chromate Anions and TNP in Aqueous Phase. *Inorg. Chem.* **2017**, *56*, 2627–2638.

(284) Lustig, W. P.; Mukherjee, S.; Rudd, N. D.; Desai, A. V.; Li, J.; Ghosh, S. K. Metal-Organic Frameworks: Functional Luminescent and Photonic Materials for Sensing Applications. *Chem. Soc. Rev.* **2017**, *46*, 3242–3285.

(285) Lalonde, M.; Bury, W.; Karagiaridi, O.; Brown, Z.; Hupp, J. T.; Farha, O. K. Transmetalation: Routes to Metal Exchange within Metal-Organic Frameworks. *J. Mater. Chem. A* **2013**, *1*, 5453–5468.

(286) Asha, K. S.; Bhattacharjee, R.; Mandal, S. Complete Transmetalation in a Metal–Organic Framework by Metal Ion Metathesis in a Single Crystal for Selective Sensing of Phosphate Ions in Aqueous Media. *Angew. Chemie - Int. Ed.* **2016**, *55*, 11528–11532.

(287) Song, X.; Kim, T. K.; Kim, H.; Kim, D.; Jeong, S.; Moon, H. R.; Lah, M. S. Post-Synthetic Modifications of Framework Metal Ions in Isostructural Metal-Organic Frameworks: Core-Shell Heterostructures via Selective Transmetalations. *Chem. Mater.* **2012**, *24*, 3065–3073.

(288) Sun, Y.; Zhou, H.-C. Recent Progress in the Synthesis of Metal–organic Frameworks. *Sci. Technol. Adv. Mater.* **2015**, *16*, 054202.

(289) Li, H.; Li, Q.; He, Y.; Zhang, N.; Xu, Z.; Wang, Y. Facile Fabrication of Magnetic Metal-Organic Framework Composites for the Highly Selective Removal of Cationic Dyes. *Materials* **2018**, *11*, 744.

(290) Park, J.; Oh, M. Construction of Flexible Metal-Organic Framework (MOF) Papers through MOF Growth on Filter Paper and Their Selective Dye Capture. *Nanoscale* **2017**, *9*, 12850–12854.

(291) Zhao, X.; Wang, K.; Gao, Z.; Gao, H.; Xie, Z.; Du, X.; Huang, H. Reversing the Dye Adsorption and Separation Performance of Metal–Organic Frameworks via Introduction of −SO_3H Groups. *Ind. Eng. Chem. Res.* **2017**, *56*, 4496–4501.

(292) Zhang, S. R.; Li, J.; Du, D. Y.; Qin, J. S.; Li, S. L.; He, W. W.; Su, Z. M.; Lan, Y. Q. A Multifunctional Microporous Anionic Metal-Organic Framework for Column-Chromatographic Dye Separation and Selective Detection and Adsorption of Cr^{3+}.

J. Mater. Chem. A **2015**, *3*, 23426–23434.

(293) Zhu, Y.; Wang, Y. M.; Zhao, S. Y.; Liu, P.; Wei, C.; Wu, Y. L.; Xia, C. K.; Xie, J. M. Three N-H Functionalized Metal-Organic Frameworks with Selective CO_2 uptake, Dye Capture, and Catalysis. *Inorg. Chem.* **2014**, *53*, 7692–7699.

(294) Han, S.; Wei, Y.; Valente, C.; Lagzi, I.; Gassensmith, J. J.; Coskun, A.; Stoddart, J. F.; Grzybowski, B. A. Chromatography in a Single Metal-Organic Framework (MOF) Crystal. *J. Am. Chem. Soc.* **2010**, *132*, 16358–16361.

(295) Kumar N., Khullar S. and Mandal S. K., *ACS Omega*, **2018**, *3*, 11062–11070.

APPENDIX

Table A1. Crystal data and structure refinement parameters for **1**.

Compound	**1**
Empirical formula	$C_{42}H_{50}N_6Ni_2O_{10}$
Formula weight	916.30
Temperature/K	100
Crystal system	monoclinic
Space group	$P2_1/n$
a/Å	10.1941(14)
b/Å	15.966(2)
c/Å	12.8443(18)
α/°	90
β/°	103.751(6)
γ/°	90
Volume/Å^3	2030.6(5)
Z	2
ρ_{calc}g/cm^3	1.499
μ/mm^{-1}	0.994
F(000)	960.0
Crystal size/mm^3	0.3 × 0.2 × 0.2
Radiation	MoKα (λ = 0.71073)
2Θ range for data collection/°	4.144 to 50.92
Index ranges	$-12 \leq h \leq 10$, $-15 \leq k \leq 19$, $-15 \leq l \leq 12$
Reflections collected	13196
Independent reflections	3619 [R_{int} = 0.1129, R_{sigma} = 0.1871]
Data/restraints/parameters	3619/0/362
Goodness-of-fit on F^2	0.961
Final R indexes [I>=2σ (I)]	R_1 = 0.0609, wR_2 = 0.0972
Final R indexes [all data]	R_1 = 0.1748, wR_2 = 0.1286
Largest diff. peak/hole / e Å^{-3}	0.46/-0.49

$R_1 = \Sigma||F_o| - |F_c||/\Sigma|F_o|$. $wR_2 = [\Sigma w(F_o^2 - F_c^2)^2/\Sigma w(F_o^2)^2]^{1/2}$, where $w = 1/[\sigma^2(F_o^2) + (aP)^2 + bP]$, $P = (F_o^2 + 2F_c^2)/3$.

Table A2.Crystal data and structure refinement parameters for **2⊃fumarate** and **3⊃succinate**.

Compound	**2⊃fumarate**	**3⊃Hsuccinate**
Empirical formula	$C_{42}H_{71}N_6Ni_2O_{19}$	$C_{46}H_{72}N_6Ni_2O_{18}$
Formula weight	1081.46	1114.51
Temperature/K	100	100
Crystal system	Monoclinic	monoclinic
Space group	$P2_1/c$	$P2_1/c$
a/Å	18.912(3)	9.425(3)
b/Å	19.007(4)	13.788(5)
c/Å	15.065(3)	19.461(8)
α/°	90	90
β/°	111.363(5)	97.28(2)
γ/°	90	90
Volume/$Å^3$	5043.3(17)	2508.6(16)
Z	4	2
$\rho_{calc}g/cm^3$	1.424	1.475
μ/mm^{-1}	0.825	0.830
F(000)	2292.0	1180.0
Crystal size/mm^3	0.25 × 0.21 × 0.21	0.2 × 0.2 × 0.2
Radiation	MoKα (λ = 0.71073)	MoKα (λ = 0.71073)
2Θ range for data collection/°	2.312 to 50.062	4.22 to 48.998
Index ranges	$-22 \le h \le 22$, $-22 \le k \le 22$, $-17 \le l \le 17$	$-9 \le h \le 10$, $-16 \le k \le 15$, $-22 \le l \le 22$
Reflections collected	35007	11551
Independent reflections	8873 [R_{int} = 0.0539, R_{sigma} = 0.0472]	4091 [R_{int} = 0.1714, R_{sigma} = 0.2283]
Data/restraints/parameters	8873/0/629	4091/0/337
Goodness-of-fit on F^2	1.083	1.029
Final R indexes [I>=2σ (I)]	R_1 = 0.0473, wR_2 = 0.1379	R_1 = 0.1069, wR_2 = 0.2844
Final R indexes [all data]	R_1 = 0.0649, wR_2 = 0.1465	R_1 = 0.2260, wR_2 = 0.3519
Largest diff. peak/hole / e $Å^{-3}$	1.03/-0.63	1.07/-0.71

$R_1 = \Sigma||F_o| - |F_c||/\Sigma|F_o|$. $wR_2 = [\Sigma w(F_o^2 - F_c^2)^2/\Sigma w(F_o^2)^2]^{1/2}$, where $w = 1/[\sigma^2(F_o^2) + (aP)^2 + bP]$, $P = (F_o^2 + 2F_c^2)/3$.

Table A3. Crystal data and structure refinement parameters for **2⊃ClO_4^-** and **2⊃I^-**.

Compound	**2⊃ClO_4^-**	**2⊃I^-**
Empirical formula	$C_{38}H_{64}Cl_2N_6Ni_2O_{20}$	$C_{38}H_{64}I_2N_6Ni_2O_{12}$
Formula weight	1113.27	1168.17
Temperature/K	100	100
Crystal system	triclinic	monoclinic
Space group	*P*-1	$P2_1/n$
a/Å	13.438(8)	9.0415(12)
b/Å	13.478(7)	18.726(2)
c/Å	14.245(8)	14.6333(19)
α/°	94.133(9)	90
β/°	99.165(7)	104.040(10)
γ/°	94.604(7)	90
Volume/$Å^3$	2529(2)	2403.6(6)
Z	2	2
$\rho_{calc}g/cm^3$	1.462	1.614
μ/mm^{-1}	0.928	2.129
F(000)	1168.0	1184.0
Crystal size/mm^3	0.25 × 0.2 × 0.2	0.23 × 0.23 × 0.23
Radiation	MoKα (λ = 0.71073)	MoKα (λ = 0.71073)
2Θ range for data collection/°	2.906 to 50.172	3.6 to 50.364
Index ranges	$-16 \le h \le 15$, $-10 \le k \le 16$, $-15 \le l \le 16$	$-10 \le h \le 10$, $-22 \le k \le 22$, $-17 \le l \le 16$
Reflections collected	32553	15882
Independent reflections	8902 [R_{int} = 0.0919, R_{sigma} = 0.1286]	4276 [R_{int} = 0.1261, R_{sigma} = 0.1764]
Data/restraints/parameters	8902/0/623	4276/0/285
Goodness-of-fit on F^2	1.080	0.966
Final R indexes [I>=2σ (I)]	R_1 = 0.0884, wR_2 = 0.2537	R_1 = 0.0697, wR_2 = 0.1362
Final R indexes [all data]	R_1 = 0.1717, wR_2 = 0.2930	R_1 = 0.1811, wR_2 = 0.1762
Largest diff. peak/hole / e $Å^{-3}$	1.02/-0.72	0.68/-1.21

$R_1 = \Sigma||F_o| - |F_c||/\Sigma|F_o|$. $wR_2 = [\Sigma w(F_o^2 - F_c^2)^2/\Sigma w(F_o^2)^2]^{1/2}$, where $w = 1/[\sigma^2(F_o^2) + (aP)^2 + bP]$, $P = (F_o^2 + 2F_c^2)/3$.

Table A4. Crystal data and structure refinement parameters for **3⊃ClO_4^-**, **3⊃Cl^-** and **3⊃NO_3^-**.

Compound	**3⊃ClO_4^-**	**3⊃Cl^-**	**3⊃NO_3^-**
Empirical formula	$C_{38}H_{64}Cl_2N_6Ni_2O_{19}$	$C_{38}H_{74}Cl_2N_6Ni_2O_{16}$	$C_{38}H_{66}N_8Ni_2O_{18}$
Formula weight	1097.27	1059.35	1040.40
Temperature/K	100	296.15	100
Crystal system	monoclinic	monoclinic	monoclinic
Space group	$P2_1/n$	$P2_1/c$	$P2_1/n$
a/Å	9.7364(17)	9.5349(10)	9.114(5)
b/Å	14.868(3)	14.1156(16)	18.192(9)
c/Å	17.882(3)	19.310(3)	14.651(7)
α/°	90	90	90
β/°	103.399(8)	100.472(7)	104.145(7)
γ/°	90	90	90
Volume/$Å^3$	2518.1(8)	2555.6(5)	2356(2)
Z	2	2	2
$\rho_{calc}g/cm^3$	1.447	1.377	1.467
μ/mm^{-1}	0.930	0.909	0.880
F(000)	1152.0	1124.0	1100.0
Crystal size/mm^3	0.23 × 0.21 × 0.21	0.2 × 0.2 × 0.2	0.2 × 0.25 × 0.25
Radiation	MoKα (λ = 0.71073)	MoKα (λ = 0.71073)	MoKα (λ = 0.71073)
2Θ range for data collection/°	3.604 to 50.192	3.596 to 50.254	3.638 to 51.534
Index ranges	-11 ≤ h ≤ 11, -17 ≤ k ≤ 17, -20 ≤ l ≤ 21	-11 ≤ h ≤ 11, -16 ≤ k ≤ 15, -21 ≤ l ≤ 23	-10 ≤ h ≤ 11, -21 ≤ k ≤ 20, -11 ≤ l ≤ 17
Reflections collected	16287	16978	14814
Independent reflections	4454 [R_{int} = 0.1481, R_{sigma} = 0.2223]	4523 [R_{int} = 0.1064, R_{sigma} = 0.1091]	4163 [R_{int} = 0.0382, R_{sigma} = 0.0468]
Data/restraints/parameters	4454/0/321	4523/0/310	4163/0/312
Goodness-of-fit on F^2	0.874	1.179	1.064
Final R indexes [I>=2σ (I)]	R_1 = 0.0737, wR_2 = 0.1623	R_1 = 0.1543, wR_2 = 0.3739	R_1 = 0.0504, wR_2 = 0.1121
Final R indexes [all data]	R_1 = 0.2101, wR_2 = 0.2073	R_1 = 0.1963, wR_2 = 0.3936	R_1 = 0.0670, wR_2 = 0.1231
Largest diff. peak/hole / e $Å^{-3}$	0.78/-0.64	2.35/-1.08	0.63/-0.77

$R_1 = \Sigma||F_o| - |F_c||/\Sigma|F_o|$. $wR_2 = [\Sigma w(F_o^2 - F_c^2)^2/\Sigma w(F_o^2)^2]^{1/2}$, where $w = 1/[\sigma^2(F_o^2) + (aP)^2 + bP]$, $P = (F_o^2 + 2F_c^2)/3$.

Table A5. Crystal data and structure refinement parameters for **4**.

Compound	**4**
Empirical formula	$C_{39}H_{60}Cl_2N_6Ni_2O_{15}$
Formula weight	1041.25
Temperature/K	296.15
Crystal system	monoclinic
Space group	*C*2/*c*
a/Å	19.6167(11)
b/Å	17.6351(11)
c/Å	14.9578(9)
α/°	90
β/°	118.420(5)
γ/°	90
Volume/Å^3	4550.9(5)
Z	4
ρ_{calc}g/cm^3	1.520
μ/mm^{-1}	1.018
F(000)	2184.0
Crystal size/mm^3	0.3 × 0.3 × 0.25
Radiation	MoKα (λ = 0.71073)
2Θ range for data collection/°	3.302 to 50.288
Index ranges	-23 ≤ h ≤ 18, -20 ≤ k ≤ 20, -16 ≤ l ≤ 17
Reflections collected	14036
Independent reflections	4049 [R_{int} = 0.0479, R_{sigma} = 0.0449]
Data/restraints/parameters	4049/0/299
Goodness-of-fit on F^2	1.044
Final R indexes [I>=2σ (I)]	R_1 = 0.0502, wR_2 = 0.1311
Final R indexes [all data]	R_1 = 0.0658, wR_2 = 0.1450
Largest diff. peak/hole / e Å^{-3}	0.81/-1.26

$R_1 = \Sigma||F_o| - |F_c||/\Sigma|F_o|$. $wR_2 = [\Sigma w(F_o^2 - F_c^2)^2/\Sigma w(F_o^2)^2]^{1/2}$, where $w = 1/[\sigma^2(F_o^2) + (aP)^2 + bP]$, $P = (F_o^2 + 2F_c^2)/3$.

Table A6. Crystal data and structure refinement parameters for **17**.

Compound	**17**
Empirical formula	$C_{22}H_{29}N_3NiO_6$
Formula weight	490.19
Temperature/K	100
Crystal system	monoclinic
Space group	$P2_1/n$
a/Å	10.2641(8)
b/Å	16.8498(13)
c/Å	13.0024(10)
α/°	90
β/°	98.545(3)
γ/°	90
Volume/Å^3	2223.8(3)
Z	4
ρ_{calc}g/cm^3	1.464
μ/mm^{-1}	0.916
F(000)	1032.0
Crystal size/mm^3	0.3 × 0.2 × 0.2
Radiation	MoKα (λ = 0.71073)
2Θ range for data collection/°	3.984 to 50.212
Index ranges	$-11 \leq h \leq 12$, $-18 \leq k \leq 20$, $-15 \leq l \leq 15$
Reflections collected	18501
Independent reflections	3952 [R_{int} = 0.0242, R_{sigma} = 0.0221]
Data/restraints/parameters	3952/6/306
Goodness-of-fit on F^2	1.044
Final R indexes [I>=2σ (I)]	R_1 = 0.0249, wR_2 = 0.0617
Final R indexes [all data]	R_1 = 0.0292, wR_2 = 0.0641
Largest diff. peak/hole / e Å^{-3}	0.32/-0.26

$R_1 = \Sigma||F_o| - |F_c||/\Sigma|F_o|$. $wR_2 = [\Sigma w(F_o^2 - F_c^2)^2/\Sigma w(F_o^2)^2]^{1/2}$, where $w = 1/[\sigma^2(F_o^2) + (aP)^2 + bP]$, $P = (F_o^2 + 2F_c^2)/3$.

Table A7. Crystal data and structure refinement parameters for **22**.

Compound	**22**
Empirical formula	$C_{44}H_{50}N_6O_8Zn_2$
Formula weight	921.64
Temperature/K	150
Crystal system	monoclinic
Space group	$P2_1/n$
a/Å	9.0471(3)
b/Å	28.4567(9)
c/Å	17.1935(5)
α/°	90
β/°	93.004(2)
γ/°	90
Volume/Å^3	4420.4(2)
Z	4
ρ_{calc}g/cm^3	1.385
μ/mm^{-1}	1.143
F(000)	1920.0
Crystal size/mm^3	0.23 × 0.21 × 0.2
Radiation	MoKα (λ = 0.71073)
2Θ range for data collection/°	2.862 to 50.104
Index ranges	$-9 \leq h \leq 10$, $-28 \leq k \leq 33$, $-19 \leq l \leq 20$
Reflections collected	27783
Independent reflections	7831 [R_{int} = 0.0398, R_{sigma} = 0.0388]
Data/restraints/parameters	7831/6/551
Goodness-of-fit on F^2	1.069
Final R indexes [I>=2σ (I)]	R_1 = 0.0839, wR_2 = 0.2500
Final R indexes [all data]	R_1 = 0.0990, wR_2 = 0.2645
Largest diff. peak/hole / e Å^{-3}	1.93/-1.03

$R_1 = \Sigma||F_o| - |F_c||/\Sigma|F_o|$. $wR_2 = [\Sigma w(F_o^2 - F_c^2)^2/\Sigma w(F_o^2)^2]^{1/2}$, where $w = 1/[\sigma^2(F_o^2) + (aP)^2 + bP]$, $P = (F_o^2 + 2F_c^2)/3$.

Table A8. Crystal data and structure refinement parameters for **23** and **24**.

Compound	**23**	**24**
Empirical formula	$C_{48}H_{46}Cd_2N_6O_{12}$	$C_{52}H_{52}Cd_2N_6O_{12}$
Formula weight	1123.71	1177.79
Temperature/K	296.15	296.15
Crystal system	monoclinic	orthorhombic
Space group	$P2_1/c$	$Pna2_1$
a/Å	9.793(6)	48.934(3)
b/Å	13.367(8)	10.4335(6)
c/Å	18.230(11)	9.7348(5)
α/°	90	90
β/°	91.74(3)	90
γ/°	90	90
Volume/Å^3	2385(2)	4970.1(5)
Z	2	4
ρ_{calc}g/cm^3	1.565	1.574
μ/mm^{-1}	0.960	0.925
F(000)	1136.0	2392.0
Crystal size/mm^3	0.4 × 0.4 × 0.4	0.2 × 0.25 × 0.2
Radiation	MoKα (λ = 0.71073)	MoKα (λ = 0.71073)
2Θ range for data collection/°	3.778 to 47.06	1.664 to 50.03
Index ranges	$-10 \le h \le 10$, $-14 \le k \le 11$, $-20 \le l \le 18$	$-49 \le h \le 58$, $-11 \le k \le 12$, $-11 \le l \le 8$
Reflections collected	12085	32799
Independent reflections	3384 [R_{int} = 0.2274, R_{sigma} = 0.3953]	7915 [R_{int} = 0.0832, R_{sigma} = 0.0837]
Data/restraints/parameters	3384/2/310	7915/1/657
Goodness-of-fit on F^2	0.974	1.074
Final R indexes [I>=2σ (I)]	R_1 = 0.1198, wR_2 = 0.2424	R_1 = 0.0534, wR_2 = 0.1082
Final R indexes [all data]	R_1 = 0.3158, wR_2 = 0.3244	R_1 = 0.0769, wR_2 = 0.1235
Largest diff. peak/hole / e Å^{-3}	1.16/-1.18	0.74/-1.11
Flack parameter		0.00(2)

$R_1 = \Sigma||F_o| - |F_c||/\Sigma|F_o|$. $wR_2 = [\Sigma w(F_o^2 - F_c^2)^2/\Sigma w(F_o^2)^2]^{1/2}$, where $w = 1/[\sigma^2(F_o^2) + (aP)^2 + bP]$, $P = (F_o^2 + 2F_c^2)/3$.

Table A9. Crystal data and structure refinement parameters for **33**.

Compound	**33**
Empirical formula	$C_{64}H_{49}Cu_2N_8O_{13}$
Formula weight	1265.19
Temperature/K	273.15
Crystal system	triclinic
Space group	*P*-1
a/Å	14.540(15)
b/Å	14.636(14)
c/Å	15.391(16)
α/°	65.02(3)
β/°	74.68(3)
γ/°	88.05(3)
Volume/Å^3	2852(5)
Z	2
ρ_{calc}g/cm^3	1.473
μ/mm^{-1}	0.821
F(000)	1302.0
Crystal size/mm^3	0.2 × 0.4 × 0.4
Radiation	MoKα (λ = 0.71073)
2Θ range for data collection/°	4.05 to 50
Index ranges	$-17 \leq h \leq 17$, $-17 \leq k \leq 17$, $-18 \leq l \leq 18$
Reflections collected	34778
Independent reflections	9811 [R_{int} = 0.2509, R_{sigma} = 0.3296]
Data/restraints/parameters	9811/0/769
Goodness-of-fit on F^2	0.897
Final R indexes [I>=2σ (I)]	R_1 = 0.1163, wR_2 = 0.2669
Final R indexes [all data]	R_1 = 0.2676, wR_2 = 0.3188
Largest diff. peak/hole / e Å^{-3}	1.00/-0.56

$R_1 = \Sigma||F_o| - |F_c||/\Sigma|F_o|$. $wR_2 = [\Sigma w(F_o^2 - F_c^2)^2/\Sigma w(F_o^2)^2]^{1/2}$, where $w = 1/[\sigma^2(F_o^2) + (aP)^2 + bP]$, $P = (F_o^2 + 2F_c^2)/3$.

Table A10. Crystal data and structure refinement parameters for **34**.

Compound	**34**
Empirical formula	$C_{64}H_{42}Mn_2N_{10}O_{14}$
Formula weight	1284.95
Temperature/K	273.15
Crystal system	monoclinic
Space group	*C*2/*c*
a/Å	17.728(2)
b/Å	18.087(2)
c/Å	10.0169(14)
α/°	90
β/°	90
γ/°	90
Volume/Å^3	3211.9(7)
Z	2
ρ_{calc}g/cm^3	1.329
μ/mm^{-1}	0.464
F(000)	1316.0
Crystal size/mm^3	0.2 × 0.2 × 0.2
Radiation	MoKα (λ = 0.71073)
2Θ range for data collection/°	6.07 to 50
Index ranges	$-20 \leq h \leq 21$, $-21 \leq k \leq 21$, $-11 \leq l \leq 11$
Reflections collected	9793
Independent reflections	2315 [R_{int} = 0.1027, R_{sigma} = 0.1543]
Data/restraints/parameters	2315/15/213
Goodness-of-fit on F^2	1.061
Final R indexes [I>=2σ (I)]	R_1 = 0.1102, wR_2 = 0.2931
Final R indexes [all data]	R_1 = 0.1578, wR_2 = 0.3133
Largest diff. peak/hole / e Å^{-3}	1.64/-1.03

$R_1 = \Sigma||F_o| - |F_c||/\Sigma|F_o|$. $wR_2 = [\Sigma w(F_o^2 - F_c^2)^2/\Sigma w(F_o^2)^2]^{1/2}$, where $w = 1/[\sigma^2(F_o^2) + (aP)^2 + bP]$, $P = (F_o^2 + 2F_c^2)/3$.

Table A11. Crystal data and structure refinement parameters for **37**.

Compound	**37**
Empirical formula	$C_{32}H_{19}N_3O_5Zn$
Formula weight	590.87
Temperature/K	273.15
Crystal system	monoclinic
Space group	*C*2/*c*
a/Å	19.7922(19)
b/Å	30.2684(19)
c/Å	21.0201(12)
α/°	90
β/°	112.831(6)
γ/°	90
Volume/Å^3	11606.1(16)
Z	8
ρ_{calc}g/cm^3	0.676
μ/mm^{-1}	0.445
F(000)	2416.0
Crystal size/mm^3	0.32 × 0.32 × 0.32
Radiation	MoKα (λ = 0.71073)
2Θ range for data collection/°	4.466 to 50.158
Index ranges	$-23 \leq h \leq 23$, $-36 \leq k \leq 36$, $-25 \leq l \leq 25$
Reflections collected	140197
Independent reflections	10290 [R_{int} = 0.1291, R_{sigma} = 0.0491]
Data/restraints/parameters	10290/0/358
Goodness-of-fit on F^2	0.996
Final R indexes [I>=2σ (I)]	R_1 = 0.0814, wR_2 = 0.2513
Final R indexes [all data]	R_1 = 0.1027, wR_2 = 0.2725
Largest diff. peak/hole / e Å^{-3}	0.62/-0.54

$R_1 = \Sigma||F_o| - |F_c||/\Sigma|F_o|$. $wR_2 = [\Sigma w(F_o^2 - F_c^2)^2/\Sigma w(F_o^2)^2]^{1/2}$, where $w = 1/[\sigma^2(F_o^2) + (aP)^2 + bP]$, $P = (F_o^2 + 2F_c^2)/3$.

Table A12. Crystal data and structure refinement parameters for **40**.

Compound	**40**
Empirical formula	$C_{124}H_{125.03}N_{12}Ni_2O_{25.05}$
Formula weight	2301.60
Temperature/K	296.15
Crystal system	monoclinic
Space group	*C*2/*c*
a/Å	28.7220(7)
b/Å	11.5612(3)
c/Å	18.7167(4)
α/°	90
β/°	116.2580(10)
γ/°	90
Volume/Å^3	5573.8(2)
Z	2
ρ_{calc}g/cm^3	1.371
μ/mm^{-1}	0.420
F(000)	2419.0
Crystal size/mm^3	0.2 × 0.4 × 0.4
Radiation	MoKα (λ = 0.71073)
2Θ range for data collection/°	3.162 to 50.084
Index ranges	$-34 \leq h \leq 33$, $-13 \leq k \leq 13$, $-22 \leq l \leq 22$
Reflections collected	20195
Independent reflections	4938 [R_{int} = 0.0301, R_{sigma} = 0.0275]
Data/restraints/parameters	4938/0/433
Goodness-of-fit on F^2	1.067
Final R indexes [I>=2σ (I)]	R_1 = 0.0698, wR_2 = 0.1929
Final R indexes [all data]	R_1 = 0.0810, wR_2 = 0.2043
Largest diff. peak/hole / e Å^{-3}	1.35/-1.38

$R_1 = \Sigma||F_o| - |F_c||/\Sigma|F_o|$. $wR_2 = [\Sigma w(F_o^2 - F_c^2)^2/\Sigma w(F_o^2)^2]^{1/2}$, where $w = 1/[\sigma^2(F_o^2) + (aP)^2 + bP]$, $P = (F_o^2 + 2F_c^2)/3$.

Table A13. Crystal data and structure refinement parameters for **41**.

Compound	**41**
Empirical formula	$C_{56}H_{42}CoN_6O_8$
Formula weight	985.88
Temperature/K	100.15
Crystal system	monoclinic
Space group	*C*2/*c*
a/Å	28.4911(19)
b/Å	11.6372(7)
c/Å	18.7187(12)
α/°	90
β/°	115.865(4)
γ/°	90
Volume/Å^3	5584.6(6)
Z	4
ρ_{calc}g/cm^3	1.173
μ/mm^{-1}	0.362
F(000)	2044.0
Crystal size/mm^3	0.2 × 0.2 × 0.2
Radiation	MoKα (λ = 0.71073)
2Θ range for data collection/°	3.178 to 50.268
Index ranges	$-33 \leq h \leq 33$, $-13 \leq k \leq 13$, $-22 \leq l \leq 22$
Reflections collected	22010
Independent reflections	4958 [R_{int} = 0.0301, R_{sigma} = 0.0254]
Data/restraints/parameters	4958/0/318
Goodness-of-fit on F^2	1.071
Final R indexes [I>=2σ (I)]	R_1 = 0.0542, wR_2 = 0.1485
Final R indexes [all data]	R_1 = 0.0613, wR_2 = 0.1539
Largest diff. peak/hole / e Å^{-3}	1.10/-1.51

$R_1 = \Sigma||F_o| - |F_c||/\Sigma|F_o|$. $wR_2 = [\Sigma w(F_o^2 - F_c^2)^2/\Sigma w(F_o^2)^2]^{1/2}$, where $w = 1/[\sigma^2(F_o^2) + (aP)^2 + bP]$, $P = (F_o^2 + 2F_c^2)/3$.

Table A14. Crystal data and structure refinement parameters for **50** and **51**.

Compound	**50**	**51**
Empirical formula	$C_{57}H_{40}CoN_6O_9$	$C_{32}H_{31}N_4O_4Zn$
Formula weight	1011.88	600.98
Temperature/K	273.15	296.15
Crystal system	triclinic	monoclinic
Space group	*P*-1	$P2_1/n$
a/Å	10.7303(13)	13.6640(7)
b/Å	11.2351(14)	15.6172(7)
c/Å	20.184(2)	15.9640(8)
α/°	79.963(3)	90
β/°	75.978(3)	105.724(3)
γ/°	89.201(3)	90
Volume/Å^3	2323.7(5)	3279.1(3)
Z	2	4
ρ_{calc}g/cm^3	1.446	1.217
μ/mm^{-1}	0.439	0.787
F(000)	1046.0	1252.0
Crystal size/mm^3	0.3 × 0.3 × 0.35	0.25 × 0.25 × 0.25
Radiation	MoKα (λ = 0.71073)	MoKα (λ = 0.71073)
2Θ range for data collection/°	2.112 to 50.148	3.488 to 50.134
Index ranges	$-12 \le h \le 12$, $-13 \le k \le 13$, $-24 \le l \le 22$	$-16 \le h \le 16$, $-18 \le k \le 18$, $-18 \le l \le 17$
Reflections collected	28812	23627
Independent reflections	8207 [R_{int} = 0.0484, R_{sigma} = 0.0586]	5804 [R_{int} = 0.0337, R_{sigma} = 0.0344]
Data/restraints/parameters	8207/0/665	5804/4/364
Goodness-of-fit on F^2	1.075	1.128
Final R indexes [I>=2σ (I)]	R_1 = 0.0793, wR_2 = 0.2203	R_1 = 0.0823, wR_2 = 0.2599
Final R indexes [all data]	R_1 = 0.0965, wR_2 = 0.2332	R_1 = 0.0991, wR_2 = 0.2804
Largest diff. peak/hole / e Å^{-3}	1.12/-0.74	0.93/-0.52

$R_1 = \Sigma||F_o| - |F_c||/\Sigma|F_o|$. $wR_2 = [\Sigma w(F_o^2 - F_c^2)^2/\Sigma w(F_o^2)^2]^{1/2}$, where $w = 1/[\sigma^2(F_o^2) + (aP)^2 + bP]$, $P = (F_o^2 + 2F_c^2)/3$.

Table A15. Crystal data and structure refinement parameters for **52**.

Compound	**52**
Empirical formula	$C_{62}H_{51}Cd_2N_7O_{13}$
Formula weight	1326.89
Temperature/K	100.15
Crystal system	monoclinic
Space group	$P2_1/n$
a/Å	14.0127(3)
b/Å	26.6466(5)
c/Å	14.9480(3)
α/°	90
β/°	91.3290(10)
γ/°	90
Volume/Å^3	5579.94(19)
Z	4
ρ_{calc}g/cm^3	1.579
μ/mm^{-1}	0.836
F(000)	2688
Crystal size/mm^3	0.2 × 0.2 × 0.2
Radiation	MoKα (λ = 0.71073)
2Θ range for data collection/°	3.056 to 50.114
Index ranges	-15 ≤ h ≤ 16, -31 ≤ k ≤ 31, -17 ≤ l ≤ 17
Reflections collected	38596
Independent reflections	9858 [R_{int} = 0.0409, R_{sigma} = 0.0391]
Data/restraints/parameters	9858/25/752
Goodness-of-fit on F^2	1.086
Final R indexes [I>=2σ (I)]	R_1 = 0.0464, wR_2 = 0.1281
Final R indexes [all data]	R_1 = 0.0597, wR_2 = 0.1414
Largest diff. peak/hole / e Å^{-3}	1.97/-0.83

$R_1 = \Sigma||F_o| - |F_c||/\Sigma|F_o|$. $wR_2 = [\Sigma w(F_o^2 - F_c^2)^2/\Sigma w(F_o^2)^2]^{1/2}$, where $w = 1/[\sigma^2(F_o^2) + (aP)^2 + bP]$, $P = (F_o^2 + 2F_c^2)/3$.

Table A16. Crystal data and structure refinement parameters for **56** and **Desolvated 56**.

Compound	**56**	**Desolvated 56**
Chemical Formula	$C_{23}H_{26}N_4O_7Zn$	$C_{20}H_{15}N_3O_4Zn$
Formula Weight	535.85	426.72
Temperature (K)	100	100
Wavelength (Å)	0.71073	0.71073
Crystal System	Monoclinic	Monoclinic
Space Group	$P2_1/n$	$P2_1/n$
a (Å)	8.7542(8)	8.485(5)
b (Å)	16.4242(15)	14.529(9)
c (Å)	15.9879(15)	14.073(8)
a (°)	90	90
β (°)	91.709(2)	94.11(3)
g (°)	90	90
Z	4	4
V ($Å^3$)	2297.7(4)	1730.4(17)
Density (mg/cm^3)	1.549	1.638
μ(mm^{-1})	1.122	1.454
F(000)	1112	872
Theta (°) Range for Data Coll.	1.78 to 25.00	2.02 to 25.40
Reflections Collected	12340	8187
Independent Reflections	4026	3130
Reflections with I >2σ(I))	3076	1399
R_{int}	0.0467	0.138
No. of Parameters refined	313	253
GOF on F^2	1.091	0.980
Final $R_1{}^a/wR_2{}^b$ (I >2σ(I))	0.0443/0.1123	0.0817/0.1894
Weighted R_1/wR_2(all data)	0.0606/0.1215	0.1826/0.2307
Largest diff. peak and hole($eÅ^{-3}$)	0.704 and -0.722	0.768 and -0.473

R1 = Σ||Fo| − |Fc||/Σ|Fo|. wR2 = [Σw(Fo2 − Fc2)2/Σw(Fo2)2]1/2, where w = 1/[σ2(Fo2) + (aP)2 + bP], P = (Fo2 + 2Fc2)/3.

Table A17. Crystal data and structure refinement parameters for **56Cu**.

Compound	**56Cu**
Empirical formula	$C_{24}H_{22.5}CuN_5O_5$
Formula weight	524.51
Temperature/K	296.15
Crystal system	monoclinic
Space group	*C*2/*c*
a/Å	23.6116(7)
b/Å	16.1125(7)
c/Å	15.9893(10)
α/°	90
β/°	129.655(2)
γ/°	90
Volume/$Å^3$	4683.3(4)
Z	8
$\rho_{calc}g/cm^3$	1.488
μ/mm^{-1}	0.979
F(000)	2164.0
Crystal size/mm^3	0.4 × 0.4 × 0.4
Radiation	MoKα (λ = 0.71073)
2Θ range for data collection/°	3.59 to 50.024
Index ranges	$-28 \leq h \leq 28$, $-19 \leq k \leq 13$, $-19 \leq l \leq 19$
Reflections collected	10976
Independent reflections	4117 [R_{int} = 0.0600, R_{sigma} = 0.0883]
Data/restraints/parameters	4117/5/332
Goodness-of-fit on F^2	0.932
Final R indexes [I>=2σ (I)]	R_1 = 0.0422, wR_2 = 0.0763
Final R indexes [all data]	R_1 = 0.0798, wR_2 = 0.0857
Largest diff. peak/hole / e $Å^{-3}$	0.42/-0.43

$R_1 = \Sigma||F_o| - |F_c||/\Sigma|F_o|$. $wR_2 = [\Sigma w(F_o^2 - F_c^2)^2/\Sigma w(F_o^2)^2]^{1/2}$, where $w = 1/[\sigma^2(F_o^2) + (aP)^2 + bP]$, $P = (F_o^2 + 2F_c^2)/3$.

Table A18. Crystal data and structure refinement parameters for **57**.

Compound	**57**
Empirical formula	$C_{20}H_{22}N_3O_{7.5}Zn$
Formula weight	489.77
Temperature/K	296.15
Crystal system	monoclinic
Space group	$P2_1/n$
a/Å	8.576(3)
b/Å	17.760(6)
c/Å	15.790(6)
α/°	90
β/°	93.828(7)
γ/°	90
Volume/Å^3	2399.6(15)
Z	4
ρ_{calc}g/cm^3	1.356
μ/mm^{-1}	1.068
F(000)	1012.0
Crystal size/mm^3	0.2 × 0.4 × 0.4
Radiation	MoKα (λ = 0.71073)
2Θ range for data collection/°	5.172 to 50
Index ranges	$-10 \leq h \leq 10$, $-18 \leq k \leq 21$, $-18 \leq l \leq 18$
Reflections collected	14052
Independent reflections	4208 [R_{int} = 0.1559, R_{sigma} = 0.1922]
Data/restraints/parameters	4208/0/326
Goodness-of-fit on F^2	0.985
Final R indexes [I>=2σ (I)]	R_1 = 0.0913, wR_2 = 0.2473
Final R indexes [all data]	R_1 = 0.1995, wR_2 = 0.3261
Largest diff. peak/hole / e Å^{-3}	1.25/-0.71

$R_1 = \Sigma||F_o| - |F_c||/\Sigma|F_o|$. $wR_2 = [\Sigma w(F_o^2 - F_c^2)^2/\Sigma w(F_o^2)^2]^{1/2}$, where $w = 1/[\sigma^2(F_o^2) + (aP)^2 + bP]$, $P = (F_o^2 + 2F_c^2)/3$.

Table A19. Crystal data and structure refinement parameters for **58**.

Compound	**58**
Empirical formula	$C_{20.75}H_{18.75}CdN_{3.25}O_{5.25}$
Formula weight	510.04
Temperature/K	296.15
Crystal system	monoclinic
Space group	$P2_1/n$
a/Å	8.762(5)
b/Å	16.803(10)
c/Å	17.619(10)
α/°	90
β/°	98.609(8)
γ/°	90
Volume/Å^3	2565(3)
Z	4
ρ_{calc}g/cm^3	1.321
μ/mm^{-1}	0.883
F(000)	1024.0
Crystal size/mm^3	0.4 × 0.4 × 0.4
Radiation	MoKα (λ = 0.71073)
2Θ range for data collection/°	3.368 to 50.408
Index ranges	$-10 \leq h \leq 10$, $-20 \leq k \leq 20$, $-20 \leq l \leq 21$
Reflections collected	19452
Independent reflections	4586 [R_{int} = 0.0208, R_{sigma} = 0.0164]
Data/restraints/parameters	4586/29/325
Goodness-of-fit on F^2	1.078
Final R indexes [I>=2σ (I)]	R_1 = 0.0404, wR_2 = 0.1443
Final R indexes [all data]	R_1 = 0.0430, wR_2 = 0.1476
Largest diff. peak/hole / e Å^{-3}	1.47/-0.37

$R_1 = \Sigma||F_o| - |F_c||/\Sigma|F_o|$. $wR_2 = [\Sigma w(F_o^2 - F_c^2)^2/\Sigma w(F_o^2)^2]^{1/2}$, where $w = 1/[\sigma^2(F_o^2) + (aP)^2 + bP]$, $P = (F_o^2 + 2F_c^2)/3$.

Table A20. Crystal data and structure refinement parameters for **60**.

Compound	**60**
Empirical formula	$C_{20}H_{15}N_3O_4Zn$
Formula weight	426.72
Temperature/K	296.15
Crystal system	monoclinic
Space group	$P2_1/n$
a/Å	10.2320(7)
b/Å	20.9065(11)
c/Å	12.3544(7)
α/°	90
β/°	99.025(4)
γ/°	90
Volume/Å^3	2610.1(3)
Z	4
ρ_{calc}g/cm^3	1.086
μ/mm^{-1}	0.964
F(000)	872.0
Crystal size/mm^3	0.2 × 0.2 × 0.2
Radiation	MoKα (λ = 0.71073)
2Θ range for data collection/°	3.866 to 50.18
Index ranges	-12 ≤ h ≤ 12, -24 ≤ k ≤ 23, -11 ≤ l ≤ 14
Reflections collected	15470
Independent reflections	4589 [R_{int} = 0.1058, R_{sigma} = 0.1447]
Data/restraints/parameters	4589/0/253
Goodness-of-fit on F^2	0.918
Final R indexes [I>=2σ (I)]	R_1 = 0.0899, wR_2 = 0.2409
Final R indexes [all data]	R_1 = 0.1574, wR_2 = 0.2692
Largest diff. peak/hole / e Å^{-3}	1.34/-0.48

$R_1 = \Sigma||F_o| - |F_c||/\Sigma|F_o|$. $wR_2 = [\Sigma w(F_o^2 - F_c^2)^2/\Sigma w(F_o^2)^2]^{1/2}$, where $w = 1/[\sigma^2(F_o^2) + (aP)^2 + bP]$, $P = (F_o^2 + 2F_c^2)/3$.

Table A21. Crystal data and structure refinement parameters for **64**.

Compound	**64**
Empirical formula	$C_{49}H_{57}N_9O_{16}Zn_2$
Formula weight	1158.77
Temperature/K	296.15
Crystal system	triclinic
Space group	*P*-1
a/Å	12.067(2)
b/Å	14.876(3)
c/Å	16.250(3)
α/°	88.118(2)
β/°	76.278(2)
γ/°	85.614(2)
Volume/Å^3	2825.2(9)
Z	2
ρ_{calc}g/cm^3	1.362
μ/mm^{-1}	0.921
F(000)	1204.0
Crystal size/mm^3	0.4 × 0.4 × 0.4
Radiation	MoKα (λ = 0.71073)
2Θ range for data collection/°	2.58 to 50.474
Index ranges	-14 ≤ h ≤ 14, -17 ≤ k ≤ 17, -19 ≤ l ≤ 19
Reflections collected	31035
Independent reflections	10182 [R_{int} = 0.0629, R_{sigma} = 0.0838]
Data/restraints/parameters	10182/0/700
Goodness-of-fit on F^2	1.045
Final R indexes [I>=2σ (I)]	R_1 = 0.0651, wR_2 = 0.1789
Final R indexes [all data]	R_1 = 0.0957, wR_2 = 0.2058
Largest diff. peak/hole / e Å^{-3}	1.05/-0.52

$R_1 = \Sigma||F_o| - |F_c||/\Sigma|F_o|$. $wR_2 = [\Sigma w(F_o^2 - F_c^2)^2/\Sigma w(F_o^2)^2]^{1/2}$, where $w = 1/[\sigma^2(F_o^2) + (aP)^2 + bP]$, $P = (F_o^2 + 2F_c^2)/3$.

Table A22. Selected bond lengths (Å) for **1**.

Ni1-O1	2.213(4)	Ni1-N1	2.131(4)
Ni1-O2	2.107(3)	Ni1-N2	2.048(5)
Ni1-O3	2.053(4)	Ni1-N3	2.079(5)

Table A23. Selected bond lengths (Å) for **2⊃fumarate**, **2⊃ClO_4^-** and **2⊃I^-**.

2⊃fumarate

Ni1-O1	2.144(2)	Ni2-N4	2.066(2)
Ni1-O3	2.041(2)	Ni2-N5	2.144(3)
Ni1-O2	2.171(2)	Ni2-O5	2.182(2)
Ni1-N1	2.082(2)	Ni2-O4	2.102(2)
Ni1-N2	2.147(3)	Ni2-O6	2.072(2)
Ni1-N3	2.079(3)	Ni2-N6	2.071(3)

2⊃ClO_4^-

Ni1-O6	2.069(7)	Ni2-O3	2.074(7)
Ni1-O5	2.122(7)	Ni2-O1	2.105(7)
Ni1-N6	2.140(8)	Ni2-O2	2.187(7)
Ni1-N5	2.039(9)	Ni2-N1	2.052(9)
Ni1-N4	2.067(8)	Ni2-N2	2.151(8)
Ni1-O4	2.249(7)	Ni2-N3	2.073(8)

2⊃I^-

Ni1-O2	2.215(6)	Ni1-N2	2.078(8)
Ni1-O1	2.067(6)	Ni1-N3	2.051(8)
Ni1-O3	2.101(6)	Ni1-N1	2.178(7)

Table A24. Selected bond lengths (Å) for **3⊃succinate**, **3⊃ClO_4^-**, **3⊃NO_3^-** and **3⊃Cl^-**.

3⊃Hsuccinate

Ni01-O1	2.068(9)	Ni01-N1	2.104(11)
Ni01-O2	2.230(9)	Ni01-N2	2.164(11)
Ni01-O3	2.106(9)	Ni01-N3	2.102(11)

3⊃ClO_4^-

Ni1-O1	2.144(6)	Ni1-N1	2.064(6)
Ni1-O2	2.133(5)	Ni1-N2	2.133(7)
Ni1-O3	2.072(5)	Ni1-N3	2.058(7)

3⊃NO_3^-

Ni1-O3	2.072(2)	Ni1-N4	2.087(3)
Ni1-O1	2.079(3)	Ni1-N3	2.164(2)
Ni1-O2	2.214(2)	Ni1-N2	2.070(2)

3⊃Cl^-

Ni1-O1	2.133(9)	Ni1-N1	2.094(11)
Ni1-O2	2.160(9)	Ni1-N2	2.135(11)
Ni1-O3	2.056(10)	Ni1-N3	2.063(12)

Table A25. Selected bond lengths (Å) for **4**, **17** and **22**.

4

Ni1-O1	2.121(2)	Ni1-O2	2.132(2)
Ni1-N1	2.145(3)	Ni1-N2	2.052(3)
Ni1-O3	2.099(2)	Ni1-N3	2.075(3)

17

Ni1-O4	2.1675(12)	Ni1-N1	2.1108(14)
Ni1-O3	2.1217(11)	Ni1-N2	2.1317(14)
Ni1-O5	2.0828(12)	Ni1-N3	2.0474(14)

22

Zn1-O1	2.339(7)	Zn2-O4	2.250(8)
Zn1-O8	2.248(11)	Zn2-O5	2.251(9)
Zn1-N1	2.447(7)	Zn2-N4	2.320(8)
Zn1-N2	2.332(7)	Zn2-N5	2.431(7)
Zn1-N3	2.302(7)	Zn2-N6	2.349(9)

Table A26. Selected bond lengths (Å) for **24** and **25**.

24

Cd1-N1	2.29(2)	Cd1-O2	2.442(15)
Cd1-N2	2.42(2)	Cd1-O1	2.24(2)
Cd1-N3	2.35(2)	Cd1-O3	2.482(17)
Cd1-O4	2.333(17)		

25

Cd1-O1	2.231(8)	Cd2-O3	2.374(7)
Cd1-O14	2.229(8)	Cd2-O4	2.373(7)
Cd1-N1	2.298(10)	Cd2-N5	2.355(9)
Cd1-N2	2.506(8)	Cd2-O8	2.260(8)
Cd1-N3	2.303(10)	Cd2-N7	2.458(9)
		Cd2-N8	2.363(10)

Table A27. Selected bond lengths (Å) for **33** and **34**.

33

Cu01-O1	1.872(9)	Cu02-O4	1.863(8)
Cu01-N2	1.831(10)	Cu02-O7	2.010(9)
Cu01-N1	1.942(11)	Cu02-N7	1.852(9)
Cu01-O10	2.015(10)	Cu02-N8	1.955(12)
Cu01-N3	1.890(7)	Cu02-N6	1.937(11)

34

Mn1-O1	2.240(5)	Mn1-N2^{1}	2.193(7)
Mn1-O1^{1}	2.240(5)	Mn1-N2	2.193(7)
Mn1-O2	2.209(5)	Mn1-O2^{1}	2.209(5)

Table A28. Selected bond lengths (Å) for **37, 40** and **41**.

37

Zn1-O2	1.937(3)	Zn1-N1	2.036(3)
Zn1-O3	1.935(4)	Zn1-N2[1]	2.030(4)

40

Ni1-O1[1]	2.109(2)	Ni1-O2[1]	2.059(3)
Ni1-O1	2.109(2)	Ni1-N1	2.099(3)
Ni1-O2	2.059(3)	Ni1-N1[1]	2.099(3)

41

Co1-O1	2.1451(18)	Co1-O3[1]	2.078(2)
Co1-O1[1]	2.1450(18)	Co1-N1	2.154(2)
Co1-O3	2.078(2)	Co1-N1[1]	2.154(2)

Table A29. Selected bond lengths (Å) for **50, 51** and **52**.

50

Co1-N1	1.712(4)	Co1-N4	1.799(4)
Co1-N2	1.789(4)	Co1-N5	1.795(4)
Co1-N3	1.696(4)	Co1-N6	1.781(4)

51

Zn01-O1[1]	2.066(4)	Zn01-O3	2.022(5)
Zn01-N1	2.070(4)	Zn01-O4	2.457(5)
Zn01-O2[1]	2.386(4)	Zn01-N3[2]	2.076(14)

52

Cd1-O1	2.271(3)	Cd2-O3	2.270(3)
Cd1-O5[1]	2.420(3)	Cd2-O5[2]	2.479(3)
Cd1-O7	2.292(3)	Cd2-O6[2]	2.555(3)
Cd1-O11	2.308(3)	Cd2-O7[3]	2.339(3)
Cd1-N1	2.305(4)	Cd2-N3[4]	2.315(4)
Cd1-N4	2.299(4)	Cd2-N6[5]	2.349(4)

codes: [1, 2, 3, 4]

Table A30. Selected bond lengths (Å) for **56**, **desolvated 56** and **56Cu**.

56

Zn1-O1	1.989(2)	Zn1-N3	2.059(3)
Zn1-O3	2.059(2)	Zn1-N2	2.088(3)
Zn1-N1	2.399(3)		

Desolvated 56

Zn1-O1	1.938(7)	Zn1-N3	2.116(8)
Zn1-O3	2.007(7)	Zn1-N2	2.065(8)
Zn1-N1	2.340(8)		

56Cu

$Cu1\text{-}O_1^1$	1.995(2)	$Cu1\text{-}N3^2$	2.074(3)
$Cu1\text{-}O_3$	1.958(2)	$Cu1\text{-}N1^2$	2.046(3)

Table A31. Selected bond lengths (Å) for **57** and **58**.

57

Zn1-O1	2.009(7)	Zn1-N1	2.313(8)
$Zn1\text{-}N1^2$	2.069(11)	Zn1-N3	2.057(11)
Zn1-O3	1.998(7)		

58

Cd1-O1	2.248(3)	Cd1-N1	2.315(4)
Cd1-O2	2.609(4)	Cd1-N3	2.487(3)
$Cd1\text{-}O3^1$	2.264(4)	Cd1-N4	2.337(4)
$Cd1\text{-}O4^1$	2.640(4)		

Table A32. Selected bond lengths (Å) for **60** and **64**.

60

$Zn1\text{-}O2^1$	1.986(6)	$Zn1\text{-}N3^2$	2.061(7)
Zn1-O3	1.957(6)	$Zn1\text{-}N1^3$	2.003(7)

64

Zn01-O1	1.954(3)	Zn02-O2[1]	1.933(3)
Zn01-O5[1]	1.955(3)	Zn02-O4	1.930(3)
Zn01-N2[2]	2.045(4)	Zn02-N3[3]	2.080(4)
Zn01-O6[1]	1.926(3)	Zn02-O9	1.931(4)

Table A33. Selected bond angles (°) for **1**.

1

O2-Ni1-O1	61.49(15)	N2-Ni1-O2	91.63(17)
O2-Ni1-N1	108.00(17)	N2-Ni1-O3	176.56(19)
O3-Ni1-O1	88.53(15)	N2-Ni1-N1	82.94(19)
O3-Ni1-O2	91.33(15)	N2-Ni1-N3	93.61(18)
O3-Ni1-N1	94.48(17)	N3-Ni1-O1	111.35(17)
O3-Ni1-N3	83.66(17)	N3-Ni1-O2	171.49(17)
N1-Ni1-O1	169.19(16)	N3-Ni1-N1	79.33(18)
N2-Ni1-O1	94.42(19)		

Table A34. Selected bond angles (°) for **2⊃fumarate**, **2⊃ClO_4^-** and **2⊃I^-**.

2⊃fumarate

O1-Ni1-O2	61.08(8)	O6-Ni2-N5	96.25(9)
O1-Ni1-N2	169.09(8)	N6-Ni2-O5	91.69(9)
O3-Ni1-O1	91.36(9)	N6-Ni2-O4	90.79(9)
O3-Ni1-O2	90.14(9)	N6-Ni2-O6	177.76(9)
O3-Ni1-N1	84.60(9)	N6-Ni2-N5	82.83(10)
O3-Ni1-N2	94.18(9)	N4-Ni2-O5	113.05(9)
O3-Ni1-N3	176.45(10)	N4-Ni2-O4	171.46(9)
N1-Ni1-O1	108.94(9)	N4-Ni2-O6	85.90(9)
N1-Ni1-O2	168.69(9)	N4-Ni2-N6	95.98(10)
N1-Ni1-N2	80.97(9)	N4-Ni2-N5	81.41(9)
N2-Ni1-O2	109.46(9)	N5-Ni2-O5	165.09(8)
N3-Ni1-O1	91.72(10)	O4-Ni2-O5	61.39(9)
N3-Ni1-O2	89.80(9)	O4-Ni2-N5	104.67(9)

N3-Ni1-N1	96.07(10)	O6-Ni2-O5	88.70(9)
N3-Ni1-N2	82.49(10)	O6-Ni2-O4	87.46(9)

2⊃ClO_4^-

O6-Ni1-O5	88.3(3)	O3-Ni2-O1	86.6(3)
O6-Ni1-N6	99.4(3)	O3-Ni2-O2	87.5(3)
O6-Ni1-O4	88.3(3)	O3-Ni2-N2	97.6(3)
O5-Ni1-N6	107.1(3)	O1-Ni2-O2	60.9(2)
O5-Ni1-O4	60.2(3)	O1-Ni2-N2	106.1(3)
N6-Ni1-O4	165.2(3)	N1-Ni2-O3	178.6(3)
N5-Ni1-O6	177.7(3)	N1-Ni2-O1	92.1(3)
N5-Ni1-O5	92.3(3)	N1-Ni2-O2	91.7(3)
N5-Ni1-N6	82.6(3)	N1-Ni2-N2	83.0(3)
N5-Ni1-N4	93.8(3)	N1-Ni2-N3	94.5(3)
N5-Ni1-O4	90.0(3)	N2-Ni2-O2	165.9(3)
N4-Ni1-O6	85.4(3)	N3-Ni2-O3	86.8(3)
N4-Ni1-O5	171.1(3)	N3-Ni2-O1	170.6(3)
N4-Ni1-N6	80.2(3)	N3-Ni2-O2	112.1(3)
N4-Ni1-O4	113.3(3)	N3-Ni2-N2	81.4(3)

2⊃I^-

O1-Ni1-O2	90.0(2)	N2-Ni1-N1	80.4(3)
O1-Ni1-O3	87.9(3)	N3-Ni1-O2	91.5(3)
O1-Ni1-N2	86.1(3)	N3-Ni1-O1	178.3(3)
O1-Ni1-N1	97.2(3)	N3-Ni1-O3	92.1(3)
O3-Ni1-O2	61.4(2)	N3-Ni1-N2	94.1(3)
O3-Ni1-N1	107.1(3)	N3-Ni1-N1	81.1(3)
N2-Ni1-O2	111.8(3)	N1-Ni1-O2	166.3(3)
N2-Ni1-O3	171.0(3)		

Table A35. Selected bond angles (°) for **3⊃succinate**, **3⊃ClO_4^-**, **3⊃NO_3^-** and **3⊃Cl^-**.

3⊃Hsuccinate

O1-Ni01-O2	61.7(4)	N1-Ni01-O2	90.1(4)
O1-Ni01-O3	89.2(4)	N1-Ni01-O3	178.3(4)
O1-Ni01-N1	90.9(4)	N1-Ni01-N2	80.6(4)
O1-Ni01-N2	105.8(4)	N3-Ni01-N2	80.9(4)
O1-Ni01-N3	170.5(4)	N2-Ni01-O2	164.5(4)
O3-Ni01-O2	91.5(4)	N3-Ni01-O2	112.8(4)
O3-Ni01-N2	97.7(4)	N3-Ni01-O3	83.0(4)
N3-Ni01-N1	97.0(4)		

3⊃ClO_4^-

O2-Ni1-O1	61.4(2)	N1-Ni1-N2	80.9(3)
O2-Ni1-N2	106.9(2)	N2-Ni1-O1	167.4(2)
O3-Ni1-O1	87.0(2)	N3-Ni1-O1	91.5(3)
O3-Ni1-O2	87.7(2)	N3-Ni1-O2	88.8(2)
O3-Ni1-N2	97.4(2)	N3-Ni1-O3	176.5(2)
N1-Ni1-O1	111.2(3)	N3-Ni1-N1	96.6(3)
N1-Ni1-O2	171.1(3)	N3-Ni1-N2	83.5(3)
N1-Ni1-O3	86.9(2)		

3⊃NO_3^-

O3-Ni1-O1	89.66(9)	N4-Ni1-N3	80.44(10)
O3-Ni1-O2	90.81(8)	N3-Ni1-O2	165.31(9)
O3-Ni1-N4	85.15(9)	N2-Ni1-O3	178.13(9)
O3-Ni1-N3	96.13(8)	N2-Ni1-O1	91.45(10)
O1-Ni1-O2	61.12(8)	N2-Ni1-O2	91.04(8)
O1-Ni1-N4	172.27(8)	N2-Ni1-N4	93.89(10)
O1-Ni1-N3	105.87(9)	N2-Ni1-N3	82.12(9)
N4-Ni1-O2	113.13(9)		

3⊃Cl⁻

O1-Ni1-O2	61.7(4)	N1-Ni1-O1	110.0(4)
O1-Ni1-N2	168.4(4)	N1-Ni1-O2	168.9(5)
O1-Ni1-C1	31.7(4)	N1-Ni1-N2	80.6(5)
O2-Ni1-C1	30.1(4)	N1-Ni1-C1	141.4(5)
O3-Ni1-O1	88.5(4)	N2-Ni1-O2	108.3(4)
O3-Ni1-O2	88.9(4)	N2-Ni1-C1	138.0(5)
O3-Ni1-N1	83.3(4)	N3-Ni1-O1	92.8(4)
O3-Ni1-N2	97.4(4)	N3-Ni1-O2	91.4(4)
O3-Ni1-N3	178.6(5)	N3-Ni1-N1	96.6(5)
O3-Ni1-C1	89.0(4)	N3-Ni1-N2	81.2(4)

Table A36. Selected bond angles (°) for **4**, **17** and **22**.

4

O1-Ni1-N1	169.89(10)	N2-Ni1-O3	178.37(10)
O1-Ni1-O2	61.76(9)	N2-Ni1-O2	89.03(10)
O3-Ni1-O1	84.51(9)	N2-Ni1-N3	92.58(11)
O3-Ni1-N1	98.67(10)	N3-Ni1-O1	109.21(10)
O3-Ni1-O2	91.78(10)	N3-Ni1-N1	80.64(11)
O2-Ni1-N1	108.41(10)	N3-Ni1-O3	86.41(10)
N2-Ni1-O1	94.63(10)	N3-Ni1-O2	170.94(10)
N2-Ni1-N1	82.41(10)		

17

O3-Ni1-O4	61.85(4)	N1-Ni1-N2	79.37(5)
O3-Ni1-N2	99.26(5)	N2-Ni1-O4	159.71(5)
O5-Ni1-O4	84.89(5)	N3-Ni1-O4	114.54(5)
O5-Ni1-O3	86.48(5)	N3-Ni1-O3	175.97(5)
O5-Ni1-N1	173.79(5)	N3-Ni1-O5	91.45(5)
O5-Ni1-N2	102.20(5)	N3-Ni1-N1	94.69(5)
N1-Ni1-O4	91.70(5)	N3-Ni1-N2	84.55(5)
N1-Ni1-O3	87.34(5)		

22

O8-Zn1-N1	115.1(6)	O4-Zn2-O5	127.6(3)
$O1^1$-Zn1-N1	131.5(2)	O4-Zn2-N4	96.5(3)
O8-Zn1-$O1^1$	111.8(6)	O4-Zn2-N5	130.2(3)
O8-Zn1-N2	101.4(3)	O4-Zn2-N6	93.1(3)
O8-Zn1-N3	98.4(4)	O5-Zn2-N4	93.8(4)
N2-Zn1-$O1^1$	107.8(3)	O5-Zn2-N5	102.1(3)
N2-Zn1-N1	74.6(2)	O5-Zn2-N6	105.6(4)
N3-Zn1-$O1^1$	88.4(2)	N4-Zn2-N5	75.0(3)
N3-Zn1-N1	73.5(3)	N4-Zn2-N6	146.4(3)
N3-Zn1-N2	147.2(3)	N6-Zn2-N5	74.2(3)

Table A37. Selected bond angles (°) for **24** and **25**.

24

N1-Cd1-N2	70.6(9)	O4-Cd1-N3	100.4(8)
N1-Cd1-N3	143.4(10)	O4-Cd1-O2	77.0(6)
N1-Cd1-O4	103.5(8)	O4-Cd1-O3	53.5(6)
N1-Cd1-O2	87.5(8)	O2-Cd1-O3	124.6(6)
N1-Cd1-O3	82.1(6)	O1-Cd1-N1	103.3(7)
N2-Cd1-O2	138.8(6)	O1-Cd1-N2	96.6(7)
N2-Cd1-O3	87.5(7)	O1-Cd1-N3	86.6(6)
N3-Cd1-N2	73.3(9)	O1-Cd1-O4	122.0(7)
N3-Cd1-O2	125.0(8)	O1-Cd1-O2	54.0(5)
N3-Cd1-O3	90.5(6)	O1-Cd1-O3	174.1(7)
O4-Cd1-N2	140.9(7)		

25

O1-Cd1-N1	92.5(3)	N5-Cd2-O4	146.9(3)
O1-Cd1-N2	130.8(3)	N5-Cd2-N7	72.9(3)
O1-Cd1-N3	98.0(3)	N5-Cd2-N8	107.8(3)
O14-Cd1-O1	125.7(3)	N8-Cd2-O3	155.0(3)

O14-Cd1-N1	111.4(3)	O8-Cd2-O3	89.7(3)
O14-Cd1-N2	103.1(3)	O8-Cd2-O4	88.6(3)
O14-Cd1-N3	89.4(3)	O8-Cd2-N5	105.8(3)
N1-Cd1-N2	73.4(3)	O8-Cd2-N7	165.0(3)
N1-Cd1-N3	144.6(3)	O8-Cd2-N8	95.3(3)
N3-Cd1-N2	74.2(3)	N8-Cd2-O4	100.0(3)
O3-Cd2-N7	105.3(3)	N8-Cd2-N7	71.5(3)
O4-Cd2-N7	100.4(3)	N5-Cd2-O3	94.3(3)
O4-Cd2-O3	55.5(3)		

Table A38. Selected bond angles (°) for **33** and **34**.

33

O1-Cu01-N1	95.2(5)	O4-Cu02-O7	88.2(4)
O1-Cu01-O101	84.9(5)	O4-Cu02-N8	94.7(4)
O1-Cu01-N3	105.0(4)	O4-Cu02-N6	102.6(4)
N2-Cu01-O1	167.4(4)	N7-Cu02-O4	163.7(4)
N2-Cu01-N1	79.4(5)	N7-Cu02-O7	107.6(4)
N2-Cu01-O101	106.4(5)	N7-Cu02-N8	80.9(5)
N2-Cu01-N3	78.6(4)	N7-Cu02-N6	79.8(5)
N1-Cu01-O101	90.1(4)	N8-Cu02-O7	91.2(4)
N3-Cu01-N1	157.2(5)	N6-Cu02-O7	99.0(4)
N3-Cu01-O101	102.0(4)	N6-Cu02-N8	160.1(4)

34

$O1^{1}$-Mn1-O1	87.9(3)	N1-Mn1-N2	71.45(16)
$O2^{1}$-Mn1-$O1^{1}$	57.52(18)	N2-Mn1-$O1^{1}$	121.4(2)
O2-Mn1-O1	57.52(18)	$N2^{1}$-Mn1-$O1^{1}$	86.4(2)
$O2^{1}$-Mn1-O1	135.28(19)	$N2^{1}$-Mn1-O1	121.4(2)
O2-Mn1-$O1^{1}$	135.28(19)	N2-Mn1-O1	86.4(2)
O2-Mn1-$O2^{1}$	166.1(3)	N2-Mn1-O2	86.8(2)
N1-Mn1-O1	136.03(13)	N2-Mn1-$O2^{1}$	88.8(2)

N1-Mn1-O1[1]	136.03(13)	N2[1]-Mn1-O2[1]	86.8(2)
N1-Mn1-O2[1]	83.07(13)	N2[1]-Mn1-O2	88.8(2)
N1-Mn1-O2	83.07(13)	N2[1]-Mn1-N2	142.9(3)
N1-Mn1-N2[1]	71.45(16)		

Table A39. Selected bond angles (°) for **37, 40** and **41**.

37

O2-Zn1-N1	115.77(15)	O3-Zn1-N1	99.56(14)
O2-Zn1-N2[1]	115.45(15)	O3-Zn1-N2[1]	110.81(16)
O3-Zn1-O2	107.60(15)	N2[1]-Zn1-N1	106.52(14)

40

O1-Ni1-O1[1]	180.0	O2[1]-Ni1-N1	87.83(11)
O2-Ni1-O1	91.39(9)	O2-Ni1-N1[1]	87.83(11)
O2-Ni1-O1[1]	88.61(9)	N1[1]-Ni1-O1[1]	90.27(10)
O2[1]-Ni1-O1[1]	91.39(9)	N1[1]-Ni1-O1	89.73(9)
O2[1]-Ni1-O1	88.61(9)	N1-Ni1-O1	90.27(10)
O2-Ni1-O2[1]	180.00(7)	N1-Ni1-O1[1]	89.73(9)
O2-Ni1-N1	92.17(11)	N1-Ni1-N1[1]	180.0
O2[1]-Ni1-N1[1]	92.16(11)		

41

O1[1]-Co1-O1	180.0	O3[1]-Co1-O1	89.99(8)
O1-Co1-N1[1]	90.66(7)	O3[1]-Co1-O3	180.00(11)
O1[1]-Co1-N1[1]	89.34(7)	O3-Co1-N1	91.98(9)
O1-Co1-N1	89.34(7)	O3-Co1-N1[1]	88.02(8)
O1[1]-Co1-N1	90.66(7)	O3[1]-Co1-N1	88.02(8)
O3[1]-Co1-O1[1]	90.01(8)	O3[1]-Co1-N1[1]	91.98(9)
O3-Co1-O1[1]	89.99(8)	N1-Co1-N1[1]	180.0
O3-Co1-O1	90.01(8)		

Table A40. Selected bond angles (°) for **50, 51** and **52**.

50

N1-Co1-N2	82.94(16)	N3-Co1-N4	100.32(17)
N1-Co1-N4	81.56(17)	N3-Co1-N5	81.93(18)
N1-Co1-N5	96.91(18)	N3-Co1-N6	83.01(18)
N1-Co1-N6	98.15(18)	N5-Co1-N4	92.03(16)
N2-Co1-N4	164.47(17)	N6-Co1-N2	90.81(17)
N2-Co1-N5	90.75(16)	N6-Co1-N4	90.46(17)
N3-Co1-N1	177.80(17)	N6-Co1-N5	164.94(18)
N3-Co1-N2	95.19(17)	N3-Co1-N4	100.32(17)

51

$O1^{1}$-Zn01-N1	107.37(16)	O3-Zn01-$O1^{1}$	143.87(17)
$O1^{1}$-Zn01-$O2^{1}$	56.94(15)	O3-Zn01-N1	94.68(17)
$O1^{1}$-Zn01-O4	102.24(17)	O3-Zn01-$O2^{1}$	94.46(14)
$O1^{1}$-Zn01-$N3^{2}$	93.0(4)	O3-Zn01-O4	56.10(18)
N1-Zn01-$O2^{1}$	93.13(15)	O3-Zn01-$N3^{2}$	112.7(6)
N1-Zn01-O4	149.57(18)	$N3^{2}$-Zn01-$O2^{1}$	149.9(4)
N1-Zn01-$N3^{2}$	97.1(8)	$N3^{2}$-Zn01-O4	88.1(9)
$O2^{1}$-Zn01-O4	97.15(17)		

52

O1-Cd1-$O5^{1}$	164.31(11)	O3-Cd2-$O5^{2}$	138.72(11)
O1-Cd1-O7	91.95(11)	O3-Cd2-$O6^{2}$	87.51(11)
O1-Cd1-O11	90.31(11)	O3-Cd2-$O7^{3}$	146.47(12)
O1-Cd1-N1	100.01(12)	O3-Cd2-$N3^{4}$	97.10(12)
O1-Cd1-N4	86.79(12)	O3-Cd2-$N6^{5}$	82.48(12)
O7-Cd1-$O5^{1}$	75.24(11)	$O5^{2}$-Cd2-$O6^{2}$	51.83(10)
O7-Cd1-O11	176.74(11)	$O7^{3}$-Cd2-$O5^{2}$	73.30(10)
O7-Cd1-N1	92.60(13)	$O7^{3}$-Cd2-$O6^{2}$	125.13(10)
O7-Cd1-N4	87.06(12)	$O7^{3}$-Cd2-$N6^{5}$	90.73(12)

O11-Cd1-O5[1]	102.15(11)	N3[4]-Cd2-O5[2]	89.93(11)
N1-Cd1-O5[1]	89.75(12)	N3[4]-Cd2-O6[2]	89.12(11)
N1-Cd1-O11	89.31(13)	N3[4]-Cd2-O7[3]	91.42(12)
N4-Cd1-O5[1]	83.59(11)	N3[4]-Cd2-N6[5]	176.65(13)
N4-Cd1-O11	90.73(12)	N6[5]-Cd2-O5[2]	88.23(11)
N4-Cd1-N1	173.20(13)	N6[5]-Cd2-O6[2]	87.54(11)

Table A41. Selected bond angles (°) for **56**, **desolvated 56** and **56Cu**.

56

O1-Zn1-N3	107.49(11)	O1-Zn1-O3	91.11(9)
N3-Zn1-O3	102.97(11)	O1-Zn1-N2	93.18(11)
N3-Zn1-N2	150.47(12)	O3-Zn1-N2	97.32(10)
O1-Zn1-N1	130.53(10)	N3-Zn1-N1	75.50(10)
O3-Zn1-N1	137.45(10)	N2-Zn1-N1	75.04(10)

Desolvated 56

O1-Zn1-N3	92.5(3)	O1-Zn1-O3	103.0(3)
N3-Zn1-O3	89.3(3)	O1-Zn1-N2	107.4(3)
N3-Zn1-N2	149.2(3)	O3-Zn1-N2	108.1(3)
O1-Zn1-N1	113.8(3)	N3-Zn1-N1	74.9(3)
O3-Zn1-N1	140.1(3)	N2-Zn1-N1	75.7(3)

56Cu

O1[1]-Cu1-N3[2]	106.36(11)	O3-Cu1-N3[2]	98.11(10)
O1[1]-Cu1-N1[2]	97.80(11)	O3-Cu1-N1[2]	135.47(10)
O3-Cu1-O1[1]	96.71(9)	N1[2]-Cu1-N3[2]	117.46(11)

Table A42. Selected bond angles (°) for **57** and **58**.

57

O1-Zn1-N1^{2}	98.5(3)	O3-Zn1-N1^{2}	96.2(4)
O1-Zn1-N1	116.8(3)	O3-Zn1-N1	129.0(3)
O1-Zn1-N3	98.2(4)	O3-Zn1-N3	95.3(4)
N1^{2}-Zn1-N1	77.0(4)	N3-Zn1-N1^{2}	153.7(5)
O3-Zn1-O1	114.2(3)	N3-Zn1-N1	77.4(4)

58

O1-Cd1-O2	52.82(13)	O3^{1}-Cd1-N4	86.37(13)
O1-Cd1-O3^{1}	109.71(14)	N1-Cd1-O2	82.62(14)
O1-Cd1-O4^{1}	76.75(15)	N1-Cd1-O4^{1}	83.58(15)
O1-Cd1-N1	109.04(14)	N1-Cd1-N3	71.39(13)
O1-Cd1-N3	134.30(13)	N1-Cd1-N4	141.75(14)
O1-Cd1-N4	97.14(15)	N3-Cd1-O2	83.08(11)
O2-Cd1-O4^{1}	118.57(12)	N3-Cd1-O4^{1}	144.78(13)
O3^{1}-Cd1-O2	162.19(13)	N4-Cd1-O2	92.19(12)
O3^{1}-Cd1-O4^{1}	52.34(13)	N4-Cd1-O4^{1}	130.49(13)
O3^{1}-Cd1-N1	109.24(14)	N4-Cd1-N3	70.36(13)
O3^{1}-Cd1-N3	112.94(12)		

Table A43. Selected bond angles (°) for **60** and **64**.

60

O2^{1}-Zn1-N3^{2}	100.1(3)	O3-Zn1-N3^{2}	105.7(3)
O2^{1}-Zn1-N1^{3}	111.4(3)	O3-Zn1-N1^{3}	110.3(3)
O3-Zn1-O2^{1}	98.2(3)	N1^{3}-Zn1-N3^{2}	127.1(3)

64.

O1-Zn01-O5[1]	109.55(15)	O2[1]-Zn02-N3[3]	108.50(14)
O1-Zn01-N2[2]	103.98(15)	O4-Zn02-O2[1]	96.21(15)
O5[1]-Zn01-N2[2]	123.29(16)	O4-Zn02-N3[3]	104.38(16)
O61-Zn01-O1	91.27(15)	O4-Zn02-O9	120.86(16)
O6[1]-Zn01-O5[1]	113.93(16)	O9-Zn02-O2[1]	122.72(18)
O6[1]-Zn01-N2[2]	109.51(16)	O9-Zn02-N3[3]	102.76(16)

List of Publications

1. **Sandeep Kumar** and Sanjay K. Mandal, "Capturing the structural diversification upon thermal desolvation of a robust metal organic framework via a single-crystal-to-single-crystal transformation", *CrystEngComm*, **2015**, *17*, 8801-8806.

http://dx.doi.org/10.1039/C5CE01116G

2. Vijay Gupta, Sadhika Khullar, **Sandeep Kumar** and Sanjay K. Mandal, "Construction of a robust pillared-layer framework based on the rare paddlewheel subunit [Mn^{II}_2(μ-$O_2CR)_4L_2$]: synthesis, crystal structure and magnetic properties", *Dalton Trans.*, **2015**, *44*, 16778-16784. http://dx.doi.org/10.1039/C5DT02354H

Vita

The author, Sandeep Kumar, was born on November 21, 1989 in Sonipat (Haryana) in India. He earned his B.Sc. (Medical) from Hindu College Sonipat, Maharishi Dyanand University Rohtak, Haryana and M.Sc. (Inorganic Chemistry) from Kurukshetra University Kurukshetra (KUK), Haryana in 2008 and 2010, respectively. He joined Indian Institute of Science Education and Research Mohali (IISERM) with a fellowship from MHRD, Govt. of India, to pursue his Ph.D. degree in Chemistry under the supervision of Professor Sanjay K. Mandal in January, 2013.